Edited by
A. Rashid bin Mohd Yusoff

Graphene-based Energy Devices

Related Titles

Yusoff, A.R.b.M. (ed.)

Graphene Optoelectronics
Synthesis, Characterization, Properties, and Applications

2014
Print ISBN: 978-3-527-33634-0
also available in digital formats

Beguin, F., Frackowiak, E. (eds.)

Supercapacitors
Materials, Systems, and Applications

2013
Print ISBN: 978-3-527-32883-3
also available in digital formats

Rao, C.N., Sood, A.K. (eds.)

Graphene
Synthesis, Properties, and Phenomena

2013
Print ISBN: 978-3-527-33258-8
also available in digital formats

Fujita, S., Suzuki, A.

Electrical Conduction in Graphene and Nanotubes

2013
Print ISBN: 978-3-527-41151-1
also available in digital formats

Malic, E., Knorr, A.

Graphene and Carbon Nanotubes
Ultrafast Relaxation Dynamics and Optics

2013
Print ISBN: 978-3-527-41161-0
also available in digital formats

Akasaka, T.T. (ed.)

Chemistry of Nanocarbons

2010
Print ISBN: 978-0-470-72195-7
also available in digital formats

Edited by A. Rashid bin Mohd Yusoff

Graphene-based Energy Devices

WILEY-VCH
Verlag GmbH & Co. KGaA

The Editor

Prof. A. Rashid bin Mohd Yusoff
Department of Information Display
Dongdaemoon-ku
130–701 Seoul
South Korea

Cover
iStockphoto© scanrail
iStockphoto© geopaul

All books published by **Wiley-VCH** are carefully produced. Nevertheless, authors, editors, and publisher do not warrant the information contained in these books, including this book, to be free of errors. Readers are advised to keep in mind that statements, data, illustrations, procedural details or other items may inadvertently be inaccurate.

Library of Congress Card No.: applied for

British Library Cataloguing-in-Publication Data
A catalogue record for this book is available from the British Library.

Bibliographic information published by the Deutsche Nationalbibliothek
The Deutsche Nationalbibliothek lists this publication in the Deutsche Nationalbibliografie; detailed bibliographic data are available on the Internet at <http://dnb.d-nb.de>.

© 2015 Wiley-VCH Verlag GmbH & Co. KGaA, Boschstr. 12, 69469 Weinheim, Germany

All rights reserved (including those of translation into other languages). No part of this book may be reproduced in any form – by photoprinting, microfilm, or any other means – nor transmitted or translated into a machine language without written permission from the publishers. Registered names, trademarks, etc. used in this book, even when not specifically marked as such, are not to be considered unprotected by law.

Print ISBN: 978-3-527-33806-1
ePDF ISBN: 978-3-527-69030-5
ePub ISBN: 978-3-527-69032-9
Mobi ISBN: 978-3-527-69033-6
oBook ISBN: 978-3-527-69031-2

Typesetting Laserwords Private Limited, Chennai, India
Printing and Binding Markono Print Media Pte Ltd., Singapore

Printed on acid-free paper

Contents

List of Contributors *XIII*
Preface *XIX*

1 Fundamental of Graphene *1*
Seong C. Jun
1.1 Introduction *1*
1.2 Synthesis of Graphene *3*
1.2.1 Mechanical Cleavage *3*
1.2.2 Epitaxial Growth *4*
1.2.3 CVD Growth of Graphene *4*
1.2.4 Solution-Based Graphene *5*
1.2.4.1 Ultrasonication *6*
1.2.4.2 Intercalation *7*
1.2.4.3 Chemical Exfoliation *7*
1.2.5 Synthesis of Composite Material Based on Graphene Oxide *8*
1.3 Characterization of Graphene *12*
1.3.1 AFM (Atomic Force Microscopy) *14*
1.3.2 SEM *16*
1.3.3 TEM/SEAD/EELS *16*
1.3.4 XPS *20*
1.3.5 XRD *21*
1.3.6 Raman *23*
1.3.7 Photoluminesces (PL) Measurement *23*
1.4 Optical Property Modification of Graphene *25*
1.4.1 Absorption Property Modification of Graphene (Terahertz, UV – Visible – NIR) *25*
1.4.1.1 Absorption Property of Thermally Annealed Graphene Oxide *25*
1.4.1.2 Absorption Property Plasma Defected Graphene *26*
1.4.2 PL Property Modification of Graphene *29*
1.4.2.1 PL Properties of Oxygen Plasma Treated Graphene *29*
1.4.2.2 Substrate Effect *30*

1.4.2.3 Pd Grafted Graphene Oxide *35*
1.5 Optoelectric Application of Graphene *39*
References *45*

2 Graphene-Based Electrodes for Lithium Ion Batteries *49*
Ronghua Wang, Miaomiao Liu, and Jing Sun
2.1 Introduction *49*
2.2 The Working Principle of LIBs *50*
2.3 Graphene-Based Cathode Materials for LIBs *51*
2.4 Graphene-Based Anode Materials for LIBs *53*
2.4.1 Graphene as Anodes for LIBs *54*
2.4.2 Graphene-Based Composites as Anodes for LIBs *56*
2.4.2.1 The Lithium Storage Mechanisms of Anode Materials *57*
2.4.2.2 Graphene–Si/Sn Composites as Anodes for LIBs *58*
2.4.2.3 Graphene–Metal Oxide Composites as Anodes for LIBs *62*
2.4.2.4 Graphene–TiO_2/MoS_2 Composites as Anodes for LIBs *65*
2.5 Two-Dimensional (2D) Flexible and Binder-Free Graphene-Based Electrodes *67*
2.5.1 Graphene-Based Flexible Anode Materials for LIBs *67*
2.5.1.1 2D Flexible and Binder-Free Graphene Electrodes *67*
2.5.1.2 2D Flexible and Binder-Free Graphene-Based Hybrid Anode Electrodes *69*
2.5.2 Graphene-Based Flexible Cathode Materials for LIBs *73*
2.6 Three-Dimensional Macroscopic Graphene-Based Electrodes *74*
2.7 Summary and Perspectives *78*
References *79*

3 Graphene-Based Energy Devices *85*
Wei-Ren Liu
3.1 Introduction *85*
3.2 Graphene for Li-Ion Batteries *85*
3.2.1 Anode Materials *85*
3.2.2 Cathode Materials *100*
3.3 Graphene for Supercapacitors *105*
3.4 Graphene for Li–Sulfur Batteries *111*
3.5 Graphene for Fuel Cells *114*
3.6 Graphene for Solar Cells *116*
3.7 Summary *118*
References *118*

4 Graphene-Based Nanocomposites for Supercapacitors *123*
Xuanxuan Zhang, Tao Hu, and Ming Xie
4.1 Introduction *123*
4.2 Graphene-Based Supercapacitors *124*
4.2.1 EDLCs *125*

4.2.2 Graphene/Metal Oxide Nanocomposites *128*
4.2.3 Graphene/Conducting Polymer Composites *129*
4.2.3.1 PANI-Graphene Nanocomposites *129*
4.2.3.2 PPy–Graphene Nanocomposite *132*
4.2.3.3 PEDOT–Graphene Nanocomposite *134*
4.2.4 Atomic Layer Deposition for Graphene/Metal Oxide Nanocomposites *134*
4.3 Issues and Perspectives *136*
References *138*

5 High-Performance Supercapacitors Based on Novel Graphene Composites *145*
Junwu Xiao, Yangyang Xu, and Shihe Yang
5.1 Introduction *145*
5.2 Graphene Synthesis Methods *148*
5.2.1 The "Top-Down" Approach *148*
5.2.2 The "Bottom-Up" Approach *150*
5.3 Graphene-Based Electrodes for Supercapacitors *151*
5.3.1 Graphene *151*
5.3.2 Graphene-Based Composites *152*
5.3.2.1 Graphene–Carbon Material Composites *153*
5.3.2.2 Graphene/Metal Oxide Composites *154*
5.3.2.3 Graphene–Conducting Polymer Composites *158*
5.3.2.4 Graphene/Metal Oxide–Conducting Polymer Composites *164*
5.4 Conclusions and Prospects *165*
References *166*

6 Graphene for Supercapacitors *171*
Richa Agrawal, Chunhui Chen, Yong Hao, Yin Song, and Chunlei Wang
6.1 Introduction *171*
6.1.1 Electrochemical Capacitors *171*
6.1.1.1 Fundamentals of a Capacitor *172*
6.1.1.2 Classification of Electrochemical Capacitors *174*
6.1.2 Graphene as a Supercapacitor Material *175*
6.2 Electrode Materials for Graphene-Based Capacitors *176*
6.2.1 Double-Layer Capacitance-Based Graphene Electrode Materials *176*
6.2.1.1 Electrodes Based on Graphene Synthesized by Reduction of Graphene Oxide *176*
6.2.1.2 Activated-Graphene-Based Electrodes *177*
6.2.1.3 Graphene and Other Carbon Nanostructure Composite Electrodes *179*
6.2.1.4 Nitrogen-Doped-Graphene-Based Electrodes *180*
6.2.2 Graphene/Pseudocapacitive Material Composite Based Electrode Materials *183*

6.2.2.1 Graphene/Conducting Polymer Composite Electrodes *183*
6.2.2.2 Graphene/Transition-Metal Oxide Composite Electrodes *186*
6.3 Graphene-Based Asymmetric Supercapacitors *189*
6.3.1 Asymmetric Capacitors Based on Graphene and Pseudocapacitive Materials *193*
6.3.2 Graphene-Based Lithium-Ion Capacitors *195*
6.4 Graphene-Based Microsupercapacitors *199*
6.5 Summary and Outlook *204*
Acknowledgments *205*
References *205*

7 Graphene-Based Solar-Driven Water-Splitting Devices *215*
Jian Ru Gong
7.1 Introduction *215*
7.2 Basic Architectures of Solar-Driven Water-Splitting Devices *216*
7.3 Promising Prospects of Graphene in Solar-Driven Water-Splitting Devices *217*
7.4 Graphene-Based Integrated Photoelectrochemical Cells *219*
7.5 Graphene-Based Mixed-Colloid Photocatalytic Systems *227*
7.6 Graphene-Based Photovoltaic/Electrolyzer Devices *235*
7.7 Conclusions and Perspectives *241*
References *241*

8 Graphene Derivatives in Photocatalysis *249*
Luisa M. Pastrana-Martínez, Sergio Morales-Torres, José L. Figueiredo, Joaquim L. Faria, and Adrián M.T. Silva
8.1 Introduction *249*
8.2 Graphene Oxide and Reduced Graphene Oxide *250*
8.2.1 Synthesis *250*
8.2.2 Properties *252*
8.3 Synthesis of Graphene-Based Semiconductor Photocatalysts *254*
8.3.1 Mixing Method *255*
8.3.2 Sol–Gel Process *255*
8.3.3 Hydrothermal and Solvothermal Methods *256*
8.4 Photocatalytic Applications *257*
8.4.1 Photodegradation of Organic Pollutants *258*
8.4.2 Photocatalytic Splitting of H_2O *262*
8.4.3 Photocatalytic Reduction of CO_2 *264*
8.4.4 Other Applications: Dye-Sensitized Solar Cells *266*
8.5 Conclusions and Outlook *267*
Acknowledgments *268*
References *268*

9 Graphene-Based Photocatalysts for Energy Applications: Progress and Future Prospects *277*
Wanjun Wang, Donald K.L. Chan, and Jimmy C. Yu
9.1 Introduction *277*
9.1.1 Synthesis of Graphene-Based Photocatalysts *278*
9.1.2 *Ex Situ* Hybridization Strategy *279*
9.1.3 *In Situ* Growth Strategy *279*
9.1.3.1 Hydrothermal Method *279*
9.1.3.2 Electrochemical and Electrophoretic Deposition *281*
9.1.3.3 Chemical Vapor Deposition *281*
9.1.3.4 Photochemical Reaction *282*
9.2 Energy Applications *283*
9.2.1 Photocatalytic Hydrogen Evolution *283*
9.2.2 Photocatalytic Reduction of Carbon dioxide *285*
9.2.3 Environmental Remediation *286*
9.2.3.1 Photodegradation of Organic Dyes *287*
9.2.3.2 Water Disinfection *287*
9.3 Conclusions and Outlook *287*
References *288*

10 Graphene-Based Devices for Hydrogen Storage *295*
Hou Wang and Xingzhong Yuan
10.1 Introduction *295*
10.2 Storage of Molecular Hydrogen *297*
10.2.1 Graphene-Based Metal/Metal Oxide *299*
10.2.2 Doped Graphene *300*
10.3 Storage of Atomic Hydrogen Based on Hydrogen Spillover *301*
References *304*

11 Graphene-Supported Metal Nanostructures with Controllable Size and Shape as Advanced Electrocatalysts for Fuel Cells *307*
Minmin Liu and Wei Chen
11.1 Introduction *307*
11.2 Fuel Cells *308*
11.2.1 Configuration and Design of PEMFCs *309*
11.2.2 Direct Methanol Fuel Cells (DMFCs) *310*
11.2.3 Direct Formic Acid Fuel Cells (DFAFCs) *313*
11.2.4 Direct Alcohol Fuel Cells (DAFCs) and Biofuel Cells *314*
11.3 Graphene-Based Metal Nanostructures as Electrocatalysts for Fuel Cells *315*
11.3.1 Graphene-Supported Metal Nanoclusters *315*
11.3.2 Graphene-Supported Monometallic and Alloy Metal Nanoparticles (NPs) *317*
11.3.3 Graphene-Supported Core–shell Nanostructures *321*
11.3.4 Graphene-Supported Hollow Nanostructures *322*

11.3.5 Graphene-Supported Cubic Nanostructures *325*
11.3.6 Graphene-Supported Nanowires and Nanorods *326*
11.3.7 Graphene-Supported Flower-Like Nanostructures *329*
11.3.8 Graphene-Supported Nanodendrites *331*
11.3.9 Other Graphene-Supported 2D or 3D Nanostructures *333*
11.4 Conclusions *333*
Acknowledgments *334*
References *335*

12 Graphene-Based Microbial Fuel Cells *339*
Yezhen Zhang and Jian S. Ye
12.1 Introduction *339*
12.2 MFC *340*
12.2.1 The Working Principle of MFC *340*
12.2.2 The Advantages of MFCs *341*
12.2.3 The Classification of MFCs *342*
12.2.3.1 Dual-Chamber and Single-Chamber MFCs *342*
12.2.3.2 Direct and Indirect MFCs *344*
12.2.3.3 Heterotrophic, Photosynthetic Autotroph, and Sediment MFCs *344*
12.2.3.4 Intermittent and Continuous MFCs *344*
12.2.3.5 Pure Bacteria and Mixed Bacteria MFCs *345*
12.3 The Development History of MFCs *345*
12.4 The Application Prospect of MFC *346*
12.4.1 Micro Batteries Embedded in the Body *346*
12.4.2 Mobile Power Supply *346*
12.4.3 Photosynthesis to Produce Electricity *346*
12.4.4 Biosensor *347*
12.4.5 Power Supply in Remote Areas or Open Sea *347*
12.4.6 Treatment of Organic Wastewater *347*
12.5 Problems Existing in the MFCs *348*
12.6 Graphene-Based MFC *348*
12.6.1 Anode *348*
12.6.2 Membrane *350*
12.6.3 Cathode *350*
References *351*

13 Application of Graphene-Based Materials to Improve Electrode Performance in Microbial Fuel Cells *355*
Li Xiao and Zhen He
13.1 Introduction *355*
13.2 Graphene Materials for Anode Electrodes in MFCs *357*
13.2.1 Graphene Nanosheets *357*
13.2.2 Three-Dimensional Graphene *359*
13.2.3 Graphene Oxide *361*
13.3 Graphene Materials for Cathode Electrodes in MFCs *361*

13.3.1 Bare Graphene *362*
13.3.2 Polymer Coating with Graphene as a Dopant *363*
13.3.3 Metal Coating with Graphene as a Supporter *363*
13.3.4 Nitrogen-Doped Graphene *364*
13.4 Outlook *366*
References *367*

14 Applications of Graphene and Its Derivative in Enzymatic Biofuel Cells *371*
A. Rashid bin Mohd Yusoff
14.1 Introduction *371*
14.2 Membraneless Enzymatic Biofuel Cells *372*
14.3 Modified Bioanode and Biocathode *375*
14.3.1 Electrochemically Reduced Graphene Oxide and Multiwalled Carbon Nanotubes/Zinc Oxide *375*
14.3.2 Graphene/Single-Walled Carbon Nanotubes *376*
14.4 Conclusion *376*
Acknowledgment *377*
References *377*

15 Graphene and Its Derivatives for Highly Efficient Organic Photovoltaics *379*
Seung J. Lee and A. Rashid bin Mohd Yusoff
15.1 Introduction *379*
15.2 Various Applications in Solar Cells *380*
15.2.1 Conductive Electrodes *380*
15.2.1.1 Transparent Conductive Anodes *380*
15.2.1.2 Transparent Conductive Cathodes *384*
15.2.2 Active Layer *385*
15.2.2.1 Light-Harvesting Materials *385*
15.2.2.2 Schottky Junctions *388*
15.2.3 Charge Transport Layer *390*
15.2.3.1 Hole Transport Layer *390*
15.2.4 Electron Transport Layer *395*
15.2.4.1 Interfacial Layer in Tandem Solar Cells *398*
15.3 Conclusion *402*
Acknowledgment *402*
References *402*

16 Graphene as Sensitizer *407*
Mohd A. Mat-Teridi, Mohd A. Ibrahim, Norasikin Ahmad-Ludin, Siti Nur Farhana Mohd Nasir, Mohamad Yusof Sulaiman, and Kamaruzzaman Sopian
16.1 Graphene as Sensitizer *407*
16.2 Graphene as Storage Current Collector *410*

16.2.1 Anode Current Collector *411*
16.2.1.1 Li-Ion Storage *412*
16.2.1.2 Fuel Cells *412*
16.2.2 Cathode Current Collector *413*
16.2.2.1 Li-Ion Storage *414*
16.2.2.2 Fuel Cells *414*
16.3 Graphene as Photoanode Additive *415*
16.3.1 DSSC Application *415*
16.3.2 OPV Application *416*
16.3.3 Lithium-Ion Battery *417*
16.3.4 Sensor Application *418*
16.3.5 Transparent Conductive Films *419*
16.3.6 Photocatalytic Application *420*
16.4 Graphene as Cathode Electrocatalyst *420*
16.4.1 N-Doped Graphene *421*
16.4.2 B-, P-, S-, and Se-Doped Graphene *422*
16.5 Conclusions *423*
Acknowledgment *424*
References *424*

Index *431*

List of Contributors

Richa Agrawal
Florida International University
Department of Mechanical and Materials Engineering
10555 W. Flagler Street
EC 3463
Miami, FL 33174
USA

Norasikin Ahmad-Ludin
Universiti Kebangsaan Malaysia
Solar Energy Research Institute (SERI)
43600 Selangor
Malaysia

Donald K.L. Chan
The Chinese University of Hong Kong
Institute of Environment Energy and Sustainability
Department of Chemistry
Shatin, N.T.
Hong Kong
P. R. China

Chunhui Chen
Florida International University
Department of Mechanical and Materials Engineering
10555 W. Flagler Street
EC 3463
Miami, FL 33174
USA

Wei Chen
Chinese Academy of Sciences
Changchun Institute of Applied Chemistry
State Key Laboratory of Electroanalytical Chemistry
130022 Changchun
Jilin
P. R. China

Siti Nur Farhana Mohd Nasir
Universiti Kebangsaan Malaysia
Solar Energy Research Institute (SERI)
43600 Selangor
Malaysia

Joaquim L. Faria
Chemical Engineering
Department
Faculdade de Engenharia
Universidade do Porto
LCM - Laboratory of Catalysis
and Materials
Associate Laboratory LSRE-LCM
Rua Dr. Roberto Frias
4200-465 Porto
Portugal

José L. Figueiredo
Chemical Engineering
Department
Faculdade de Engenharia
Universidade do Porto
LCM - Laboratory of Catalysis
and Materials
Associate Laboratory LSRE-LCM
Rua Dr. Roberto Frias
4200-465 Porto
Portugal

Jian Ru Gong
National Center for Nanoscience
and Technology
Laboratory for Nanodevices
11 Beiyitiao Zhongguancun
100190 Beijing
P. R. China

Yong Hao
Florida International University
Department of Mechanical and
Materials Engineering
10555 W. Flagler Street
EC 3463
Miami, FL 33174
USA

Zhen He
Virginia Polytechnic Institute
and State University
Department of Civil and
Environmental Engineering
403 Durham Hall
Blacksburg, VA 24061
USA

Tao Hu
Northeastern University
Laboratory for Anisotropy and
Texture of Materials of Ministry
of Education
Shenyang 110819
P. R. China

Mohd A. Ibrahim
Universiti Kebangsaan Malaysia
Solar Energy Research Institute
(SERI)
43600 Selangor
Malaysia

Seong C. Jun
Yonsei University
School of Mechanical
Engineering
262 Seongsanno
120-749 Seoul
Republic of Korea

Seung J. Lee
Kyung Hee University
Advanced Display Research
Center
Department of Information
Display
130-701 Seoul
Republic of Korea

Miaomiao Liu
Chinese Academy of Sciences
Shanghai Institute of Ceramics
State Key Laboratory of High Performance Ceramics and Superfine Microstructure
1295 DinXi Road
200050 Shanghai
P. R. China

Minmin Liu
Chinese Academy of Sciences
Changchun Institute of Applied Chemistry
State Key Laboratory of Electroanalytical Chemistry
130022 Changchun
Jilin
P. R. China

and

University of Chinese Academy of Sciences
Graduate Faculty
100039 Beijing
P. R. China

Wei-Ren Liu
Chang Yuan University
Department of Chemical Engineering
200 Chung-Pei Road
32023 Chung Li
Taiwan

Mohd A. Mat-Teridi
Universiti Kebangsaan Malaysia
Solar Energy Research Institute (SERI)
43600 Selangor
Malaysia

A. Rashid bin Mohd Yusoff
Kyung Hee University
Department of Information Display
Advanced Display Research Center
Dongdaemoon-gu
130–701 Seoul
South Korea

Sergio Morales-Torres
Chemical Engineering Department
Faculdade de Engenharia
Universidade do Porto
LCM - Laboratory of Catalysis and Materials
Associate Laboratory LSRE-LCM
Rua Dr. Roberto Frias
4200-465 Porto
Portugal

Luisa M. Pastrana-Martínez
Chemical Engineering Department
Faculdade de Engenharia
Universidade do Porto
LCM - Laboratory of Catalysis and Materials
Associate Laboratory LSRE-LCM
Rua Dr. Roberto Frias
4200-465 Porto
Portugal

Jian Shan Ye
South China University of Technology
College of Chemistry and Chemical Engineering
Wushan Road
Guangzhou 510641
P. R. China

Adrián M.T. Silva
Chemical Engineering Department
Faculdade de Engenharia
Universidade do Porto
LCM - Laboratory of Catalysis and Materials
Associate Laboratory LSRE-LCM
Rua Dr. Roberto Frias
4200-465 Porto
Portugal

Yin Song
Florida International University
Department of Mechanical and Materials Engineering
10555 W. Flagler Street
EC 3463
Miami, FL 33174
USA

Kamaruzzaman Sopian
Universiti Kebangsaan Malaysia
Solar Energy Research Institute (SERI)
43600 Selangor
Malaysia

Mohamad Yusof Sulaiman
Universiti Kebangsaan Malaysia
Solar Energy Research Institute (SERI)
43600 Selangor
Malaysia

Jing Sun
Chinese Academy of Sciences
Shanghai Institute of Ceramics
State Key Laboratory of High Performance Ceramics and Superfine Microstructure
1295 DinXi Road
200050 Shanghai
P. R. China

Li Xiao
University of Wisconsin-Milwaukee
Department of Civil Engineering and Mechanics
Milwaukee, WI 53211
USA

Junwu Xiao
Huazhong University of Science and Technology
Department of Chemistry and Chemical Engineering
Luoyu Road
Wuhan 430074
P. R. China

Ming Xie
NingBo ATMK Lithium Ion Technologies Inc.
NingBo
Zhejiang
P. R. China

Yangyang Xu
Huazhong University of Science and Technology
Department of Chemistry and Chemical Engineering
Luoyu Road
Wuhan 430074
P. R. China

Chunlei Wang
Florida International University
Department of Mechanical and Materials Engineering
10555 W. Flagler Street
EC 3463
Miami, FL 33174
USA

Hou Wang
Hunan University
College of Environmental
Science and Engineering
410082 Changsha
P. R. China

Ronghua Wang
Chinese Academy of Sciences
Shanghai Institute of Ceramics
State Key Laboratory of High
Performance Ceramics and
Superfine Microstructure
1295 DinXi Road
200050 Shanghai
P. R. China

Wanjun Wang
The Chinese University of Hong
Kong
Institute of Environment Energy
and Sustainability
Department of Chemistry
Shatin, N.T.
Hong Kong
P. R. China

Shihe Yang
The Hong Kong University of
Science and Technology
Department of Chemistry
Clear Water Bay
Kowloon 999077
Hong Kong

Jimmy C. Yu
The Chinese University of Hong
Kong
Institute of Environment Energy
and Sustainability
Department of Chemistry
Shatin, N.T.
Hong Kong
P. R. China

Xingzhong Yuan
Hunan University
College of Environmental
Science and Engineering
410082 Changsha
P. R. China

Xuanxuan Zhang
NingBo ATMK Lithium Ion
Technologies Inc.
NingBo
Zhejiang
P. R. China

Yezhen Zhang
Nanyang Normal University
College of Chemistry and
Pharmacy Engineering
Wolong Road
Nanyang 473061
P. R. China

Preface

Graphene, the nanoscale wonder material, is one of the hottest areas of materials science research. Discovered in 2004 by two Russian scientists, Andrei Geim and Kostya Novoselov at the University of Manchester, graphene's revolutionary physical properties won the two scientists the 2010 Nobel Prize in Physics. Since then, considerable efforts have been put forward to fully utilize graphene as an energy material, and today huge advancements have been realized in developing highly efficient energy conversion and storage devices. In this context, this book aims to provide an overview of the recent advancements of research in the field of energy conversion and storage. Researchers from various fields, namely physics, chemistry, materials science, biology, and engineering, have contributed a variety of chapters based on their research expertise in these fields.

This book is organized into two areas, namely fundamentals and applications. In the fundamentals chapter (Chapter 1), the readers are introduced to the basic and important aspects of graphene, followed by its synthesis. In the synthesis part, it discusses mechanical cleavage, which is one of the simplest methods to obtain graphene from highly ordered pyrolytic graphite. Besides, this chapter also discusses epitaxial growth, chemical vapor deposition, and solution processing, which includes ultrasonication, intercalation, and chemical exfoliation. Chapter 1 also deals with various characterization methods, such as atomic force microscopy, scanning electron microscopy, transmission electron microscopy, X-ray photoelectron spectroscopy, X-ray diffraction, Raman spectroscopy, and photoluminescence. Finally, the chapter ends with a discussion on the optical properties of graphene and also some optoelectric applications of graphene.

The second, large, part of this book can be divided into two different fields: namely (i) graphene-based energy storage and (ii) graphene-based energy conversion. In graphene-based energy storage devices are included lithium-ion batteries, supercapacitors, photochemical water splitting, photocatalysis, and hydrogen storage. The last portion of this second part comprises fuel cells, microbial biofuel cells, enzymatic biofuel cells, polymer solar cells, and sensitizers.

The second part of this book begins with a "combo" of chapters dealing with lithium-ion batteries, namely Chapters 2 and 3. Chapter 2 introduces some basic working principles of lithium-ion batteries, the application of graphene as cathode and anode materials for lithium-ion batteries, and graphene-based flexible cathode and anode materials. On the other hand, Chapter 3 provides some extra

discussions on graphene for supercapacitors, lithium– sulfur batteries, fuel cells, and solar cells.

Chapters 4, 5, and 6 are devoted to high-performance graphene supercapacitors. Starting with electric double-layer capacitors, Chapter 4 mostly brings us to a new dimension where an in-depth discussion is provided on graphene/metal oxide nanocomposites and graphene/conducting polymer composites as main materials in supercapacitors. Chapter 5 starts with some synthesis routes of graphene, including top-down and bottom-up approaches, and discusses graphene/metal oxide/conducting polymer nanocomposite supercapacitors. Chapter 6 looks different from Chapters 4 and 5 because it deals with the fundamentals of capacitors and electrochemical capacitors. In addition, this chapter also introduces capacitors based on double-layer capacitance, which consist of electrodes based on graphene synthesized by the reduction of graphene oxide, activated graphene, graphene and carbon nanostructure composites, and nitrogen-doped graphene. Electrodes based on graphene/pseudocapacitive material composites and graphene-based asymmetric supercapacitors are also discussed in detail. Finally, Chapter 6 ends with a discussion on graphene-based microsupercapacitors.

Chapter 7 deals with water splitting, which is one of the energy storage mechanisms. This chapter begins with the basic building blocks of solar-driven water-splitting devices and discusses the prospects of graphene in this type of devices. It also introduces the combination of graphene with a variety of semiconductors for application in integrated photochemical cells. The highly oxidized and exfoliated products of pristine graphite provide a great convenience for the development of graphene-based mixed photocatalytic systems. This chapter also touches upon graphene-based electrolyzer device which convert sunlight into electricity and provide the essential voltage for the electrolysis of water. Some good conclusions and perspectives finally end this chapter.

Chapters 8 and 9 focus on graphene-based photocatalysis. The first part of Chapter 8 deals with the synthesizing mechanism of graphene and graphene oxide as well as their properties. It also discusses graphene-based semiconductor photocatalysts, which utilize a single titanium dioxide (rutile) crystal as the photoanode and platinum as the counterelectrode. The chapter ends with a discussion of various photocatalytic applications such as photodegradation of organic pollutants, photocatalytic splitting of H_2O, photocatalytic reduction of CO_2, and other applications. Chapter 9 starts with the synthesis methods of graphene-based photocatalysts including *ex situ* and *in situ* hybridization strategies. In the latter case, the hydrothermal method is considered as a powerful and versatile tool to synthesize inorganic nanocrystals. Recently, the electrochemical and electrophoretic depositions have been attracting huge attention because they do not require any post-synthetic transfer of the composite materials. For example, a constant current has been successfully applied to seed nanoparticles on reduced graphene oxide followed by the growth of nanoparticles under the constant potential mode. The discussion continues with chemical vapor deposition and photochemical reaction. The chapter ends with some discussions on

energy applications, photocatalytic hydrogen evolution, photocatalytic reduction of carbon dioxide, and environmental remediation.

Chapter 10 deals with graphene-based hydrogen storage, which consists of cryogenic liquids, high-pressure gas cells, low-temperature adsorbates, metal hydrides, and chemical storage. Moreover, this chapter also discusses the storage of molecular hydrogen and graphene-based metal/metal oxide nanoparticles which have recently attracted a lot of attention for hydrogen storage. In addition, graphenes doped with elements such as boron, aluminum, silicon, or nitrogen are discussed in detail for significantly enhancing their hydrogen binding capacity. The chapter ends with a discussion on the storage of atomic hydrogen based on hydrogen spillover.

The last part of this book is focused on fuel cells, microbial biofuel cells, enzymatic biofuel cells, polymer solar cells, and sensitizers. The first part of Chapter 11 deals mostly with the configuration and design of proton exchange membrane fuel cells, direct methanol fuel cells, direct formic acid fuel cells, and direct alcohol fuel cells. The second part discusses graphene/metal nanostructures that have been used as electrocatalysts including metal nanoclusters (Au, Ag, and Cu), monometallic particles and alloy nanoparticles, core@shell nanostructures, hollow nanostructures, cubic nanostructures, nanowires and nanorods, flower-like nanostructures, nanodendrites, and two- or three-dimensional (3D) nanostructures.

Chapters 12 and 13 are focused on graphene in microbial fuel cells. Chapter 12 discusses the basic working principle of microbial fuel cells, some of their advantages, and their classification. It is followed by a history and some future prospects of microbial fuel cells. Finally, this chapter deals with graphene-based microbial fuel cells with regard to their various aspects such as the anode, membrane, and cathode. Chapter 13 deals with the improvement of electrode performance in microbial fuel cells. It begins with graphene and its derivatives such as nanosheets, 3D graphene, and graphene oxide as anode electrodes. The discussion continues with graphene materials as cathode electrodes, which include bare graphene, coated graphene, and doped graphene. Finally, the chapter ends with some positive outlook and a detailed discussion on the future improvement in graphene-based microbial fuel cells.

Chapter 14 introduces another type of fuel cells, namely enzymatic biofuel cells. This chapter is rather short because research in this field has just started. The first part of this chapter deals with membraneless enzymatic biofuel cells, while the second part discusses modified anodes and cathodes. These include electrochemically reduced graphene oxide and graphne-single-walled carbon nanotubes.

Chapter 15 discusses various applications of graphene in solar cells. Today, graphene has been successfully employed in organic solar cells as the anode, the hole and electron interfacial layer, as well as the top electrode. This chapter also touches upon the possibility of replacing the currently used transparent electrode, indium tin oxide (ITO). The use of graphene as an intermediate layer in tandem solar cells is also discussed.

Chapter 16 finally deals with graphene as sensitizer in storage current collectors and anode and cathode current collectors. Moreover, this chapter also covers the field of photoanode additives in dye-sensitized solar cells. Finally, this chapter introduces graphene as a cathode electrocatalyst, which includes nitrogen-, boron-, phosphorous-, sulfur-, and selenium-doped graphene.

This book has brought together materials from various sources, including the authors' previously published articles, their latest experiments and lecture notes. All materials in this book have been organized, reviewed, and now presented in a consistent and more readable way because they have been reviewed very thoroughly and reformulated. It has been a great pleasure writing and at the same time editing this book on the graphene-based energy conversion and storage devices. For me, this book was a labor of love, and the adventure involved in compiling the content along a unifying theme was a great enriching experience and sufficient reward in and of itself. I hope that all readers will similarly find great enrichment and understanding as they explore the pages of this book. Finally, I would like to thank my lovely wife Sharifah Nurilyana and our families for their support and understanding. Special thanks also go to my students, colleagues, and, in particular, my director, Jin Jang, for fruitful discussions and help.

Seoul
23 October 2014 *A. Rashid bin Mohd Yusoff*

1
Fundamental of Graphene

Seong C. Jun

1.1
Introduction

Graphene, a single-atom-thick sheet of hexagonally arrayed sp^2-bonded carbon atoms, has got a significant attention due to its unique electronic [1], mechanical [2], and thermal [3] properties all derived from the unique details of its electronic band structure. Due to its flexibility, graphene provides infinite possibilities in various fields [4, 5] and the peculiar dispersion relation of carbon's π electrons is responsible for its unique properties [1].

There are different ways to produce "pristine" graphene. The graphene synthesis can be mainly classified into exfoliation [6], chemical vapor deposition (CVD) [7], arc discharge [8], and reduction of graphene oxide (GO) [9]. One method for isolation of a sheet of graphene is through the mechanical exfoliation from a graphite crystal, but this is not scalable beyond one small flake of graphene, making graphene with lateral dimensions on the order of tens to hundreds of micrometers. But reports are also showing the development of patterned graphene through the mechanical exfoliation of patterned graphite.

The important large-scale synthesis of graphene includes the thermal decomposition of silicon carbide [10] and CVD growth. The formation of carbon layers with sp^2 bonding, on the SiC substrate could be obtained through the sublimation of Si by heating the *C*-face or Si-face in ultrahigh vacuum (UHV) at temperatures ranging from 1000 to 1500 °C and the thermal decomposition of hydrocarbons. CVD method has raised much attention for graphene synthesis due to high quality with large surface area. Gas-phase synthesis of graphene platelets and arc discharge synthesis of multilayered graphene are also reported.

Exfoliation of graphite in solvents is a method for obtaining dispersions of GO to yield individual layers of GO and offers potential for the production of cost-effective, large-scale production of graphene [9]. Based on recent studies, GO consists of phenol hydroxyl and epoxide functional groups on the top and bottom surfaces of each sheet and sp^2-hybridized carbons containing carboxyl and carbonyl groups mostly at the sheet edges and these groups offer tremendous opportunities for access to functionalized graphene-based materials [11]. The oxidation

Graphene-based Energy Devices, First Edition. Edited by A. Rashid bin Mohd Yusoff.
© 2015 Wiley-VCH Verlag GmbH & Co. KGaA. Published 2015 by Wiley-VCH Verlag GmbH & Co. KGaA.

of graphite to GO breaks up the sp^2-hybridized structure of the stacked graphene sheets and the disruption of graphene lattice is reflected in an increase in interlayer spacing from 0.335 nm for graphite to more than 1 nm for GO. In GO, the ratio of sp^2/sp^3 fractions opens up possibilities for new functionalities and possesses a finite electronic band gap generated by the disruption of π-networks due to the formation of oxygen-containing groups. Thus, it is possible to modify the electronic structure by means of chemical or physical treatments with different gases to reduce the connectivity of the electron network [12–14]. In contrast to pristine graphene, in which all atoms are sp^2 hybridized, GO also contains sp^3 carbon atoms covalently bonded to oxygen-bearing functional groups.

Characterization of graphene involves various microscopic and spectroscopic techniques such as: X-ray diffraction (XRD), transmission electron microscopy (TEM), low energy electron diffraction (LEED), Raman spectroscopy, scanning electron microscopy (SEM), and so on. These characterization tools can be used for characterizing the structural, chemical, electrical, and even magnetic properties of graphene. The intrinsic ripples of freely suspended graphene have been addressed by Monte Carlo simulation TEM and optical microscopy studies can be used to find the number of layers and the presence of defects [15, 16]. Optical microscopy is based on the contrast arising from the interference of the reflected light beams at the interfaces. Contrast in SEM can also be used to determine the number of graphene layers [17]. Using TEM, by viewing the edges of the film, it is possible to analyze the number of layers. TEM can also be used to evaluate the number of graphene layers and to assess the crystalline quality of the graphene films [10]. TEM images provide images of sp^2 clusters as well as defects. The diffraction experiments provide knowledge of the orientation of the crystal lattice and different crystal grains can be mapped. Electron diffraction is an effective tool, in which the intensities of diffraction peaks do not change much with the incidence angle for single layer graphene. But, in bilayer graphene, there is a change in intensity with different incidence angles. Thus, by comparing the relative intensities of the electron diffraction pattern, it is possible to determine the number of layers. The thickness of graphene layers can be obtained by atomic force microscopy (AFM) in the tapping mode. Fluctuations in height for graphene platelets deposited on different Si substrate could be studied by scanning tunneling microscopy (STM).

Raman spectroscopy is the principal tool to examine the quality of graphene crystals; it is a nondestructive tool and does not require vacuum. Raman spectroscopy is a tool for finding the number of graphene layers by manipulating the position and shape of the 2D band, which is around 2700 cm^{-1}. Raman spectra of GO consists of prominent spectral features, called G at ~1586 cm^{-1}, D bands ~1350 cm^{-1}, and 2D at 2697 cm^{-1} [18]. Raman spectra of all disordered carbons are dominated by the relatively sharp G and D features of the sp^2 sites. The G and 2D peaks represent the E_{2g} vibrational and out-of-plane modes within aromatic carbon rings, respectively. The G band is a degenerated optical phonon mode at the Brillouin zone center and is induced by a single resonance process. The peak near 1350 cm^{-1} is denoted with the D band (in

plane carbon ring breathing mode (A_{1g} mode)), which is forbidden in perfect graphite. This process requires a scattering at defect sites in order to conserve the momentum. Photoluminescence (PL) in such carbon systems usually is a consequence of the recombination of localized e–h pairs in sp^2 clusters [19]. Excitation wavelength-dependent PL emission from the GO and graphene quantum dots were also observed and the PL peak shifted from 430 to 515 nm when the excitation wavelength was changed from 320 to 420 nm [13]. Bao *et al.* [20] reported intense PL from chemically modified graphene, where oxygen plasma treatment was applied to introduce band gap opening in graphene and the degree of band gap opening is proportional to the degree of oxidation. The effects of oxygen plasma treatments on the PL properties of single- and few-layer graphene (FLG) growth by the CVD process were described by Gokus *et al.*, and they observed visible luminescence from oxygen plasma-treated graphene that has been attributed the emission to carbon–oxygen-related localized states [21]. It is possible to induce ripples on the graphene surface, which can alter the local electrical and optical properties of graphene; thus, modified ripple engineering can be used for possible application in various devices.

1.2 Synthesis of Graphene

1.2.1 Mechanical Cleavage

Mechanical cleavage is one of the simplest methods to obtain graphene from highly ordered pyrolytic graphite (HOPG) ensuring its smooth edge structure. Mechanical cleavage is a general and novel method to exfoliate bulky crystals, such as hexagonal boron nitride (h-BN), or Molybdenum disulfide (MoS_2), to few-layer ultrasharp, single-crystal layer. This was the method used to exfoliate and isolate a few graphene sheets of micrometer size in the research of Andre Geim and Konstantin Novoselov of University of Manchester; they won a Nobel Prize in Physics in 2004 [6]. This method also called the *tapping method* involves the use of Scotch Tape to separate the graphene sheet from graphite flakes. Few-flakes of graphite are loaded on Scotch Tape and continuous alternation of attaching and detaching exfoliates graphite into FLG. To transfer and visualize the graphene, we need to stick the tape on a target Si/SiO_2 wafer and examine the wafer with an optical microscope. The graphene and few layers of it are almost transparent to the naked eye; however, by adding graphene layers to the Si/SiO_2 wafer, which is usually oxidized about 300 nm, the graphene interferes with the light and shifts the color; this allows us to distinguish its existence and even the layer difference from mono, or few-layer to multilayer graphene. Figure 1.1 shows how to stick graphene-exfoliated Scotch Tape to wafer, and Figure 1.1b shows the optical microscope image of a graphene-attached wafer.

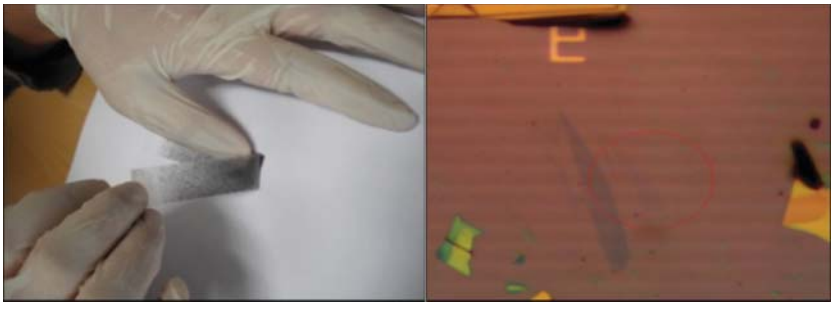

(a) (b)

Figure 1.1 (a, b) Mechanical exfoliation of graphene.

1.2.2
Epitaxial Growth

Epitaxial growth graphene has attracted tremendous attention due to the fabrication problem of mechanical exfoliated graphene. A few layers of graphite growth on SiC surface (0001) was already known by the epitaxial growth mechanism. In 1975, the graphite covering on SiC was obtained by heating the SiC crystal in oxygen at a low pressure above 1000 °C[10]. The existence of low vacuum at high temperature conditions leads to a depletion of Si, resulting in a high portion of the carbon layer turning to graphite layers. LEED patterns are usually employed to shows the states of obtained graphite layers. Annealing above typical temperatures affects reconstruction, for example, Si-rich $(\sqrt{3} \times \sqrt{3})$ R30° structure transforms into carbon-rich structure $(6\sqrt{3} \times 6\sqrt{3})$ R30° [22]. Since the reconstruction of carbon-rich structure is a precursor to graphene on SiC, that structures attract attention. The different band position of SiC and graphene or a few layers of graphene leads to barriers at the junction, affecting electrical properties including photoemission. There are around 3 eV energy gap attributed to relative position difference of band structure. Through many researches, homogeneous large area graphene are synthesized [23]. Substrates are treated chemical mechanical polishing. Then, the graphene growth process is conducted under highly isothermal conditions at very high temperatures with ambient Ar condition. Also, various substrates are employed such as Ru [24], Ir [25], and Pt [26].

1.2.3
CVD Growth of Graphene

Graphene can be grown by the CVD process on the catalytic metal substrates. Usually, metal foils, dimensions about 20 cm with thickness of few micrometres, or metal-deposited substrates are used. Various metals can be applied including Ni, Cu, Pd, which are the catalysts of carbon [7]. The metal substrate sample is then loaded in reactors of 2-in.-wide quartz tube and the temperature increased with

Ar, H_2, or its mixture condition. In case of copper, which is the most widely used, the loaded copper was heated up to 1000 °C or more, with hydrogen gas. After reaching the target temperature, the sample is then subjected to annealing; it is reported that this flattens the target surface and also affects the carbon solubility of the substrate metal. Usually, copper foil is annealed for 30 min with a sustaining flow rate and pressure of H_2 gas. Also, in the case of copper, this heat-treatment results in adequate grain size required for the making of higher-quality graphene films. After 30 min of annealing, the gas phase of carbon source including CH_4 gas or C_2H_2 gas flows with Ar/H_2 mixture, matching the unique recipe that depends on the metals or gas mixture rates. By this step, carbon from the gas source is diffused into the copper foil. The process is terminated by enabling far rapid cooling to room temperature, usually without the flowing of the carbon source gases. After the rapid cooling process, the diffused carbon from copper comes on the surface and a monolayer of carbon hexagonal film formed as graphene.

The graphene film that is grown on metal films or substrates is then transferred on to the target substrate [27]. The most general and widely used technique is to use the PMMA (polymethylmethacrylate) polymer. The PMMA is coated on graphene-metal substrates and then the metal is etched out using a specific etchant. The isotropic wet etching removes metal and some graphene residue from the bottom surface of the metal substrates. The remaining PMMA-graphene film on the metal etchant is then rinsed with deionized (DI) for 1 or 2 days, thereby ensuring that there is no Cu etchant residue on its surface and transferred carefully on to the target substrate. The substrate then goes through cleaning and annealing with high vacuum and temperature conditions for removing PMMA adhesion. Generally, to confirm the purity of the graphene film on a target substrate, Raman spectroscopy and other versatile characterizations (electrical resistance or optical transmittance in a visible region) are used.

The Figure 1.2 shows schematic of graphene growth process. In case of the picture on the right, the graphene sample was grown on Cu foils, 50 μm thick at temperatures of 1000 °C with carbon obtained from a mixture of methane (CH_4) and hydrogen (H_2) gas and transferred on Si/SiO_2 with PMMA and Cu etchant. The SEM image shows the uniform deposition of graphene on the substrate and the bottom picture shows that graphene is transferred to the Si/SiO_2 substrate.

1.2.4
Solution-Based Graphene

In the nineteenth century, graphite oxide was synthesized by the Brodie, Staudenmaier, and Hummers methods [9]. From then on there have been various preparation methods of solution-based graphene including not only chemical methods but also a physical method. Exfoliating graphene with solution processes was in practice since the material attracted tremendous attention because of its advantages. Moreover, solution-based graphene has many advantages of fabricating devices such as roll-to-roll and printable processes especially with regard to mass production. Solution-based graphene synthesized by the above-mentioned

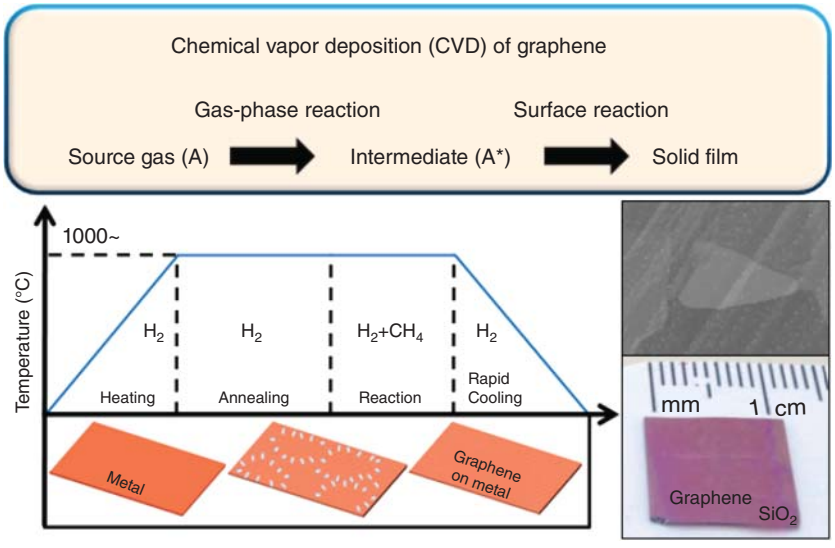

Figure 1.2 Chemical vapor deposition process of graphene.

methods are exfoliated from graphite, which is one of the allotropes of carbon, piled up on graphene layers with AB stacking. The idea of exfoliating graphene from graphite originated due to the weakening interaction between the layers.

1.2.4.1 **Ultrasonication**

Graphene dispersion prepared by the physical method is exfoliated by horn ultrasonication of natural graphite flakes in an aqueous solution with sodium cholate as a stabilizing agent and density gradient ultracentrifugation [28]. Compared with the covalent bonding of carbons in a graphene monolayer sheet composed of benzene rings, each graphene flake is combined by van der Waals force due to the interaction of p_z orbitals of carbon atoms in graphene; these combinations are possibly broken by horn ultrasonication. However, since these separated flakes are hydrophobic they gather as colloid; sodium cholate is dissolved in the solution to disperse graphene flakes. The hydrophobic face of sodium cholate is combined with the graphene flakes, while the hydrophilic face is combined with an aqueous solution consisting of liposome followed by sedimentation centrifugation to remove the thicker flakes that are broken imperfectly by horn ultrasonication. Then, by density gradient ultracentrifugation, it is possible to separate the exfoliated graphene with different thicknesses. The average thickness of the graphene flakes with the least buoyant density is around 1 nm measured by AFM. Also, graphene flakes having different layers are confirmed by Raman shift by comparing the intensity of G band and 2D band. The graphene flakes obtained from physical methods have D band-related disorders, which are due to the defect present within the flakes and because of their tiny size.

1.2.4.2 Intercalation

Another physical method for exfoliating graphite is the potassium-intercalation process [29]. Naturally occurring graphite is accumulated in AB stacking and carbon atoms of the upper graphene layer are positioned within the center of the benzene ring of the lower graphene layer. Alkali metals easily intercalate the layered structure of graphite, affecting the interlayer spacing related to the van der Waals force. However, graphene flakes exfoliated by intercalation shows low yield and are unstable.

1.2.4.3 Chemical Exfoliation

On the other hand, the chemical method needs oxidants, such as oxygen atoms, to break the interaction between the graphene flakes. As mentioned earlier, graphene flakes are combined by van der Waals force, that results from the π interaction of the different layers of graphene flakes. When carbon atoms composed benzene rings repeated, the orbitals of carbon hybridize each other, changing sp^3 orbitals to sp^2 and p_z orbitals. Comparing sp^3 shows three-dimensional structures; sp^2 exhibits planar shapes and combines each carbon as a σ bond. The remaining orbital, p_z of each carbon, composes delocalized electron clouds, which affect the van der Waals force. Therefore, if the delocalized orbitals are affected by the different bonding combinations, the force between the flakes becomes weak. Usually, by using oxidants, oxygen atoms are effective on the forces. In the chemical exfoliation method, strong acids and oxidants are used to synthesize GO. In recent days, the Hummers method is the most employed with some modifications made. Naturally occurring graphite powder is used to synthesize graphite oxide, which is the primary stage of material (GO), having weaker bonding than normal graphite states. The modified Hummers method comprises two-step oxidation processes. After the pre-oxidation step using potassium peroxodisulfate and phosphorus pentoxide in sulfur acid condition, pre-oxidized graphite that is aged a few hours is oxidized again with potassium permanganate, followed by filtering and washing with HCl for eliminating metal ions from oxidants. Next, the oxidized graphite in membrane filter is dialyzed by stirring distilled water to purify the residual salts and acid. The suspension is sonicated for exfoliation and centrifuged for removing the graphite powder that is not reacting with the oxidant. However, GO suspension, well dispersed in purified water, shows relatively lower properties than graphene due to the lower number of participating delocalized carriers resulting from oxygen-related functional groups including carboxyl, carbonyl, and epoxide groups. According to previous researches, these functional groups are placed in different positions such as phenol hydroxyl and epoxide groups on both the surfaces, and carboxyl and carbonyl groups at the edges of flakes [11]. These groups makes GO with tuneable properties for various application. In order to reduce GO, thermal and chemical reduction means are employed [30, 31]. rGO, which retains the properties of single-layer graphene can be fabricated on a device with reduction at various conditions, regulated by vaporized hydrazine or high temperature annealing under noble gas condition.

Suspension state GO is normally reduced by chemical modification by mixing various chemicals such as hydrazine, hydroquinone, and $NaBH_4$. These reduction methods change the atomic ratio of GO from sp^3 bond composed of carbon and oxygen to sp^2 bond of benzene rings demonstrated with elemental analysis, Raman spectroscopy, and X-ray photoelectron spectroscopy (XPS). The changes reveal various properties, since carboxyl and hydroxyl groups decreases with the reduction process. The deconvolution of XPS shows a different ratio since the bonding ratio between carbon to carbon bond and carbon to oxygen changes. Also, the vibration-scattering changes according to orbital transition effects on Raman scattering peak the intensity ratio. GO naturally exhibits negative charges that come from ionized functional groups, which make it disperse in water easily. Hexylamine-modified graphene is obtained using an amine within the methanol solution before the hydrazine reduction process [32]. Modified graphene contains more nitrogen atoms than unmodified graphene measured by element analysis and XPS, thereby showing more intensity of carbon and nitrogen. Since amine groups on graphene flakes reveal positive charges when the ligand is ionized, different applications can be adapted. Also, layer-by-layer graphene tends to show strong interactions rather than the same charged functionalized graphene.

1.2.5
Synthesis of Composite Material Based on Graphene Oxide

Nano composites or hybrid materials have inspired passionate research over past decades because of their new optical, electronic, thermal, mechanical, and catalytic properties. Graphene-based materials can be prepared for composite with various other materials, such as metal, polymer, and biomolecule. Forming composite with pristine graphene sheet has known to be difficult, because it is chemically stable and nonactive. In contrast, GO has many functional groups including oxygen, which is helpful for bonding with other particles; hence, it is more used for synthesis of composite. Hybrid materials of graphene sheet have been studied for its modified energy level distribution, which causes to improve its characteristics. Numerous research groups have tried to prepare graphene and metal or metal oxides decorated graphene. This has resulted in a novel kind of composite material and possibly brought in new functionality and properties [33–36].

The demonstration of structural property and chemical bonding between graphene sheets and inserted material can be facilitated by various measurements, such as XPS, XRD, TEM, SEM, and so on. The TEM and SEM are high-resolution imaging techniques for monitoring the surface profile of materials. XRD is helpful to confirm the structure of materials. And XPS measures the bonding energy between atoms for observing the chemical relation. Furthermore, many detecting methods exist such as electron energy-loss spectroscopy (EELS), high resolution transmission electron microscope (HR-TEM), high-angle annular dark-field (HAADF)-scanning transmission electron microscope (STEM), and energy dispersive spectroscopy (EDS). According to the material state, we should choose the proper experiment [13, 37–39].

The studied metals are gold, silver, copper, cobalt, nickel, palladium, titanium, and so on. There is no end to this list. Also the states of metals are various, for example, homogeneous nanoparticle (NP), ion, and molecule composed of metal cation and anion. Particularly, Ag is considerably exploited for synthesis with graphene/GO [40]. Thus, many preparation methods are reported and widely used for advanced experiments. Ag/graphene composite exhibits the catalytic activity for the oxygen-reduction reaction of graphene and can become a cathode in alkaline fuel cells because it can help to solve the methanol cross-over problem from the anode. Also, optical property of Ag/graphene can be modified by the interaction between orbitals in Ag and carbon atoms [40, 41].

The preparation of graphene with metal nanoparticles hybrid material usually, done by using chemically mixing and heating or vapor deposit. Thus, an extremely important factor is the condition under which the experiment is done – conditions such as temperature, concentration of solution, operating time – because these conditions contribute to the exfoliation of graphene sheets and NP dispersion. The methods of synthesis for Ag/graphene developed earlier are going to be discussed in this chapter. The method for Ag/graphene involves use of reduced GO, which closer to graphene, for facile synthesis. The GO was adsorbed on the 3-aminopropyltriethoxysilane-modified Si/SiO_x substrate. Then, the GO reduced to form rGO. The Ag particles are grown on the reduced GO by heating them at 75 °C for 30 min in $AgNO_3$ solution. The reduced GO becomes decorated with Ag particles. Another method is that $Ag[(imH)_2]NO_3$ was added in the NH_3 solution with dispersed GO at a pH of 9.5. The compound of Ag complex and GO was heated in the nitrogen atmosphere as inert gas. The TEM image in Figure 1.3 shows an Ag NP grown on the single-layer GO surface.

Similarly, samples having Au can be produced by adding $[Au(bipy)Cl_2]NO_3$ with heating raised temperature until 573 K at a rate of 5 K min^{-1}. Other transition metals can build a composite with GO, such as Co, Ni, and Cu with Ammine complexes $[Co(NH_3)_6]^{3+}$, $[Ni(NH_3)_6]^{2+}$, $[Cu(NH_3)_4]^{+}$, which were used as intercalates to create the precursors and metal-decorated graphene. Figure 1.4 represents the TEM images of Cu–Gr heated at 673 K (Figure 1.4a), Co–Gr heated at 673 K (Figure 1.4b), and Ni–Gr heated at 673 K (Figure 1.4c). These images resemble the images of Pt, Pd, or Ru samples that we reported. Micropore or mesopore was not discovered on the carbon surface. Therefore, the mesoporous structure estimated by the isotherm measurement is responsible for the room between exfoliated graphene sheets and the empty space in wrinkled parts on the graphene sheets. Redox reaction between GO and Fe^{2+} is preparation route for Fe_3O_4/rGO composite (reduced graphene oxide). Redox reaction of GO with Fe^{2+}, in water/NH_4OH (pH 9) solution and collected by applying magnet.

Composites combine not only with metal but also with a kind of polymer. Functional groups, for instance, alcohol, aldehyde, ester, carboxylic acid, and amide, on the GO surface are beneficial for chemical reaction. The polymer as multiphase solid material has also various functional groups and these can assist bonding

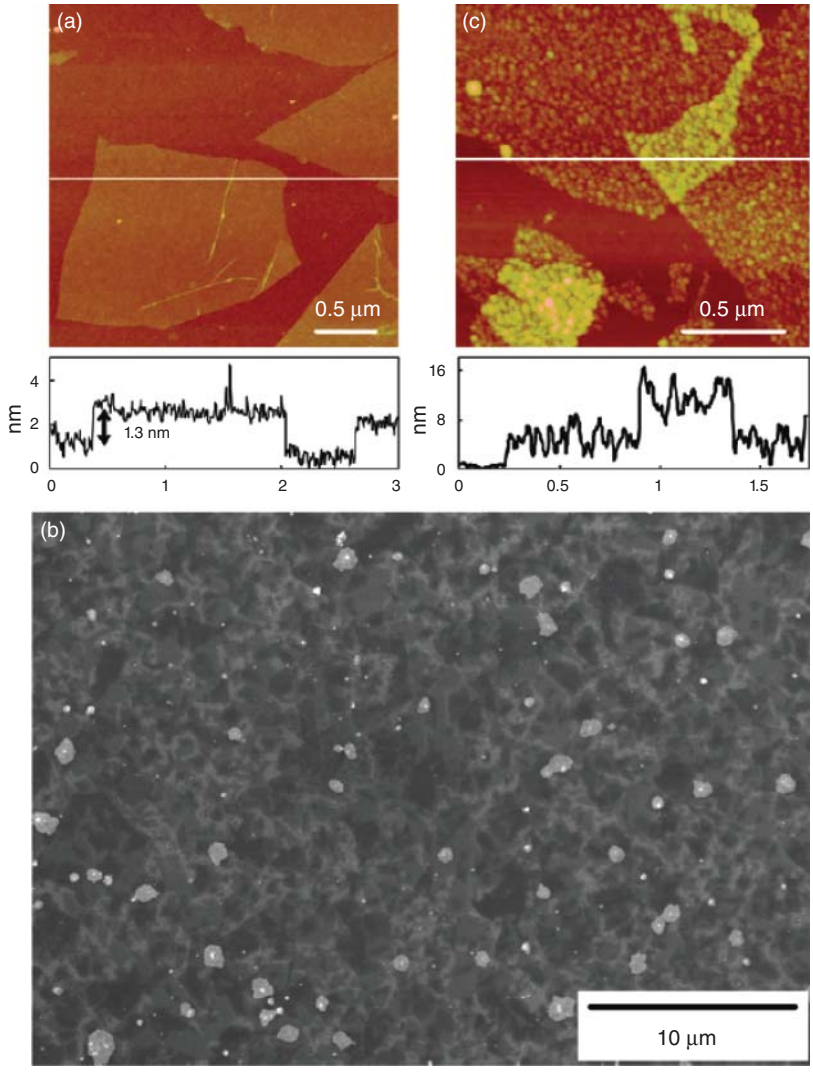

Figure 1.3 (a) Tapping mode AFM topographic image and height profile of single-layer GO adsorbed on APTES-modified SiO_x substrate. (b) SEM image of Ag particles grown on rGO surface. (c) Tapping mode AFM topographic image and height profile of Ag NPs grown on single-layer GO surface.

with other materials [39, 42]. Many research programs in this field used polymer for sensing, bonding, and filtering by the characteristic of selective attachment. They developed numerous devices to interact with biomolecules like protein, DNA, and metal particles. The graphene and polymer composite provides a way to the production of a wide innovative class of graphene-based materials and their use in a variety of applications. This chapter presents the general method

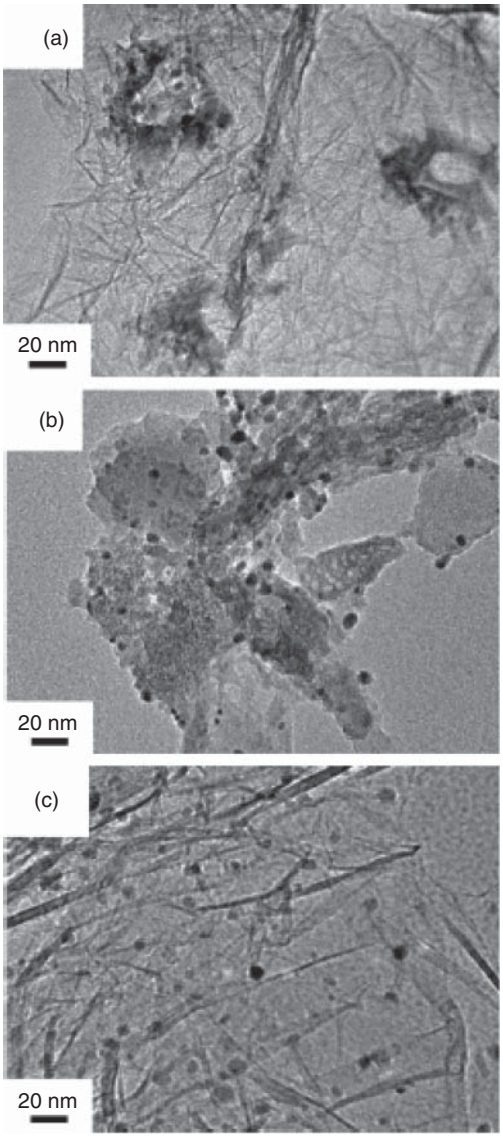

Figure 1.4 TEM images of Cu–Gr heated at 673 K (a), Co–Gr heated at 673 K (b), and Ni–Gr heated at 673 K (c).

of graphene–polymer composites by exfoliation of graphite and dispersion in polymer at molecular scale. For example, a polystyrene–graphene composite, the electrically conductive graphene–polymer nanocomposites, is formed by the solution phased mixing of the exfoliated phenyl isocyanate-treated graphite oxide sheets with polystyrene, followed by their chemical reduction. These composites represent the individual graphene sheets well dispersed via the polymer matrix.

Similar performances have been accomplished with other styrenic polymers such as acrylonitrile-butadiene-styrene and styrene-butadiene rubbers. Chemical reduction was indispensable for inducing electrical conductivity because composite samples become insulating before phenyl isocyanate–treated graphite oxide sheets were reduced. In addition, the existence of the polymer in solution during the reduction process contributes to preventing the agglomeration among the sheets because the sheets of GO covered with the polymer. The graphene–polymer composite fabrication process starts from preparation of graphite oxide sheets by exfoliation graphite powder. After graphite oxide sheets are treated with phenyl isocyanate, they are mixed with dissolved polystyrene in dimethylformamide (DMF). Composite powder obtained from coagulation of graphene and polymer through reduction by *N*,*N*-dimethylhydrazine in methanol. In Figure 1.5, the morphology of graphene/polysterene composite is represented by SEM and TEM images. In addition, many other modifying methods with polymers report that characteristics are improved based on the agent used. Some methods are introduced that graphene makes composite with octadecyl amine by reduction in the stabilization medium and with poly-L-lysine by covalent modification with alkyl amine/amino acid by nucleophilic substitution. We can benefit from the advantages of these methods such as enhancing conductivity as well as capacitance, mechanical property, and heat capacity.

Lastly, some other atoms such as europium in lanthanoids and palladium are used for composite with graphene-based material [39]. These composites demonstrated the PL characteristics in visible light range and opened the possibility of display device material. Similarly, these atoms combined due to chemically mixing in solution and annealing. The performance of PL with heat and oxygen plasma treated GO is explained in a later chapter.

1.3 Characterization of Graphene

Graphene, a single-atom-thick sheet of hexagonally arrayed sp^2 bonded carbon atoms, has been able to get significant attention due to its unique electronic, mechanical, and thermal properties all derived from the unique details of its electronic band structure. On the basis of recent studies, GO consists of phenol hydroxyl and epoxide functional groups on the top and bottom surfaces of each sheet and sp^2 hybridized carbons containing carboxyl and carbonyl groups mostly at the sheet edges and these groups offer tremendous opportunities to access functionalized graphene-based materials. The oxidation of graphite to GO breaks up the sp^2 hybridized structure of the stacked graphene sheets and the disruption of graphene lattice is reflected in an increase in interlayer spacing from 0.335 nm for graphite to more than 1 nm for GO. In GO, the ratio of the sp^2/sp^3 fractions opens up possibilities for new functionalities and possesses a finite electronic band gap generated by the disruption of π-networks due to

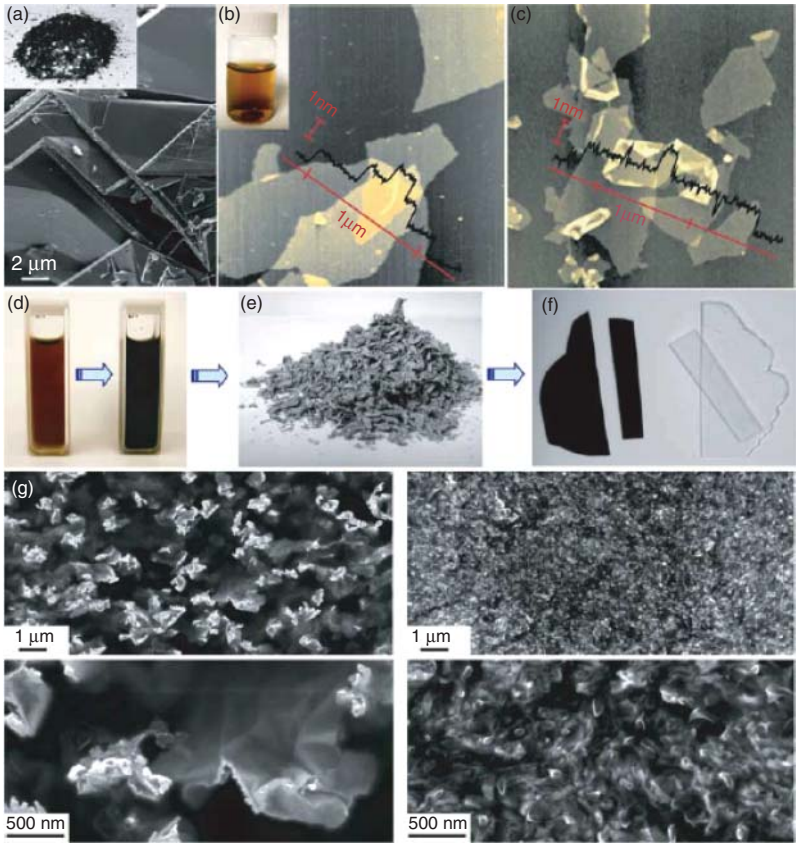

Figure 1.5 Process flow of graphene–polymer composite fabrication. (a) SEM and digital image (inset) of natural graphite. (b) A typical AFM noncontact-mode image of graphite oxide sheets deposited onto a mica substrate from an aqueous dispersion (inset) with superimposed cross section measurements taken along the red line indicating a sheet thickness of, 1 nm. (c) AFM image of phenyl isocyanate-treated graphite oxide sheets on mica and profile plot showing the, 1 nm thickness. (d) Suspension of phenyl isocyanate-treated graphite oxide 1 mg ml^{-1} and dissolved polystyrene in DMF before (left) and after (right) reduction by *N,N*-dimethylhydrazine. (e) Composite powder as obtained after coagulation in methanol. (f) Hot-pressed composite (0.12 vol% of graphene) and pure polystyrene of the same 0.4-mm thickness and processed in the same way. (g) Low (top row) and high (bottom row) magnification SEM images obtained from a fracture surface of composite samples of 0.48 vol% (left) and 2.4 vol% (right).

the formation of oxygen-containing groups. Thus, it is possible to modify the electronic structure by means of chemical or physical treatments with different gases to reduce the connectivity of the electron network. TEM can also use to evaluate the number of graphene layers and to assess the crystalline quality of the graphene films. TEM images provide images of sp^2 clusters as well as

defects. The diffraction experiments provide knowledge of the orientation of the crystal lattice and different crystal grains can be mapped. Raman spectroscopy provides information about the number of graphene layers and can provide information about the differences between HOPG, FLG, and graphene. PL spectra can be used to understand the sp^2 and sp^3 clusters. In contrast to pristine graphene, in which all atoms are sp^2 hybridized, GO also contains sp^3 carbon atoms covalently bonded to oxygen-bearing functional groups and the PL in such carbon systems usually is a consequence of recombination of localized e–h pairs in sp^2 clusters. Excitation wavelength-dependent PL emission from the GO and graphene quantum dots were also observed and the PL peak shifted from 430 to 515 nm when the excitation wavelength was changed from 320 to 420 nm.

1.3.1 AFM (Atomic Force Microscopy)

This measurement method of imaging can effectively represent the surface profile at the nanometer scale. AFM is a scanning probe microscopy type with very high resolution, in the order of fractions of a nanometer, more than 1000 times better than the optical diffraction limit. However, this method is not suitable for imaging large regions of material. The profile is obtained by interaction between the surfaces with a mechanical probe. Piezoelectric elements are used for accurate and precise movements and sensing the force by electronic signal change [43, 44]. Imaging modes are mainly of two types – the static mode with the deflection of the cantilever and the dynamic mode that uses the vibration at the fundamental resonance frequency. In the static mode operation, the tip is connected to the surface of the sample as close as needed. Thus, static mode AFM, which is always conducted in contact with the entire force, is repulsive. The force is maintained constant during dragging on the surface to notify deflection.

In the dynamic mode, the tip of the cantilever stays a distance from the sample surface. The cantilever oscillated at its resonance frequency, where the amplitude of oscillation is typically between few picometer to few nanometer (<10 nm) [45]. Above the surface, the van der Waals forces or any other long-range force performances act to decrease the resonance frequency of the cantilever. From this derivation, measuring the tip-to-sample distance at each point of scanning area leads to building the topographic image of the sample surface. This method, called *noncontact AFM*, is a preferred method to contact AFM for measuring soft samples, for example, biology sample and organic thin film, because noncontact mode AFM does not cause damage to the tip or sample degradation effects that are sometimes observed after taking overflowing scans with contact AFM.

Distinguishing between the GO and the graphene layers in the AFM image is difficult just using the topographic contrast factor. Phase imaging, which is tapping-mode AFM, allows the separation of both the materials [46]. The separation is possible, because the AFM tip undergoes a different force with

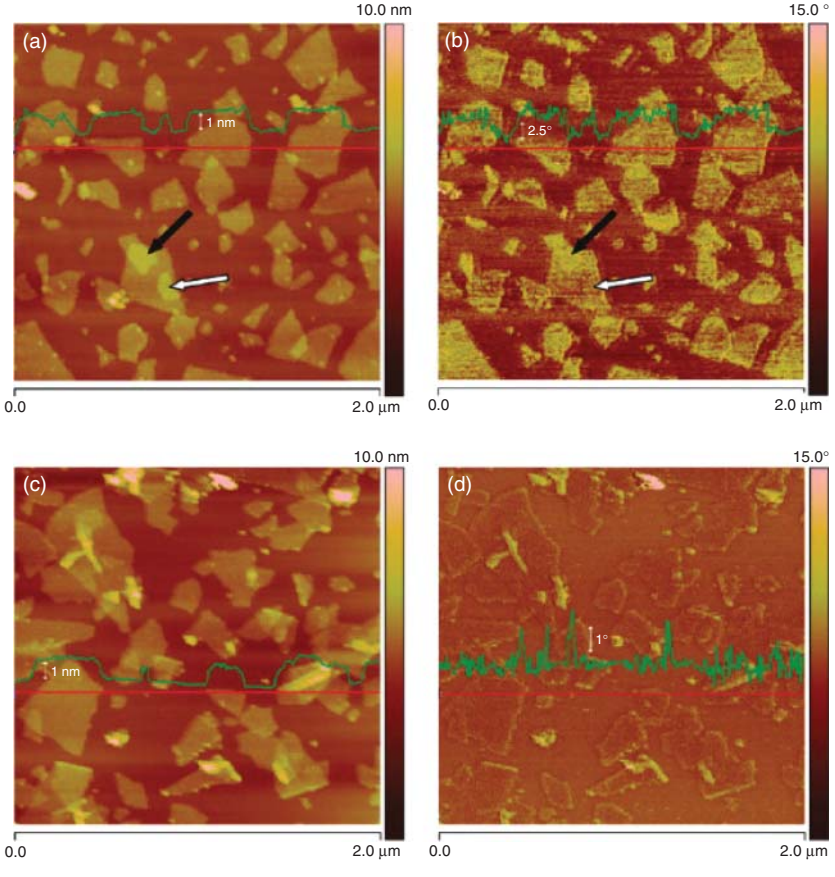

Figure 1.6 Height (a, c) and corresponding phase (b, d) tapping-mode AFM images of unreduced (a, b) and chemically reduced (c, d) graphene oxide nanosheets deposited from aqueous dispersions onto freshly cleaved HOPG. The images were recorded in the attractive regime of tip sample interaction. Superimposed onto each image is a line profile taken along the marked red line.

pristine graphene and its functionalized group. The thickness of two-dimensional materials, particularly graphene, can be measured by AFM using the repulsive mode [47]. The thickness of the unreduced GO is ~1.0 nm and that of chemically rGO is 0.6 nm. This difference in the thickness and the phase contrast arises from the hydrophilicity difference due to the distinct oxygen functional group in the reduction process as represented in Figure 1.6 [19, 48].

In the previous research, AFM has been exploited for mechanical and structural characterization of graphene because it can feel the small force from the tip of the probe [48]. In the future, new AFM modes will be developed and other modes for graphene are already suggested about mechanical, frictional, electrical, magnetic, and even elastic properties of graphene flakes (Figure 1.7).

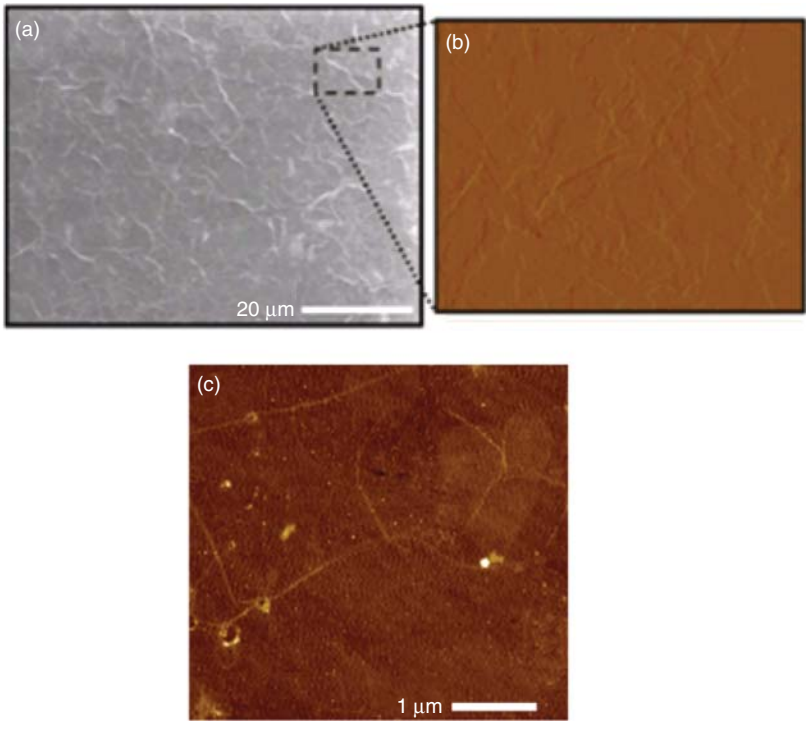

Figure 1.7 (a–c) AFM images of GO film and graphene transferred onto a fused silica substrate.

1.3.2 SEM

Graphene or GO deposited on substrates need to be morphologically characterize for more analysis. SEM is employed in order to obtain more detailed information. The number of not only graphene but also functionalized graphene layers can be classified by using this method under highly optimized conditions [17, 49]. Since, distinguishable contrast between graphene and non-graphene position reveals defects, edges and wrinkles on the surface. Graphene is easily detected because it has high mobility, and it shows as a semimetal. However, the SEM image shows representative electronic structures rather than topology because of its semimetallic property.

1.3.3 TEM/SEAD/EELS

GO sample was deposited on the standard holey-carbon-film-covered copper grids and loaded into the microscope for TEM measurements to study GO lattice. HR-TEM images of pristine GO and oxygen plasma–treated GO with different

oxygen pressure illustrate that, atomic structures get in order at an optimum oxygen pressure and disordered thereafter (Figure 1.8a and 1.24b). TEM images show that during the oxygen plasma treatment, the thermal energy favors the further clustering of the sp^2 phase, thereby stimulating the connection between ordered rings and oxygen atoms attached to graphene sites randomly and convert sp^2 carbon bonds to sp^3 bonds. Thus, initially the sp^2 clusters in GO are small and separated by an amorphous and highly disordered sp^3-bonded matrix, which forms a high tunnel barrier between the clusters. During heat treatment, the thermal energy favors the further clustering of the sp^2 phase, thereby stimulating the connection between ordered rings and moving from polycrystalline to the two-dimensional nano-crystalline graphene.

From the selective area electron diffraction (SAED) pattern, a typical sharp, polycrystalline ring pattern is obtained for GO-1 film (inset of Figure 1.8a). Strikingly, clear diffraction spots are observed (GO-3) characteristics of internal short-range crystalline order; the sixfold pattern is consistent with a hexagonal lattice (inset of Figure 1.8b). This simple hexagonal pattern of sharp spots is similar to that obtained from graphite oxide and leads immediately to several conclusions that the GO films are not completely amorphous and the lack of any diffraction spots other than those corresponding to the graphite structure shows that any oxygen-containing functional groups present do not form super lattice-type ordered arrays. This implies that an appreciable fraction of oxygen atoms is involved in linkage between carbon atoms. However, for GO-4 (inset of Figure 1.8c) the pattern again shows disordered nano-crystalline pattern when compared to GO-3. Also the existence of some disorder is obvious from the broadening of the diffraction spots. This broadening shows that a disturbance exists in the stacking of the closely packed planes. A similar behavior is also observed for the electron diffraction patterns of graphite.

First diffraction rings in GO have a lattice spacing of 0.76 nm, which have been identified to be the (110) reflections. After oxygen plasma treatment, the corresponding spacing are 2.1 and 2.4 nm respectively, which is larger than the interplanar spacing of pristine GO. This can be attributed to the presence of oxygen functional groups on the GO layers. The EELS spectrum, as shown in Figure 1.9, the carbon K-edge region shows a peak at 285 eV that corresponds to transitions from the 1s to the π^* states ($1s-\pi^*$), and a peak at 291 eV that corresponds to transitions from the 1s to the σ^* states ($1s-\sigma^*$). Figure 1.9a shows $1s-\pi^*$ transitions as oxygen plasma treated (GO-3, GO-4). The higher-order π^* and σ^* resonances in GO at ~292.5 and ~293.5 eV may be assigned mainly to the presence of carbon atoms bonded to oxygen atoms by epoxide and carbonyl bonds. Lower energy plasmon excitations are observed from the films in Figure 1.9b. Previous reports show that for monolayer GO, the plasmon energy of the pristine GO sheet is at 24.5 eV and the plasmon energy decreases almost linearly with sp^3 fraction. sp^3 hybridization induced by oxygen-containing groups increases this value in GO. The experimentally recorded $\pi^* + \sigma^*$ plasmon energies for a single-layer and five-layer graphene are 16.6 and 18 eV respectively. Thus, in the present study, a plasmon energy of 19.2 eV corresponds to four to six layers of GO. Thus, GO-3 and

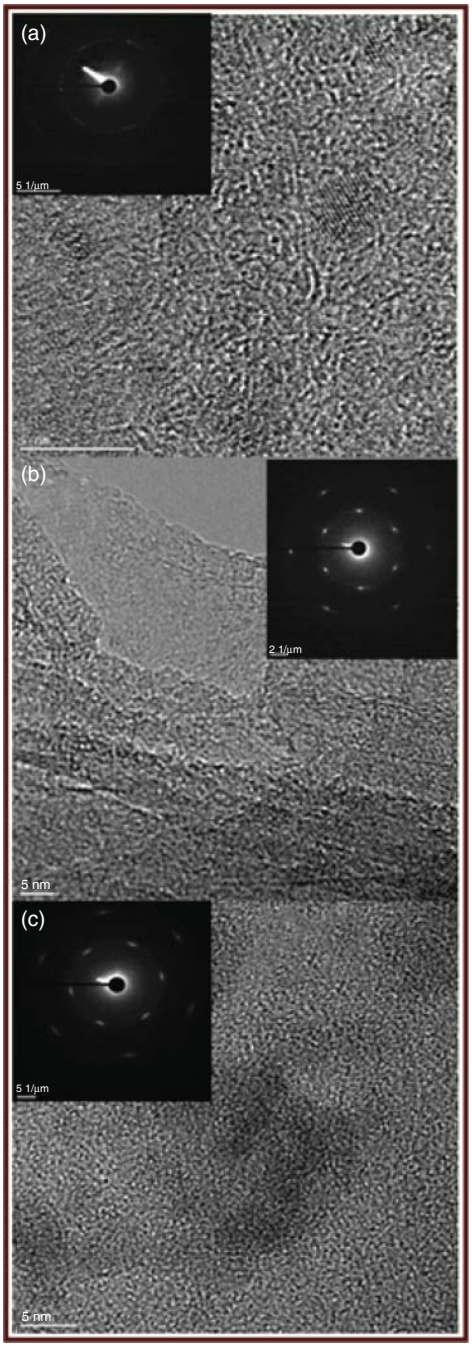

Figure 1.8 HR-TEM images of (a) GO-1, (b) GO-3, and (c) GO-4 films. Inset shows the corresponding SAED pattern.

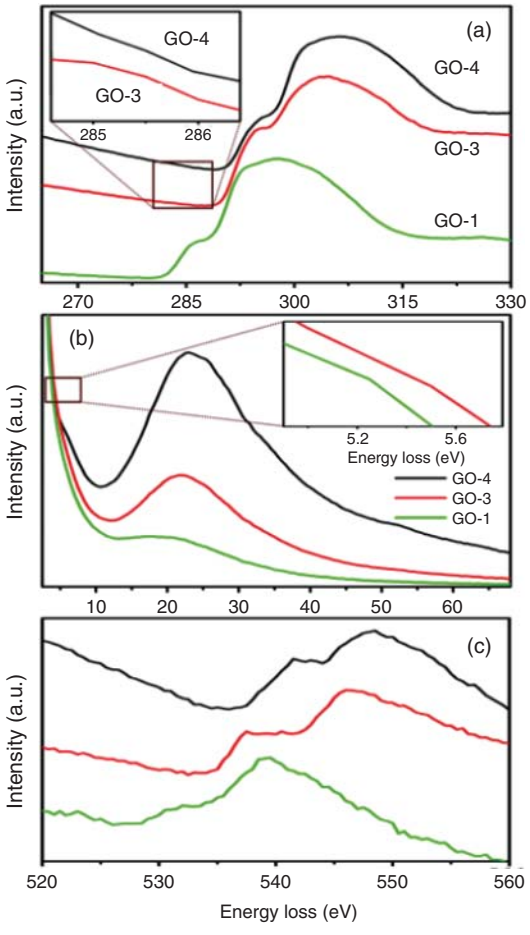

Figure 1.9 (a) EELS analysis of C K-edge, (b) lower energy plasmons resonance of GO-1, GO-3, and GO-4 films, and (c) shows O K-edge spectrum of GO films. Inset of (a) shows 1s–π* transitions from GO-3 and GO-4 films. Inset of (b) shows low energy plasma excitations of π* electrons in the GO-1 and GO-3 films.

GO-4 samples in Figure 1.9b give peak values of around 21 and 22 eV respectively and reports show that the plasmon energy of an amorphous carbon of ~45% fraction of sp^3 bond is around 24 eV. This confirms that the oxygen plasma treatment increases sp^3 bonding. The low-energy plasma excitations of π* electrons in the GO film is ~5.2 eV (Figure 1.9b) and the π* electrons in single-layer GO is ~5 eV, which shows that our film consists of three to five layers of GO. GO-1 shows a peak around 539.7 eV in Figure 1.9b,c; this may possibly be due to higher-order π* resonance of all oxygen atoms and higher-order σ* resonance of the 1,2-epoxy linkages in the GO sample. In the GO-3 film, the absorption corresponds to a peak value of ~536.7 eV and this seems to arise from σ* and higher-order π* resonances

of only epoxy bond. Peak corresponds to 545 eV and this arises from the oxygen atom from the C═O and O–C═O groups; the intensity of this peak increases, which shows the dominance of carbonyl groups in the advanced oxidation stages.

1.3.4 XPS

The XPS analysis shows us the bonding distribution through the intensities of each binding energy. In the case of graphene, the C–C bonding of sp^2 carbon in 284.8 eV is shifted from the oxidized defect in GO. In Figure 1.10a, the XPS results reveals two different peaks of carbon bonds (sp^2) and its intensity decreases with plasma-oxidation treatment for CVD graphene. In most cases, the CVD graphene has its own inherent defect from its fabrication process, which makes it difficult to have the single Gaussian peak only for sp^2 carbon. Figure 1.10b shows the XPS results of GO, which correspond to sp^2 carbon at 284.8 eV, and the other C═O or O–C═O around 288 eV. Especially, dramatic depressed sp^2 carbon peak rather than CVD graphene shows the formation of oxygen-related defects. Generally, there are several different functional groups in GO, which are characterized by the appearance of several XPS spectral peaks. The XPS C1s spectra of GO consist of four peaks that correspond to sp^2 carbon at 284.8 eV, O–H/O–C–O at 286.2 eV, C═O at 287.8 eV, O–C═O at 288.5 eV and COOH groups at 289.3 eV. The peak at 290.2 eV is from plasmon, which is a collective behavior of delocalized valence electrons of GO. It can be considered that the main bonding configuration of carbon atoms in the film is C–C. A sheet of GO consists of a hexagonal ring–based carbon network having both sp^2 hybridized carbon atoms and sp^3 hybridized carbons bearing hydroxyl and epoxide functional groups on either side of the sheet. Thus, the sp^2 clusters in GO vary in size and separated by an amorphous and highly disordered sp^3 bonded matrix, which forms a high tunnel barrier between the clusters.

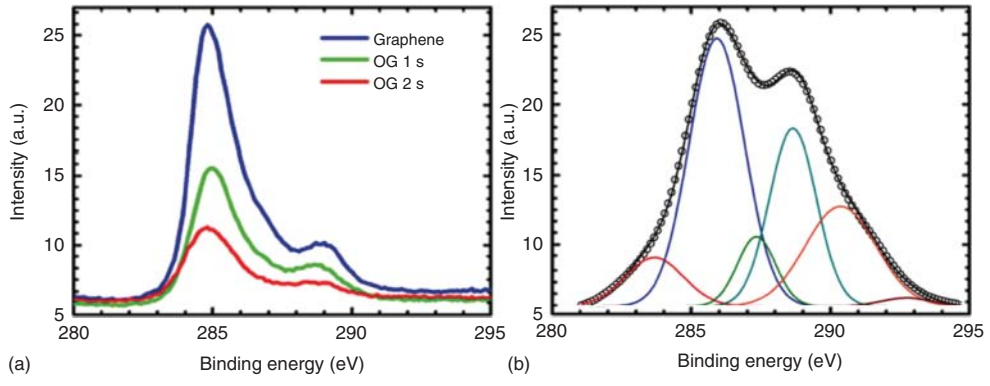

Figure 1.10 (a, b) XPS of graphene and graphene oxide.

1.3.5 XRD

XRD is used for confirming the material structure of a crystal by measuring the angles and intensities of these diffracted beams [50–52], in which the crystalline atoms lead a beam of X-rays to diffract into many specific directions. This measurement can expect the spatial density of electrons in crystal because X-ray beam interact with electrons. From this expectation, the mean positions of the atoms in the crystal can be estimated; also their chemical bonds, their defect and various other information [53–55] can be deduced. There are many crystalline materials, for example, salts, minerals, metals, semiconductors as well as inorganic, organic, and biological molecules. XRD measurement plays a key role for characterization of these materials, such as the size of atoms, the lengths and types of chemical bonds, and the atomic-scale differences among the combined materials [56–60].

For measurement, a crystal lies on a goniometer and gradually rotated while being emitted with X-rays, gathering a diffraction pattern of regularly spaced spots known as *reflections*. X-ray crystallography is related to several other methods for determining atomic structures. Similar diffraction patterns can be obtained by scattering electrons or neutrons, which are likewise interpreted as a Fourier transform.

XRD gives three types of structural information of graphene materials – the interplane distance of the lattices, graphene material thickness and the number of graphene layers. First, the base principle of XRD for material is Bragg's law [61], $n\lambda = 2d_{(hkl)}\sin\theta$, where λ is the wavelength of the X-ray, θ is the scattering angle, n is an integer representing the order of the diffraction peak, d is the interplane distance of the lattices, and (hkl) are Miller indices. Graphite or multilayered graphene has (002) planes; d_{002} becomes the interlayer distance. Scattering from entering X-ray occurs on each graphene plane. As changing the incoming angle, the X-ray beam undergoes path length difference by multiplying n (integer) of the beam wavelength λ. The beams scattered among the adjacent graphene planes could combine practically. Consequently, the XRD peak of the (002) facet of graphene exhibit a d_{002} value and the clue acquired for the lattice size and quality.

Using Sherrer's equation [61], the graphene thickness can be expected, which is expressed by $D_{002} = K\lambda/B\cos\theta$, where D_{002} is the thickness of crystallite, graphene thickness, K is a constant dependent on the crystallite shape (0.89), λ is the X-ray wavelength, and B is the full width at half maximum (FWHM), and θ is the scattering angle [61]. From Sherrer's equation, the number of graphene (N_{GP}) layers can be determined using the following equation (Ju *et al.*, 62): $N_{GP} = D_{002}/d_{002}$. From XRD crystallography, we can understand the formation during the GO reduction and the finally reduced graphene. The interlayer distance of graphene-based materials is different because there are many defects, nanoholes, and intercalated molecules, which are oxygen-bonded functional groups and H_2O molecules. The materials composed with smallest interlayer distance is graphite, 3.348–3.360 Å [63], as shown in

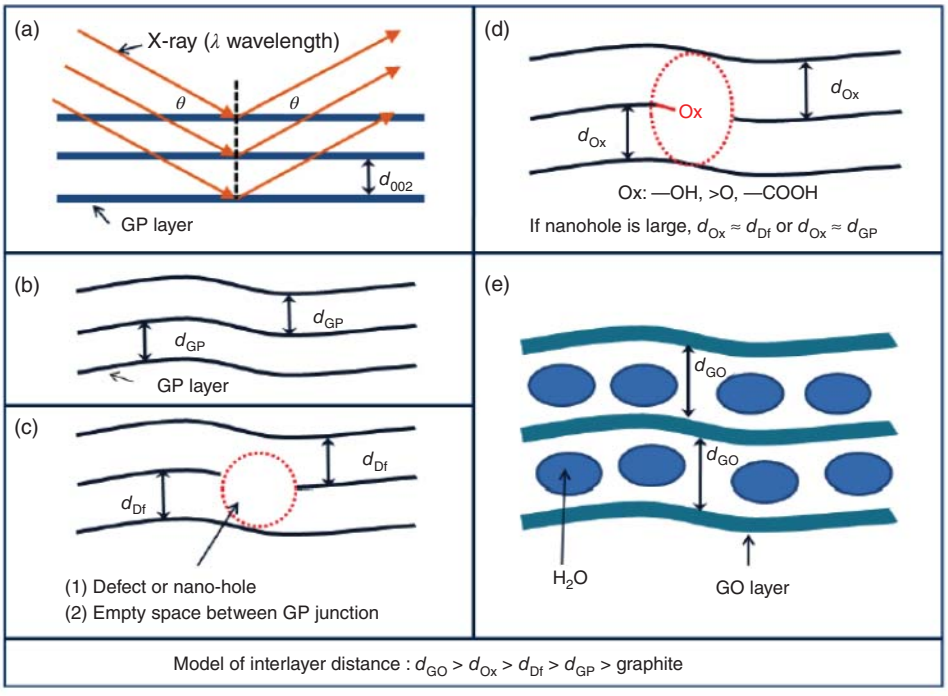

Figure 1.11 Bragg's law for graphene (GP) or graphite (002) planes (a), and models for d_{002} of GO (e), and thermally reduced GP (b–d). In this model, the order of interlayer distance becomes graphite $< d_{GP} < d_{Df} < d_{Ox} < d_{GO}$.

Figure 1.11 [63]. The interlayer distance order is graphite < graphene < defect and nanohole < oxygen bonded functional groups < GO. Particularly, GO has the largest distance about ~5–9 Å because of the inclusion of H_2O between the layers. If defects in the layer are sufficiently large, the space of oxide groups and H_2O molecules can be ignored. Thus, the order could change the distance of (oxygen bonded functional groups) ≈ (defect and nanohole) or (oxygen bonded functional groups) ≈ (graphene). GO has an intermediate structure with oxygen bonded functional groups and defect and nanohole during thermal reduction, and through bottom-up layer stacking, the resultant graphene evolves toward graphite as crystal growth with the removal of gap by oxygen and defects.

In various annealing conditions, GO and graphene films show temperature-dependent XRD patterns. From the change of XRD patterns shown in Figure 1.12, we can figure out that the structure and bonding states of thermally reduced GO depend on the annealing temperature [64]. As increasing temperatures, the (002) peak of a GO film on the left side moves continuously toward the right with a variance in intensity and FWHM as seen from Figure 1.13.

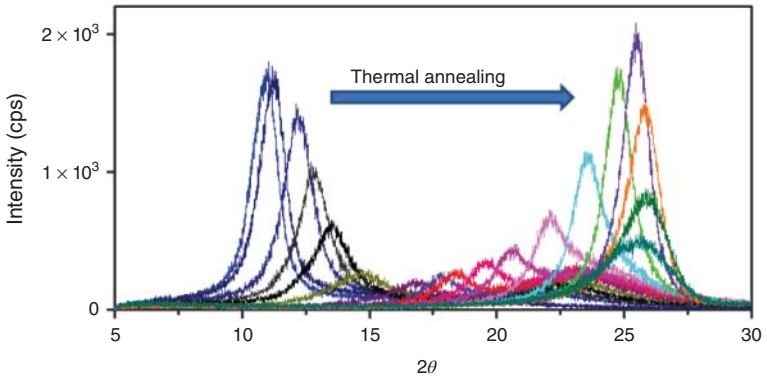

Figure 1.12 Total plot for measured in situ XRD patterns of GO/GP films obtained at room temperature to 1000 °C.

1.3.6
Raman

Raman spectra of GO consists of prominent spectral features, called G at ~1586 cm^{-1}, D bands ~1350 cm^{-1}, and 2D at 2697 cm^{-1}. Raman spectra of all disordered carbons are dominated by the relatively sharp G and D features of the sp^2 sites. The G and 2D peaks represent the E_{2g} vibrational and out-of-plane modes within aromatic carbon rings, respectively. G band is a degenerated optical phonon mode at the Brillouin zone center and is induced by a single-resonance process. The peak near 1350 cm^{-1} is denoted with the D band (in plane carbon ring breathing mode (A_{1g} mode)), which is forbidden in perfect graphite. This process requires a scattering at defect sites in order to conserve the momentum. Previous reports show that the dominant peaks in the D mode spectra originate from phonons between the K and M points of the Brillouin zone. The D mode is dispersive; it varies with photon excitation energy, even when the G peak is not dispersive and its intensity is strictly connected to the presence of sixfold aromatic rings. The G band corresponds to graphite-like sp^2 carbon and D band corresponds to disordered sp^2 carbon induced by the linking with sp^3 carbon atoms. The D peak ultimately gives a relative measure of the amount of sp^3 carbons in the surrounding. Defects such as impurity atoms, functional groups, heptagon–hexagon pairs, folding, and so on, of the graphene layers give rise to the D band. The cooperation between D and G peaks gives rise to a G0 peak near 2931 cm^{-1}.

1.3.7
Photoluminesces (PL) Measurement

Graphene, which is semimetal in nature, the highest occupied molecular orbital (HOMO) and the lowest unoccupied molecular orbital (LUMO) meets in K point, making it a zero band gap material and opening of a band gap can be

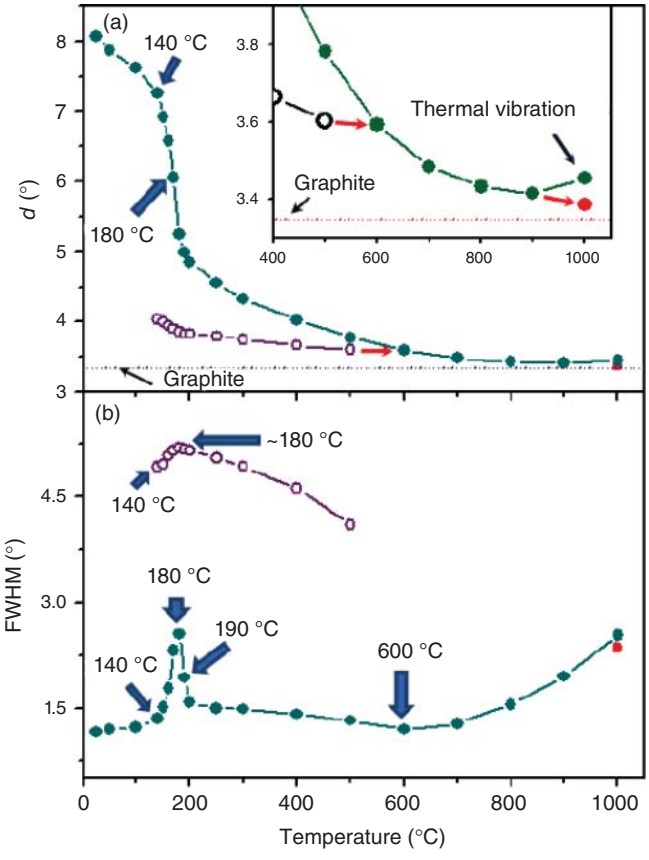

Figure 1.13 FWHM (a) and d_{002} (b) plots for XRD patterns of Figure 1.4. The inset shows a magnified image of (a).

possible due to the functionalization of its lattice with oxygen atom. GO has an electronic structure similar to that of graphene, except for the states near Fermi level and oxygen-related states. The formation of sp^2 clusters in sp^3 matrix is expected to produce quantum confinement effects, which result in an opening of the band gap, at the Fermi level. In graphene, $\pi-\pi^*$ bands degenerate at the K point and coinciding with the Fermi level makes it the zero band gap. But in GO, the π states disappeared near the Fermi level because of bonding between the π and oxygen-related states causing electron transfer from carbon to oxygen and shifting the HOMO state downward results opening of a band gap. Since sigma bands away from the Fermi level and π bands close to it so that the $\pi-\pi^*$ band controls the band gap. Entire π bands lie within the $\sigma-\sigma^*$ gap and the $\pi-\pi^*$ energy states are highly localized due to the large $\sigma-\sigma^*$ gap of the sp^3 matrix. Thus, electron confinement in sp^2 clusters are possible because sp^3 carbon sites act as large repulsive barriers for carrier and thus sp^2 clusters of a smaller size result in larger $\pi-\pi^*$ splitting. Since π and π^* states form the band edge, the size

of the gap depends on the size of the sp^2 clusters and the width of optical gap is found to vary inversely with the sp^2 cluster size. Recombination via emission of photons takes place because electron–hole pairs are localized due to a deep potential well, which separates carriers from extended sigma states.

1.4
Optical Property Modification of Graphene

1.4.1
Absorption Property Modification of Graphene (Terahertz, UV–Visible–NIR)

The optical properties of graphene, GO [65], and rGO shows fairly similar tendency that as GO becomes reduced, it shows properties similar to those of graphene and plasma oxidized graphene (OG) shows what are similar as GO. Therefore, it is significantly essential to figure out tunable transmittance feature for expecting absorbance between graphene and GO with two of treatment, annealing and oxygen plasma (Figure 1.14).

1.4.1.1 Absorption Property of Thermally Annealed Graphene Oxide

Thermal annealing is a very powerful tool to reduce GO. While the chemical method is applicable, still the reduction rate of thermal annealing is the highest. For heating the GO up to 850 °C, most of the oxygen functional groups are reduced and it is shown that only the aromatic rings are still alive. The Raman analysis in Figure 1.15 presents that the GO is reduced by thermal annealing, where its G-peak is shifted to graphene and the D peak increases due to the reduced oxygen atoms. The G-peak shift shows us that the carrier density of GO increases similarly to graphene and that the physical properties of rGO resemble those of graphene. Moreover, when the GO is annealed up to 850 °C,

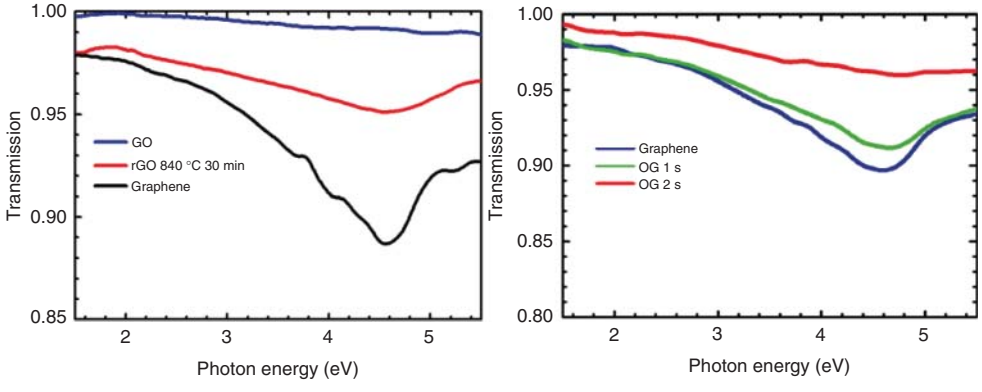

Figure 1.14 Transmission spectrum of graphene and graphene oxide with heat treatment (left) for reduction of GO and Oxygen plasma treatment (right) for making defect and oxidation. OG is equalt to oxygen plasma treated graphene.

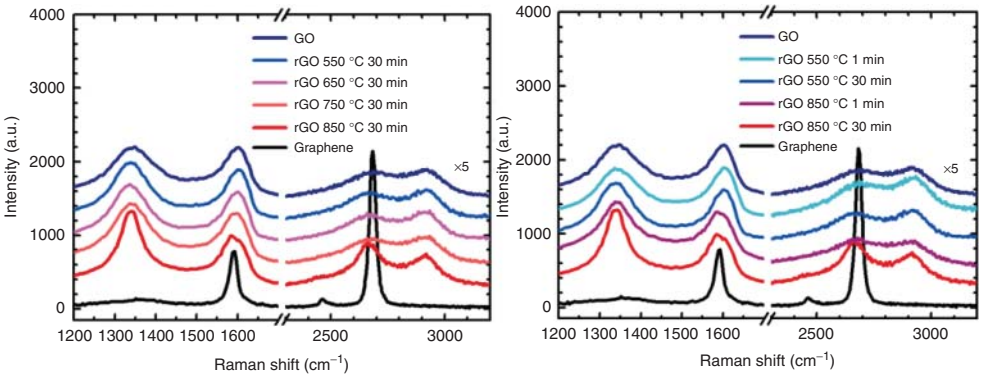

Figure 1.15 Raman spectra of thermally reduced graphene oxide.

the 2D peak dramatically increases, where the crystal structure of graphene is formed by reduction. Also, Raman data show the temperature-dependent, but time-independent reduction of GO.

The ultraviolet (UV)–visible absorption property of thermal rGO in Figure 1.16 shows what similar with the result of Raman spectra. First of all, the monolayer GO and rGO thin films were highly transparent, close to 99%, in the optical range of 1.5–5.5 eV. The transmission of more than 98% at 1.5 eV in rGO is fairly close to the corresponding value of 97.7% in graphene. When the GO is thermally annealed and the annealing rate getting increased, the rGO exhibits lower transmission of 96–98% and a dip in transmission at 4.55 eV. This dip feature at 4.55 eV clearly indicates the restoration of monolayer behavior in rGO as this feature matches the feature in the transmission spectrum of monolayer graphene grown by CVD. This is the same as predicted that the direct inter-band transition in graphene expected at 5.1 eV is smeared out by a strong electron–hole interaction, and the resulting resonant excitonic absorption causes a distinct absorption peak to appear at a redshifted energy of 4.55 eV. Therefore, from the absence and presence of this dip feature in GO and rGO, the restoration of monolayer behavior in rGO has been confirmed. Moreover, the peak for the resonant excitonic absorption becomes stronger and narrower with increasing annealing temperature. A systematic redshift in the absorption peak energy from 4.62 to 4.55 eV is also notable from the absorbance spectra. The 850 °C treatment appears to be the most effective in restoring monolayer-like behavior with its absorption peak energy matching that of monolayer graphene.

1.4.1.2 Absorption Property Plasma Defected Graphene

The oxygen plasma treatment on graphene causes disorder and a doping effect. OG processed by plasma oxidation has several distinct physical properties such as high transparency, low mobility, and a moderate free carrier density [12]. Optical properties in the visible region show the quantized universal absorbance $\pi e^2/\hbar c = 0.023$, where c, e, and $\hbar$ are the speed of light in vacuum, the electronic charge, and the reduced Planck constant, respectively. In the UV

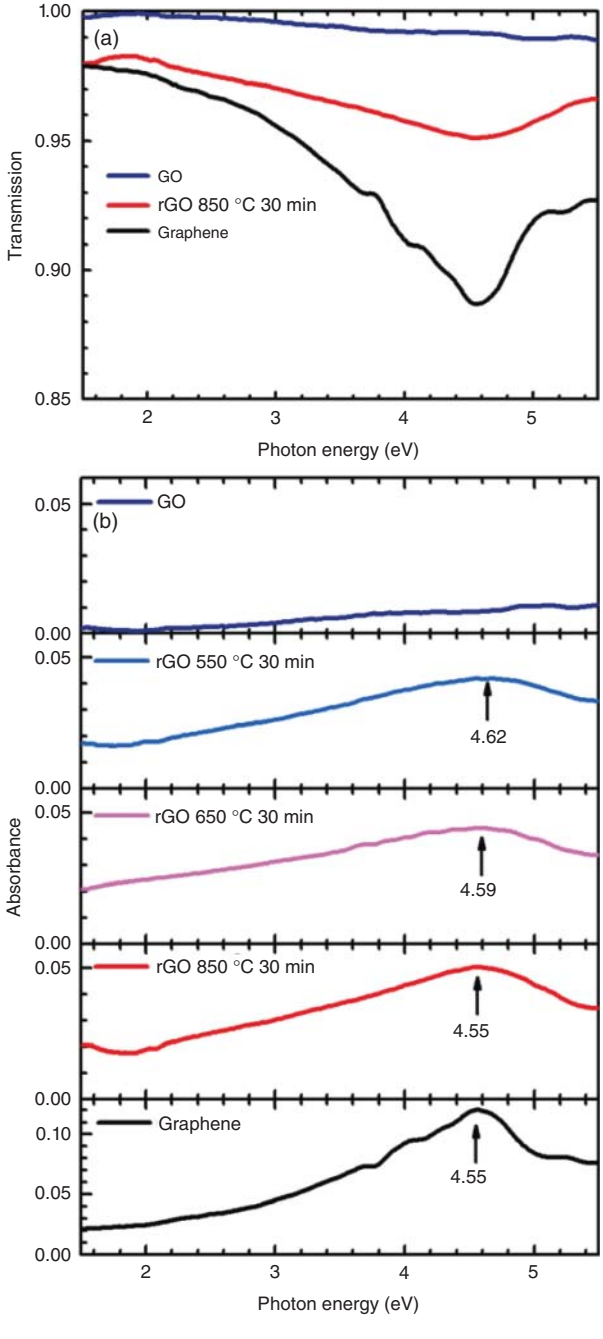

Figure 1.16 (a, b) Visible absorption spectra of thermally reduced graphene oxide.

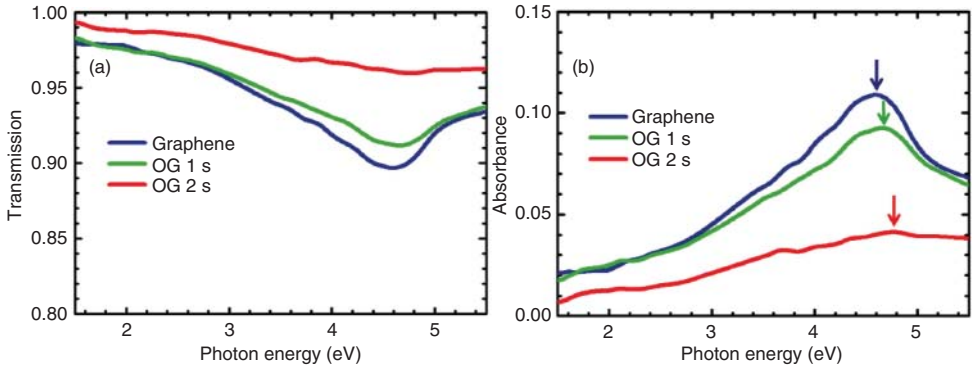

Figure 1.17 The transmission (a) and the absorbance (b) spectra of graphene and oxidized graphene, 1 s oxidization graphene (OG 1 s) and 2 s oxidization graphene (OG 2 s), in the visible and ultraviolet regions.

region, the electron–hole excitonic absorption at around 4.55 eV is one of the main characteristic features of graphene.

In Figure 1.17a, the transmission spectra of graphene and OG in the visible and UV region are compared with the oxidation time. The transmission of OG 1 s is not much different from that of graphene; in contrast, for OG 2 s, the transmission closer to 100% is higher than that of graphene in the visible range. The increase of transmission with the oxidation process is due to a free carrier density decrease and a metal–insulator transition. The result is consistent with the redshift of the Raman G peak and weakened electron–hole excitonic peak resonance in the UV region in Figure 1.17b.

The free carrier dynamics and a metal–insulator transition are well noticed in the terahertz region. Figure 1.18a shows the terahertz time-domain electric field amplitude through vacuum, a fused silica substrate, the graphene film, and the OG films on a fused silica substrate. The time delay compared to that in vacuum

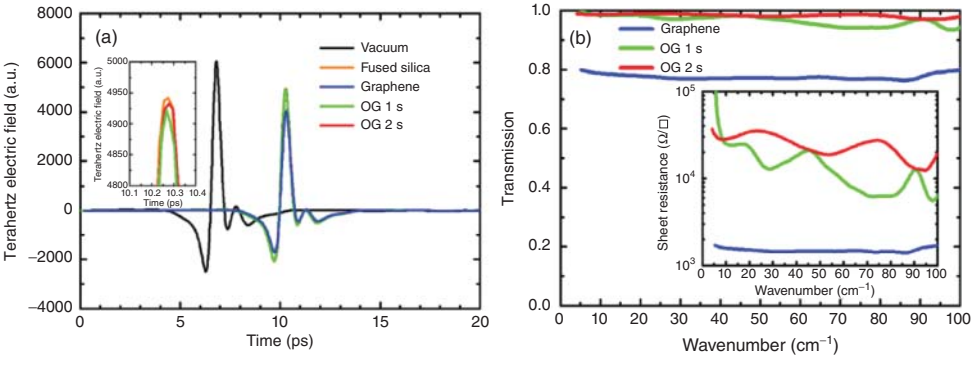

Figure 1.18 Terahertz time-domain electric field (a, main), enlarged terahertz pulse peaks (a, inset), transmission spectra (b, main), and calculated optical sheet resistances (b, inset) of graphene and oxidized graphene in the terahertz region.

is related to their real part of the refractive index and thickness. Furthermore, the terahertz pulse peaks show an amplitude increase due to plasma oxidation. Figure 1.18b shows the transmission spectra (main) and the calculated sheet resistance (inset) of graphene and the OG films. The transmission spectra in the terahertz region shows a free carrier density decrease and again consistent with previous transmission changes in the visible and UV range. The optical sheet resistance $\rho(\omega)$ is obtained from the absorbance $A(\omega) = (4\pi/c)/\rho(\omega)$. The transmission (close 100%) and optical sheet resistance of OG 2 s are higher than those of OG 1 s and of graphene in the terahertz range. The increase in the optical sheet resistance with the oxidation process is again related to a metal–insulator transition. The decrease in the free carrier density directly leads to an increase in DC resistivity. The transparent OG with tunable sheet resistance can be thus conveniently fabricated from our graphene by plasma oxidation, as confirmed by visible–UV and terahertz spectroscopy results.

1.4.2 PL Property Modification of Graphene

1.4.2.1 PL Properties of Oxygen Plasma Treated Graphene

The oxygen plasma treatment to GO causes not only the defect on graphene but also the change in distributions in oxygen functional groups: epoxy to carbonyl. By this physical property modification, the PL spectra becoming redshifted depends on the plasma pressure [66]. Figure 1.19 shows Raman analysis. The GO-1 is pristine GO, and as it becomes GO-4, the oxygen pressure increases. Raman spectra of all disordered carbons are dominated by the relatively sharp G and D features of the sp^2 sites. Also, the G and 2D peaks represent the E_{2g} vibrational and out-of-plane modes within aromatic carbon rings. Due to the oxygen plasma treatment, the intensity of the D peak increases compared to the G peak intensity. The prominent D peak in the Raman spectra is from the structural imperfections created by the attachment of hydroxyl and epoxide groups on the carbon basal plane. This indicates the increased density of structural defects due to oxygen plasma treatment.

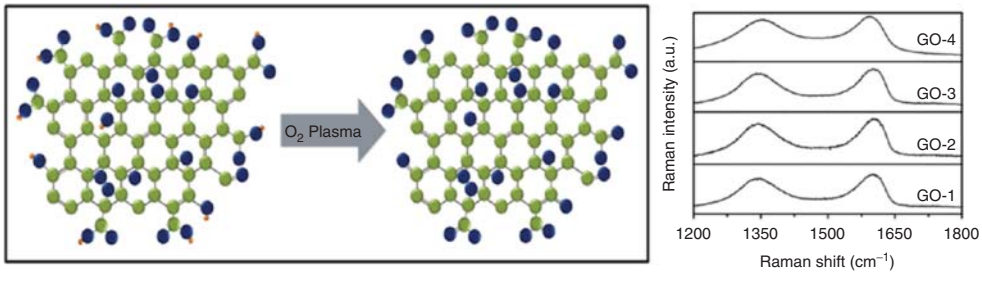

Figure 1.19 Oxygen functional group modification from epoxy to carbonyl and Raman spectra of oxygen plasma–treated graphene oxide dependent to oxygen pressure.

The PL emission spectra of the GO film, showed in Figure 1.20, presents the wavelength of 487 nm where they remain almost constant with plasma treatment with 200 nm excitation. However, as the oxygen plasma treated to GO thin films, the shoulder peak at 530 nm disappears gradually with increasing oxygen pressure (from left to right) and resulting in a much broad emission. The emission intensity of higher wavelength emission (550–650 nm) from the graphene decreases considerably by oxygen plasma treatment.

This results are considerable with the XPS analysis in Figure 1.21 present that it is clear that when oxygen pressure increases sp^3 hybridization increases due to the incorporation of oxygen resulting in O–C–O, C═O, and O–C═C linkage. The epoxy and carbonyl groups usually induce non-radiative recombination of localized electron–hole (e–h) pairs, which leads to the non-emissive property of GO. The oxidation increases reactive sites such as epoxy and carbonyl groups and hence decreases the emission efficiency of the sp^2 domains on GO nanosheets. Moreover, XPS analysis shows that as oxygen pressure increases carbonyl groups increase. For oxygen-treated films it can be inferred that due to the presence of an increased number of carbonyl groups, most of the electrons excited to the high levels relax non-radiatively, which decreases the PL emission in higher wavelength region. Moreover, for these samples, the nonuniformity of graphene edges and the potential for dangling bonds are thought to have significant influence on their chemical properties and reactivity, which may also decrease the PL emission in the higher wavelength region.

1.4.2.2 Substrate Effect

Optical and structural properties of GO are varied with the changes of substrates. Substrates significantly influence the properties because the interaction between substrate and GO modifies the electron band structure [19]. Graphene is semimetallic since its HOMO and LUMO are in contact, resulting in the zero band gap material [67]. However, graphene on a SiC substrate shows a band gap of around 0.26 eV possibly due to the interaction of a substrate. The presence of oxygen-related functional groups increases the possibility of reactivity. If graphene and their substrates have interactions yield band gap then its applications in transistor or optoelectronic devices could considered due modified band structures. In this section, we will compare four types of fabricated devices; G1 for GO/Au NPs/quartz, G2 for GO/ITO/glass (indium tin oxide), G3 for GO/quartz, and G4 for GO/SiO_2/Si. We can confirm that GO has different types of oxygen-related functional groups by EELS analysis. The peak at 285 eV reveals that the 1s for carbon to the π^* state transition exists in the range of carbon K-edge spectrum, and the peak at 291 eV represents 1s for carbon to the σ^* state transition within the same ranges. The peak of 539.7 eV within the range of oxygen K-edge spectrum means that higher-order π^* resonance of every oxygen and σ^* resonance of the 1,2-epoxy linkage exist [68]. Around 200 nm absorption peak of UV–visible are exhibited on every sample corresponding to π–π^* transition attributed to carbon bonding in aromatic sp^2 clusters. There are some variations of UV–visible spectra in all samples due to changes of linkages with epoxide and

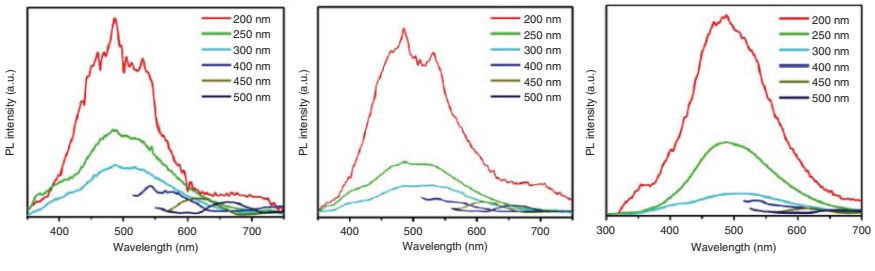

Figure 1.20 Oxygen plasma–dependent PL property modification of graphene oxide.

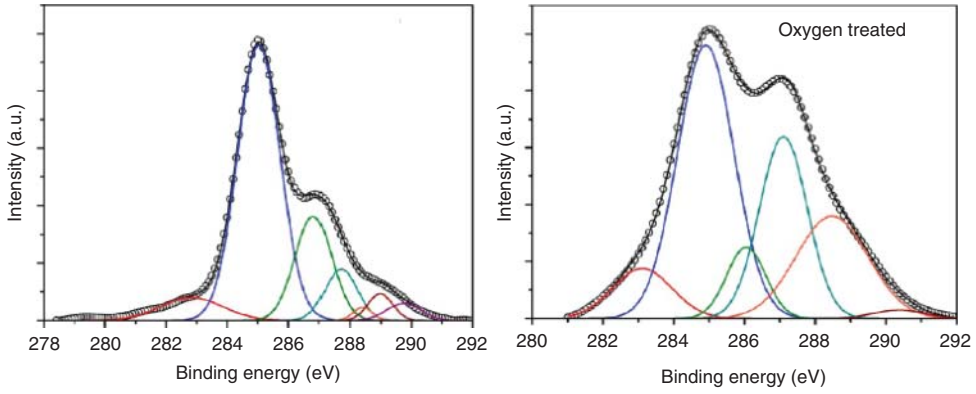

Figure 1.21 XPS analysis of graphene oxide with oxygen plasma treatment.

peroxide. There is an extra peak around 420 nm with the G1 because gold NP generates surface plasmon resonance affecting additional absorption. Also, G1 shows almost a constant value of absorption in the whole visible range. Therefore, substrates are enough influential to the absorption value, which correspond to the band gap. G2 shows almost absent value of Fourier transform infrared (FTIR) peak around 1600 cm^{-1} for carboxyl group vibration and 1726 cm^{-1} for C═O stretching vibration related to carbonyl and carboxyl groups [69]. Compared to normal GO having ~10.5° ($d = 0.83$ nm) measured by XRD, G2 shows 24° ($d = 0.36$ nm) due to a low number of oxygen functional groups, while G4 has a peak of 11.26° ($d = 0.789$ nm) originated from the diffraction plane (002) in agreement with the FTIR spectrum [63]. Also, the D band of Raman shift can present oxygen functionalities in different films because of the band related with oxygen content in GO. Gold NPs act as a hot spot generating localized surface plasmon polariton, which leads to the changes of lattice parameter resulting in shift of G and D bands. The XPS spectrum specified with C1s shows how much oxygen functionalities exist in the films. As of the same results of the previous measurement, G2 shows the lowest peak ratio of 286.2 eV for O–H/O–C–O and 288.4 eV for C═O since oxygen atoms are transferred from GO to ITO. Also, the indium XPS spectrum shows that the peak for $3d_{5/2}$ moves higher after treated with oxygen plasma (443.7 – 444.02 eV) and the results of shift happens with respect to the work functions. Thus, GO is reduced when it is deposited on ITO substrates. G3 shows a lower intensity value of peak at around 286.2 eV for O–C–O than G1 and G4 because the number of epoxide linkage is small. In the XPS of G1, there are additional peaks; 285.4 eV for defected sp^2 and 283.9 eV for Au–C hybrid bond. The defected peak position affects the overall peak of XPS in binding energy according to carbon atoms out of sp^2 configuration. Thus, gold NP makes delocalized bond to localize in it, resulting in the disorder of sp^3. Since GO is composed of sp^2 clusters in sp^3 matrix, quantum confinement opens the band gap at the K-point. This is related to the oxygen functionalities that make the HOMO levels lower. Those samples show similar PL peaks of 495, 540, and

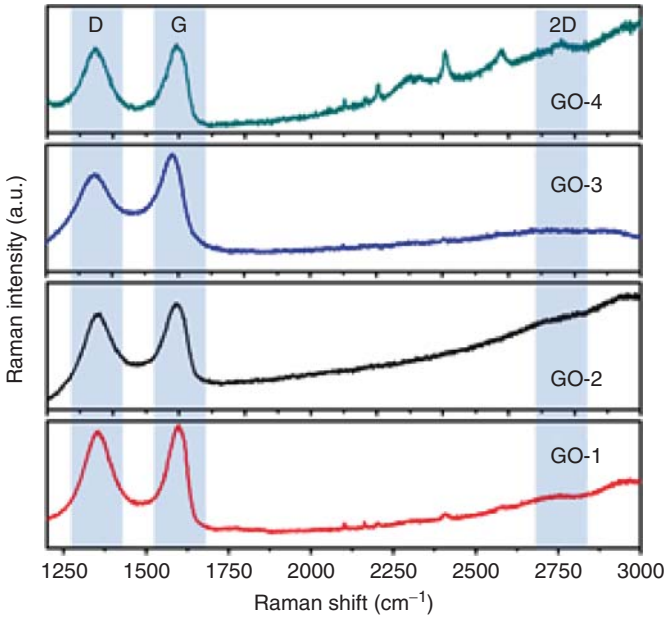

Figure 1.22 Raman spectra of graphene oxide films (GO-1, GO-2, GO-3, and GO-4).

650 nm corresponding to the size of clusters (1.2, 1.3, and 1.4 nm, respectively). For getting information for the substrate effect on Raman spectra, Raman analysis of GO films coated on different substrates are presented in Figure 1.22. The films are named as GO-1 (GO/Au/quartz), GO-2 (GO/ITO/glass), GO-3 (GO/quartz), and GO-4 (GO/SiO_2/Si). GO-2, GO-3, and GO-4 films show spectral features, called G around 1590 cm^{-1}, D ~1350 cm^{-1}, and 2D at ~2697 cm^{-1}. But for GO-1 (GO/Au/quartz) film G band, D band, and 2D band positions are found to be 1579, 1339, and 2709 cm^{-1}, respectively. G band, G0, and 2D band positions are almost constant for GO-2, GO-3, and GO-4 films with a slight variation in D band nature. Since D band depends on the oxygen content in GO, this could be due to the changes in oxygen functionalities in different films. But for GO-1 (GO/Au/quartz) film G band, D band, and 2D band positions vary strongly compared to other films. The changes in these band positions are interpreted as the local field enhancement in the nanostructure of the gold-coated quartz substrate. There is a possibility of the generation of local field at the contact areas of the two structures by coupling the localized surface plasmon of the gold NPs with the surface plasmon polariton of the graphene film, which leads to the changes in the graphene lattice parameter with the corresponding G and D peak shifts. The graphene–gold bond is covalent in nature; such bonding would change its lattice constant as well as the electronic properties. Also, there is a possibility that the lattice mismatch between the graphene lattice and the interfacial gold layer may cause a compressive stress on graphene; hence the shift of the G band Raman peak frequencies. The

relation introduced for point-like defects in nanocrystalline graphene established that I_D/I_G varies inversely with the distance of an average distance between defects (L_D) $\frac{I_D}{I_G} = \frac{C(\lambda)}{L_D^2}$. Where, C is variable depend on wavelength. With an increase of the ID/IG ratio, there is an increase of the crystallite boundaries and a reduction of the crystallite size. But Ferrari reported that Tuinstra–Koenig relation is not valid above a critical defect density where the cluster size (La) of sp^2 is smaller than 2 nm; the ID/IG ratio increases with the number of aromatic rings, opposite to what is expected from the Tuinstra–Koenig Relation. For La below about 2 nm, they proposed a second amorphization stage and according to the phenomenological model for this stage, the ratio decreases as the crystallite size is reduced: $ID/IG = C'La^2$, where $C = 0.0055$ and La in angstroms. In the first stage, the increase of the ID/IG ratio indicates an increase in the disorder, while in the second stage, the increase of the ID/IG ratio indicates a decrease in the disorder.

A different size of cluster shows different PL emission because the amount of delocalized orbital. G1 shows different dominant peak positions of 435 and 450 nm. The d orbital of Au and π orbital of aromatic carbon has interactions, effecting on defected sp^2 hybridized carbon atoms of band structure. The interaction modifies the band structures related with Fermi level, electron phonon coupling. Thus, GO films on different substrates vary the optoelectronic properties such as PL and absorption related with band structures. The substrates affect tremendously the structural and optical properties such as interlayer spacing, sp^2 cluster confinement changes, and band structure. The blueshift of PL emission is shown in gold buffers between GO and the substrate with respect to generating defected sp^2 sites. The luminescence emission of films at various excitations ranging from 200 to 450 nm for GO films coated on different substrates are shown in Figure 1.23 and inset of Figure 1.23c shows emission from GO solution. The films are named as GO-1 (GO/Au/quartz), GO-2 (GO/ITO/glass), GO-3 (GO/quartz), and GO-4 (GO/SiO_2/Si). Figure 1.22 shows the emission from substrates (Au/quartz, ITO/glass, SiO_2, quartz), which is also shown for reference.

The schematic representations of band level diagram of corresponding films are shown in Figure 1.24. GO-2, GO-3, and GO-4 (GO/SiO_2/Si) films show almost a similar PL emission behavior with the peak emission corresponding to around 495 nm (2.5 eV marked as γ), 540 nm emission (around 2.3 eV, marked as δ), and 650 nm emission (around 1.9 eV, marked as ϕ) in Figure 1.24a,b. In addition to these emissions, the GO-1 (GO/Au/quartz) film shows emission peaks around 435 nm (2.83 eV, marked as α), 450 nm (2.74 eV, marked as β), and 580 nm (2.13 eV, marked ε) in Figure 1.24d,e,f. The average cluster size of around 1.2 nm corresponds to an emission around 495 nm (2.5 eV marked as γ); the larger clusters (1.3 nm) give 540 nm emission (around 2.3 eV, marked as δ) and much larger clusters (1.4 nm) result 650 nm emission (around 1.9 eV, marked as ϕ) in Figure 1.24a and 3.11b. Emissions around 425 and 350 nm correspond to emission from substrate (marked as "s" in Figure 1.24a). sp^2 clusters of different size ranges release excitation-dependent emission. At 200 nm excitation, emissions from all clusters are observed resulting in a broad emission ranging from 400 to 600 nm. However,

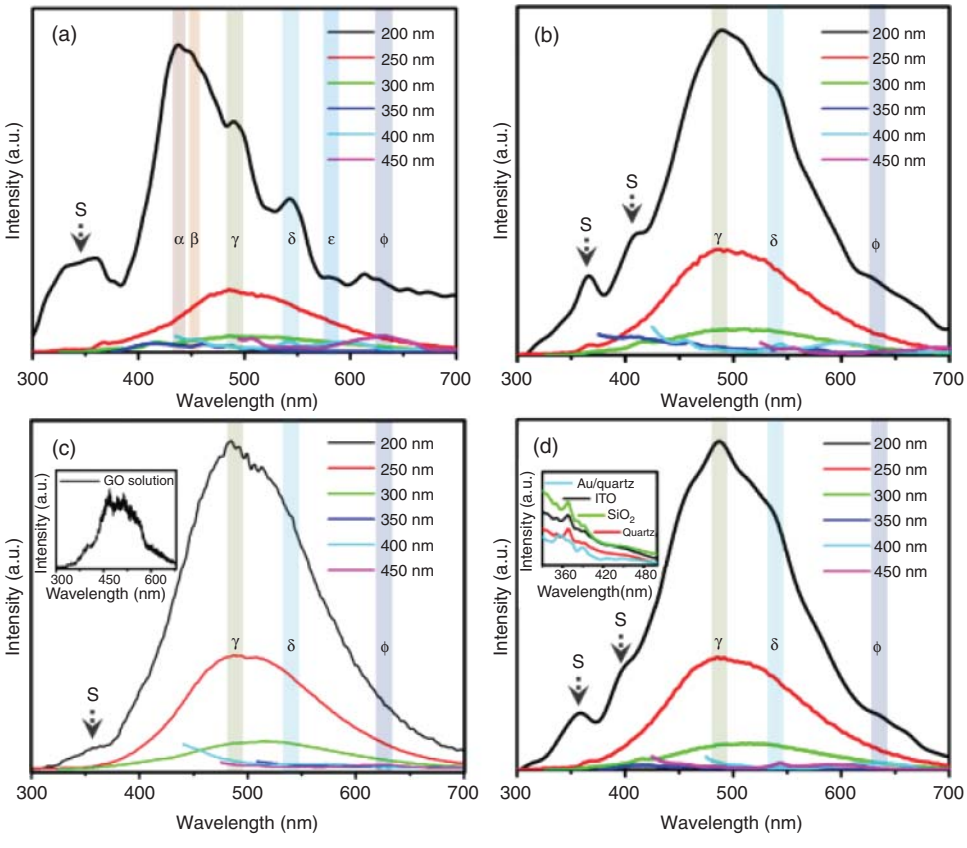

Figure 1.23 PL spectra of graphene oxide films (a) GO-1, (b) GO-2, (c) GO-3, and (d) GO-4 showing excitation-dependent PL emission. Inset of (c) shows emission from GO solution, Inset of (d) shows emission from substrates (Au/quartz, ITO/glass, SiO_2, quartz).

when excited using higher wavelength, radiation emission from selected clusters (large clusters) are only observed. This may be the reason for reduction of PL emission intensity in higher excitation wavelengths. Attractive interaction between the d-orbital's of gold atoms and the π-orbital of the sp^2-hybridized carbon atoms can create some defected sp^2 levels, which results in some additional localized energy level in π*, which accounts for the variation in PL emission when compared to other films. In the Au/quartz film, the observed peaks in Figure 1.24a are around 435 nm (2.83 eV, marked as α), 450 nm (2.74 eV, marked as β), 495 nm (2.5 eV, marked as γ), 540 nm (2.3 eV, marked as δ), 580 nm (2.13 eV, marked as ε), and 650 nm (1.9 eV, marked as ϕ). These transitions are shown in Figure 1.24b.

1.4.2.3 Pd Grafted Graphene Oxide

In order to apply graphene for the application of electronic and optoelectronic devices, graphene overcomes its limitations attributed from the lack of a band gap.

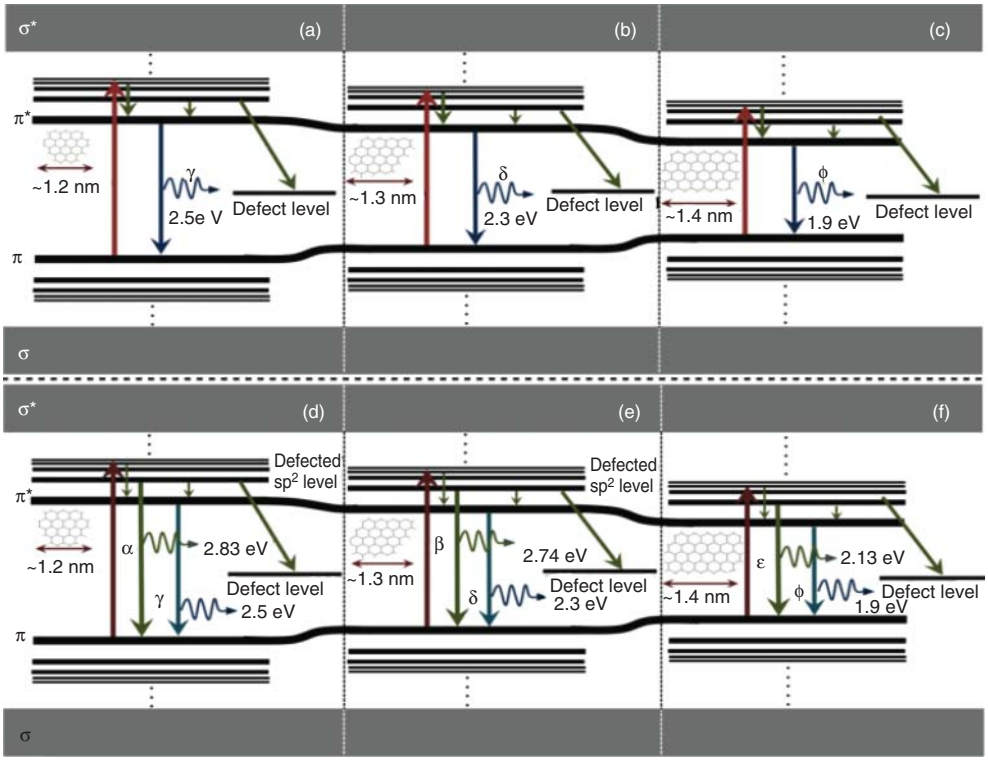

Figure 1.24 (a–f) Schematic representation of band level diagram of GO for GO-1, GO-2, GO-3, and GO-4 films.

As modification methods, many research groups have been studying optoelectronic properties of GO functionalized with NPs of metal or semiconductors such as TiO_2, Co_3O_4, Pt, Pd, Ag, and Au. Various application fields including optics, electronics, catalysis, and sensors are adopted graphene-based matrix mixed with NPs mentioned above. Confined electrons in localized sp^2 orbital affect the optical properties of GO such as optical absorptions and broadband fluorescence in the spectral region from UV to near infrared. Remarkable physical and chemical properties of palladium and palladium oxide attract tremendous attention in transition metal and metal oxide dopant application respectively. Particularly, applications in sensors and optoelectronic devices are possible because of its catalytic properties as well as the composite structure of graphene-supported palladium [13]. Similar spacing in both carbon aromatic structure in graphene (0.246 nm) and interlayer of palladium (0.225 nm) is evidence that composite structure is possible. Palladium grafting affects photoluminescent property since it regulates the reduction of GO. Pristine GO has more structural defects than GO and rGO is obtained from bonding with oxygen and carbon atoms, transforming orbital to sp^3. EELS shows that the absorption peak of 536.7 eV is detected due to the resonance of epoxide bond, which appears to be σ^*

and higher-order π*. Ungrafted GO emits yellow-green PL from defect-trapped excitons. As the annealing process progressed, the restoration rate increased resulting in the decrease of yellow-green PL and increase of blue PL. FTIR spectra of GO shows that decrease of peak (1730 cm^{-1}) correspond to carbon and oxygen double bonds with respect to annealing. The sp^2 site originating blue PL emission increases when GO is reduced. The annealing process, that is, thermal heating in low pressure Ar environment condition results in the elimination of functional groups; as a consequence, sp^3 transforms to sp^2 clusters. The role of palladium decorating GO for PL emission was investigated, and various measurement techniques were used to analyze the origin of PL emission. Palladium enhances the probability of reduction since palladium acts as a reducing agent, increasing the C═C–C aromatic ring vibration. Also, sp^2 fractions are enhanced compared to pristine GO due to the synthesis of palladium oxide, and further annealing affects strongly the increase of the restoration rate related to the blue PL emission. The tailoring effects of palladium are confirmed with various measurement techniques such as XPS, Raman, EELS, UV–visible absorption, FTIR, and so on. Compared to interplanar distance of pristine GO, palladium grafted GO shows a larger value of lattice spacing due to the presence of palladium identified as (002) reflections. Transitions from the 1s to σ* due to palladium changes peak position of EELS corresponding to the carbon K-edge region, and palladium generates a peak of its M 4,5 edge. The peak intensity of FTIR shows that positions of 1050, 1100, and 1200 cm^{-1} correspond to a single bond of carbons, single bond of carbon and oxygen, and C–O–C stretching vibration respectively are equally dominant before annealing in grafted samples. As annealing temperature increases, C–C stretching vibration peak (1050 cm^{-1}) gets intensive. In the case of ungrafted GO, it also shows similar tendency of peak intensity in annealing, but dominant intensity increase rate is lower than grafted GO. With the XPS spectrum, carbon and oxygen-related functional groups of GO can be detected clearly. Since the aromatic bonding of carbon is dominant, the most intensive peak is positioned at 284.6 eV rather than any other peaks such as 286.2 eV for O–H/O–C–O, 287.8 eV for C═O, 288.5 eV for O–C═O, and 289.3 eV for carboxyl group. Thus, as the annealing temperature increases, the relative intensity of 284.8 eV increases because of restoration in sp^2 clusters from sp^3 sites. Comparing both pristine and grafted GO with the XPS spectrum, the restoration rate of palladium grafted GO is higher than pristine GO. In agreement with the above measurement, UV–visible absorption shows broad peaks related to the π–π* transition in various sized clusters of sp^2 ranging from 240 to 260 nm. Also, the range of 295–305 nm related to n to π transition with respect to the linkage of epoxide (C–O–C) and peroxide (R–O–O–R). Also, the overall range of visible absorption is enhanced as sp^2 clusters increases with respect to reduction, and grafted GO shows that it absorbs a visible range relatively more than pristine GO. Thus, we can infer that palladium acts as a reducing agent. The conjugation electron within the GO increases as oxygen extracted from functional groups, resulting in the restoration of aromatic sp^2. Since palladium grafting affects the alternation of bonding alternating between single and double bond of carbon

within the sp^2 network, palladium-grafted samples show extra peaks related to the combination modes of phonons for in-plane transverse optical (iTO) and in-plane transverse acoustic (iTA) around K-point (2300 cm^{-1}) and an overtone away from the K-point (2400 cm^{-1}). With those investigations, the structural changes are demonstrated, and effects on band structures are strongly related with PL emissions. Palladium on GO sheets tailors photoluminescent property and annealing effects, which also related to PL emission. The area of sp^2 clusters increases related to the $\sigma-\sigma^*$ band when palladium is decorated on GO. PL peaks are emitted around 465 and 485 nm are enhanced when palladium is grafted on increasing the annealing temperature. With the results of XPS, Raman, UV–visible investigations, we can infer that those blue PL (465 and 485 nm) is attributed to sp^2 clusters with an area of a different size. Also, the decrease of yellow-green emission with reduction reveals that the peak is originated from the defect site. Moreover, the quenching effect is stronger when palladium is grafted on GO. The PL emission (Figure 1.25) consists of peaks around 465, 485, 505, and 536 nm. All films (GOPd and GO) show the peak emission around 465 nm (~2.66 eV marked as α) and 485 nm (2.5 eV marked as β), attributed to radiative recombination of electron–hole pairs (e–h pairs) generated within localized $\pi-\pi^*$ states (schematically shown in Figure 1.26).

Peak emission around 505 nm (2.44 eV, marked as γ) and 530 nm (2.32 eV, marked as δ) corresponds to emission from defect states due to oxygen functionalities as schematically shown in Figure 1.26a–e. The presence of oxygen functionalities may give rise to defect states in the $\pi-\pi^*$ gap. Thus, in GOPd and GO films, the γ and δ peak emission intensity get reduced with the annealing temperature. With annealing, defect density reduces due to the removal of oxygen functionalities and thereby reducing the intensity of γ and δ peaks (Figure 1.25b). Also PL emission intensity from annealed GOPd films (GOPd-3 and GOPd-4) is lower when compared to annealed GO films (GO-3 and GO-4). This could be

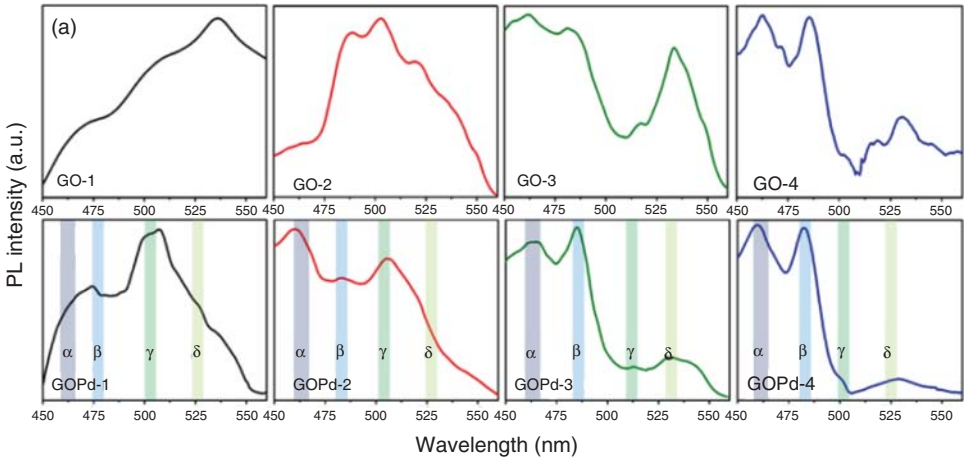

Figure 1.25 PL emission spectra of (a) Pd grafted and (b) ungrafted GO films.

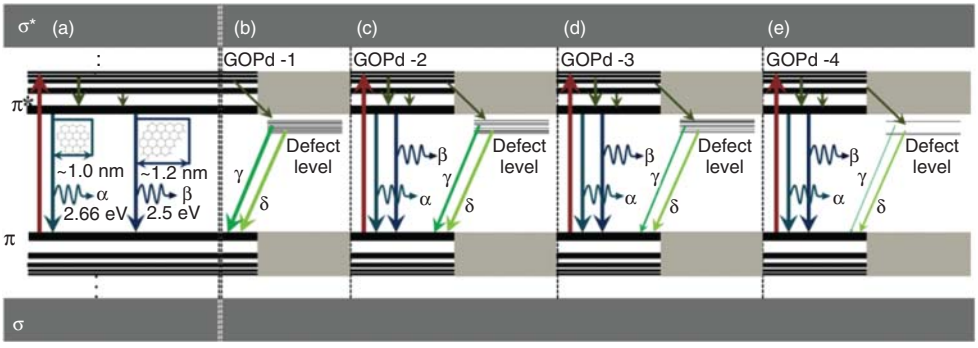

Figure 1.26 (a–e) Schematic representation of band level diagram of GOPd films.

due to the decrease in defect density in GOPd films compared to GO films. As reduction of GO increased (GOPd-4), yellow-green emission (γ, δ) decreased and blue PL became the prominent emission. Since the restoration of electronic conjugation is happening in graphene with reduction, the blue PL emission is expected to originate from sp^2 clusters and the yellow-green PL from trapped states. Irregular PL spectra suggest that trapped states influence the emission spectra. In GOPd film, with annealing temperature, the blue emission is enhanced while the green-yellow emission intensity is reduced. Even though the quenching of green-yellow emission was also observed in ungrafted films, quenching was more prominent in annealed grafted films.

1.5 Optoelectric Application of Graphene

Massless electrons behave as Dirac fermions, with a linear energy–momentum relation [70–72], on the bi-dimensional structure of graphene. As a result, electronic properties of graphene is arisen from a two-dimensional gas of charged particles derived by the relativistic Dirac equation. Carriers mimicking particles are with zero effective mass and the Fermi velocity of electron is $10^6\,m\,s^{-1}$ [71, 72]. The mobilities of graphene, up to $10^6\,cm^2\,V^{-1}\,s^{-1}$, are reported in suspended samples. Graphene is a potential material for nanoelectronics, particularly high frequency, by combining with near-ballistic transport at normal ambience [73].

Graphene also exhibits extraordinary optical properties. It can be transparent although being a single atom level thickness [74, 15, 75]. The linear dispersion relationship with Dirac electrons leads widespread applications in photonics. Saturable absorption is a remarkable characteristic of graphene as a consequence of Pauli blocking [76]. Nonequilibrium carriers in graphene cause hot luminescence [77]. Graphene can also produce the PL by chemical and mechanical treatment. Graphene is a prime candidates for photonic and optoelectronic applications

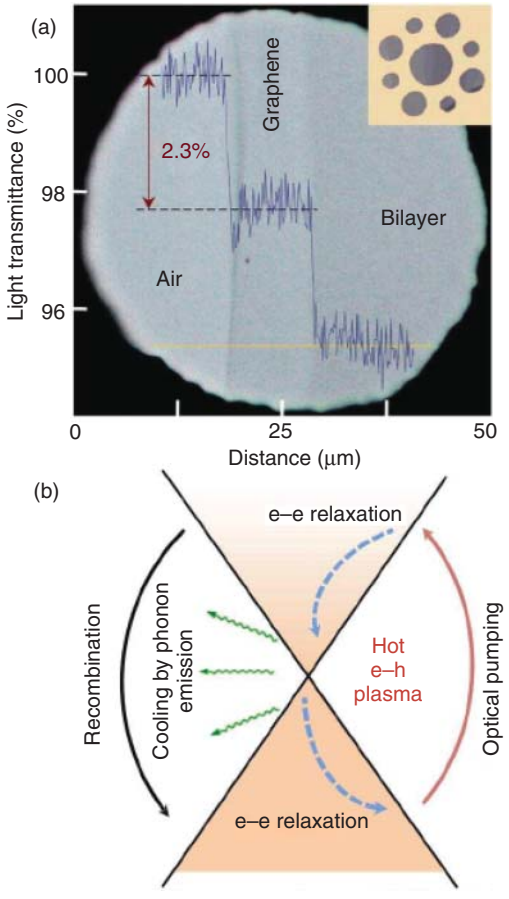

Figure 1.27 (a, b) Transmittance for increasing number of layers. Schematic of photoexcited electron kinetics in graphene, with possible relaxation mechanisms for the nonequilibrium electron population.

thanks to unique physical properties such as light transmittance and small band gap with dirac point [21, 78] (Figure 1.27).

Low-sheet resistance R_s and high transparency is required for optoelectronic devices such as displays, touch screens, light-emitting diodes, solar cells. For a rectangle of length L and width W, the resistance R is:

$$R = \frac{\rho}{d} \times \frac{L}{W} = R_s \times \frac{L}{W}$$

In a thin film $R_s = \rho/d$, where d is the film thickness and $\rho = 1/\sigma_{dc}$ is the resistivity. The number of squares of side W that can be covered on the resistor without overlapping can be seen as the term L/W.

Semiconductor-based transparent materials [79] for electrode are various: zinc oxide (ZnO) [80], doped indium oxide (In_2O_3) [81], tin oxide (SnO_2) [79], as well

as ternary compounds based on their combinations. The most famous material is a doped n-type semiconductor composed of In_2O_3 and SnO_2 with 9 : 1 proportion, called *indium tin oxide* (*ITO*) [79]. The impurities as Sn atoms acting as n-type donors effect on the electrical and optical properties of ITO considerably. ITO has ~80% transmittance and R_s as low as $10\,\Omega\,\text{sq.}^{-1}$ on glass, and $\sim 60-300\,\Omega\,\text{sq.}^{-1}$ on polyethylene terephthalate (PET) [82]. ITO undergoes critical limitations with cost from scarcity of Indium, processing requirements, difficulties in pattering, sensitivity to acidic and basic environments [79, 82]. Also, ITO is brittle and weak at external impulse; in addition, it can easily wear out if it is bending such as touch screens and flexible displays. For overcoming the disadvantages of ITO, metal grids [83], metallic nanowires [84], and other metal oxides [81–84] have been studied. Graphene and graphene-based materials exhibit the considerable performance for transparent conductor. Graphene films show much higher transmittance and wider useful wavelength range than single-wall carbon nanotube films, thin metallic films and ITO. In Figure 1.28, compared to several transparent conductor materials, transmittance and sheet resistance is described. The graphene is more transparent than any other materials for the widespread wavelength range. Sheet resistance is also lower and better than ITO, nanotube, and Ag nanowire mesh.

A photovoltaic device concerned with the solar cell, photo detector transfer energy from light to electricity [85]. The efficiency of energy conversion is defined by the ratio of maximum and incident power, $\eta = P_{max}/P_{in}$, where P_{max} is determined by voltage and current in circuit. Silicon with η up to ~25% is the dominant material for photovoltaic device [85, 86]. The use of polymers in Polymer-based organic photovoltaic cells is for light absorption with efficient charge transport. Even though polymer cells have lower η, they have the advantage of manufacturing economically compared to Si cells by a roll-to-roll process [87]. An organic photovoltaic cell is a transparent conductor used for a photoactive layer and the electrode. Dye-sensitized solar cells consist of a liquid electrolyte as a charge transport medium. As incoming light from outside, the dye molecules absorb the incident photon producing electron–holes pairs. The electrons are transported to the cathode. Dye molecules regenerate by absorbing electrons from a liquid electrolyte. Current the most well-known material is ITO used as photoanode and cathode with Pt coating. The optical properties of graphene can satisfy the requirements for photovoltaic devices. First, graphene is a transparent conductor, which is beneficial for window. Second, graphene is photoactive material due to unique dispersion relation between energy and momentum. Moreover, graphene has very high mobility and low effective mass of electron for charge transport. Lastly, graphene has a catalytic character to other material for fast interaction. The various photovoltaic device applications such as inorganic, organic, and dye-sensitized solar cell, organic light emitting device (OLED), photodetector are shown in Figure 1.29.

Electroluminescent material is needed for organic light-emitting device between two charge-injecting electrodes, and at least one of which is transparent [88]. The HOMO and the LUMO capture the hole and electron at the anode and cathode. This capturing process is connected to matching the work function

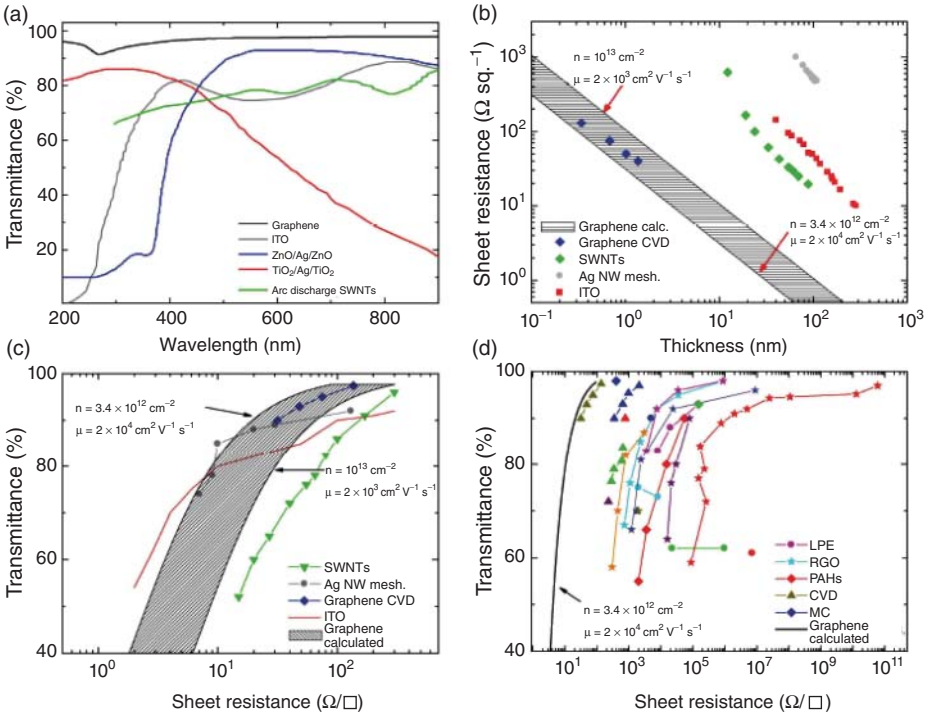

Figure 1.28 (a) Transmittance for different transparent conductors: GTCFs (Graphene-based transparent conductive film) 37, single wall carbon nanotubes (SWNTs) 73, ITO74, ZnO-Ag-ZnO75, TiO_2/Ag/TiO_2 76, where Agis silver and TiO_2 is titanium dioxide. (b) Thickness dependence of R_s blue rhombuses, roll to roll GTCFs37; red squares, ITO74; gray dots, metal wires74; green rhombuses, SWNT73. Two limiting lines for GTCFs are also plotted (hatched area), using typical values for n and μ. (c) Transmittance versus R_s for different transparent conductors: blue rhombuses, roll to roll GTCFs37; red line, ITO74; gray dot, metal wires74; green triangles, SWNTs73. Hatched area, limiting lines for GTCFs calculated using n and μ as in (b). (d) Transmittance versus R_s for GTCFs grouped according to production strategies: CVD35–37,77, micromechanical cleavage (MC)78, organic synthesis68, LPE (liquid-phase exfoliation) of pristine graphene42,43,47,78 or GO52,54,79–81. A theoretical line as for Equation 8 is also plotted for comparison.

of the anode and cathode. OLED have been explored a number of applications in ultrathin television and other display screens, for example, the monitor of computer and mobile phone. Because organic light-emitting devices have advantage of the low power consumption, high image quality and are possible to manufacturing ultrathin device. Similarly in other applications, ITO with 4.4–4.5 eV is mainly exploited material for display even though it has several limitations such as mechanical property, since ITO is brittle, and limited bending and cost issue [89]. Moreover, ITO has a tendency of diffusing into the active OLED layers, which result in a decline of performance over time. The graphene

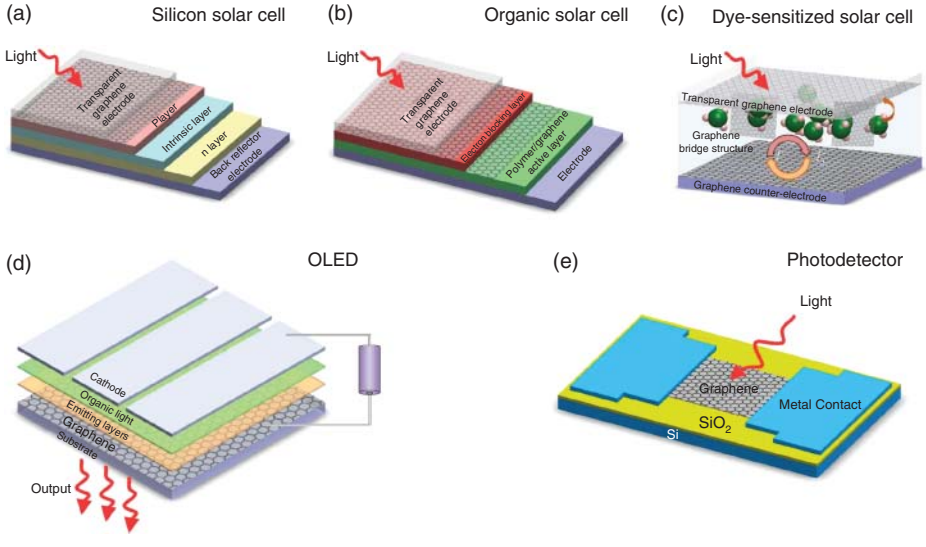

Figure 1.29 Schematic representation of (a) inorganic,(b) organic, and (c) dye-sensitized solar cell, (d) organic light emitting device (OLED), and (e) photodetector.

can alter ITO with 4.5 eV work function and easy to obtain as well as flexible mechanical property included in graphene. Figure 1.30 shows the expected OLED design with graphene without the diffusion problem.

The photodetective device measured photon flux or optical power by transferring the absorbed photon energy into electricity. Photodetectors has copious applications such as remote controls, DVD players, and so on [90]. The excited electrons by photon energy move from the valence to conduction band and electron–hole carries generate the electric current. The band gap limits absorption of light over broad wavelength range because the light with long-wavelength and low quantum energy cannot excite the electron. The graphene can deal with the light from UV to terahertz [91, 92]. Consequently, photodetector made of graphene could work through extensive range of wavelength. Furthermore, the response time of graphene is promising due to great mobility with zero effective mass.

Nonlinear optical and electro-optical properties are necessary for most photonic applications [93]. Laser manufacturers with laser sources providing nano- to sub-picosecond pulses handle with basic research, material processing, circuit board printing, as well as metrology and even eye surgery, and so on. Mode-locking is the most important technique of ultrafast laser systems, which needs the nonlinear optical elements, called *saturable absorber*. Saturable absorber converts the continuous wave beam into a sequence of ultrafast optical pulses [94]. The nonlinear materials require fast response time, strong nonlinearity, and wide useful wavelength range. In addition, in terms of manufacturer, the advantages are high-power handling, low-power consumption, cheap and easy ways of setting up the optical system. Presently, the dominant material of saturable absorber is made

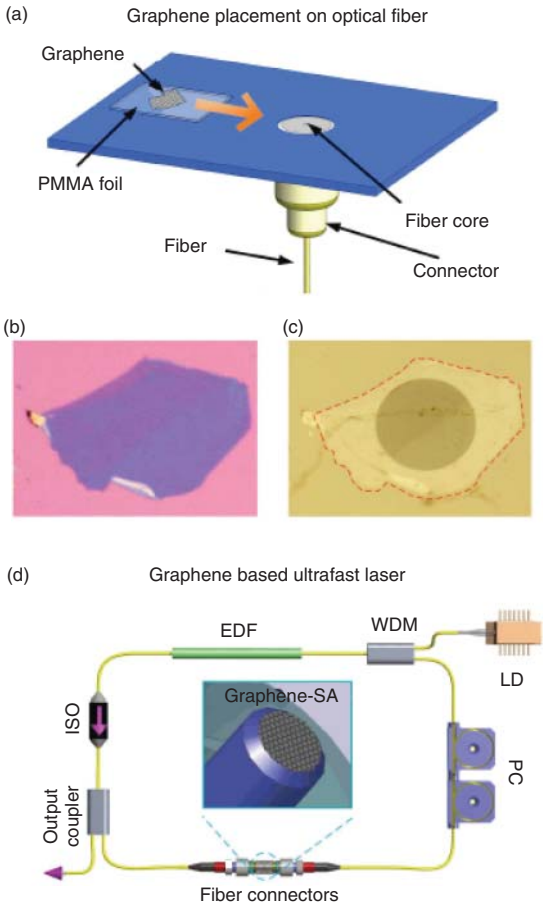

Figure 1.30 (a) An optical fiber is mounted onto a holder. Once detached from the original substrate, a polymer/graphene membrane is slid and aligned with the fiber core. (b) Flake originally deposited on SiO_2/Si. (c) The same flake after deterministic placement. (d) Graphene-mode locked ultrafast laser: a graphene saturable absorber is placed between two fiber connectors. An Erbium doped fiber (EDF) is the gain medium, pumped by a laser diode (LD) via a wavelength-division-multiplexer (WDM). An isolator (ISO) maintains unidirectional operation. A polarization controller (PC) optimizes mode-locking.

by semiconductor saturable absorber mirror. However, it has the disadvantages of tuning range, fabrication and packaging. First, single-wall nanotube was trying to replace the earlier material with low cost and possibility of operating wavelength by controlling of diameter [95]. Graphene can solve the problems of traditional materials (such as Silicon, CNTs etc.,) for the following reasons: Graphene has no restriction of operating wavelength and ultrafast carrier momentum. Compared to conventional materials with mirror or nanotube, it is not necessary to consider the band gap.

References

1. Schedin, F. *et al.* (2007) Detection of individual gas molecules adsorbed on graphene. *Nat. Mater.*, **6** (9), 652–655.
2. Lee, C. *et al.* (2008) Measurement of the elastic properties and intrinsic strength of monolayer graphene. *Science*, **321** (5887), 385–388.
3. Xiao, N. *et al.* (2011) Enhanced thermopower of graphene films with oxygen plasma treatment. *ACS Nano*, **5** (4), 2749–2755.
4. Eda, G., Fanchini, G., and Chhowalla, M. (2008) Large-area ultrathin films of reduced graphene oxide as a transparent and flexible electronic material. *Nat. Nanotechnol.*, **3** (5), 270–274.
5. Wu, Q. *et al.* (2010) Supercapacitors based on flexible graphene/polyaniline nanofiber composite films. *ACS Nano*, **4** (4), 1963–1970.
6. Novoselov, K.S. *et al.* (2004) Electric field in atomically thin carbon films. *Science*, **306** (5696), 666–669.
7. Obraztsov, A.N. *et al.* (2007) Chemical vapor deposition of thin graphite films of nanometer thickness. *Carbon*, **45** (10), 2017–2021.
8. Gattia, D.M., Vittori Antisari, M., and Marazzi, R. (2007) AC arc discharge synthesis of single-walled nanohorns and highly convoluted graphene sheets. *Nanotechnology*, **18** (25), 255604.
9. Hummers, W.S. Jr., and Offeman, R.E. (1958) Preparation of graphitic oxide. *J. Am. Chem. Soc.*, **80** (6), 1339.
10. Van Bommel, A.J., Crombeen, J.E., and Van Tooren, A. (1975) LEED and Auger electron observations of the SiC(0001) surface. *Surf. Sci.*, **48** (2), 463–472.
11. Wang, Z. *et al.* (2009) Direct electrochemical reduction of single-layer graphene oxide and subsequent functionalization with glucose oxidase. *J. Phys. Chem. C*, **113** (32), 14071–14075.
12. Choi, K. *et al.* (2013) Terahertz and optical study of monolayer graphene processed by plasma oxidation. *Appl. Phys. Lett.*, **102** (13), 131901.
13. Rani, J.R. *et al.* (2013) Controlling the luminescence emission from palladium grafted graphene oxide thin films via reduction. *Nanoscale*, **5** (12), 5620–5627.
14. Lim, J. *et al.* (2013) Terahertz, optical, and Raman signatures of monolayer graphene behavior in thermally reduced graphene oxide films. *J. Appl. Phys.*, **113** (18).
15. Nair, R.R. *et al.* (2008) Fine structure constant defines visual transparency of graphene. *Science*, **320** (5881), 1308.
16. Meyer, J.C. *et al.* (2007) The structure of suspended graphene sheets. *Nature*, **446** (7131), 60–63.
17. Tung, V.C. *et al.* (2009) High-throughput solution processing of large-scale graphene. *Nat. Nanotechnol.*, **4** (1), 25–29.
18. Ferrari, A.C. *et al.* (2006) Raman spectrum of graphene and graphene layers. *Phys. Rev. Lett.*, **97** (18), 187401.
19. Rani, J.R. *et al.* (2013) Substrate and buffer layer effect on the structural and optical properties of graphene oxide thin films. *RSC Adv.*, **3** (17), 5926–5936.
20. Bao, Q. *et al.* (2010) Graphene-polymer nanofiber membrane for ultrafast photonics. *Adv. Funct. Mater.*, **20** (5), 782–791.
21. Gokus, T. *et al.* (2009) Making graphene luminescent by oxygen plasma treatment. *ACS Nano*, **3** (12), 3963–3968.
22. Bostwick, A. *et al.* (2008) Photoemission studies of graphene on SiC: growth, interface, and electronic structure. *Adv. Solid State Phys.*, **47**, 159–170.
23. Virojanadara, C. *et al.* (2008) Homogeneous large-area graphene layer growth on 6H-SiC(0001). *Phys. Rev. B: Condens. Matter*, **78** (24), 245403.
24. Sutter, P.W., Flege, J.I., and Sutter, E.A. (2008) Epitaxial graphene on ruthenium. *Nat. Mater.*, **7** (5), 406–411.
25. N'Diaye, A.T. *et al.* (2008) Structure of epitaxial graphene on Ir(111). *New J. Phys.*, **10**.
26. Otero, G. *et al.* (2010) Ordered vacancy network induced by the growth of epitaxial graphene on Pt(111). *Phys. Rev. Lett.*, **105** (21), 216102.
27. Regan, W. *et al.* (2010) A direct transfer of layer-area graphene. *Appl. Phys. Lett.*, **96** (11), 113102.
28. Green, A.A. and Hersam, M.C. (2009) Solution phase production of graphene

with controlled thickness via density differentiation. *Nano Lett.*, **9** (12), 4031–4036.
29. Ziambaras, E. *et al.* (2007) Potassium intercalation in graphite: a van der Waals density-functional study. *Phys. Rev. B: Condens. Matter*, **76** (15), 155425.
30. McAllister, M.J. *et al.* (2007) Single sheet functionalized graphene by oxidation and thermal expansion of graphite. *Chem. Mater.*, **19** (18), 4396–4404.
31. Stankovich, S. *et al.* (2007) Synthesis of graphene-based nanosheets via chemical reduction of exfoliated graphite oxide. *Carbon*, **45** (7), 1558–1565.
32. Compton, O.C. *et al.* (2010) Electrically conductive "alkylated" graphene paper via chemical reduction of amine-functionalized graphene oxide paper. *Adv. Mater.*, **22** (8), 892–896.
33. Chandra, V. *et al.* (2010) Water-dispersible magnetite-reduced graphene oxide composites for arsenic removal. *ACS Nano*, **4** (7), 3979–3986.
34. Zhu, X. *et al.* (2011) Reduced graphene oxide/tin oxide composite as an enhanced anode material for lithium ion batteries prepared by homogenous coprecipitation. *J. Power Sources*, **196** (15), 6473–6477.
35. Wu, Z.S. *et al.* (2012) Graphene/metal oxide composite electrode materials for energy storage. *Nano Energy*, **1** (1), 107–131.
36. Feng, H., Li, Y., and Li, J. (2012) Strong reduced graphene oxide-polymer composites: hydrogels and wires. *RSC Adv.*, **2** (17), 6988–6993.
37. Bai, H. *et al.* (2011) Graphene oxide/conducting polymer composite hydrogels. *J. Mater. Chem.*, **21** (46), 18653–18658.
38. Li, B. *et al.* (2011) Cu 2O@reduced graphene oxide composite for removal of contaminants from water and supercapacitors. *J. Mater. Chem.*, **21** (29), 10645–10648.
39. Stankovich, S. *et al.* (2006) Graphene-based composite materials. *Nature*, **442** (7100), 282–286.
40. Zhou, X. *et al.* (2009) In situ synthesis of metal nanoparticles on single-layer graphene oxide and reduced graphene oxide surfaces. *J. Phys. Chem. C*, **113** (25), 10842–10846.
41. Shen, J. *et al.* (2011) One-pot hydrothermal synthesis of Ag-reduced graphene oxide composite with ionic liquid. *J. Mater. Chem.*, **21** (21), 7795–7801.
42. Chen, G.H. *et al.* (2001) Dispersion of graphite nanosheets in a polymer matrix and the conducting property of the nanocomposites. *Polym. Eng. Sci.*, **41** (12), 2148–2154.
43. Binnig, G., Quate, C.F., and Gerber, C. (1986) Atomic force microscope. *Phys. Rev. Lett.*, **56** (9), 930–933.
44. Lang, K.M. *et al.* (2004) Conducting atomic force microscopy for nanoscale tunnel barrier characterization. *Rev. Sci. Instrum.*, **75** (8), 2726–2731.
45. Gross, L. *et al.* (2009) The chemical structure of a molecule resolved by atomic force microscopy. *Science*, **325** (5944), 1110–1114.
46. Parades, J.I. *et al.* (2008) Graphene oxide dispersions in organic solvents. *Langmuir*, **24** (19), 10560–10564.
47. Paredes, J.I. *et al.* (2009) Atomic force and scanning tunneling microscopy imaging of graphene nanosheets derived from graphite oxide. *Langmuir*, **25** (10), 5957–5968.
48. Singh, V. *et al.* (2011) Graphene based materials: past, present and future. *Prog. Mater. Sci.*, **56** (8), 1178–1271.
49. Kim, K.S. *et al.* (2009) Large-scale pattern growth of graphene films for stretchable transparent electrodes. *Nature*, **457** (7230), 706–710.
50. Barlow, W. (1883) Probable nature of the internal symmetry of crystals. *Nature*, **29** (738), 186–188.
51. Sohncke, L. (1884) Probable nature of the internal symmetry of crystals. *Nature*, **29** (747), 383–384.
52. Compton, A.H. (1923) A quantum theory of the scattering of X-rays by light elements. *Phys. Rev.*, **21** (5), 483–502.
53. Bragg, W.H. (1908) The nature of γ and X-rays. *Nature*, **77** (1995), 270–271.
54. Bragg, W.H. (1910) XXXIX. The consequence of the corpuscular hypothesis of the γ and X rays, and the range of β rays. *Philos. Mag. Ser. 6*, **20** (117), 385–416.

55. Bragg, W. (1912) On the direct or indirect nature of the ionization by X-rays. *Philos. Mag.*, **23**, 647–650.
56. von Laue, M. (1915) Concerning the Detection of X-ray Interferences. Nobel Lecture, *http//www.nobelprize.org/nobel_prizes/physics/laureates/1914/* (accessed 30 August 2014).
57. Ford, W.E. and Dana, E.S. (1932) *A Textbook of Mineralogy*, John Wiley & Sons, Inc., New York, p. 438.
58. Bragg, W. (1913) The structure of some crystals as indicated by their diffraction of X-rays. *Proc. R. Soc. London, Ser. A*, **89** (610), 248–277.
59. Bragg, W., James, R.t., and Bosanquet, C. (1921) The intensity of reflexion of X-rays by rock-salt.—Part II. *London, Edinburgh Dublin Philos. Mag. J. Sci.*, **42** (247), 1–17.
60. Bragg, W.L. (1914) The analysis of crystals by the X-ray spectrometer. *Proc. R. Soc. London, Ser. A*, **89** (613), 468–489.
61. Culity, B. and Stock, S. (1978) *Elements of X-ray Diffraction*, Edison Wesley, London.
62. Hye-Mi, Ju, Seung Hun, Huh, Seong-Ho, Choi, Hong-Lim, Lee (2010) Structures of thermally and chemically reduced graphene, Materials Letters, **64**, (3), 357–360, ISSN 0167-577X, *http://dx.doi.org/10.1016/j.matlet.2009.11.016.* (*http://www.sciencedirect.com/science/article/pii/S0167577X0900857X*)
63. Li, Z. *et al.* (2007) X-ray diffraction patterns of graphite and turbostratic carbon. *Carbon*, **45** (8), 1686–1695.
64. Huh, S.H. (2011) *Thermal Reduction of Graphene Oxide*, Chapter, INTECH.
65. Lim, J. *et al.* (2013) Terahertz, optical, and Raman signatures of monolayer graphene behavior in thermally reduced graphene oxide films. *J. Appl. Phys.*, **113** (18), 183502–183502-5.
66. Rani, J. *et al.* (2012) Epoxy to carbonyl group conversion in graphene oxide thin films: effect on structural and luminescent characteristics. *J. Phys. Chem. C*, **116** (35), 19010–19017.
67. Zhou, S. *et al.* (2007) Substrate-induced bandgap opening in epitaxial graphene. *Nat. Mater.*, **6** (10), 770–775.
68. Saxena, S., Tyson, T.A., and Negusse, E. (2010) Investigation of the local structure of graphene oxide. *J. Phys. Chem. Lett.*, **1** (24), 3433–3437.
69. Titelman, G. *et al.* (2005) Characteristics and microstructure of aqueous colloidal dispersions of graphite oxide. *Carbon*, **43** (3), 641–649.
70. Wallace, P. (1947) The band theory of graphite. *Phys. Rev.*, **71** (9), 622.
71. Geim, A.K. and Novoselov, K.S. (2007) The rise of graphene. *Nat. Mater.*, **6** (3), 183–191.
72. Charlier, J.-C. *et al.* (2008) *Electron and Phonon Properties of Graphene: their Relationship with Carbon Nanotubes, in Carbon Nanotubes*, Springer, pp. 673–709.
73. Lemme, M.C. *et al.* (2007) A graphene field-effect device. *IEEE Electron Device Lett.*, **28** (4), 282–284.
74. Casiraghi, C. *et al.* (2007) Rayleigh imaging of graphene and graphene layers. *Nano Lett.*, **7** (9), 2711–2717.
75. Blake, P. *et al.* (2007) Making graphene visible. *Appl. Phys. Lett.*, **91**, 063124.
76. Hasan, T. *et al.* (2009) Nanotube–polymer composites for ultrafast photonics. *Adv. Mater.*, **21** (38-39), 3874–3899.
77. Lui, C.H. *et al.* (2010) Light emission from graphene induced by femtosecond laser pulses. *Bull. Am. Phys. Soc.*, **1**, Z22.008.
78. Eda, G. *et al.* (2010) Blue photoluminescence from chemically derived graphene oxide. *Adv. Mater.*, **22** (4), 505–509.
79. Hamberg, I. and Granqvist, C.G. (1986) Evaporated Sn-doped In 2 O 3 films: Basic optical properties and applications to energy-efficient windows. *J. Appl. Phys.*, **60** (11), R123–R160.
80. Minami, T. (2005) Transparent conducting oxide semiconductors for transparent electrodes. *Semicond. Sci. Technol.*, **20** (4), S35.
81. Holland, L. and Siddall, G. (1953) The properties of some reactively sputtered metal oxide films. *Vacuum*, **3** (4), 375–391.
82. Granqvist, C.G. (2007) Transparent conductors as solar energy materials: a panoramic review. *Sol. Energy Mater. Sol. Cells*, **91** (17), 1529–1598.

83. Lee, J.-Y. *et al.* (2008) Solution-processed metal nanowire mesh transparent electrodes. *Nano Lett.*, **8** (2), 689–692.

84. De, S. *et al.* (2009) Silver nanowire networks as flexible, transparent, conducting films: extremely high DC to optical conductivity ratios. *ACS Nano*, **3** (7), 1767–1774.

85. Chapin, D., Fuller, C., and Pearson, G. (1954) A new silicon p-n junction photocell for converting solar radiation into electrical power. *J. Appl. Phys.*, **25** (5), 676–677.

86. Green, M.A. *et al.* (1999) Solar cell efficiency tables (version 13). *Prog. Photovoltaics Res. Appl.*, **7** (1), 31–37.

87. Krebs, F.C. (2009) All solution roll-to-roll processed polymer solar cells free from indium-tin-oxide and vacuum coating steps. *Org. Electron.*, **10** (5), 761–768.

88. Burroughes, J. *et al.* (1990) Light-emitting diodes based on conjugated polymers. *Nature*, **347** (6293), 539–541.

89. Giovannetti, G. *et al.* (2008) Doping graphene with metal contacts. *Phys. Rev. Lett.*, **101** (2), 026803.

90. Saleh, B. and Teich, M. (2007) *Fundamentals of Photonics*, Chapter 7, John Wiley & Sons, Inc., NewYork.

91. Dawlaty, J.M. *et al.* (2008) Measurement of ultrafast carrier dynamics in epitaxial graphene. *Appl. Phys. Lett.*, **92**, 042116.

92. Wright, A., Cao, J., and Zhang, C. (2009) Enhanced optical conductivity of bilayer graphene nanoribbons in the terahertz regime. *Phys. Rev. Lett.*, **103** (20), 207401.

93. Boyd, R.W. (2003) *Nonlinear Optics*, Academic Press.

94. Keller, U. (2003) Recent developments in compact ultrafast lasers. *Nature*, **424** (6950), 831–838.

95. Wang, F. *et al.* (2008) Wideband-tuneable, nanotube mode-locked, fibre laser. *Nat. Nanotechnol.*, **3** (12), 738–742.

2
Graphene-Based Electrodes for Lithium Ion Batteries

Ronghua Wang, Miaomiao Liu, and Jing Sun

2.1
Introduction

As a kind of carbon material, graphene sheet (GS) has attracted increasing attention in a variety of fields because of its high theoretical specific surface area ($2600\ m^2\ g^{-1}$), good flexibility, superior chemical/thermal stability, and extraordinary electrical, thermal, and mechanical properties. The unique structure and outstanding properties render graphene highly promising for a wide range of applications in electronics, sensors, and energy storage/conversion.

In the field of lithium ion batteries (LIBs), graphene has wide potential windows and rich surface chemistry, and thus can be used as electrode material individually. Also, the high conductivity and unique layered structure make graphene a predominant matrix to form hybrids with other cathode and anode materials. Significant synergistic effects often occur in graphene/other material composites, which will greatly enhance the overall electrochemical performance: On one hand, the conductivity of cathode or anode materials can be significantly increased after compositing with graphene, which will improve the electron transport and rate capability of the electrode; on the other, the good mechanical property of graphene can help maintain the microstructure of electrode materials and improve the cyclic stability. Besides, graphene has an extremely large aspect ratio and excellent structural flexibility; thus it can act as building blocks to self-assemble into two-dimensional (2D) flexible and free-standing electrode as well as three-dimensional (3D) macroscopic aerogels. This is of great importance to promote the development of new electrode structures and new types of LIBs.

In this review, we will summarize recent research progress on the synthesis methods, structural design, and electrochemical performance of graphene-based electrodes for high-performance LIBs, including graphene-based cathode materials, graphene-based anode materials, 2D graphene-based flexible electrodes, and 3D macroscopic graphene-based electrodes.

Graphene-based Energy Devices, First Edition. Edited by A. Rashid bin Mohd Yusoff.
© 2015 Wiley-VCH Verlag GmbH & Co. KGaA. Published 2015 by Wiley-VCH Verlag GmbH & Co. KGaA.

2.2 The Working Principle of LIBs

LIB, with its high-energy density, high voltage, and environmental friendliness, is widely considered as one of the most probable candidates for electric vehicle power source [1, 2]. As schematically illustrated in Figure 2.1, an LIB typically consists of a positive electrode (cathode), a negative electrode (anode), a porous membrane (allowing lithium ions to travel through) separating the two electrodes, and an electrolyte (playing the role of conducting lithium ions during charge and discharge).

A typical LIB can be represented as follows [3]:

$$(-)\ C_n|1\ \ \mathrm{mol\,l^{-1}}\ \mathrm{LiPF_6} - \mathrm{EC} + \mathrm{DEC}|\mathrm{LiMO}_x(+) \tag{2.1}$$

where C indicates a carbonaceous material and M stands for a metal. On the cathode, the following reaction takes place:

$$\mathrm{LiMO}_x - y\mathrm{e}^- \underset{\text{discharge}}{\overset{\text{charge}}{\rightleftharpoons}} \mathrm{Li}_{1-y}\mathrm{MO}_x + y\mathrm{Li}^+ \tag{2.2}$$

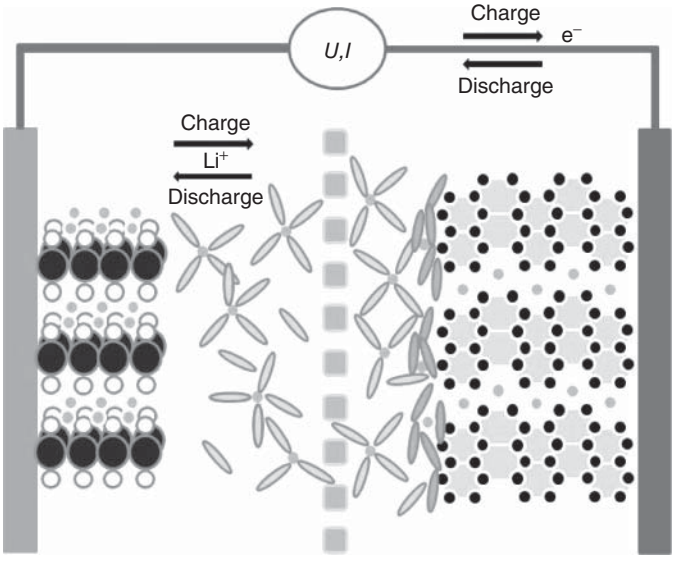

Figure 2.1 The scheme of a common LIB: (a) aluminum current collector; (b) metal oxide cathode active material; (c) porous separator in organic electrolyte; (d) solid electrolyte interface layer; (e) graphite anode active material; and (f) copper current collector. (Reproduced with permission [3]. Copyright (2013), Royal Society of Chemistry.)

On the anode, the following reaction occurs:

$$C_n + y\mathrm{Li}^+ + y\mathrm{e}^- \underset{\text{discharge}}{\overset{\text{charge}}{\rightleftharpoons}} \mathrm{Li}_y\mathrm{C}_n \tag{2.3}$$

The overall reaction can be expressed as below:

$$\mathrm{LiMO}_x + \mathrm{C}_n \underset{\text{discharge}}{\overset{\text{charge}}{\rightleftharpoons}} \mathrm{Li}_{1-y}\mathrm{MO}_x + \mathrm{Li}_y\mathrm{C}_n \tag{2.4}$$

During the charging process, lithium ions will deintercalate from the cathode into the electrolyte, diffuse across the porous separator, and intercalate into the carbonaceous anode. During the discharging process, the lithium ions will deintercalate from the anode and intercalate back to the empty sites between layers of the cathode. Because of the lithium ion transfer mechanism, LIB is also called the *rocking chair* battery.

The capacity of LIBs is defined as the amount of charge that can be obtained via the charging and discharging processes under specific conditions. The theoretical capacity of LIBs determined by the amount of an active material, and is given by [4]:

$$C_\mathrm{o} = 26.8n\frac{m_o}{M} = \frac{1}{q}m_\mathrm{o}\ (\mathrm{Ah}) \tag{2.5}$$

where C_o in ampere hour is the theoretical capacity, m_o in grams is the mass of the active material participating in the electrochemical reaction, M in grams per mole is the molar weight of the active material, n is the number of electron involved in the reaction, and q is the electrochemical equivalence. For example, the theoretical capacity of a graphite anode with six-coordinated carbon atoms for each Li ion (LiC_6) is calculated as below [4]:

$$\mathrm{LiC}_6 \rightarrow \mathrm{Li}^+ + \mathrm{C}_6 + \mathrm{e}^- \tag{2.6}$$

$$\mathrm{LiC}_6 = 26.8 \times \frac{1}{78.94} \times 1000 = 339.50\ (\mathrm{mAh\ g^{-1}}) \tag{2.7}$$

However, the currently available LIBs cannot satisfy the ever-increasing requirements from massive power-storage devices used in, for example, electric vehicles and grid power management. Electrodes play a very important role in the development of high-performance batteries. Research efforts have thus been largely devoted to improving current electrode materials or exploring new ones.

2.3 Graphene-Based Cathode Materials for LIBs

The development of cathode materials with excellent electrochemical properties is currently a key task in LIB research. At present, the most attractive cathode materials for LIBs are LiMPO_4 (M = Fe, Co, Mn, V), lithium metal (Mn, Co, Ni) oxide,

V_2O_5, and so on [5]. However, their practical applications are limited by the sluggish kinetics of electron and Li^+ transport, resulting in low specific capacities at high rates and poor cyclability. Graphene, with its high conductivity, high specific surface area, and structure flexibility, becomes an ideal material to composite with cathode materials to overcome the ionic and electronic transport limitations. By compositing with graphene, the electrochemical performance of cathode materials can be significantly boosted with the aid of a conductive network.

The olivine-type $LiFePO_4$ is one of the most intensively studied materials because of its high capacity, excellent cycle life, thermal stability, environmentally friendliness, and low cost [6–8]. The first publication on $LiFePO_4$/GS composites was by Ding and coworkers [9] in 2010, obtained via a coprecipitation method. The composites, in which 100-nm $LiFePO_4$ nanocrystals uniformly decorated on the surface of GS, delivered an initial specific capacity of 160 mAh g^{-1} at 0.2 C, while the value was only 113 mAh g^{-1} for bare $LiFePO_4$. Zhou *et al.* [10] developed a combined spray-drying and annealing route to prepare $LiFePO_4$/GS. $LiFePO_4$ nanoparticles were homogeneously wrapped by loosely packed graphene 3D networks to form a microsized spherical secondary structure. Such a special nanostructure was of benefit for Li^+ diffusion, resulting in a high specific capacity of 70 mAh g^{-1} at 60 C discharge rate and a capacity decay rate of <15% when being cycled under 10 C charging and 20 C discharging for 1000 times. In another study, a low-temperature polyol method was explored to prepare graphene-wrapped $LiFePO_4$ nanorod composites, which delivered excellent discharge capacities of 164, 156.7, and 121.5 mAh g^{-1} with remarkable capacity retention ratios of 99, 97.9, and 98.6% after 100 cycles at current rates of 0.1, 1, and 10 C, respectively (Figure 2.2a,b) [11].

Besides $LiFePO_4$, other cathode materials/GS composites have also been intensively explored. Dai and coworkers [6] presented a two-step approach for the synthesis of $LiMn_{0.75}Fe_{0.25}PO_4$ nanorods on GS (Figure 2.2c): Fe-doped Mn_3O_4 nanoparticles were first selectively grown onto GO (graphene oxide) by controlled hydrolysis; the oxide nanoparticle precursors then reacted solvothermally with Li and phosphate ions and were *in situ* transformed into $LiMn_{0.75}Fe_{0.25}PO_4$ nanorods on GS. The $LiMn_{0.75}Fe_{0.25}PO_4$/GS composite, with its high electrical conductivity, ideal nanorod morphology, and intimate interfacial interactions, delivered an ultrahigh-rate capacity (132 and 107 mAh g^{-1} at high discharge rates of 20 and 50 C, respectively) and excellent cyclic stability (Figure 2.2 d-e). Rao *et al.* [12] prepared $LiNi_{1/3}Mn_{1/3}Co_{1/3}O_2$/GS composites by the microemulsion and ball-milling route, which could deliver a reversible capacity of 153 mAh g^{-1} at a rate of 5 C, which was much higher than that of bare $LiNi_{1/3}Mn_{1/3}Co_{1/3}O_2$. The improved performance was attributed to the grain connectivity and high electronic conductivity.

V_2O_5 is one of the most promising candidates for cathodes of LIBs because of its intercalation structure, low cost, and high-energy density. Recently, V_2O_5/GS composites were investigated as cathodes for LIBs. For example, Yang and Liu [13] have developed a modified hydrothermal method using graphite as precursor to prepare ultralong V_2O_5 nanowire (NW)/GS composites. As a result

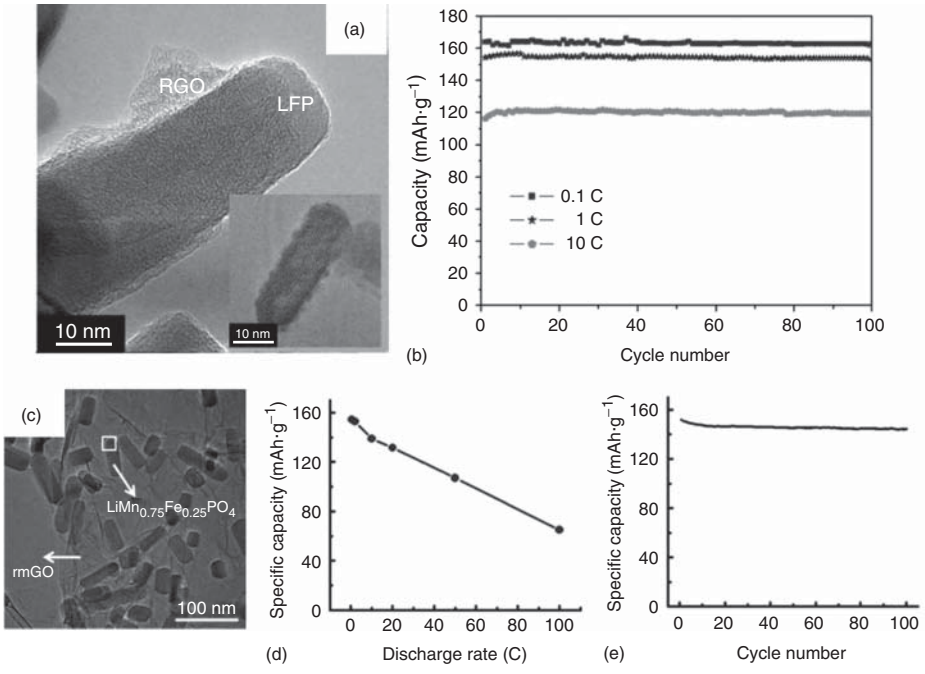

Figure 2.2 (a,b) HRTEM images and rate capabilities of $LiFePO^4$/graphene composites. (Reproduced with permission [11]. Copyright (2012), Royal Society of Chemistry.) (c–e) TEM image, rate capability, and cyclic stability of $LiMn_{0.75}Fe_{0.25}PO_4$/graphene. rmGO in the Figure 2.2c represents reduced mildly oxidized graphene oxide. (Reproduced with permission [6]. Copyright (2011), John Wiley & Sons, Inc.)

of the improved conductivity, V_2O_5/GS composites showed a specific capacity of 190 mAh g^{-1} after 50 cycles. V_2O_5 with extremely stable cycling was further achieved by preparing V_2O_5/GS composites using a facile vacuum filtration method [14]. They could deliver a capacity of 0.1 Ah g^{-1} after 100 000 cycles at a current density of 10 A g^{-1}. The improvement could be ascribed to the GSs, which are excellent electronic conductors and could reduce the polarization of LIBs.

The principle of using graphene to improve the properties of cathode materials can be briefly summarized as the follows: First, graphene with its high conductivity can enhance the conductance of electrode materials compared to their unmodified counterparts. Second, the good mechanical property of graphene can maintain the microstructure of cathode materials and improve the cyclic stability. Although many improvements on lithium storage performance have been achieved, the effect of the graphene precursor GO on the morphology of cathode materials, the interfacial interactions between cathode materials and GS, and the rational design of the nanostructure still need to be intensively explored.

2.4 Graphene-Based Anode Materials for LIBs

In recent years, the anode material, as one of the important components of LIBs system, has been another key bottleneck that restricts the popular applications of LIBs. Commonly, graphite (3D network of graphene) is widely used as the commercial anode material by intercalating Li ions reversibly in interlayer spaces [(0002) planes]. However, graphite can achieve a maximum specific capacity of only 372 mAh g^{-1} with a LiC_6 intercalation mechanism [15, 16]. This material suffers from poor capacity, which makes it hard to meet the needs of high-performance devices. Thus, it is necessary to exploit new anode materials to obtain high capacity. It is worth noting that, since the first report in 2004, graphene has drawn global attention due to its high surface area, fast charge-carrier mobility, and strong mechanical property [17]. All these properties facilitate lithium ions to insert/extract quickly and reversibly on the surface of graphene. More importantly, it has been calculated that lithium adsorption can take place on both sides of the GS, further attaining twice the theoretical capacity as compared with graphite through the formation of Li_2C_6 [3, 18]. Apart from the Li_2C_6 intercalation capacity, there exist additional storage sites for higher capacity due to the imperfection of graphene, such as the layer edges and covalent sites, the nanopores/cavities and defect sites, oxygen-containing functional groups, or heteroatom sites [19]. Besides, graphene is used not only as the anode material individually but also is a predominant matrix to hybrid with other materials. Significant synergistic effects often occur in graphene/other material composites, further enhancing their overall electrochemical performance [20]. Taking all the above factors into consideration, graphene-base materials are expected to be prospective anode materials for next-generation LIBs.

2.4.1 Graphene as Anodes for LIBs

It is well known that the development of graphene opens up a new field for next-generation LIBs. To ensure the advantage of graphene as anode material, several works have theoretically studied the lithium storage properties of graphene. Back in 1995, Dahn and coworkers [18] proposed that there was only one layer of intercalated lithium for each carbon sheet of graphite. However, in carbons composed mainly of a single layer, Li atoms at the same areal density presumably could be adsorbed on each side of the sheet, resulting in two layers of lithium for each carbon sheet, and hence a theoretical maximum capacity of 740 mAh g^{-1}. In another work, Sato *et al.* [21] studied the transport mechanism in disordered carbon by using high-resolution microscopy and lithium-7 nuclear magnetic resonance (NMR). The result indicated the existence of Li_2 covalent molecule in carbon material. This extra covalent site of lithium offered better performance for LIBs. Theoretically, the disordered graphene promised to be a high-performance anode material owing to the greatly enhanced capacity.

Driven by the pioneering theoretical studies, many experimental investigations have been conducted to investigate graphene as anode for LIBs. Song *et al.* [22] prepared graphene nanosheets by the oxidation, expansion, and ultrasonication treatments of graphite. The specific capacity of GS could reach 502 mAh g^{-1} at the current density of 0.2 mA cm^{-2} after 30 cycles, which is much higher than that of graphite (265 mAh g^{-1}). Similarly, Wang *et al.* [23] synthesized GSs from graphite powder through oxidation followed by rapid thermal expansion in a nitrogen atmosphere. After 40 cycles, it could maintain the reversible specific capacity of 848 mAh g^{-1} at 100 mA g^{-1}. The excellent performance of graphene could be ascribed to its Li_2C_6 intercalation mechanism and the disordered carbon or defects of GS. As shown in Figure 2.3, some lithium ions are inserted/extracted reversibly between the (002) planes by forming Li_2C_6. Meanwhile, lithium ions may be stored on the defects at the edge and internal sites. To better prove the function of disordered carbon and defects, Pan *et al.* [24] synthesized graphene nanosheets with structural parameters tunable via different reduction methods, such as hydrazine reduction, low-temperature pyrolysis, and electron beam irradiation. The highly disordered GS exhibited high reversible capacities of 794–1054 mAh g^{-1} at 50 mA g^{-1}, which is larger than that of pure GS (540 mAh g^{-1}) reported previously [25], indicating their huge advantage for lithium storage.

Recently, heteroatomic doping, such as nitrogen and boron atoms, has been shown as a novel way to tailor the properties of graphene. The doping effects could induce defects and disordered surface morphology, enhanced

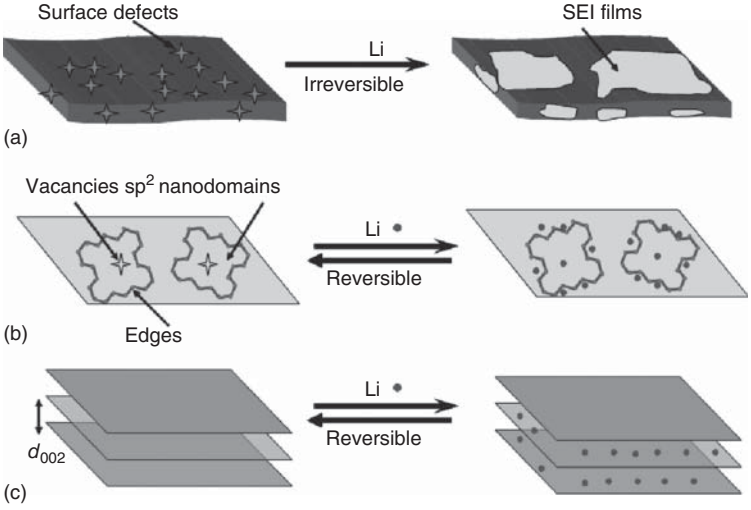

Figure 2.3 (a) Irreversible Li storage at the interface between graphene and electrolyte. (b) Reversible Li storage at edge sites and internal defects (vacancies, etc.) of nanodomains embedded in GS. (c) Reversible Li storage between (002) planes. (Reproduced with permission [24]. Solid Electrolyte Interphase. Copyright (2009), American Chemical Society.)

electrode–electrolyte wettability, and improved electrical conductivity. All these effects are favorable for rapid lithium adsorption and electron transport, thereby rendering its promising use for LIBs. In a typical example, nitrogen- and boron-doped GSs with 3.06% and 0.88% doping level were prepared for use in high-power, high-energy LIBs [26]. The doped graphene electrodes delivered an exceptionally high capacity of 1043 and 1549 mAh g^{-1} at 50 mA g^{-1} for N- and B-doped graphene, respectively. In another example, Cui *et al.* [27] obtained nitrogen-doped graphene nanosheets with 2% nitrogen content by heat treatment of GO under an ammonia atmosphere. The as-prepared electrode showed a highly reversible capacity of 900 mAh g^{-1} at 42 mA g^{-1}, further demonstrating the potential applications of the doping graphene.

Although graphene as anode material for LIBs has made great achievements, there is still a big challenge. The intractable issue is the easy agglomeration and restacking of graphene during drying because of van der Waals forces, which significantly limits the electron and ion transport, consequently leading to undesirable performance. Considering the above problem, more effective ways to prepare high-performance graphene anodes for practical applications should be urgently pursued.

2.4.2
Graphene-Based Composites as Anodes for LIBs

As discussed above, the existing problem limits the development of graphene in LIBs. To solve this issue, combining graphene with other anode materials, such as Si [28–30], Sn [31], metal sulfides [32, 33], and metal oxides [34–37], to fabricate graphene-based composites is considered to be an efficient and practical method (Figure 2.4). This combination can fully use the advantages of both graphene and other anode materials as active materials, further favorably

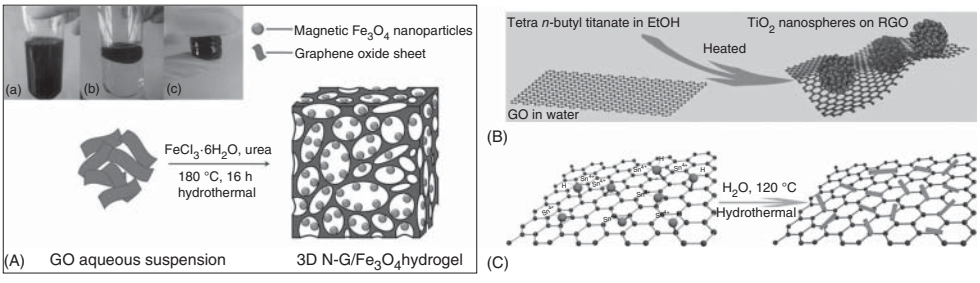

Figure 2.4 Schematic of the preparation of graphene-based composites with synergistic effects between graphene and other anode materials. (A) A scheme for the synthesis process of 3D N-doped graphene (GN)/Fe_3O_4 hydrogels. (Reproduced with permission [38]. Copyright (2013), Royal Society of Chemistry.) (B) Illustration of the synthesis process of TiO_2-reduced graphene oxide composite (TGC) from GO. (Reproduced with permission [39]. Copyright (2012), Royal Society of Chemistry.) (C) Schematic diagram of the one-step hydrothermal synthesis of SnO_2/GS. (Reproduced with permission [40]. Copyright (2012), Royal Society of Chemistry.)

affecting the electrochemical performance of the composites synergistically [20]. First, as a flexible confinement material, graphene would homogeneously support and disperse anode materials with well-organized size and shape, suppressing the agglomeration and volume change of other anode materials. Second, other anode materials separate graphene and prevent restacking, providing better immersion and diffusion of electrolyte ions for efficient reactions during the lithium storage process. Finally, this composite structure forms a perfectly conductive network, which increases the conductivity, shortens the ion transport paths, and further boosts the performance at high current density. In consequence, graphene-based composites are expected to make incredible achievements in LIBs.

2.4.2.1 The Lithium Storage Mechanisms of Anode Materials

To better take advantage of graphene-based composites, the key point is to figure out the lithium storage mechanisms. Research on anodes for LIBs is directed toward materials that can perform through three different mechanisms (Figure 2.5) [16, 20, 41].

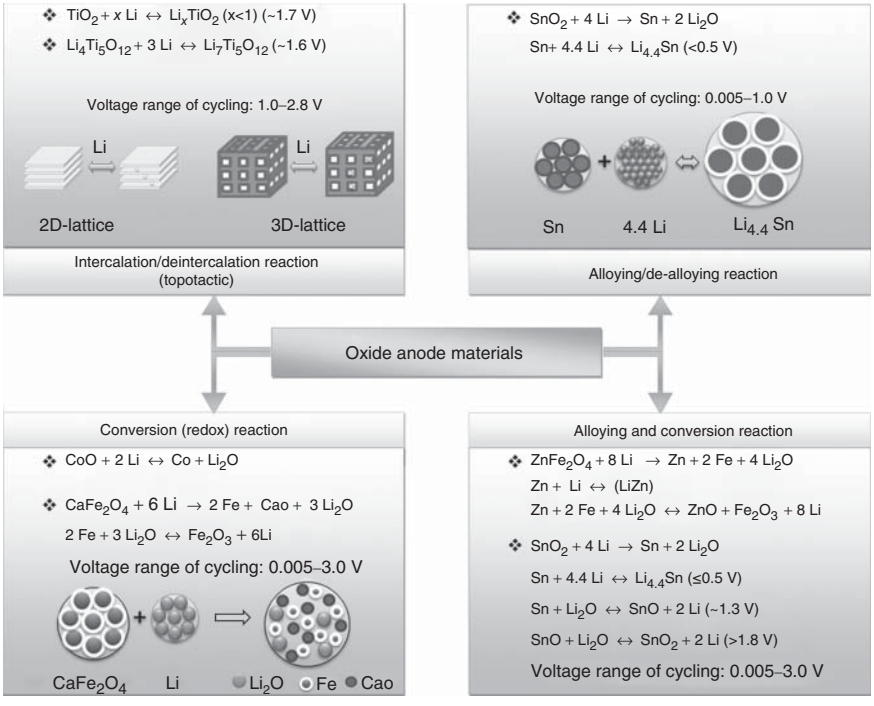
$TiO_2 + x\,Li \leftrightarrow Li_xTiO_2$ (x<1) (~1.7 V)
$Li_4Ti_5O_{12} + 3\,Li \leftrightarrow Li_7Ti_5O_{12}$ (~1.6 V)
Voltage range of cycling: 1.0–2.8 V
Li
Li
2D-lattice
3D-lattice
Intercalation/deintercalation reaction (topotactic)
$SnO_2 + 4\,Li \rightarrow Sn + 2\,Li_2O$
$Sn + 4.4\,Li \leftrightarrow Li_{4.4}Sn$ (<0.5 V)
Voltage range of cycling: 0.005–1.0 V
Sn
4.4 Li
$Li_{4.4}$ Sn
Alloying/de-alloying reaction
Oxide anode materials
Conversion (redox) reaction
$CoO + 2\,Li \leftrightarrow Co + Li_2O$
$CaFe_2O_4 + 6\,Li \rightarrow 2\,Fe + Cao + 3\,Li_2O$
$2\,Fe + 3\,Li_2O \leftrightarrow Fe_2O_3 + 6Li$
Voltage range of cycling: 0.005–3.0 V
$CaFe_2O_4$
Li
Li_2O
Fe
Cao
Alloying and conversion reaction
$ZnFe_2O_4 + 8\,Li \rightarrow Zn + 2\,Fe + 4\,Li_2O$
$Zn + Li \leftrightarrow (LiZn)$
$Zn + 2\,Fe + 4\,Li_2O \leftrightarrow ZnO + Fe_2O_3 + 8\,Li$
$SnO_2 + 4\,Li \rightarrow Sn + 2\,Li_2O$
$Sn + 4.4\,Li \leftrightarrow Li_{4.4}Sn$ (≤0.5 V)
$Sn + Li_2O \leftrightarrow SnO + 2\,Li$ (~1.3 V)
$SnO + Li_2O \leftrightarrow SnO_2 + 2\,Li$ (>1.8 V)
Voltage range of cycling: 0.005–3.0 V

Figure 2.5 Classification of oxide anode materials based on the reversible Li insertion and extraction process: Intercalation–deintercalation, alloying–dealloying, and conversion (redox) reaction. In favorable cases, the latter two processes can act synergistically to give rise to large and stable capacities. Selected examples are given. Schematic diagram of the process is shown. The voltages shown are versus Li metal. (Reproduced with permission [41]. Copyright (2013), American Chemical Society.)

1) Alloying–dealloying mechanism. The Li alloy reaction mechanism is as follows:

$$M_xO_y + 2ye^- + 2yLi^+ \leftrightarrow x[M]^0 + yLi_2O$$

$$M + ze^- + zLi^+ \rightarrow Li_zM$$

The elements M, such as Si, Sn, and so on, forming alloys with lithium have been investigated widely. The process involves a large reversible capacity in the reaction: Sn (or Si) + 4.4Li ↔ $Li_{4.4}$Sn (or Si), which usually occurs at low potentials (≤1.0 V vs Li). Thus these anode materials possess high theoretical specific capacity (4200 and 992 mAh g^{-1} for Si and Sn, respectively). However, the large volume effect (>300%) during charge/discharge leads to the severe aggregation of electrode materials, electrode pulverization, and loss of electrical contact with current collectors, thereby limiting their extensive applications.

2) Conversion mechanism. The reaction below is the conversion mechanism:

$$M_xO_y + 2ye^- + 2yLi^+ \leftrightarrow x[M]^0 + yLi_2O$$

Metal oxides (SnO_2, Fe_3O_4, Co_3O_4, NiO) belong to this mechanism. The above materials also have high theoretical specific capacities (600–1000 mAh g^{-1}). Simultaneously, they suffer from the severe volume expansion and poor conductivity, which are urgent issues to be solved.

3) Intercalation–deintercalation mechanism. The following is the reaction mechanism:

$$M_xO_y + ze^- + zLi^+ \leftrightarrow Li_zM_xO_y$$

Anode materials with a 2D layer or 3D network crystal structure, such as TiO_2 and metal chalcogenides (MoS_2, TiS_2), follow this reaction mechanism, which can reversibly intercalate lithium into the lattice with a small volume change, similar to graphite. Therefore, this kind of anode materials exhibits long life cycling due to the structural stability. Nevertheless, the drawbacks, including low specific capacity and poor conductivity, hinder their progress as LIBs. With better understanding of the advantages and disadvantages of these anode materials, researchers may be able to design superior graphene-based composites that could show the synergistic effects fully and exhibit enhanced electrochemical performance.

2.4.2.2 Graphene–Si/Sn Composites as Anodes for LIBs

Of all the attractive electrode materials following the alloying mechanism, silicon (Si) is considered one of the most prospective anode materials because of its highest theoretical specific capacity (4200 mAh g^{-1}), low operating potential, and low cost [42]. Up to now, Si anode materials with different morphologies have been fabricated, such as Si nanoparticles [43], nanosheets [44], hollow nanospheres [45], NWs [46], and nanotubes [47] (Figure 2.6). Despite the improvement in

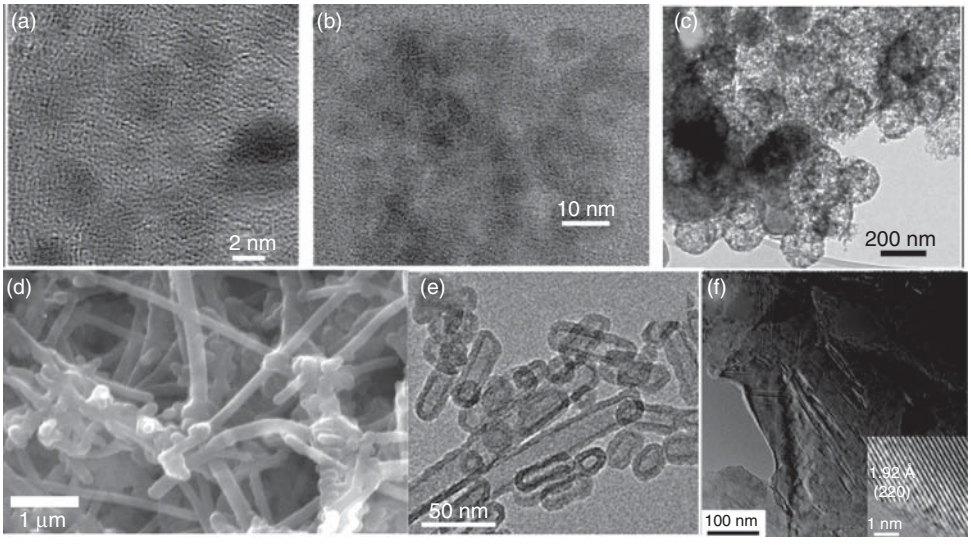

Figure 2.6 Silicon materials with different morphologies: *Ex situ* TEM images of (a) 5 nm and (b) 10 nm sized Si nanoparticles (red lines indicate *n*-Si particles). (Reproduced with permission [43]. Copyright (2010), John Wiley & Sons, Inc.) (c) TEM image of the Si-SiC/C hollow nanosphere. (Reproduced with permission [45]. Copyright (2010), Royal Society of Chemistry.) (d) Scanning electron microscope (SEM) image of Si-coated carbon nanofibers (CNFs). (Reproduced with permission [46]. Copyright (2009), American Chemical Society.) (e) TEM image of Si nanotubes. (Reproduced with permission [47]. Copyright (2013), Elsevier.) (f) TEM image of Si nanotubes. (Reproduced with permission [44]. Copyright (2011), American Chemical Society.)

performance, owing to the elaborate designation of morphology, they are not satisfactory. Si anodes still suffer from high cost, difficulty in scaling up, poor cycling stability resulting from huge volume change (>300%) during the alloying–dealloying processes, and inefficient utilization due to the poor electrical conductivity [48]. Therefore, it is a major topic of interest to explore a cost-effective conductive material to buffer the volume change and improve the conductivity of Si anode. Fortunately, graphene meets all of the features described above. The overall volume change of the silicon/graphene structure is smaller (24%) than that of the original silicon particles upon full lithiation, as shown by theoretical calculation [29]. As a result, incorporating graphene with Si to generate composites is a great way to prepare high-performance anode materials (Figure 2.7).

Zhou and coworkers [51] synthesized Si/graphene composites by hybrid electrostatic assembly between negatively charged GO and positively charged aminopropyltriethoxysilane-modified Si nanoparticles, followed by heat treatment. The GSs formed a continuous conductive path and covered the highly dispersed Si nanoparticles well. This novel structure could provide not only the alleviating spaces needed for volume changes during the lithiation and delithiation processes but also excellent conductivity to improve the efficient

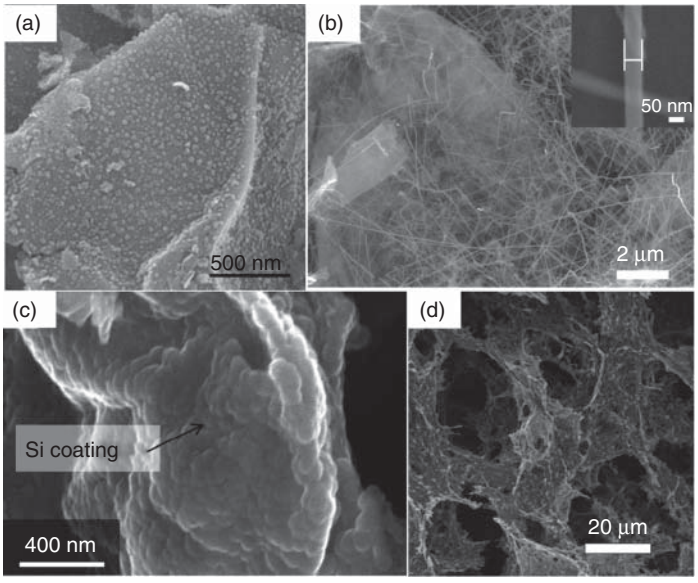

Figure 2.7 The Si/graphene composites: (a) SEM image of the Si/GS. (Reproduced with permission [28]. Copyright (2012), Royal Society of Chemistry.) (b) SEM image of the CVD-synthesized Si NW/GO composite. (Reproduced with permission [49]. Copyright (2014), Royal Society of Chemistry.) (c) SEM micrograph of Si-coated graphene. (Reproduced with permission [50]. Copyright (2011), John Wiley & Sons, Inc.) (d) SEM image of the Si/GS aerogel. (Reproduced with permission [30]. Copyright (2013), Elsevier.)

utilization of Si nanoparticles. Thus the Si/graphene electrode exhibited superior performance with a discharge capacity of 822 mAh g^{-1} after 100 cycles at a current density of 0.1 A g^{-1}, which is much higher than that of Si nanoparticles (16 mAh g^{-1} after only 30 cycles). In another study, a Si/GS aerogel was successfully prepared by the simple self-assembly of GS [30]. The aerogel architecture possessed a more efficient framework to form a 3D conductive network as well as to buffer the large volume changes. As a result, the Si/GS electrode displayed a high discharge capacity of 1481 mAh g^{-1} after 50 cycles and a high-rate capability of 705 mAh g^{-1} at 5000 mA g^{-1}.

To ensure good chemical bonding and electronic conduction between Si nanoparticles and graphene, a number of studies have focused on the magnesiothermic reduction process, through which Si nanoparticles *in situ* grew and riveted on GSs (Figure 2.8). For example, a 3D porous architecture of Si/graphene nanocomposite was constructed through magnesiothermic reduction, in which Si nanoparticles were stably anchored on the graphene nanosheets through a thin SiO_x layer [28]. Such a unique 3D architecture improved substantially the rate capability of the Si anode, showing a reversible capacity of 900 mAh g^{-1} with very little fading when the current density was increased from 100 mA g^{-1} up to 1 A g^{-1}. Du *et al.* [52] synthesized well-organized Si/graphene composites by magnesiothermal reduction of the *in situ* generated SiO_2 nanoparticles on GSs.

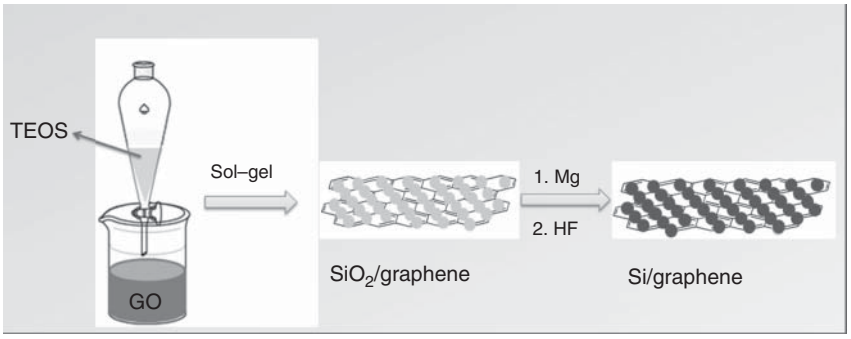

Figure 2.8 Illustration of the preparation process of the Si/graphene composite through magnesiothermic reduction.

Si nanoparticles of 5 nm were uniformly anchored on graphene. The Si/graphene composite delivered long cycling stability with a capacity of 1374 mAh g^{-1} over 120 cycles. The excellent performance derived from the unique structure, which could offer high conductivity and accommodate the severe volume changes.

Not only Si nanoparticles but also other morphologies of Si were used to compound with graphene as well. Ren *et al.* [49] reported a novel hierarchical Si nanowire (Si NW)/GS composite as anode, which retained a high specific capacity of 2300 mAh g^{-1} over 100 cycles. The remarkable performance of Si NW/GS composite was attributed to the enhanced contacts between the Si NWs and the GS overcoats, wherein GS buffered the volume change of Si NWs, further maintaining the structural integrity of the electrode. In another work, Evanoff *et al.* [50] studied continuous Si films conformally deposited on the GSs via SiH_4 decomposition at 500 °C. The obtained anode delivered a high specific reversible capacity of 2000 mAh g^{-1} at a current density of 140 mA g^{-1}.

In addition to Si materials, Sn is another promising candidate as LIBs for its high theoretical capacity (992 mAh g^{-1}) and low discharge potential, which belongs to alloying mechanism. However, a dramatic volume change commonly occurs in Sn, just like Si, which leads to severe pulverization, further causing rapid capacity decay and poor cyclability. Similarly, an effective route to overcome this issue is to design Sn/graphene composites. In recent research, Wang *et al.* [31] investigated the lithium storage properties of graphene by first-principles calculations. The results revealed that lithium could be stored on both sides of GSs, proving the advantage of graphene theoretically. Simultaneously, they prepared a Sn/graphene nanocomposite, in which Sn nanoparticles with the size of 2–5 nm act as a spacer to effectively separate graphene nanosheets. The Sn/graphene composite delivered a reversible capacity of 508 mAh g^{-1} after 100 cycles, which is an enhanced performance compared to bare graphene electrode (255 mAh g^{-1}) and bare Sn electrode (failed). In another work, a novel 3D porous graphene networks was built by the *in situ* chemical vapor deposition (CVD) technique. The networks were anchored with small and uniform Sn nanoparticles encapsulated with graphene shells by using metal precursors as catalyst and a

self-assembly of NaCl particles as template [53]. In this unique structure, the CVD-synthesized graphene shells could effectively not only avoid the direct exposure of encapsulated Sn to the electrolyte and preserve the structural and interfacial stabilization of Sn nanoparticles but also suppress the aggregation of Sn nanoparticles and buffer the volume expansion. At the same time, the interconnected 3D porous graphene networks led to remarkably enhanced electrical conductivity and structural integrity of the overall electrode. Consequently, this 3D hybrid anode exhibited extremely long cycling stability even at high current density, achieving a high capacity of 682 mAh g^{-1} at 2 A g^{-1} and maintaining ~96.3% after 1000 cycles. It reveals that the construction of graphene-based composites is required for improving the performance of LIBs.

2.4.2.3 Graphene–Metal Oxide Composites as Anodes for LIBs

As described above, most metal oxides (SnO_2, Fe_2O_3, Fe_3O_4, Co_3O_4, NiO, Mn_3O_4) follow a conversion mechanism, functioning via redox reactions and offering high capacities (600–1000 mAh g^{-1}). Nevertheless, the severe volume expansion and poor conductivity limit their practical applications for LIBs. Fortunately, the emergence of graphene overcomes this issue. Several works have proved that the combination of graphene with metal oxides yields a significant increase in reversible capacity and rate capacity. There are a large number of approaches to prepare graphene–metal oxide composites (Figure 2.9). Among them, the physical mixing method is the original one. In 2009, Honma *et al.* [54] reassembled graphene nanosheets in the presence of SnO_2 nanoparticles: that is, GSs were distributed between SnO_2 nanoparticles. Such a structure limited the volume expansion upon lithium insertion, thereby avoiding the stress formed during the cycling. The obtained SnO_2/GS showed a reversible capacity of 810 mAh g^{-1}. After 30 cycles, the charge capacity was maintained at 570 mAh g^{-1}, about 70% retention of the reversible capacity. Du and coworkers [55] synthesized an α-Fe_2O_3/GS composite using $Fe(OH)_3$ sol and GO as precursors by a facile hydrothermal method (Figure 2.10a). The optimized α-Fe_2O_3/GS composite could deliver a reversible capacity of 950 mAh g^{-1} after 70 cycles at 100 mA g^{-1}, which is notably higher than that of α-Fe_2O_3 materials (200 mAh g^{-1}). It was different from achieving effective electronic conduction by a physical mixing process. Thus the performance was improved, but not sufficiently. It was still a big challenge to further optimize the performance of composite materials. To create good structural integrity and electronic conduction between metal oxides and graphene, coupling agents were used to form covalent bonds. As shown in Figure 2.10b, Feng *et al.* [35] synthesized graphene-encapsulated Co_3O_4 (Co_3O_4/GS) by assembly between negatively charged GO and positively charged Co_3O_4, in which Co_3O_4 nanoparticles were first modified by surface grafting of aminopropyltrimethoxysilane (APS). The GSs were wrapped around the surface of Co_3O_4 nanoparticles, which separated individual nanoparticles and retained a continuous conductive network to connect all the nanoparticles. Benefiting from the unique structure, the resulting Co_3O_4/GS possessed a high and stable reversible capacity of 1000 mAh g^{-1} after 130 cycles.

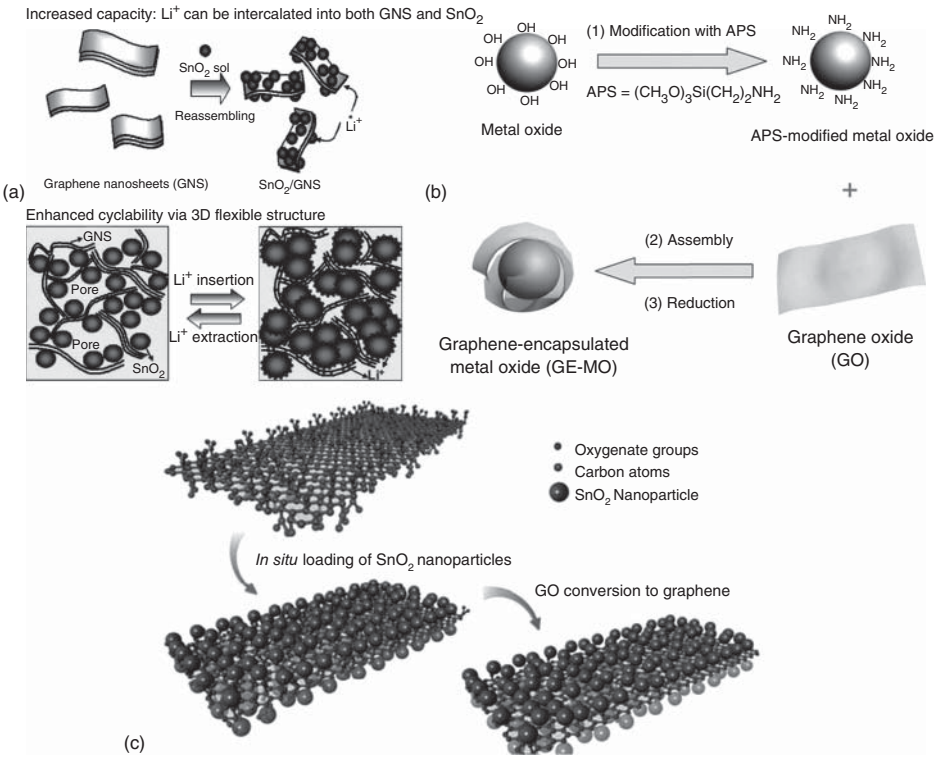

Figure 2.9 The preparation methods of graphene–metal oxide composites: (a) Schematic illustration for the physical mixing method to prepare SnO_2/GS. (Reproduced with permission [54]. Copyright (2009), American Chemical Society.) (b) Coupling-agent method for the preparation of graphene–metal oxides. (Reproduced with permission [35]. Copyright (2010), John Wiley & Sons, Inc.) (c) *In situ* chemical synthesis for the preparation of SnO_2/GS. (Reproduced with permission [56]. Copyright (2010), Royal Society of Chemistry.)

Compared to the above methods, *in situ* chemical synthesis could effectively improve the dispersion of nanoparticles on the graphene and enhance the interface contact, further optimizing the electrochemical performance of composite materials. For example, a well-organized composite of graphene nanosheets decorated with Fe_3O_4 particles was fabricated through *in situ* reduction of iron hydroxide between GSs (Figure 2.10c) [57]. The GS/Fe_3O_4 composite displayed a reversible specific capacity of 1026 mAh g^{-1} after 30 cycles at 35 mA g^{-1} and 580 mAh g^{-1} after 100 cycles at 700 mA g^{-1}, indicating superior rate capability and long cycle stability. The excellent performance could be attributed to the unique structure: that is, GS formed an effective matrix for the individual dispersion of Fe_3O_4 particles, playing the function of buffering the volume change and providing a highway for electron transport. In another work, Chen *et al.* [59] developed a facile one-step hydrothermal procedure for the *in situ* preparation of

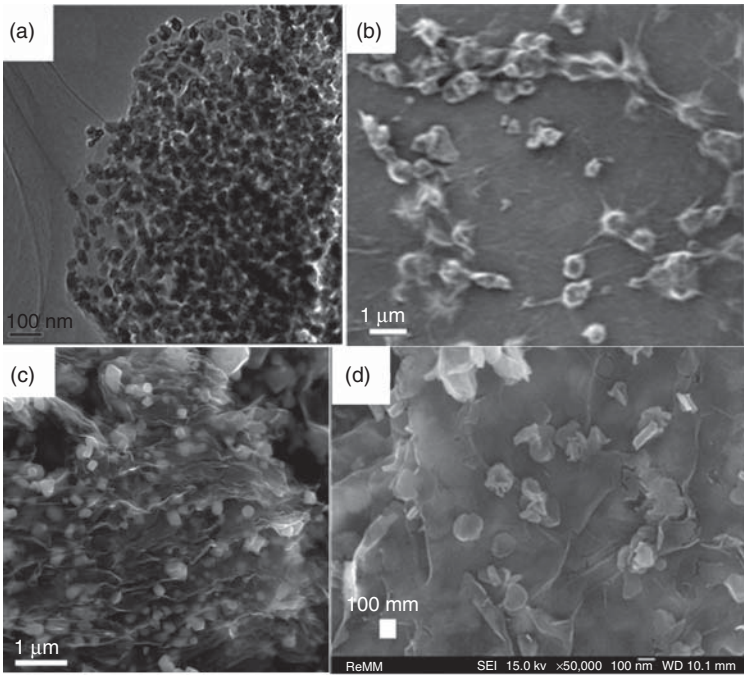

Figure 2.10 (a) SEM image of Fe_2O_3/graphene composite. (Reproduced with permission [55]. Copyright (2013), Royal Society of Chemistry.) (b) SEM image of graphene-encapsulated Co_3O_4. (Reproduced with permission [35]. Copyright (2010), John Wiley & Sons, Inc.) (c) SEM image of the cross-section of Fe_3O_4/graphene composite. (Reproduced with permission [57]. Copyright (2010), American Chemical Society.) (d) SEM image of NiO/graphene. (Reproduced with permission [58]. Copyright (2012), Elsevier.)

SnO_2/GS. Owing to the *in situ* chemical synthesis, ultrafine SnO_2 nanoparticles with an average diameter of 3 nm were uniformly decorated on or encapsulated in the GSs. The structure significantly shortened lithium diffusion length within each SnO_2 particle and graphene, further enhancing lithium and electron diffusion. Therefore, the as-prepared SnO_2/GS electrode delivered an increased reversible capacity of up to 1813 mAh g^{-1} after over 1000 cycles under a high current density of 2 A g^{-1}. Ryu *et al.* [58] fabricated a graphene/NiO composite by simple *in situ* chemical precipitation (Figure 2.10d). NiO nanoparticles were used as spacers to keep the GSs separated. Additionally, GSs were overlapped with each other to assemble a three-dimensional conducting network for fast electron transfer. As a result, the resulting electrode could deliver a specific capacity of 856 mAh g^{-1} even at a high current density of 5000 mA g^{-1}. Thus, it is believed that *in situ* chemical synthesis is an extremely efficient way to prepare high-performance LIBs.

As is well known, nitrogen-doped graphene would improve Li storage properties significantly by offering more active sites and enhancing the interaction between carbon and lithium compared to graphene. Therefore, N-doped

graphene–metal oxide nanocomposites are expected to be excellent electrode materials for LIBs. In a recent study, Sun *et al.* [60] synthesized Fe_2O_3/GN composite by a one-step hydrothermal strategy. Fe_2O_3 particles with size of 100–200 nm were uniformly anchored on the surface of GNs. Owing to its better conductivity and uniformity, the Fe_2O_3/GN composite exhibited much better electrochemical performance than Fe_2O_3/pristine graphene and pure Fe_2O_3, achieving a reversible capacity of 1012 mAh g^{-1} after 100 cycles. In another work, Park *et al.* [61] developed a facile hydrothermal route to grow small Mn_3O_4 nanoparticles on the surface of N-doped graphene using hydrazine hydrate both as a reducing agent and a nitrogen source. The N-doped graphene/Mn_3O_4 exhibited a high specific capacity 800 mAh g^{-1}, which was more stable and higher performance than graphene/Mn_3O_4 (703 mAh g^{-1}). The enhanced cycling performance was caused by the nitrogen doping, which was favorable for fast electron and ion transfer by decreasing the energy barrier, thus leading to higher electrochemical performance.

2.4.2.4 Graphene–TiO_2/MoS_2 Composites as Anodes for LIBs

Apart from the anode materials discussed above, another type of commonly used materials is the insertion type, which follows the intercalation mechanism, such as MoS_2 and TiO_2. MoS_2 possesses a special layered molecular structure. In this unique structure, Mo and S atoms form two-dimensional layers by strong covalent forces, and then these individual layers are stacked by van der Waals bonds. The weak interaction facilitates Li ions to insert and extract without large volume change. Therefore, MoS_2 is a prospective material for efficient storage and release of Li ions. Yet, the poor conductivity and aggregation limit its practical applications. Graphene, as a perfect conductive matrix, presents the unique advantage once again. Chen *et al.* [32] employed a facile, *in situ*, solution-phase reduction method to synthesize MoS_2/GS composites (Figure 2.11a–c). The electrode showed extraordinary capacity, up to 1300 mAh g^{-1}, and excellent rate capability and cycling stability. The excellent property of MoS_2/GS could be attributed to the *in situ* introduced graphene, which provided a conductive matrix to disperse the MoS_2 nanoplates and accommodate the volume changes during cycling. In addition to its use as the 2D matrix to anchor MoS_2, graphene could form 3D architecture by self-assembly to support MoS_2. The unique 3D architecture could offer rich sites to absorb lithium ions, an integrated network to improve conductivity, and a large space to buffer the volume change. Zhang *et al.* [62] fabricated a MoS_2-coated three-dimensional graphene network (MoS_2/3DGN) by a facile CVD method. The 3D GN was composed of interconnected GSs, and was used as a template to deposit MoS_2. The MoS_2/3D GN delivered reversible capacities of 877 and 665 mAh g^{-1} at 100 and 500 mA g^{-1} after 50 cycles, respectively, exhibiting its superior rate and cycling performance.

TiO_2 is known for intercalating lithium into the lattice with a small volume change. It has also been mixed with GSs to prepare LIB anode materials with an enhanced electrochemical performance. Lee *et al.* [37] designed a unique sandwich-like structure by directly growing rutile TiO_2 nanorobs onto GS

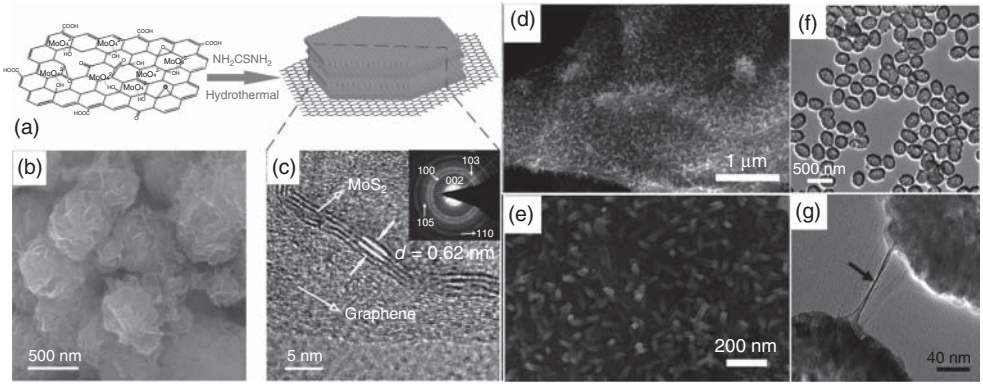

Figure 2.11 (a–c) The characterization of MoS_2/GS. (Reproduced with permission [32]. Copyright (2011), Royal Society of Chemistry.) (a) Schematic diagram of the *in situ* synthesis of MoS_2/GS. (b) SEM image of MoS_2/GS composites. (c) HRTEM image of MoS_2 layers on graphene (inset is the electron diffraction pattern of the MoS_2 nanosheets on graphene.). (d,e) SEM images of TONRAs-GS nanocomposites. (Reproduced with permission [37]. Copyright (2012), Royal Society of Chemistry.) (f,g) TEM images of GS/hollow TiO_2 composite (the black arrow in (g) shows the folding of GS between connected TiO_2 hollow particles). (Reproduced with permission [63]. Copyright (2011), Royal Society of Chemistry.)

sheets (TONRAs-GS) to improve the electrochemical properties of rutile TiO_2 (Figure 2.11d,e). The unique sandwich-like structure could provide larger electrode–electrolyte contact area and rapid Li ion transfer, give more electron transfer access, and prevent aggregation of electroactive materials during cycling, leading to an improved performance. Remarkably, the TONRAs-GS nanocomposite showed a specific capacity of 190 and 117 mAh g^{-1} at 0.2 and 2 C, much higher than bare TONRs (36 and 11 mAh g^{-1}). In another example, Lou *et al.* [63] reported a rational design of GS-wrapped anatase TiO_2 hollow particles (Figure 2.11f,g). The graphene/TiO_2 hollow particles delivered a reversible capacity of 90 mAh g^{-1} over 180 cycles, while the pure TiO_2 could give only 60 mAh g^{-1}. The significantly enhanced lithium storage capacity of GS/TiO_2 could be probably ascribed to the GS wrapping, which not only created a highly conductive network, which allowed efficient electron conduction among the TiO_2 hollow particles, but also boosted the structural integrity during extended charge/discharge cycling.

In summary, the combination of anode materials with different reaction mechanisms, composites, and GSs to prepare graphene-based composites has been demonstrated to display significantly improved electrochemical performance compared with the pure anode material or graphene. The presence of graphene in the composite plays a number of roles, such as preventing the nanosized active particles from aggregation, efficiently buffering the volume expansion and contraction of the particles during cycling, enhancing the rate capability due to its excellent electric conductivity, and reversibly storing lithium ions. In turn, the

composite also benefits from the particles, which could act as spacers between GSs, enabling a highly accessible surface.

2.5
Two-Dimensional (2D) Flexible and Binder-Free Graphene-Based Electrodes

With the advent of flexible electronics, flexible LIBs have attracted great attention as a promising power source in the emerging field of flexible and wearable electronic devices such as roll-up displays, touch screens, wearable sensors, and implantable medical devices [64]. The traditional electrode of LIBs is formed from a current collector which is coated with a mixture of an active material, an electrical conductor, and a polymer binder (Figure 2.12a). This type of electrode is not suitable for flexible or bendable electrode, because the active material layer will easily detach from the substrate following repeated deformation. In addition, polymer binders will generate many discontinuous channels which retard ion transport and cause an undesirable decrease in electrical conductivity [65–68]. In this regard, the development of free-standing and binder-free electrode materials is highly desirable for flexible and bendable LIBs (Figure 2.12b). Graphene has an extremely large aspect ratio and excellent structural flexibility, and thus can be easily assembled layer by layer into a macroscopic, flexible, and strong graphene membrane. These intriguing features make it attractive as a promising flexible, free-standing electrode for flexible power sources, and recent studies have demonstrated its promise in such applications.

2.5.1
Graphene-Based Flexible Anode Materials for LIBs

2.5.1.1 2D Flexible and Binder-Free Graphene Electrodes

Graphene-based papers can be easily obtained by a simple vacuum filtration method: the flow of water during vacuum filtration will cause the generation of a directing force, which drives GO or GS to assemble layer by layer and form an ordered layered film. The first investigation of graphene paper as a

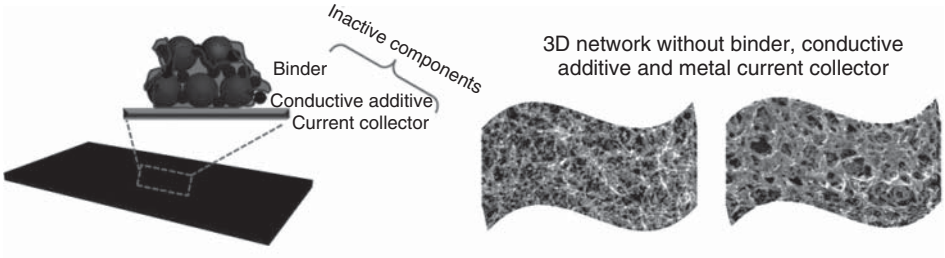
Inactive components
Binder
Conductive additive
Current collector
3D network without binder, conductive additive and metal current collector
(a) Commerical electrode for batteries
(b) Flexible CNT/graphene based electrodes for batteries

Figure 2.12 Schematic of (a) conventional and (b) flexible electrode components in LIBs. (Reproduced with permission [64]. Copyright (2014), Royal Society of Chemistry.)

flexible electrode material was carried out by Wallace's group [69, 70]. Although graphene paper had good mechanical properties (tensile strength 293.3 MPa, Young's modulus 41.8 GPa), high conductivity (351 S m^{-1}), and a large initial discharge capacity (680 mAh g^{-1}), the irreversible capacity was very serious, retaining only 84 mAh g^{-1} at the second cycle. This may due to the fact that GSs tend to tightly restack together driven by large π−π interactions, which severely inhibit the diffusion and penetration of electrolyte into the film. To solve this problem, the CNTs were randomly dispersed between GSs to prevent its restacking and increase cross-plane electric conductivity of the paper [71]. As a result, the hybrid paper exhibited an initial reversible specific capacity of ~375 mAh g^{-1} (second cycle) and 330 mAh g^{-1} at the 100th cycle, greatly improving the cyclic stability. In another study, Kung and coworkers [72] reported a combined ultrasonic vibration and mild acid oxidation approach to increase the cross-plane ion diffusion by introducing in-plane carbon vacancy defects (pores) into GS (Figure 2.13a,b). These in-plane pores provided a high density of new, cross-plane ion diffusion channels that facilitated charge transport and

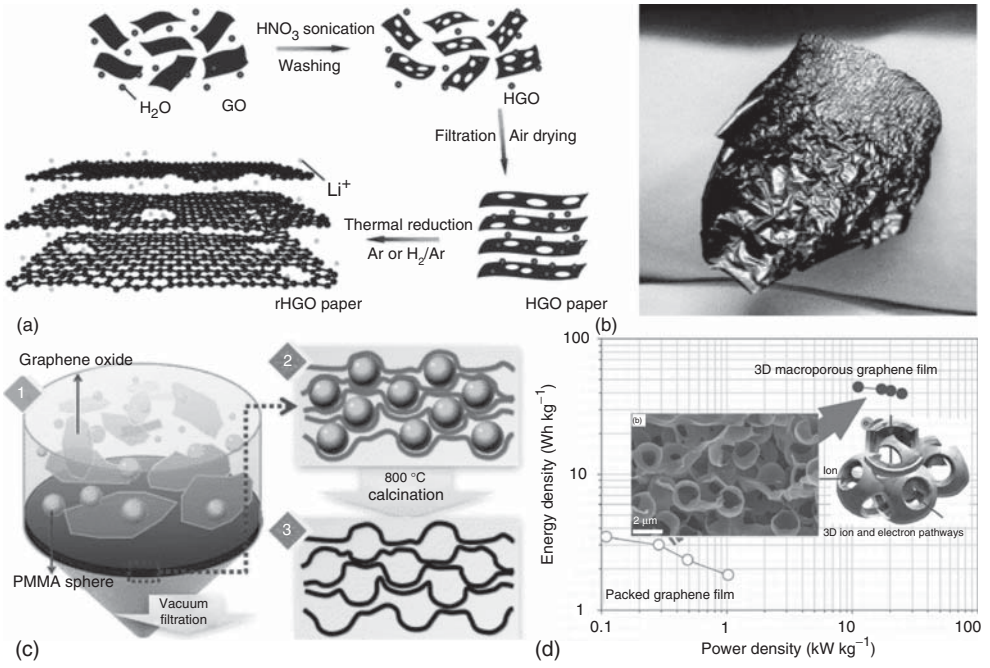

Figure 2.13 (a,b) Schematic drawing of the formation of holey graphene paper and the digital image. (Reproduced with permission [72]. Copyright (2011), American Chemical Society.) (c) Illustration of the fabrication of a macroporous bubble graphene film. (Reproduced with permission [73]. Copyright (2012), Royal Society of Chemistry.) (d) Illustration of 3D ionic and electronic transport pathways in the porous electrode, and the inset is a highly magnified SEM image of the bubble graphene film. (Reproduced with permission [74]. Copyright (2012), American Chemical Society.)

storage at high rates. High capacities of ~150 and 70 mAh g^{-1} were achieved at 13.3 and 26.6 C without any capacity decay up to 1000 cycles. Additionally, macroporous bubble graphene films were constructed by using GO as carbon precursor and a polymer as template, such as poly(methyl methacrylate) (PMMA) spheres [73] and polystyrene (PS) colloidal particles [74, 75] (Figure 2.13c). Such a macroporous structure can not only provide 3D ion and electron pathways but also greatly increase the contact area between the electrode and the electrolyte, thus significantly improving the energy density and power density of the electrode compared to those of a packed graphene film (Figure 2.13d). Recently, Liu *et al.* [76] prepared an interconnected porous graphene network by mechanically pressing a graphene aerogel. The free-standing graphene paper was highly flexible with a 3D porous structure, delivering a capacity of 557 mAh g^{-1} at a current density of 200 mA g^{-1}.

In addition to chemically exfoliated graphene, CVD-grown graphene has higher electrical conductivity and lower structural defects, and could also be filtrated to fabricate graphene papers. For example, Cao *et al.* [77] used expanded vermiculite as a layered template in the CVD process to produce bulk materials containing GSs of the order of hundreds of micrometers at a gram scale (Figure 2.14a–c). Owing to the large sheet size, the as-obtained GSs were easily fabricated into flexible graphene papers with low surface density and good conductivity (Figure 2.14d). The obtained graphene paper exhibited a greatly enhanced reversible capacity (1350 mAh g^{-1} at 50 mA g^{-1}) and cycling performance compared to the graphene papers fabricated using reduced GO. Based on the CVD route, monolayer graphene grown on a Cu foil, together with a lithium foil anode, was further used to sandwich a thin solid polymer electrolyte, forming a flexible all-solid-state battery with a total thickness of 50 mm (inset in Figure 2.14e) [78]. The battery can be bent to a radius of less than 1 mm and can drive an LED (light emitting diode) (Figure 2.14e–g). As a result of the rapid surface Li^+ absorption/diffusion and electron transport in monolayer graphene, a high volumetric energy density of 10 Wh l^{-1} was achieved at a power density of 50 W l^{-1} with good cyclic stability over 100 cycles.

Although some progress has been made on 2D flexible and binder-free graphene electrodes, further increasing the initial Coulombic efficiency and revealing the lithium storage mechanisms remain the key aspects of current research. Additionally, there is no obvious voltage plateau to provide a stable potential output, and the specific capacity of pure graphene paper is still too low to meet practical applications [64]. In view of these problems, electrochemically active second phases with higher capacity and better cyclic stability are expected to be combined to further improve the lithium storage performance of flexible graphene electrodes.

2.5.1.2 2D Flexible and Binder-Free Graphene-Based Hybrid Anode Electrodes

Up to now, great efforts have been devoted to prepare graphene-based free-standing and binder-free hybrid electrodes. For instance, a flexible graphene film was used as the current collector, upon which metal oxides were attached by

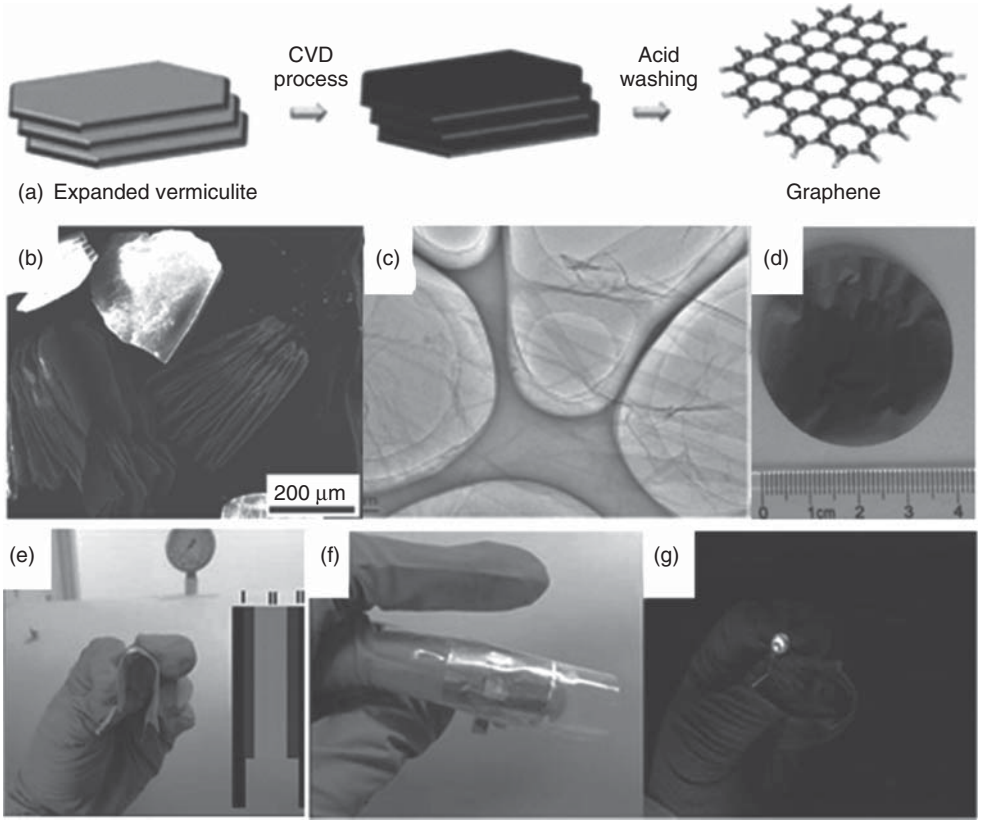

Figure 2.14 (a) Illustration of the formation of graphene using expanded vermiculite as template. (b) SEM images of the expanded vermiculite templates. (c) TEM images of the CVD graphene. (d) A photograph of the as-prepared graphene paper. (Reproduced with permission [77]. Copyright (2013), Royal Society of Chemistry.) (e,f) Flexible graphene battery undergoing deformation: inset in (e) shows the sandwich structure of the battery: (I) graphene on Cu foil as a cathode, (II) polymer electrolyte, and (III) lithium foil as an anode. (g) Graphene monolayer battery powering a LED. (Reproduced with permission [78]. Copyright (2013), Royal Society of Chemistry.)

chemical deposition [67, 79] or hydrothermal reaction [80]. Such approaches usually produce low loading and aggregation of metal oxides; thus the improvement on the overall hybrid electrode performance was limited. Another way was based on vacuum filtration, by which various active materials (such as Fe_3O_4 [81], Co_3O_4 [82], SnO_2 [34, 83], TiO_2 [84, 85], MnO_2 [68, 86], V_2O_5 [14], and silicon [87–89]) were incorporated into the graphene scaffold [68]. Specifically, both components were homogeneously mixed and filtered to produce paper-like electrodes, in which graphene formed a 3D conductive network to behave as a mechanical support and embedded-in current collector. From the viewpoint of structure, on one hand, the electroactive materials introduced into graphene film can not only suppress the tight restacking of GSs but also increase the available surface area,

leading to high electrochemical activity. On the other hand, graphene can also act as a support to induce a uniform dispersion of second phases on its surface [64]. All these will consequently improve the lithium storage performance.

Metal oxides have attracted extensive interest because of their high theoretical capacity. Guo *et al.* [83] first prepared a flexible, free-standing SnO_2 nanoparticle/GS paper by vacuum filtration of GO and SnO_2 nanoparticles, followed by a thermal reduction (Figure 2.15a). Compared with single graphene paper, the hybrid paper showed a higher capacity because of the hybridization with high-capacity SnO_2 nanoparticles. Compared with the pure SnO_2 nanoparticles, the hybrid paper exhibited a better cycling stability because of the hybridization with the excellent flexible and electroconductive graphene. Li and coworkers fabricated SnO_2/N-doped graphene sandwich papers, using 7,7,8,8-tetracyanoquinodimethane anion ($TCNQ^-$) as both the nitrogen source and the complexing agent [34]. When used in LIBs, the material exhibited a

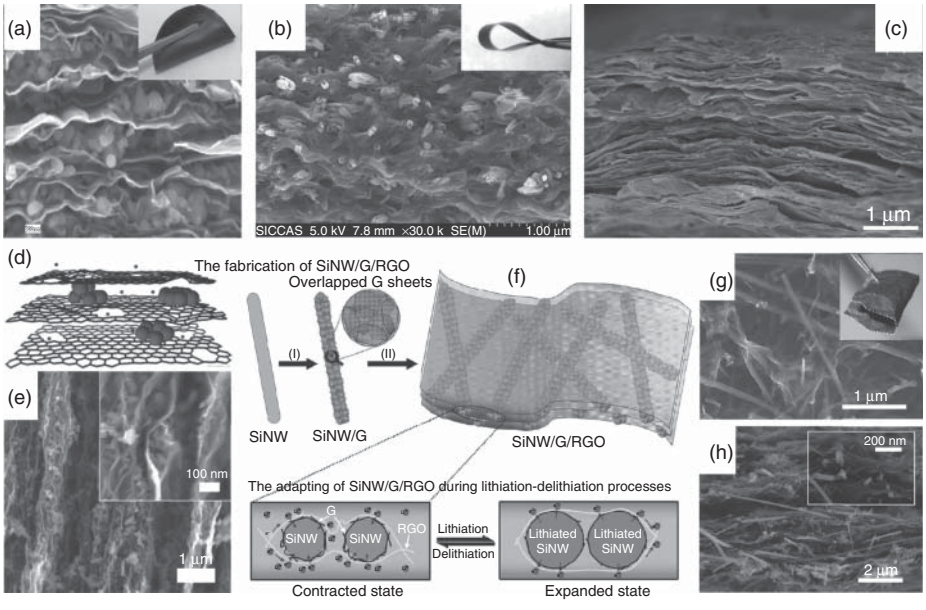

Figure 2.15 (a) Cross-sectional SEM image of SnO_2 nanoparticles/GS paper. (Reproduced with permission [83]. Copyright (2012), American Chemical Society.) (b) Cross-sectional SEM image of hollow Fe_3O_4 nanospindles/GS film. (Reproduced with permission [81]. Copyright (2013), Royal Society of Chemistry.) (c) Cross-sectional SEM image of Co_3O_4 nanosheets/GS film. (Reproduced with permission [82]. Copyright (2013), Royal Society of Chemistry.) (d) A schematic drawing of a composite electrode material constructed by a graphenic scaffold with in-plane carbon vacancy defects. (e) SEM image of the cross-section of a Si nanoparticles/GS paper. (Reproduced with permission [87]. Copyright (2011), John Wiley & Sons, Inc.) (f) Schematic of the fabrication of a dual-sheath-protected Si NWs/GS/RGO electrode and its lithiation/delithiation. (g) Cross-section and (e) top-surface SEM images of Si NWs/GS/RGO electrode. (Reproduced with permission [88]. Copyright (2013), American Chemical Society.)

large capacity (918 mAh g^{-1} at 100 mA g^{-1}), high-rate capability (504 mAh g^{-1} at 5 A g^{-1}), and excellent cycling stability resulting from its unique features, namely excellent electronic conductivity related to the sandwich structure, short transportation length for both lithium ions and electrons, and elastomeric space to accommodate volume changes upon Li insertion/extraction. Recently, Sun *et al.* [81] designed porous, free-standing, hollow Fe_3O_4 nanospindle/GS films to enhance ion diffusion kinetics (Figure 2.15b). The hybrid film had a loosely layered three-dimensional structure and many pores existed between the spindles and the GS. This pore-enriched nanostructure provided not only abundant open channels for ion transport but also sufficient buffer space for volume expansion of Fe_3O_4. As a result, the hybrid electrode exhibited high specific capacities (1555 mAh g^{-1} at 100 mA g^{-1}) and excellent cyclic stability (940 and 660 mAh g^{-1} at 200 and 500 mA g^{-1} after 50 cycles, respectively), which are much superior to those of traditional electrodes and pure Fe_3O_4 electrodes. Afterwards, hierarchically structured Co_3O_4 nanosheets/GS films were designed to strengthen interfacial interactions with the assistance of electrostatic attractive interactions (Figure 2.15c) [82]. A high capacity of 1400 mAh g^{-1} was achieved at 100 mA g^{-1} because of the morphological compatibility coupled with strong interfacial interactions between Co_3O_4 nanosheets and GSs. Besides, other metal oxides, such as MnO_2 nanotubes [86] and TiO_2 nanosheets [85], were also incorporated with GSs to form hybrid films.

Apart from metal oxides, as mentioned above, Si is another promising anode material because of ultrahigh specific capacity, natural abundance, and low cost. Free-standing Si nanoparticle/GS films were first prepared by vacuum filtration of Si nanoparticles and GO together with thermal reduction [90]. The hybrid film delivered a capacity of >2200 mAh g^{-1} after 50 cycles and >1500 mAh g^{-1} after 200 cycles with a decreasing rate of 0.5% per cycle. Thus, the cyclic stability still needs to be improved. Based on this work, Kung *et al.* [87] further optimized the nanostructure of Si/GS film, by introducing in-plane, nanometer-sized carbon vacancies into GS via mild acid etching (Figure 2.15d,e). The in-plane carbon vacancies created new diffusion channels for facile ion transport throughout the hybrid film, thus overcoming the characteristic high resistance of graphene material for Li ion transport. Consequently, this Si/GS free-standing and binder-free electrode achieved an unprecedented reversible capacity of around 1100 mAh g^{-1} at 8 A g^{-1}, a rate equivalent to full discharge in 8 min, repeatable up to 99.9% between cycles for over 150 cycles. Apart from 0D nanoparticles, Zhi and coworkers [89] developed a new anode prototype consisting of 2D GS-sandwiched 1D Si nanowires (Si NWs/GS). Such 1D/2D combination enables the formation of a 3D porous structure which facilitates the fast diffusion of lithium ions, delivering a large capacity of 3350 mAh g^{-1} at 840 mA g^{-1} and high-rate capacity of 1200 mAh g^{-1} at 8.4 A g^{-1}. Furthermore, Si NWs were presheathed with overlapped GS by CVD to form core–sheath nanocables (Si NWs/GS), and were in turn sandwiched between reduced GO to construct dual-sheath-protected flexible Si NWs/GS/RGO electrodes (Figure 2.15f) [88]. In the architecture, the inner GS-sealed sheaths prevented the direct exposure of Si NWs to the

electrolyte, enabling the structural and interfacial stabilization. Meanwhile, the flexible and conductive RGO overcoats accommodated the volume change of embedded Si NWs/GS nanocables, maintaining the structural and electrical integrity of the electrode (Figure 2.15g,h). Based on the nanostructure design, the electrodes exhibited a high reversible specific capacity of 1600 mAh g^{-1} at 2.1 A g^{-1}, 80% capacity retention after 100 cycles, and superior rate capability (500 mAh g^{-1} at 8.4 A g^{-1}) based on the total electrode weight.

2.5.2 Graphene-Based Flexible Cathode Materials for LIBs

Cathode materials are currently one of the bottlenecks for the production of high-performance LIBs. Therefore, graphene-based flexible cathode materials have also been intensively explored. For example, V_2O_5/GS cathode paper and graphene anode paper were integrated to build a flexible lithium rechargeable battery (Figure 2.16a,b) [67]. V_2O_5/GS paper was fabricated by using a pulsed

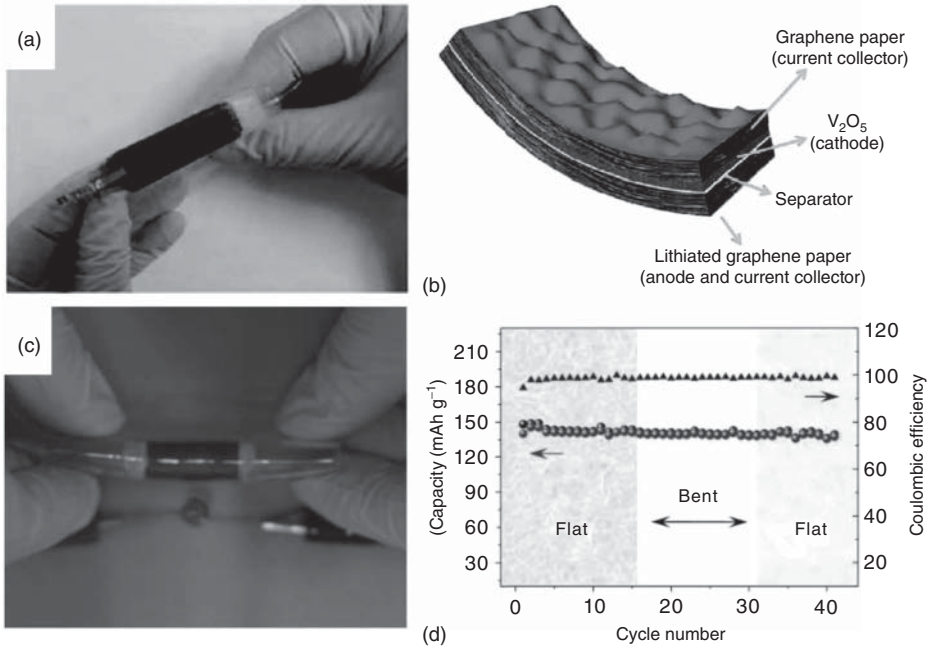

Figure 2.16 (a) Photograph of the assembled flexible Li battery based on graphene paper, which is thin, lightweight, and flexible enough to be rolled up or twisted. (b) Schematic drawing of the flexible Li battery based on graphene paper. V_2O_5/graphene paper and electrochemically lithiated-graphene paper were used as cathode and anode, respectively, which were separated by a separator dipped in liquid electrolyte. (Reproduced with permission [67]. Copyright (2011), Royal Society of Chemistry.) (c) Photograph of a full battery with $LiFePO_4$/GF cathode and $Li_4Ti_5O_{12}$/GF anode lighting a red LED device under bending. (d) Cyclic performance of the battery under flat and bent states [93].

laser deposition technique, while graphene paper served as a template and current collector. The graphene paper anode was electrochemically lithiated prior to cell integration because lithium is initially not present either in the anode or in the cathode. As shown in Figure 2.16a, the flexible battery was able to operate when rolled up or twisted, with the first charge capacity of ~15 mAh cm^{-2}, showing its potential application in flexible electronic equipment. Recently, 3D porous conductive graphite foam (GF), which was synthesized using Ni foam template-directed CVD, was developed as a free-standing, lightweight current collector, upon which $LiFePO_4$ was drop-cast to produce a cathode material for LIBs [91, 92]. Benefitting from the light weight (~9.5 mg cm^{-3}) and highly conductive interconnected network (~1.3×10^5 S m^{-1} at 300 K), the $LiFePO_4$/GF cathode presented excellent electrochemical stability up to 5 V versus Li/Li^+ and superior rate capacity of 70 mAh g^{-1} at 1280 mA g^{-1}. Afterwards, Li *et al.* [93] developed thin, lightweight, and flexible $LiFePO_4$/GF and $Li_4Ti_5O_{12}$/GF electrodes by *in situ* hydrothermal deposition, which could simultaneously obtain high charge and discharge rates up to 200 C. They further assembled a thin, lightweight, and flexible full LIB by sealed $LiFePO_4$/GF and $Li_4Ti_5O_{12}$/GF electrodes with polydimethylsiloxane (PDMS), using $LiPF_6$ in ethylene carbonate/dimethyl carbonate as the electrolyte. The flexible full battery, with a total thickness of <800 μm, showed no structural failure after repeatedly bending to a radius of <5 mm and was able to power a red LED when bent (Figure 2.16c). Combining the mechanical flexibility and high-rate performance of these electrodes, the full LIB can deliver an initial discharge capacity of 143 mAh g^{-1} at 0.2 C and an energy density of 110 Wh kg^{-1} based on the total mass of $LiFePO_4$/GF and $Li_4Ti_5O_{12}$/GF electrodes. Also, the flexible cell can be repeatedly bent to a radius of <5 mm without loss of its excellent performance (Figure 2.16d), demonstrating its great potential for use in next-generation flexible electronics.

2.6 Three-Dimensional Macroscopic Graphene-Based Electrodes

Graphene-based aerogel is a 3D macroscopic graphene architecture constructed by the self-assembly of GSs. Graphene can be seen as macromolecules that have a planar structure and also many dangling bonds on its edges. Driven by a noncovalent (van der Waals force, π–π stacking interactions, hydrogen bond) or covalent interactions, GSs can partially overlap or coalesce and self-assemble into stable 3D macroscopic hydrogels with a high surface area, porous structure, and continuous graphene backbone [94–96]. These structural features not only prevent individual GSs from aggregating and restacking during the process of assembly but also facilitate the easy access of electrolyte and fast diffusion of electrons. Moreover, 3D porous frameworks can accommodate the volume change of metal oxides and sulfides, and prevent their aggregation during cycle processes, resulting in excellent electrochemical performance [97, 98]. All these have made the graphene-based aerogel as an attractive electrode material in the field of LIBs.

In 2011, Chen *et al.* [99] pioneered the capture of preprepared Fe_3O_4 into 3D graphene network by a mild chemical reduction (~90 °C without stirring) with the aid of $NaHSO_3$ reducing agents. The obtained Fe_3O_4/GS aerogel exhibited a capacity of 1000 mAh g^{-1} at 200 mA g^{-1}. Theoretically, any nanoparticles homogeneously dispersed in the aqueous suspension can be embedded into the graphene network to form a 3D nanoparticle/GS hydrogel. Although the whole process is simple, mild, and universal, long-term dialysis with ultrapure water is required to remove the large amount of reducing agents. Additionally, since the as-prepared nanoparticles and GSs are only physically contacted, the interfacial interactions are inferior and need to be further improved. Later, Yu *et al.* [100] found that ferrous ions ($FeSO_4$) could act both as a reducing agent to induce the assembly of GS and simultaneously as a precursor to achieve the *in situ* growth of α-FeOOH nanorods and Fe_3O_4 nanoparticles on GS under mild conditions (Figure 2.17a–d). Therefore, this approach requires no additional reducing agent and also greatly improves interfacial interactions with *in situ* growth.

Apart from chemical reduction method, hydrothermal treatment is another generally employed approach to fabricate the 3D graphene architecture. For instance, a nitrogen-doped graphene aerogel with Fe_3O_4 nanoparticles (Fe_3O_4/GN) was synthesized by mixing of GO aqueous suspension, iron acetate, and polypyrrole (as nitrogen source) via a combined hydrothermal method, freeze-drying, and a thermal treatment process (Figure 2.17e) [101]. The as-prepared Fe_3O_4/GN exhibited an interconnected, porous, 3D graphene framework with continuous macropores in the micrometer size range. Fe_3O_4 nanoparticles (20–80 nm) were uniformly deposited on GN (Figure 2.17f,g). However, the specific surface area was only 110 m^2 g^{-1}, indicating a serious aggregation of GN. Furthermore, the same authors fabricated 3D graphene foams cross-linked with Fe_3O_4 nanospheres (~200 nm) encapsulated with graphene (Fe_3O_4/GS/GF) [102]. The graphene shells suppressed the aggregation of Fe_3O_4 and buffered the volume expansion, while the interconnected 3D graphene networks reinforced the core–shell structure of Fe_3O_4/GS and thus enhanced the electrical conductivity of the overall electrode. As a result, Fe_3O_4/GS/GF delivered a high reversible capacity of 1059 mAh g^{-1} at 93 mA g^{-1} over 150 cycles, and excellent rate capability (363 mAh g^{-1} at 4800 mA g^{-1}). Recently, Ajayan and coworkers [97] synthesized 3D porous MoS_2/GS or FeO_x/GS hybrid architectures using GO aqueous suspension and $(NH_4)_2MoS_4$ or $FeCl_3$ as precursors through a hydrothermal reaction. The resulting aerogels possessed high surface area (285 and 265 m^2 g^{-1} for MoS_2/GS and FeO_x/GS, respectively), a porous structure, and a continuous graphene backbone. Accordingly, a high specific capacity (1100–1200 mAh g^{-1} at 0.5 C) and long cycle life (3000 cycles for MoS_2 and 1500 cycles for FeO_x with almost 100% capacity retention) were achieved at different charge and discharge rates.

Although the hydrothermal method can successfully induce the self-assembly of graphene, GO was partially reduced in mild reduction conditions. Recently, Sun and coworkers [1] developed a novel solvothermal-induced self-assembly approach, using colloid sol as precursor, to construct monolithic 3D metal

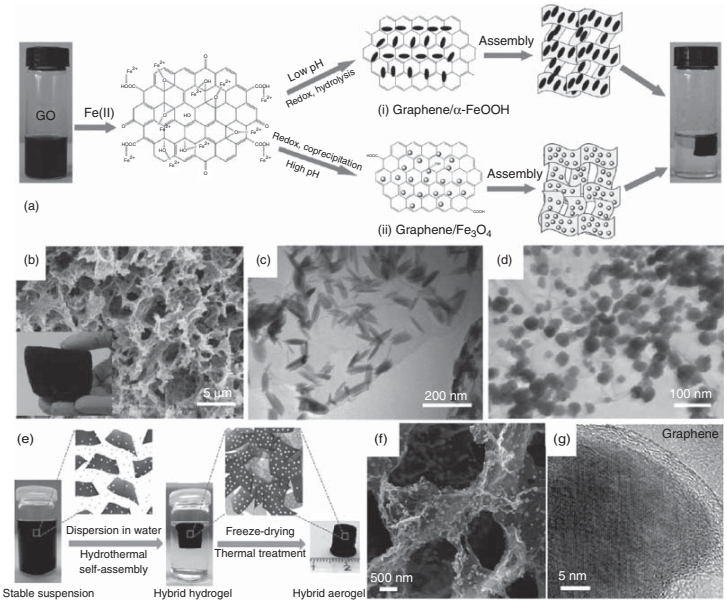

Figure 2.17 (a) Schematic illustration of the formation mechanism of the α-FeOOH/GS and Fe_3O_4/GS hydrogels. (b) SEM image of α-FeOOH/GS and its digital photograph (the inset in (b)). (c,d) TEM images of α-FeOOH/GS and Fe_3O_4/GS aerogels, respectively. (Reproduced with permission [100]. Copyright (2012), American Chemical Society.) (e) Fabrication process of the 3D Fe_3O_4/GN aerogels by hydrothermal treatment. (f) SEM image and (g) HRTEM image of Fe_3O_4/GN aerogels. (Reproduced with permission [101]. Copyright (2012), American Chemical Society.)

oxide/GS aerogels. Compared with the general hydrothermal treatment, solvothermal treatment can further restrict the coarsening of the resulting nanocrystals, enable a more thorough reduction of GS, and endow the composite a higher electrical conductivity. As a proof of concept, Fe_2O_3/GS aerogels were synthesized based on the $Fe(OH)_3$ sol (Figure 2.18a). The resultant Fe_2O_3/GS aerogels, with uniform deposition of Fe_2O_3 of 20–50 nm, possessed the key factors for high-performance electrodes: macroporous structures, large surface area (212.1 $m^2 g^{-1}$), high electrical conductivity (277.5 S m^{-1}), and good electrode homogeneity (Figure 2.18b–d). As a result, the Fe_2O_3/GS electrode delivered a high capacity of 733 mAh g^{-1} during 1000 charge/discharge cycles even at 2000 mA g^{-1}, with a capacity decay as low as 0.027% per cycle (Figure 2.18e). Importantly, the solvothermal-induced self-assembly process is a versatile approach for the fabrication of metal oxide/GS hydrogels. Furthermore, the colloidal precursor is not limited to hydroxide colloids but can be extended to oxide colloids. For example, macroscopic SnO_2/GN aerogels were also obtained when using SnO_2 sol as precursor (crystal size of 3–7 nm) [2]. Benefiting from the combined N-doped property and 3D graphene frameworks, the SnO_2/GN

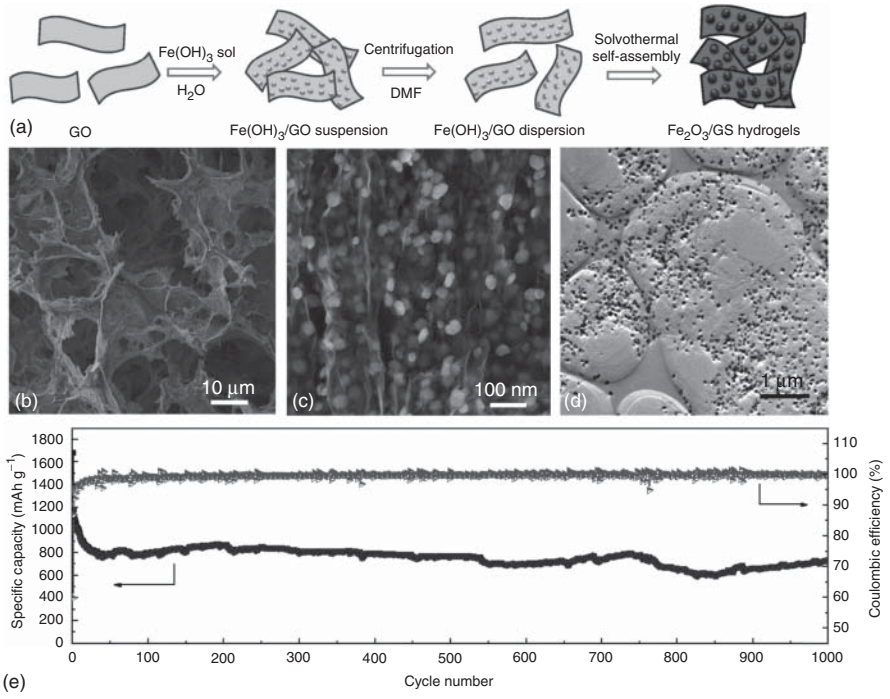

Figure 2.18 (a) Schematic illustration of preparation of Fe_2O_3/GS aerogels by a solvothermal-induced self-assembly approach, using $Fe(OH)_3$ sol as precursor. (b,c) SEM and (d) TEM images of Fe_2O_3/GS aerogels. (e) Cycle performance of Fe_2O_3/GS aerogels at a current density of 2000 mA g^{-1}. (Reproduced with permission [1]. Copyright (2014), John Wiley & Sons, Inc.)

exhibited superior rate capability (1126, 855, and 614 mAh g^{-1} at 1000, 3000, and 6000 mA g^{-1}, respectively) and extraordinarily prolonged cycling stability at high current densities (905 mAh g^{-1} after 1000 cycles at 2000 mA g^{-1}).

2.7 Summary and Perspectives

We have reviewed the recent advances of graphene-based electrodes in LIBs, including grahene-based cathode materials, graphene-based anode materials, new type 2D flexible and binder-free graphene-based electrodes, and 3D macroscopic graphene-based electrodes (aerogels), highlighting them as a promising class of advanced electrode materials for LIBs. Although considerable research progress and breakthroughs have been made in this field, several problems and challenges still need to be resolved before this promising material can be practically widely used in people's everyday life.

1) In the case of graphene-based traditional electrode, intensive researches have demonstrated that integration of active materials and graphene can fully use each component via synergistic effects, and consequently improve the lithium storage performance. However, the following aspects should be the future research focus in order to further boost the electrochemical performance. On one hand, researches should understand in depth and clarify the lithium storage mechanisms of graphene-based electrodes, as well as the relationships between microstructure and electrochemical behavior. In this regard, *in situ* transmission electron microscope (TEM) and atomic force microscope (AFM) techniques need to be developed to directly observe the dynamic behaviors and clarify the fundamental mechanisms of the active materials. On the other hand, further efforts should also be focused on the design of novel nanostructure, the control of the size, morphology, and dispersibility of the active materials, and improvement of the interfacial interactions between active materials and graphene.
2) Although a large number of 2D flexible graphene-based cathodes and anodes have been reported, the development of simple, low-cost, and large-scale fabrication process is urgently required. And also, the state-of-the-art reports were mainly focused on the preparation of flexible and binder-free graphene-based electrodes. Considering the final industrial implementation, high-performance and flexible cathode and anode materials should be assembled together for developing practical flexible LIB devices, not merely high-performance electrodes in some aspects. Therefore, lightweight and flexible packaging materials with exceptional barrier properties, shape-deformable highly conductive electrolytes, and integration technologies of full battery systems are worth exploring and yet very challenging. Moreover, the current flexible graphene-based electrodes were often tested in a rigid half-cell, or even full LIB cells were only tested by simply bending them without quantitative analysis. More in-depth analyses combined with

mechanical studies are highly desired to precisely characterize the lithium storage behavior of flexible LIBs under twisting and bending conditions.

3) As for 3D macroscopic graphene-based aerogels, the understanding of self-assembly mechanisms and the inherent properties of those materials is still far from sufficient and need to be explored. And also, how to enhance the strength of aerogels and precisely control the pore size distribution remains a large scientific and technological challenge. Furthermore, the development of cost-effective and large-scale approaches to construct graphene-based aerogels is another important issue. These aspects should gain increased research attention.

With continuous exploitation, we believe that graphene-based electrodes for LIBs will realize many practical applications such as portable tools, electrical vehicles, and also many flexible and wearable electronic devices.

References

1. Wang, R., Xu, C., Du, M., Sun, J., Gao, L., Zhang, P., Yao, H., and Lin, C. (2014) Solvothermal-induced self-assembly of Fe_2O_3/GS aerogels for high li-storage and excellent stability. *Small*, **10** (11), 2260–2269.
2. Wang, R., Xu, C., Sun, J., Gao, L., and Yao, H. (2014) Solvothermal-induced 3D macroscopic SnO_2/nitrogen-doped graphene aerogels for high capacity and long-life lithium storage. *ACS Appl. Mater. Interfaces*, **6** (5), 3427–3436.
3. Xu, C.H., Xu, B.H., Gu, Y., Xiong, Z.G., Sun, J., and Zhao, G. (2013) Graphene-based electrodes for electrochemical energy storage. *Energy Environ. Sci.*, **6** (5), 1388–1414.
4. Guo, B.K., Xu, H., Wang, X.Y., and Xiao, L.X. (2002) *Lithium Ion Batteries*, Central South University Press, Changsha, pp. 7–11.
5. Chen, L., Zhang, M., and Wei, W. (2013) Graphene-based composites as cathode materials for lithium ion batteries. *J. Nanomater.*, 2013, 940389–940397.
6. Wang, H.L., Yang, Y., Liang, Y.Y., Cui, L.F., Casalongue, H.S., Li, Y.G., Hong, G.S., Cui, Y., and Dai, H.J. (2011) $LiMn_{1-x}Fe_xPO_4$ nanorods grown on graphene sheets for ultrahigh-rate-performance lithium ion batteries. *Angew. Chem. Int. Ed.*, **50** (32), 7364–7368.
7. Wang, R., Xu, C., Sun, J., Gao, L., Jin, J., and Lin, C. (2013) Controllable synthesis of nano-$LiFePO_4$ on graphene using Fe_2O_3 precursor for high performance lithium ion batteries. *Mater. Lett.*, **112** (1), 207–210.
8. Wang, G., Liu, H., Liu, J., Qiao, S., Lu, G.M., Munroe, P., and Ahn, H. (2010) Mesoporous $LiFePO_4$/C nanocomposite cathode materials for high power lithium ion batteries with superior performance. *Adv. Mater.*, **22** (44), 4944–4948.
9. Ding, Y., Jiang, Y., Xu, F., Yin, J., Ren, H., Zhuo, Q., Long, Z., and Zhang, P. (2010) Preparation of nano-structured $LiFePO_4$/graphene composites by co-precipitation method. *Electrochem. Commun.*, **12** (1), 10–13.
10. Zhou, X.F., Wang, F., Zhu, Y.M., and Liu, Z.P. (2011) Graphene modified $LiFePO_4$ cathode materials for high power lithium ion batteries. *J. Mater. Chem.*, **21** (10), 3353–3358.
11. Oh, S.W., Huang, Z.D., Zhang, B.A., Yu, Y., He, Y.B., and Kim, J.K. (2012) Low temperature synthesis of graphene-wrapped $LiFePO_4$ nanorod cathodes by the polyol method. *J. Mater. Chem.*, **22** (33), 17215–17221.
12. Rao, C.V., Reddy, A.L.M., Ishikawa, Y., and Ajayan, P.M. (2011) $LiNi_{1/3}Co_{1/3}Mn_{1/3}O_2$-graphene composite as a promising cathode for

lithium-ion batteries. *ACS Appl. Mater. Interfaces*, **3** (8), 2966–2972.

13. Liu, H. and Yang, W. (2011) Ultralong single crystalline V_2O_5 nanowire/graphene composite fabricated by a facile green approach and its lithium storage behavior. *Energy Environ. Sci.*, **4** (10), 4000–4008.
14. Lee, J.W., Lim, S.Y., Jung, H.M., Hwang, T.H., Kang, J.K., and Choi, J.W. (2012) Extremely stable cycling of ultra-thin V_2O_5 nanowire-graphene electrodes for lithium rechargeable battery cathodes. *Energy Environ. Sci.*, **5** (12), 9889–9894.
15. Wang, G., Shen, X., Yao, J., and Park, J. (2009) Graphene nanosheets for enhanced lithium storage in lithium ion batteries. *Carbon*, **47** (8), 2049–2053.
16. Huang, X., Zeng, Z., Fan, Z., Liu, J., and Zhang, H. (2012) Graphene-based electrodes. *Adv. Mater.*, **24** (45), 5979–6004.
17. Wang, H.B., Maiyalagan, T., and Wang, X. (2012) Review on recent progress in nitrogen-doped graphene synthesis, characterization, and its potential applications. *ACS Catal.*, **2** (5), 781–794.
18. Dahn, J.R., Zheng, T., Liu, Y.H., and Xue, J.S. (1995) Mechanisms for lithium insertion in carbonaceous materials. *Science*, **270**, 590–593.
19. Kaskhedikar, N.A. and Maier, J. (2009) Lithium storage in carbon nanostructures. *Adv. Mater.*, **21** (25-26), 2664–2680.
20. Wu, Z.S., Zhou, G., Yin, L.C., Ren, W., Li, F., and Cheng, H.M. (2012) Graphene/metal oxide composite electrode materials for energy storage. *Nano Energy*, **1** (1), 107–131.
21. Sato, K., Noguchi, M., Demachi, A., Oki, N., and Endo, M. (1994) A mechanism of lithium storage in disordered carbon. *Science*, **264** (22), 556–558.
22. Guo, P., Song, H., and Chen, X. (2009) Electrochemical performance of graphene nanosheets as anode material for lithium-ion batteries. *Electrochem. Commun.*, **11** (6), 1320–1324.
23. Lian, P., Zhu, X., Liang, S., Li, Z., Yang, W., and Wang, H. (2010) Large reversible capacity of high quality graphene sheets as an anode material for lithium-ion batteries. *Electrochim. Acta*, **55** (12), 3909–3914.
24. Pan, D., Wang, S., Zhao, B., Wu, M., Zhang, H., Wang, Y., and Jiao, Z. (2009) Li storage properties of disordered graphene nanosheets. *Chem. Mater.*, **21** (14), 3136–3142.
25. Yoo, E., Kim, J., Hosono, E., Zhou, H.S., Kudo, T., and Honma, I. (2008) Large reversible Li storage of graphene nanosheet families for use in rechargeable lithium ion batteries. *Nano Lett.*, **8** (8), 2277–2282.
26. Wu, Z.S., Ren, W.C., Xu, L., Li, F., and Cheng, H.M. (2011) Doped graphene sheets as anode materials with superhigh rate and large capacity for lithium ion batteries. *ACS Nano*, **5** (7), 5463–5471.
27. Wang, H., Zhang, C., Liu, Z., Wang, L., Han, P., Xu, H., Zhang, K., Dong, S., Yao, J., and Cui, G. (2011) Nitrogen-doped graphene nanosheets with excellent lithium storage properties. *J. Mater. Chem.*, **21** (14), 5430–5434.
28. Xin, X., Zhou, X., Wang, F., Yao, X., Xu, X., Zhu, Y., and Liu, Z. (2012) A 3D porous architecture of Si/graphene nanocomposite as high-performance anode materials for Li-ion batteries. *J. Mater. Chem.*, **22** (16), 7724–7730.
29. Tang, H., Tu, J.P., Liu, X.Y., Zhang, Y.J., Huang, S., Li, W.Z., Wang, X.L., and Gu, C.D. (2014) Self-assembly of Si/honeycomb reduced graphene oxide composite film as a binder-free and flexible anode for Li-ion batteries. *J. Mater. Chem. A*, **2** (16), 5834–5840.
30. Park, S.H., Kim, H.K., Ahn, D.J., Lee, S.I., Roh, K.C., and Kim, K.B. (2013) Self-assembly of Si entrapped graphene architecture for high-performance Li-ion batteries. *Electrochem. Commun.*, **34**, 117–120.
31. Wang, G.X., Wang, B., Wang, X.L., Park, J., Dou, S.X., Ahn, H., and Kim, K. (2009) Sn/graphene nanocomposite with 3D architecture for enhanced reversible lithium storage in lithium ion batteries. *J. Mater. Chem.*, **19** (44), 8378–8384.
32. Chang, K. and Chen, W. (2011) In situ synthesis of MoS_2/graphene nanosheet composites with extraordinarily high

electrochemical performance for lithium ion batteries. *Chem. Commun.*, **47** (14), 4252–4254.

33. Yin, J., Cao, H., Zhou, Z., Zhang, J., and Qu, M. (2012) SnS_2@reduced graphene oxide nanocomposites as anode materials with high capacity for rechargeable lithium ion batteries. *J. Mater. Chem.*, **22** (45), 23963–23970.
34. Wang, X., Cao, X., Bourgeois, L., Guan, H., Chen, S., Zhong, Y., Tang, D.M., Li, H., Zhai, T., Li, L., Bando, Y., and Golberg, D. (2012) N-doped graphene-SnO_2 sandwich paper for high-performance lithium-ion batteries. *Adv. Funct. Mater.*, **22** (13), 2682–2690.
35. Yang, S., Feng, X., Ivanovici, S., and Müllen, K. (2010) Fabrication of graphene-encapsulated oxide nanoparticles: towards high-performance anode materials for lithium storage. *Angew. Chem. Int. Ed.*, **49** (45), 8408–8411.
36. Qiu, D., Bu, G., Zhao, B., Lin, Z., Pu, L., Pan, L., and Shi, Y. (2014) In situ growth of mesoporous Co_3O_4 nanoparticles on graphene as a high-performance anode material for lithium-ion batteries. *Mater. Lett.*, **119** (15), 12–15.
37. He, L., Ma, R., Du, N., Ren, J., Wong, T., Li, Y., and Lee, S.T. (2012) Growth of TiO_2 nanorod arrays on reduced graphene oxide with enhanced lithium-ion storage. *J. Mater. Chem.*, **22** (36), 19061–19066.
38. Chang, Y., Li, J., Wang, B., Luo, H., He, H., Song, Q., and Zhi, L. (2013) Synthesis of 3D nitrogen-doped graphene/Fe_3O_4 by a metal ion induced self-assembly process for high-performance Li-ion batteries. *J. Mater. Chem. A*, **1** (46), 14658–14665.
39. Cao, H., Li, B., Zhang, J., Lian, F., Kong, X., and Qu, M. (2012) Synthesis and superior anode performance of TiO_2@reduced graphene oxide nanocomposites for lithium ion batteries. *J. Mater. Chem.*, **22** (19), 9759–9766.
40. Xu, C., Sun, J., and Gao, L. (2012) Direct growth of monodisperse SnO_2 nanorods on graphene as high capacity anode materials for lithium ion batteries. *J. Mater. Chem.*, **22** (3), 975–979.
41. Reddy, M.V., Subba Rao, G.V., and Chowdari, B.V.R. (2013) Metal oxides and oxysalts as anode materials for Li ion batteries. *Chem. Rev.*, **113** (7), 5364–457.
42. Chan, C.K., Peng, H., Liu, G., McIlwrath, K., Zhang, X.F., Huggins, R.A., and Cui, Y. (2007) High-performance lithium battery anodes using silicon nanowires. *Nat. Nanotechnol.*, **3** (1), 31–35.
43. Kim, H., Seo, M., Park, M.H., and Cho, J. (2010) A critical size of silicon nano-anodes for lithium rechargeable batteries. *Angew. Chem. Int. Ed.*, **49** (12), 2146–2149.
44. Lu, Z., Zhu, J., Sim, D., Zhou, W., Shi, W., Hng, H.H., and Yan, Q. (2011) Synthesis of ultrathin silicon nanosheets by using graphene oxide as template. *Chem. Mater.*, **23** (24), 5293–5295.
45. Wen, Z., Lu, G., Cui, S., Kim, H., Ci, S., Jiang, J., Hurley, P.T., and Chen, J. (2014) Rational design of carbon network cross-linked Si-SiC hollow nanosphere as anode of lithium-ion batteries. *Nanoscale*, **6** (1), 342–351.
46. Cui, L.F., Yang, Y., Hsu, C.M., and Cui, Y. (2009) Carbon-silicon core-shell nanowires as high capacity electrode for lithium ion batteries. *Nano Lett.*, **9** (9), 3370–3374.
47. Wen, Z., Lu, G., Mao, S., Kim, H., Cui, S., Yu, K., Huang, X., Hurley, P.T., Mao, O., and Chen, J. (2013) Silicon nanotube anode for lithium-ion batteries. *Electrochem. Commun.*, **29**, 67–70.
48. Lai, J., Guo, H., Wang, Z., Li, X., Zhang, X., Wu, F., and Yue, P. (2012) Preparation and characterization of flake graphite/silicon/carbon spherical composite as anode materials for lithium-ion batteries. *J. Alloys Compd.*, **530** (25), 30–35.
49. Ren, J.G., Wang, C., Wu, Q.H., Liu, X., Yang, Y., He, L., and Zhang, W. (2014) A silicon nanowire-reduced graphene oxide composite as a high-performance lithium ion battery anode material. *Nanoscale*, **6** (6), 3353–3360.

50. Evanoff, K., Magasinski, A., Yang, J., and Yushin, G. (2011) Nanosilicon-coated graphene granules as anodes for Li-ion batteries. *Adv. Energy Mater.*, **1** (4), 495–498.
51. Zhou, M., Pu, F., Wang, Z., Cai, T., Chen, H., Zhang, H., and Guan, S. (2013) Facile synthesis of novel Si nanoparticles-graphene composites as high-performance anode materials for Li-ion batteries. *Phys. Chem. Chem. Phys.*, **15** (27), 11394–11401.
52. Du, Y., Zhu, G., Wang, K., Wang, Y., Wang, C., and Xia, Y. (2013) Si/graphene composite prepared by magnesium thermal reduction of SiO2 as anode material for lithium-ion batteries. *Electrochem. Commun.*, **36**, 107–110.
53. Qin, J., He, C.N., Zhao, N.Q., Wang, Z.Y., Shi, C.S., Liu, E.Z., and Li, J.J. (2014) Graphene networks anchored with Sn@graphene as lithium ion battery anode. *ACS Nano*, **8** (2), 1728–1738.
54. Paek, S.M., Yoo, E., and Honma, I. (2009) Enhanced cyclic performance and lithium storage capacity of SnO_2/graphene nanoporous electrodes with three-dimensionally delaminated flexible structure. *Nano Lett.*, **9** (1), 72–75.
55. Du, M., Xu, C., Sun, J., and Gao, L. (2013) Synthesis of alpha-Fe_2O_3 nanoparticles from $Fe(OH)_3$ sol and their composite with reduced graphene oxide for lithium ion batteries. *J. Mater. Chem. A*, **1** (24), 7154–7158.
56. Zhang, L.S., Jiang, L.Y., Yan, H.J., Wang, W.D., Wang, W., Song, W.G., Guo, Y.G., and Wan, L.J. (2010) Mono dispersed SnO_2 nanoparticles on both sides of single layer graphene sheets as anode materials in Li-ion batteries. *J. Mater. Chem.*, **20** (26), 5462–5467.
57. Zhou, G., Wang, D.W., Li, F., Zhang, L., Li, N., Wu, Z.-S., Wen, L., Lu, G.Q., and Cheng, H.M. (2010) Graphene-wrapped Fe_3O_4 anode material with improved reversible capacity and cyclic stability for lithium ion batteries. *Chem. Mater.*, **22** (18), 5306–5313.
58. Hwang, S.G., Kim, G.O.K., Yun, S.R., and Ryu, K.S. (2012) NiO nanoparticles with plate structure grown on graphene as fast charge-discharge anode material for lithium ion batteries. *Electrochim. Acta*, **78** (1), 406–411.
59. Chen, Y., Song, B.H., Chen, R.M., Lu, L., and Xue, J.M. (2014) A study of the superior electrochemical performance of 3 nm SnO_2 nanoparticles supported by graphene. *J. Mater. Chem. A*, **2** (16), 5688–5695.
60. Du, M., Xu, C., Sun, J., and Gao, L. (2012) One step synthesis of Fe_2O_3/nitrogen-doped graphene composite as anode materials for lithium ion batteries. *Electrochim. Acta*, **80** (1), 302–307.
61. Park, S.K., Jin, A., Yu, S.H., Ha, J., Jang, B., Bong, S., Woo, S., Sung, Y.E., and Piao, Y. (2014) In situ hydrothermal synthesis of Mn_3O_4 nanoparticles on nitrogen-doped graphene as high-performance anode materials for lithium ion batteries. *Electrochim. Acta*, **120** (20), 452–459.
62. Cao, X., Shi, Y., Shi, W., Rui, X., Yan, Q., Kong, J., and Zhang, H. (2013) Preparation of MoS_2-coated three-dimensional graphene networks for high-performance anode material in lithium-ion batteries. *Small*, **9** (20), 3433–3438.
63. Chen, J.S., Wang, Z., Dong, X.C., Chen, P., and Lou, X.W. (2011) Graphene-wrapped TiO_2 hollow structures with enhanced lithium storage capabilities. *Nanoscale*, **3** (5), 2158–2161.
64. Zhou, G., Li, F., and Cheng, H.-M. (2014) Progress in flexible lithium batteries and future prospects. *Energy Environ. Sci.*, **7** (4), 1307–1338.
65. Chen, X.C., Wei, W., Lv, W., Su, F.Y., He, Y.B., Li, B.H., Kang, F.Y., and Yang, Q.H. (2012) Graphene-based nanostructure with expanded ion transport channels for high rate li-ion battery. *Chem. Commun.*, **48** (47), 5904–5906.
66. Noerochim, L., Wang, J.Z., Chou, S.L., Wexler, D., and Liu, H.K. (2012) Free-standing single-walled carbon nanotube/SnO_2 anode paper for flexible lithium-ion batteries. *Carbon*, **50** (3), 1289–1297.
67. Gwon, H., Kim, H.S., Lee, K.U., Seo, D.H., Park, Y.C., Lee, Y.S., Ahn, B.T.,

and Kang, K. (2011) Flexible energy storage devices based on graphene paper. *Energy Environ. Sci.*, **4** (4), 1277–1283.

68. Li, Z.P., Mi, Y.J., Liu, X.H., Liu, S., Yang, S.R., and Wang, J.Q. (2011) Flexible graphene/MnO_2 composite papers for supercapacitor electrodes. *J. Mater. Chem.*, **21** (38), 14706–14711.

69. Dikin, D.A., Stankovich, S., Zimney, E.J., Piner, R.D., Dommett, G.H.B., Evmenenko, G., Nguyen, S.T., and Ruoff, R.S. (2007) Preparation and characterization of graphene oxide paper. *Nature*, **448** (7152), 457–460.

70. Chen, H., Müller, M.B., Gilmore, K.J., Wallace, G.G., and Li, D. (2008) Mechanically strong, electrically conductive, and biocompatible graphene paper. *Adv. Mater.*, **20** (18), 3557–3561.

71. Hu, Y., Li, X., Wang, J., Li, R., and Sun, X. (2013) Free-standing graphene–carbon nanotube hybrid papers used as current collector and binder free anodes for lithium ion batteries. *J. Power. Sources*, **237** (1), 41–46.

72. Zhao, X., Hayner, C.M., Kung, M.C., and Kung, H.H. (2011) Flexible holey graphene paper electrodes with enhanced rate capability for energy storage applications. *ACS Nano*, **5** (11), 8739–8749.

73. Chen, C.M., Zhang, Q., Huang, C.H., Zhao, X.C., Zhang, B.S., Kong, Q.Q., Wang, M.Z., Yang, Y.G., Cai, R., and Sheng Su, D. (2012) Macroporous 'bubble' graphene film via template-directed ordered-assembly for high rate supercapacitors. *Chem. Commun.*, **48** (57), 7149–7151.

74. Choi, B.G., Yang, M.H., Hong, W.H., Choi, J.W., and Huh, Y.S. (2012) 3D macroporous graphene frameworks for supercapacitors with high energy and power densities. *ACS Nano*, **6** (5), 4020–4028.

75. Wang, Z.L., Xu, D., Wang, H.G., Wu, Z., and Zhang, X.B. (2013) In situ fabrication of porous graphene electrodes for high-performance energy storage. *ACS Nano*, **7** (3), 2422–2430.

76. Liu, F., Song, S., Xue, D., and Zhang, H. (2012) Folded structured graphene paper for high performance electrode materials. *Adv. Mater.*, **24** (8), 1089–1094.

77. Ning, G., Xu, C., Cao, Y., Zhu, X., Jiang, Z., Fan, Z., Qian, W., Wei, F., and Gao, J. (2013) Chemical vapor deposition derived flexible graphene paper and its application as high performance anodes for lithium rechargeable batteries. *J. Mater. Chem. A*, **1** (2), 408–414.

78. Wei, D., Haque, S., Andrew, P., Kivioja, J., Ryhanen, T., Pesquera, A., Centeno, A., Alonso, B., Chuvilin, A., and Zurutuza, A. (2013) Ultrathin rechargeable all-solid-state batteries based on monolayer graphene. *J. Mater. Chem. A*, **1** (9), 3177–3181.

79. Xiao, F., Li, Y.Q., Zan, X.L., Liao, K., Xu, R., and Duan, H.W. (2012) Growth of metal–metal oxide nanostructures on freestanding graphene paper for flexible biosensors. *Adv. Funct. Mater.*, **22** (12), 2487–2494.

80. Yuan, C.Z., Yang, L., Hou, L.R., Li, J.Y., Sun, Y.X., Zhang, X.G., Shen, L.F., Lu, X.J., Xiong, S.L., and Lou, X.W. (2012) Flexible hybrid paper made of monolayer Co_3O_4 microsphere arrays on rGO/CNTs and their application in electrochemical capacitors. *Adv. Funct. Mater.*, **22** (12), 2560–2566.

81. Wang, R.H., Xu, C.H., Sun, J., Gao, L., and Lin, C.C. (2013) Flexible free-standing hollow Fe_3O_4/graphene hybrid films for lithium-ion batteries. *J. Mater. Chem. A*, **1** (5), 1794–1800.

82. Sun, J., Wang, R.H., Xu, C.H., Liu, Y.Q., Gao, L., and Lin, C.C. (2013) Free-standing and binder-free lithium-ion electrode based on robust layered assembly of graphene and Co_3O_4 nanosheets. *Nanoscale*, **5** (15), 6960–6967.

83. Liang, J., Zhao, Y., Guo, L., and Li, L. (2012) Flexible free-standing graphene/SnO_2 nanocomposites paper for Li-ion battery. *ACS Appl. Mater. Interfaces*, **4** (11), 5742–5748.

84. Hu, T., Sun, X., Sun, H.T., Yu, M.P., Lu, F.Y., Liu, C.S., and Lian, J. (2013) Flexible free-standing graphene-TiO_2 hybrid paper for use as lithium ion battery anode materials. *Carbon*, **51**, 322–326.

85. Li, N., Zhou, G., Fang, R., Li, F., and Cheng, H.M.h. (2013) TiO_2/graphene sandwich paper as an anisotropic electrode for high rate lithium ion batteries. *Nanoscale*, **5** (17), 7780–7784.
86. Yu, A.P., Park, H.W., Davies, A., Higgins, D.C., Chen, Z.W., and Xiao, X.C. (2011) Free-standing layer-by-layer hybrid thin film of graphene-MnO_2 nanotube as anode for lithium ion batteries. *J. Phys. Chem. Lett.*, **2** (15), 1855–1860.
87. Zhao, X., Hayner, C.M., Kung, M.C., and Kung, H.H. (2011) In-plane vacancy-enabled high-power Si–graphene composite electrode for lithium-ion batteries. *Adv. Energy Mater.*, **1** (6), 1079–1084.
88. Wang, B., Li, X.L., Zhang, X.F., Luo, B., Jin, M.H., Liang, M.H., Dayeh, S.A., Picraux, S.T., and Zhi, L.J. (2013) Adaptable silicon-carbon nanocables sandwiched between reduced graphene oxide sheets as lithium ion battery anodes. *ACS Nano*, **7** (2), 1437–1445.
89. Wang, B., Li, X.L., Luo, B., Jia, Y.Y., and Zhi, L.J. (2013) One-dimensional/two-dimensional hybridization for self-supported binder-free silicon-based lithium ion battery anodes. *Nanoscale*, **5** (4), 1470–1474.
90. Lee, J.K., Smith, K.B., Hayner, C.M., and Kung, H.H. (2010) Silicon nanoparticles-graphene paper composites for Li ion battery anodes. *Chem. Commun.*, **46** (12), 2025–2027.
91. Chen, Z.P., Ren, W.C., Gao, L.B., Liu, B.L., Pei, S.F., and Cheng, H.M. (2011) Three-dimensional flexible and conductive interconnected graphene networks grown by chemical vapour deposition. *Nat. Mater.*, **10** (6), 424–428.
92. Ji, H., Zhang, L., Pettes, M.T., Li, H., Chen, S., Shi, L., Piner, R., and Ruoff, R.S. (2012) Ultrathin graphite foam: a three-dimensional conductive network for battery electrodes. *Nano Lett.*, **12** (5), 2446–2451.
93. Li, N., Chen, Z., Ren, W., Li, F., and Cheng, H.M. (2012) Flexible graphene-based lithium ion batteries with ultrafast charge and discharge rates. *Proc. Natl. Acad. Sci.U.S.A.*, **109** (43), 17360–17365.
94. Sudeep, P.M., Narayanan, T.N., Ganesan, A., Shaijumon, M.M., Yang, H., Ozden, S., Patra, P.K., Pasquali, M., Vajtai, R., Ganguli, S., Roy, A.K., Anantharaman, M.R., and Ajayan, P.M. (2013) Covalently interconnected three-dimensional graphene oxide solids. *ACS Nano*, **7** (8), 7034–7040.
95. Xu, Y., Sheng, K., Li, C., and Shi, G. (2010) Self-assembled graphene hydrogel via a one-step hydrothermal process. *ACS Nano*, **4** (7), 4324–4330.
96. Han, Z., Tang, Z., Li, P., Yang, G., Zheng, Q., and Yang, J. (2013) Ammonia solution strengthened three-dimensional macro-porous graphene aerogel. *Nanoscale*, **5** (12), 5462–5467.
97. Gong, Y.J., Yang, S.B., Liu, Z., Ma, L.L., Vajtai, R., and Ajayan, P.M. (2013) Graphene-network-backboned architectures for high-performance lithium storage. *Adv. Mater.*, **25** (29), 3979–3984.
98. Jiang, L.L. and Fan, Z.J. (2014) Design of advanced porous graphene materials: from graphene nanomesh to 3D architectures. *Nanoscale*, **6** (4), 1922–1945.
99. Chen, W.F., Li, S.R., Chen, C.H., and Yan, L.F. (2011) Self-assembly and embedding of nanoparticles by in situ reduced graphene for preparation of a 3D graphene/nanoparticle aerogel. *Adv. Mater.*, **23** (17), 5679–5683.
100. Cong, H.P., Ren, X.C., Wang, P., and Yu, S.H. (2012) Macroscopic multifunctional graphene-based hydrogels and aerogels by a metal ion induced self-assembly process. *ACS Nano*, **6** (3), 2693–2703.
101. Wu, Z.S., Yang, S.B., Sun, Y., Parvez, K., Feng, X.L., and Mullen, K. (2012) 3D nitrogen-doped graphene aerogel-supported Fe_3O_4 nanoparticles as efficient eletrocatalysts for the oxygen reduction reaction. *J. Am. Chem. Soc.*, **134** (22), 9082–9085.
102. Wei, W., Yang, S.B., Zhou, H.X., Lieberwirth, I., Feng, X.L., and Müllen, K. (2013) 3D graphene foams cross-linked with pre-encapsulated Fe_3O_4 nanospheres for enhanced lithium storage. *Adv. Mater.*, **22** (21), 2909–2914.

3
Graphene-Based Energy Devices

Wei-Ren Liu

3.1
Introduction

Owing to excellent properties of graphite reported so far, such as Young's modulus (>1060 GPa), electron conductivity (10^4 S m^{-1}), thermal conductivity (~3000 W m^{-1} K^{-1}), light weight, and low cost, it is widely used in many applications. By downsizing graphite from the micro to the nano scale, namely graphene, the applications would, in future, widen to polymer composites, anode materials for Li-ion batteries, supercapacitors, hydrogen storage materials, adsorbers, and catalysts. In this chapter, we introduce the applications of graphene for energy devices, such as Li-ion batteries, Li–sulfur batteries, fuel cells, and solar cells.

3.2
Graphene for Li-Ion Batteries

3.2.1
Anode Materials

In order to develop next-generation anode materials with an energy density higher than the theoretical capacity of 372 mAh g^{-1} for the graphite anode, much attention has been paid on alloy-based anode materials. However, the poor cycle life of these anodes due to the dramatic volume change during charge/discharge processes results in difficulty for their commercialization. Nowadays, graphene has been emerging as a fascinating material for applications in transistors, transparent electrodes, sensors, and energy materials with many unusual physical, chemical, and mechanical properties. Graphene nanosheets (GNSs), obtained from chemical exfoliation of graphite, have been proposed for the application of anode materials for Li-ion batteries. The corresponding research on GNS for Li-ion batteries is introduced in this section.

In 1994, Sato *et al.* proposed a covalent molecular model of LiC_2, which indicated that the lithium ion could be trapped by carbon in an arobatic structure.

Graphene-based Energy Devices, First Edition. Edited by A. Rashid bin Mohd Yusoff.
© 2015 Wiley-VCH Verlag GmbH & Co. KGaA. Published 2015 by Wiley-VCH Verlag GmbH & Co. KGaA.

The formation of LiC_2 in amorphous carbon could give a reversible capacity of as high as 1116 mAh g^{-1}. However, these amorphous carbon-based anodes synthesized from different precursors typically deliver reversible capacity in the range of 400–700 mAh g^{-1}. According to the covalent molecular model of Li_2, the highest theoretical capacity could be approached as long as the *d* spacing of the graphene layer in the (002) direction exceeds 0.4 nm. Pan *et al.* [1] synthesized graphene-based anodes by different reducing processes, including chemical reduction agents, thermal reduction, electron beam, and so on, to demonstrate the electrochemical properties of graphene-based anode materials. Their results indicate that graphene anodes derived from thermal exfoliation at low temperatures and electron beam etching give a higher reversible capacity of ~600 mAh g^{-1}.

In order to investigate the relationship between the structural properties of graphene and the reaction mechanism of lithium for Li-ion batteries, Kostecki *et al.* [2] synthesized single-layer and few-layer graphenes by chemical vapor deposition (CVD). By an *in situ* Raman technique, as shown in Figure 3.1, they could show that the reaction mechanism of lithium is quite similar for single-layer graphene and few-layer graphene. From first-principles calculations, it has been

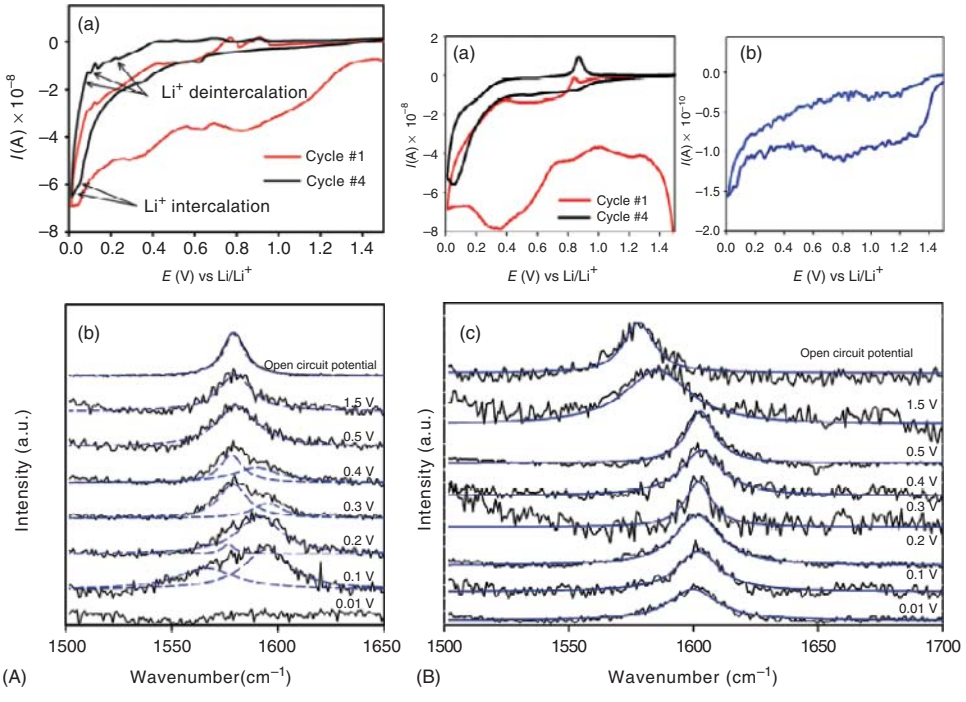

Figure 3.1 (A: a,b) CV curves of few-layer graphene in the first two cycles and *in situ* Raman spectra of few-layer graphene during charging process. (B: a–c) CV curves of single-layer graphene in the first and second cycle and *in situ* Raman spectra of single-layer graphene during the charging process [2].

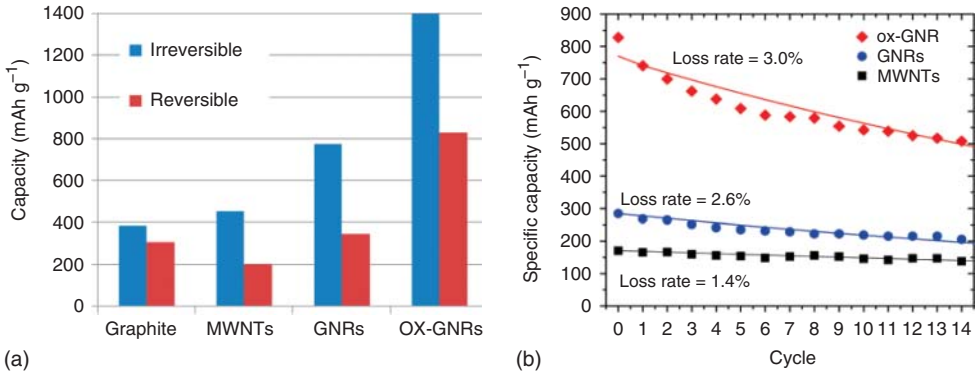

Figure 3.2 (a) Charge/discharge capacities of graphite, multilayer carbon nanotubes, multilayer graphene, and oxide multilayer graphene. (b) Cycling tests of multilayer carbon nanotubes, multilayer graphene, and oxidized multilayer graphene [4].

found that the degree of charge transfer is lower than that in graphite, which might be due to the strong repulsive force resulting from the lithium located at edge sites.

Barone *et al.* [3] studied the diffusion mechanism of lithium in graphene by using density functional theory. As the dimension of graphene reduces to 1, both reactivity and diffusion are affected as a result of the edge effect of graphene materials. With decreasing width of graphene, the diffusion barrier and diffusion length decrease. The energy difference and diffusivity coefficient could be reduced and increased to 0.15 eV and two orders of magnitude, respectively.

Apart from CVD or chemical exfoliation, recently, many other approaches have been investigated for the characterization of graphene. Fahlman *et al.* [4] synthesized quasi-one-dimentional graphene nanoribbons (GNRs) by cutting multilayer carbon nanotubes. Four different morphhologies of carbon-based materials, namely graphite, multilayer carbon nanotubes, GNRs, and oxidized GNRs, were synthesized for Li-ion batteries for carrying out tests of charge/discharge capacity and life cycle tests, as shown in Figure 3.2a,b, respectively. The electrochemcial tests indicate that the reversible capacity of reduced GNRs is much higher than that of bare multiwalled carbon nanotubes (MWCNTs), namely ~200–370 mAh g^{-1}. In addition, the charge and dischrge capacities of oxidized GNRs are 1400 and 820 mAh g^{-1}, respectively, which gives a coulombic efficiency of 53%. The enhanced capacity of oxidized GNRs might be due to the contribution of functional groups on the surface.

Uthaisar *et al.* [5] synthesized reduced graphene oxide (RGO) by different thermal reduction processes. Table 3.1 shows the atomic compositions of these samples obtained by elemental analysis and X-ray photoelectron spectroscopy (XPS) measurements. By Hummers' method, the carbon/oxygen ratio (C/O ratio) of GO is 1.2. The oxygen content is as high as 33 mol%. During the thermal reduction process, the C/O ratio could be increased to 4.2–11.6 and the oxygen content could be reduced to 7–17 mol%. Figure 3.3 shows the electrochemical

Table 3.1 Composite of EG and RGO from elemental analysis and XPS [5].

Materials	Elemental analysis						XPS		
	%C	%H	%O	%H + %O	C/O	C/(O + H)	%C	%H + %O	C/(O + H)
EG	100	—	—	—	—	—	95	5	19
GO	40	27	33	60	1.2	0.7	39	61	0.6
RGO (at 250 °C, vacuum)	71	11	17	29	4.2	2.4	72	28	2.6
RGO (at 250 °C, Ar)	73	11	16	27	4.6	2.7	68	32	2.1
RGO (at 250 °C, Ar + H_2)	72	12	16	28	4.5	2.6	69	31	2.2
RGO (at 600 °C, Ar + H_2)	74	15	11	26	6.7	2.9	74	26	2.8
RGO (at 900 °C, Ar + H_2)	81	12	7	19	11.6	4.3	83	17	4.9

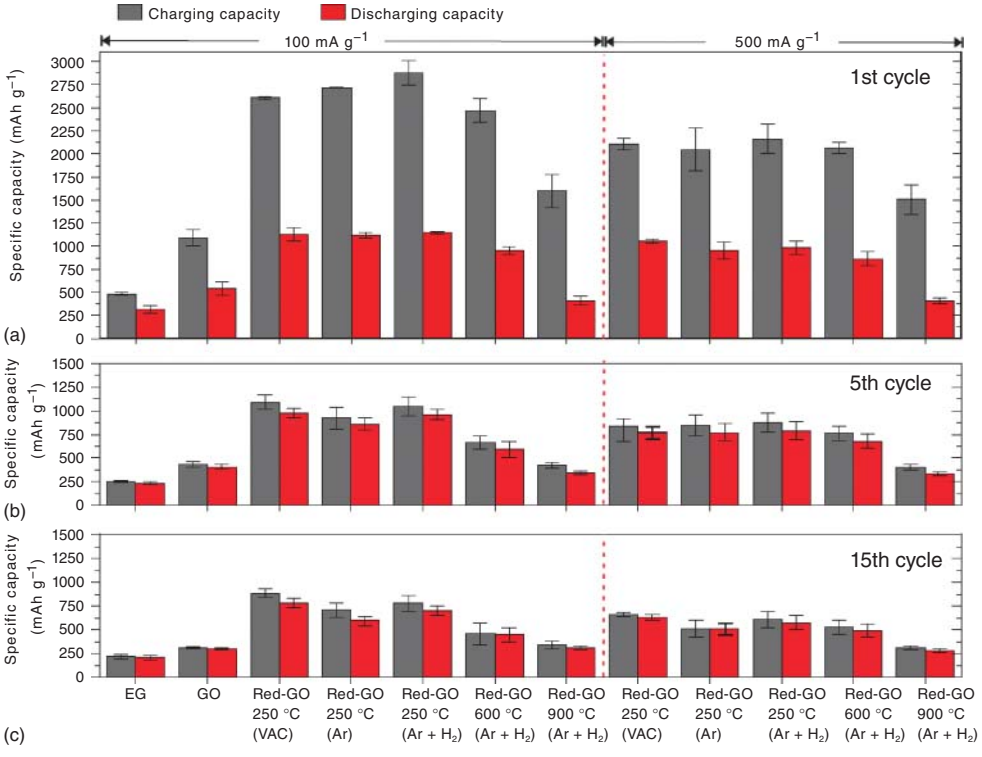

Figure 3.3 (a) First-cycle specific capacity of ethylene glycol (EG), GO, and reduced-GO (irreversible and reversible), and extended cycling capacity of these materials with temperature effects and atmosphere condition. (b,c) Two sets of experiments at different current rates (100 and 500 mA g^{-1}) are shown in each panel [5].

properties of RGO under different reduction processes. The charge and discharge capacity of GO (Graphite oxides) are 1000 and 500 mAh g^{-1}, respectively. After the reduction process, the reversible capacity increased from 500 to 1000 mAh g^{-1}. The higher Li intake capacity could be attributed to the defects and types of oxygen groups.

Lee *et al.* [6] synthesized graphite oxides with different oxidation degrees through the oxidation of graphite from one to three times. The photographs displayed in Figure 3.4 show that the color of graphite oxides changes from brown to yellow and the charge capacity of these samples increases with increase in the number of times of oxidation. The cycling tests of GO-1, GO-2, and GO-3 are shown in Figure 3.4. The result indicates that all of them exhibit good stability and GO-3 gives the highest capacity of ~2000 mAh g^{-1}. Chen *et al.* reported a facile approach to obtain an all-carbon structure with expanded ion channels, which showed excellent rate performance. Figure 3.5 shows the flowchart to synthesize the graphene-based nanostructure. Figure 3.6a–c displays the different morphologies of the graphene nanostructure from loose stacking to tight stacking. The electrochemical tests are shown in Figure 3.6d. The results demonstrate that loose stacking of PGNs (porous graphene nanosheets) delivers the highest Li^+ storage capacity even at a very high discharge rate, which approaches 480 mAh g^{-1} after 100 cycles at a current density of 500 mA g^{-1} and 320 mAh g^{-1} after 300 cycles at 2 A g^{-1}. Liu *et al.* [7, 8] also reported RGOs prepared via controlled thermal and chemical reduction processes. The structure, surface

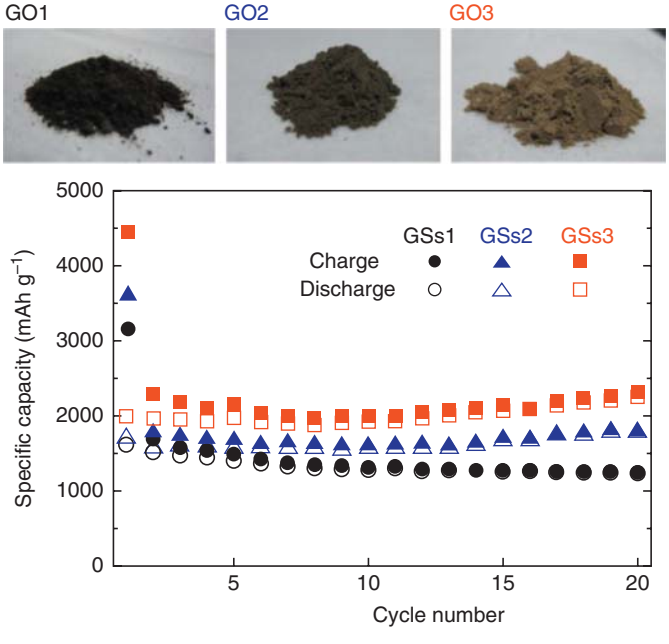

Figure 3.4 Cycle performance of GSs1, GSs2, and GSs3 at a current density of 100 mA g^{-1}. Upper inset: Photo images of GO-1, GO-2, and GO-3 samples [6].

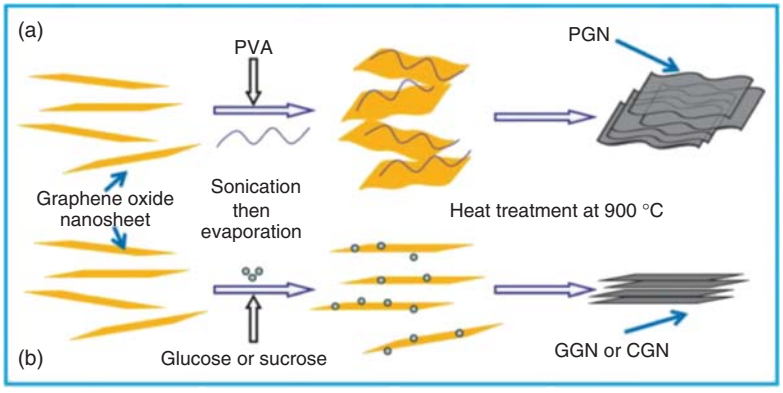

Figure 3.5 Scheme for the assembly process of graphene-based nanostructure. (a) PGN with expanded structure in which GNSs are loosely stacked and (b) GGN or CGN in which GNSs are tightly stacked [9].

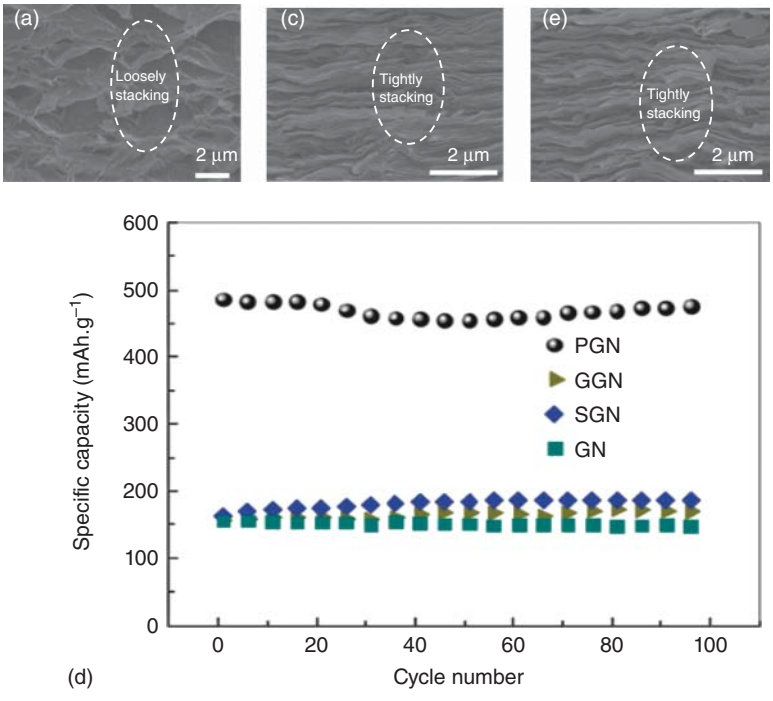

Figure 3.6 SEM images of (a) PGN, (b) GGN, and SGN. (d) Cycling tests of GN, SGN, GGN, and PGN at 500 mA g^{-1} [9].

chemistry, and electrochemical behaviors of RGOs were investigated by Raman spectroscopy, N_2 adsorption, temperature-programmed desorption, Fourier transform infrared spectroscopy, XPS, and charge/discharge measurements. The enhanced reversible capacity of RGOs is attributed to specific functionalities rather than to the exceptionally large specific surface area or structural defects. The contributed capacities at a potential higher than 1.5 V and in region of 0.8–1.5 V are attributed predominantly to phenol groups and cyclic edge ether groups, respectively. These findings may be beneficial to the material design of graphene-based anodes with high energy density.

Hu *et al.* [10] systematically studied the electrochemical performance of free-standing graphene paper as anodes for LIBs. Figure 3.7 displays the schematic diagram for the fabrication of graphene paper through vacuum-assisted filtration of a GNS dispersion to obtain papers with different thicknesses. Figure 3.8 shows

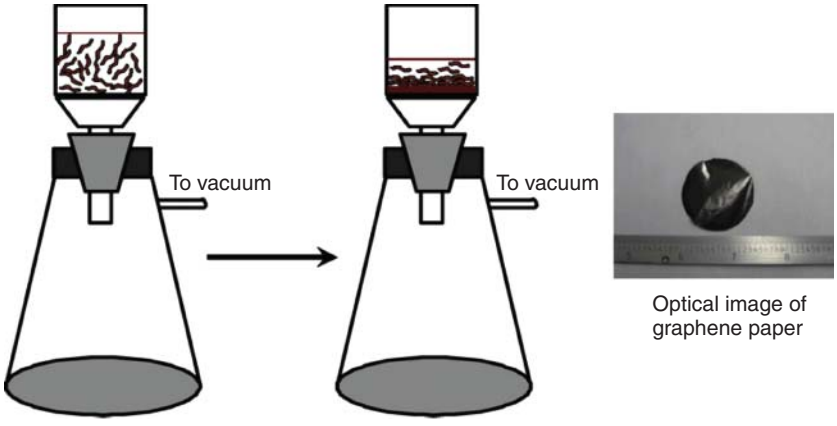

Figure 3.7 Schematic diagram for the fabrication of graphene paper through vacuum-assisted filtration of GNS dispersion and a photograph of the as-prepared graphene [10].

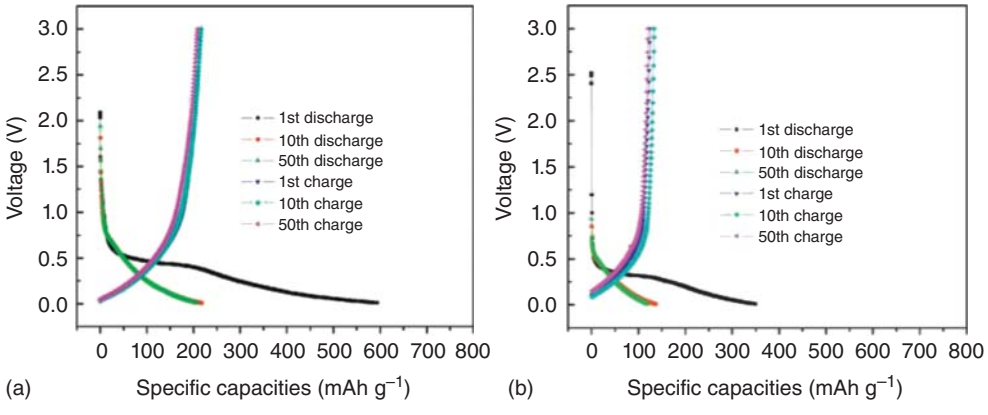

Figure 3.8 Charge and discharge curves of (a) 1.5-μm and (b) 3-μm graphene paper [10].

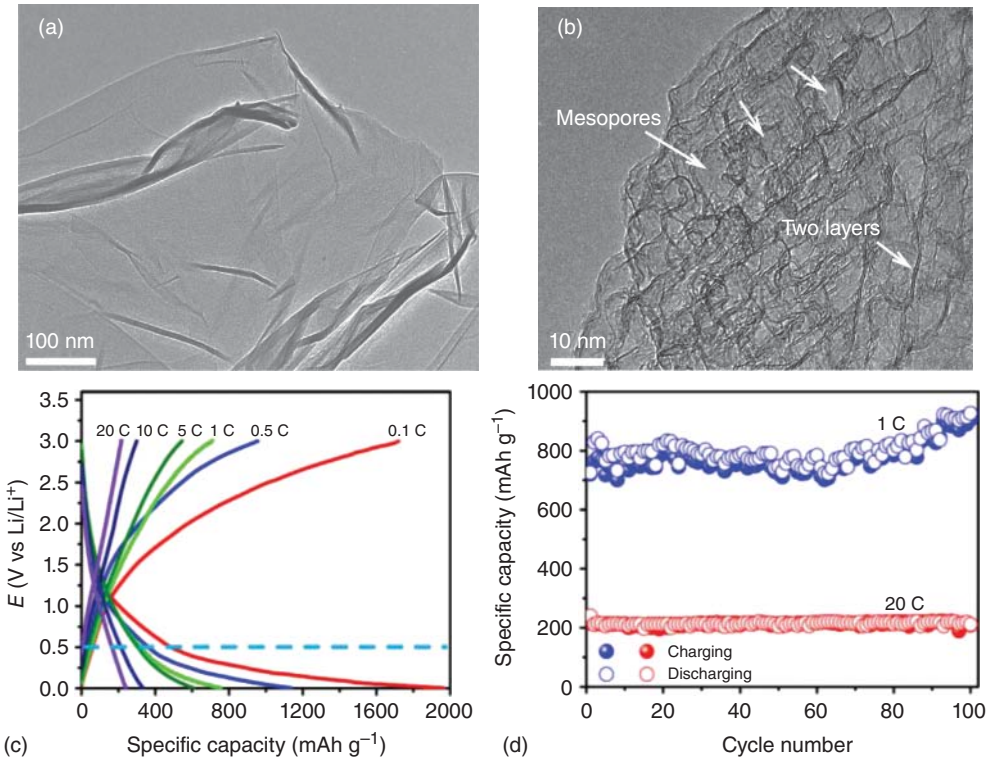

Figure 3.9 TEM images of (a) typical graphene and (b) porous graphene. (c) Galvanostatic charge/discharge curves of the porous graphene electrode at 0.1–20 C. (d) Cycling performance of the porous graphene electrode at 1 and 20 C [11].

the electrochemical tests of 1.5- and 3-μm graphene papers. The 1.5-μm graphene paper gives rise to an initial reversible capacity of ~200 mAh g^{-1} at a current density of 100 mA g^{-1}, whereas the 3-μm graphene paper gives only ~140 mAh g^{-1}. The decrease in capacity with paper thickness is associated with the dense restacking of GNSs and the larger aspect ratio of the paper.

Fan *et al.* [11] obtained porous graphene anode materials by CVD using porous MgO sheets as template. Figure 3.9a,b shows the transmission electron microscopy (TEM) images of as-synthesized graphene and porous graphene. Figure 3.9c,d further displays the rate capability and cycling test result of porous graphene. These results indicate that the porous property of graphene exhibits a high and reversible capacity (1723 mAg h^{-1}), excellent rate capability, and cycling stability.

Yang *et al.* [12] reported graphene sheets coated with a thin layer of nitrogen-enriched carbon that possess excellent rate capability and cycle performance at various current rates. Figure 3.10a demonstrates the synthetic process of carbon-coated graphene, namely GSNC. Figure 3.10b displays the scanning electron microscopy (SEM) image of GSNC. Figure 3.10c shows the rate capacity

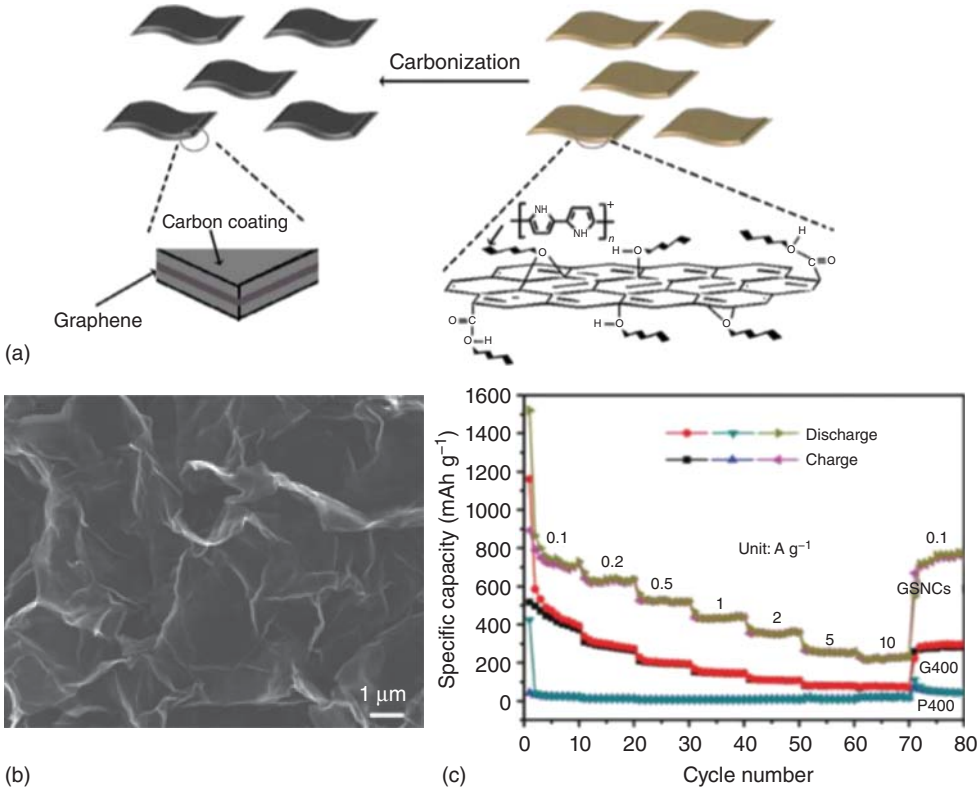

Figure 3.10 (a) Schematic illustration of the synthesis process of GSNS. (b) SEM image of GSNCs. (c) Rate performance of GSNC, G400, and P400 [12].

of the composite anode and other graphene-based anodes. These results demonstrate that the carbon coating not only incorporates the nitrogen atoms but also reduces the aggregation of graphene sheets, which can facilitate the storage and transportation of lithium within the anode.

Jiang *et al.* [13] synthesized porous graphene by a hydrothermal method followed by etching with KOH and ball-milling, called *holey graphene* (*HG*). The TEM images of graphene oxides and HG are shown in Figure 3.11a,b, respectively. The electrochemical tests of rate capability and cycling test of the randomly stacked holey graphene (RSHG) anodes (shown in Figure 3.11c,d) exhibit high rate capability with excellent cycling stability due to the porous, sponge-like structure of graphene resulting from the treatments of KOH and ball-milling.

Apart from chemical exfoliation and CVD, another potential approach is electrochemical exfoliation [14–21]. Yang *et al.* [14] proposed a mechanism of cathodic exfoliation of graphite electrodes. Figure 3.12 displays the cathodic exfoliation process carried out for 0, 1, 60, and 180 min. In addition, the authors also tried different systems of electrolytes, such as $LiPF_6$ in PC, $TBAPF_6$ in AN, $TBAPF_6$ in DMF (dimethylformamide), $TBAPF_6$ in PC, and so on. The

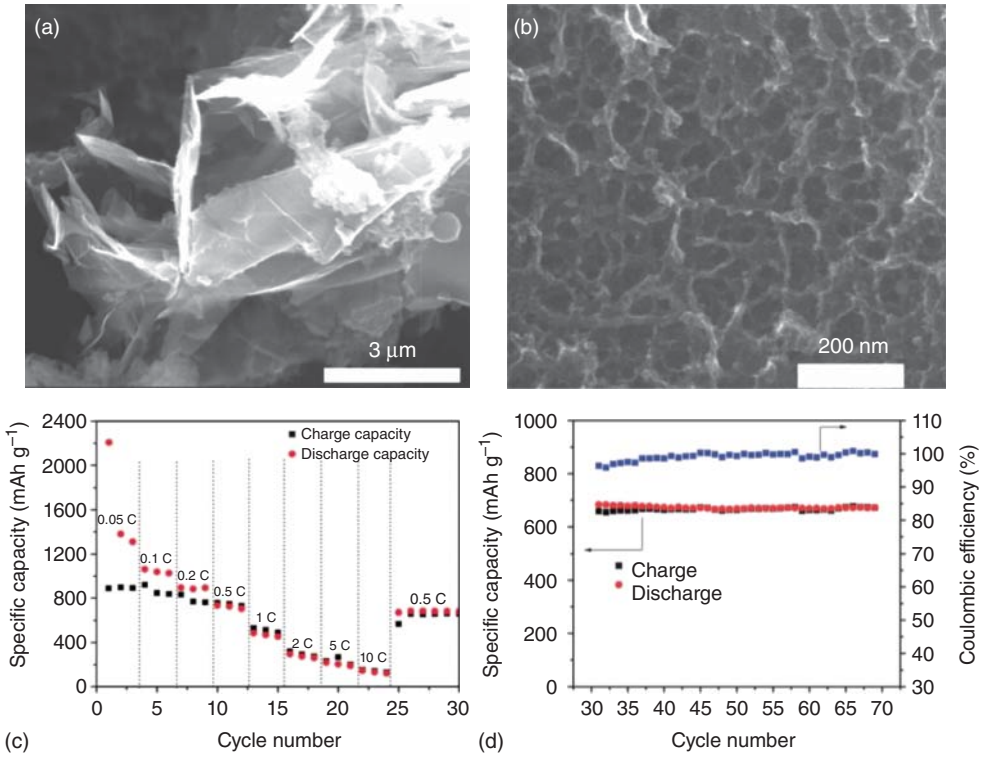

Figure 3.11 TEM images of (a) graphene oxides (GOs) and (b) holey graphene (HG). (c) Rate capabilities and cycle performance of the randomly stacked HGs (RSHGs) at rates from 0.05 to 10 C. (d) Cyclability and coulombic efficiencies of the RSHG at 0.5 C rate between 3.0 and 0.01 V versus Li/Li^+ [13].

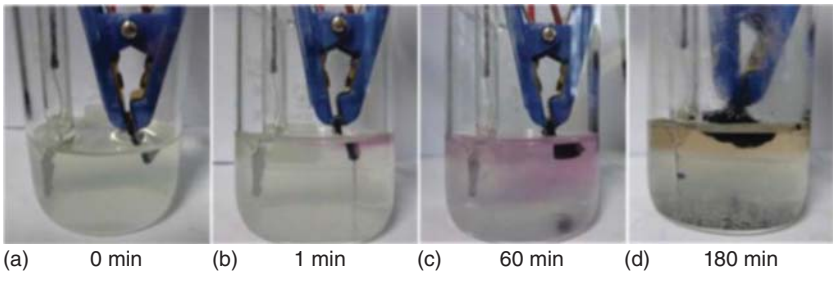

Figure 3.12 Images of electrochemical cathodic exfoliation of graphite [14].

corresponding observations are summarized in Table 3.2. Figure 3.13c,d shows the cycling performance and rate capability of GS anode materials. The high reversible capacity, good cycling life, and excellent capability demonstrate that graphene sheets (GSs) could be promising candidates as anode materials for use in Li-ion batteries.

Table 3.2 Cathodic exfoliation of graphite under different experimental conditions [14].

Electrolyte	Voltage (V)	Current density (mA cm^{-2})	Phenomenon
	−5	0.3	No exfoliation; even exfoliated for 4 h/no bubbles
1 M $LiPF_6$ (in PC)	−10	2.0	No exfoliation; even exfoliated for 4 h/bubbles
	−30	10.4	Small amount of exfoliated sheets for 4 h/large bubbles
0.5 M $TBAPF_6$ (in AN)	−5	1.9	No exfoliation observed; exfoliated for 4 h/no bubbles
	−10	5.9	Exfoliation/bubbles
	−30	26.6	Large amounts of exfoliated sheets precipitated/bubbles
0.5 M $TBAPF_6$ (in DMF)	−5	1.0	No exfoliation; exfoliated for 4 h/no bubbles
	−10	3.4	Exfoliation sheets surrounded the cathode/no bubbles
	−30	14.1	Large amounts of exfoliated sheets/bubble
	−5	0.2	No exfoliation; even exfoliated for 4 h/no bubbles
	−10	1.4	Exfoliation for 0.5 h/obvious bubbles
	−30	5.9	Large amounts of exfoliated sheets/bubble
10 ml 0.5 M $TBAPF_6$ (in AN) + 0.5 ml C_2H_5OH	−10	5.7	Exfoliation/large bubbles
10 ml 0.5 M $TBAPF_6$ (in DMF) + 0.5 ml C_2H_5OH	−10	3.2	The exfoliation rate became slower/bubbles
10 ml 0.5 M $TBAPF_6$ (in PC) + 0.5 ml C_2H_5OH	−10	1.2	Exfoliation for 0.5 h/bubbles

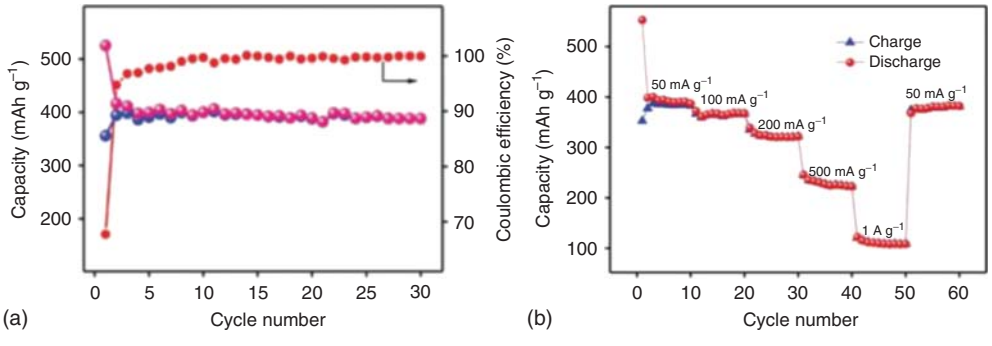

Figure 3.13 (a) Cycling property and coulombic efficiency of the GS electrode. (b) Rate capability of the GS electrode [14].

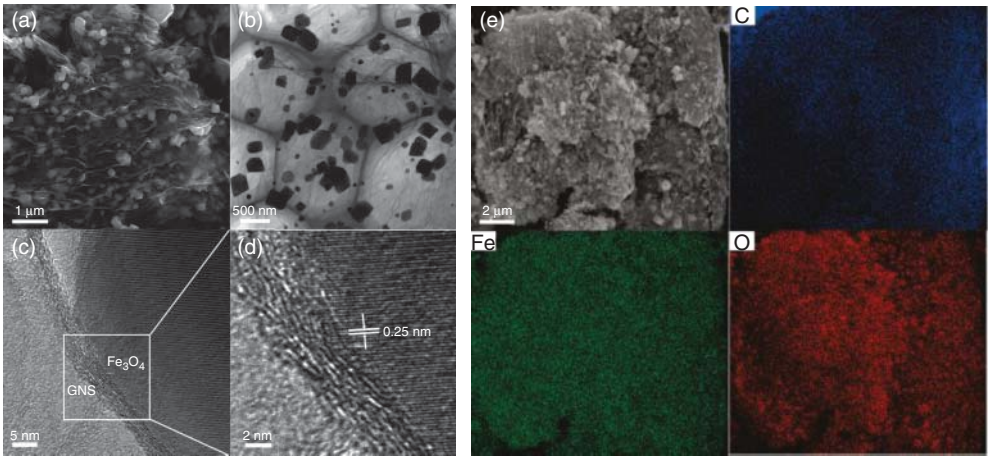

Figure 3.14 (a) SEM images of GNS/Fe_3O_4 composite materials. (b–d) TEM images of GNS/Fe_3O_4 TEM image. (e) EDX mapping for C, Fe, and O in the composite [22].

In addition to their use for pure anodes, GNSs could also be used for composite anodes for Li-ion batteries. From the view point of composite anode, GNSs have also been used to serve not only as a buffer matrix to accommodate the volume expansion of alloy-based anodes during cycling processes but also as a conductive network for enhancing the rate capability. Zhou *et al.* [22] synthesized GNS/Fe_3O_4 nanoporous composite anodes with high specific surface area by an *in situ* chemical reduction process of $Fe(OH)_2$. The results of SEM, TEM, and energy-dispersive X-ray (EDX) mapping shown in Figure 3.14 demonstrate that Fe_3O_4 nanoparticles with particle sizes of 100–200 nm were homogeneously dispersed on the surface of GNS. The electrochemical tests in Figure 3.15 show an obvious plateau located at ~0.8 V, which might be due to the typical intercalation of lithium into Fe_3O_4 ($Fe_3O_4 + 8e^- + 8Li^+ \leftrightarrows 3Fe^0 + 4Li_2O$) with a theoretical capacity of 922 mAh g^{-1}. The rate capability shown in Figure 3.15d further demonstrates a reversible capacity as high as 600 mAh g^{-1} at 1750 mA g^{-1}. These results prove that graphene could be a highway for lithium ions to charge and discharge at high rates. The structural and cycle stability of Fe_3O_4 could be also dramatically improved by introducing graphene as a buffer matrix for these alloy-based anode materials for Li-ion batteries.

Wu *et al.* [23] reported Co_3O_4/GNS nanocomposite materials by a soft chemistry process. The schematic diagram is shown in Figure 3.16. In the first step, $Co(OH)_2$ and graphene solution in basic condition are mixed. Then the mixture is sintered at 450 °C. Afterward, 10–30-nm Co_3O_4/GNS composites could be successfully synthesized. Figure 3.17 shows the SEM and TEM images of Co_3O_4/GNS composites, which demonstrate a homogenous distribution of nano-sized Co_3O_4 coated onto the graphene surface. Figure 3.18 shows the electrochemical tests of GNS, Co_3O_4, and Co_3O_4/GNS composites in terms of charge/discharge curves and cycling tests. As shown in Figure 3.18d, the

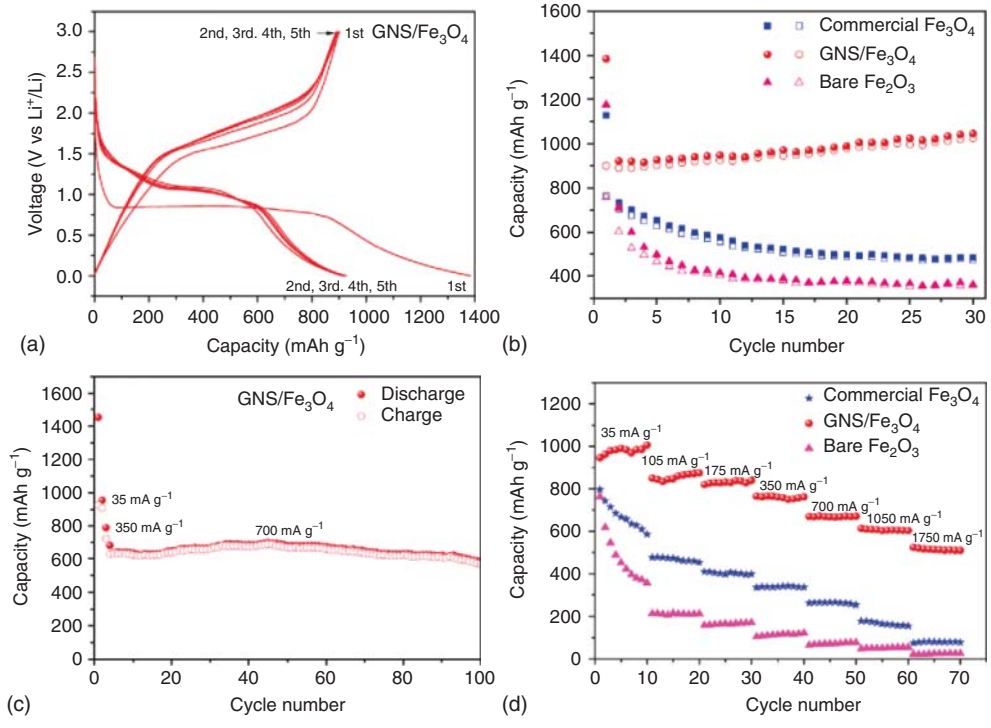

Figure 3.15 (a) Charge/discharge curves of GNS/Fe_3O_4 composite anode material in the first five cycles. (b) Cycling tests of commercial Fe_3O_4, GNS/Fe_3O_4 composite, and bare Fe_3O_4 at a current density of 35 mA g^{-1}. (c) Cycling tests of a GNS/Fe_3O_4 composite anode at current densities of 35, 350, and 700 mA g^{-1}. (d) Rate capability of commercial Fe_3O_4, GNS/Fe_3O_4 composite, and bare Fe_3O_4 [22].

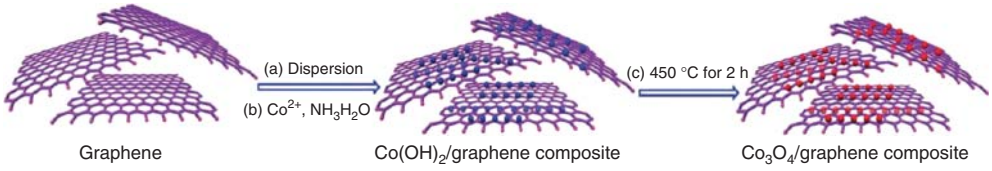

Figure 3.16 Schematic diagram of Co_3O_4/GNSs composite. (a) Mixing GNS and IPA/H_2O with 1 : 1 vol%. (b) Synthesize $Co(OH)_2$/GNS composite in basic condition. (c) Sintering at high temperature [23].

cyclability of Co_3O_4 could be enhanced by introducing GNS as a buffer matrix. The reversible capacity of Co_3O_4/GNS composites was ~1000 mAh g^{-1} even after 30 cycles.

Chou *et al.* [24] physically mixed 40-nm silicon and GNS derived from hydrothermal reaction at the molar ratio of 1 : 1 and studied the surface morphology and electrochemical properties. Figure 3.19a,b shows the SEM images of the Si/GNS composite. Nano silicon particles were homogeneously coated

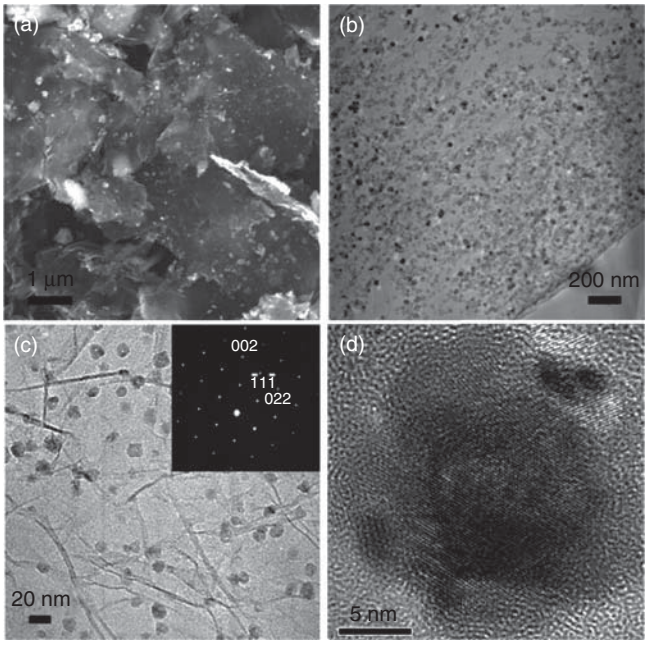

Figure 3.17 (a) SEM image of the Co_3O_4/GNS composite. (b–d) TEM images of Co_3O_4/GNS composite. The inset in (c) shows the selected-area diffraction pattern [23].

by graphene. Figure 3.19c displays the capacities and cycling performance of graphene, nano silicon, and Si/graphene composite, as well as the values calculated for Si. The Si/graphene composite gives a better cycling performance. Figure 3.19d compares the AC impedances of pure nano silicon and the Si/graphene composite. The result indicates that the impedance could be dramatically reduced by adding graphene as a matrix.

Sun *et al.* [25] at the University of Western Ontario prepared graphene by a modified Hummer's method and coated SnO_2 via an atomic layer deposition (ALD) process. The SEM and TEM images of pure graphene and SnO_2/graphene composite are shown in Figure 3.20a–c, respectively. The flexible nature of graphene could buffer the volume expansion of Sn during the charge and discharge processes. Figure 3.21d shows the cycling tests of these materials. For pure graphene, the first charge and first discharge capacity are 900 and 420 mAh g^{-1}, respectively. The irreversible capacity loss in the first cycle is as high as 50%, which could be due to the formation of a solid–electrolyte interphase (SEI). After 100 cycles, the capacity of pure graphene reduces to ~280 mAh g^{-1}. On the other hand, for the SnO_2/graphene composite, the first charge and first discharge capacity are 1250 and 800 mAh g^{-1}, respectively. After 150 cycles, the capacity is still 400 mAh g^{-1}.

Kung *et al.* [26] reported a composite of Si nanoparticles highly dispersed between graphene sheets and supported by a 3D network of graphite formed

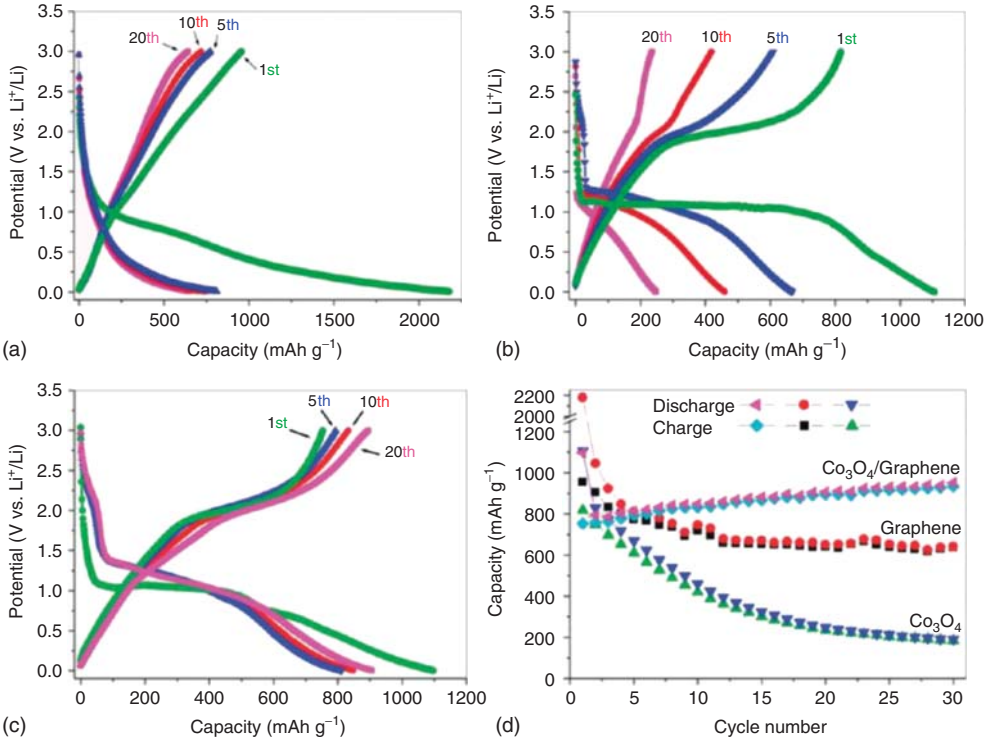

Figure 3.18 Charge/discharge curves of (a) GNS, (b) Co_3O_4, and (c) Co_3O_4/GNS composite at 1st, 5th, 10th, and 20th cycles under a current density of 50 mA g^{-1}. (d) Cycling tests of GNS, Co_3O_4, and Co_3O_4/GNS composite [24].

by reconstituting regions of graphene stacks, which exhibit high Li-ion storage capacities and cycling stability. Figure 3.21a displays a graphene oxide solution with different solid contents of 0.25, 1.2, and 2.5 mg ml^{-1}. Figure 3.21b shows the TEM image displaying the distribution of nano-sized silicon particles on graphene oxide. Figure 3.21c shows the Si/graphene composite paper prepared by a vacuum-assisted filtration approach. The thickness of the Si/graphene composite paper is about 10 μm. Figure 3.21d shows the cycling test of the composite paper. The electrode was prepared with a storage capacity >2200 mAh g^{-1} after 50 cycles and >1500 mAh g^{-1} after 200 cycles, which decreased by <0.5% per cycle. The post annealing of Si/graphene composite paper is very important. Table 3.3 displays the sheet resistances, resistivity, and conductivity of the composite paper under different reducing conditions. Without annealing, the sheet resistance of Si/graphene oxide is as high as $2.9 \times 10^5\ \Omega$ sq.$^{-1}$, which could be reduced to 153 Ω sq.$^{-1}$ for 550 °C and 60 Ω sq.$^{-1}$ for 850 °C under a thermally reducing atmosphere of 4% H_2/96% Ar.

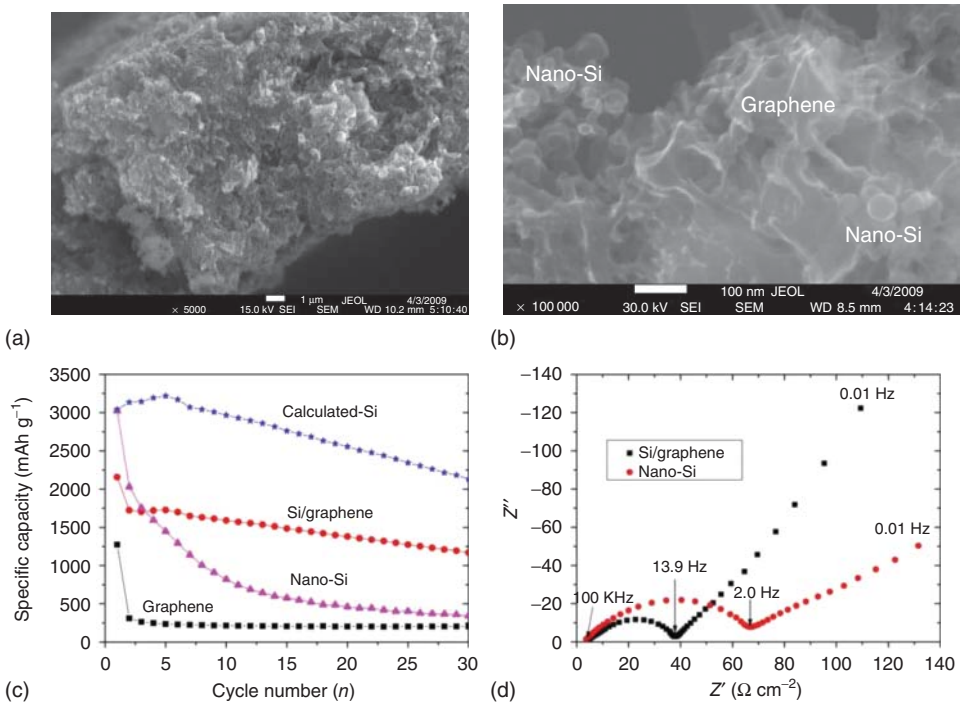

Figure 3.19 (a,b) SEM morphologies of Si/GNS composite. (c) Cycling tests of graphene, nano silicon, Si/graphene, and calculated Si. (d) AC impedances of nano-Si and Si/graphene composite in the charged state of 0.2 V [24].

Table 3.3 The sheet resistances, resistivity, and conductivity of reduced graphene oxide in different reducing temperature [26].

	Reduction temperature			Unreduced SGO sample
	550 °C	700 °C	850 °C	
Sheet resistance (Ω sq.$^{-1}$)	153	107	60	2.9×10^5
Resistivity (Ω · cm)	0.076	0.053	0.030	146
Conductivity (S · cm^{-1})	13.1	18.7	33.1	0.0068

3.2.2 Cathode Materials

In order to enhance the capacity, rate performance, and cycle life of cathode materials, graphene-coated cathode materials have been widely studied [27–33]. He *et al.* [27] synthesized graphene-coated $Li[Li_{0.2}Mn_{0.54}Ni_{0.13}Co_{0.13}]O_2$ by the spray-drying method. Figure 3.22 shows the SEM and TEM images of graphene-coated $Li[Li_{0.2}Mn_{0.54}Ni_{0.13}Co_{0.13}]O_2$. The primary particle of

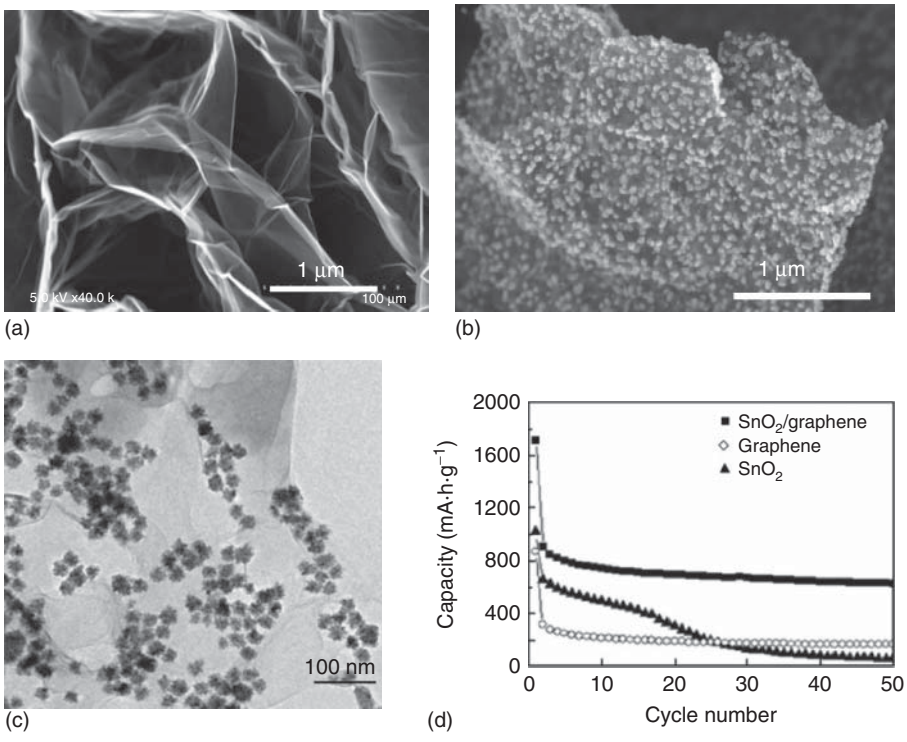

Figure 3.20 SEM images of (a) pure graphene and (b) SnO_2/graphene composite. (c) TEM image SnO_2/graphene composite. (d) Cycling performance of SnO_2, graphene, and SnO_2/graphene composite [25].

$Li[Li_{0.2}Mn_{0.54}Ni_{0.13}Co_{0.13}]O_2$ is about 1 μm, and the thickness of the graphene layer is about 2.3 nm. Figure 3.23 displays the charge/discharge tests, rate capability, and AC impedances of the bare cathode and graphene-coated cathode. From the AC impedance, the semicircle in the lower frequency resulting from charge transfer resistance could be dramatically reduced by graphene coating. Thus, as shown in Figure 3.23b, the capacity and rate capability could also be enhanced by the graphene coating. Sun *et al.* [28] reported a free-standing $VO_{2.07}$RGO composite film formed by a hydrothermal process. Figure 3.24 shows the SEM, TEM, and photo images of the $VO_{2.07}$RGO composite film. Figure 3.25 demonstrates the charge/discharge tests, cycling performance, rate capability, and AC impedances of $VO_{2.07}$ with and without RGO. The electrochemical tests show that the cathode film delivers a high reversible capacity of 160 mAh g^{-1} and good cycling stability with a capacity retention of 83% after 200 cycles in the voltage range between 2.0 and 3.5 V.

Ding *et al.* [29] reported nanostructured-graphene-supported $LiMn_{1/3}Ni_{1/3}Co_{1/3}O_2$ (LMNCO) prepared by the coprecipitation method. A schematic diagram of this synthetic process is shown in Figure 3.26. Figure 3.27a shows the TEM image of graphene-supported LMNCO. Approximately 50-nm LMNCO

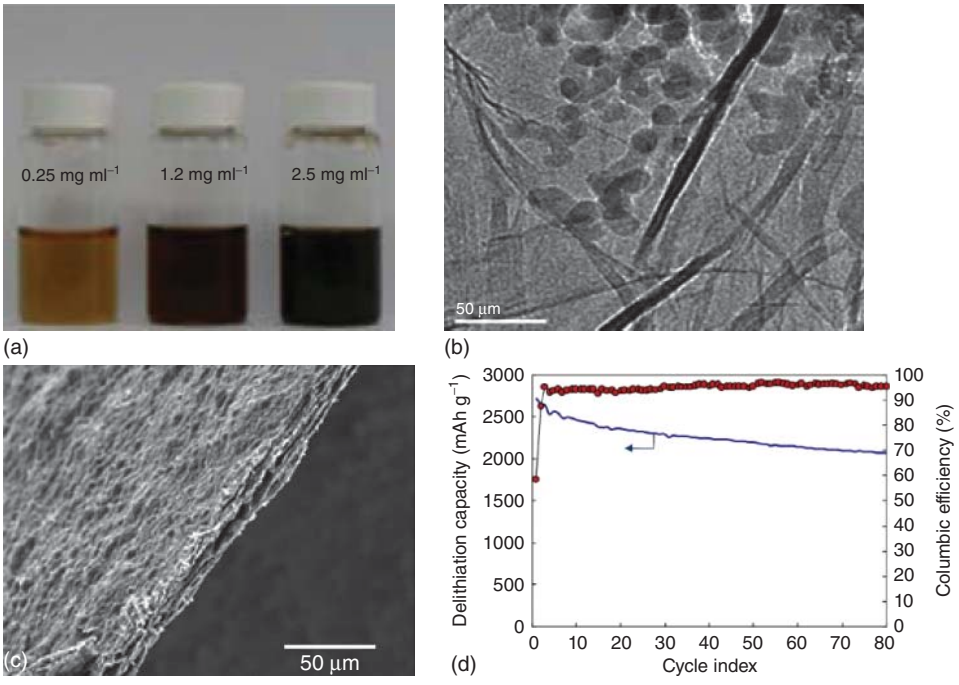

Figure 3.21 (a) The photoimages of graphene oxide solutions with different solid content. (b) TEM image of Si/graphene composite. (c) SEM cross-sectional image of Si/graphene electrode. (d) Cycling performance and coulombic efficiency of a Si/graphene composite anode [26].

nanoparticles are homogeneously coated by graphene. Figure 3.27b–d is the corresponding electrochemical tests. These results demonstrate that graphene-supported LMNCO exhibits a high initial discharge capacity of 175 mAh g^{-1} and 0.2 V and a high capacity retention of 95.5% after 50 cycles by incorporating only 1.6% graphene.

Prabakar *et al.* [30] chose graphene to form efficient conducing networks and to suppress the formation of a solid–electrolyte interface layer in a sandwiched composite with $LiNi_{0.5}Mn_{1.5}O_4$ (LNMO). Figure 3.28A displays a schematic diagram of the graphene-sandwiched LNMO structure prepared in a solution by self-assembly. Figure 3.28B,C shows the TEM and SEM images of LNMO–G2.5% composite. Figure 3.28D gives a rate capability of the series of LNMO cathode materials. The LNMO–G2.5% composite with a sandwiched structure showed the best electrochemical performance. The efficient conducing network and the significant suppression of the electrolyte decomposition allowed it to exhibit greater capacity and better capacity retention than bare LNMO. Wang *et al.* [31] reported a carbon-coated $LiFePO_4$ modified with RGO using an ultrasonic-assisted rheological phase method coupled with carbothermal treatment. Figure 3.29 shows the TEM micrograph and the electrochemical performance of the composite cathode. The composite with 5 wt% RGO exhibited high

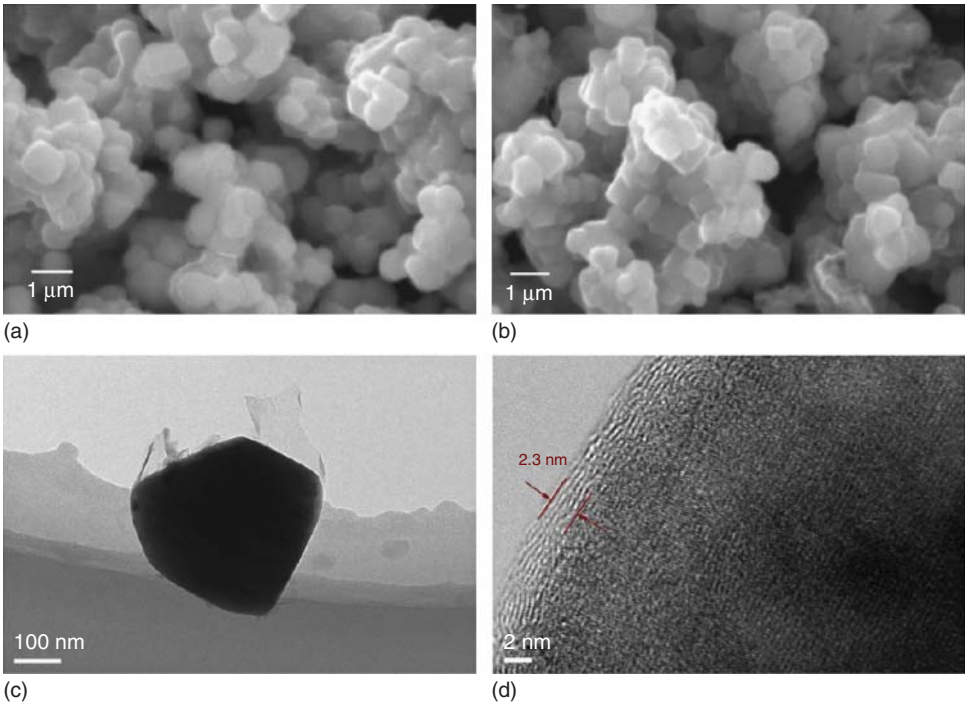

Figure 3.22 SEM images of (a) pristine $Li[Li_{0.2}Mn_{0.54}Ni_{0.13}Co_{0.13}]O_2$ particle and (b) graphene-coated Li $[Li_{0.2}Mn_{0.54}Ni_{0.13}Co_{0.13}]O_2$. (c) TEM image of the graphene-coated particle. (d) HRTEM image of the graphene-coated particle [27].

specific capacity and superior rate performance with the discharge capacities of 160.4 mAh g^{-1} at 0.2 C and 115.0 mAh g^{-1} at 20 C. The sample also demonstrated excellent cycling stability with only 10% capacity decay at 10 C after 1000 cycles. Ha *et al.* [32] reported a chemically activated graphene (CA-G) via activation by KOH to enhance the electrochemical performance of $LiFePO_4$. Figure 3.30 displays the schematic diagrams of preparation of (a) CA-G by activation and (b) CA-G/LFP by annealing. Figure 3.31a,b demonstrates the TEM images of pure GO and porous graphene-coated $LiFePO_4$. Figure 3.32a shows the cycling performance of $LiFePO_4$, G/LFP, and CA-G/LFP at 100 mA g^{-1}. In cycling tests, bare $LiFePO_4$ and normal graphene/LFP displayed similar cycling performance. However, for porous graphene/LFP, namely CA-G/LFP, the composite gave much better cyclability. The mechanism for enhancing the rate capability of $LiFePO_4$ and their remarkable achievement of CA-G/LFP is demonstrated in Figure 3.33a and Figure 3.33b, respectively. Under a charging current of 5000 mA g^{-1}, the capacity of CA-G/LFP still maintains 65 mAh g^{-1}, which is much higher than those of $LiFePO_4$ and G/LFP. A cartoon to explain the excellent rate performance is given in Figure 3.34. Lithium ions have to go around the electrode materials in the G/LFP electrode, but can take shortcuts by going through pores in CA-G in the CA-G/LFP electrode.

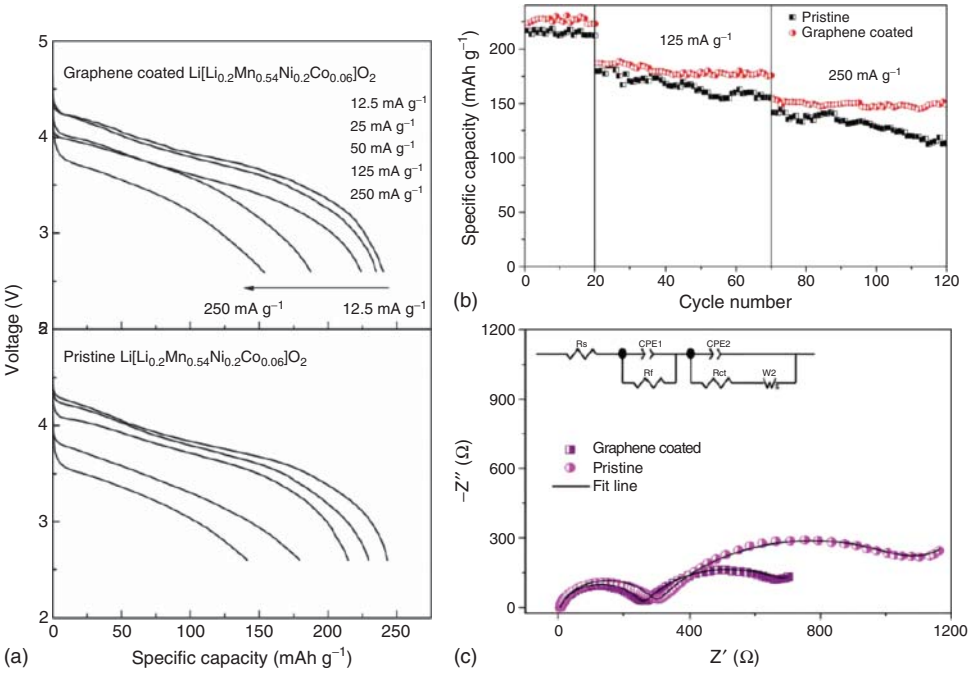

Figure 3.23 (a) Discharge curve at various *C* rates. (b) Cycling performance at several *C* rates. (c) AC impedance measurement of both samples. The inset shows the equivalent circuit for curve-fitting [27].

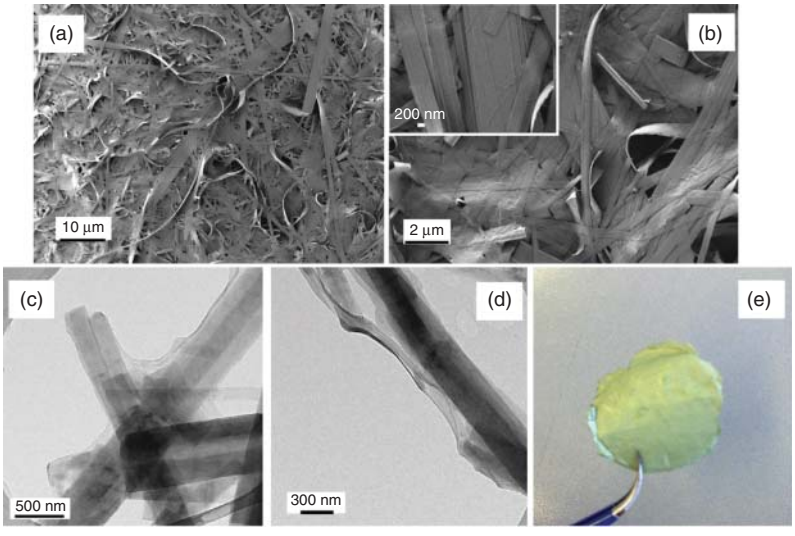

Figure 3.24 (a,b) SEM and (c,d) TEM images of the $V_2O_5{\cdot}xH_2O$/RGO film on the intertwining network of above ribbons without addition of any binders [28] (e) The appearance of $V_2O_5 \cdot xH_2O$/RGO film.

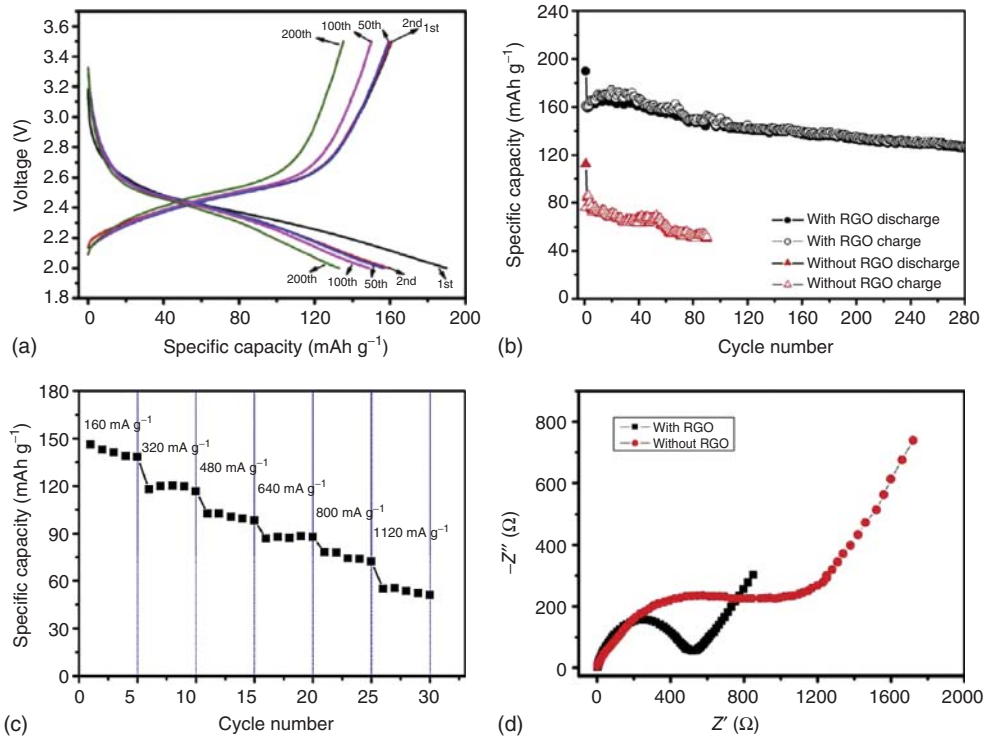

Figure 3.25 (a) Voltage of VO_x/RGO film at a current density of 70 mA g^{-1}. (b) Cycling performance of VO_x/RGO film and the VO_x film without RGO. (c) Rate capability of VO_x/RGO. (d) Electrochemical impedance spectra of these two film electrodes measured at the 20th fully discharged state [28].

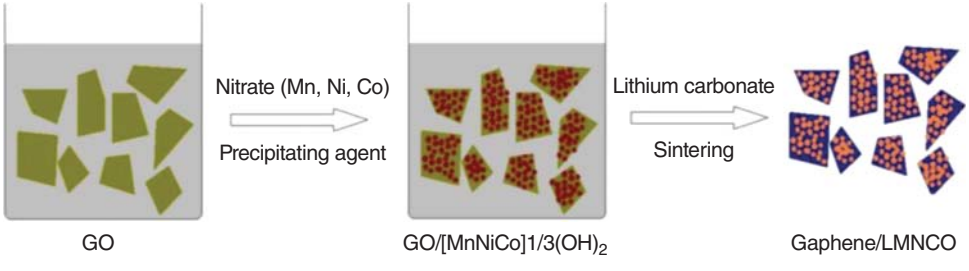

Figure 3.26 Illustration of the preparation of graphene-supported LMNCO [29].

3.3 Graphene for Supercapacitors

A supercapacitor is an energy device with high power density and excellent cycle life of more than 100 000 times. According to the storage mechanism,

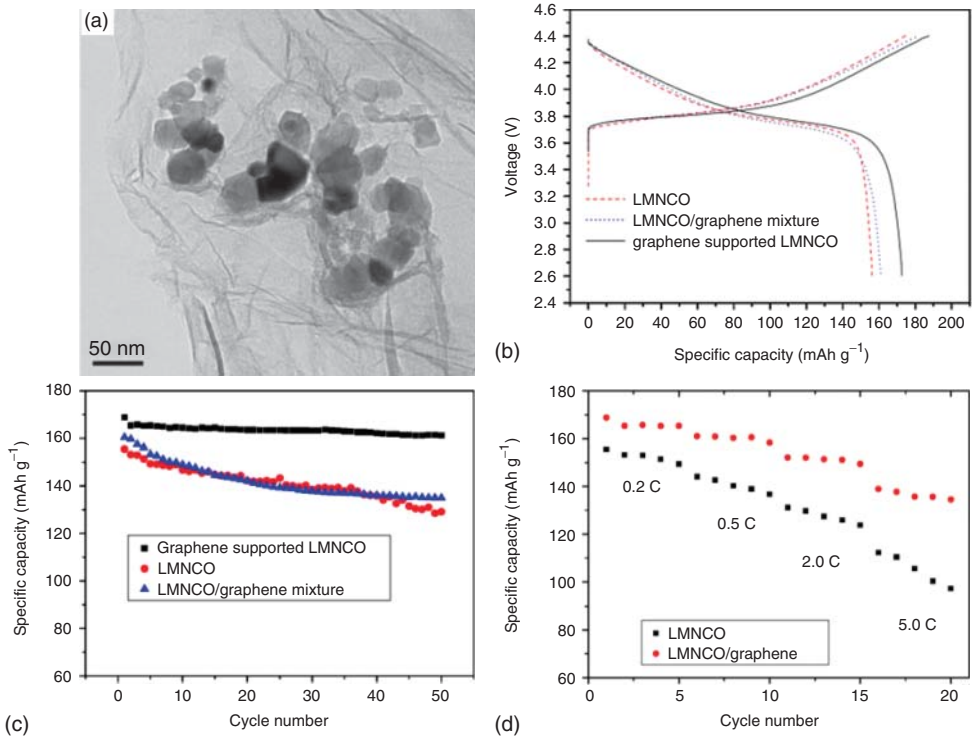

Figure 3.27 (a) TEM image of graphene-supported LMNCO. (b) Charge/discharge curves of LMNCO and LMNCO/graphene mixture. (c) Cycling performance of LMNCO, LMNCO/graphene, and graphene-supported LMNCO. (d) Rate capability of LMNCO and LMNCO/graphene [29].

supercapacitors can be divided into electric double-layer capacitors (EDLCs) and pseudo capacitors. The former operates by using the adsorption of cations and anions onto the electrode; the latter functions from the reversible oxidation/reduction reactions to provide electrical storage. Figure 3.34 and Table 3.4 summarize specific capacitances of common materials for supercapacitor applications [34]. Because of their merits of a large, open, flat layer with high surface area and excellent electronic transport properties, GNSs have been considered a promising electrode material for supercapacitors [34–40]. The capacitance of graphene can approach ~200 F g^{-1} [34, 35], even though the specific surface area of graphene is not high compared to activated carbon. However, the high electronic conductivity and porous structure with meso pores instead of micropores demonstrate excellent electrochemical performance in supercapacitors. In addition, by combining graphene and a high-working-voltage ionic liquid, the energy density is even more than 100 Wh kg^{-1}, which approaches that of the Li-ion battery system [37]. These results demonstrate

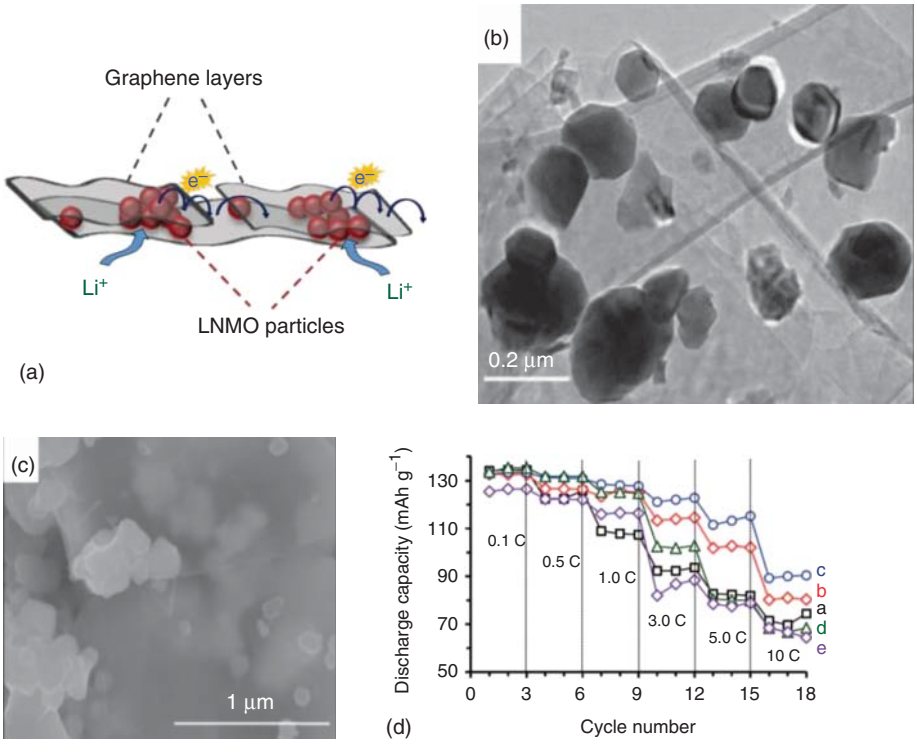

Figure 3.28 (A) Schematic diagram showing a graphene-sandwiched LNMO structure prepared in a solution by self-assembly. (B,C) TEM and SEM images of LNMO-G2.5%. (D) Rate capability of (a) LNMO, (b) LNMO–G1%, (c) LNMO–G2.5%, (d) LNMO–G5%, and (e) a composite prepared by a powder mixture of LNMO with 2.5 wt% graphene [30].

the potential of graphene for use in supercapacitors. Fan *et al.* [38] reported an easy synthesis of PGNs using the etching of graphene by MnO_2. Figure 3.35 shows an illustration of the formation of porous graphene material with pores on the surface of the sheet. The corresponding electrochemical tests are shown in Figure 3.36. The results indicate that the PGNs exhibit a specific capacitance of $154\,F\,g^{-1}$ at $500\,mV\,s^{-1}$ in 6 M KOH, compared to a value of $67\,F\,g^{-1}$ for GNSs, and a low capacitance loss of 12% after 5000 cycles. Krishnamoorthy *et al.* [39] designed graphene oxides with various degrees of oxidation, and studied the formation of various oxygen-containing functional groups at different stages of oxidation and their influence on the chemical and structural properties. Figure 3.37 demonstrates the electrochemical tests on these GO samples. The results support the view that the tunable properties of GO can provide new, positive features in the development of GO-based device applications.

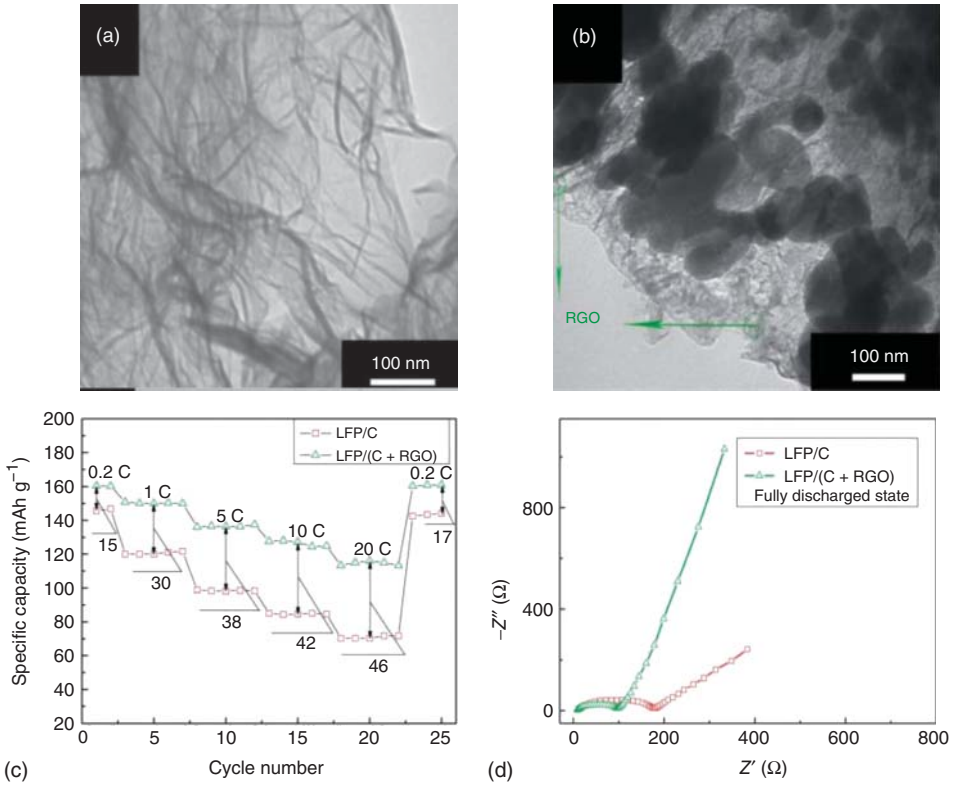

Figure 3.29 TEM images of (a) GO and (b) LFP/(C + RGO). (c) Rate performances of LFP/C (□) and LFPO (C + RGO) (Δ). (d) Electrochemical impedance spectroscopic (EIS) profile of LFP/C and LFP/(C + RGO) at the fully discharged state [31].

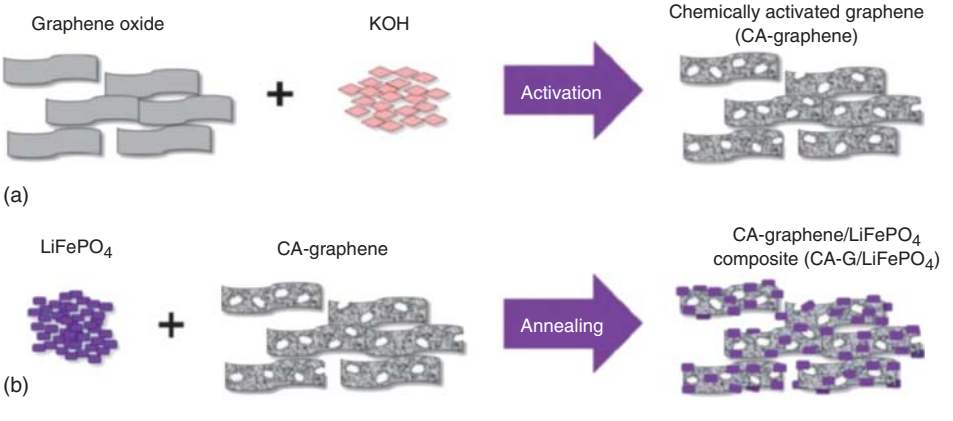

Figure 3.30 Schematic diagrams of preparation of (a) CA-graphene by activation and (b) CA-G/LFP by annealing [32].

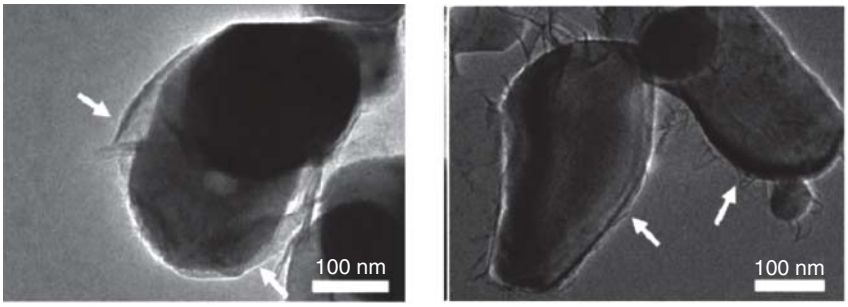

Figure 3.31 TEM images of (a) G/LFP and (b) CA-G/LEP.

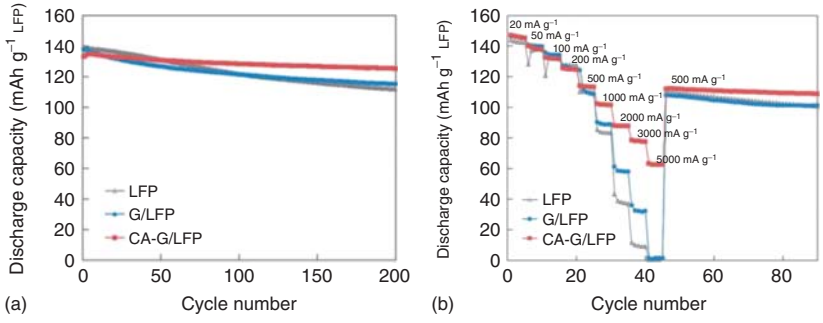

Figure 3.32 Cycling performance (a) and rate capability (b) of $LiFePO_4$, G/LFP, and CA-G/LFP at 100 mA g^{-1} [32].

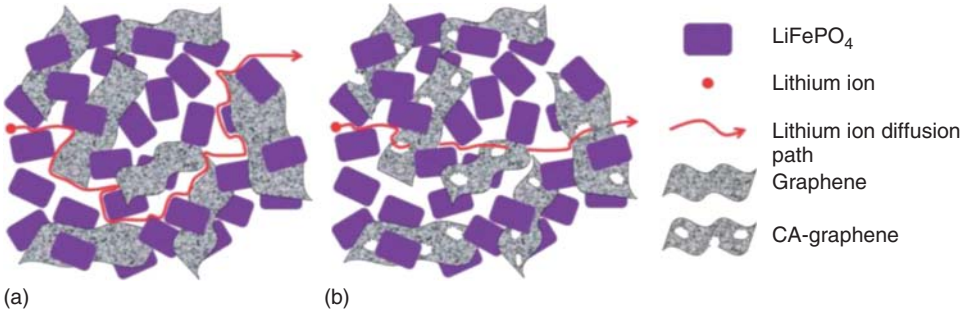

Figure 3.33 Conceptual illustrations of lithium ion diffusion pathways in (a) G/LFP and (b) CA-G/LFP [32].

Table 3.4 A comparison of various carbon electrode materials for supercapacitors [34].

Carbon	Specific surface area (m^2g^{-1})	Density (cm^{-3})	Electrical conductivity(S cm^{-1})	Cost	Aqueous electrolyte		Organic electrolyte	
					Fg^{-1}	Fcm^{-3}	Fg^{-1}	Fcm^{-3}
Fullerene	1100–1400	1.72	10^{-8}–10^{-1418}	Medium	—	—	—	—
CNTs	120–500	0.6	10^{4}–10^{519}	High	50–100	<60	<60	<30
Graphene	2630	>1	10^{6}	High	100–205	>100–205	80–110	>80–110
Graphite	10	2.26	10^{423}	Low	—	—	—	—
ACs	1000–3500	0.4–0.7	0.1–1	Low	<200	<80	<100	<50
Templated porous carbon	500–3000	0.5–1	0.3–10	High	120–350	<200	60–140	<100
Functionalized porous carbon	300–2200	0.5–0.9	>300	Medium	150–300	<180	100–150	>90
Activated carbon fibers	1000–3000	0.3–0.8	5–10	Medium	120–370	<150	80–200	<120
Carbon aerogles	400–1000	0.5–0.7	1–10	Low	100–125	<80	<80	<40

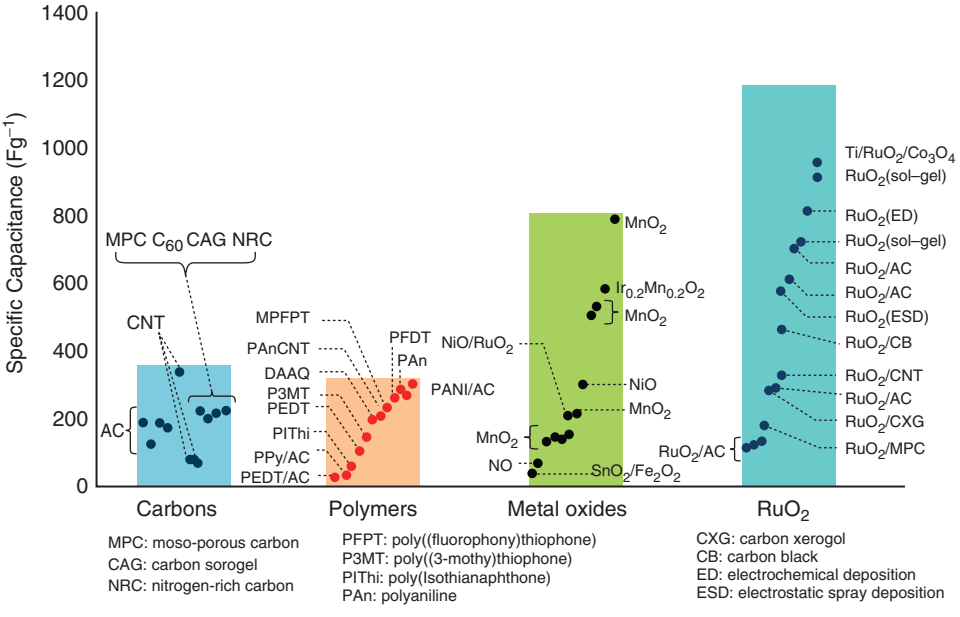

Figure 3.34 Summary of common materials for supercapacitors [34].

3.4
Graphene for Li–Sulfur Batteries

Rechargeable lithium batteries with sulphur cathode, called *lithium–sulfur* (*Li–S*) batteries, are expected to deliver a theoretical energy density up to 2600 Wh kg^{-1} [41–47]. However, the insulating nature of the sulfur and the high solubility of the lithium polysulfide in the liquid electrode impede the commercialization of Li–S batteries [41]. One of the strategies to stabilize sulfur cathodes is to develop an electron-conductive matrix to not only improve the conductivity but also inhibit the dissolution of lithium–sulfur during charge/discharge processes. The carbon could be mesoporous carbon, microporous carbon, hierarchical porous carbon, microporous carbon spheres, hollow carbon spheres, or carbon nanotubes [44]. GNSs, as a unique two-dimensional carbon, have also been used to confine the sulfur compounds for Li–S batteries because of their electronic properties, large specific surface area, and excellent mechanical properties [45].

Zhou *et al.* [42] proposed a graphene-coated mesoporous carbon/sulfur (RGO/CMK-3/S) composite cathode material. Figure 3.38a shows a schematic of the RGO/CMK-3/S composite. Figure 3.38b displays the TEM image of this composite. Figure 3.38c demonstrates the cycling tests of CMK-3/S and the RGO/CMK-3/S composite. The results show that the RGO/CMK-3/S composite with 53.14 wt% sulfur presents a reversible discharge capacity of 734 mAh g^{-1} after 100 cycles at 0.5 C. Lu *et al.* [43] reported an approach to assemble a

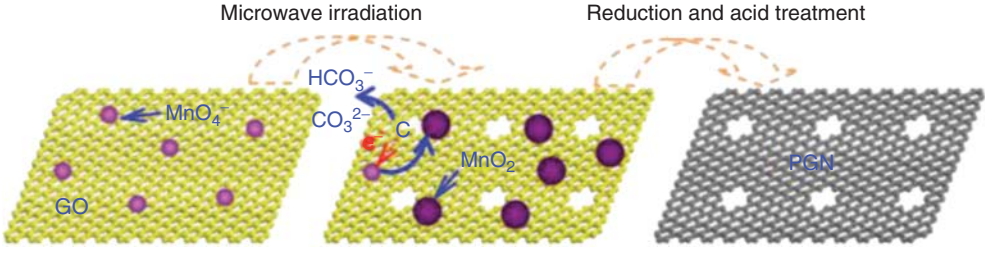

Figure 3.35 Illustration of the formation of porous graphene material with pores on the surface of sheet [38].

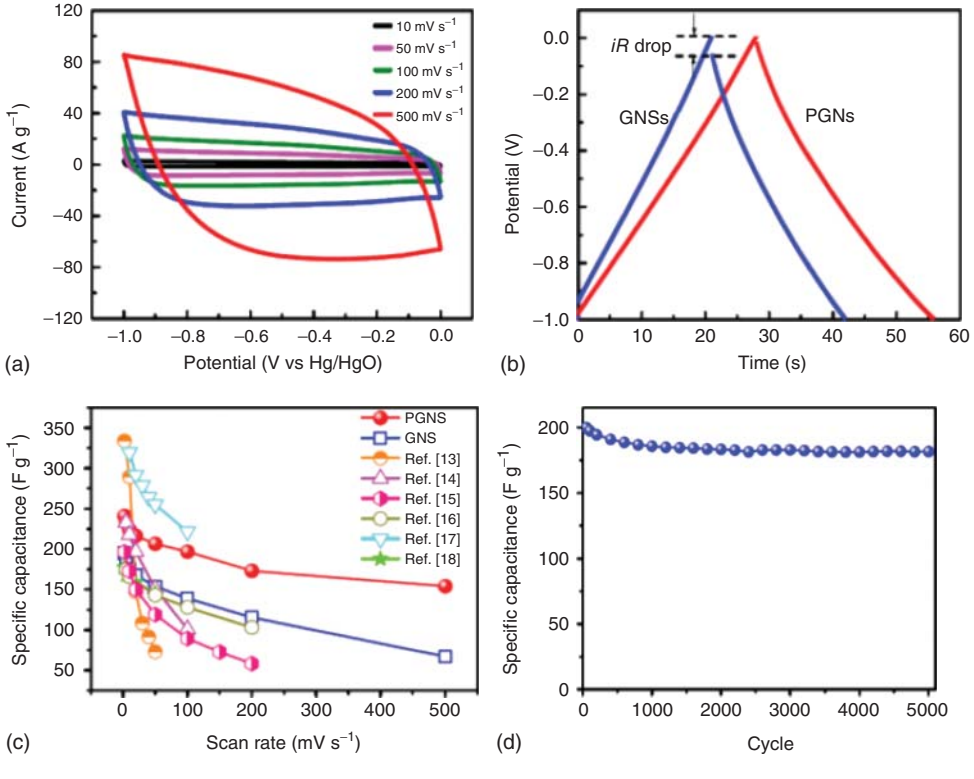

Figure 3.36 (a) CV curves of the PGN electrode at different scan rates of 10, 50, 100, 200, and 500 mV s^{-1} in 6 M KOH. (b) Galvanostatic charge/discharge curves of PGNs and GNSs at a current density of 50 mA cm^{-2}. (c) Specific capacitance of PGNs, GNSs, commercial activated carbon, thermally exfoliated graphene, activated carbon and carbide-derived carbon with different scan rates. (d) Cycle stability of the PGN electrode at 100 mV s^{-1} for 5000 cycles [38].

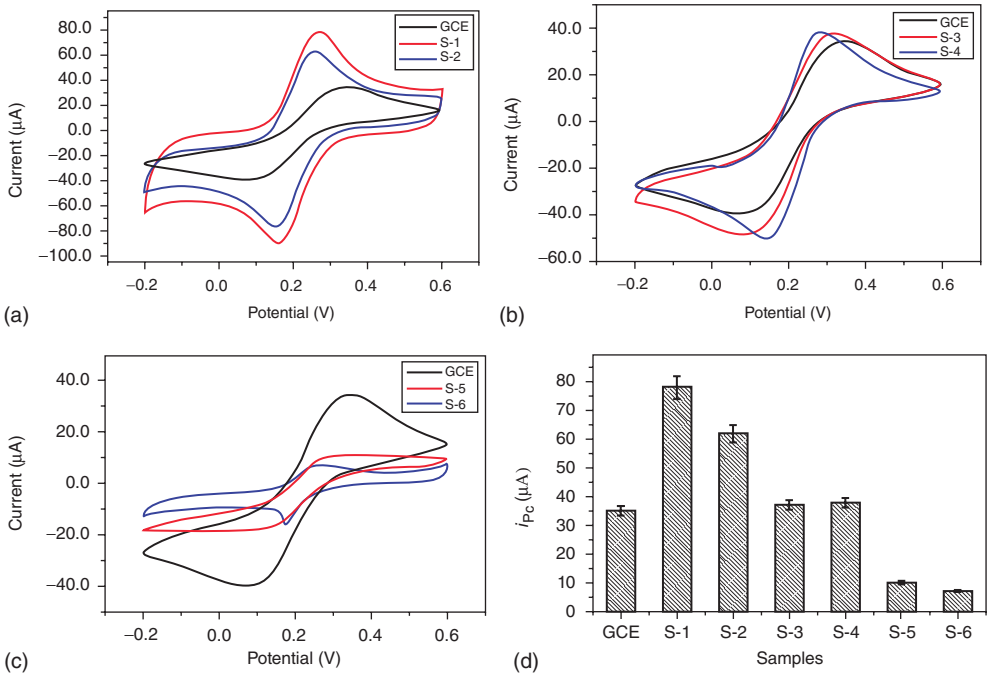

Figure 3.37 (a–c) Cyclic voltammetry of GO samples (S-1 to S-6) modified on glassy carbon electrode (GCE) in 5 mM $K_3[Fe(CN)_6]$ containing 0.1 M KCl solution. (d) Comparison of i_{pc} of the samples with different oxidation levels [39].

graphene–sulfur–carbon nanofiber (G-S-CNF) coaxial structured nanocomposite with sulfur sandwiched between graphene and CNFs, which can be used as cathode for Li–S batteries with significantly improved cycle stability and capacity. Figure 3.39a demonstrates a schematic illustration of the assembled G-S-CNF multilayered coaxial nanocomposites, and Figure 3.39b shows the cycling tests of S-CNFs and G-S-CNFs. The composite cathode of G-S-CNFs with an initial capacity of 745 mAh g^{-1} was able to maintain ~273 mAh g^{-1} even after 1500 charge/discharge cycles at a high rate of 1 C, representing an extremely low decay rate of 0.043% per cycle after 1500 cycles. Zhou *et al.* [44] reported a graphene–sulfur hybrid material with sulfur nanocrystals anchored on interconnected fibrous graphene obtained by a facile one-pot strategy using a sulfur/carbon disulfide/alcohol mixed solution. Figure 3.40a displays an illustration of the formation of the G-S hybrid and a schematic of the fabrication of a self-supporting electrode. Figure 3.40b,c shows the capacity at different current densities and the cycling performance of these composite cathodes. The results demonstrate that the G-S hybrid cathodes give excellent electrochemical performance with high specific capacity, good rate performance, and stable cyclability over 100 cycles.

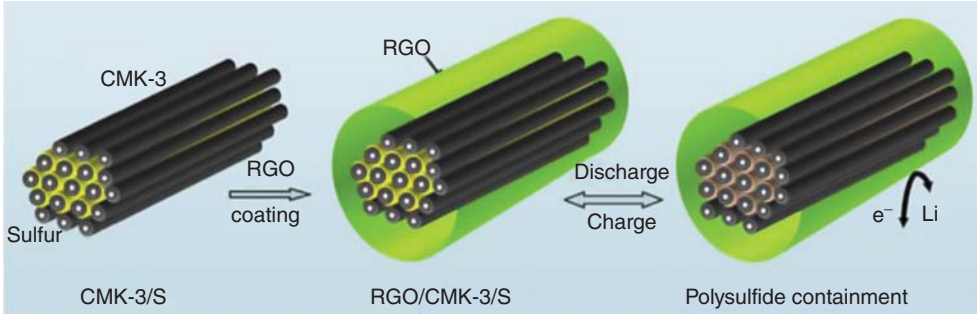

(a)

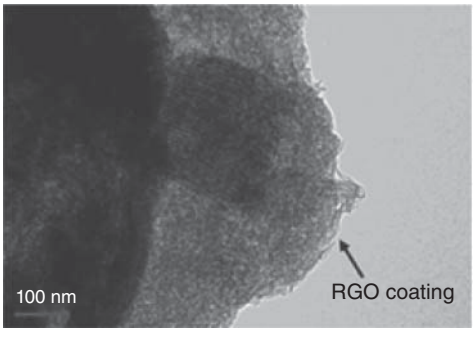

(b)

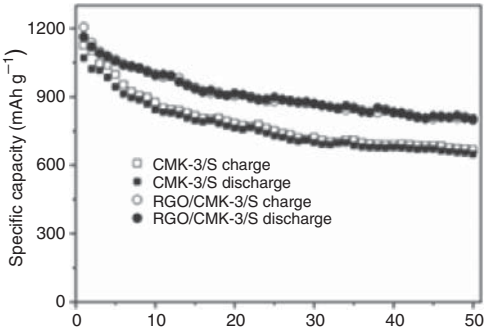

(c)

Figure 3.38 (a) Scheme of RGO/CMK-3/S composite for improving the cathode performance. (b) TEM image of RGO/CMK-3/S composite. (c) Cycling tests of CMK-3/S and RGO/CMK-3/S composite [42].

3.5 Graphene for Fuel Cells

Fuel cells constitute a green energy device to transfer chemical reactions to electrical energy. The reactions involve the oxidation of hydrogen and reduction of oxygen. In general, the reaction rate of these redox reactions could be enhanced by adding nano-sized catalysts in a porous support. Traditionally, activated carbon or carbon black has been used as the support because of their high specific surface area. Owing their open structure, high electric conductivity, and specific surface area, graphene-based materials have drawn much attention to the application of graphene on fuel cells [48–54]. It has been proved that graphene could replace traditional carbon-based materials as an alternative matrix for catalyst loading. The loading density of a catalyst such as Pt in graphene is much higher than that in other carbon-based materials [48–50]. As shown in Figure 3.41, nitrogen-doped graphene exhibits much better performance than Pt/carbon black and pure graphene [48]. For hydrogen storage materials, alloy-based materials such as $LaNi_5$, TiFe, MgNi, and so on,

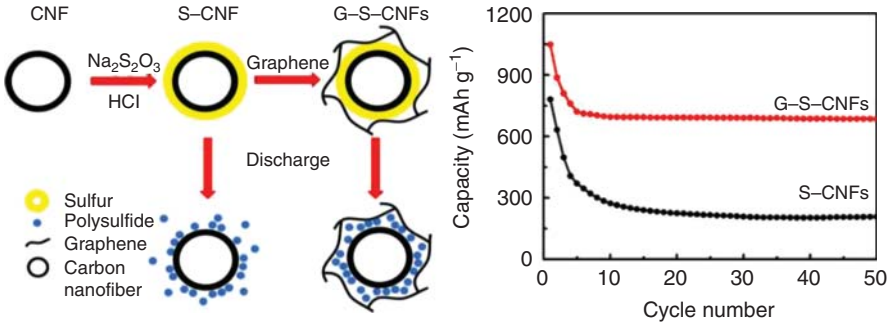

Figure 3.39 (a) Schematic illustration of the assembled G-S-CNF multilayered coaxial nanocomposites for improving cathode performance. (b) Cycling tests of S-CNFs and G-S-CNFs [43].

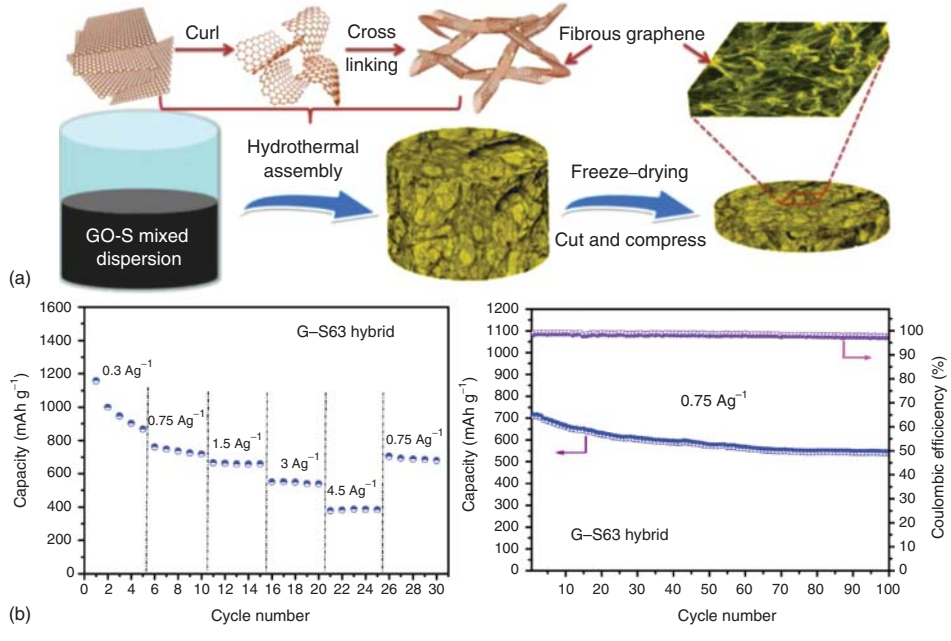

Figure 3.40 (a) Illustration of the formation of the G-S hybrid and schematic of the fabrication of a self-supporting electrode. (b) Capacity at different current densities of the G-S62 cathode. (c) Cycling performance and coulombic efficiency of the G-S63 cathode at 0.75 A g^{-1} for 100 cycles after the high current density test [44].

have been widely used. However, the content of hydrogen storage is smaller than 2 wt%. In addition, the disadvantages of alloy-based catalysts are that they expansive and of high specific gravity, which limit their applications to fuel cells. For developing novel hydrogen storage materials, much attention has been drawn to graphene. Rao *et al.* [50] demonstrated that 3–4 layers of

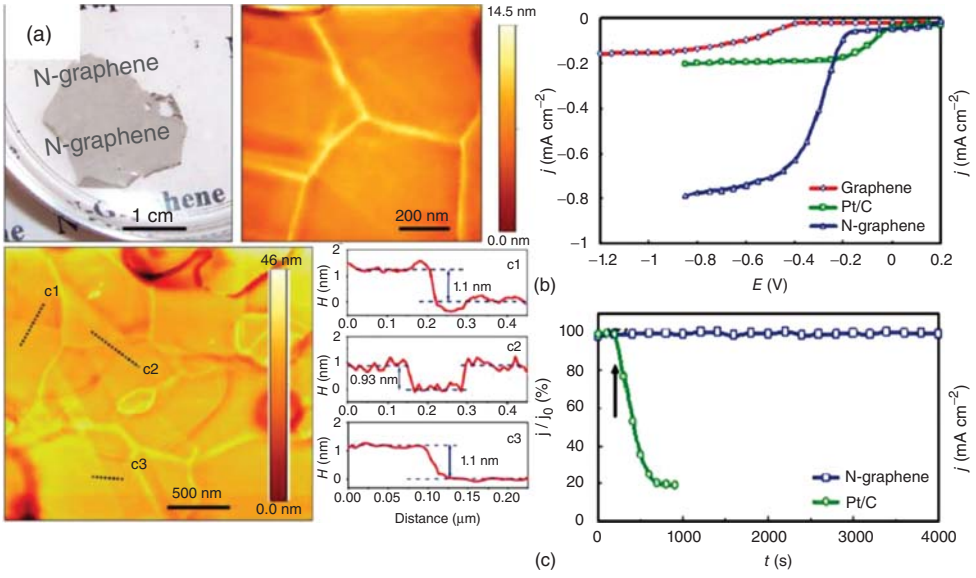

Figure 3.41 (a) Photo and AFM images of N-doped graphene. (b) Oxygen reduction reaction (ORR) curves of graphene, Pt/C, and N-doped graphene. (c) Cycling performance of N-doped graphene and Pt/C composite [48].

GNSs are potential candidates to be an absorber for H_2 and CO_2. For H_2, the storage content is 3.11 wt% under 100 bar and 298 K. For CO_2, on the other hand, the absorption content is 2.1 – 3.5 wt% under 1 bar and 195 K. According to theoretical calculations, the absorption content is as high as 7.7 wt%, which completely approaches the requirement of the United States Department of Energy (DoE) of 6 wt%. Thus, graphene could be a promising material for hydrogen storage.

3.6 Graphene for Solar Cells

Graphene could also be used for solar cells. The absorption of a single graphene layer was published in 2008. Graphene absorbs 2.3% of white light. And the transparency at near-IR for graphene is much better than for indium tin oxide (ITO). This indicates that more light in the near-IR range can penetrate the device of the solar cells and the solar cell efficiency can be enhanced. In addition, the work function of graphene is about 4.2 eV, which is similar to that of carbon nanotubes. Hence, graphene could also act as an electrode for dye-sensitized solar cells. From these points of view, much work has been done for studying the application of graphene to solar cells [55 – 62].

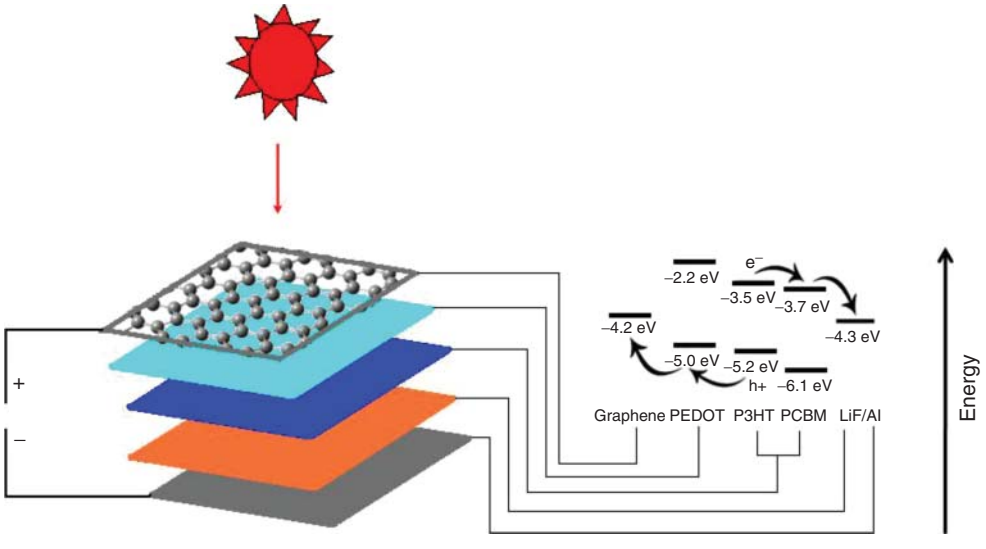

Figure 3.42 Schematic diagram and work function of dye-sensitized solar cells and their corresponding materials [56].

Müllen *et al.* [58] used graphene as a counterelectrode for dye-sensitized solar cell applications, as shown in Figure 3.42. Under a solar simulation condition of 98.3 mW cm^{-2}, its short-circuit photocurrent density (I_{SC}), open-circuit voltage (OCV), and fill factor (FF) are 1.01 mA cm^{-2}, 0.7 V, and 0.36, respectively. The efficiency is about 0.26%. Hong *et al.* [56] reported a graphene/polyethylenedioxythiophene (PEDOT)-poly(styrenesulfonate) (PSS) composite electrode as a counterelectrode with a thickness of 60 nm. The transparency was >80%, and the efficiency was as high as 4.6%, which is superior to that of a pure PEDOT-PSS electrode of 2.3%. The performance is close to that of platinum. Compared to a PEDOT-PSS electrode, thanks to the properties of higher specific surface area and structural defects, graphene exhibits high catalytic activity. Thus, the current density and FF can be enhanced by the addition of a small content of graphene.

Wang *et al.* [58] reported transparent, conductive, ultrathin films as an alternative to the ubiquitously employed metal oxide window electrodes for solid-state dye-sensitized solar cells. Figure 3.43 shows an illustration of a solar cell based on a graphene electrode and the energy level diagram of graphene/TiO_2/dye/spiro-OMeTAD/Au device. In optoelectronic devices, proper contact between the electrode and p/n type material important for charge collection. The calculated work function of graphene is 4.42 eV. Thus, it can replace the fluorine tin oxide (FTO) electrode (work function ~4.4 eV). The results show a high conductivity of 550 S cm^{-1} and a transparency of more than 70% over 1000–3000 nm [58].

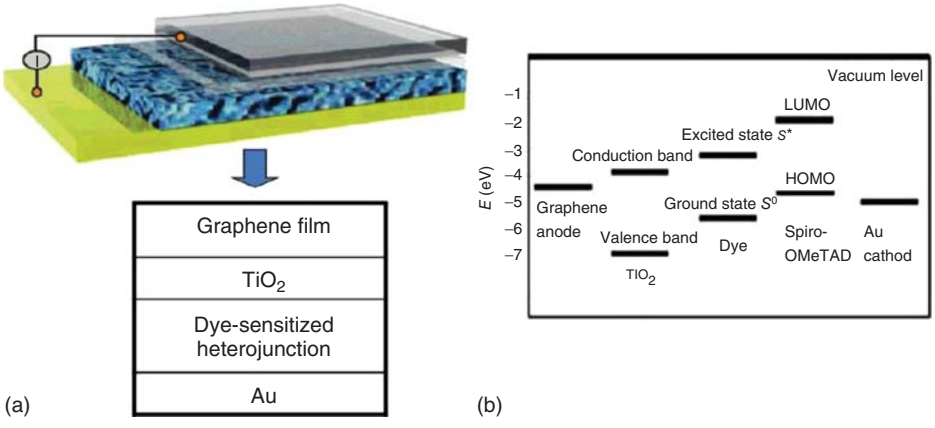

Figure 3.43 (a) Illustration of a schematic of dye-sensitized solar cells. The four layers (from bottom to top) are Au, dye-sensitized heterojunction, compact TiO_2, and graphene film. (b) The energy level diagram of graphene/TiO_2/dye/spiro-OMeTAD/Au device [58].

3.7 Summary

This chapter focused on the application aspects of graphene-based materials on energy storage devices, including Li-ion batteries, supercapacitors, fuel cells, Li–sulfur batteries, and solar cells. The critical challenges, nowadays, for the applications of graphene on energy materials lie in (i) how to propose cost-effective and environmentally friendly processes to synthesize graphene; (ii) how to synthesize structure-tunable graphene with different geometry; and (iii) how to control the functional groups of graphene for different blending systems. Graphene, indeed, is a promising candidate for energy material applications because of its merits of high electronic conductivity, high specific surface area, light weight, and tunable chemical and physical properties. It is believed graphene could change the world of basic science, nanotechnology and energy-based applications in the near future.

References

1. Pan, D., Wang, S., Zhao, B., Wu, M.H., Zhang, H.J., Wang, Y., and Jiao, Z. (2009) Li storage properties of disordered graphene nanosheets. *Chem. Mater.*, **21**, 3136–3142.
2. Pollak, E., Geng, B., Jeon, K.-J., Lucas, I.T., Richardson, T.J., Wang, F., and Kostecki, R. (2010) The interaction of Li^+ with single-layer and few-layer graphene. *Nano Lett.*, **10**, 3386–3388.
3. Uthaisar, C. and Barone, V. (2010) Edge effects on the characteristics of Li diffusion in graphene. *Nano Lett.*, **10**, 2838–2842.
4. Bharwaj, T., Antic, A., Paven, B., Barone, V., and Fahlman, B.D. (2010) Enhanced electrochemical lithium storage by graphene nanoribbons. *J. Am. Chem. Soc.*, **132**, 12556–12558.

5. Uthaisar, C., Barone, V., and Fahlman, B.D. (2013) On the chemical nature of thermally reduced graphene oxide and its electrochemical Li intake capacity. *Carbon*, **61**, 558–567.
6. Lee, W., Suzuki, S., and Miyayama, M. (2013) Lithium storage properties of graphene sheets derived from graphite oxides with different oxidation degree. *Ceram. Int.*, **39**, S753–S756.
7. Kuo, S.-L., Liu, W.-R., and Wu, H.-C. (2012) Lithium storage behavior of graphene nanosheets-based materials. *J. Chin. Chem. Soc.*, **59** (10), 1220–1225.
8. Kuo, S.-L., Liu, W.-R., Kuo, C.-P., Wu, N.-L., and Wu, H.-C. (2013) Lithium storage in reduced graphene oxides. *J. Power Sources*, **244**, 552–556.
9. Chen, X.-C., Wei, W., Lv, W., Su, F.-Y., He, Y.-B., Li, B., Kang, F., and Yang, Q.-H. (2012) A graphene-based nanostructure with expanded ion transport channels for high rate Li-ion batteries. *Chem. Commun.*, **48**, 5904–5906.
10. Hu, Y., Li, X., Geng, D., Cai, M., Li, R., and Sun, X. (2013) Influence of paper thickness on the electrochemical performances of graphene papers as an anode for lithium ion batteries. *Electrochem. Acta*, **91**, 227–233.
11. Liu, Y., Fan, Q., Tang, N., Wan, X., Liu, L., Lv, L., and Du, Y. (2013) Study of electronic and magnetic properties of nitrogen doped graphene oxide. *Carbon*, **60**, 538–561.
12. Yang, Y.Q., Wu, K., Pang, R.Q., Zhou, X.J., Zhang, Y., Wu, X.C., Wu, C.G., Wu, H.X., and Guo, S.W. (2013) Graphene sheets coated with a thin layer of nitrogen-enriched carbon as a high-performance anode for lithium-ion batteries. *RSC Adv.*, **3**, 14016–14020.
13. Jiang, Z.Q., Pei, B., and Manthiram, A. (2013) Randomly stacked holey graphene anodes for lithium ion batteries with enhanced electrochemical performance. *J. Mater. Chem. A*, **1**, 7775–7781.
14. Yang, Y., Ji, X., Yang, X., Wang, C., Song, W., Chen, Q., and Banks, C.E. (2013) Electrochemically triggered graphene sheets through cathodic exfoliation for lithium ion batteries anodes. *RSC Adv.*, **3**, 16130–16135.
15. Liu, N., Luo, F., Wu, H., Liu, Y., Zhang, C., and Chen, J. (2008) One-step ionic-liquid-assisted electrochemical synthesis of ionic-liquid-functionalized graphene sheets directly from graphite. *Adv. Funct. Mater.*, **18**, 1518–1525.
16. Zhou, M., Tang, J., Cheng, Q., Xu, G., Cui, P., and Qin, L.C. (2013) Few-layer graphene obtained by electrochemical exfoliation of graphite cathode. *Chem. Phys. Lett.*, **572**, 61–65.
17. Su, C.Y., Lu, A.Y., Xu, Y.P., Chen, F.R., Khlobystov, A.N., and Li, L.J. (2011) High-quality thin graphene films from fast electrochemical exfoliation. *ACS Nano*, **5**, 2332–2339.
18. Geng, Y., Zheng, Q.B., and Kim, J.-K. (2011) Effects of stage, intercalant species and expansion technique on exfoliation of graphite intercalation compound into graphene sheets. *J. Nanosci. Nanotechnol.*, **11**, 1084–1091.
19. Wang, G.X., Wang, B., Park, J., Wang, Y., Sun, B., and Yao, J. (2009) Highly efficient and large-scale synthesis of graphene by electrolytic exfoliation. *Carbon*, **47**, 3242–3246.
20. Wang, J., Manga, K.K., Bao, Q., and Loh, K.P. (2011) High-yield synthesis of few-layer graphene flakes through electrochemical expansion of graphite in propylene carbonate electrolyte. *J. Am. Chem. Soc.*, **133**, 8888–8891.
21. Morales, G.M., Schifani, P., Ellis, G., Ballesteros, C., Martínez, G., Barbero, C., and Salavagione, H.J. (2011) High-quality few layer graphene produced by electrochemical intercalation and microwave-assisted expansion of graphite. *Carbon*, **49**, 2809–2816.
22. Zhou, G., Wang, D.-W., Li, F., Zhang, L., Li, N., Wu, Z.-S., Wen, L., Lu, G.Q., and Cheng, H.-M. (2010) Graphene-wrapped Fe_3O_4 anode material with improved reversible capacity and cyclic stability for lithium ion batteries. *Chem. Mater.*, **22**, 5306–5313.
23. Wu, Z.-S., Ren, W., Wen, L., Gao, L., Zhao, J., Chen, Z., Zhou, G., Li, F., and Cheng, H.-M. (2010) Graphene anchored with Co_3O_4 nanoparticles as anode of lithium ion batteries with enhanced reversible capacity and cyclic performance. *ACS Nano*, **4** (6), 3187–3194.

24. Chou, S.-L., Wang, J.-Z., Choucair, M., Liu, H.-K., Stride, J.A., and Dou, S.-X. (2010) Enhanced reversible lithium storage in a nanosize silicon/graphene composite. *Electrochem. Commun.*, **12**, 303–306.
25. Li, X., Geng, D., Meng, X., Wang, J., Liu, J., Li, Y., Wang, D., Yang, J., Li, R., and Sun, A.X. (2010) 15th International Meeting on Lithium Battery, 15th IMLB Meeting.
26. Lee, J.K., Smith, K.B., Hayner, C.M., and Kung, H.H. (2010) Silicon nanoparticles–graphene paper composites for Li ion battery anodes. *Chem. Commun.*, **46**, 2025–2027.
27. He, Z., Wang, Z., Guo, H., Li, X., Xianwen, W., Yue, P., and Wang, J. (2013) A simple method of preparing graphene-coated $Li[Li_{0.2}Mn_{0.54}Ni_{0.13}Co_{0.13}]O_2$ for lithium-ion batteries. *Mater. Lett.*, **91**, 261–264.
28. Sun, Y., Yang, S.-B., Lv, L.-P., Lieberwirth, I., Zhang, L.-C., Ding, C.-X., and Chen, C.-H. (2013) A composite film of reduced graphene oxide modified vanadium oxide nanoribbons as a free standing cathode material for rechargeable lithium batteries. *J. Power Sources*, **241**, 168–172.
29. Ding, Y.-H., Ren, H.-M., Huang, Y.-Y., Chang, F.-H., He, X., Fen, J.-Q., and Zhang, P. (2013) Co-precipitation synthesis and electrochemical properties of graphene supported $LiMn_{1/3}Ni_{1/3}Co_{1/3}O_2$ cathode materials for lithium-ion batteries. *Nanotechnology*, **24**, 375401–375408.
30. Prabakar, S.J.R., Hwang, Y.-H., Lee, B., Sohn, K.-S., and Pyo, M. (2013) Graphene-sandwiched $LiNi_{0.5}Mn_{1.5}O_4$ cathode composites for enhanced high voltage performance in Li ion batteries. *J. Electrochem. Soc.*, **160** (6), A832–A837.
31. Wang, B., Wang, D., Wang, Q., Liu, T., Guo, C., and Zhao, X. (2013) Improvement of the electrochemical performance of carbon-coated $LiFePO_4$ modified with reduced graphene oxide. *J. Mater. Chem. A*, **1**, 135–144.
32. Ha, J., Park, S.-K., Yu, S.-H., Jin, A., Jang, B., Bong, S., Kim, I., Sung, Y.-E., and Piao, Y. (2013) A chemically activated graphene-encapsulated $LiFePO_4$ composite for high-performance lithium ion batteries. *Nanoscale*, **5**, 8647–8655.
33. Song, B., Lai, M.O., Liu, Z., Liu, H., and Lu, L. (2013) Graphene-based surface modification on layered Li-rich cathode for high-performance Li-ion batteries. *J. Mater. Chem. A*, **1**, 9954–9965.
34. Zhang, L.L., Zhou, R., and Zhao, X.S. (2010) Graphene-based materials as supercapacitor electrodes. *J. Mater. Chem.*, **20**, 5983–5992.
35. Wang, H., Hao, Q., Yang, X., Lu, L., and Wang, X. (2009) Graphene oxide doped polyaniline for supercapacitors. *Electrochem. Commun.*, **11**, 1158–1161.
36. Lv, W., Tang, D.-M., He, Y.-B., You, C.-H., Shi, Z.-Q., Chen, X.-C., Chen, C.-M., Hou, P.-X., Liu, C., and Yang, Q.-H. (2009) Low-temperature exfoliated graphenes: vacuum-promoted exfoliation and electrochemical energy storage. *ACS Nano*, **3**, 3730–3736.
37. Liu, C., Yu, Z., Neff, D., Zhamu, A., and Jang, B.Z. (2010) Graphene-based supercapacitor with an ultrahigh energy density. *Nano Lett.*, **10**, 4863–4868.
38. Fan, Z.G., Zhao, Q.K., Li, T.Y., Yan, Y., Ren, Y.M., Feng, J., and Wei, T. (2012) Easy synthesis of porous graphene nanosheets and their use in supercapacitors. *Carbon*, **50**, 1699–1703.
39. Krishnamoorthy, K.K., Veerapandian, M., Yun, K.S., and Kim, S.-J. (2013) The chemical and structural analysis of graphene oxide with different degrees of oxidation. *Carbon*, **53**, 38–49.
40. Mhamane, D., Suryawanshi, A., Banerjee, A., Aravindan, V., Ogale, S., and Srinivasan, M. (2013) Non-aqueous energy storage devices using graphene nanosheets synthesized by green route. *AIP Adv.*, **3**, 042112.
41. Wang, X.F., Wang, Z.X., and Chen, L.Q. (2013) Reduced graphene oxide film as a shuttle-inhibiting interlayer in a lithium-sulfur battery. *J. Power. Sources*, **242**, 65–69.
42. Zhou, X.Y., Xie, J., Yang, J., Zou, Y.L., Tang, J.J., Wang, S.C., Ma, L., and Liao, Q.C. (2013) Improving the performance of lithium–sulfur batteries by graphene coating. *J. Power. Sources*, **243**, 993–1000.

43. Lu, S.T., Cheng, Y.W., Wu, X.H., and Liu, J. (2013) Significantly improved long-cycle stability in high-rate Li-S batteries enabled by coaxial graphene wrapping over sulfur-coated carbon nanofibers. *Nano Lett.*, **13**, 2485–2489.
44. Zhou, G.M., Yin, L.-C., Wang, D.-W., Li, L., Pei, S.F., Gentle, I.R., Li, F., and Cheng, H.-M. (2013) Fibrous hybrid of graphene and sulfur nanocrystals for high-performance lithium-sulfur batteries. *ACS Nano*, **7** (6), 5367–5375.
45. Ding, B., Yuan, C.Z., Shen, L.F., Xu, G.Y., Nie, P., Lai, Q.X., and Zhang, X.G. (2013) Porous nitrogen-doped carbon nanotubes derived from tubular polypyrrole for energy-storage applications. *J. Mater. Chem. A*, **1**, 1096–1101.
46. Xiao, M., Huang, M., Zeng, S.S., Han, D.M., Wang, S.J., Sun, L.Y., and Meng, Y.Z. (2013) Sulfur@graphene oxide core–shell particles as a rechargeable lithium–sulfur battery cathode material with high cycling stability and capacity. *RSC Adv.*, **3**, 4914–4916.
47. Lu, L.Q., Lu, L.J., and Wang, Y. (2013) Sulfur film-coated reduced graphene oxide composite for lithium–sulfur batteries. *J. Mater. Chem. A*, **1**, 9173–9181.
48. Seger, B. and Kamat, P.V. (2009) Electrocatalytically active graphene-platinum nanocomposites. Role of 2-D carbon support in PEM fuel cells. *J. Phys. Chem. C*, **113**, 7990–7995.
49. Si, Y. and Samulski, E.T. (2009) Exfoliated graphene separated by platinum nanoparticles. *Chem. Mater.*, **20**, 6792–6707.
50. Ghosh, A., Subrahmanyam, K.S., and Rao, C.N.R. (2008) Uptake of H_2 and CO_2 by graphene. *J. Phys. Chem. C*, **112**, 15704–15707.
51. Guo, Y.H., Lan, X.X., Cao, J.X., Xu, B., Xia, Y.D., Yin, J., and Liu, Z.G. (2013) A comparative study of the reversible hydrogen storage behavior in several metal decorated graphyne. *Int. J. Hydrogen Energy*, **38**, 3987–3993.
52. Lee, S.G., Lee, M.H., Choi, H.C., Yoo, D.S., and Chung, Y.-C. (2013) Effect of nitrogen induced defects in Li dispersed graphene on hydrogen storage. *Int. J. Hydrogen Energy*, **38**, 4611–4617.
53. Lee, S.G., Lee, M.H., and Chung, Y.-C. (2013) Enhanced hydrogen storage properties under external electric fields of N-doped graphene with Li decoration. *Phys. Chem. Chem. Phys.*, **15**, 3243–3248.
54. Li, F., Gao, J.F., Zhang, J., Xu, F., Zhao, J., and Sun, L.X. (2013) Graphene oxide and lithium amidoborane: a new way to bridge chemical and physical approaches for hydrogen storage. *J. Mater. Chem. A*, **1**, 8016–8022.
55. Fan, B.H., Mei, X.G., Sun, K., and Ouyang, J.Y. (2008) Conducting polymer/carbon nanotube composite as counter electrode of dye-sensitized solar cells. *Appl. Phys. Lett.*, **93**, 143103.
56. Hong, W.J., Xu, Y.X., Lu, G.W., Li, C., and Shi, G.Q. (2008) Transparent graphene/PEDOT–PSS composite films as counter electrodes of dye-sensitized solar cells. *Electrochem. Commun.*, **10**, 1555–1558.
57. Eda, G. and Chhowalla, M. (2009) Chemically derived graphene oxide: towards large–area thin–film electronics and optoelectronics. *Adv. Mater.*, **22** (22), 2392–2415.
58. Wang, X., Zhi, L., and Müllen, K. (2008) Transparent, conductive graphene electrodes for dye-sensitized solar cells. *Nano Lett.*, **8** (1), 323–327.
59. Park, H., Rowehl, J.A., Kim, K.K., Bulovic, V., and Kong, J. (2010) Doped graphene electrodes for organic solar cells. *Nanotechnology*, **21**, 505204.
60. Tsai, T.-H., Chiou, S.-C., and Chen, S.-M. (2011) Enhancement of dye-sensitized solar cells by using graphene-TiO_2 composites as photoelectrochemical working electrode. *Int. J. Electrochem. Sci.*, **6**, 3333–3343.
61. Miao, X.C., Tongay, S., Petterson, M.K., Berke, K., Rinzler, A.G., Appleton, B.R., and Hebard, A.F. (2012) High efficiency graphene solar cells by chemical doping. *Nano Lett.*, **12**, 2745–2750.
62. Li, X.M., Zhu, H.W., Wang, K.L., Cao, A., Wei, J.Q., Li, C.Y., Jia, Y., Li, Z., Li, X., and Wu, D. (2010) Graphene-on-silicon schottky junction solar cells. *Adv. Mater.*, **22**, 2743–2748.

4
Graphene-Based Nanocomposites for Supercapacitors

Xuanxuan Zhang, Tao Hu, and Ming Xie

4.1
Introduction

Supercapacitors, also called *ultracapacitors*, as potential electrochemical energy storage devices are applied in a variety of military and commercial applications because of their long cycling lifetime, low maintenance cost, and extraordinarily high power density [1, 2]. A hybrid system combining lithium-ion batteries and supercapacitors has also been attracting the attention of researchers. Supercapacitors can be primary energy devices for power assist during acceleration and hill climbing, as well as for recovery of braking energy. Lithium-ion batteries can provide the energy during cruising. The hybrid system combines the power performance of supercapacitors with the greater energy storage capability of lithium-ion batteries. The hybrid system can also extend the life, downsize the volume, and reduce the cost of batteries.

There are two types of supercapacitors (SCs): electric double-layer capacitors (EDLCs) and pseudocapacitors. EDLCs are non-faradaic supercapacitors which store energy using the adsorption of both anions and cations [3, 4]. Currently, most of state-of-the-art EDLCs devices are based on high-surface-area carbon [5–11], such as porous activated carbon (AC). A main issue with AC-based SC electrodes is that the entire surface area is not electrochemically accessible by the electrolyte because of their small micropore size (pore size <2 nm) and hydrophobic graphene-like surface [12, 13]. Therefore, carbon has a low surface-area-normalized specific capacitance of $10-40\,\mu F\,cm^{-1}$ [2, 14] The commercial SC based on AC and organic electrolyte has only an energy density of $\sim 7\,Wh\,kg^{-1}$ [15], although its power density can be as high as $10\,kW\,kg^{-1}$ as shown in Figure 4.1. Therefore, it is essential to develop novel electrode materials with large accessible specific surface area (SSA) and better electrolyte affinity, contributing to a higher energy density.

Unlike EDLCs which store energy through physical adsorption, pseudocapacitive materials [17] store energy through a faradaic process, which involves fast and reversible redox reactions between the electrolyte and electroactive materials on the electrode surface [18]. In principle, the electroactive species, which possess

Graphene-based Energy Devices, First Edition. Edited by A. Rashid bin Mohd Yusoff.
© 2015 Wiley-VCH Verlag GmbH & Co. KGaA. Published 2015 by Wiley-VCH Verlag GmbH & Co. KGaA.

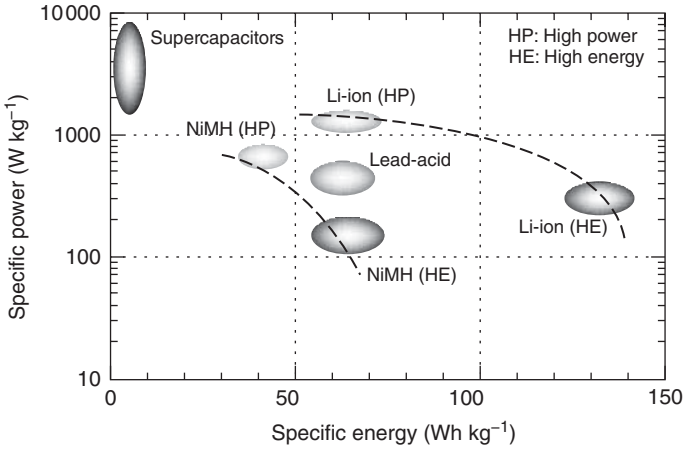

Figure 4.1 Specific power versus specific energy of modern storage devices [16]. (Reproduced with permission from Database r2009 IEEE.)

various valence/oxidation states, have pseudo charge storage abilities. The most widely explored electroactive materials include (i) transition-metal oxides [10], hydroxides, or nitrides; [19] (ii) conducting polymers (CPs) [20] such as polyaniline (PANI), polypyrrole (PPy), and polythiophene (PTh); and (iii) materials possessing oxygen- and nitrogen-containing surface functional groups [9, 11].

Graphene [21, 22] is an excellent electronic conductor [23, 24] and has a high theoretical SSA of 2630 $m^2 g^{-1}$ [25], high chemical stability [21], and excellent mechanical properties [26]. The two-dimensional sheet structure of graphene provides an excellent building block and ideal conductive platform for accommodating nano-sized electrochemically active materials. The flexible mesopore and macropore structures [27] of graphene allow nanoscale materials to fill the void space while at the same time providing conduction channels for the transport of electrons. By combining graphene and pseudocapacitance materials, researchers have successfully created novel nanocomposites with high capacitance and long stability.

In this chapter, we will review the progress on graphene-based nanocomposites for supercapacitors. The main focus will be on graphene-based EDLCs, conductive polymers, and metal oxides. We will describe the uniqueness of atomic layer deposition (ALD) as a synthesis technique. In the end, we will address issues and perspectives for the future.

4.2 Graphene-Based Supercapacitors

Generally, graphene-based porous materials are synthesized by reduction from graphite oxide (GO) by the Hummers method [28]. GO can be reduced either by

thermal exfoliation or by chemical exfoliation. The detailed of synthesis can be found elsewhere [29]. Briefly, graphite powders are added to a mixture of concentrated H_2SO_4 and $NaNO_3$ and stirred in an ice bath. $KMnO_4$ is added carefully to the solution, and then maintained for 30 min at 35 °C, followed by the slow addition of deionized (DI) water. Afterwards, additional DI water containing H_2O_2 is added to the solution. The solid is obtained from centrifugation followed by washing with excess DI water, HCl, and ethanol. The final yellow-brown GO powder is then dried in vacuum. Graphene sheets are produced by thermal exfoliation of the as-synthesized GO powders [30]. Strictly speaking, the product should not be called graphene but reduced graphene oxide (rGO). Different from CVD (chemical vapor deposition) graphene, rGO has more layers and many functional groups and defects on surface. Therefore, the mechanical and electrical properties of rGO are very different those of CVD graphene. However, these functional groups and defects are usually beneficial as initial nucleation sites to grow other nanomaterials by the hydrothermal process and vapor deposition. In this chapter, we will use the term rGO for graphene made by reduction.

4.2.1 EDLCs

Ruoff *et al.* [25] demonstrated that a supercapacitor based on chemically modified graphene (CMG) electrodes exhibited specific capacitances of 135 and 99 F g^{-1} with KOH and organic electrolytes, respectively, as shown in Figure 4.2. Additionally, the high electrical conductivity gives these materials exceptional performance over a wide range of voltage scan rates.

To further exploit the adsorption potential of graphene with a larger SSA, the same group used a simple chemical activation method to synthesize activated microwave-exfoliated graphene oxide with extremely large surface area (~3100 m^2 g^{-1}) [5]. As shown in Figure 4.3, the sp^2-bonded carbon with low oxygen and hydrogen content has a continuous three-dimensional network of highly curved, atom-thick walls that form primarily 0.6–5 nm wide pores. High specific capacitances of 165, 166, and 166 F g^{-1} can be achieved at current densities of 1.4, 2.8, and 5.7 A g^{-1}, respectively, indicating their exceptional rate capability. The energy density was calculated to be about 70 Wh kg^{-1}, with a power density at ~250 kW kg^{-1}. Moreover, the activated CMG showed very impressive cycling stability such that 97% of its initial capacity was preserved after 10 000 charge/discharge cycles at a current density of 2.5 A g^{-1}.

Besides increasing the pore distribution and SSA of rGO, doping heteroatoms (nitrogen or boron) can also effectively enhance its electrochemical performance [11, 31]. An electrode based on N-doped rGO from a simple plasma treatment exhibited lower resistivity [11]. A large specific capacitance of 282 F g^{-1} at a high current density of 1 A g^{-1} could be achieved, which is significantly higher than that of pristine rGO (69 F g^{-1} reported in the literature). In addition, excellent cycle life (>200 000) and high rate capability were achieved as well. These dramatic enhancements can be attributed to the N configuration at

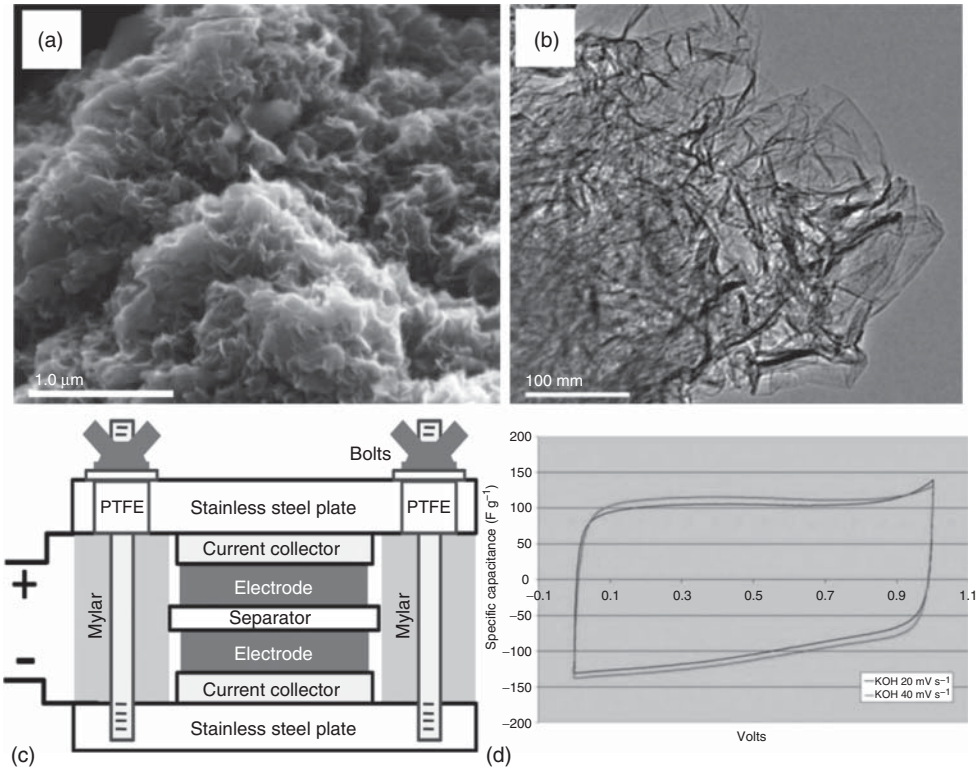

Figure 4.2 (a) SEM image of the surface of "particles" composed of agglomerated CMG platelets. (b) TEM image showing individual CMG platelets extending from a particle composed of agglomerated CMG platelets. (c) Schematic of the ultracapacitor test cell assembly. (d) CV plots obtained from cyclic voltammogram measurements of electrodes consisting of the CMG material, with KOH electrolyte. (Reprinted with permission from Ref. [25]. Copyright (2008), American Chemistry Society.)

the basal planes, which enhances the binding energy to accommodate more electrolyte ions.

Although graphene is predicted to have a large surface area, the electrochemical performance of rGO is strongly affected by the inevitable aggregation or restacking of individual graphene sheets [25, 32, 33]. To avoid the aggregation of single-layer graphene sheets, different strategies have been developed [34, 35]. Intercalating "stabilizers" or "spacers" such as polymers, nanoparticles, or carbon nanotubes into the graphene layers has proved to be an easy and effective method [36–43]. Besides the works shown in Table 4.1, Li *et al.* [44] demonstrated that water, the very "soft" matter, can also serve as an effective "spacer" to prevent the restacking of chemically reduced GO sheets. The obtained self-stacked, solvated graphene (SSG) film gave no detectable X-ray diffraction (XRD) peak at 22.7°, indicating that, despite of being arranged in a nearly parallel manner, the rGO sheets in the SSG film remain largely separated by water, which allows fast ion

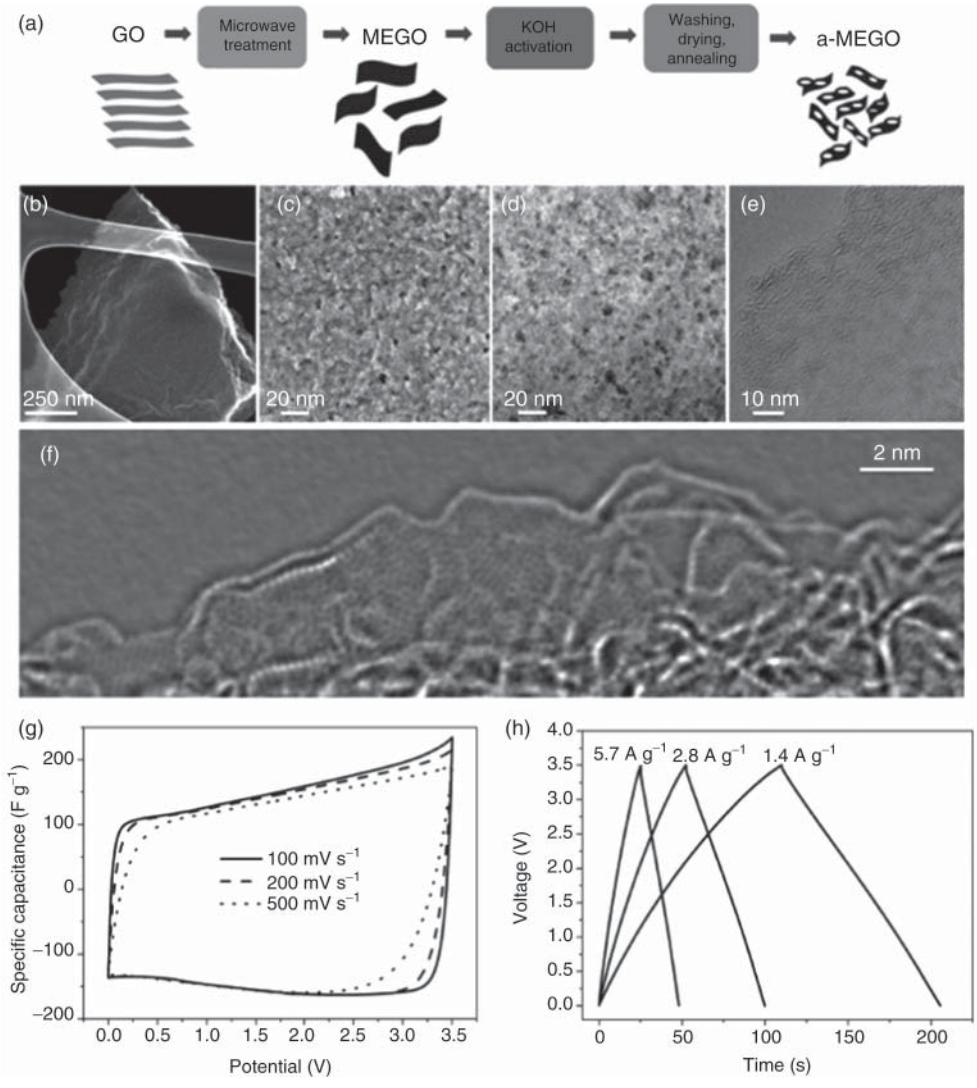

Figure 4.3 (a) Schematic showing the microwave exfoliation/reduction of graphene oxide (GO) and the following chemical activation of microwave-exfoliated graphene oxide (MEGO) with KOH that creates pores while retaining high electrical conductivity. (b) Low-magnification SEM image of a 3D activate microwave-exfoliated graphene oxide (a-MEGO) piece. (c) High-resolution SEM image of a different sample region which demonstrates the porous morphology. (d) ADF-STEM image of the same area as (c), acquired simultaneously. (e) High-resolution phase-contrast electron micrograph of the thin edge of an a-MEGO chunk, taken at 80 kV. (f) Exit wave reconstructed HRTEM image from the edge of a-MEGO. (g) CV curves at different scan rates. (h) Galvanostatic charge/discharge curves of a-MEGO-based supercapacitor under different constant currents. (Reproduced with permission from Ref. [25]. Copyright (2011), American Association for the Advancement of Science.)

Table 4.1 rGO with the concept of "spacer."

Material	Capacitance	Condition	References
rGO/CNT	2.8 mF cm^{-2}	KCl, 50 V s^{-1}	[37]
rGO/carbon black	138 F g^{-1}	6 M KOH, 10 V s^{-1}	[38]
rGO/carbon spheres	198 F g^{-1}	6 M KOH, 175 mA g^{-1}	[39]
rGO/CNT	385 F g^{-1}	6 M KOH, 10 V s^{-1}	[40]
rGO/CNT	120 F g^{-1}	1 M H_2SO_4, 1 V s^{-1}	[41]
rGO/mesoporous carbon spheres	171 F g^{-1}	6 M KOH, 10 m V s^{-1}	[42]
rGO/activated carbon	210 F g^{-1}	6 M KOH, 1 mV s^{-1}	[43]

diffusion in the SSG film. The SSG-film-based SC exhibited superior performance without the need for any other binders or conducting additives. A high specific capacitance of 215.0 F g^{-1} can be reached for a SSG film, with a mass loading of 0.45 mg cm^{-2} of chemically converted graphene (CCG) in an aqueous electrolyte. More significantly, even at an ultrafast charge/discharge rate of 1080 A g^{-1}, a capacitance of 156.5 F g^{-1} could be obtained, which means that the SC can be charged/discharged at the millisecond scale.

4.2.2 Graphene/Metal Oxide Nanocomposites

As reported by Conway *et al.* [45], the capacitance of pseudocapacitive materials can be 10–100 times higher than that of EDLCs. This is because the pseudocapacitance involves faradaic charge reactions. Figure 4.4 summarizes the general electrochemical features of pseudocapacitive materials. In 1970s, RuO_2 was first reported as a pseudocapactive material [46]. The storage of protons from the electrolyte resulted in a faradaic charge-transfer reaction.

However, RuO_2 is very expensive, which limits its use to only some military applications. The pseudocapacitive behavior of MnO_2 was first investigated in 1999 by Goodenough in a KCl aqueous electrolyte [48]. However, unlike RuO_2 with the high electronic conductivity, MnO_2 has conductivity varying from 10^{-7} to 10^{-3} S cm^{-1} [49]. In addition, the ion diffusivity also affects the performance of pseudocapacitive materials. Therefore, compounding with conductive materials and going to the nanoscale are possible solutions. Carbon has high electrical conductivity and can be formed in various high-surface-area configurations such as porous carbon or rGO powder. If these high-surface-area forms of carbon are then coated with an ultrathin film of a pseudocapacitance material, the electrical conductivity will be extremely high even if the pseudocapacitance material is a poor electrical conductor. Electrons can easily tunnel through dielectric insulators if the insulator thicknesses are in the ultrathin range of 10–50 Å. The coupling rGO and pseudocapacitive metal oxides turns out to be an effective solution, as shown in Table 4.2. Besides MnO_2, other common pseudocapacitance materials, such as

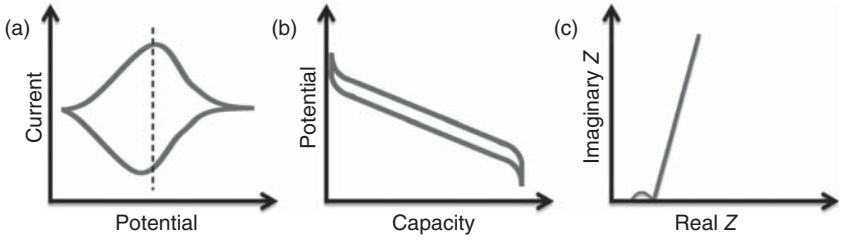

Figure 4.4 The general electrochemical features of pseudocapacitive materials. (a) In a cyclic voltammetry experiment, the shape is rectangular and if peaks are present, they are broad and exhibit a small peak-to-peak voltage separation. (b) In a galvanostatic experiment, the shape is sloping so that a capacitance value, dQ/dE, may be assigned at each point, and the voltage hysteresis is small. Here, *Q* is the capacity and *E* is the potential window. (c) In an AC impedance experiment, the Nyquist representation will contain a vertical line with a phase angle of 90° or less. A semicircle at high frequencies, associated with charge-transfer resistance, may also be present. (Reproduced with permission from Ref. [47]. Copyright (2011), American Association for the Advancement of Science.)

TiO_2, NiO, Co_3O_4, Fe_2O_3, and ZnO, are also included in Table 4.2. However, the cost and abundance of transition-metal oxides have not been carefully examined for future practical large-scale production. Table 4.3 estimates the merit in terms of dollars per farad for the common metal oxides based on the price of their metal elements ($\$\,MT^{-1}$) and their theoretical capacity ($F\,g^{-1}$). The high cost of Co and Sn limits their potential application, and thus more attention should be focused on metal oxides with much lower dollars per farad, such as Fe, Mn, and Ti.

4.2.3 Graphene/Conducting Polymer Composites

PANI, PPy, PTh, and their variations [62] are the most widely studied CPs. CPs have a characteristic structure with aromatic rings. Each carbon atom links with two adjacent carbon atoms by σ bonds to form the rings. The 2p orbitals of carbon atoms form delocalized π bonds perpendicular to the carbon planes. CPs have been widely studied as electrode materials for supercapacitors because of their high capacitance, easy production, and low cost. However, their poor conductivity and weak flexibility prevent them from being further applied to high-performance supercapacitors, especially for high-performance flexible supercapacitors. rGO-CPs have turned out to be able to enhance the electrical conductivity and the mechanical strength of polymer composites [63].

4.2.3.1 PANI-Graphene Nanocomposites

Because of its low cost, strong electrochemical activity, and satisfactory electrochemical stability, rGO/PANI nanocomposites have attracted much attention. Usually, there are two ways to form rGO/PANI nanocomposites. One is by *in situ* growth or polymerization of PANI on graphene sheets, and the other is to grow or polymerize PANI on graphene sheets by electrochemical synthesis.

Table 4.2 G–metal oxide nanocomposites.

Nature of electrode	Preparation method	Mass loading of active materials (mg cm^{-2})	Electrolyte	Maximum capacitance (F g^{-1})	Capacitance retention	References
G/MnO_2	Hydrothermal	2	1 M Na_2SO_4	121	100% after 10 000 cycles	[50]
G/Mn_3O_4	Two-step coating	0.1	0.5 M Na_2SO_4	380	95% after 3000 cycles	[51]
G/Mn_3O_4	Microwave irradiation	1.9	1 M Na_2SO_4	310	95.4% after 15 000 cycles	[52]
GO/MnO_2	Soft chemical route	5.6–15.2	1 M Na_2SO_4	216	84.1% after 1000 cycles	[53]
G/RuO_2	Sol–gel	5	1 M H_2SO_4	570	97.9% after 1000 cycles	[54]
G/$Ni(OH)_2$	Two-step method	1	1 M KOH	1335	No decay for 2000 cycles	[55]
G/Fe_3O_4	Solvothermal process	—	1 M KOH	480	No decay for 10 000 cycles	[56]
G/CeO_2	Wet chemistry	0.4–0.6	3 M KOH	208	—	[34]
G/$Co(OH)_2$	Soft chemistry	5.6–8.4	6 M KOH	972.5	—	[57]
G/Co_3O_4	Microwave	—	6 M KOH	243.2	95.6% after 2000 cycles	[58]
G/ZnO	Wet chemistry	1	0.1 M Na_2SO_4	308	93.5% after 1500 cycles	[59]
G/TiO_2	ALD	2–3	1 M KOH	84	87.5% for 1000 cycles	[60]
G/Al_2O_3/TiO_2	ALD	1–2	1 M KOH	97.5	No decay for 1000 cycles	[61]

Table 4.3 Dollars per farad for the common transition-metal oxides.

Metal	Oxide	$ kg^{-1} 3-month average[a)]	Theoretical capacity (F g^{-1})[b)]	$ F^{-1}
Mn	MnO_2	3.84	1839	2
Ti	TiO_2	11.16	2000	6
Fe	Fe_3O_4	5.2	690	8
Ni	NiO	18.38	2133	9
Sn	SnO_2	24.93	1060	24
Co	Co_3O_4	26	664	39

a) Prices obtained from *MetalPrices.com*, Winter 2013.
b) Theoretical capacity obtained based on 1 electron transfer and 0.6 V window. $C = nF/(VM)$, where n is the charge transfer number, F is the Faraday constant, and M is the molecular weight.

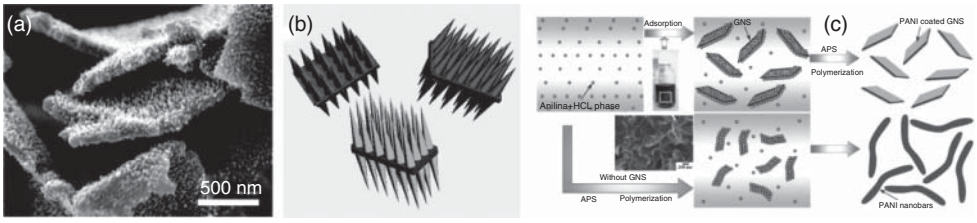

Figure 4.5 (a,b) Vertical PANI nanowire/graphene hierarchical structures for supercapacitors. (c) Illustration of the process of preparing graphene/PANI composites. (Reproduced with permission from Ref. [64].)

Xu *et al.* [55] reported a method by *in situ* growth of vertical PANI nanowires on graphene oxide sheets, with a tunable morphology and hierarchical structure (Figure 4.5a,b). It showed a specific capacitance of 555 F g^{-1} at 0.2 A g^{-1} and 227 F g^{-1} at 2 A g^{-1}. Yan *et al.* [64] reported a graphene/PANI composite synthesized by an *in situ* polymerization method. A high specific capacitance of 1046 F g^{-1} at 1 mV s^{-1} scan rate with the energy density of 39 Wh kg^{-1} was obtained. Chemically modified graphene and PANI nanofiber composites were prepared also by using an *in situ* polymerization method under acidic conditions (Figure 4.5c). The obtained GO/PANI composites were reduced to graphene/PANI followed by reoxidation and reprotonation of the reduced PANI. SCs based on this graphene/PANI composite showed a specific capacitance of 480 F g^{-1} and good cycling stability [65]. A novel method for synthesizing PANI/graphene nanocomposites was developed starting from *in situ* polymerization of PANI on the graphene surfaces followed by hot sodium hydroxide reduction and acid redoping. The resulting supercapacitor had a specific capacitance of 1126 F g^{-1} and 84% retention after 1000 cycles [66]. Li *et al.* [67] investigated the electrochemical properties of the graphene nanosheets/PANI nanofiber composite, prepared by an *in situ* polymerization method in 1 M H_2SO_4 solution and obtained a remarkable capacitance of 1130 F g^{-1} at 5 mV s^{-1} scan rate.

An electrochemically synthesized graphene/PANI nanocomposite film was fabricated on indium tin oxide (ITO) starting from GO and aniline, with a specific capacitance of 640 F g^{-1} and retention of 90% after 1000 charge/discharge cycles [59]. Jiang *et al.* proposed to prepare electrochemically reduced graphene oxide (ERGO)/PANI composites by an easy electrochemical technique in a single step. It was found that the ERGO/PANI films exhibited high mechanical stability and flexibility (Figure 4.6b). The two-electrode cells (Figure 4.6a,c) acted as electrochemical capacitors (ECs) after sufficient voltage cycling and exhibited relatively large specific capacitances (195–243 F g^{-1} at a scan rate of 100 mV s^{-1}) with excellent cycle life (retention of 83% capacitance after 20 000 charge/discharge cycles) [68]. A novel graphene/PANI nanocomposite material synthesized using chemical precipitation technique was reported as an electrode for supercapacitors. A specific capacitance of 300–500 F g^{-1} at a current density of 0.1 A g^{-1} was observed over grapheme/PANI nanocomposite materials [70].

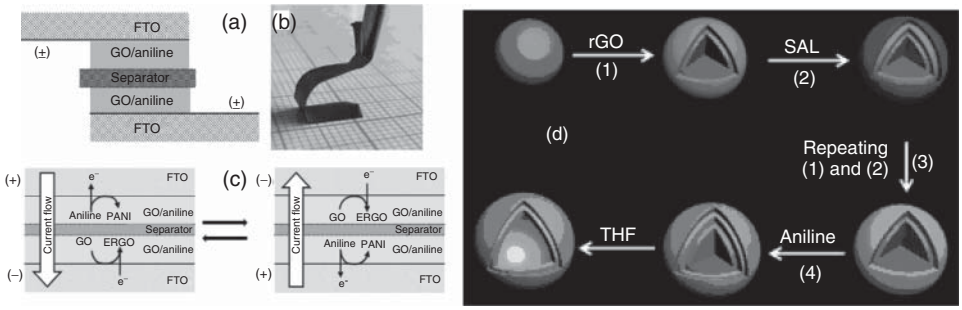

Figure 4.6 (a) Illustration of a two-electrode cell for the electrochemical conversion of GO/aniline film to ERGO/PANI composite. (b) Photographs of ERGO/PANI 4 : 1 composite films bending at a sharp angle. (c) Illustration for generation of ERGO/PANI composites in a two-electrode cell. (d) Illustration of the preparation of graphene/PANI hybrid hollow microspheres combining the LBL assembly technique. ((a–c) Reproduced with permission from Ref. [68]. (d) Reproduced with permission from Ref. [69] Copyright (2014), Springer.)

The significantly enhanced stability in the nanocomposites was confirmed by the 92% retention after 2000 cycles, which is much higher than for pure PANI nanowires (74%). By combining the layer-by-layer (LBL) assembly technique with *in situ* chemical oxidative polymerization after etching the templates, graphene/PANI hybrid hollow microspheres with the specific capacitance of 633 F g^{-1} in a 1.0 M H_2SO_4 electrolyte were prepared for high-performance supercapacitor application (Figure 4.6d) [69].

Other methods to synthesize PANI/graphene composite films have also been reported. Wu *et al.* [71] successfully prepared a sandwiched layer structured PANI/graphene composite films by using a vacuum filtration method. An SC based on the composite films showed an electrochemical capacitance of 210 F g^{-1} at 0.3 A g^{-1}. Wang *et al.* [72] reported the preparation of free-standing, flexible graphene/PANI composite paper by an *in situ* electropolymerization method and obtained a gravimetric capacitance of 233 F g^{-1} and volumetric capacitance of 135 F cm^{-3} for the composite. Novel PANI/rGO nanocomposite-based supercapacitor electrodes were fabricated by the *in situ* grafting of an aniline monomer to the edge of the graphene oxide followed by the polymerization and reduction of GO, resulting in a capacitance of 250 F g^{-1} and conductivity of 8.66 S cm^{-1} [73]. The other studies of the graphene/PANI composite are summarized in Table 4.4.

4.2.3.2 PPy–Graphene Nanocomposite

Mini *et al.* [77] reported a high-performance pseudocapacitive electrode material based on graphene and PPy, prepared by electropolymerization. The as-prepared material showed an extremely high capacitance value of 1510 F g^{-1} at 10 mV s^{-1} scan rate with area capacitance of 151 mF cm^{-2} and volume capacitance of 151 F cm^{-3} at the same scan rate. Although the material exhibited high specific capacitance, it showed only a low energy density (5.7 Wh kg^{-1}). Das *et al.* [78] explored a facile route to synthesize a graphene/PPy nanofiber composite using

Table 4.4 The specific capacitances of graphene-based/PANI nanocomposites.

GO/CPs composite	Specific capacitance ($F\ g^{-1}$)	Electrolyte	Voltage window (V)	Current load or scan rate	References
Graphene/PANI	555	1.0 M H_2SO_4	−0.2 to 0.8 (vs AgCl|Ag)	0.2 $A\ g^{-1}$	[55]
Graphene/PANI	233 (three-electrode)	1.0 M H_2SO_4	−0.2 to 0.8 (vs AgCl|Ag)	2 $mV\ s^{-1}$	[72]
rGO/PANI	361 (three-electrode)	1.0 M H_2SO_4	−0.1 to 0.7 (vs AgCl|Ag)	0.3 $A\ g^{-1}$	[74]
Graphene/PANI	480 (three-electrode)	2.0 M H_2SO_4	−0.2 to 0.8 (vs AgCl|Ag)	0.1 $A\ g^{-1}$	[65]
Graphene/PANI	640 (three-electrode)	1.0 M H_2SO_4	−0.6 to 1.2 (vs AgCl|Ag)	0.1 $A\ g^{-1}$	[59]
GO/PANI	325 (three-electrode)	1.0 M H_2SO_4	−0.2 to 0.8 (vs AgCl|Ag)	0.5 $A\ g^{-1}$	[75]
Graphene/PANI	1130 (three-electrode)	1.0 M H_2SO_4	−0.2 to 0.8 (vs AgCl|Ag)	5 $mV\ s^{-1}$	[67]
Graphene/PANI	1126 (three-electrode)	1.0 M H_2SO_4	−0.2 to 0.8 (vs AgCl|Ag)	1 $mV\ s^{-1}$	[66]
Graphene/PANI	1046 (three-electrode)	1.0 M H_2SO_4	−0.2 to 0.8 (vs AgCl|Ag)	1 $mV\ s^{-1}$	[64]
Graphene/PANI	301 (three-electrode)	1.0 M H_2SO_4	−0.2 to 0.8 (vs AgCl|Ag)	10 $mA\ cm^{-2}$	[76]
Graphene/PANI	210 (three-electrode)	1.0 M H_2SO_4	−0.2 to 0.8 (vs AgCl|Ag)	0.3 $A\ g^{-1}$	[71]
ERGO/PANI-4 : 1	243 (two-electrode)	4.0 M H_2SO_4	−1.4 to 1.4	100 $mV\ s^{-1}$	[68]
—	233 (two-electrode)	2 M HCl	—	—	—
—	196 (two-electrode)	2.0 M $HClO_4$	—	—	—
Graphene/PANI	633 (three-electrode)	1 M H_2SO_4	−0.2 to 0.8 (vs AgCl|Ag)	10 $mA\ cm^{-2}$	[69]

the biopolymer sodium alginate. Although the specific capacitance obtained was 466 $F\ g^{-1}$ at 10 $mV\ s^{-1}$ scan rate in 1 M KCl solution, it showed high energy density (165.7 $Wh\ kg^{-1}$). Tang *et al.* [79] prepared uniform graphene/PPy nanocomposites by an *in situ* intercalative chemical polymerization. Such a uniform nanostructure together with the observed high conductivities (the highest 1980 $S\ m^{-1}$) endowed the graphene/PPy composites with high specific capacitance (650 $F\ g^{-1}$) and good cycling stability (Figure 4.7a,b).

Zhang *et al.* [80] prepared PPy on graphene *in situ*, resulting in 482 $F\ g^{-1}$ capacitance with <5% decrease in 1000 cycles. Layered conducting PPy/graphene oxide sandwiches exhibited a specific capacitance of over 500 $F\ g^{-1}$ with a good rate performance and cycle stability. Multilayered PPy nanowire/graphene nanocomposites can also prepared by a capillary-driven self-assembly for binder-free supercapacitor electrodes with a capacitance of 165 $F\ g^{-1}$ [65]. A composite

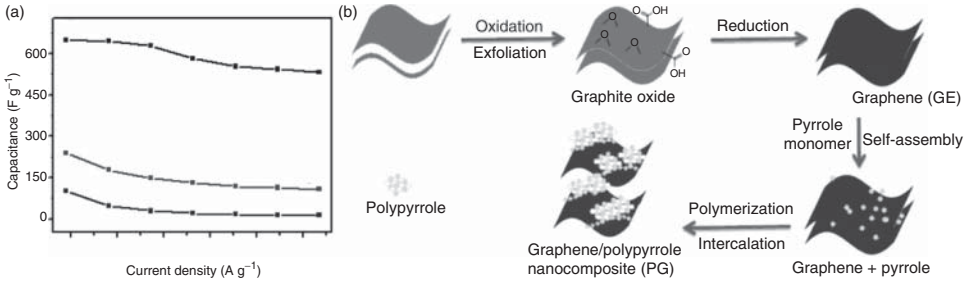

Figure 4.7 (a) The specific capacitance curves of PG10:1Graphene (GE) and PPy at different current densities. (b) Illustration of the preparation procedure for GE/PPy nanocomposite. (Reproduced with permission from Ref. [79] Copyright (2013), Elseiver.)

film based on graphene oxide and electrochemically prepared PPy showed a specific capacitance of 424 F g^{-1} at 1 A g^{-1} current density in 1 M H_2SO_4 [81]. Liu *et al.* [82] fabricated a novel composite based on PPy nanotubes and chemically reduced graphene sheets, and reported a specific capacitance of 400 F g^{-1} at a current density of 0.3 A g^{-1}. A novel hierarchical graphene/PPy nanosheet composite, prepared by an *in situ* chemical oxidation polymerization method, exhibited a large electrochemical capacitance of 318.6 F g^{-1} at a scan rate of 2 mV s^{-1} [83]. Bose *et al.* [84] reported a composite of PPy and graphene, which exhibited a specific capacitance of 267 F g^{-1} at 100 mV s^{-1} scan rate. Davies *et al.* [85] proposed a simple method for the preparation of flexible, uniform graphene/PPy composite films using a pulsed electropolymerization technique and obtained a specific capacitance value of 237 F g^{-1} for the composite. More results of the graphene/PPy composites are summarized in Table 4.5.

4.2.3.3 PEDOT–Graphene Nanocomposite

Zhao and Zhang [74] prepared an rGO/PEDOT composite by *in situ* polymerization and obtained a remarkable capacitance of 108 F g^{-1} at 0.3 A g^{-1} current density in 1 M H_2SO_4 solution. Dolui *et al.* [88] developed a novel method to prepare polythiophene/graphene oxide (PTh/GO) composites by liquid/liquid interfacial polymerization (Figure 4.8) and obtained a specific capacitance value of 99 F g^{-1} at the scan rate 50 mV s^{-1} for the composite. Other results of the graphene/PTh composites are summarized in Table 4.6.

4.2.4 Atomic Layer Deposition for Graphene/Metal Oxide Nanocomposites

At present, the most common synthesis techniques for nanocomposites of graphene/metal oxides involve wet chemistry, including sol–gel, hydrothermal, and electroplating [90–92]. None of these techniques can fully utilize the high surface area of graphene or control the metal oxide deposition in the nanometer regime.

Table 4.5 Specific capacitance of graphene-based/PPy composites.

GO/CPs composite	Specific capacitance ($F\,g^{-1}$)	Electrolyte	Voltage window (V)	Current load or scan rate	References
Graphene/PPy	1510	1.0 M H_2SO_4	−0.2 to 0.8 (vs AgCl|Ag)	10 $mV\,s^{-1}$	[77]
Graphene/PPy	650	1.0 M H_2SO_4	−0.2 to 0.8 (vs AgCl|Ag)	0.45 $A\,g^{-1}$	[79]
EG/rGO/PPy	420	1.0 M H_2SO_4	−0.3 to 0.7 (vs AgCl|Ag)	0.5 $A\,g^{-1}$	[86]
Graphene/PPy	466	1.0 M KCl	−0.8 to 0.8 (vs AgCl|Ag)	10 $mV\,s^{-1}$	[78]
Graphene/PPy	482	1.0 M H_2SO_4	−0.2 to 0.8 (vs AgCl|Ag)	0.5 $A\,g^{-1}$	[80]
Graphene/PPy	424	1.0 M H_2SO_4	−0.2 to 0.8 (vs AgCl|Ag)	1 $A\,g^{-1}$	[81]
Graphene/PPy	409	1.0 M KCl	−0.2 to 0.8 (vs AgCl|Ag)	10 $mV\,s^{-1}$	[78]
Graphene/PPy	400	1.0 M H_2SO_4	−0.6 to 0.4 (vs AgCl|Ag)	0.3 $A\,g^{-1}$	[82]
Graphene/PPy	318.6	1.0 M H_2SO_4	−0.6 to 0.4 (vs AgCl|Ag)	2 $mV\,s^{-1}$	[83]
Graphene/PPy	285	1.0 M H_2SO_4	−0.2 to 0.8 (vs AgCl|Ag)	0.5 $A\,g^{-1}$	[87]
Graphene/PPy	267	1.0 M H_2SO_4	−0.2 to 0.8 (vs AgCl|Ag)	100 $mV\,s^{-1}$	[84]
rGO/PPy	249	1.0 M H_2SO_4	−0.6 to 0.4 (vs AgCl|Ag)	0.3 $A\,g^{-1}$	[74]
Graphene/PPy	237	1.0 M H_2SO_4	−0.6 to 0.4 (vs AgCl|Ag)	10 $mV\,s^{-1}$	[85]
Graphene/PPy	165	1.0 M H_2SO_4	−0.2 to 0.8 (vs AgCl|Ag)	1 $A\,g^{-1}$	[65]

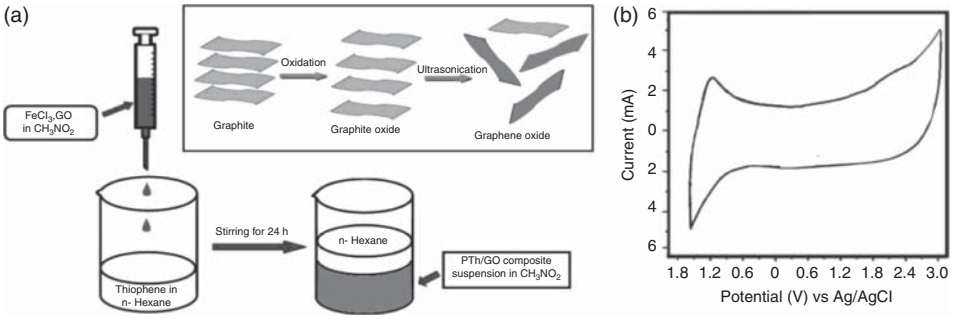

Figure 4.8 (a) Fabrication process for PTh/GO composites. (b) Cyclic voltammograms of polythiophene/graphene oxide (PTGO3) composite obtained at a scan rate of 50 $mV\,s^{-1}$. (Reproduced with permission from Ref. [88] Copyright (2014), Society of Chemical Industry.)

ALD has emerged as an important thin-film deposition technique which provides several benefits compared to pulsed-laser deposition (PLD), magnetron sputtering, thermal spray, and CVD [93]. Semiconductor processing has been one of the main motivations for the recent development of ALD. However, the uniqueness of ALD is its ability to deposit conformal thin films on high-aspect-ratio substrates [94, 95] or nanoparticles [96, 97] and to control the film thickness at the angstrom scale, which opens another novel avenue for applications of ALD in energy storage. In addition, the chemical bonding between graphene and metal oxides defined by ALD can effectively enhance the stability of metal oxides on graphene, leading to improved cycling performance.

Table 4.6 Specific capacitance of graphene-based/PTh composites.

GO/CPs composite	Specific capacitance (F g^{-1})	Electrolyte	Voltage window (V)	Current load or scan rate	References
G/PEDOT	370	2.0 M HCl	0–1 (vs AgCl|Ag)	50 mV s^{-1}	[89]
G/PTh	176	2.0 M HCl	0–1 (vs AgCl|Ag)	50 mV s^{-1}	[89]
rGO/PEDOT	108 (three-electrode)	1.0 M H_2SO_4	−0.4 to 0.6 (vs AgCl|Ag)	0.3 A g^{-1}	[74]
polythiophene/graphene oxide (PTh/GO3)	99 (three-electrode)	0.1 M $LiClO_4$	1.8–3.0 (vs AgCl|Ag)	50 mV s^{-1}	[88]

Xie *et al.* [60] reported the growth of a conformal coating of anatase TiO_2 quantum dots on rGO via ALD. As a potential SC material, the TiO_2/G composites exhibited a capacity of 75 and 84 F g^{-1} at a scan rate of 10 mV s^{-1} for composites grown using 50 and 100 ALD cycles, respectively. The nearly identical Nyquist plots of the TiO_2/G composites, compared to those of pure graphene, demonstrated that the composites possess excellent conductivity for charge transfer and open structures for ion diffusion. In addition, even with 3–4 times additional mass loading, the composites exhibit no obvious degradation with respect to the electrochemical performance. By using ALD, the same group also reported the conformal coating of amorphous TiO_2 thin films onto the surface of both rGO and CNTs via ALD [61]. The subnanometer-thick Al_2O_3 adhesion layer plays a critical role on such deposition, which cannot be realized by other common deposition techniques. No capacity loss was observed even after 2000 cycles. Boukhalfa *et al.* [98] reported the growth of V_2O_5 by ALD on a carbon nanotube paper. A remarkable capacitance of up to 1550 F g^{-1} per active mass of the vanadium oxide and up to 600 F g^{-1} per mass of the composite electrode were achieved. The authors were able to precisely determine the optimum thickness by tuning the thickness of V_2O_5, which no technique other than ALD can offer.

4.3 Issues and Perspectives

Although much progress has been made on graphene-based SCs, there are still some issues be addressed. When making a Ragone plot, people should only use data obtained from a two-electrode configuration. The three-electrode configuration can be used to identify the material properties, but does not reflect the device's performance [99]. In addition, the mass loading of the active material greatly affects the measurement. It is misleading to take advantage of the high capacity by a low active material mass loading to compare with the commercial device, which generally has a high mass loading on the order of ~10 mg cm^{-2}.

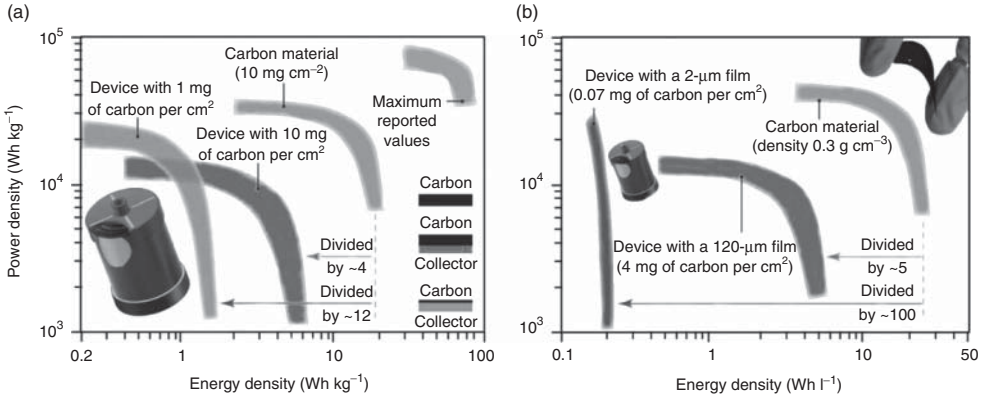

Figure 4.9 Two Ragone plots of power density versus energy density for the same ECs on a gravimetric (per weight) basis in (a) and on a volumetric basis in (b). The plots show that excellent properties of carbon materials will not translate in to medium- and large-scale devices if thin-film and/or low-density electrodes are used. (Reproduced with permission from Ref. [101]. Copyright (2011), American Association for the Advancement of Science.)

Furthermore, most of articles report energy/power density only based on electrodes, but not including the weight of electrolyte, separator, packing, and current collector. The commercial devices take all of those weights into considerations. Another important parameter that is important but often ignored is the tap density, particularly for graphene-based materials. Because of its extremely low density (~0.3 g cm^{-3}), although graphene-based SCs may have a high capacity (F g^{-1}), they have almost the same volumetric density (~5 Wh l^{-1}) [100] as commercial AC-based SCs in Figure 4.9. Those issues are well known in industry but, surprisingly, not quite recognized by the academia yet.

In order to push graphene-based SCs forward, the commercialization is the biggest issue. Cost and production consistency are of equal importance. So far, none of synthesis techniques has shown sufficient commercialization potential. Even if the potential exists, production consistency is a major concern. So far, no solution-based method has been largely adapted in the battery industry. One of the important issues is production consistency. ALD can be a perfect solution because of its unique reaction mechanism, but its economic feasibility has to be proven. In addition, further improvement in the energy density of SCs will be challenging. Hybrid electrode materials to combine EDLC capacitance together with fast and highly reversible pseudocapacitive materials or battery materials are being studied. This concept can combine both the advantages and expand the voltage to a large window. However, this concept is still in its infancy, and much work needs to be done, such as electrode material design, electrode compatibility, and the interface between the electrolyte and electrodes. Looking forward, SCs, mostly EDLCs, will play a bigger role in energy storage and harvesting, especially in fields that need ultrafast charge/discharge. SCs will not replace batteries, but in many cases

they can form a hybrid system with batteries. SCs can increase system efficiency and lifetime, and lower the demand on and cost of batteries.

References

1. Winter, M. and Brodd, R.J. (2004) What are batteries, fuel cells, and supercapacitors? *Chem. Rev.*, **104** (10), 4245–4269.
2. Burke, A. (2000) Ultracapacitors: why, how, and where is the technology. *J. Power Sources*, **91** (1), 37–50.
3. Ramachandran, R., Mani, V., Chen, S.M., Saraswathi, R., and Lou, B.S. (2013) Recent trends in graphene based electrode materials for energy storage devices and sensors applications. *Int. J. Electrochem. Sci.*, **8** (10), 11680–11694.
4. Zhu, Y.W., Murali, S., Cai, W.W., Li, X.S., Suk, J.W., Potts, J.R., and Ruoff, R.S. (2010) Graphene and graphene oxide: synthesis, properties, and applications. *Adv. Mater.*, **22**, 3906; **22** (46), 5226.
5. Zhu, Y.W., Murali, S., Stoller, M.D., Ganesh, K.J., Cai, W.W., Ferreira, P.J., Pirkle, A., Wallace, R.M., Cychosz, K.A., Thommes, M., Su, D., Stach, E.A., and Ruoff, R.S. (2011) Carbon-based supercapacitors produced by activation of graphene. *Science*, **332** (6037), 1537–1541.
6. Futaba, D.N., Hata, K., Yamada, T., Hiraoka, T., Hayamizu, Y., Kakudate, Y., Tanaike, O., Hatori, H., Yumura, M., and Iijima, S. (2006) Shape-engineerable and highly densely packed single-walled carbon nanotubes and their application as super-capacitor electrodes. *Nat. Mater.*, **5** (12), 987–994.
7. Bordjiba, T., Mohamedi, M., and Dao, L.H. (2008) New class of carbon-nanotube aerogel electrodes for electrochemical power sources. *Adv. Mater.*, **20** (4), 815–819.
8. Ania, C.O., Khomenko, V., Raymundo-Pinero, E., Parra, J.B., and Beguin, F. (2007) The large electrochemical capacitance of microporous doped carbon obtained by using a zeolite template. *Adv. Funct. Mater.*, **17** (11), 1828–1836.
9. Li, W.R., Chen, D.H., Li, Z., Shi, Y.F., Wan, Y., Wang, G., Jiang, Z.Y., and Zhao, D.Y. (2007) Nitrogen-containing carbon spheres with very large uniform mesopores: the superior electrode materials for EDLC in organic electrolyte. *Carbon*, **45** (9), 1757–1763.
10. Simon, P. and Gogotsi, Y. (2008) Materials for electrochemical capacitors. *Nat. Mater.*, **7** (11), 845–854.
11. Jeong, H.M., Lee, J.W., Shin, W.H., Choi, Y.J., Shin, H.J., Kang, J.K., and Choi, J.W. (2011) Nitrogen-doped graphene for high-performance ultracapacitors and the importance of nitrogen-doped sites at basal planes. *Nano Lett.*, **11** (6), 2472–2477.
12. Kinoshita, K., Electrochemical Society (1992) *Electrochemical Oxygen Technology*, John Wiley & Sons, Inc., New York, p. xiv, 431 p.
13. Hsieh, C.-T. and Teng, H. (2002) Influence of oxygen treatment on electric double-layer capacitance of activated carbon fabrics. *Carbon*, **40** (5), 667–674.
14. Qu, D.Y. and Shi, H. (1998) Studies of activated carbons used in double-layer capacitors. *J. Power Sources*, **74** (1), 99–107.
15. Long, J.W., Belanger, D., Brousse, T., Sugimoto, W., Sassin, M.B., and Crosnier, O. (2011) Asymmetric electrochemical capacitors-Stretching the limits of aqueous electrolytes. *MRS Bull.*, **36** (7), 513–522.
16. Thounthong, P., Chunkag, V., Sethakul, P., Davat, B., and Hinaje, M. (2009) Comparative study of fuel-cell vehicle hybridization with battery or supercapacitor storage device. *IEEE Trans. Veh. Technol.*, **58** (8), 3892–3904.
17. Jayalakshmi, M. and Balasubramanian, K. (2008) Simple capacitors to supercapacitors – An overview. *Int. J. Electrochem. Sci.*, **3** (11), 1196–1217.

18. Zhang, L.L. and Zhao, X.S. (2009) Carbon-based materials as supercapacitor electrodes. *Chem. Soc. Rev.*, **38** (9), 2520–2531.
19. Choi, D., Blomgren, G.E., and Kumta, P.N. (2006) Fast and reversible surface redox reaction in nanocrystalline vanadium nitride supercapacitors. *Adv. Mater.*, **18** (9), 1178–1182.
20. Rudge, A., Davey, J., Raistrick, I., Gottesfeld, S., and Ferraris, J.P. (1994) Conducting polymers as active materials in electrochemical capacitors. *J. Power Sources*, **47** (1-2), 89–107.
21. Geim, A.K. and Novoselov, K.S. (2007) The rise of graphene. *Nat. Mater.*, **6** (3), 183–191.
22. Novoselov, K.S., Geim, A.K., Morozov, S.V., Jiang, D., Zhang, Y., Dubonos, S.V., Grigorieva, I.V., and Firsov, A.A. (2004) Electric field effect in atomically thin carbon films. *Science*, **306** (5296), 666–669.
23. Stankovich, S., Dikin, D.A., Dommett, G.H.B., Kohlhaas, K.M., Zimney, E.J., Stach, E.A., Piner, R.D., Nguyen, S.T., and Ruoff, R.S. (2006) Graphene-based composite materials. *Nature*, **442** (7100), 282–286.
24. Miller, J.R., Outlaw, R.A., and Holloway, B.C. (2010) Graphene double-layer capacitor with ac line-filtering performance. *Science*, **329** (5999), 1637–1639.
25. Stoller, M.D., Park, S.J., Zhu, Y.W., An, J.H., and Ruoff, R.S. (2008) Graphene-based ultracapacitors. *Nano Lett.*, **8** (10), 3498–3502.
26. Geim, A.K. (2009) Graphene: status and prospects. *Science*, **324** (5934), 1530–1534.
27. Wu, Z.S., Ren, W.C., Wang, D.W., Li, F., Liu, B.L., and Cheng, H.M. (2010) High-energy MnO_2 nanowire/graphene and graphene asymmetric electrochemical capacitors. *ACS Nano*, **4** (10), 5835–5842.
28. Hummers, W.S. and Offeman, R.E. (1958) Preparation of graphitic oxide. *J. Am. Chem. Soc.*, **80** (6), 1339.
29. Tan, Y.B. and Lee, J.M. (2013) Graphene for supercapacitor applications. *J. Mater. Chem. A*, **1** (47), 14814–14843.
30. McAllister, M.J., Li, J.L., Adamson, D.H., Schniepp, H.C., Abdala, A.A., Liu, J., Herrera-Alonso, M., Milius, D.L., Car, R., Prud'homme, R.K., and Aksay, I.A. (2007) Single sheet functionalized graphene by oxidation and thermal expansion of graphite. *Chem. Mater.*, **19** (18), 4396–4404.
31. Hu, T., Sun, X., Sun, H.T., Xin, G.Q., Shao, D.L., Liu, C.S., and Lian, J. (2014) Rapid synthesis of nitrogen-doped graphene for a lithium ion battery anode with excellent rate performance and super-long cyclic stability. *Phys. Chem. Chem. Phys.*, **16** (3), 1060–1066.
32. Schniepp, H.C., Li, J.L., McAllister, M.J., Sai, H., Herrera-Alonso, M., Adamson, D.H., Prud'homme, R.K., Car, R., Saville, D.A., and Aksay, I.A. (2006) Functionalized single graphene sheets derived from splitting graphite oxide. *J. Phys. Chem. B*, **110** (17), 8535–8539.
33. Stankovich, S., Dikin, D.A., Piner, R.D., Kohlhaas, K.A., Kleinhammes, A., Jia, Y., Wu, Y., Nguyen, S.T., and Ruoff, R.S. (2007) Synthesis of graphene-based nanosheets via chemical reduction of exfoliated graphite oxide. *Carbon*, **45** (7), 1558–1565.
34. Wang, Y., Guo, C.X., Liu, J.H., Chen, T., Yang, H.B., and Li, C.M. (2011) CeO_2 nanoparticles/graphene nanocomposite-based high performance supercapacitor. *Dalton Trans.*, **40** (24), 6388–6391.
35. Liu, C.G., Yu, Z.N., Neff, D., Zhamu, A., and Jang, B.Z. (2010) Graphene-based supercapacitor with an ultrahigh energy density. *Nano Lett.*, **10** (12), 4863–4868.
36. Weng, Z., Su, Y., Wang, D.W., Li, F., Du, J.H., and Cheng, H.M. (2011) Graphene-cellulose paper flexible supercapacitors. *Adv. Energy Mater.*, **1** (5), 917–922.
37. Beidaghi, M. and Wang, C.L. (2012) Micro-supercapacitors based on interdigital electrodes of reduced graphene oxide and carbon nanotube composites with ultrahigh power handling performance. *Adv. Funct. Mater.*, **22** (21), 4501–4510.
38. Wang, G.K., Sun, X., Lu, F.Y., Sun, H.T., Yu, M.P., Jiang, W.L., Liu, C.S., and Lian, J. (2012) Flexible pillared graphene-paper electrodes for high-performance electrochemical supercapacitors. *Small*, **8** (3), 452–459.

39. Guo, C.X. and Li, C.M. (2011) A self-assembled hierarchical nanostructure comprising carbon spheres and graphene nanosheets for enhanced supercapacitor performance. *Energy Environ. Sci.*, **4** (11), 4504–4507.
40. Fan, Z.J., Yan, J., Zhi, L.J., Zhang, Q., Wei, T., Feng, J., Zhang, M.L., Qian, W.Z., and Wei, F. (2010) A three-dimensional carbon nanotube/graphene sandwich and its application as electrode in supercapacitors. *Adv. Mater.*, **22** (33), 3723–3728.
41. Yu, D.S. and Dai, L.M. (2010) Self-assembled graphene/carbon nanotube hybrid films for supercapacitors. *J. Phys. Chem. Lett.*, **1** (2), 467–470.
42. Lei, Z.B., Christov, N., and Zhao, X.S. (2011) Intercalation of mesoporous carbon spheres between reduced graphene oxide sheets for preparing high-rate supercapacitor electrodes. *Energy Environ. Sci.*, **4** (5), 1866–1873.
43. Zheng, C., Zhou, X.F., Cao, H.L., Wang, G.H., and Liu, Z.P. (2014) Synthesis of porous graphene/activated carbon composite with high packing density and large specific surface area for supercapacitor electrode material. *J. Power Sources*, **258**, 290–296.
44. Yang, X.W., Zhu, J.W., Qiu, L., and Li, D. (2011) Bioinspired effective prevention of restacking in multilayered graphene films: towards the next generation of high-performance supercapacitors. *Adv. Mater.*, **23** (25), 2833–2838.
45. Conway, B.E., Birss, V., and Wojtowicz, J. (1997) The role and utilization of pseudocapacitance for energy storage by supercapacitors. *J. Power Sources*, **66** (1-2), 1–14.
46. Trasatti, S. and Buzzanca, G. (1971) Ruthenium dioxide – new interesting electrode material – Solid state structure and electrochemical behaviour. *J. Electroanal. Chem.*, **29** (2), A1–A5.
47. Augustyn, V., Simon, P., and Dunn, B. (2014) Pseudocapacitive oxide materials for high-rate electrochemical energy storage. *Energy Environ. Sci.*, **7** (5), 1597–1614.
48. Lee, H.Y. and Goodenough, J.B. (1999) Supercapacitor behavior with KCl electrolyte. *J. Solid State Chem.*, **144** (1), 220–223.
49. Ghodbane, O., Pascal, J.L., and Favier, F. (2009) Microstructural effects on charge-storage properties in MnO_2-based electrochemical supercapacitors. *ACS Appl. Mater. Interfaces*, **1** (5), 1130–1139.
50. Lee, J.W., Hall, A.S., Kim, J.D., and Mallouk, T.E. (2012) A facile and template-free hydrothermal synthesis of Mn3O4 nanorods on graphene sheets for supercapacitor electrodes with long cycle stability. *Chem. Mater.*, **24** (6), 1158–1164.
51. Yu, G.H., Hu, L.B., Liu, N.A., Wang, H.L., Vosgueritchian, M., Yang, Y., Cui, Y., and Bao, Z.A. (2011) Enhancing the supercapacitor performance of graphene/MnO_2 nanostructured electrodes by conductive wrapping. *Nano Lett.*, **11** (10), 4438–4442.
52. Yan, J., Fan, Z.J., Wei, T., Qian, W.Z., Zhang, M.L., and Wei, F. (2010) Fast and reversible surface redox reaction of graphene-MnO_2 composites as supercapacitor electrodes. *Carbon*, **48** (13), 3825–3833.
53. Chen, S., Zhu, J.W., Wu, X.D., Han, Q.F., and Wang, X. (2010) Graphene oxide-MnO_2 nanocomposites for supercapacitors. *ACS Nano*, **4** (5), 2822–2830.
54. Wu, Z.S., Wang, D.W., Ren, W., Zhao, J., Zhou, G., Li, F., and Cheng, H.M. (2010) Anchoring hydrous RuO_2 on graphene sheets for high-performance electrochemical capacitors. *Adv. Funct. Mater.*, **20** (20), 3595–3602.
55. Xu, J., Wang, K., Zu, S.-Z., Han, B.-H., and Wei, Z. (2010) Hierarchical nanocomposites of polyaniline nanowire arrays on graphene oxide sheets with synergistic effect for energy storage. *ACS Nano*, **4** (9), 5019–5026.
56. Shi, W.H., Zhu, J.X., Sim, D.H., Tay, Y.Y., Lu, Z.Y., Zhang, X.J., Sharma, Y., Srinivasan, M., Zhang, H., Hng, H.H., and Yan, Q.Y. (2011) Achieving high specific charge capacitances in Fe3O4/reduced graphene oxide

nanocomposites. *J. Mater. Chem.*, **21** (10), 3422–3427.

57. Chen, S., Zhu, J.W., and Wang, X. (2010) One-step synthesis of graphene-cobalt hydroxide nanocomposites and their electrochemical properties. *J. Phys. Chem. C*, **114** (27), 11829–11834.
58. Yan, J., Wei, T., Qiao, W.M., Shao, B., Zhao, Q.K., Zhang, L.J., and Fan, Z.J. (2010) Rapid microwave-assisted synthesis of graphene nanosheet/Co_3O_4 composite for supercapacitors. *Electrochim. Acta*, **55** (23), 6973–6978.
59. Feng, X.-M., Li, R.-M., Ma, Y.-W., Chen, R.-F., Shi, N.-E., Fan, Q.-L., and Huang, W. (2011) One-step electrochemical synthesis of graphene/polyaniline composite film and its applications. *Adv. Funct. Mater.*, **21** (15), 2989–2996.
60. Sun, X., Xie, M., Wang, G.K., Sun, H.T., Cavanagh, A.S., Travis, J.J., George, S.M., and Lian, J. (2012) Atomic layer deposition of TiO_2 on graphene for supercapacitors. *J. Electrochem. Soc.*, **159** (4), A364–A369.
61. Sun, X., Xie, M., Travis, J.J., Wang, G.K., Sun, H.T., Lian, J., and George, S.M. (2013) Pseudocapacitance of amorphous TiO_2 thin films anchored to graphene and carbon nanotubes using atomic layer deposition. *J. Phys. Chem. C*, **117** (44), 22497–22508.
62. Murugan, A.V., Muraliganth, T., and Manthiram, A. (2009) Rapid, facile microwave-solvothermal synthesis of graphene nanosheets and their polyaniline nanocomposites for energy strorage. *Chem. Mater.*, **21** (21), 5004–5006.
63. Ramanathan, T., Abdala, A.A., Stankovich, S., Dikin, D.A., Herrera Alonso, M., Piner, R.D., Adamson, D.H., Schniepp, H.C., Chen, X., Ruoff, R.S., Nguyen, S.T., Aksay, I.A., Prud'Homme, R.K., and Brinson, L.C. (2008) Functionalized graphene sheets for polymer nanocomposites. *Nat. Nanotechnol.*, **3** (6), 327–331.
64. Yan, J., Wei, T., Shao, B., Fan, Z., Qian, W., Zhang, M., and Wei, F. (2010) Preparation of a graphene nanosheet/polyaniline composite with high specific capacitance. *Carbon*, **48** (2), 487–493.
65. Zhang, K., Zhang, L.L., Zhao, X.S., and Wu, J. (2010) Graphene/polyaniline nanofiber composites as supercapacitor electrodes. *Chem. Mater.*, **22** (4), 1392–1401.
66. Wang, H., Hao, Q., Yang, X., Lu, L., and Wang, X. (2010) A nanostructured graphene/polyaniline hybrid material for supercapacitors. *Nanoscale*, **2** (10), 2164–2170.
67. Li, J., Xie, H., Li, Y., Liu, J., and Li, Z. (2011) Electrochemical properties of graphene nanosheets/polyaniline nanofibers composites as electrode for supercapacitors. *J. Power Sources*, **196** (24), 10775–10781.
68. Jiang, X., Setodoi, S., Fukumoto, S., Imae, I., Komaguchi, K., Yano, J., Mizota, H., and Harima, Y. (2014) An easy one-step electrosynthesis of graphene/polyaniline composites and electrochemical capacitor. *Carbon*, **67**, 662–672.
69. Mu, B., Zhang, W., and Wang, A. (2014) Template synthesis of graphene/polyaniline hybrid hollow microspheres as electrode materials for high-performance supercapacitor. *J. Nanopart. Res.*, **16**, 2432.
70. Gómez, H., Ram, M.K., Alvi, F., Villalba, P., Stefanakos, E., and Kumar, A. (2011) Graphene-conducting polymer nanocomposite as novel electrode for supercapacitors. *J. Power Sources*, **196** (8), 4102–4108.
71. Wu, Q., Xu, Y., Yao, Z., Liu, A., and Shi, G. (2010) Supercapacitors based on flexible graphene/polyaniline nanofiber composite films. *ACS Nano*, **4** (4), 1963–1970.
72. Wang, D.-W., Li, F., Zhao, J., Ren, W., Chen, Z.-G., Tan, J., Wu, Z.-S., Gentle, I., Lu, G.Q., and Cheng, H.-M. (2009) Fabrication of graphene/polyaniline composite paper via in situ anodic electropolymerization for high-performance flexible electrode. *ACS Nano*, **3** (7), 1745–1752.
73. Kumar, N.A., Choi, H.-J., Shin, Y.R., Chang, D.W., Dai, L., and Baek, J.-B. (2012) Polyaniline-grafted reduced graphene oxide for efficient electrochemical supercapacitors. *ACS Nano*, **6** (2), 1715–1723.

74. Zhang, J. and Zhao, X.S. (2012) Conducting polymers directly coated on reduced graphene oxide sheets as high-performance supercapacitor electrodes. *J. Phys. Chem. C*, **116** (9), 5420–5426.
75. Gedela, V.R. and Srikanth, V.V.S.S. (2014) Electrochemically active polyaniline nanofibers (PANi NFs) coated graphene nanosheets/PANi NFs composite coated on different flexible substrates. *Synth. Met.*, **193**, 71–76.
76. Liu, S., Liu, X., Li, Z., Yang, S., and Wang, J. (2011) Fabrication of free-standing graphene/polyaniline nanofibers composite paper via electrostatic adsorption for electrochemical supercapacitors. *New J. Chem.*, **35** (2), 369–374.
77. Mini, P.A., Balakrishnan, A., Nair, S.V., and Subramanian, K.R.V. (2011) Highly super capacitive electrodes made of graphene/poly(pyrrole). *Chem. Commun.*, **47** (20), 5753–5755.
78. Sahoo, S., Dhibar, S., Hatui, G., Bhattacharya, P., and Das, C.K. (2013) Graphene/polypyrrole nanofiber nanocomposite as electrode material for electrochemical supercapacitor. *Polymer*, **54** (3), 1033–1042.
79. Liu, Y., Wang, H., Zhou, J., Bian, L., Zhu, E., Hai, J., Tang, J., and Tang, W. (2013) Graphene/polypyrrole intercalating nanocomposites as supercapacitors electrode. *Electrochim. Acta*, **112**, 44–52.
80. Zhang, D., Zhang, X., Chen, Y., Yu, P., Wang, C., and Ma, Y. (2011) Enhanced capacitance and rate capability of graphene/polypyrrole composite as electrode material for supercapacitors. *J. Power Sources*, **196** (14), 5990–5996.
81. Chang, H.-H., Chang, C.-K., Tsai, Y.-C., and Liao, C.-S. (2012) Electrochemically synthesized graphene/polypyrrole composites and their use in supercapacitor. *Carbon*, **50** (6), 2331–2336.
82. Liu, J., An, J., Ma, Y., Li, M., and Ma, R. (2012) Synthesis of a graphene-polypyrrole nanotube composite and its application in supercapacitor electrode. *J. Electrochem. Soc.*, **159** (6), A828–A833.
83. Xu, C., Sun, J., and Gao, L. (2011) Synthesis of novel hierarchical graphene/polypyrrole nanosheet composites and their superior electrochemical performance. *J. Mater. Chem.*, **21** (30), 11253–11258.
84. Bose, S., Kim, N.H., Kuila, T., Lau, K., and Lee, J.H. (2011) Electrochemical performance of a graphene–polypyrrole nanocomposite as a supercapacitor electrode. *Nanotechnology*, **22** (29), 295202.
85. Davies, A., Audette, P., Farrow, B., Hassan, F., Chen, Z., Choi, J.-Y., and Yu, A. (2011) Graphene-based flexible supercapacitors: pulse-electropolymerization of polypyrrole on free-standing graphene films. *J. Phys. Chem. C*, **115** (35), 17612–17620.
86. Liu, Y., Zhang, Y., Ma, G., Wang, Z., Liu, K., and Liu, H. (2013) Ethylene glycol reduced graphene oxide/polypyrrole composite for supercapacitor. *Electrochim. Acta*, **88**, 519–525.
87. Si, P., Ding, S., Lou, X.-W., and Kim, D.-H. (2011) An electrochemically formed three-dimensional structure of polypyrrole/graphene nanoplatelets for high-performance supercapacitors. *RSC Adv.*, **1** (7), 1271–1278.
88. Bora, C., Pegu, R., Saikia, B.J., and Dolui, S.K. (2014) Synthesis of polythiophene/graphene oxide composites by interfacial polymerization and evaluation of their electrical and electrochemical properties. *Polym. Int.*, DOI 10.1002/pi.4739.
89. Alvi, F., Ram, M.K., Basnayaka, P., Stefanakos, E., Goswami, Y., Hoff, A., and Kumar, A. (2011) Electrochemical supercapacitors based on graphene-conducting polythiophenes nanocomposite. *ECS Trans.*, **35** (34), 167–174.
90. Liu, J.H., Chen, J.S., Wei, X.F., Lou, X.W., and Liu, X.W. (2011) Sandwich-like, stacked ultrathin titanate nanosheets for ultrafast lithium storage. *Adv. Mater.*, **23** (8), 998–1002.
91. Wang, D.H., Choi, D.W., Li, J., Yang, Z.G., Nie, Z.M., Kou, R., Hu, D.H., Wang, C.M., Saraf, L.V., Zhang, J.G., Aksay, I.A., and Liu, J. (2009) Self-assembled TiO(2)-graphene hybrid nanostructures for enhanced Li-ion insertion. *ACS Nano*, **3** (4), 907–914.

92. Li, N., Liu, G., Zhen, C., Li, F., Zhang, L.L., and Cheng, H.M. (2011) Battery performance and photocatalytic activity of mesoporous anatase TiO_2 nanospheres/graphene composites by template-free self-assembly. *Adv. Funct. Mater.*, **21** (9), 1717–1722.
93. George, S.M. (2010) Atomic layer deposition: an overview. *Chem. Rev.*, **110** (1), 111–131.
94. Elam, J.W., Routkevitch, D., Mardilovich, P.P., and George, S.M. (2003) Conformal coating on ultrahigh-aspect-ratio nanopores of anodic alumina by atomic layer deposition. *Chem. Mater.*, **15** (18), 3507–3517.
95. Gordon, R.G., Hausmann, D., Kim, E., and Shepard, J. (2003) A kinetic model for step coverage by atomic layer deposition in narrow holes or trenches. *Chem. Vap. Deposition*, **9** (2), 73–78.
96. McCormick, J.A., Rice, K.P., Paul, D.F., Weimer, A.W., and George, S.M. (2007) Analysis of Al_2O_3 atomic layer deposition on ZrO_2 nanoparticles in a rotary reactor. *Chem. Vap. Deposition*, **13** (9), 491–498.
97. Ferguson, J.D., Weimer, A.W., and George, S.M. (2000) Atomic layer deposition of ultrathin and conformal Al_2O_3 films on BN particles. *Thin Solid Films*, **371** (1-2), 95–104.
98. Boukhalfa, S., Evanoff, K., and Yushin, G. (2012) Atomic layer deposition of vanadium oxide on carbon nanotubes for high-power supercapacitor electrodes. *Energy Environ. Sci.*, **5** (5), 6872–6879.
99. Stoller, M.D. and Ruoff, R.S. (2010) Best practice methods for determining an electrode material's performance for ultracapacitors. *Energy Environ. Sci.*, **3** (9), 1294–1301.
100. Yu, G.H., Xie, X., Pan, L.J., Bao, Z.N., and Cui, Y. (2013) Hybrid nanostructured materials for high-performance electrochemical capacitors. *Nano Energy*, **2** (2), 213–234.
101. Gogotsi, Y. and Simon, P. (2011) True performance metrics in electrochemical energy storage. *Science*, **334** (6058), 917–918.

5
High-Performance Supercapacitors Based on Novel Graphene Composites

Junwu Xiao, Yangyang Xu, and Shihe Yang

5.1
Introduction

The global energy consumption is accelerating at an alarming rate and will soon exhaust all fossil fuel resources. Sustainable, renewable, and environmentally friendly technologies for energy generation, storage, and conversion are high on the agenda of public and private enterprises. Electrochemical capacitors, also called *supercapacitors*, are one of the energy storage modalities. In light of their excellent power density, fast charging rate, and extended cycle life, supercapacitors have immense application potential in portable electronics and electric vehicles [1], and thus have been attracting growing research interest in recent years. In general, two major types of supercapacitors exist depending on the underlying energy storage mechanism: electric double-layer capacitors (EDLCs) and pseudocapacitors [2–4]. EDLCs store energy by the electrostatic accumulation of charges in the electric double layer near the electrode/electrolyte interface, as shown in Figure 5.1. The electrode materials for EDLCs are generally carbonaceous materials, such as activated carbon (AC), mesoporous carbon, carbon nanotubes, and graphene. The electric double-layer (EDL) capacitance is closely dependent on the surface area, which can be calculated using the following equation [5]:

$$C = \frac{\varepsilon_r \varepsilon_o}{d} A \tag{5.1}$$

where ε_r and ε_0 are the relative dielectric constant and the dielectric constant of vacuum, respectively, A is the specific surface area of the electrode accessible to the electrolyte ions, and d is the effective thickness of the EDL. Because of the nature of energy storage mechanism of EDLCs, charges are not transferred between the electrode materials and the electrolyte. Thus, the EDLCs have good cycling stability, but do not exhibit a high enough energy density to meet the ever-growing need for peak-power assistance in electric vehicles.

Pseudocapacitors use an energy storage mechanism similar to that of electrochemical batteries, but the fast and the reversible faradaic reactions for energy storage primarily occur at the interface or near the interface of

Graphene-based Energy Devices, First Edition. Edited by A. Rashid bin Mohd Yusoff.
© 2015 Wiley-VCH Verlag GmbH & Co. KGaA. Published 2015 by Wiley-VCH Verlag GmbH & Co. KGaA.

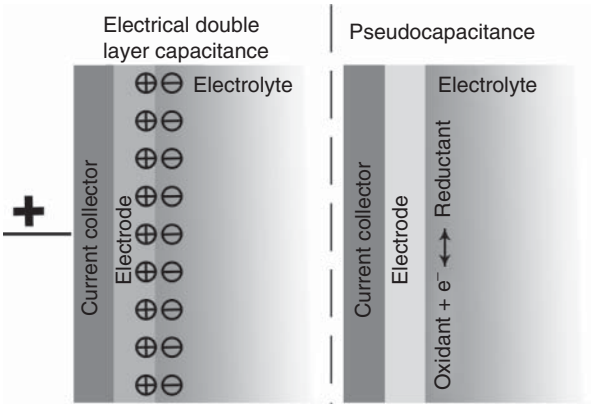

Figure 5.1 Schematic illustration of the charge storage process of electrochemical double-layer capacitance and pseudocapacitance.

electrolyte–electrode materials, as shown in Figure 5.1. The electrode materials for pseudocapacitors are usually transition-metal compounds and conducting polymers. The theoretical value of the pseudocapacitive electrode materials is closely related to the mean number of the electrons transferred in the redox reaction (n), the Faraday constant (F), the molar mass (M), and the operating voltage window (V), and is calculated as follows [6]:

$$C = \frac{nF}{MV} \tag{5.2}$$

EDLCs have good electrochemical cyclic stability, but their capacitance value is often low. Pseudocapacitors, on the other hand, can obviously enhance the specific capacitance and energy density by using interfacial reversible faradaic reactions to store energy, but they exhibit relatively poor cyclic stability. Comprehensive utilization of EDLC and pseudocapacitor electrode materials has proven to be an effective method by which high performance may be achieved.

A performance metric of supercapacitors is the capacity of electrodes to store and release energy. The specific capacitance (C) is one of the most important parameters related to the performance of a supercapacitor, which is defined as follows:

$$C = \frac{Q}{V} \tag{5.3}$$

where Q is the charge stored on the electrode per unit mass, and V is the operation voltage window. In a three-electrode configuration, when the electrode materials are charged/discharged in an operating voltage window at a constant current, the value of C_s can be deduced from the discharge curve according to the following equation:

$$C_s = \frac{i}{|(dV/dt)m|} \tag{5.4}$$

where dV/dt is the slope of the discharge curve, i is the discharge current, and m is the mass of electrode materials. When the discharge curve can be treated as linear, dV/dt is close to V/t, where t is the time period for the overall potential decrease in the discharge curve. Then, Equation 5.4 can be approximated as follows:

$$C_s = \frac{i\Delta t}{\Delta V m} = \frac{Q}{\Delta V m} \tag{5.5}$$

where Q is the overall charge released during the discharge process. In a two-electrode configuration, the two working electrodes are separated by a separator. The overall capacitor is considered as two subcapacitors in series. Therefore, the total capacitance (C_{total}) is calculated according to the following equation:

$$\frac{1}{C_{total}} = \frac{1}{C_{s,1}} + \frac{1}{C_{s,2}} \tag{5.6}$$

where $C_{s,1}$ and $C_{s,2}$ are the specific capacitances of the negative and positive electrodes, respectively.

The energy and power densities are other important parameters related to the performance of supercapacitors. Energy density is the ability to store energy and it determines how long the supercapacitors can act as a power source, represented by Equation 5.7:

$$E = \frac{1}{2}CV^2 \tag{5.7}$$

where C represents the capacitance and V is the operation voltage window. Power density is the rate of energy transfer per unit volume, area, or mass, and it determines how fast the energy can be discharged or charged. The maximum power achievable by supercapacitors is given by

$$P = \frac{V^2}{4\mathrm{ESR}} \tag{5.8}$$

where V represents the operation voltage window, and ESR is the equivalent series resistance.

Graphene is a single layer of sp^2 carbon atoms arranged hexagonally, and has excellent electrical mobility, extremely high surface area, and perfect mechanical properties. Thus, not surprisingly, graphene is envisioned to find a wide spectrum of applications, especially for energy storage and conversion. However, there are several critical factors of the graphene material that warrant consideration in order for it to perform as an electrochemical capacitor. First, the EDL capacitance energy storage mechanism of graphene imposes a limit on its electrochemical capacitor performance, since it depends on the electrolyte-ion-accessible surface area of graphene. Second, as a two-dimensional (2D) nanosheet graphene has a strong propensity to aggregate as a result of the interlayer $\pi-\pi$ interaction. This usually destabilizes graphene in a single-layer form for most graphene supercapacitors, and makes a large portion of the graphene surface practically inaccessible to the electrolyte ions. Third, the surface wettability of graphene affects the physical adsorption of electrolyte ions (EDLC) and the interfacial redox reaction (pseudocapacitance). In general,

perfect graphene is chemically inert, which makes it difficult for aqueous and organic electrolytes to wet the graphene surface [7]. The introduction of defects such as oxygenate functionalities is beneficial to wetting of graphene but at the cost of a reduction in electrical conductivity [8]. The extremely large surface area and the excellent electrical and mechanical properties of graphene can be best exploited when it is hybridized with pseudocapacitive materials, which can have high capacitance but low conductivity and poor mechanical robustness. Indeed, the deposition of pseudocapacitive materials, such as metal oxides and/or hydroxides and conducting polymers, on graphene sheets cannot only prevent the self-aggregation of graphene nanosheets but also improve the electrical conductivity of the pseudocapacitive materials, thereby providing a path to optimize the electrochemical capacitor performance. There have already been a number of excellent reviews in the literature about graphene/polymer, graphene/metal oxide, and 3D carbon-based materials for energy storage and conversion applications [9–17]. The present critical review is focused on the most recent research on the applications of graphene-based materials as electrodes for supercapacitors. The emphasis is to review and weigh up the research progress in how to anchor carbon materials, metal oxides, and conducting polymers onto the atomically thin graphene layers to enhance the electrochemical capacitor performance.

5.2 Graphene Synthesis Methods

Since the discovery of graphene, and it was shown to have exceptional electronic, mechanical, and thermal properties, many routes for its synthesis have been reported. They are generally divided into "top-down" and "bottom-up" approaches. In the "top-down" approach, graphene is obtained via the exfoliation of natural or synthetic graphite using, for example, mechanical exfoliation, chemical exfoliation [18, 19], liquid-phase exfoliation [20], electrochemical exfoliation, and so on [18]. In contrast, the "bottom-up" approach is characterized by the direct formation of graphene from organic molecules such as methane and other hydrocarbon sources [21], and examples are epitaxial growth [22] and chemical vapor deposition (CVD) [23]. In this section, we will review some synthesis methods of graphene.

5.2.1 The "Top-Down" Approach

The mechanical exfoliation of graphite to produce graphene using a tape was first reported by Kurz and coworkers in 1990 [24], and was subsequently developed by Geim and coworkers in 2004 [25]. The method is suitable for producing high-quality graphene for laboratory research because of the few

graphene processing steps required, and is easily repeatable in generating few-layer graphenes with 10 μm thickness. However, it is unsuitable for large-scale production because of the slow and labor-intensive nature of the process. Similar to mechanical exfoliation, graphite can be exfoliated into graphene via liquid-phase exfoliation, in which ultrasonic agitation supplies the energy for cleaving graphene from graphite in water or organic solvents containing surfactants [12]. Liquid-phase exfoliation can produce large, high-quality graphene without defects and oxygen-containing groups. However, it is difficult to obtain a high concentration of graphene suspension and recover the solvent. In addition, few-layer graphene instead of a single-layer graphene is dominant in the suspension.

The availability of processable graphene in large quantities is a prerequisite for exploiting its wide applications [26]. The chemical exfoliation method is thought to be an efficient route for synthesizing graphene on a large scale and at low cost [18]. During the chemical exfoliation process, the well-stacked graphite is first oxidized to graphite oxides [27]. Graphite oxides are then delaminated into graphene oxides (GOs), since the oxidation can increase the *d* spacing and weaken the interaction between adjacent graphene layers. To restore the electrical conductivity, the GOs are subsequently reduced into reduced graphene oxides (rGOs) [28]. Graphite oxides also can be thermally exfoliated into graphene [29–32]. The chemical structure of GO is shown in Figure 5.2 [33]. It can be found that there are abundant reactive oxygen-containing groups (carboxylic acid groups at the edges, epoxy and hydroxyl groups on the basal planes) in the GO structure, which play a significant role in the preparation of graphene-based nanocomposites. The nucleation and growth of nanostructure precursors could be initiated via the covalent bonding between the precursors and the GO surface groups. Particularly, the precursors preferentially nucleate on the basal and edge defects and grow into desired nanostructures, since the functional groups mainly distribute themselves on the basal and edge defects, as seen from Figure 5.2. For the reduction of GO to rGO, different methods

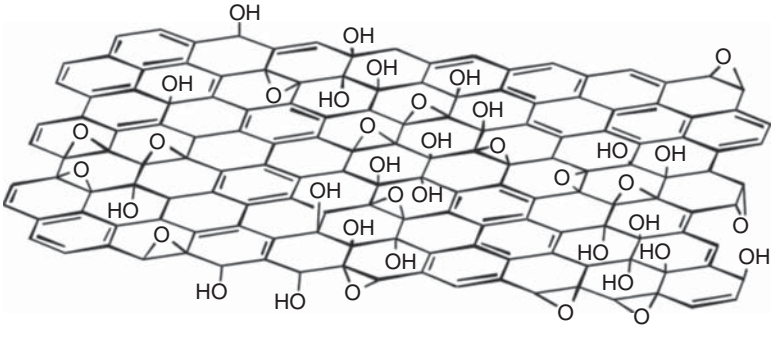

Figure 5.2 Proposed schematic (Lerf–Klinowski model) of the graphene oxide (GO) structure. (Reprinted with permission from Ref. [33]. Copyright (1998), Elsevier.)

including chemical reduction and electrochemical reduction have been reported. For the chemical reaction method, the commonly used reducing reagents include N_2H_4 [28], KOH [34], $NaBH_4$ [35], and HI [36]. However, the as-formed rGOs are prone to self-agglomeration and are poorly dispersed in water. Some of the reducing agents are toxic and unstable, making the processing difficult. In addition, because of the disruption of the sp^2 framework structure during the oxidation process, simply reducing GO would not remove all the morphological defects, making rGO a nonideal electric conductor [28, 37–39]. The electrochemical reduction method can be used to reduce GO to rGO without the use of toxic reducing agents, but it is difficult to process rGO on a large scale. Thus, in comparison with mechanical and liquid-phase exfoliation, chemical exfoliation has the advantages of scalability and low cost although it is difficult to obtain single-layer high-quality graphene because of the defect creation during exfoliation.

5.2.2 The "Bottom-Up" Approach

Although graphene can be exfoliated from natural or synthetic graphite via the "top-down" approaches as described above, these approaches are not suitable for producing large-area, high-quality graphene films. Therefore, much effort is recently focused on the development of "bottom-up" approaches to grow large-area, high-quality graphene films on extended surfaces. The common "bottom-up" approach for growing graphene is via CVD, in which hydrocarbon compounds are pyrolyzed on the surface of a metal catalyst at high temperatures [40]. According to the different solubility of carbon in the metal catalysts, the growth mechanisms can be divided into two types, schematically illustrated in Figure 5.3; they are the carbon segregation and/or precipitation mechanism, and the surface growth mechanism [41]. The former relies on the high solubility of carbon in metal catalysts such as Ni (Figure 5.3a). Specifically, the hydrocarbon compounds decompose at high temperatures to form carbon species, which dissolve in the metal catalysts. In the following cooling process, the carbon species dissolved in the metal precipitate out from the surface of the metal followed by nucleation and growth to form graphene. Thus, the number of graphene layers is strongly dependent on the cooling rate. In the surface growth mechanism, on the other hand, the carbon precursors first adsorb on the surface of the catalysts such as Cu, instead of diffusing into the bulk, and then nucleate and grow to form a graphene island, and finally form graphene by continuous growth (Figure 5.3b). High-quality, large-area graphene films have been successfully synthesized via the "bottom-up" approach. However, it is extremely difficult to the control the manufacturing process, and this increases the manufacturing cost. In addition, the as-formed graphene film cannot be easily manipulated.

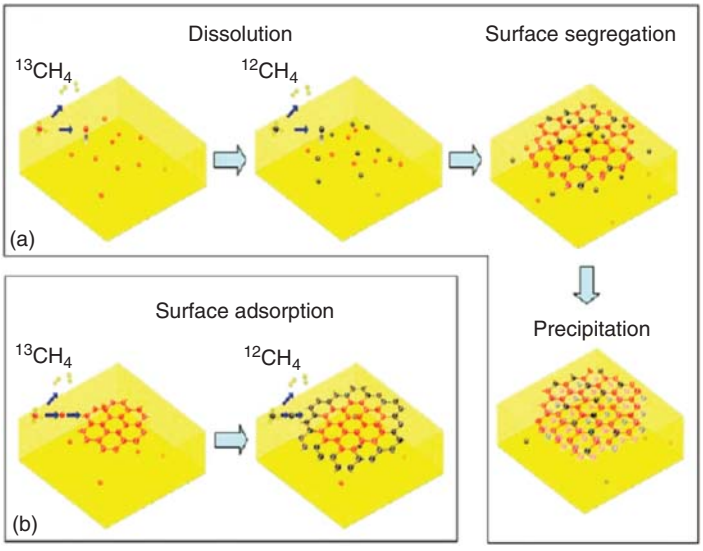

Figure 5.3 Schematic illustration of the possible growth mechanisms of graphene via the chemical vapor deposition (CVD) process. (a) The carbon segregation/precipitation mechanism. (b) The surface growth mechanism. (Reprinted with permission from Ref. [41]. Copyright (2009), American Chemical Society.)

5.3
Graphene-Based Electrodes for Supercapacitors

5.3.1
Graphene

Graphene has a theoretical high surface area ($2630\,m^2\,g^{-1}$), very high intrinsic electrical conductivity in its plane, good chemical stability, and high mechanical strength, making it an excellent candidate for EDLC materials. The first and arguably the most important factor is the effective surface area of graphene, which determines the capacitance and, by extension, the supercapacitor performance, according to Equation 5.1. The effective surface area determines how large the electrode/electrolyte interface would be. Although graphene has a large theoretical surface area, this area will not result in high EDLC if it is not accessible to ions. Therefore, it should be noted that the capacitance is largely dependent on the layering and stacking configuration of graphene, and much research has been conducted to create graphene structures that display large ion-accessible surface areas. In addition, porosity, along with pore volume and pore size distribution, also plays an important role in the capacitance of an electrode.

The rGO electrodes formed by the reduction of GO have a specific surface area of $705\,m^2\,g^{-1}$, which is much less than the aforementioned theoretical value of graphene, resulting in poor electrochemical capacitor performance. The specific

capacitance of rGO-based supercapacitors reach 135 and 99 F g^{-1} in aqueous and organic electrolytes, respectively [42, 43], since rGO generally suffers from serious agglomeration and restacking after removal from the dispersed solutions and drying due to the van der Waals interactions between the rGO nanosheets (Figure 5.4a). Although doping heteroatoms into graphene structure, such as in N-doped graphene sheets (NGSs), increases the electrical conductivity arising from the N-doping-assisted network restoration [46, 47], and thus improves the electrochemical performance [48], NGS still has a low specific surface area, just like rGO. Thus, the current challenge is to develop graphene materials with a single layer or a few layers combined with less agglomeration, a tailored pore-size distribution, and high electrical conductivity to optimize the supercapacitor performance. Ruoff and coworkers [49] reported a simple activation of microwave-exfoliated graphene oxide (MEGO) with KOH. The as-formed MEGO sheets activated by KOH yielded a continuous 3D network of pores of diameter ranging from ~1 to ~10 nm. The specific surface area achieved was 3100 m^2 g^{-1}, which is even higher than the theoretical value of graphene. Hence, the supercapacitor devices based on such electrode materials exhibited a specific capacitance of 166 F g^{-1} at a current of 5.7 A g^{-1} in an organic electrolyte, and an energy density of ~70 Wh kg^{-1} at the power density of ~75 kW kg^{-1}. However, a binder should be introduced in the electrode preparation, which influences the performance of supercapacitors. To avoid introduction of the binder, the vacuum filtration method was reported to the fabricate graphene films (Figure 5.4b), which constitute a new class of mechanically strong, highly conductive, and anisotropic films [44]. However, the as-formed graphene film also has low ion-accessible surface area and high ion-transport resistance, which significantly limit the performance of supercapacitor devices. Li and coworkers reported a graphene film electrode prepared by capillary compression with a continuous ion-transport network into which a nonvolatile liquid electrolyte permeated. Electrochemical capacitors based on this graphene film could obtain volumetric energy densities of 60 Wh l^{-1} [50]. Besides the two-dimensional graphene film, three-dimensional (3D) graphene hydrogels, prepared by the hydrothermal reduction method, were also explored as electrodes for supercapacitors [45]. The graphene hydrogels have a highly interconnected 3D network structure (Figure 5.4c). Flexible supercapacitors based on such a structure exhibited a high mass specific capacitance of 186 F g^{-1}, an unprecedented areal specific capacitance of 372 mF cm^{-2}, a low leakage current (10.6 μA), excellent cycling stability, and extraordinary mechanical flexibility.

5.3.2 Graphene-Based Composites

The agglomeration and restacking of graphene nanosheets during the drying process decrease the electrolyte-ion-accessible surface area, and thus limit the electrochemical performance. To take full advantage of graphene in supercapacitors, dispersing carbon materials, metal oxides/hydroxides, and conducting polymer

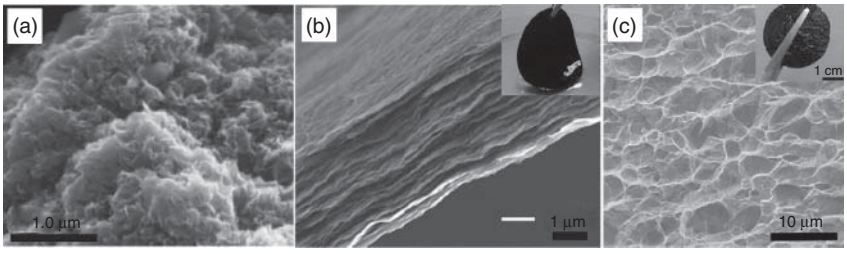

Figure 5.4 SEM images of (a) rGO powder, (b) graphene film, and (c) three-dimensional graphene hydrogel (inset: the corresponding digital photograph). (Reprinted with permission from Refs [42, 44, 45]. Copyright (2008), American Chemical Society, Copyright (2011), Wiley-VCH Verlag, and Copyright (2013), American Chemical Society.)

onto graphene to form graphene-based composites is considered an effective and practical method. These materials can not only prevent the agglomeration and restacking of graphene during the drying process but also contribute to the specific capacitance themselves to the composites, and thus improve the whole supercapacitor performance.

5.3.2.1 Graphene–Carbon Material Composites

Carbon materials such as AC, carbon black (CB), carbon nanotubes (CNTs), and mesoporous carbon spheres (MCSs) have been reported to be introduced into graphene to enhance the electrochemical performance. Yan and coworkers [51] prepared graphene/CB composites by the ultrasonication and *in situ* reduction methods. The incorporation of CB as the spacer not only could increase the distance between the graphene sheets and improve electrolyte–electrode accessibility but also provide a rapid diffusion path for better edge plane participation in double-layer capacitance. As a result, the as-formed graphene/CB composite electrodes could achieve a specific capacitance of 175 F g^{-1}, which is higher than that of graphene layers (122.6 F g^{-1}). However, CB itself almost has no specific capacitance because of the limitation in specific surface area.

In recent studies, CNTs have replaced CB and have been combined with graphene to investigate the effects on the supercapacitor performance. CNTs have excellent conductivities, high surface areas, and mechanical properties, and thus can act as ideal spacers and binders to hold the graphene sheets together. Huang *et al.* [52] reported rGO/CNTs hybrid films formed by simply casting an aqueous GO and CNT dispersion on a Ti substrate. However, such a fabrication process makes it impossible to prevent the agglomeration of the atomically thin graphene sheets, which leads to reduction of the electrochemically active surface area. To overcome this problem, a hybrid graphene/CNT film was formed by a sequential self-assembly of poly(ethyleneimine)-modified graphene nanosheets and acid-treated CNTs in an aqueous electrolyte [53]. This architecture enabled the full utilization of the maximum active surface area of graphene nanosheets by using a CNT layer as a spacer to enhance the permeation of electrolyte ions inside the structure and reduce the agglomeration of graphene nanosheets along the

vertical direction. As a result, the stacked multilayers of graphene and CNTs offer better electrochemical capacitor performance than pristine graphene and CNT electrodes. However, the acid treatment process tends to damage the structure of CNTs, and poly(ethyleneimine) is introduced into the graphene/CNT film, thus worsening the electrical conductivity.

Besides the physical mixing of graphene and CNTs, CNTs can also be *in situ* grown on graphene to form a 3D hybrid structure. Fan *et al.* [54] have developed 3D CNTs/graphene sandwich structures in which CNT pillars were grown in between the graphene layers by CVD (Figure 5.5). This approach can avoid the destruction of the structure of CNTs, and restore the electrical conductivity of GO without using the toxic reducing agent. The special structure allows the high-rate transportation of electrolyte ions and electrons throughout the electrode matrix, resulting in excellent electrochemical performance of this hybrid material. Supercapacitor devices based on this structure exhibit a specific capacitance of 385 F g^{-1} at 10 mV s^{-1} in 6 M KOH solution. To further decrease the extent of damage of the graphene structure during the preparation process, the vertically aligned CNTs can be directly intercalated on the thermally expanded highly ordered pyrolytic graphite (HOPG) instead of GO to form the 3D pillared, vertically aligned CNT/graphene architecture [55]. In a departure from the use of CNTs with graphene, MCS could also act as the spacer to inhibit the aggregation of graphene layers, and exhibited good supercapacitance performance in aqueous and organic electrolytes [56]. For example, a specific capacitance of 180 F g^{-1} was achieved, with an energy density of 62.8 W h kg^{-1} at a power density of 0.16 kW kg^{-1} in the tetraethylammonium tetrafluoroborate ($TEABF_4$) electrolyte. Such a good capacitance performance can be ascribed to the structure of the graphene/MCS composites, which exhibit high effective surface area and short diffusion length with the resulting low diffusion resistance and better capacitive performances.

5.3.2.2 Graphene/Metal Oxide Composites

Just like carbon materials, metal oxides can also act as a spacer to inhibit the agglomeration and restacking of the graphene layer. More importantly, metal oxides can exhibit high specific capacitance via the redox reaction at the interface of the electrode material and the electrolyte. However, the application of these pseudocapacitive electrode materials is largely limited by the following two factors: First is that metal oxides have low conductivity. The other is that the electrochemical reaction often occurs at the surface of the electrode, resulting in ineffective utilization of the active material. In the graphene/metal oxides composites, graphene can provide the conductive pathway to improve the electrical conductivity of metal oxides. Many approaches have been reported to load metal oxides on graphene sheets with the aim of enhancing the effective surface area and introducing additional pseudocapacitance. With the emphasis on metal oxide/graphene composites, different metal oxides, such as those of ruthenium, manganese, cobalt, nickel, copper, iron, and vanadium, have been incorporated in to graphene and their electrochemical properties have been studied intensively.

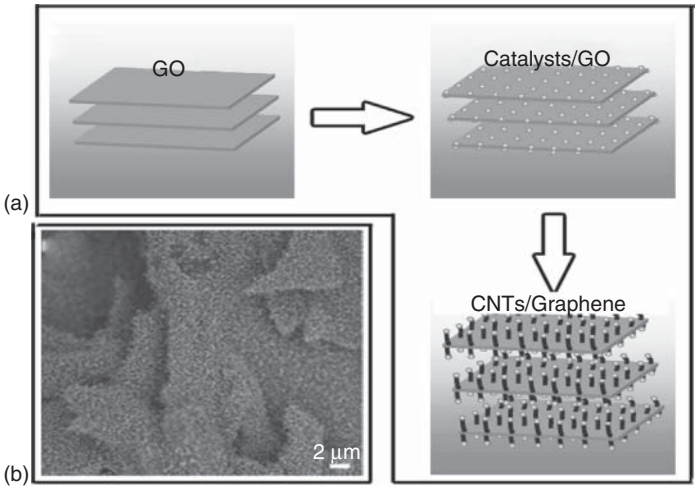

Figure 5.5 (a) Schematic illustrating the formation process of CNT/graphene hybrid materials, in which CNTs are grown in between graphene nanosheets via chemical vapor deposition method. (b) SEM images of CNT/graphene composites. (Reprinted with permission from Ref. [54]. Copyright (2010), Wiley-VCH Verlag.)

Ruthenium oxide, especially hydrous and amorphous RuO_2, is one of the most promising electrode materials for supercapacitors because of its high specific capacitance, highly reversible redox reactions over a wide potential range, and long cycle life. The hydrous RuO_2/rGO composites (RuO_2/rGO) were prepared by the sol–gel process and subsequent low-temperature annealing [57]. The graphene sheets (GSs) are well separated by RuO_2 nanoparticles and, simultaneously, the RuO_2 nanoparticles are anchored by the rich oxygen-containing functional groups of rGO. Combining the benefits from the advantages of rGO and RuO_2 in the composites, the RuO_2/rGO composites exhibit a specific capacitance of ~570 F g^{-1} at a scan rate of 1 mV s^{-1}, enhanced rate capability, and excellent electrochemical stability (~97.9% retention after 1000 cycles). RuO_2 also can be successfully deposited on rGO sheets by combining a hydrothermal process and low-temperature annealing [58, 59]. Unlike pure crystalline RuO_2 exhibiting poor electrochemical performance, the composites present superior capacitive properties. For example, the RuO_2/rGO composite electrodes containing 40 wt% of Ru exhibited higher specific capacitance (551 F g^{-1} at 1 A g^{-1}) and improved rate capability and cycle performance when compared to rGO and RuO_2. In addition, increasing the electroactive area of RuO_2 nanoparticles can further enhance the electrochemical performance. Soin *et al.* [60] reported that well-dispersed RuO_2 nanoparticles with a diameter of less than 2 nm were formed on few-layer graphene nanoflakes using a combination of low-base-pressure radio frequency magnetron sputtering and the subsequent electrochemical cycling in acidic media. Thus, the as-formed composite electrodes achieved a specific capacitance of 650 F g^{-1}, which was much higher than those of the RuO_2/rGO

composites described above. To avoid the introduction of the additional toxic reducing agent during the reduction process of GO to rGO, the microwave hydrothermal method was developed for synthesizing RuO_2/rGO nanocomposites [61]. During the preparation process, the reduction of GO to rGO and the oxidation of Ru^{3+} ions to RuO_2 are simultaneously achieved. The as-formed RuO_2/rGO nanocomposite electrode showed a specific capacitance of 497 F g^{-1} at 0.5 A g^{-1}, and maintained 88% of the specific capacitance as the discharging current density was increased from 0.5 to 16 A g^{-1}.

RuO_2, although is a good electrode material, it is both costly and toxic. Recently, the studies have largely shifted to cheaper alternative metal oxides such as nickel, cobalt, and manganese oxides. Manganese oxides, such as MnO_2 and Mn_3O_4, have been demonstrated to be promising electrode materials because of their low cost, environmental friendliness, and high theoretical capacitance. They can deliver specific capacitances ranging from 700 to 1380 F g^{-1}, as MnO_2 is deposited with a few hundred nanometers thickness. However, commercial MnO_2 exhibits a specific capacitance of only ~200 F g^{-1} because of the limited electroactive area and poor electrical conductivity. To improve the electrochemical performance of MnO_2, one promising strategy is the direct deposition of MnO_2 nanomaterials on large-surface-area materials, such as carbon nanotubes and graphene. GO is rich in functional groups for anchoring MnO_2 on the surface, which has been widely investigated as a suitable support for MnO_2 loading. Up until now, various morphologies of MnO_2 nanomaterials, such as nanorods [62–66], needle-like MnO_2 [67–69], nanowires [70], nanosheets [66, 71], flower-like MnO_2 [67, 72], wrapped honeycomb MnO_2 nanospheres [73], urchin-like MnO_2 [74], hollow spheres [75], and nanowall [76], have been anchored on graphene sheets to form the MnO_2/graphene nanocomposites. Besides the morphologies of MnO_2, the electrical conductivity of the GO support also influences the electrochemical performance of the MnO_2/rGO nanocomposites. GOs fabricated from commercial expanded graphite possess more functional groups and larger interplanar gaps for loading MnO_2 nanomaterials, as compared to commercial graphite powder, and thus offer larger specific capacitance (307.7 F g^{-1} at 0.1 A g^{-1}) and better electrochemical activity [77]. Kim *et al.* [78] found that the types of reducing agents added in the reduction process from GO to rGO are closely related to the electrochemical performance of the MnO_2/rGO nanocomposites. The H-rGO/MnO_2 composite reduced by hydrazine hydrate shows higher electrical conductivity than S-rGO/MnO_2 reduced by sodium borohydride, because the former has a lower concentration of oxygen-containing functional groups. Thus, the as-formed H-rGO/MnO_2 electrode displayed a specific capacitance of 327.5 F g^{-1} at 10 mV s^{-1}, which is higher than that of the S-rGO/MnO_2 electrode (278.6 F g^{-1}). However, the introduction of the binder during the preparation of electrodes influenced the electrical conductivity, resulting in the deterioration of the electrochemical performance. Ge and coworkers [79] have developed a low-cost "dip and dry" processes to fabricate hierarchical MnO_2/rGO nanostructured sponges without using a binder. Figure 5.6a schematically shows the formation process of MnO_2/rGO sponges. On the smooth surface of a

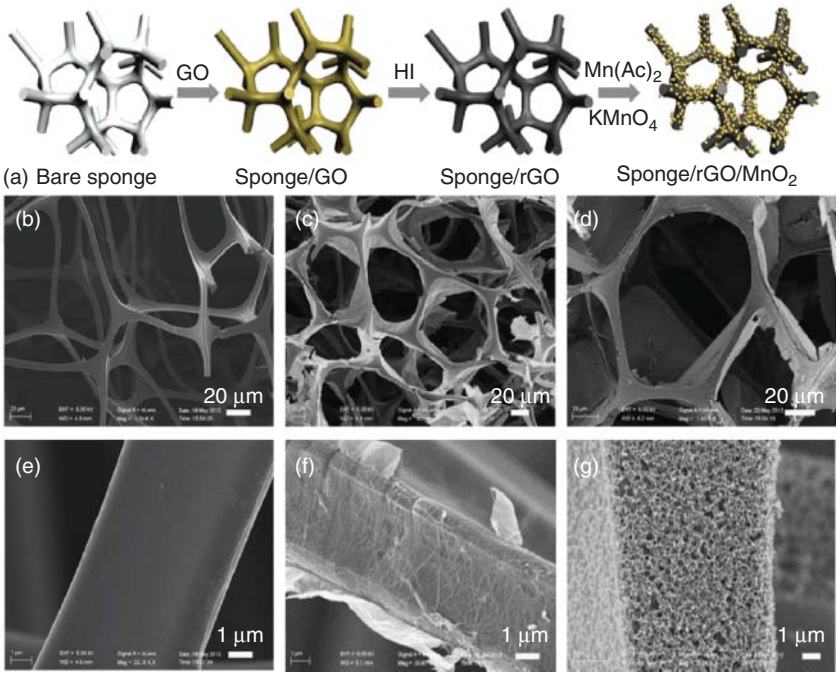

Figure 5.6 (a) Schematic illustration of the whole dip-coating process. (b–d) SEM images of bare sponge, sponge/rGO, and sponge/rGO/MnO_2, respectively. (e–g) High-magnification SEM images of bare sponge, sponge/rGO, and sponge/rGO/MnO_2, respectively. (Reprinted with permission from Ref. [79]. Copyright (2013), Elsevier.)

commercial sponge (Figure 5.6b,e), the rGO nanosheets were homogeneously deposited to form the three-dimensional interconnected macro-network rGO sponge (Figure 5.6c,f). Then, MnO_2 nanomaterials were loaded on the rGO sponge to form the MnO_2/rGO sponge-based supercapacitors (Figure 5.6d,g). Apart from MnO_2, Mn_3O_4 nanomaterials anchored on the graphene sheets were also widely investigated for supercapacitors [80, 81].

Cobalt and nickel oxides were also investigated to be incorporated with graphene for supercapacitors. The basic combination mode is the attachment of cobalt and nickel oxides onto the surface or intercalation into the interlayer of large patches of graphene-based materials [82–87]. Different from the cobalt and nickel oxides grown on the surface of rGO sheets, rGO platelets can be incorporated into Co_3O_4 scrolls, as demonstrated by Zhou and coworkers [88] . This assembly enables almost every single Co_3O_4 scroll to be connected with the rGO platelets, thus leading to remarkable electrochemical performances. In addition, Yang *et al.* [89] have developed a novel strategy for the fabrication of metal oxide/rGO nanocomposites, in which the metal oxide nanoparticles are wrapped with graphene sheets, driven by the mutual electrostatic interactions between negatively charged GO and positively charged metal oxide nanoparticles.

The formation process is schematically illustrated in Figure 5.7. Compared to the monometallic cobalt and nickel oxides, $NiCo_2O_4$ has at least two orders of magnitude higher electric conductivity and rich redox reactions, and thus is more suitable for the electrode materials [90]. $NiCo_2O_4$ exhibited a specific capacitance of 658 F g^{-1} at 1 A g^{-1}, which is higher than that of cobalt oxides (60 F g^{-1}) and nickel oxides (194 F g^{-1}). To further improve the electrical conductivity of $NiCo_2O_4$, Wang and coworkers [91] used charge-bearing nanosheets as building blocks to construct the $NiCo_2O_4$/rGO composites. Co/Ni hydroxides intercalated by the *p*-aminobenzoate (PABA) ion and graphene oxide (GO) as positively and negatively charged building blocks were assembled to form heterostructured nanohybrids through electrostatic interactions. The subsequent thermal treatment led to the formation of $NiCo_2O_4$ and rGO. The as-obtained $NiCo_2O_4$/rGO composite exhibited an initial specific capacitance of 835 F g^{-1} at a specific current of 1 A g^{-1}, which is much higher than that of pristine $NiCo_2O_4$. The $NiCo_2O_4$ is stoichiometric and has a molar ratio of Co/Ni fixed at 2 : 1, and thus the study of the properties of Co/Ni oxides at other compositions has been out of reach. Yang and Xiao [82] chose amorphous precursors in disordered states and with high solubility, which allowed the coexistence of Co^{2+} and Ni^{2+} in any molar ratio. The amorphous precursors could then be crystallized and thermally decomposed into single-phase $Co_xNi_{1-x}O$ with various molar ratios of Co/Ni anchored on the rGO sheets. The electrochemical results revealed that the $Co_xNi_{1-x}O$/rGO nanocomposite electrodes could achieve peak specific capacitance when the Co/Ni molar ratio is close to 1.

Besides manganese oxides, cobalt oxides, and nickel oxides, other metal oxides have also been reported to be grown on graphene sheets for supercapacitors. For example, vanadium oxide nanomaterials with various morphologies have been reported to be anchored on rGO sheets via a one-step electrochemical deposition method [92] and hydrothermal process [93–95]. Compared to pure V_2O_5 microspheres, the rod-like V_2O_5/rGO nanocomposites exhibited a higher specific capacitance of 537 F g^{-1} at a current density of 1 A g^{-1} and better stability even after 1000 charge/discharge cycles [93]. Fe_3O_4 [96–99], SnO_2 [100, 101], ZnO [102, 103], TiO_2 [104, 105], and CuO [106, 107] have also been reported to be anchored on the rGO sheets for improving the electrochemical performance.

5.3.2.3 Graphene–Conducting Polymer Composites

Conducting polymers can offer capacitive behaviors because of the presence of a delocalized π-electron conjugation system, which can enable fast and reversible redox reactions. When the redox process happens, electrolyte ions are transferred to and released from the polymer backbone [9]. In addition, conducting polymers also have the advantages of cost effectiveness, environmental benignity, high conductivity in a doped state, and adjustable redox activity through chemical modifications. Thus, conducting polymers are considered as good electrode materials for supercapacitors. However, the limitation of using conducting polymers as standalone materials for supercapacitors is that they can rapidly degrade as a result of swelling and shrinkage, resulting in poor cycle stability. The introduction of

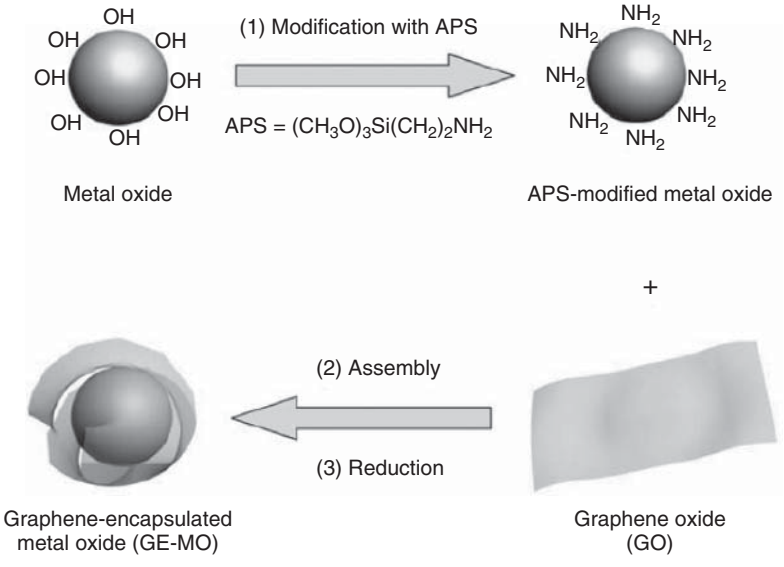

Figure 5.7 Fabrication of graphene-encapsulated metal oxide (GE-MO) including (1) modification of the metal oxide by grafting aminopropyltrimethoxysilane (APS) to render the oxide surface positively charged, (2) hybrid assembly between positively charged oxide nanoparticles and negatively charged graphene oxide by electrostatic interactions, and (3) chemical reduction. (Reprinted with permission from Ref. [89]. Copyright (2010), Wiley-VCH Verlag.)

conducting polymers into graphene not only can prevent the agglomeration and restacking of graphene during the drying process to enhance the EDL capacitance of graphene but also can improve the mechanical and electrochemical cycling stability of the polymers. Thus, a combination of graphene and electrically conducting polymers is beneficial for improving the electrochemical performance. In the conducting polymer/graphene composites, the interaction between graphene and conducting polymers is a significant factor in defining the capacitance, rather than the specific surface area of graphene. A variety of polymers such as polypyrrole (PPy), polyaniline (PANI), poly(3,4-ethylenedioxythiophene) (PEDOT), and polythiphene (PT) grown on the graphene sheets were investigated for electrode materials.

To exploit the potential of conducting polymer/graphene nanocomposites for supercapacitors, a variety of methods have been developed, including solution mixing, layer-by-layer self-assembly, *in situ* polymerization, electrochemical polymerization, oxidation polymerization, and liquid/liquid interfacial polymerization. Solution mixing requires both graphene and the conducting polymers to be stably dispersed in a common solvent. The GO precursors have a good dispersibility in water or polar organic solvents, while conducting polymers are usually insoluble in polar solvents. Thus, to date, only a few conducting polymer/graphene nanocomposites have been prepared by solution mixing. Shi *et al.* [108] have developed a facile method to synthesize the PANI nanofiber/graphene

composite film via the vacuum filtration of mixed dispersions of PANI nanofibers and graphene sheets (Figure 5.8). In this case, the negatively charged graphene sheets and positively charged PANI nanofibers were self-assembled, through electrostatic interaction, into a uniform composite film by filtration. Supercapacitor devices based on this PANI/graphene composite film showed a large a large specific capacitance of 210 F g^{-1} at 0.3 A g^{-1}, as well as greatly improved electrochemical stability and rate performance. However, this technique cannot be applied to the preparation of uniform composites, as GO interacts strongly with the polymer resulting in the aggregation of both graphene and the polymer. Furthermore, the mixture of graphene and conducting polymers frequently tends to form gels if their concentrations are sufficiently high [109]. Inspired by the oppositely charged GO and PANI, a layer-by-layer self-assembly approach was employed to prepare the PANI/rGO multilayer films [110]. The electrochemical results revealed that the multilayer-based electrode composed of 15 PANI/rGO bilayers exhibited a volumetric capacitance of 584 F cm^{-3} at a current density of 30 A cm^{-3}, and even maintained a value of 170 F cm^{-3} at 100 A cm^{-3}. Besides the van der Waals forces between graphene and PANI, the amine-group-connected PANI/graphene can make the interaction between graphene and PANI more intimate [111]. PANI nanofiber is grafted onto rGO via the formation of amine groups, which decreases the interfacial resistance and thus improves the electrochemical performance. Supercapacitors based on these amine-group-connected PANI/graphene composites could further improve the electrochemical performance, and exhibited a specific capacitance of 579.8 and 361.9 F g^{-1} at current densities of 0.3 and 1 A g^{-1}, respectively.

Besides solution mixing and layer-by-layer self-assembly, the monomers can be directly polymerized on the graphene sheets to form conducting polymer/graphene nanocomposites. This process is called *in situ polymerization*. Many conducting polymer/graphene nanocomposites can be prepared using this approach. Conducting polymers prefer to grow on the surface of graphene sheets rather than in solution, probably because of the preferential adsorption of the monomer molecules on graphene sheets via electrostatic, $\pi-\pi$ stacking, and hydrogen bonding interactions [16]. Wang *et al.* [112] have reported the polymerization of aniline monomers on GO sheets via the *in situ* polymerization method. Although GO has poor electrical conductivity because of the oxidation during the exfoliation process, GO-doped PANI still has a conductivity of 10 S cm^{-1}, which is higher than that of pristine PANI (2 S cm^{-1}). Thus, supercapacitors based on the PANI/GO nanocomposites exhibited a higher specific capacitance (531 F g^{-1}) than PANI-based supercapacitors (216 F g^{-1}) measured under the same condition. To increase the electrical conductivity of GO, PANI was deposited on rGO directly reduced from GO via the *in situ* polymerization method. In the PANI/rGO composites, the rGO sheets prefer to agglomerate together, and thus hinder the performance of the as-prepared composite electrodes [113–117]. To prevent the agglomeration of graphene sheets, Wang *et al.* [118] have developed an *in situ* polymerization–reduction/dedoping–redoping process to prepare the PANI/graphene hybrid materials, and thus enhance the

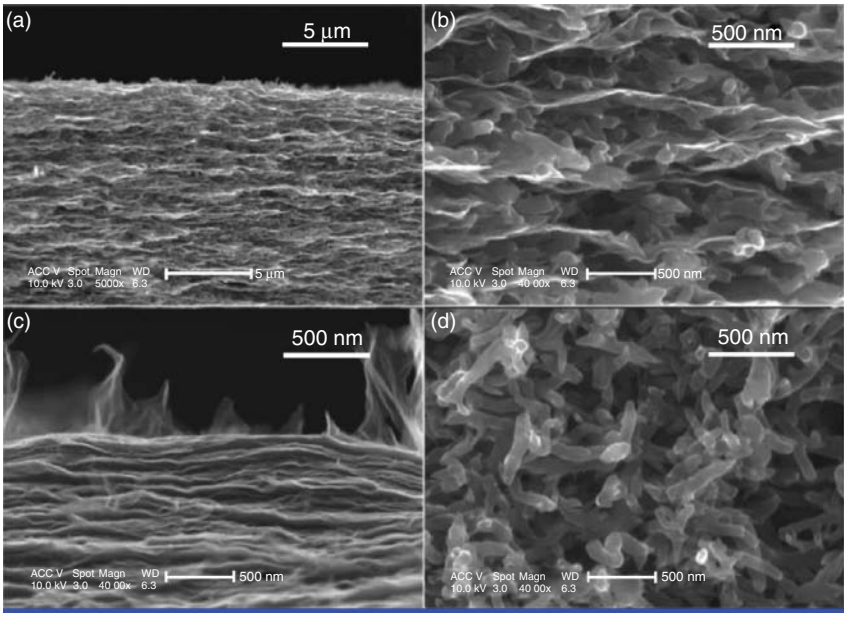

Figure 5.8 Cross-sectional SEM images of (a,b) PANI/graphene, (c) pure graphene, and (d) PANI nanofiber films by vacuum filtration. (Reprinted with permission from Ref. [108]. Copyright (2010), American Chemical Society.)

electrochemical capacitor performance. In the preparation process, sodium hydroxide acted as the reducing and dedoping agent for PANI. In addition, using an *in situ* polymerization of aniline in the presence of well-dispersed GO in acidic solution followed by reduction with GO with hydrazine and reoxidation of PANI by the oxidant, PANI nanofibers were uniformly grown on the rGO sheets to inhibit the agglomeration of graphene sheets [119]. The formation process is schematically shown in Figure 5.9. Supercapacitors based on this PANI/rGO nanocomposite showed a specific capacitance of 480 F g^{-1} at a current density of 0.1 A g^{-1}. However, during the reduction and reoxidation processes, the chemical and electronic structure of PANI were unavoidably destroyed, leading to a degradation of capacitor performance. Mao *et al.* [120] reported a mild condition to prepare PANI nanofiber/graphene composites by *in situ* polymerization of aniline in the presence of surfactants, such as tetrabutylammonium hydroxide, and sodium dodecyl benzenesulfonate-stabilized graphene under acidic condition. A homogeneous dispersion of individual graphene sheets within the polymer matrix was achieved as a result of the good dispersibility of surfactant-stabilized graphene in the aqueous phase. The composite electrodes achieved a high specific capacitance of 526 F g^{-1} at a current density of 0.2 A g^{-1} with good cycling stability. Typically, the aniline polymerization on the graphene surface was carried out using oxidants such as $(NH_4)_2S_2O_8$ or $FeCl_3$, resulting in inhomogeneity of PANI on the graphene sheets. Sathish and coworkers [121]

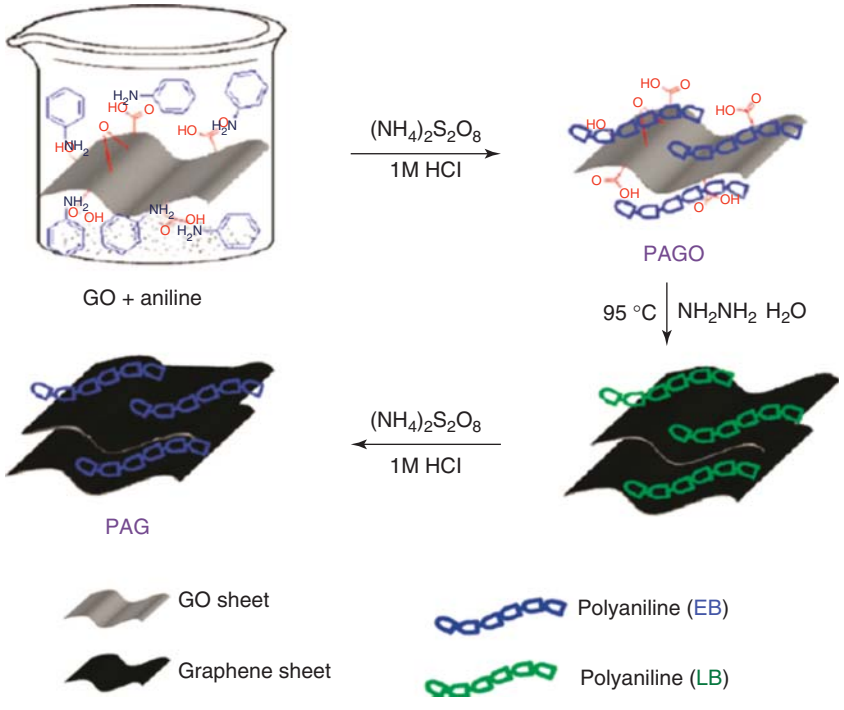

Figure 5.9 Schematic illustrating the preparation process of PANI/graphene composites via *in situ* polymerization. (Reprinted with permission from Ref. [119]. Copyright (2010), American Chemical Society.)

have developed a method in which MnO_2 grown on graphene sheets acted as the oxidant to initiate the polymerization of PANI, resulting in the formation of a uniform PANI film on the graphene sheets. Supercapacitors based on this PANI/graphene nanocomposite, obtained via the oxidative polymerization of aniline, showed increased specific capacitance by ~15–40% over the value reported previously.

The irreversible mechanical deformation in the repetitive redox process of conducting polymers results in poor cycle stability. It can be improved by introducing graphene sheets and altering the morphologies of the conducting polymers. Based on this background, Xu *et al.* [122] were able to control the morphologies of PANI in the graphene/polymer composites via tuning the polymerization conditions, and investigated its influence on the electrochemical performance. At a concentration of aniline less than 0.05 M, most active nucleation sites were generated on GO nanosheet surfaces at the beginning of polymerization through the heterogeneous nucleation (Route i in Figure 5.10a), resulting in the formation of PANI nanowire arrays on the GO sheets (Figure 5.10b). When the concentration of aniline was increased to over 0.06 M, homogeneous nucleation took place after the initial nucleation on the solid surface (Route ii in Figure 5.10a), leading to the formation of randomly connected PANI nanowires on the GO sheets (Figure 5.10c).

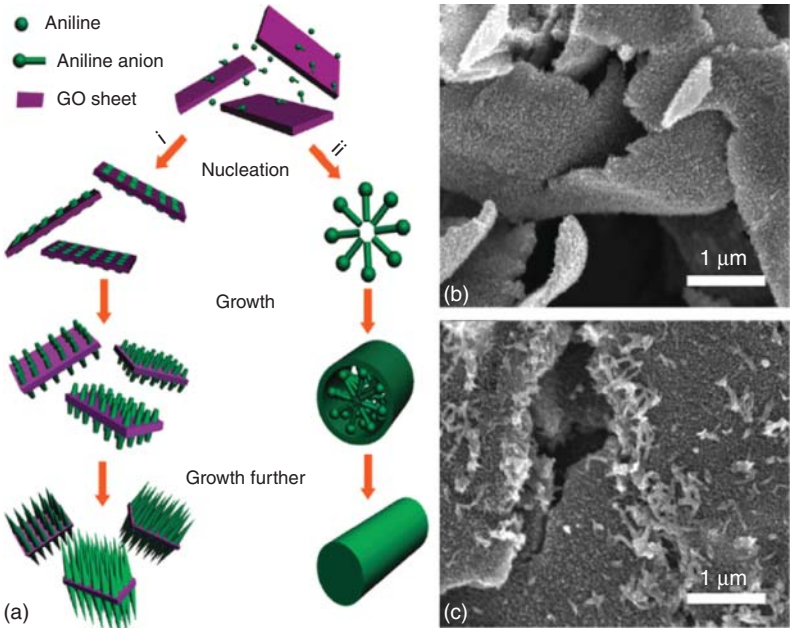

Figure 5.10 (a) Schematic illustration of the nucleation and growth mechanism of PANI on the GO sheets via the heterogeneous nucleation (Route i) and homogenous nucleation (Route ii). SEM images of PANI/GO nanocomposites formed at (b) 0.05 M and (c) 0.06 M of aniline. Reprinted with permission from Ref. [122]. Copyright (2010) American Chemical Society.

Electrochemical results revealed that the PANI nanowire arrays on the rGO sheets exhibited better cycling stability, in comparison with random PANI nanowires on the rGO sheets, maybe because the vertical nanowire arrays were conducive to strain relaxation and thus allowed them to decrease the breaking during the doping/dedoping process of counter ions [123, 124].

In comparison with the *in situ* polymerization approach, electrochemical polymerization can yield mechanically stable composite films, which can be directly used as the electrodes of energy storage devices, and is a versatile, facile, and environmentally friendly way for doping during the synthesis and polymerization without violent stirring. Furthermore, the electrochemical polymerization process is controlled by the electrochemical reaction, and thus can be modulated by the applied potentials and current densities. Wang *et al.* [125] have developed an *in situ* anodic electropolymerization method to prepare PANI on free-standing graphene paper. Supercapacitors based on this PANI/graphene paper exhibited a specific capacitance of 233 F g^{-1}. Owing to the agglomerated layer-like structure of the free-standing graphene paper, it has almost no contribution to the electrochemical capacitance, and thus the capacitance is mainly contributed by the pseudocapacitance of PANI. To inhibit the agglomeration of graphene, Feng *et al.* [126] have prepared PANI/graphene composites using a GO suspension and

aniline as the starting material for the electrochemical deposition. The as-obtained composite electrodes had a specific capacitance of 640 F g^{-1} and a retention of 90% after 1000 charge/discharge cycles. To fully explore the EDL capacitance of rGO and solve the poor dispersion of aniline monomers in the polar solvents during the electrochemical polymerization process, Gao and coworkers [127] integrated the layer-by-layer self-assembly with electrochemical polymerization techniques to prepare the PANI/rGO composites. Compared to the pure PANI electrode, the PANI/rGO multilayer composite electrodes displayed an improved capacitive performance (5.16 F cm^{-2}), good rate capability, and improved cycle performance, with capacity retention of about 93% after 1000 charge/discharge cycles. In comparison with graphene, GO in the composites was demonstrated to have a higher conductivity as a result of the increase of the doping degree of PANI [119]. GO also exhibited higher specific capacitance, excellent rate performance, and good cycle stability because of an additional pseudocapacitance effect of the attached oxygen-containing functional groups on its basal planes [128]. Based on this background, Zhang *et al.* [129] have investigated the influence of GO on the electrochemical performance of the PANI/GO composites prepared via a one-step electrochemical codeposition method. The maximum specific capacitance of the PANI/GO composite achieved was 1136.4 F g^{-1} at a scan rate of 1 mV s^{-1} with a GO concentration of 10 mg l^{-1}, which is almost twofold higher than that of PANI (484.5 F g^{-1}), and retained over 89% of its initial capacitance after 1000 cycles.

5.3.2.4 Graphene/Metal Oxide–Conducting Polymer Composites

To develop the electrode materials for supercapacitors with high energy densities, metal oxide/graphene composites with high mass loading of the oxides have been investigated. A high mass loading of metal oxides, however, would typically increase the electrode resistance because of the high-density packing of the metal oxides, and also reduce the effective surface area for pseudocapacitance. Cui and coworkers [130] have proposed a 3D conductive-layer wrapping method to design ternary systems based on graphene/MnO_2/CNTs or graphene/MnO_2/conducting polymers to enhance the electric conductivity (Figure 5.11a), and thus improve the electrochemical performance. Introducing the conductive interlayer can increase the specific capacitance by as much as 45%, with capacitance values peaking at 380 F g^{-1}. However, they just deposited the conducting layer on the surface of the outmost metal oxides but could not completely explore the potential of electrochemical performance. Li *et al.* [131] have developed an efficient method for coupling the controlled growth of metal oxides and graphene sheets by employing PANI as the coupling linker to construct unique 2D nanohybrids (Figure 5.11b). These nanohybrids have a well-defined 2D morphology, confined metal oxides within the PANI nanostructures, controllable particle size, and high specific surface areas. Such unique structural features give rise to their outstanding electrochemical performance. The graphene/PANI/Co_3O_4 composites with GO to aniline weight ratios of 1 : 10 achieved the specific capacitance of 938 F g^{-1} at a scan rate of 10 mV s^{-1}.

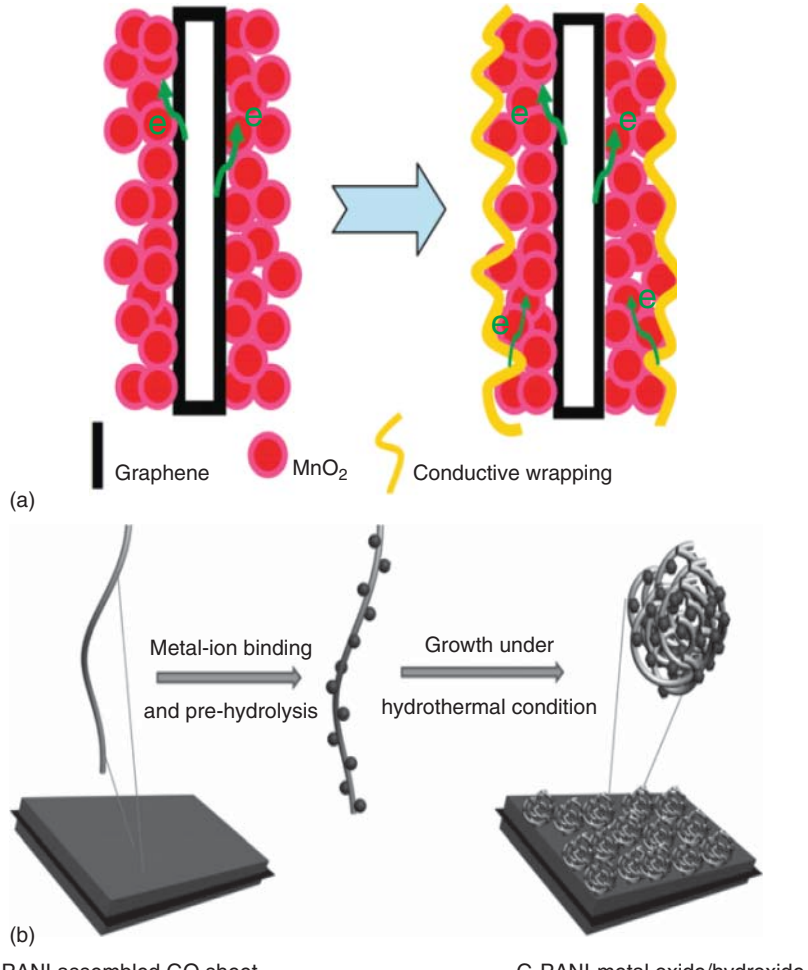

Figure 5.11 (a) Schematic illustration showing conductive wrapping of graphene/MnO_2 (GM) to introduce an additional electron transport path. (Reprinted with permission from Ref. [130]. Copyright (2011), American Chemical Society.) (b) The overall synthetic procedure of graphene (G)-PANI-metal oxide/hydroxide hybrids. (Reprinted with permission from Ref. [131]. Copyright (2013), Wiley-VCH Verlag.)

5.4 Conclusions and Prospects

Research on graphene-based materials as electrodes for supercapacitors is a rapidly advancing field. In this chapter, we summarized the progress in the development of preparation methods of graphene and graphene-based composites, as well as the applications of these materials in supercapacitors. In the field of graphene-based supercapacitor devices, since pristine graphene can only achieve

a specific capacitance of ~100 F g^{-1}, there has been considerable research on how graphene could be integrated with carbon materials, metal oxides, and conducting polymers to produce hybrids with excellent electrochemical properties. Much progress has been made in this direction, as we have summarized in this review.

One of the bottlenecks of graphene-based electrodes lies in the low volumetric and mass energy density for supercapacitor devices, which are mainly influenced by the current collector, electrode materials, and the electrolyte. Current collectors, such as nickel foam and carbon fiber papers, occupy a large portion of the volume and mass in these devices, but they have almost no contribution to energy storage and thus severely limit the overall electrochemical performance. In contrast, graphene not only can exhibit the EDL capacitance by itself but also has a low mass density, good electrical conductivity and chemical stability, and high specific surface area, making it a good current collector material for loading the additional electrode materials. Thus, the development of free-standing graphene-based materials as electrodes can further improve the electrochemical performance of supercapacitor devices. Much more work needs be done to develop free-standing graphene-based electrode materials, which include (i) developing facile methods to produce graphene from graphite in a large quantity and high quality; (ii) self-assembling graphene nanosheets into a 3D graphene scaffold with a large specific surface area, high electrical conductivity, and hierarchical porous structure; (iii) optimizing the structures and components to be loaded onto the graphene scaffold to attain the maximum possible specific capacitance; (iv) searching for appropriate electrolytes to widen the operation voltage window of the graphene-based materials; and (v) developing flexible, solid-state, smart supercapacitor devices.

References

1. Huang, Y., Liang, J.J., and Chen, Y.S. (2012) *Small*, **8**, 1805–1834.
2. Simon, P. and Gogotsi, Y. (2008) *Nat. Mater.*, **7**, 845–854.
3. Choi, H.J., Jung, S.M., Seo, J.M., Chang, D.W., Dai, L.M., and Baek, J.B. (2012) *Nano Energy*, **1**, 534–551.
4. Long, J.W., Belanger, D., Brousse, T., Sugimoto, W., Sassin, M.B., and Crosnier, O. (2011) *MRS Bull.*, **36**, 513–522.
5. Zhang, L.L., Zhou, R., and Zhao, X.S. (2010) *J. Mater. Chem.*, **20**, 5983–5992.
6. Conway, B.E. (1999) *Electrochemical Supercapacitors: Scientific Fundamentals and Technological Applications*, Plenum Publisher, New York.
7. Fang, M., Tang, Z.Y., Lu, H.B., and Nutt, S. (2012) *J. Mater. Chem.*, **22**, 109–114.
8. Sreeprasad, T.S. and Berry, V. (2013) *Small*, **9**, 341–350.
9. Wang, G., Zhang, L., and Zhang, J. (2012) *Chem. Soc. Rev.*, **41**, 797–828.
10. Xu, C., Xu, B., Gu, Y., Xiong, Z., Sun, J., and Zhao, X.S. (2013) *Energy Environ. Sci.*, **6**, 1388–1414.
11. Zhi, M., Xiang, C., Li, J., Li, M., and Wu, N. (2013) *Nanoscale*, **5**, 72–88.
12. Hou, J., Shao, Y., Ellis, M.W., Moore, R.B., and Yi, B. (2011) *Phys. Chem. Chem. Phys.*, **13**, 15384–15402.
13. Zhu, J., Chen, M., He, Q., Shao, L., Wei, S., and Guo, Z. (2013) *RSC Adv.*, **3**, 22790–22824.
14. Chang, H. and Wu, H. (2013) *Energy Environ. Sci.*, **6**, 3483–3507.
15. Tan, Y.B. and Lee, J.-M. (2013) *J. Mater. Chem. A*, **1**, 14814–14843.

16. Kim, H., Abdala, A.A., and Macosko, C.W. (2010) *Macromolecules*, **43**, 6515–6530.
17. Zhai, Y., Dou, Y., Zhao, D., Fulvio, P.F., Mayes, R.T., and Dai, S. (2011) *Adv. Mater.*, **23**, 4828–4850.
18. Park, S. and Ruoff, R.S. (2009) *Nat. Nanotechnol.*, **4**, 217–224.
19. Dikin, D.A., Stankovich, S., Zimney, E.J., Piner, R.D., Dommett, G.H.B., Evmenenko, G., Nguyen, S.T., and Ruoff, R.S. (2007) *Nature*, **448**, 457–460.
20. Hernandez, Y., Nicolosi, V., Lotya, M., Blighe, F.M., Sun, Z.Y., De, S., McGovern, I.T., Holland, B., Byrne, M., Gun'ko, Y.K., Boland, J.J., Niraj, P., Duesberg, G., Krishnamurthy, S., Goodhue, R., Hutchison, J., Scardaci, V., Ferrari, A.C., and Coleman, J.N. (2008) *Nat. Nanotechnol.*, **3**, 563–568.
21. Allen, M.J., Tung, V.C., and Kaner, R.B. (2010) *Chem. Rev.*, **110**, 132–145.
22. Berger, C., Song, Z.M., Li, X.B., Wu, X.S., Brown, N., Naud, C., Mayou, D., Li, T.B., Hass, J., Marchenkov, A.N., Conrad, E.H., First, P.N., and de Heer, W.A. (2006) *Science*, **312**, 1191–1196.
23. Kim, K.S., Zhao, Y., Jang, H., Lee, S.Y., Kim, J.M., Kim, K.S., Ahn, J.H., Kim, P., Choi, J.Y., and Hong, B.H. (2009) *Nature*, **457**, 706–710.
24. Seibert, K., Cho, G.C., Kütt, W., Kurz, H., Reitze, D.H., Dadap, J.I., Ahn, H., Downer, M.C., and Malvezzi, A.M. (1990) *Phys. Rev. B*, **42**, 2842–2851.
25. Novoselov, K.S., Geim, A.K., Morozov, S.V., Jiang, D., Zhang, Y., Dubonos, S.V., Grigorieva, I.V., and Firsov, A.A. (2004) *Science*, **306**, 666–669.
26. Li, D., Muller, M.B., Gilje, S., Kaner, R.B., and Wallace, G.G. (2008) *Nat. Nanotechnol.*, **3**, 101–105.
27. Hummers, W.S. and Offeman, R.E. (1958) *J. Am. Chem. Soc.*, **80**, 1339.
28. Stankovich, S., Dikin, D.A., Piner, R.D., Kohlhaas, K.A., Kleinhammes, A., Jia, Y., Wu, Y., Nguyen, S.T., and Ruoff, R.S. (2007) *Carbon*, **45**, 1558–1565.
29. Schniepp, H.C., Li, J.L., McAllister, M.J., Sai, H., Herrera-Alonso, M., Adamson, D.H., Prud'homme, R.K., Car, R., Saville, D.A., and Aksay, I.A. (2006) *J. Phys. Chem. B*, **110**, 8535–8539.
30. McAllister, M.J., Li, J.L., Adamson, D.H., Schniepp, H.C., Abdala, A.A., Liu, J., Herrera-Alonso, M., Milius, D.L., Car, R., Prud'homme, R.K., and Aksay, I.A. (2007) *Chem. Mater.*, **19**, 4396–4404.
31. Wu, Z.S., Ren, W.C., Gao, L.B., Liu, B.L., Jiang, C.B., and Cheng, H.M. (2009) *Carbon*, **47**, 493–499.
32. Wu, Z.S., Ren, W.C., Gao, L.B., Zhao, J.P., Chen, Z.P., Liu, B.L., Tang, D.M., Yu, B., Jiang, C.B., and Cheng, H.M. (2009) *ACS Nano*, **3**, 411–417.
33. He, H., Klinowski, J., Forster, M., and Lerf, A. (1998) *Chem. Phys. Lett.*, **287**, 53–56.
34. Fan, X.B., Peng, W.C., Li, Y., Li, X.Y., Wang, S.L., Zhang, G.L., and Zhang, F.B. (2008) *Adv. Mater.*, **20**, 4490–4493.
35. Shin, H.J., Kim, K.K., Benayad, A., Yoon, S.M., Park, H.K., Jung, I.S., Jin, M.H., Jeong, H.K., Kim, J.M., Choi, J.Y., and Lee, Y.H. (2009) *Adv. Funct. Mater.*, **19**, 1987–1992.
36. Pei, S.F., Zhao, J.P., Du, J.H., Ren, W.C., and Cheng, H.M. (2010) *Carbon*, **48**, 4466–4474.
37. Eda, G., Fanchini, G., and Chhowalla, M. (2008) *Nat. Nanotechnol.*, **3**, 270–274.
38. Gomez-Navarro, C., Weitz, R.T., Bittner, A.M., Scolari, M., Mews, A., Burghard, M., and Kern, K. (2007) *Nano Lett.*, **7**, 3499–3503.
39. Kang, H., Kulkarni, A., Stankovich, S., Ruoff, R.S., and Baik, S. (2009) *Carbon*, **47**, 1520–1525.
40. Li, X.S., Cai, W.W., An, J.H., Kim, S., Nah, J., Yang, D.X., Piner, R., Velamakanni, A., Jung, I., Tutuc, E., Banerjee, S.K., Colombo, L., and Ruoff, R.S. (2009) *Science*, **324**, 1312–1314.
41. Li, X.S., Cai, W.W., Colombo, L., and Ruoff, R.S. (2009) *Nano Lett.*, **9**, 4268–4272.
42. Stoller, M.D., Park, S., Zhu, Y., An, J., and Ruoff, R.S. (2008) *Nano Lett.*, **8**, 3498–3502.
43. Wang, Y., Shi, Z., Huang, Y., Ma, Y., Wang, C., Chen, M., and Chen, Y. (2009) *J. Phys. Chem. C*, **113**, 13103–13107.
44. Yang, X., Qiu, L., Cheng, C., Wu, Y., Ma, Z.-F., and Li, D. (2011) *Angew. Chem. Int. Ed.*, **50**, 7325–7328.

45. Xu, Y., Lin, Z., Huang, X., Liu, Y., Huang, Y., and Duan, X. (2013) *ACS Nano*, **7**, 4042–4049.
46. Li, X., Wang, H., Robinson, J.T., Sanchez, H., Diankov, G., and Dai, H. (2009) *J. Am. Chem. Soc.*, **131**, 15939–15944.
47. Wang, X., Li, X., Zhang, L., Yoon, Y., Weber, P.K., Wang, H., Guo, J., and Dai, H. (2009) *Science*, **324**, 768–771.
48. Qiu, Y.C., Zhang, X.F., and Yang, S.H. (2011) *Phys. Chem. Chem. Phys.*, **13**, 12554–12558.
49. Zhu, Y.W., Murali, S., Stoller, M.D., Ganesh, K.J., Cai, W.W., Ferreira, P.J., Pirkle, A., Wallace, R.M., Cychosz, K.A., Thommes, M., Su, D., Stach, E.A., and Ruoff, R.S. (2011) *Science*, **332**, 1537–1541.
50. Yang, X., Cheng, C., Wang, Y., Qiu, L., and Li, D. (2013) *Science*, **341**, 534–537.
51. Yan, J., Wei, T., Shao, B., Ma, F., Fan, Z., Zhang, M., Zheng, C., Shang, Y., Qian, W., and Wei, F. (2010) *Carbon*, **48**, 1731–1737.
52. Huang, Z.-D., Zhang, B., Oh, S.-W., Zheng, Q.-B., Lin, X.-Y., Yousefi, N., and Kim, J.-K. (2012) *J. Mater. Chem.*, **22**, 3591–3599.
53. Yu, D. and Dai, L. (2009) *J. Phys. Chem. Lett.*, **1**, 467–470.
54. Fan, Z., Yan, J., Zhi, L., Zhang, Q., Wei, T., Feng, J., Zhang, M., Qian, W., and Wei, F. (2010) *Adv. Mater.*, **22**, 3723–3728.
55. Du, F., Yu, D., Dai, L., Ganguli, S., Varshney, V., and Roy, A.K. (2011) *Chem. Mater.*, **23**, 4810–4816.
56. Lei, Z., Christov, N., and Zhao, X.S. (2011) *Energy Environ. Sci.*, **4**, 1866–1873.
57. Wu, Z.-S., Wang, D.-W., Ren, W., Zhao, J., Zhou, G., Li, F., and Cheng, H.-M. (2010) *Adv. Funct. Mater.*, **20**, 3595–3602.
58. Chen, Y., Zhang, X., Zhang, D., and Ma, Y. (2012) *J. Alloys Compd.*, **511**, 251–256.
59. Lin, N., Tian, J., Shan, Z., Chen, K., and Liao, W. (2013) *Electrochim. Acta*, **99**, 219–224.
60. Soin, N., Roy, S.S., Mitra, S.K., Thundat, T., and McLaughlin, J.A. (2012) *J. Mater. Chem.*, **22**, 14944–14950.
61. Kim, J.-Y., Kim, K.-H., Yoon, S.-B., Kim, H.-K., Park, S.-H., and Kim, K.-B. (2013) *Nanoscale*, **5**, 6804–6811.
62. Lee, M.-T., Fan, C.-Y., Wang, Y.-C., Li, H.-Y., Chang, J.-K., and Tseng, C.-M. (2013) *J. Mater. Chem. A*, **1**, 3395–3405.
63. Yu, Y., Zhang, B., He, Y.-B., Huang, Z.-D., Oh, S.-W., and Kim, J.-K. (2013) *J. Mater. Chem. A*, **1**, 1163–1170.
64. Chen, C., Fu, W., and Yu, C. (2012) *Mater. Lett.*, **82**, 133–136.
65. Kalubarme, R.S., Ahn, C.-H., and Park, C.-J. (2013) *Scr. Mater.*, **68**, 619–622.
66. Feng, X., Yan, Z., Chen, N., Zhang, Y., Ma, Y., Liu, X., Fan, Q., Wang, L., and Huang, W. (2013) *J. Mater. Chem. A*, **1**, 12818–12825.
67. Mao, L., Zhang, K., Chan, H.S.O., and Wu, J. (2012) *J. Mater. Chem.*, **22**, 1845–1851.
68. Wu, Z.-S., Ren, W., Wang, D.-W., Li, F., Liu, B., and Cheng, H.-M. (2010) *ACS Nano*, **4**, 5835–5842.
69. Li, Y., Zhao, N., Shi, C., Liu, E., and He, C. (2012) *J. Phys. Chem. C*, **116**, 25226–25232.
70. Chen, S., Zhu, J., Wu, X., Han, Q., and Wang, X. (2010) *ACS Nano*, **4**, 2822–2830.
71. Peng, L., Peng, X., Liu, B., Wu, C., Xie, Y., and Yu, G. (2013) *Nano Lett.*, **13**, 2151–2157.
72. Zhang, J. and Zhao, X.S. (2013) *Carbon*, **52**, 1–9.
73. Zhu, J. and He, J. (2012) *ACS Appl. Mater. Interfaces*, **4**, 1770–1776.
74. Yang, W., Gao, Z., Wang, J., Wang, B., Liu, Q., Li, Z., Mann, T., Yang, P., Zhang, M., and Liu, L. (2012) *Electrochim. Acta*, **69**, 112–119.
75. Chen, H., Zhou, S., Chen, M., and Wu, L. (2012) *J. Mater. Chem.*, **22**, 25207–25216.
76. Zhu, C., Guo, S., Fang, Y., Han, L., Wang, E., and Dong, S. (2011) *Nano Res.*, **4**, 648–657.
77. Yang, H., Jiang, J., Zhou, W., Lai, L., Xi, L., Lam, Y.M., Shen, Z., Khezri, B., and Yu, T. (2011) *Nanoscale Res. Lett.*, **6**, 531.
78. Kim, M., Hwang, Y., and Kim, J. (2013) *J. Power Sources*, **239**, 225–233.
79. Ge, J., Yao, H.-B., Hu, W., Yu, X.-F., Yan, Y.-X., Mao, L.-B., Li, H.-H., Li, S.-S.,

and Yu, S.-H. (2013) *Nano Energy*, **2**, 505–513.
80. Wu, Y., Liu, S., Wang, H., Wang, X., Zhang, X., and Jin, G. (2013) *Electrochim. Acta*, **90**, 210–218.
81. Wang, B., Park, J., Wang, C., Ahn, H., and Wang, G. (2010) *Electrochim. Acta*, **55**, 6812–6817.
82. Xiao, J. and Yang, S. (2012) *J. Mater. Chem.*, **22**, 12253–12262.
83. Chen, S., Zhu, J., and Wang, X. (2010) *J. Phys. Chem. C*, **114**, 11829–11834.
84. Yan, J., Wei, T., Qiao, W., Shao, B., Zhao, Q., Zhang, L., and Fan, Z. (2010) *Electrochim. Acta*, **55**, 6973–6978.
85. Wang, L., Wang, X., Xiao, X., Xu, F., Sun, Y., and Li, Z. (2013) *Electrochim. Acta*, **111**, 937–945.
86. Xiao, J. and Yang, S. (2012) *ChemPlusChem*, **77**, 807–816.
87. Wang, H.L., Casalongue, H.S., Liang, Y.Y., and Dai, H.J. (2010) *J. Am. Chem. Soc.*, **132**, 7472–7477.
88. Zhou, W., Liu, J., Chen, T., Tan, K.S., Jia, X., Luo, Z., Cong, C., Yang, H., Li, C.M., and Yu, T. (2011) *Phys. Chem. Chem. Phys.*, **13**, 14462–14465.
89. Yang, S., Feng, X., Ivanovici, S., and Muellen, K. (2010) *Angew. Chem. Int. Ed.*, **49**, 8408–8411.
90. Xiao, J. and Yang, S. (2011) *RSC Adv.*, **1**, 588–595.
91. Wang, H.-W., Hu, Z.-A., Chang, Y.-Q., Chen, Y.-L., Wu, H.-Y., Zhang, Z.-Y., and Yang, Y.-Y. (2011) *J. Mater. Chem.*, **21**, 10504–10511.
92. Zhang, W., Zeng, Y., Xiao, N., Hng, H.H., and Yan, Q. (2012) *J. Mater. Chem.*, **22**, 8455–8461.
93. Li, M., Sun, G., Yin, P., Ruan, C., and Ai, K. (2013) *ACS Appl. Mater. Interfaces*, **5**, 11462–11470.
94. Wang, H., Yi, H., Chen, X., and Wang, X. (2014) *J. Mater. Chem. A*, **2**, 1165–1173.
95. Yang, S., Gong, Y., Liu, Z., Zhan, L., Hashim, D.P., Ma, L., Vajtai, R., and Ajayan, P.M. (2013) *Nano Lett.*, **13**, 1596–1601.
96. Wang, Q., Jiao, L., Du, H., Wang, Y., and Yuan, H. (2014) *J. Power Sources*, **245**, 101–106.
97. Xu, H., Hu, Z., Lu, A., Hu, Y., Li, L., Yang, Y., Zhang, Z., and Wu, H. (2013) *Mater. Chem. Phys.*, **141**, 310–317.
98. Wang, D., Li, Y., Wang, Q., and Wang, T. (2012) *J. Solid State Electrochem.*, **16**, 2095–2102.
99. Shou, Q., Cheng, J., Zhang, L., Nelson, B.J., and Zhang, X. (2012) *J. Solid State Chem.*, **185**, 191–197.
100. Wang, B., Guan, D., Gao, Z., Wang, J., Li, Z., Yang, W., and Liu, L. (2013) *Mater. Chem. Phys.*, **141**, 1–8.
101. Lim, S.P., Huang, N.M., and Lim, H.N. (2013) *Ceram. Int.*, **39**, 6647–6655.
102. Zhang, Y., Li, H., Pan, L., Lu, T., and Sun, Z. (2009) *J. Electroanal. Chem.*, **634**, 68–71.
103. Lu, T., Zhang, Y., Li, H., Pan, L., Li, Y., and Sun, Z. (2010) *Electrochim. Acta*, **55**, 4170–4173.
104. Ramadoss, A. and Kim, S.J. (2013) *Carbon*, **63**, 434–445.
105. Qiu, Y., Yan, K., Yang, S., Jin, L., Deng, H., and Li, W. (2010) *ACS Nano*, **4**, 6515–6526.
106. Pendashteh, A., Mousavi, M.F., and Rahmanifar, M.S. (2013) *Electrochim. Acta*, **88**, 347–357.
107. Liu, Y., Ying, Y., Mao, Y., Gu, L., Wang, Y., and Peng, X. (2013) *Nanoscale*, **5**, 9134–9140.
108. Wu, Q., Xu, Y., Yao, Z., Liu, A., and Shi, G. (2010) *ACS Nano*, **4**, 1963–1970.
109. Bai, H., Li, C., Wang, X., and Shi, G. (2010) *Chem. Commun.*, **46**, 2376–2378.
110. Sarker, A.K. and Hong, J.-D. (2012) *Langmuir*, **28**, 12637–12646.
111. Liu, J., An, J., Zhou, Y., Ma, Y., Li, M., Yu, M., and Li, S. (2012) *ACS Appl. Mater. Interfaces*, **4**, 2870–2876.
112. Wang, H., Hao, Q., Yang, X., Lu, L., and Wang, X. (2009) *Electrochem. Commun.*, **11**, 1158–1161.
113. Yan, J., Wei, T., Shao, B., Fan, Z., Qian, W., Zhang, M., and Wei, F. (2010) *Carbon*, **48**, 487–493.
114. Murugan, A.V., Muraliganth, T., and Manthiram, A. (2009) *Chem. Mater.*, **21**, 5004–5006.
115. Wang, H., Hao, Q., Yang, X., Lu, L., and Wang, X. (2010) *ACS Appl. Mater. Interfaces*, **2**, 821–828.

116. Yan, J., Wei, T., Fan, Z., Qian, W., Zhang, M., Shen, X., and Wei, F. (2010) *J. Power Sources*, **195**, 3041–3045.

117. Zhang, L.L., Zhao, S., Tian, X.N., and Zhao, X.S. (2010) *Langmuir*, **26**, 17624–17628.

118. Wang, H., Hao, Q., Yang, X., Lu, L., and Wang, X. (2010) *Nanoscale*, **2**, 2164–2170.

119. Zhang, K., Zhang, L.L., Zhao, X.S., and Wu, J. (2010) *Chem. Mater.*, **22**, 1392–1401.

120. Mao, L., Zhang, K., Chan, H.S.O., and Wu, J. (2012) *J. Mater. Chem.*, **22**, 80–85.

121. Sathish, M., Mitani, S., Tomai, T., and Honma, I. (2011) *J. Mater. Chem.*, **21**, 16216–16222.

122. Xu, J., Wang, K., Zu, S.-Z., Han, B.-H., and Wei, Z. (2010) *ACS Nano*, **4**, 5019–5026.

123. Wang, K., Huang, J., and Wei, Z. (2010) *J. Phys. Chem. C*, **114**, 8062–8067.

124. Huang, J., Wang, K., and Wei, Z. (2010) *J. Mater. Chem.*, **20**, 1117–1121.

125. Wang, D.-W., Li, F., Zhao, J., Ren, W., Chen, Z.-G., Tan, J., Wu, Z.-S., Gentle, I., Lu, G.Q., and Cheng, H.-M. (2009) *ACS Nano*, **3**, 1745–1752.

126. Feng, X.-M., Li, R.-M., Ma, Y.-W., Chen, R.-F., Shi, N.-E., Fan, Q.-L., and Huang, W. (2011) *Adv. Funct. Mater.*, **21**, 2989–2996.

127. Gao, Z., Yang, W., Wang, J., Yan, H., Yao, Y., Ma, J., Wang, B., Zhang, M., and Liu, L. (2013) *Electrochim. Acta*, **91**, 185–194.

128. Xu, B., Yue, S., Sui, Z., Zhang, X., Hou, S., Cao, G., and Yang, Y. (2011) *Energy Environ. Sci.*, **4**, 2826–2830.

129. Zhang, Q., Li, Y., Feng, Y., and Feng, W. (2013) *Electrochim. Acta*, **90**, 95–100.

130. Yu, G., Hu, L., Liu, N., Wang, H., Vosgueritchian, M., Yang, Y., Cui, Y., and Bao, Z. (2011) *Nano Lett.*, **11**, 4438–4442.

131. Li, S., Wu, D., Cheng, C., Wang, J., Zhang, F., Su, Y., and Feng, X. (2013) *Angew. Chem. Int. Ed.*, **52**, 12105–12109.

6
Graphene for Supercapacitors

Richa Agrawal, Chunhui Chen, Yong Hao, Yin Song, and Chunlei Wang

6.1
Introduction

In recent years, there has been an upsurge in scientific interest of using carbon and its derivatives in a host of fields including physical, chemical, and biological sciences. Graphene, the one-atom-thick sheet (2D) of sp^2-hybridized carbon atoms arranged in a hexagonal manner, in principle is the building block of some of the most important graphitic carbon materials of all the other dimensionalities including graphite (3D), carbon nanotubes (CNTs) (1D), and fullerenes (0D). Figure 6.1 illustrates how graphene is the mother of all graphitic carbon forms [1]. Owing to its unique structure and outstanding properties, graphene has held a star status in the scientific community ever since its discovery. Graphene is known to have extraordinary electrical and thermal conductivities, very high mechanical strength [2, 3], and a very high theoretical specific surface area (SSA) ($> 2600\,m^2\,g^{-1}$). These excellent properties of graphene make it a promising candidate for a host of applications, including energy storage [4–6], electronics [7], composites [8], biotechnology [9], and so on. High electrical conductivity, excellent mechanical strength, and high theoretical surface area make this material particularly suitable for its applicability in energy storage devices as functional electrode material either by itself or in conjunction with other materials.

6.1.1
Electrochemical Capacitors

Electrochemical capacitors (ECs), often called as *ultracapacitors* or *supercapacitors*, are a class of energy storage devices that bridge the gap between conventional electrolytic capacitors and batteries. Hereafter, the words ECs, supercapacitors, and ultracapacitors will be used interchangeably in this chapter. These capacitors are characterized by high specific energy, long cycle life, and high specific power. These devices have higher power densities than batteries and have higher energy

Graphene-based Energy Devices, First Edition. Edited by A. Rashid bin Mohd Yusoff.
© 2015 Wiley-VCH Verlag GmbH & Co. KGaA. Published 2015 by Wiley-VCH Verlag GmbH & Co. KGaA.

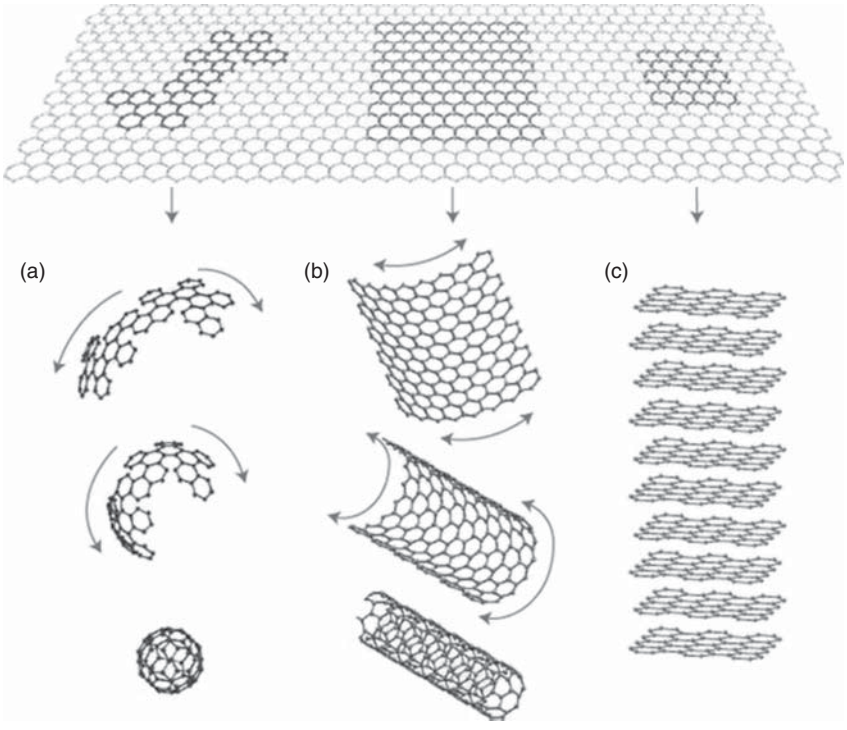

Figure 6.1 Graphene is the mother of all graphitic forms. This 2D carbon sheet can be wrapped up into (a) 0D buckyballs, (b) rolled into 1D carbon nanotubes, or (c) stacked into 3D graphite [1].

densities than conventional capacitors. Figure 6.2 depicts the special positioning of ECs in the power-specific energy plot, also known as the *Ragone plot*.

6.1.1.1 Fundamentals of a Capacitor

A typical capacitor is a passive component that stores energy electrostatically. Unlike batteries, which are active components and supply energy in chemical form, capacitors store energy in an electrostatic field. A parallel plate capacitor comprises two parallel electrodes separated by a dielectric. Upon the application of an external electric potential, the electrodes accumulate opposite charges, which generates an electric field, aiding in the storage of energy in a capacitor. The capacitance (C) of a capacitor is given as the ratio of charge on each electrode (Q) to the potential difference between them (V):

$$C = \frac{Q}{V} \tag{6.1}$$

where C is given by

$$C = \frac{\varepsilon_0 \varepsilon_r A}{D} \tag{6.2}$$

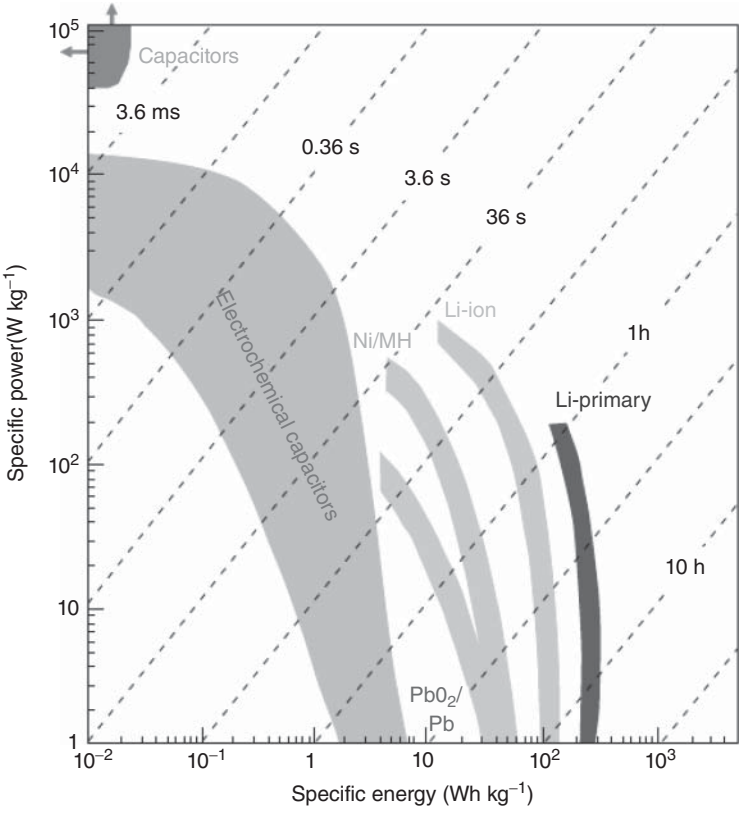

Figure 6.2 Ragone plot for different energy devices. It can be seen that electrochemical capacitors bridge the gap between conventional capacitors and batteries, with intermediate time constants [10].

where ε_0 is the electric permittivity of free space, ε_r is the relative permittivity, A is the area of the electrodes, and D is the distance between the electrodes. As evident from the equation, capacitance is governed by the nature of the dielectric, area of the plates, and the distance between the electrodes.

The primary electrochemical characteristics of any energy storage device are its energy density and power density, both of which can be expressed per unit mass (per kilogram), per unit area, or per unit volume. The energy of a capacitor is given by

$$E = \frac{1}{2}CV^2 \tag{6.3}$$

where the symbols have their usual meanings.

Power, in general, is the measure of the rate of energy delivery, that is, energy per unit time. However, the maximum power delivered by a capacitor is limited by the internal resistance of the system, also known as the *equivalent series resistance*

(*ESR*).

$$P_{\max} = \frac{V^2}{4\mathrm{ESR}} \tag{6.4}$$

As is evident from Equation 6.4, power is an inverse function of the resistance of the system – the lower the resistance, the higher the power delivered by the system. ESR can be measured as the voltage drop introduced in the discharging part of the charge/discharge curves of the system, and hence decreases the maximum voltage of a capacitor during discharge, thereby limiting the maximum power of the system. However, this is the maximum power, and, in general, the peak power in an actual system is lower than $P_{\max}$.

6.1.1.2 Classification of Electrochemical Capacitors

ECs store energy in the form of charge at the electrode/electrolyte interface of materials with high surface area. Depending on the charge storage mechanism, ECs are subdivided into (i) electrochemical double-layer capacitors (EDLCs) and (ii) pseudocapacitors. A third category, the so-called "hybrid ECs" essentially combines both EDLCs and pseudocapacitors. EDLCs, just like traditional capacitors, store charge electrostatically. Charges are stored at the electrode/electrolyte interface and the capacitance is governed by the thickness of the double layer, also known as the *Helmholtz double layer*. Upon the application of a voltage, charge accumulates on the electrode surface. This charge buildup leads to the diffusion of opposite charges across the separator, leading to the creation of a double layer on each electrode. The presence of this double layer, along with high surface electrodes and smaller distances between the electrodes, enables EDLCs to have higher energy densities than conventional capacitors. Since these capacitors are governed by non-faradaic processes, charge storage in EDLCs is highly reversible, allowing them to achieve virtually endless cycle lives. However, since the cycle life is a result of various other factors, such as electrode stability in the electrode, adhesion of the active material with the substrate, and so on, these capacitors can reach a very high number of cycles, if not endless ($\sim 10^6$), much higher than that of conventional batteries which operate on redox processes. Common EDLC materials include activated carbons (ACs), carbon aerogels, carbon nanostructures including a host of morphologies such as CNTs, onion like carbons (OLCs), carbon nanowires (CNWs), carbon nanorods, fullerenes, and graphene.

In contrast to conventional capacitors and EDLCs, pseudocapacitors store charge in a faradaic manner; or, in other words, the capacitance in this kind of capacitors arises from the transfer of charge between the electrode and electrolyte. This charge transfer is highly reversible and fast, and as a result the charging and discharging curves of these devices look like those of a typical capacitor. The latter is referred to as *pseudo* because of the reversible faradaic-type charging and discharging. Owing to a faradaic mechanism of charge storage, these capacitors in general exhibit higher specific energies and capacitances than their EDLC counterparts. Detailed mechanisms and explanations are subject of other works [11, 12]. The most widely used pseudocapacitive materials include metal

oxides (MOs) (mostly ruthenium oxide, manganese oxide, and nickel hydroxide), conducting polymers (CPs) including polyaniline (PANI), polypyrrole (PPy), polythiophene (PTH), and their derivatives.

6.1.2 Graphene as a Supercapacitor Material

Although pseudocapacitive materials exhibit higher capacity and capacitances than EDLC materials, their inherent poor electrical conductivity restricts facile electron transport and thereby lowers their power density. Moreover, redox reactions lead to poor cycling and poor robustness of the structure of the electrodes made from such materials, and all these shortcomings restrict the applications of pseudocapacitive materials in pristine forms as EC materials. The addition of carbon-based materials enables facile electron transport due to increased electrical conductivity, but also the known phenomenal mechanical properties of carbon nanostructures add to the mechanical stability of these pseudocapacitive materials. Graphene, known for its outstanding electrical and mechanical properties, is the perfect additive to prepare composite pseudocapacitor electrodes. And, hence, not only is graphene an excellent EDLC material but also an excellent alternative as a conductive additive in pseudocapacitors. Excellent review articles have been written on the use of graphene as a supercapacitor material [13–16]. Figure 6.3 shows the increasing trend in the use of graphene as a supercapacitor electrode material over recent years.

For supercapacitors, graphene can be synthesized in several ways: (i) mechanical exfoliation of graphite. Geim's group [17], for instance, used a regular scotch tape to extract thin layers of graphite from highly oriented pyrolytic graphite (HOPG); (ii) epitaxial growth on SiC wafer [18]; (iii) gas-phase synthesis by chemical vapor deposition (CVD) on catalytic metal substrates such as Ni [19] or Cu [20]; and (iv) solution-based exfoliation of graphene oxide (GO) [21], in which graphite powders are first oxidized to form graphite oxide usually by the so-called Hummer's method. This graphite oxide is then exfoliated in water. The resulting

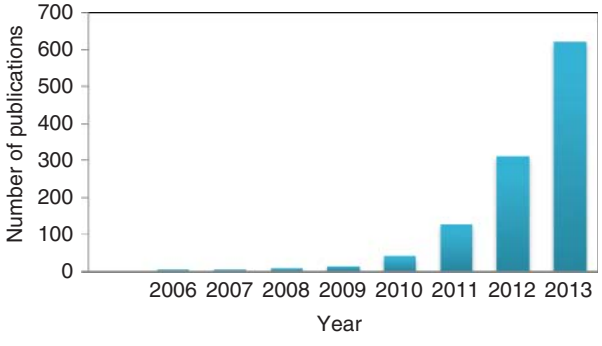

Figure 6.3 Trend for graphene-based supercapacitors over a range of years (2006–2013, Source – Web of Science).

solution is then reduced either chemically or thermally and the final product is usually designated as *reduced graphene oxide* (rGO) because of the presence of remnant oxygen-containing functional groups. This is perhaps the most widely used method for graphene synthesis owing to the ease of production and cost effectiveness. Additionally, graphene synthesized by this method is desirable for supercapacitor applications because of the presence of oxygen-containing functional groups. These groups not only lend a net pseudocapacitance to the graphene but also allow easy chemical modification because these groups act as defect sites.

6.2
Electrode Materials for Graphene-Based Capacitors

6.2.1
Double-Layer Capacitance-Based Graphene Electrode Materials

This section discusses the use of graphene-based materials for EDLCs. The resulting capacitance is predominantly double-layer capacitance.

6.2.1.1 Electrodes Based on Graphene Synthesized by Reduction of Graphene Oxide

One of the methods for synthesizing rGO is the chemical reduction of GO. This can be done by using reducing agents such as hydrazine hydrate, hydrobromic acid, glutathione (GSH), and so on. One of the benefits of using rGO instead of graphene is that the remnant oxygen and hydroxyl groups not only induce pseudocapacitive effects but also promote hydrophilicity of the otherwise hydrophobic graphene. Stankovich *et al* [22] proposed the chemical reduction of GO sheets suspended in water with hydrazine hydrate; such reduction led to the aggregation and formation of a carbon material, which they called *chemically modified graphene* (CMG), and since then hydrazine hydrate has been one of the most widely used reducing agents for GO. Later Stoller *et al* [23] explored chemically modified graphene as a supercapacitor electrode material. The resultant CMG yielded specific capacitances of 135 and 99 $F\,g^{-1}$ in aqueous and organic electrolytes, respectively. Chen *et al.* [24] prepared rGO-based supercapacitors using hydrobromic acid (HBr) as the reducing agent and tested them in a two-electrode system with liquid ionic electrolytes, namely 1-butyl-3-methylimidazolium hexafluorophosphate ($BMIPF_6$) and 1-butyl-3-methylimidazolium tetrafluoroborate ($BMIMBF_4$). The electrodes showed a higher specific capacitance of 74 $F\,g^{-1}$ at 10 $mV\,s^{-1}$ in $BMIMBF_4$ but a lower capacitance of 45 $F\,g^{-1}$ in $BMIPF_6$. However, the energy density was substantially higher in the latter owing to its wider voltage window. HBr is a mild reducing agent, as a result of which oxygen-containing functional groups were present. These oxygen groups give the graphene sheets a pseudocapacitive element, which increases the capacitance. Zhang *et al.* [25] used GSH in its reduced form as the reducing agent for GO suspension in water and achieved a specific capacitance of 238 $F\,g^{-1}$ at 0.1 $A\,g^{-1}$ and 140 $F\,g^{-1}$ at 5 $A\,g^{-1}$ in

Table 6.1 Graphene-based EDLCs prepared through reduction of graphene oxide.

Reducing agent	Electrolyte	Specific capacitance/ performance	Cyclability	References
Hydrazine hydrate	5.5 KOH (aqueous)	135 F g^{-1} for a discharge of 10 mA (aqueous)	—	Stoller *et al.* [23]
	$TEABF_4$/AC	99 F g^{-1} for a discharge of 10 mA (organic)		
Hydrobromic acid (HBr)	$BMIPF_6$	45 F g^{-1} at 10 mV s^{-1} in $BMIPF_6$	141% after 3000 cycles	Chen *et al.* [24]
	$BMIBF_4$	74 F g^{-1} at 10 mV s^{-1} in $BMIBF_4$		
Glutathione (GSH)	1 M H_2SO_4	238 F g^{-1} at 0.1 A g^{-1}	97% of the initial value after 1000 cycles	Zhang *et al.* [25]
		140 F g^{-1} at 5 A g^{-1}		
Hydrobromic acid	1 M H_2SO_4	348 F g^{-1} at 0.2 A g^{-1}	~120% after 3000 cycles	Chen *et al.* [26]
Hydrazine hydrate (gas based reduction)	30 wt% aq. KOH	205 F g^{-1} at 1 V	90% after 1200 cycles	Wang *et al.* [27]
		Power density of 10 kW kg^{-1} at the energy density of 28.5 Wh kg^{-1}		

1 M H_2SO_4 electrolyte. Moreover, a capacitive retention of 97% was achieved after 1000 cycles. Table 6.1 summarizes some of the works that have reported chemically reduced graphene oxide as electrode material for supercapacitors.

6.2.1.2 Activated-Graphene-Based Electrodes

Since capacitance is directly proportional to the area of the electrodes, increasing the surface area of the electrodes is highly crucial for improving the performance of the EC. One of the routes to increasing the accessible surface area for the electrolyte ions is through the creation of porous sites. Activation processes have been carried out extensively to create accessible pores and hence obtain a high-surface-area porous electrode structure. One of the most common activation routes for carbon-based materials is electrochemical activation. During this process, the initial carbon component with a smaller surface area develops pores and thereby achieves a much larger surface area. This enhancement in the surface area further leads to an increase in the double-layer capacitance.

Hantel *et al.* [28] synthesized partially reduced graphite oxide (GOpr) through electrochemical activation. The brunauer-Emmett-teller (BET) surface area of GOpr upon activation increased from 5 to 2687 m^2 g^{-1}. The latter value was

calculated assuming no pseudocapacitive contribution and results obtained for basal planes of graphite. As a result of this high SSA, the material delivered a high specific capacitance of 220 F g^{-1} at a scan rate of 1 mV s^{-1} in 1 M Et_4NBF_4 in acetonitrile electrolyte.

Apart from electrochemical activation, chemical treatment of graphene with KOH is another popular method to activate graphene or graphene-based composites. Chen *et al.* [29] prepared chemically activated graphene-activated carbon (GAC) composite. Upon activation, a surface area of 798 m^2 g^{-1} was achieved. The composite showed a capacitance of 122 F g^{-1} at 0.1 A g^{-1} in KOH electrolyte. Significantly, Zhu *et al.* [30] synthesized KOH-activated microwave-exfoliated graphene oxide (MEGO) and thermally exfoliated graphene oxide (TEGO) and achieved surface areas as high as 3100 m^2 g^{-1}. The MEGO powders were prepared by the irradiation of microwaves onto GO, followed by chemical treatment with KOH. The solutions were then filtered and dried, followed by heat treatment in an argon environment at 800 °C, at 400 Torr for 1 h. It was shown that chemical activation etched the MEGO surface, creating a continuous 3D network of minute pores in the range of ~1–10 nm. CV tests run in a two-electrode setup in $BMIMBF_4$/AN electrolyte showed typical rectangular curves, and charge/discharge curves showed specific capacitances of 165, 166, and 166 F g^{-1} at 1.4, 2.8, and 5.7 A g^{-1}, respectively. Furthermore, the low voltage drop in the charge/discharge curves was indicative of a low ESR of the system. Energy and power densities in $BMIMBF_4$/AN were calculated to be ~70 Wh kg^{-1} and ~250 kW kg^{-1} at 5.7 A g^{-1}, respectively. Moreover, a capacitive retention of 97% was achieved after 10 000 cycles at 2.5 A g^{-1}. This groundbreaking work thus demonstrated that simple KOH activation can be scaled up for the production of activated-graphene-based materials in a short span of time. Table 6.2 summarizes some of the studies that have reported on activated-graphene-based EDLC materials as supercapacitor electrodes.

Table 6.2 Activated-graphene-based EDLC materials.

Activation method	Electrolyte	Specific capacitance/ performance	Cyclability	References
Electrochemical activation	1 M Et_4NB_4 in acetonitrile	220 F g^{-1} at 1 mV s^{-1}		Hantel *et al.* [28]
Chemical activation using KOH	KOH	122 F g^{-1} at 0.1 A g^{-1} in KOH electrolyte	90% after 3000 cycles for KOH	Chen *et al.* [29]
Chemical activation of microwave-exfoliated graphite oxide using KOH	$BMIMBF_4$/AN	165, 166, and 166 F g^{-1} at 1.4, 2.8, and 5.7 A g^{-1}, respectively	97% of the initial value after 10 000 cycles	Zhu *et al.* [30]

6.2.1.3 Graphene and Other Carbon Nanostructure Composite Electrodes

Graphene, although packed with phenomenal properties, has a tendency to restack, and this restacking makes it almost impossible to fully exploit the benefits of the 2D graphene. One route to prevent this restacking of graphene sheets is the incorporation of "spacers" into the graphene layers, which can prevent graphene sheet stacking and help in increasing the usable surface area. Carbon nanostructures or derivatives, such as CNTs, mesoporous carbon spheres, and so on, have all been used as spacers. It should be noted that the "spacers" are not limited to carbon nanostructures: for instance other materials such as platinum nanoparticles [31], different surfactants [32], diethylene glycol [33], zinc oxide particles [34], and so on, can also serve this purpose.

Several studies have reported the use of graphene and CNT composites for supercapacitor electrodes. While both graphene and CNTs possess extraordinary properties, both these materials have a tendency to agglomerate. Therefore, it is imperative to thoroughly disperse these materials in order to fully exploit the benefits from each. Cheng *et al.* [35] synthesized graphene/single-walled carbon nanotube (SWCNT) composite films through a "blending" process and reported specific capacitances of 290.4 and 201 $F\,g^{-1}$ in aqueous and organic electrolytes, respectively. An increase of 23% in energy density and 31% in power density was noted after the addition of CNTs as compared to the pristine graphene electrodes. Moreover, an enhancement of 29% was seen in the specific capacitance after 1000 cycles when tested in an ionic liquid electrolyte. Jung *et al.* [36] synthesized graphene/CNT composites for supercapacitor applications through amide bonding. It was seen that the CNTs attached onto the edges and on the surface of graphene, which served a dual purpose: first, the CNTs inhibited the restacking of graphene; and, second, they increased the overall capacitance. The electrodes exhibited a phenomenal volumetric capacitance of 165 $F\,cm^{-3}$. This high capacitance was attributed to the enlarged interlayer spacing of up to 0.55 nm. In another study, Wang *et al.* [37] fabricated 3D few-layer graphene and multiwalled carbon nanotube (MWCNT) composites on nickel foam through a one-step ambient pressure CVD technique. The hybrid structures possessed a high SSA of 743 $m^2\,g^{-1}$, with specific capacitance, energy density, and power density of 283 $F\,g^{-1}$, 39.72 $Wh\,kg^{-1}$, and 154.67 $kW\,kg^{-1}$, respectively. Quite remarkably, the capacitance retention for the composites was reported to be 99.34% after 85 000 cycles, which proves the high stability of the electrodes. In yet another work, Yu *et al.* [38] prepared polymer-modified graphene sheets via *in situ* reduction of exfoliated graphite oxide in the presence of cationic poly(ethyleneimine) (PEI). These polymer-treated graphene sheets were then used for self-assembly with acid-oxidized MWCNTs. The resultant hybrid films showed an interconnected network of carbon structures and exhibited a specific capacitance of 120 $F\,g^{-1}$ at a high scan rate of 1 $V\,s^{-1}$.

Other carbon derivatives such as carbon black (CB) have also been employed as spacers to prevent graphene agglomeration. Yan *et al.* [39] fabricated graphene and CB composites through sonication and reduction of GO. CB particles acted as spacers and prevented the restacking on graphene sheets, thereby enhancing

the electrolyte ion accessibility to the individual graphene sheets. It was seen that the CB particles were mostly adhered to the edge surface of the graphene sheets and hence enhanced the capacitance of the system. At a scan rate of 10 mV s^{-1}, the composite exhibited a specific capacitance of 175 F g^{-1} and retained 90.9% of the initial capacitance even after 6000 cycles. This remarkable capacity retention was attributed to the capacitance arising predominantly from double-layer effects as well as minimal pseudocapacitive effects. Ma *et al.* [40] synthesized sugar-derived carbon/graphene composite materials by ultrasonication and calcination. The sugar-derived carbon nanoparticles thereby acted as spacers and prevented graphene from restacking. The composites yielded a high specific capacitance of 273 F g^{-1} at a current density of 0.5 A g^{-1} in a 6 M KOH electrolyte, in addition to a much enhanced cyclic performance as compared to typical pristine graphene nanosheets (GNSs). Table 6.3 summarizes some of the literature relating to the use of graphene and other carbon derivative composites as supercapacitor electrode materials. Figure 6.4 shows the morphologies and electrochemical performances of graphene-based EDLC materials from some of the works [24–26, 37, 40].

6.2.1.4 Nitrogen-Doped-Graphene-Based Electrodes

For certain applications, the presence of heteroatoms in the graphene lattice leads to the improvement of the device performance. This modification allows the tailoring of both the chemical and electronic properties of graphene. For instance, the addition of oxygen groups adds pseudocapacitive effects to the otherwise pure double-layer capacitance of graphene and hence enhances the overall capacitance. Similarly, the addition of nitrogen to graphene has shown significant promise in the improvement of biocompatibility of carbon devices in biosensing and the enhancement in the performance of graphene-based supercapacitors.

Several studies have been conducted on the synthesis and usage of N-enriched graphene-based materials as supercapacitor electrodes. Nolan *et al.* [44], synthesized nitrogen-doped reduced graphene oxide (N-rGO) via ammonia plasma treatment of GO. They utilized the N-rGO without the addition of any binders or supplemental conductivity enhancers and spray-coated the N-rGO as the active material onto indium tin oxide (ITO)/glass substrates. Through a series of investigation in the three-electrode setup, they concluded that the addition of nitrogen lent pseudocapacitance to the system. Jiang *et al.* [45] prepared N-doped graphene through an ammonia-assisted hydrothermal method, in which the reduction of GO and N-doping took place simultaneously. A maximum N-doping level of 7.2% was reported, and studies revealed that the oxygen content went down to 8.5% in N-doped graphene from 34.8% in GO. A maximum capacitance of 144.6 F g^{-1} was reported along with excellent long-term cycling and stability. While most of these studies used ammonia as the precursor for N-doping, Sun *et al.* [46] reported nitrogen-enriched graphene preparation via a one-step hydrothermal reaction between GO and urea. The resultant N-doped graphene nanosheets (NGSs) had nitrogen content as high as 10.13 at.%. The NGS exhibited excellent electrochemical performance with a very high capacitance of 326 F g^{-1}

Table 6.3 Graphene and other carbon-based material composites for supercapacitors.

Composite	Electrolyte	Performance	Capacitance retention	References
Graphene/SWCNT	1 M KCl (aqueous), 1 M $TEABF_4$/PC (organic)	290.4 F g^{-1} in aqueous 201 F g^{-1} in organic	Increase in capacitance by 29% after 1000 cycles in ionic liquid	Cheng *et al.* [35]
Reduced graphene oxide/carbon nanotubes	1 M $TEABF_4$ in propylene carbonate (PC)	Very high volumetric capacitance of 165 F cm^{-3} High energy density of 34.3 Wh kg^{-1} at 400 W kg^{-1}	N/A	Jung *et al.* [36]
Few layer graphene/multi-walled carbon nanotubes	6 M KOH	A high capacitance of 286 F g^{-1} Energy density of 39.72 Wh kg^{-1} Power density of 154.67 kW kg^{-1}	99.34% after 85 000 cycles	Wang *et al.* [37]
Graphene/carbon black	6 M KOH	175 F g^{-1} at 10 mV s^{-1} 118 F g^{-1} at 500 mV s^{-1}	90.9% after 6000 cycles	Yan *et al.* [39]
Sugar-derived carbon/graphene	6 M KOH	273 F g^{-1} at 0.5 A g^{-1} 209 F g^{-1} at 10 A g^{-1}	5% drop after 400 cycles, stable capacitance with slight increase after 2000 cycles	Ma *et al.* [40]
Graphene oxide (GO)/carbon nanotubes (CNT)	1 M H_2SO_4	74–119 F g^{-1} depending upon the concentration of GO and CNT at 1 mV s^{-1}	For 1 : 1 GO and CNT concentration capacitance decreases from 111 to 98 F g^{-1} after 400 cycles	Li *et al.* [41]
Reduced graphene oxide/carbon nanotubes	1 M H_2SO_4	90 F g^{-1} at 100 A g^{-1}	N/A	Qiu *et al.* [42]
Graphene/multiwalled carbon nanotubes	6 M KOH	265 F g^{-1} at 0.1 A g^{-1}	97% after 2000 cycles	Lu *et al.* [43]

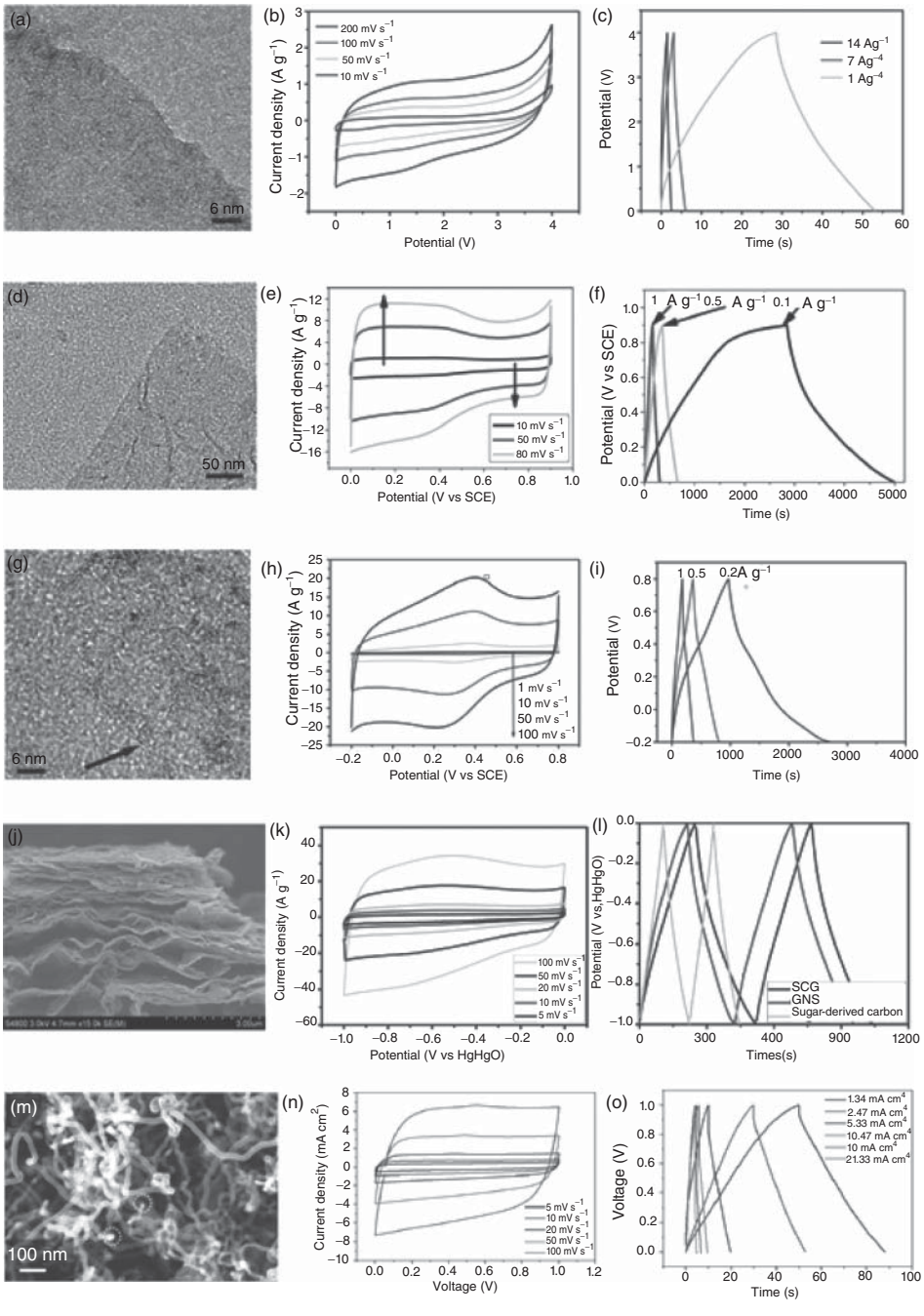
(a)
6 nm
(b)
200 mV s−1
100 mV s−1
50 mV s−1
10 mV s−1
Current density (A g−1)
Potential (V)
(c)
14 Ag−1
7 Ag−4
1 Ag−4
Potential (V)
Time (s)
(d)
50 nm
(e)
10 mV s−1
50 mV s−1
80 mV s−1
Current density (A g−1)
Potential (V vs SCE)
(f)
1 A g−1 0.5 A g−1 0.1 A g−1
Potential (V vs SCE)
Time (s)
(g)
6 nm
(h)
1 mV s−1
10 mV s−1
50 mV s−1
100 mV s−1
Current density (A g−1)
Potential (V vs SCE)
(i)
1 0.5 0.2A g−1
Potential (V)
Time (s)
(j)
(k)
100 mV s−1
50 mV s−1
20 mV s−1
10 mV s−1
5 mV s−1
Current density (A g−1)
Potential (V vs HgHgO)
(l)
SCG
GNS
Sugar-derived carbon
Potential (V vs.HgHgO)
Times(s)
(m)
100 nm
(n)
5 mV s−1
10 mV s−1
20 mV s−1
50 mV s−1
100 mV s−1
Current density (mA cm−2)
Voltage (V)
(o)
1.34 mA cm−2
2.47 mA cm−2
5.33 mA cm−2
10.47 mA cm−2
10 mA cm−2
21.33 mA cm−2
Voltage (V)
Time (s)

at a current density of 0.2 A g^{-1} and an outstanding capacitive retention of 99.58% after 2000 cycles.

6.2.2 Graphene/Pseudocapacitive Material Composite Based Electrode Materials

As mentioned earlier, pseudocapacitors exhibit rather high capacitance, but since these devices depend primarily on redox processes, they have lower cycle lives than double-layer capacitors; however, hybrid electrodes can benefit from the higher capacitances of pseudocapacitors and long cycle lives of double-layer capacitors. The most investigated pseudocapacitive materials are PANI, PPy, and polythiophene (PTP) as well as their derivatives.

6.2.2.1 Graphene/Conducting Polymer Composite Electrodes

CPs get their name because of their ability to conduct electricity. CPs such as PANI, PPy, polythiophene (PTH), and their derivatives are some of the most investigated pseudocapacitive materials. Upon oxidation, the electrolyte ions are transferred to the polymer chain, and, upon reduction, the ions detach from the chain and get released into the electrolyte, this is shown in Equation 6.5. This ion transfer takes place through the bulk of the electrodes, as a result of which the resultant specific capacitance is quite high.

$$[PPy^{+}X^{-}] + e^{-} \leftrightarrow [PPy] + X^{-} \tag{6.5}$$

However, this insertion/deinsertion leads to volumetric changes in the electrodes, which results in degradation because of swelling, shrinking, and so on, leading to a loss in the conductivity and mechanical stability. Therefore, CPs can benefit from carbon-based materials which have high mechanical strength and resilience. These carbons can act as a buffer and alleviate the stresses resulting from the volumetric changes; moreover, the addition of carbons can add to the electrical conductivity and also enhance the power capability of the device [47, 48]. Carbon fibers, CNTs, and ACs have all been employed, and graphene is the newest addition to the carbon family for this purpose.

Figure 6.4 (a–c) High-resolution transmission electron microscope (HRTEM) images of rGO, CV, and galvanostatic charge/discharge plots of rGO electrodes in $BMIPF_6$ [24]. (d–f) Transmission electron microscope (TEM) image of GG (graphene nanosheets), CV, and galvanostatic charge/discharge curves of GG in 1 M H_2SO_4 [25]. (g–i) HRTEM image of rGO, CV of the rGO electrode at different scan rates, and galvanostatic charge/discharge curves at different current densities of the rGO electrode in aqueous system [26]. (j–l) Morphology of the sugar-derived carbon/graphene (SCG), composites CV curves at different scan rates of the SCG electrodes, and a comparison of charge/discharge curves of SCG, graphene (GNS), and sugar-derived carbon electrodes [40]. (m–o) Morphology of 3-D few-layer graphene/MWCNT/NF structures, CV plots for different scan rates, and charge/discharge curves for different current densities [37].

Graphene/Polyaniline (PANI) Composites PANI is one of the most widely studied CPs because of its ease of preparation, good electronic conductivity, high specific capacitance, and environmental benignity. Tong *et al.* [49] prepared graphene/PANI composites by *in situ* polymerization of aniline monomer in a graphene dispersion under acidic environment followed by an electrophoretic deposition. It was seen that PANI showed a preferential growth on the graphene sheet surface because of the conformation of aniline molecules on graphene sheets via electrostatic, $\pi-\pi$ stacking, and hydrogen bonding. The composite exhibited a specific capacitance of 384 F g^{-1} at 0.5 A g^{-1} and a capacitive retention of 84% after 1000 cycles. Wu and coworkers [50] prepared graphene/PANI composites by the *in situ* polymerization of aniline in the presence of GO under acidic conditions, whereafter the GO was reduced by hydrazine. The resultant CMG and PANI composites exhibited specific capacitances as high as 480 F g^{-1} at 0.1 A g^{-1}. Furthermore, Wu's group [51] prepared graphene/PANI nanofiber composites by carrying out *in situ* polymerization of aniline in the presence of surfactants (tetrabutylammonium hydroxide and sodium dodecyl benzenesulfonate). It was seen that the presence of surfactants enhanced the dispersion of graphene within the polymer matrix, and a high capacitance of 526 F g^{-1} was achieved at a current density of 0.2 A g^{-1} along with good cyclability. Wang *et al.* [52] reported a high-performance electrode material based on "fibrillar" PANI doped with GO. The PANI grown on GO sheets exhibited fibril-like morphology as opposed to the granular structure of pristine PANI. The composite exhibited an enhanced conductivity, achieving a high specific capacitance of 531 F g^{-1} in the potential range 0–0.45 V for a current density of 0.2 A g^{-1}. Additionally, Wang's group [53] synthesized a sulfonated graphene/PANI nanocomposite which exhibited a specific capacitance of 763 F g^{-1} with a capacitance retention of 96% post 100 cycles. Hu *et al.* [54] synthesized graphene/PANI composite films by carrying out *in situ* electrochemical polymerization on an ITO substrate in a reverse micelle electrolyte. The composites showed a good conductive network between PANI and graphene sheets and exhibited a very high capacitance of 878.57 F g^{-1} with a charge loading of 0.5 °C at a current density of 1 A g^{-1}. Wang *et al.* [55] fabricated a free-standing and flexible graphene/PANI composite paper via an *in situ* anodic electropolymerization of PANI film on graphene paper, which showed a large specific capacitance of 233 F g^{-1}, in addition to showing favorable mechanical strength. However, since the graphene paper was prepared by filtration, the SSA of graphene was highly suppressed. Feng *et al.* [56] reported a one-step method for the electrochemical synthesis of graphene/PANI composite films using GO and PANI as starting materials. They constructed both a biosensor and a supercapacitor based on the composite film. The supercapacitor exhibited a specific capacitance of 640 F g^{-1} with a capacitive retention of 90% after 1000 charge/discharge cycles.

Graphene/PPy Composites PPy is another widely studied conductive polymer owing to its high electrical conduction with high stability, water solubility of the pyrrole monomer, the ease of PPy synthesis, and cost effectiveness. Unlike PANI,

it shows good electrical activity in aprotic aqueous and nonaqueous electrolytes; however, in general, PPy exhibits lower specific capacitance than PANI. When combined with carbon materials, PPy shows the same synergism with EDLC materials as talked about earlier.

To improve the performance of PPy-based supercapacitors, Sahoo and coworkers [57] prepared graphene/PPy nanocomposites with different weight ratios of graphene by the *in situ* oxidative polymerization method and reported specific capacitance values as high as 409 F g^{-1}. Oliveira *et al.* [58] used an interfacial oxidative polymerization method to prepare functionalized graphene sheets and PPy composites for fabricating supercapacitors. The specific capacitance of these composite electrodes was measured to be 277.8 F g^{-1}. This was mainly due to the growth of p-type PPy on the surface of the negatively charged, carboxylate-functionalized graphene sheets. This synergism between functionalized graphene and PPy led to a higher energy storage capacity than the graphene-only or polymer-only films. Another feasible strategy to fabricate graphene/PPy composites is to start with GO instead of graphene sheets. GO is highly water soluble and can therefore be better dispersed in an aqueous, polymerizable monomer solution and can later be reduced to obtain an rGO/PPy composite. A flexible free-standing PPy/GO nanocomposite paper has been prepared in a one-step *in situ* chemical oxidation polymerization method [59]. In this system, the structural features of the nanocomposite were indicative of the $\pi-\pi$ electron stacking interaction between PPy and GO. The paper exhibited a specific capacitance of ~330 F g^{-1} at a scan rate of 100 mV s^{-1} and a capacitive retention of 91% after 700 cycles. Liu *et al.* [60] reported graphene/PPy composites prepared via *in situ* oxidative polymerization of pyrrole monomers in aqueous GO solutions, followed by chemical reduction using ethylene glycol (EG). The EG-rGO/PPy composite showed a high specific capacitance of over 420 F g^{-1} at a current density of 0.5 A g^{-1} and a capacitive retention of 93% after 200 cycles, as opposed to the pristine PPy which showed a capacitance of 200 F g^{-1} under the same testing conditions.

Davies *et al.* [61] fabricated flexible, uniform graphene/PPy composite films using pulsed electropolymerization and reported a high specific capacitance of 237 F g^{-1}. Si *et al.* [62] reported an environment-friendly, facile electrochemical strategy to prepare PPy/graphene nanocomposites by elctropolymerization followed by electrochemical reduction. The composite exhibited a high surface area of ~136.5 m^2 g^{-1}. Additionally, the electrochemically prepared hybrid material showed a high specific capacitance of 285 F g^{-1} at a discharge rate of 0.5 A g^{-1}, along with excellent cycling stability.

Graphene/Polyethylenedioxythiophene (PEDOT) Composites Polyethylenedioxythiophene (PEDOT) is a popular polythiophene derivative, which has high conductivity, a wide potential window (1.2–1.5 V), and good thermal and chemical stability and has been reported to undergo fast redox reactions. PEDOT has been used as an electrode material for supercapacitor applications in various electrolytic solutions [63–65]. However, compared to PANI and PPy, PEDOT has

been less investigated for composites with graphene materials as supercapacitor electrodes. Alvia *et al.* [66] synthesized a graphene/PEDOT nanocomposite using a chemical oxidative polymerization which showed a specific capacitance of 374 F g^{-1}. In their work, Zhang and Zhao [67] compared the electrochemical performances of graphene composites with PANI, PPy, and PEDOT. It was found that rGO/PANI, rGO/PPy, and rGO/PEDOT composites exhibited specific capacitances of 361, 248, and 108 F g^{-1}, respectively, at a current density of 0.3 A g^{-1}.

6.2.2.2 Graphene/Transition-Metal Oxide Composite Electrodes

Transition-metal oxides such as RuO_2, NiO_x, manganese oxides (MnO_2, Mn_3O_4), Fe_3O_4, and PbO_2 undergo fast, reversible redox reactions at their surfaces, which lend them a pseudocapacitive character. Since pseudocapacitors have higher specific capacitances in general than their EDLC counterparts, MOs exhibit higher specific energies, and therefore much research has been carried out in tailoring MOs to suit to the energy needs. However, since pseudocapacitance is a result of faradaic processes, MOs suffer from poor cycling and relatively shorter cycle longevity as compared to EDLCs. One of the methods to enhance the cyclability and shorter lifespans of MOs is the addition of EDLC materials. These MO/EDLC composites can be used either in the symmetric configuration or in the asymmetric configuration depending upon the energy needs.

The synergism between GO and MOs can be summarized as follows:

1) MOs suffer from poor electrical conductivity and hence can benefit from the excellent conductivity of graphene.
2) Graphene, although having a very large theoretical SSA, has a high tendency of agglomeration and restacking; the MO, on the other hand, can suppress this restacking by acting as "spacers" between the graphene sheets.
3) Graphene is an EDLC material and in principle has very high longevity in terms of cycling, and therefore can aid in improving the cycle life of the MO.

Graphene/Manganese Oxide Composites Among transition-metal oxides, manganese oxide is perhaps the most investigated pseudocapacitive material owing to its low cost, environmental benignity, and abundance. MnO_2 stores charge mainly through protonation and deprotonation in aqueous electrolytes, as per Equation 6.6:

$$MnO_2 + H^+ + e^- \leftrightarrow MnOOH \tag{6.6}$$

Equation 6.6 can be generalized as Equation 6.7 depending upon the electrolyte ion:

$$MnO_2 + X^+ + e^- \leftrightarrow MnOOX \tag{6.7}$$

These fast and reversible redox reactions give MnO_2 its pseudocapacitive character. However, MnO_2 prepared from traditional coprecipitation methods suffers from low specific capacitance owing to its low surface area [68], and since

pseudocapacitance arises because of surface adsorption of electrolyte ions, large surface area and pore size distribution are the key factors to realize the full potential of any pseudocapacitive material. While the surface area can be increased if nanostructured MnO_2 is used, the resultant structure in general is short-lived during electrochemical cycling and therefore leads to poor cycle life. Given the excellent mechanical and electrochemical stability of graphene, manganese oxides can therefore be combined with graphene in order to benefit from both these materials.

Zhao *et al.* [69] fabricated a MnO_2/graphene/nickel foam (MnO_2/EPD-G/NF) composite in which they deposited graphene on a nickel foam substrate electrophoretically followed by the electrodeposition of MnO_2 on EPD-G/NF. This composite yielded high specific capacitances of 476 and 216 F g^{-1} at current densities of 1 and 10 A g^{-1}, respectively in 0.5 M Na_2SO_4. In comparison, MnO_2/NF electrodes yielded a specific capacitance of only 357 and 114 F g^{-1} at 1 and 10 A g^{-1}, respectively, signifying that the better performance of the hybrid electrode was a result of the synergy between MnO_2 and graphene, where graphene helped to reduce the internal resistance of the MnO_2/NF electrode. Wang *et al.* [70] fabricated a graphene/MWCNT/MnO_2 nanowire composite which they referred to as a *GMM hybrid*. They deposited GM (graphene/MWCNT) structures on a nickel foam substrate through CVD. This GM foam had a high BET surface area of 497 m^2 g^{-1}. Upon the synthesis of this GM foam, α-MnO_2 nanowires (BET surface area of 22.28 m^2 g^{-1}) formed via hydrothermal synthesis were coated onto the GM foam. It was seen that, in the Graphene/MWCNT/MnO_2 (GMM) composite, the MnO_2 nanowires were homogeneously distributed and well attached to the graphene foam (GM). For an aqueous electrolyte of 2 M Li_2SO_4, the composite yielded an exceptional capacitance of 1108.79 F g^{-1} and a high power density of 799.84 kW kg^{-1}. Moreover, the composite exhibited a very high energy density of 391.7 Wh kg^{-1}, which is extraordinary for ECs. In addition, the composite showed excellent capacitance retention of 97.94% even after 13 000 cycles. In another work, Ge *et al.* [71] developed a low-cost "dip and dry" process to fabricate hierarchical graphene/MnO_2 nanostructured sponges using commercial sponges. First, macroporous commercially available sponges were cleaned with water and ethanol and cut into pieces 1 mm thick and dimensions 1 cm × 2 cm. The pieces were then dipped into a GO solution (2.6 mg ml^{-1}) followed by centrifugation, dipping in hydroiodic acid, and drying. These sponges, which were designated as sponge/rGO, were dipped into 6.9 mM $Mn(CH_3COO)_2{\cdot}4H_2O$ (hydrous manganese acetate) under moderate stirring, followed by dipping in 4.7 mM $KMnO_4$ solution and then washing and drying. The resultant composites, which were designated as sponge/rGO/MnO_2, exhibited outstanding cyclability with only ∼10% degradation in capacitance after 10 000 cycles for a scan rate of 10 mV s^{-1}. The maximum energy and power densities were reported to be 8.34 Wh kg^{-1} and 47 kW kg^{-1}, respectively, as compared to sponge/rGO which showed maximum energy and power density of 2.08 Wh kg^{-1} and 94 kW kg^{-1}, respectively.

Functionalized graphene has also been explored as an alternative to graphene. Yang *et al.* [72] prepared N-doped graphene and ultrathin MnO_2 sheet composites (NGMCs) in a one-step hydrothermal method at 120 °C. It was seen that the MnO_2 sheets were well dispersed and well adhered to the N-doped graphene framework. In a 1 M Na_2SO_4 electrolyte, specific capacitances of 257.1, 224.4, 205.6, and 192.5 F g^{-1} were achieved at current densities of 0.2, 0.5, 1, and 2 A g^{-1}, respectively. Moreover, a capacitance retention of 94.2% was observed even after 2000 cycles.

In addition to MnO_2/graphene composites, those of Mn_3O_4 and graphene have also been investigated as supercapacitor electrode materials. Wang *et al.* [73] synthesized Mn_3O_4/graphene nanocomposites by mixing graphene in EG with MnO_2 organosol, followed by ultrasonication and heat treatment. Micrographic studies showed a homogeneous distribution of Mn_3O_4 nanoparticles on GNSs. High specific capacitances of 175 and 256 F g^{-1} were reported for 1 M Na_2SO_4 and 6 M KOH electrolytes, respectively. The higher capacitance values were attributed to the synergism between Mn_3O_4 and graphene.

Other Metal Oxides/Graphene Composites Despite its high cost, RuO_2 has been one of the most extensively investigated transition-metal oxide for supercapacitors owing to its high theoretical pseudocapacitance (> 1300 F g^{-1}), long cycle life, and high electrochemical reversibility. The charge storage in RuO_2 in aqueous electrode takes place through electrochemical protonation, as shown in Equation 6.8:

$$RuO_2 + \delta H^+ + \delta e^- \leftrightarrow RuO_{2-\delta} + (OH)_\delta \quad \text{where} \quad 0 \leq \delta \leq 2 \tag{6.8}$$

over a window of ~1.2 V [10].

However, to fully exploit the benefit of RuO_2, it has to be combined with some carbon-based material in order to overcome the inherent shortcomings of MOs when used as stand-alone capacitive materials. Another advantage of using carbon materials as an additive to RuO_2 is the prevention of the formation of RuO_2 agglomerates, which hampers the complete reaction of RuO_2. Moreover, agglomerates can severely affect the capacitance as a result of decreased surface area. Graphene, therefore, holds great promise as an EDLC additive to RuO_2, and since graphene is quite prone to restacking and agglomeration itself, RuO_2 can prevent it, and vice versa.

While much effort has been invested in RuO_2 composited with other carbon derivatives, research on RuO_2/graphene composites is relatively new. Wu *et al.* [74] used GNS to prepare hydrous RuO_2/GNS composites, which they referred to as RuO_2/GNS composites (*ROGSCs*) with different percentages of ruthenium. They found that RuO_2 particles were uniformly distributed on the GNS and acted as spacers to prevent the restacking of graphene sheets. The composite with 38.3 wt% of Ru exhibited a phenomenal capacitance of 570 F g^{-1} at a scan rate of 1 mV s^{-1}, along with energy density and power density of 20.1 Wh kg^{-1} and 10 000 W kg^{-1}, respectively. A capacitance retention of 97.9% was observed after 1000 cycles for a current density of 1 A g^{-1}, which was much higher than that for pure RuO_2 electrodes (~42%). It was concluded that the particle-sheet structure

helps in realizing the best of both graphene and RuO_2 by decreasing the particle resistance and facilitating ionic motion during the charge storage process.

Other MOs such as Cu_xO, ZnO, and Fe_3O_4 have also been studied in conjunction with graphene as electrode materials. Some of the representative works have been summarized in Table 6.5. Figure 6.5 shows the morphologies and electrochemical performances of graphene and pseudocapacitive material composites from some of the works [52, 69, 71, 72].

6.3 Graphene-Based Asymmetric Supercapacitors

Despite their outstanding power densities ($10\,kW\,kg^{-1}$), typical supercapacitors suffer from low energy densities, whereas, on the other hand, secondary batteries possess very high energy densities. In order to expand the applicability of supercapacitors to areas such as electric vehicles (EVs), hybrid electric vehicles (HEVs), mobile electronic devices, and military devices [88–91] which demand high energy and high power simultaneously, superior energy density of supercapacitors is highly desirable. To address the relatively low energy densities of supercapacitors, one alternative is the utilization of asymmetric supercapacitors. Such capacitors essentially combine one faradaic electrode and one capacitive electrode, where the former serves as the energy source while the latter serves as the power source. Figure 6.6 illustrates a schematic of the asymmetrical supercapacitor [89]. According to the equation $E = \frac{1}{2}CV^2$, improvement in the energy (E) can be obtained by maximizing the specific capacitance (C) and/or the cell voltage (V). The overall cell capacitance (C) comprising two electrodes with individual capacitances C_1 and C_2 is given by Equation 6.9:

$$\frac{1}{C} = \frac{1}{C_1} + \frac{1}{C_2} \tag{6.9}$$

Since two dissimilar electrodes are used in an asymmetric capacitor, these electrodes possess different capacitances. In general, the faradaic electrode has a much larger capacitance than its EDLC counterpart, and therefore the overall capacitance exhibited by the device is $C \sim C-$, which, in principle, is the capacitance of the negative electrode. Hence, the capacitance of a capacitor in an asymmetric configuration is twice of that in a symmetric capacitor if the same negative electrode is used. As a result of this higher capacitance, the energy density of an asymmetric cell is much higher. The key considerations while choosing the materials for an asymmetric hybrid capacitor are as follows:

1) *Matching the capacity of the active materials*: Since the pseudocapacitive electrode has much higher specific capacitance than the EDLC electrode, there is a mismatch in the capacitance if the same amount of materials is loaded for each electrode. To compensate for this mismatch, larger amounts of EDLC material should be used; or in other words, the non-faradaic electrode should hold more mass than the faradaic electrode.

Table 6.4 Graphene/conducting polymer composites for supercapacitors.

Composite	Morphology	Electrolyte	Performance	Capacitance retention	References
Graphene/PANI nanorods	Fibrous morphology with appropriate pore size distribution	1 M $HClO_4$	878.57 F g^{-1} at 1 A g^{-1}	Low capacitance fading after 1000 cycles	[54]
Graphene/PANI paper	Layered structure	1 M H_2SO_4	233 F g^{-1}	N/A	[55]
Graphene/PANI	Uniform morphology with no indication of PANI and graphene agglomeration	1 M H_2SO_4	640 F g^{-1}	90% after 1000 charge/discharge cycles	[56]
Graphene nanosheets/PANI	Nano fibrillar morphology	1 M H_2SO_4	1130 F g^{-1} at 5 mV s^{-1}	87% after 1000 cycles	[75]
Graphene oxide (GO)/PANI	Hierarchical structure	1 M H_2SO_4	555 F g^{-1} at a discharge current density of 0.2 A g^{-1}	92% after 2000 cycles	[76]
Graphene oxide (GO)/PANI/CO_2	PANI nanoparticles uniformly coated on GO sheets	1 M H_2SO_4 solution	425 F g^{-1} at 0.2 A g^{-1}	83% after 500 cycles	[77]
Reduced graphene oxide/PANI	Fibrillar morphology	1 M aqueous H_2SO_4 solution	250 F g^{-1}	N/A	[78]
Graphene nanosheets/PPy	PPy homogeneously surrounded by GNS	1 M H_2SO_4	482 F g^{-1} at 0.5 A g^{-1}	95% after 1000 cycles	[79]
Graphene nanosheets/PPy	Dispersed network – polypyrrole nanowire attached to basal planes of GNS	1 M NaCl	165 F g^{-1} at 1 A g^{-1}	92% after 1000 cycles	[80]
Graphene oxide/PPy nanowires	PPy nanowires attached to the surface of GO nanosheets	1 M KCl aqueous solution	633 F g^{-1} at 1 A g^{-1}	94% after 1000 cycles	[81]
Reduced graphene oxide/PPy	PPy located on both sides of the GO sheets	1 M H_2SO_4	376 F g^{-1} at a scan rate of 25 mV s^{-1}	84% after 1000 cycles	[82]
Reduced graphene oxide (rGO)/PPy	GO/PPy composite was uniformly electropolymerized onto the surface of gold electrode	1 M H_2SO_4	424 F g^{-1} at 1 A g^{-1}	N/A	[83]
Reduced graphene oxide (rGO)/PPy	rGO/PPy composite exhibits porous structure	3 M KCl	224 F g^{-1} at 240 A g^{-1}	83% after 5000 cycles	[84]

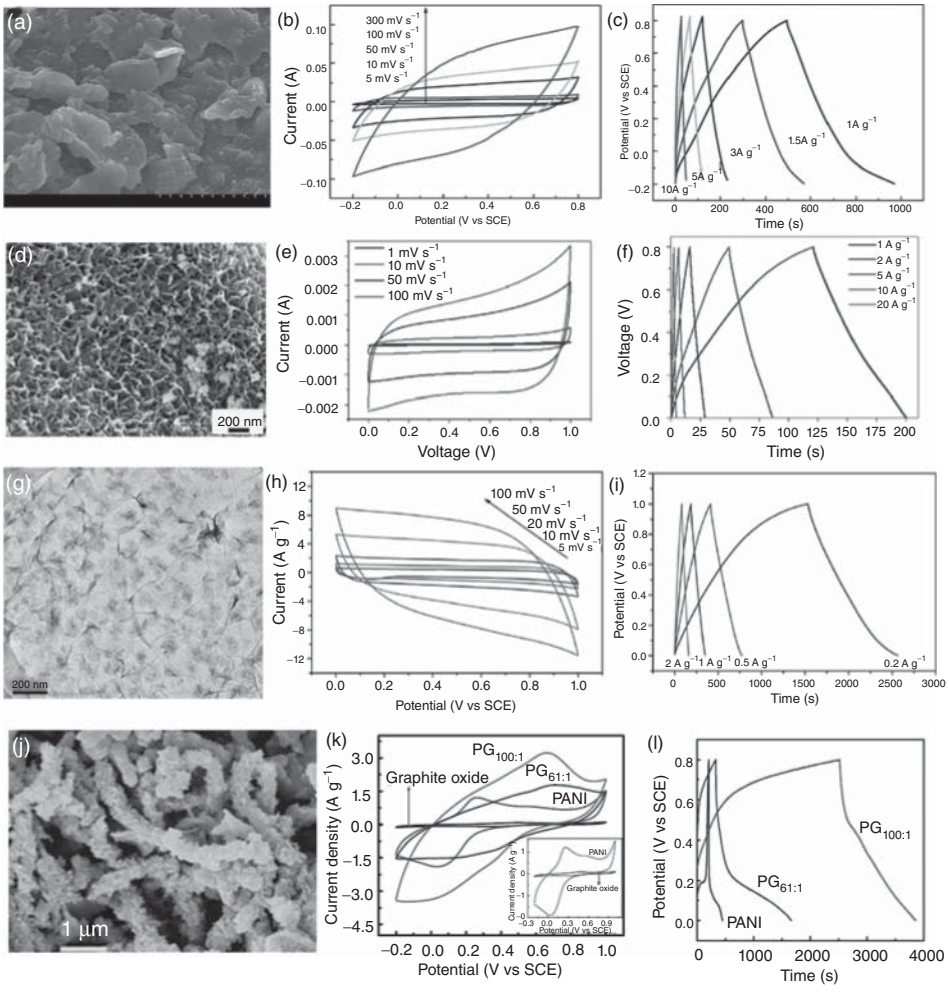

Figure 6.5 (a–c) MnO_2/EPD-G/NF composite morphology, CV curves at different scan rates, and galvanostatic charge/discharge curves of MnO_2/EPD-G/NF composite [69]. (d–f) Morphology of sponge/rGO/MnO_2 dip-coated three times, (e) CV curves of sponge/rGO/MnO_2 with three times dip deposition at different voltage scan rates (1–100 mV s^{-1}), and charge/discharge curves at different current densities [71]. (g–i) HRTEM image of NGMCs, CV curves at different scan rates, and charge/discharge curves for NGMCs [72]. (j–l) Scanning electron microscope (SEM) images of $PG_{100:1}$ (aniline:graphite oxide = 100 : 1); CV curves for PANI, graphite oxide, and PG composites for different aniline and graphite oxide ratios at a scan rate of 10 mV s^{-1}; and galvanostatic charge/discharge curves of PANI, $PG_{100:1}$, $PG_{61:1}$ at a current density of 200 mA g^{-1} [52].

Table 6.5 Graphene/metal oxide composite electrodes for supercapacitors.

Composite	Morphology	Electrolyte	Performance	Capacitance retention	References
MnO_2/graphene/nickel foam (NF)	Nanoneedle-like MnO_2 uniformly grown on porous G/NF sheets	0.5 M Na_2SO_4	476 F g^{-1} at 1 A g^{-1} 216 F g^{-1} at 10 A g^{-1}	N/A	Zhao *et al.* [69]
Graphene/MWCNTs/MnO_2	Nanowires on graphene/MWCNT foam	2 M Li_2SO_4	1108.9 F g^{-1} at 1.89 A g^{-1}	97.94% after 13 000 cycles	Wang *et al.* [70]
Reduced graphene oxide/MnO_2	Flower-like nanoparticles	1 M Na_2SO_4	450 F g^{-1} at 2 mV s^{-1} Energy density of 8.34 Wh kg^{-1} Power density of 47 kW kg^{-1}	90% after 10 000 cycles	Ge *et al.* [71]
N-doped graphene/MnO_2	Sheet-like morphology	1 M Na_2SO_4	257.1, 224.4, 205.6, and 192.5 F g^{-1} at densities of 0.2, 0.5, 1, and 2 A g^{-1}, respectively	94.2% after 2000 cycles	Yang *et al.* [72]
Graphene/Mn_3O_4	Nanoparticles	1 M Na_2SO_4 6 M KOH	175 and 256 F g^{-1} for 1 M Na_2SO_4 and 6 M KOH respectively	N/A	Wang *et al.* [73]
RuO_2/graphene	5–10 nm RuO_2 NPs well anchored to the graphene backbone	1 M H_2SO_4	570 F g^{-1} for 38.3 wt% of Ru at 1 mV s^{-1} Energy density of 20.1 Wh g^{-1} Power density of 10 000 W kg^{-1}	97.9% after 1000 cycles	Wu *et al.* [74]
Fe_3O_4/reduced graphene oxide	Nanoparticles	1 M KOH	220.1 F g^{-1} at 0.5 A g^{-1}	Capacitance increases from 180.6 to 220.1 F g^{-1} during first 800 cycles and remains stable until 3000 cycles	Wang *et al.* [85]
Reduced graphene oxide/$Co(OH)_2$	Nanoparticles	2 M KOH	476 F g^{-1} at 1 A g^{-1} 300 F g^{-1} at 10 A g^{-1}	90% after 1000 cycles	Li *et al.* [86]
Graphene/Co_3O_4	Multilayered morphology with uniform distribution of Co_3O_4	6 M KOH	331 F g^{-1} at 5 A g^{-1}	122% after 5000 cycles	Li *et al.* [87]
Graphene/ZnO	Particles	1 M KOH	Highest capacitance of 62.2 F g^{-1} and power density of 8.1 kW kg^{-1}	Only 5.1% drop after 200 cycles	Wang *et al.* [34]

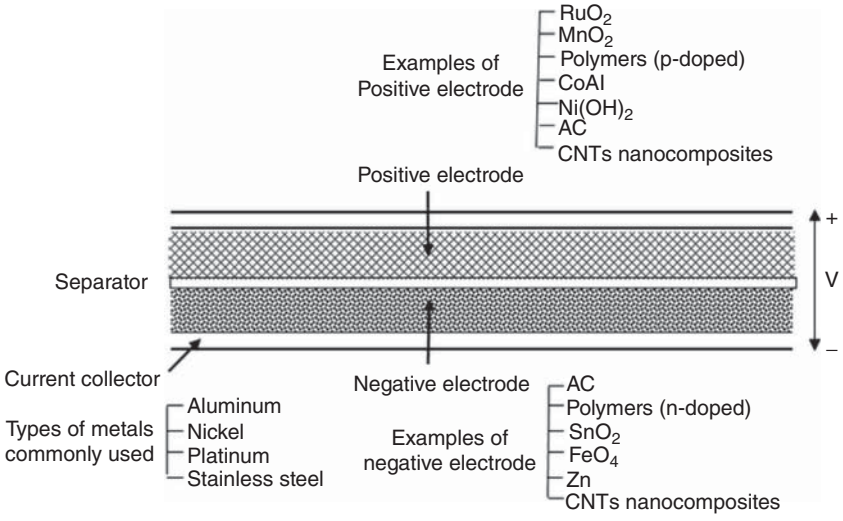

Figure 6.6 Schematic illustration of an asymmetrical supercapacitor [89].

2) *Maximizing the operational voltage of the cell*: Both the electrodes should be chosen such that their potentials are either at the high or low end of the operating voltage. Since energy increases as potential squared, the wider the voltage window, the more is the enhancement in energy.

6.3.1
Asymmetric Capacitors Based on Graphene and Pseudocapacitive Materials

Given the phenomenal properties of graphene, it is one of the most researched EDLC materials for asymmetric supercapacitors. As the complement electrode for graphene in asymmetric capacitors, most of the research to date has focused on pseudocapacitive materials, mostly transition-metal oxides and hydroxides. Typical transition-metal oxides/hydroxides include RuO_2, V_2O_5, MnO_2, $Ni(OH)_2$, Co_3O_4, $Co(OH)_2$, and Fe_3O_4, and their binary systems. In order to match with the power density of the graphene electrode, modification of the faradaic electrode is required. Two main strategies are used for this purpose: first is to increase the surface area of the electrode materials, which can be done by using either nanosized or porous materials, upon which the electrode/electrolyte interface is increased and henceforth the diffusion path is shortened. The second one is to enhance the electron transport between the active materials, which can be done by the incorporation of conductive additives into the electrode materials. Because of their high electrical conductivity, graphene-based materials are popular conductive additives for electrode materials of asymmetric capacitors.

Wu *et al.* [92] developed a high-voltage asymmetric supercapacitor based on graphene as the negative electrode and a MnO_2/graphene composite as the positive electrode in a neutral aqueous Na_2SO_4 electrolyte. The graphene

electrode was obtained by casting graphene sheets with 10 wt% acetylene black and 10 wt% polytetrafluoroethylene (PTFE) on Ni foam. Solution-phase assembly of graphene sheets and α-MnO_2 nanowires was performed to fabricate MnO_2/graphene composites. The graphene in the composite makes it electrically conductive and, furthermore, the presence of nanostructured MnO_2 effectively prevents the agglomeration of graphene sheets. An energy density of 30.4 Wh kg^{-1} was reported, which was much superior to that of graphene/graphene (~2.8 Wh kg^{-1}) symmetric capacitors. Moreover, a high energy density of 7.0 Wh kg^{-1} was recorded at a high power of 5000 W kg^{-1}, and a cyclic performance of 79% retention was noted after 1000 cycles. In another work, Cheng *et al* [93] successfully fabricated binderless supercapacitors with electroactivated graphene paper as the negative electrode and graphene films coated with MnO_2 nanoflowers as the positive electrode. The electroactivated graphene film and the MnO_2-coated graphene film were tested as symmetric supercapacitor electrodes first, which showed high specific capacitances of 245 and 328 F g^{-1}, respectively. For the asymmetric supercapacitor comprising these two electrodes, the power density reached 25.8 kW kg^{-1} and the energy density reached 11.4 Wh kg^{-1}.

In addition to graphene, activated graphene has also been investigated for asymmetric supercapacitors. In Huang's [94] recent work, porous MnO_2 nanotubes fabricated with a one-pot hydrothermal method using a polycarbonate membrane as the template were paired with activated graphene to form an asymmetric supercapacitor. An energy density of 22.5 Wh kg^{-1} and a maximum power density of 146.2 kW kg^{-1} were obtained, and this superior performance was attributed to the hierarchical structure of the porous MnO_2 nanotubes and the activated graphene. Sumboja *et al* [95] reported a template-free and simple synthesis process for flexible, rGO/MnO_2 paper electrodes. The free-standing electrodes not only combined the high conductivity of rGO and large specific capacitance of MnO_2 but also minimized the added weight of components such as current collector, binder, and other additives which reduce the overall specific capacitance of the device. An areal capacitance as high as 897 mF cm^{-2} was achieved from the rGO/MnO_2 paper, with a mass of 3.7 mg cm^{-2}, which is considerably higher than that of other flexible carbon-based electrodes. The asymmetric supercapacitor based on rGO and rGO/MnO_2 electrodes tested in bent conditions was able to yield a capacitance of 0.34 F, which confirmed the high mechanical robustness of the device, since no significant difference in electrochemical performance was reported in the bent and flat state.

Graphene has also been paired with conductive polymers to fabricate asymmetric supercapacitors. Hung *et al* [96] synthesized PANI nanofibers via a chemical method of rapid mixing. The diameter and aspect ratio of PANI nanofibers were found to be controllable by varying the aniline-to-oxidant concentration ratio. Cyclic voltammetric (CV) and electrochemical impedance spectroscopic (EIS) analyses were used to study the capacitive responses of PANI nanofibers, which were between 0.2 and 0.7 V (vs Ag/AgCl) in concentrated acidic media. The aqueous asymmetric capacitor comprising a PANI nanofiber cathode and

a graphene anode exhibited energy and power densities of 4.86 Wh kg^{-1} and 8.75 kW kg^{-1}, respectively.

Besides operating as one of the electrodes of asymmetric supercapacitor, graphene-based materials have been widely used as additives in the other active electrode materials of the capacitor. Yu *et al* [97] demonstrated a unique structure based on graphene/MnO_2 textiles, where solution-exfoliated GNSs were conformably coated onto porous textile fibers, serving as conductive 3D frameworks for the subsequent controlled electrodeposition of MnO_2 nanomaterials. The porous networks not only permitted large loading of active electrode materials but also enabled easy access of electrolyte ions to the electrodes. The resulting hybrid graphene/MnO_2-based textile exhibited a high specific capacitance of up to 315 F g^{-1} at a scan rate of 2 mV s^{-1}. The uniform coating of GNSs, the easy access of electrolyte ions to electrode surfaces, the excellent interfacial contact between MnO_2 and graphene, and the nanoflower architectures of electrodeposited MnO_2 with large electrochemically active surface area, all contributed to this excellent performance. Hybrid supercapacitors with this graphene/MnO_2 textile as the positive electrode and SWCNT textiles as the negative electrode was assembled in 0.5 M Na_2SO_4 aqueous electrolyte. A maximum energy density of 12.5 Wh kg^{-1} and a maximum power density of 110 kW kg^{-1} were achieved for the asymmetric supercapacitor at an operating voltage of 1.5 V. Furthermore, the cycling test of the asymmetric supercapacitor cells showed a ~95% capacitive retention for over 5000 cycles at a high current density of 2.2 A g^{-1}. Table 6.6 summarizes some of the works based on graphene-based electrode materials in asymmetric supercapacitors.

6.3.2
Graphene-Based Lithium-Ion Capacitors

This section discusses supercapacitor systems that essentially hybridize lithium-ion batteries (LIBs) and ECs. LIBs are known for their outstanding energy densities (150–200 Wh kg^{-1}), and therefore if an LIB electrode is coupled with an EC electrode, the resulting device can benefit from the high energy density of LIB and the high power density of the supercapacitor. For such a hybrid capacitor, a capacitive cathode and a lithium-intercalating anode are used along with a lithium-ion electrolyte. Charge is stored by the reversible adsorption/desorption of anions at the surface of the capacitive cathode, while at the anode charge is stored via a reversible insertion/extraction mechanism of the lithium ions, as illustrated in Figure 6.7 [88]. The combined effects provide an opportunity to enhance both the energy and power densities while still maintaining high cycle lives comparable to that of conventional supercapacitors. The concept of such a hybrid supercapacitor was pioneered by Amatucci *et al.* [106] based on AC and $Li_4Ti_5O_{12}$ as the supercapacitor electrode and the Li-intercalating electrode, respectively. Although theoretically enticing, such a device poses several design challenges which must be addressed in order to fully exploit the goods from the battery and capacitor electrodes. For instance, lithium-ion intercalation is a faradaic process which is far

Table 6.6 Performance summary of graphene-based electrodes in asymmetric supercapacitors.

Positive electrode	Negative electrode	Electrolyte	Current density/ scan rate	Specific capacitance/ performance	Capacitance retention	References
MnO_2 nanowire/graphene	Graphene	1 M Na_2SO_4	0.5 A g^{-1}	Specific capacitance of 24.5 F g^{-1} Energy density of 7 Wh kg^{-1} Power density of 5 kW kg^{-1}	79% after 1000 cycles	[92]
MnO_2-coated graphene	Graphene	1 M KCl	4 mA	Specific capacitance of 328 F g^{-1} Energy density of 11.4 Wh kg^{-1} Power density of 25.8 kW kg^{-1}	99% after 1300 cycles	[93]
MnO_2 nanotubes	Activated graphene	1 M Na_2SO_4	0.25 A g^{-1}	Specific capacitance of 365 F g^{-1} Energy density of 22.5 Wh kg^{-1} Power density of 146.2 kW kg^{-1}	90.4% after 3000 cycles	[94]
Reduced graphene oxide/MnO_2	rGO	1 M Na_2SO_4	10 mA g^{-1}	Specific capacitance of 113 mF cm^{-2} Energy density of 11.5 μWh cm^{-2} Power density of 3.8 mW cm^{-2}	93% after 3600 cycles	[95]
PANI	Graphene	1 M HCl		Energy density of 4.86 Wh kg^{-1} Power density of 8.75 kW kg^{-1}		[96]
Graphene/MnO_2 textile	SWCNT textiles	0.5 M Na_2SO_4		Energy density of 12.5 Wh kg^{-1} Power density of 110 kW kg^{-1}	95% after 5000 cycles	[97]
Graphene/MnO_2	Activated carbon nanofibers (ACNs)	1 M Na_2SO_4	200 mV s^{-1}	Specific capacitance of 113.5 F g^{-1} Energy density of 51.1 Wh kg^{-1} Power density of 198 kW kg^{-1}	97.3% after 1000 cycles	[98]

$Ni(OH)_2$/graphene	RuO_2/graphene	1 mol l^{-1} KOH	20 A g^{-1}	Specific capacitance of 97 F g^{-1} Energy density of 14 Wh kg^{-1} Power density of 21 kW kg^{-1}	92% after 5000 cycles	[99]
Graphene/MnO_2 composite	Graphene/MoO_3 composite	Na_2SO_4	200 mA g^{-1}	Specific capacitance of 307 F g^{-1} Energy density of 42.6 Wh kg^{-1} at a power density of 0.276 kW kg^{-1}	1000 cycles	[100]
Vertically aligned MnO_2 nanoplates	Graphene hydrogel	1 M Na_2SO_4	1 A	Specific capacitance of 41.7 F g^{-1} Energy density of 23.2 Wh kg^{-1} Power density of 1 kW kg^{-1}	83.4% after 5000 cycles	[101]
$Ni(OH)_2$/CNTs	Iron nanosheets on graphene sheets	6 M KOH	—	Energy density of 140 Wh kg^{-1}	78% after 2000 cycles	[102]
$Ni(OH)_2$/MnO_2 hybrid film	Reduced graphene oxide	1 M KOH	—	Energy density of 186 Wh kg^{-1} at a power density of 0.778 kW kg^{-1}	76% after 3000 cycles	[103]
MnO_2/graphene oxide composite	Graphene oxide (GO)	1 M HCl	0.5 A g^{-1}	Specific capacitance of 280 F g^{-1} Energy density of 35 Wh kg^{-1} Power density of 7.5 kW kg^{-1}	70% after 1000 cycles	[104]
(2D) MnO_2	Graphene nanosheets	$Ca(NO_3)_2$-SiO_2 composite gel	0.1 A g^{-1}	Specific capacitance of 774 F g^{-1} Energy density of 97.2 Wh kg^{-1}	97% after 10 000 cycles	[105]

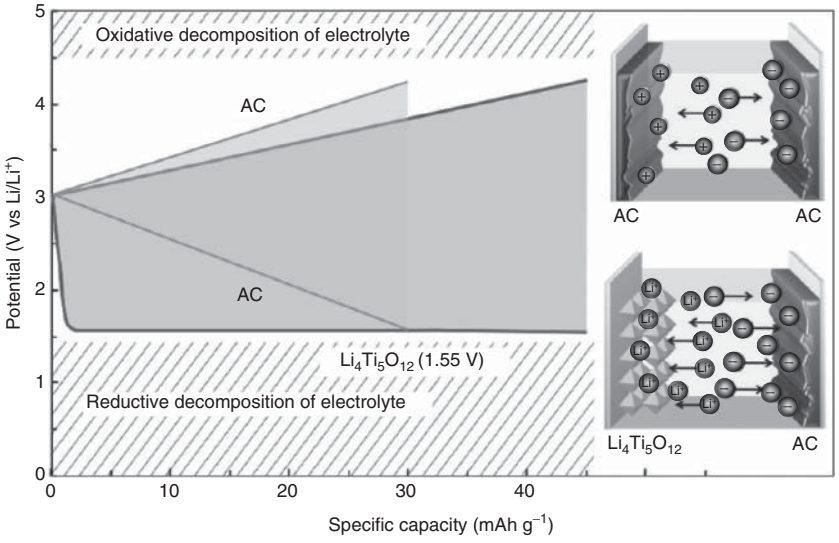

Figure 6.7 Configuration of the "nanohybrid capacitor" (NHC). The device consists of a $Li_4Ti_5O_{12}$ (LTO) negative electrode combined with an activated-carbon (AC) positive electrode. This is a hybrid system of a faradaic lithium-insertion LTO electrode and a non-faradaic AC electrode employing an anion adsorption/desorption process [88].

more sluggish than the non-faradaic adsorption and desorption of ions, and this mismatch in kinetics leads to a mismatch in power characteristics of the positive and negative electrodes, which must be addressed in order to realize the best of both electrodes. There are additional issues such as charge balancing, cycle life balancing, and so on, which also must be looked into.

Conventional Li-ion-based hybrid systems, also known as *lithium-ion capacitors* (LICs), typically use graphite as the lithium-intercalating anode and AC as the capacitive cathode in a lithium-ion electrolyte. $Li_4Ti_5O_{12}$ is another popular anode material for LICs, given its high columbic efficiency (> 95% at 1 C), a flat discharge profile at 1.55 V versus Li/Li^+, long cycle life, and cost effectiveness. Since the cathode part of LIC is essentially capacitive, most carbon materials are suitable as cathode materials for LICs. Here, in this chapter, we will focus only on cathodes involving graphene and/or graphene derivatives for LICs. Stoller *et al* [107] synthesized chemically activated graphene, "activated microwave-expanded graphite oxide (a-MEGO)", to replace AC as the cathode material. The results showed that the activated graphene material worked well in a symmetrical cell with the Li-ion electrolyte and was able to deliver specific capacitances as high as 182 F g^{-1}. In the full a-MEGO/graphite hybrid cell, specific capacitances as high as 266 F g^{-1} were reported at an operating potential of 4 V, and a gravimetric energy density of 53.2 Wh kg^{-1} was reported for the packaged cell. In a recent work by Aravindan *et al* [108], GNSs were prepared from GO by an ecofriendly trigol reduction process, which were used as the cathode of an LIC paired with commercial LTO powder. A comprehensive study of the optimal active mass loading for achieving

higher energy density without sacrificing power density is described in this work. The resultant hybrid cell delivered an exceptional cyclability for about 5000 cycles, with a maximum deliverable energy density of about 45 Wh kg^{-1}.

Graphene-based materials have also been used as additives to other materials in battery–capacitor hybrid cells. For instance, a hybrid supercapacitor with high energy and power densities was reported by Kim *et al* [109]. It comprised a composite anode of anatase TiO_2/rGO and a cathode of AC in a nonaqueous electrolyte. An energy density of 42 Wh kg^{-1} was achieved at 800 W kg^{-1} for a voltage window of 1.0–3.0 V. Even at a very high charge/discharge rate (4 s), an energy density of 8.9 Wh kg^{-1} was retained. The high energy and power characteristics of the hybrid supercapacitor were attributed to the wider potential window and enhanced electrochemical kinetics due to the unique TiO_2 nanostructure. Graphene has also been composited with V_2O_5 nanowires (VNWs) to form binder-free, flexible paper electrodes by Perera *et al* [110]. Graphene sheets were prepared using an alkaline deoxygenation process (hGO), and hybrid cells were assembled using the hGO-VNW paper electrodes as the anode and a spectracarb fiber cloth as the cathode. Electrochemical studies for various compositions of VNWs on hGO were reported. The resulting hybrid cells delivered an energy density of 38.8 Wh kg^{-1} at a power density of 455 W kg^{-1}. A maximum power density of 3.0 kW kg^{-1} was achieved at a constant current discharge rate of 5.5 A g^{-1}. The same group [111] coupled V_2O_5/rGO composites with MnO_2/rGO composites to fabricate a hybrid cell. A facile hydrothermal synthesis route was used to grow MnO_2 on rGO sheets. The hybrid supercapacitor was able to deliver an energy density of ~115 Wh kg^{-1} with a specific capacitance of 36.9 F g^{-1}. Table 6.7 summarizes some of the recent works that have investigated graphene-based electrodes for LICs.

6.4 Graphene-Based Microsupercapacitors

Miniaturized supercapacitors, also known as *microsupercapacitors*, have gained much attention in recent years. These devices find application in implantable biomedical devices, environmental sensors, microelectromechanical systems (MEMS), and also in some small personal electronics which require the power in microwatts [112]. Quite akin to their macro counterparts, microsupercapacitors can be connected in series or parallel in order to meet the voltage, current, and capacity requirements depending upon the given application. In general, for microsupercapacitors the total footprint area of the device is in the millimeter or centimeter range. Microsupercapacitors consist of either thin-film electrodes with a thickness of <10 μm or arrays of microelectrodes with micrometer-scale sizes which can either be two or three dimensional. For supercapacitors in the "macro" regime, the electrochemical performance is usually reported as specific capacitance, energy, and power densities, all in gravimetric terms, that is, per unit mass. Since any physical quantity in gravimetric terms is a direct

Table 6.7 Performance summary of graphene-based electrodes in lithium-ion capacitors.

Cathode	Anode	Electrolyte	Voltage window (V)	Specific capacitance/performance	References
Activated graphene	Graphite	1 M $LiPF_6$ in EC/DEC 1 : 1 (volume)	2–4	266 F g^{-1}	[107]
Trigol-reduced graphene oxide	LTO	1 M $LiPF_6$ in EC/DEC 1 : 1 (volume)	1–3	Energy density of 147.8 Wh kg^{-1} 163 F g^{-1} at 0.5 A g^{-1}	[108]
Activated carbon	TiO_2/rGO	1 M $LiPF_6$ in EC/DEC 1 : 1 (volume)	1–3	Energy density of 45 Wh kg^{-1} at a power density of 3.3 kW kg^{-1} Energy density of 42 Wh kg^{-1} at a power density of 0.8 kW kg^{-1}	[109]
MnO_2 nanorodes on rGO	V_2O_5 nanowire on rGO	1 M LiTFSI in dry acetonitrile	0–2	36.9 F g^{-1}	[110]
Spectracarb fiber cloth	V_2O_5 nanowire graphene composite	1 M LiTFSI in dry acetonitrile	0–2	Energy density of 15 Wh kg^{-1} at a power density of 0.4365 kW kg^{-1} 80 F g^{-1} Energy density of 38.8 Wh kg^{-1} at a power density of 0.455 kW kg^{-1}	[111]
Functionalized graphene	Modified graphite	1 M $LiPF_6$ with 3 wt% vinylene carbonate (VC) in EC/DEC 1 : 1 (volume)	2–4	Energy density of 61 Wh kg^{-1} at a power density of 1.452 kW kg^{-1}	[113]

measure of mass, and the mass of the electrode materials is almost negligible for a microsupercapactor, gravimetric parameters are rendered almost inappropriate for reporting the performance of a microsupercapacitor [114]. Hence, the key to report the performance of a microsupercapacitor accurately is the footprint area, energy, and power in terms of the areal density [115].

The first generation of microsupercapacitors followed the planar 2D architecture of conventional supercapacitors, consisting of two electrodes and a separator soaked in an electrolyte. And, to date, for cost-effective mass production the 2D design is preferred over other designs. However, owing to the small footprint area of microsupercapacitors, the areal energy density is quite low for the 2D design. One of the approaches to increase the area of the electrodes is the construction of a platform with electrodes arranged in an "interdigitated" manner. Such a design offers several advantages over the conventional 2D design [116–119]: for instance, having the electrodes in the same plane is not only easy to fabricate but also helps in achieving smaller distances between the electrodes, thereby improving electron transport and kinetics. While graphene has been extensively researched for conventional supercapacitors, its potential application in microsupercapacitors is rather newfound [120–122]. Graphene-based materials and rGO, in particular, have been widely investigated owing to their scalability, low cost, and the presence of chemically active defect sites [123–125]. This section will summarize the advantages, disadvantages, and performance of graphene-based microsupercapacitors.

A critical consideration for using graphene-based materials is the restacking of individual graphene sheets during the electrode processing, which hinders the facile accessibility of electrolyte ions to the electrode. In the conventional 2D design, the complete active surface of the graphene sheets is not always accessed. However, it was demonstrated by Yoo *et al.* [126] that having graphene electrodes side by side in an in-plane design increases the accessibility of the ions to the entire surface of graphene sheets by creating diffusion channels between the electrodes. The proposed microsupercapacitor was based on a planar architecture of opposing graphene thin films. The structure comprised graphene flakes connected along the flake edges, which provided sufficient porosity to maximize the coverage of the electrode surface. The effect of graphene edges resulted in specific capacitances of $80\,mF\,cm^{-2}$ for few-layer graphene electrodes, while much higher specific capacitances ($0.394\,mF\,cm^{-2}$) were achieved for multilayer rGO electrodes, which were almost three times higher than that of the stacked layer-by-layer structure ($0.14\,mF\,cm^{-2}$). It was concluded, therefore, that the planar geometry provided superior charge mobility and effective utilization of the electrochemical surface area by minimizing the diffusion barriers of the electrolyte ions. To further increase the electrolyte-ion accessibility to the graphene sheets and prevent restacking, CNTs can also be used as spacers. Beidaghi and Wang [127] fabricated rGO/CNT composites based microsupercapacitors by combining photolithography lift-off methods with electrostatic spray deposition. The reduction of GO and the fabrication of electrodes were both achieved by deposition of a solution of GO or GO/CNT on a heated

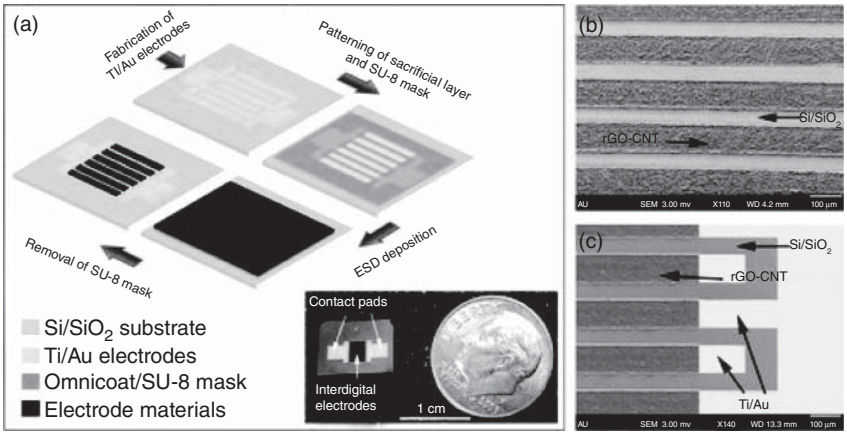

Figure 6.8 (a) Schematic drawing of fabrication procedures of microsupercapacitors. Inset: Digital photograph of a fabricated device. (b,c) Top-view SEM images of rGO/CNT-based interdigital microelectrode arrays [127].

substrate, as shown in Figure 6.8. The electrochemical results indicated high accessibility of the electrolyte ions to the electrodes and faster ionic transport for a layered structure of CNT/rGO. The microsupercapacitor with the electrode composition of 90% rGO and10% CNT exhibited a capacitance of 6.1 mF cm^{-2} at a scan rate of 0.01 V s^{-1}. Even at a very high scan rate of 50 V s^{-1}, this rGO/CNT microsupercapacitor showed a specific capacitance of 2.8 mF cm^{-2}. Another example of graphene-based interdigitated microsupercapacitors is the carpet-based microsupercapacitors based on graphene/CNTs/Ni electrodes reported by Lin *et al.* [128]. The microsupercapacitor showed an impedance phase angle of −81.58° at a frequency of 120 Hz, similar to that of commercial aluminum electrolytic capacitors. The microsupercapacitor also delivered an energy density of 2.42 mWh cm^{-3} in an ionic liquid and a maximum power density of 115 W cm^{-3} in an aqueous electrolyte at a scan rate of 400 V s^{-1}. The excellent performance of this microsupercapacitor was attributed to the seamless CNT/graphene junctions at the interface of the differing carbon allotropic forms.

Another important factor that affects the performance of microsupercapacitors is the thickness of the electrode. Generally, as the thickness of the electrode increases, the increased mass loading of the electrode material increases the electrode resistance, which results in decreased gravimetric capacitance. Although thin electrodes show less areal capacitance because of the small mass loading, their very high rate capability and frequency response outweigh the relatively low specific capacitance. Liu *et al.* [129] demonstrated a microsupercapacitor based on very thin films of graphene quantum dots (GQDs). The device was fabricated by electrophoretic deposition of 365-nm-thick films of GQD on patterned Au microelectrodes. The device showed capacitive behavior even at high CV scans rates and very small *RC* time constants of 103.6 μs in aqueous and 53.8 μs in ionic electrolytes. This remarkable performance was attributed to the small thickness of the

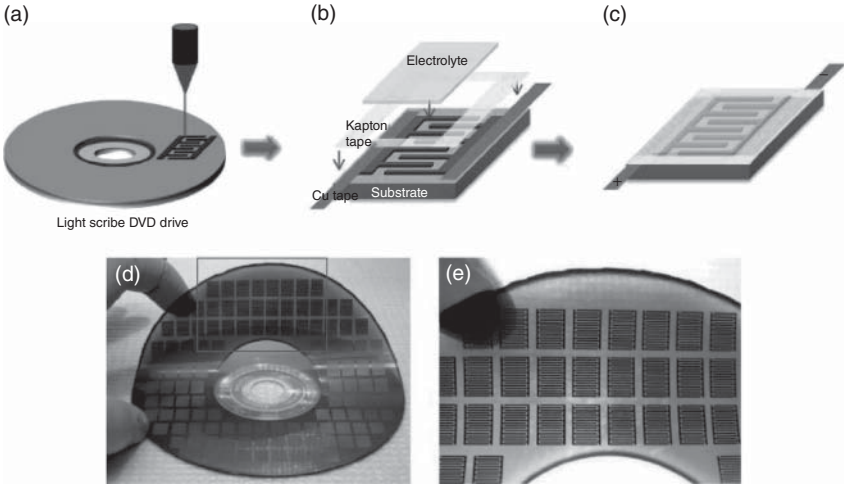

Figure 6.9 (a–c) Schematic diagram of fabrication process for microsupercapacitors by the laser scribing method. (d,e) Flexible microsupercapacitors with high areal density [132].

electrodes combined with the device architecture and good electrical conductivity of GQDs and the presence of abundant edge defects. However, this high rate performance came at the cost of specific capacitance and energy density, as device capacitance was 534.7 μF cm^{-2} in aqueous electrolyte, which was lower than that of many other reported microsupercapacitors.

Graphene based microsupercapacitors have also been fabricated using nonconventional methods for low-cost and scalable fabrication. Recently, rGO electrodes were patterned by direct laser irradiation on graphite oxide films under ambient conditions. Gao *et al.* [130] used a laser reduction technique to write rGO patterns directly on free-standing hydrated GO films for microsupercapacitors. In this device, the patterned parts of rGO served as electrodes while the hydrated GO between the electrodes served as the separator and electrolyte. The concentric circular pattern exhibited the highest specific capacitance of 0.51 mF cm^{-2} and a volumetric capacitance of 3.1 F cm^{-3}. The energy density was calculated to be 4.3×10^{-4} Wh cm^{-3}, with a power density of 1.7 W cm^{-3}. The sandwich and concentric circular pattern devices showed fairly good cyclic stabilities, with less than 35% loss of capacitance after 10 000 cycles. On the other hand, El-Kady *et al.* [131] demonstrated the fabrication of thin-film graphene electrodes by laser irradiation using a commercial light-scribe DVD burner. Later, they advanced the fabrication process design of the microsupercapacitor [132] (shown in Figure 6.9). The patterning and reduction of GO were performed in one step, with more than 100 microsupercapacitors fabricated in less than 30 min. The electrodes with smaller width and spacing showed better performance. For a device with 16 interdigitated electrodes, a stack capacitance of 3.05 F cm^{-1} (areal capacitance of 2.32 mF cm^{-2}) was recorded at a current density of 16.8 mA cm^{-3}, and 60% of this value (1.35 mF cm^{-2}) was maintained when the device was operated at an

ultrahigh current density of 18.4 A cm^{-3}. The microsupercapacitors exhibited a power density of 200 W cm^{-3}, a frequency response with an *RC* time constant of 19 ms, and a low leakage current (< 150 nA after 12 h). Another newly published study combined rGO and PANI as active materials for microelectrodes, which were prepared by in situ electrodeposition of PANI nanorods on the surface of rGO patterns [133]. This method allowed uniform and controllable in situ electrochemical growth of conducting PANI nanorod arrays on patterned rGO thin films over large areas. The as-prepared microsupercapacitors exhibited a specific capacitance of 970 F g^{-1} at a discharge current density of 2.5 A g^{-1}, as well as good stability, retaining 90% of initial capacitance after 1700 consecutive cycles.

6.5 Summary and Outlook

Given its exceptional electrical conductivity, very high theoretical SSA, and high mechanical strength, graphene as an active electrode material is extremely fascinating to the world of energy storage. At the heart of energy storage lie ECs or "supercapacitors," which bridge the gap between conventional batteries and electrolytic capacitors. These devices are able to deliver high power while still maintaining modest energy densities.

From the foregoing, it can be seen how graphene can be used as an EDLC material, both by itself and as an additive to other carbon structures. Several routes were discussed for using graphene as an EDLC material, including chemical reduction of GO, activation of graphene, addition of carbon nanostructures, and the induction of heteroatoms. Chemical reduction of GO gives rGO as the final product, and such graphene possesses oxygen-containing functional groups. The presence of these oxygen groups lends a net pseudocapacitance to graphene and hence improves the overall capacitance. Activation processes, on the other hand, are carried out to enhance the accessible surface to the electrolyte ions by the creation of porous sites. It was seen how activation of graphene leads to significant improvement in the electrochemical performance. Although theoretically ideal, graphene has a great tendency to agglomerate. The addition of other carbon structures to graphene can prevent graphene sheet restacking and ensure the high surface area of graphene. The carbon structures not only act as "spacers" or stabilizers between graphene sheets but also enhance the overall conductivity of the material. Additionally, the presence of heteroatoms in the graphene lattice can induce pseudocapacitive effects to the otherwise pure double-layer capacitance of graphene, and thereby increase the overall capacitance of the system. Moreover, these heteroatoms act as defect sites and ease the functionalization of graphene and expand its applicability.

Graphene can also be used in conjunction with pseudocapacitive materials such as CPs and transition-metal oxides as composite material electrodes. Such electrodes benefit from the synergism between graphene and the pseudocapacitive

material. Since the latter relies on faradaic processes for charge storage, the insertion/deinsertion of electrolyte ions upon prolonged cycling can lead to swelling and shrinking of the electrode, resulting in a decrease of electrical conductivity and mechanical stability. Graphene can act as a buffer and alleviate stresses resulting from these volumetric changes, thereby improving the cyclic longevity of the electrode, in addition to improving conductivity of the electrode. The pseudocapacitive electrode, on the other hand, improves the capacitance of the overall system.

Graphene has also been studied extensively in asymmetric capacitors. Such capacitors exhibit much higher energies than symmetric capacitors as a result of their high capacitance and larger voltage window. Graphene has been studied by itself as one of the electrodes of such capacitors, and had also been used as a conductive additive to the active materials of asymmetric capacitor electrodes. A special class of these asymmetric capacitors, the so-called lithium-ion capacitor, has been reviewed along with the use of graphene in such devices. Graphene has also been explored as a material for microsupercapacitors. As was seen, graphene-based electrodes significantly improved the performance of microsupercapacitors. In order to further increase the capacitance of graphene-based microsupercapacitors without compromising ion diffusion length and power, 3D interdigitated structures can be constructed by increasing the thickness of the electrodes. The merits of 3D electrodes with a small area footprint and short transport lengths will become more obvious upon further miniaturizing on-chip power systems.

To conclude, graphene-based materials hold great promise as supercapacitor electrodes. The essence is to make the full use of its high surface area, excellent electrical conductivity, rich surface bondings, and high mechanical strength, which can be challenging to realize in practice. However, high-quality graphene synthesis is still an expensive process, and therefore large-scale, cost-effective graphene production is an issue that needs to be addressed.

Acknowledgments

RA thanks the University Graduate School at Florida International University for support through a Presidential Fellowship. The authors are grateful to NSF NERC-Advanced Self-Powered Systems of Integrated Sensors and Technologies (ASSIST) for financial assistance.

References

1. Geim, A.K. and Novoselov, K.S. (2007) The rise of graphene. *Nat. Mater.*, **6**, 183–191. doi: 10.1038/nmat1849
2. Lee, J.U., Yoon, D., and Cheong, H. (2012) Estimation of Young's modulus of graphene by Raman spectroscopy. *Nano Lett.*, **12**, 4444–4448. doi: 10.1021/nl301073q
3. Booth, T.J., Blake, P., Nair, R.R. *et al.* (2008) Macroscopic graphene membranes and their extraordinary

stiffness. *Nano Lett.*, **8**, 2442–2446. doi: 10.1021/nl801412y

4. Dhanabalan, A., Li, X., Agrawal, R. *et al.* (2013) Fabrication and characterization of SnO2/graphene composites as high capacity anodes for Li-ion batteries. *Nanomaterials*, **3**, 606–614. doi: 10.3390/nano3040606
5. Liu, F., Wee Lee, C., and Im, J.S. (2013) Graphene-based carbon materials for electrochemical energy storage. *J. Nanomater.*, **2013**, Article ID 642915, 11 p.. doi: 10.1155/2013/642915
6. Beidaghi, M., Wang, Z., and Gu, L. (2012) Electrostatic spray deposition of graphene nanoplatelets for high-power thin-film supercapacitor electrodes. *J. Solid State Electrochem.*, **16**, 3341–3348. doi: 10.1007/s10008-012-1777-5
7. Schwierz, F. (2010) Graphene transistors. *Nat. Nanotech.*, **5**, 487–496. doi: 10.1038/nnano.2010.89
8. Stankovich, S., Dikin, D.A., and Dommett, H.B. (2006) Graphene-based composite materials. *Nature*, **442**, 282–286. doi: 10.1038/nature04969
9. Zhou, X. and Liang, F. (2014) Application of graphene/graphene oxide in biomedicine and biotechnology. *Curr. Med. Chem.*, **21**, 855–869.
10. Simon, P. and Gogotsi, Y. (2008) Materials for electrochemical capacitors. *Nat. Mater.*, **7**, 845–854. doi: 10.1038/nmat2297
11. Conway, B.E. (1999) *Electrochemical Supercapacitors: Scientific Fundamentals and Technological Applications*, Kluwer Academic/Plenum Publishes, New York.
12. Beguin, F. and Frackowiak, E. (eds) (2013) *Supercapacitors: Materials, Systems, and Applications*, Wiley-VCH Verlag GmbH & Co, Weinheim.
13. Huang, Y., Liang, J.J., and Chen, Y.S. (2012) An overview of the applications of graphene-based materials in supercapacitors. *Small*, **8**, 1805–1834. doi: 10.1002/smll.201102635
14. Pumera, M. (2011) Graphene-based nanomaterials for energy storage. *Energy Environ. Sci.*, **4**, 668–674. doi: 10.1039/C0EE00295J
15. Huang, X., Zeng, Z., Fan, Z. *et al.* (2012) Graphene-based electrodes. *Adv. Mater.*, **24**, 5979–6004. doi: 10.1002/adma.201201587
16. Dai, L., Chang, D.W., Baek, J.B. *et al.* (2012) Carbon nanomaterials for advanced energy conversion and storage. *Small*, **8**, 1130–1166. doi: 10.1002/smll.201101594
17. Novoselov, K.S., Geim, A.K., Morozov, S.V. *et al.* (2004) Electric field effect in atomically thin carbon films. *Science*, **306**, 666–669.
18. Riedl, C., Coletti, C., and Starke, U. (2010) Structural and electronic properties of epitaxial graphene on SiC(0 0 0 1): a review of growth, characterization, transfer doping and hydrogen intercalation. *J. Phys. D Appl. Phys.*, **43**, 374009. doi: 10.1088/0022-3727/43/37/374009
19. Kim, K.S., Zhao, Y., Jang, H. *et al.* (2009) Large-scale pattern growth of graphene films for stretchable transparent electrodes. *Nature*, **457**, 706–710.
20. Li, X., Cai, X.S., An, J. *et al.* (2009) Large-area synthesis of high-quality and uniform graphene films on copper foils. *Science*, **324**, 1312–1314.
21. Loryuenyong, V., Totepvimarn, K., Eimburanapravat, P. *et al.* (2013) Preparation and characterization of reduced graphene oxide sheets via water-based exfoliation and reduction methods. *Adv. Mater. Sci. Eng.*, **2013**, Article ID 923403, 5 pp. 1–5.
22. Stankovich, S., Dikin, D.A., Piner, R.D. *et al.* (2007) Synthesis of graphene-based nanosheets via chemical reduction of exfoliated graphite oxide. *Carbon*, **45**, 1558–1565. doi: 10.1016/j.carbon.2007.02.034
23. Stoller, M.D., Park, S., Zhu, Y. *et al.* (2008) Graphene based ultracapacitors. *Nano Lett.*, **8**, 3498–3502.
24. Chen, Y., Zhang, X., Zhang, D. *et al.* (2012) High power density of graphene-based supercapacitors in ionic liquid electrolytes. *Mater. Lett.*, **68**, 475–477. doi: 10.1016/j.matlet.2011.11.008
25. Zhang, D., Zhang, X., Chen, Y. *et al.* (2012) An environment-friendly route to synthesize reduced graphene oxide

as a supercapacitor electrode material. *Electrochim. Acta*, **69**, 364–370. doi: 10.1016/j.electacta.2012.03.024

26. Chen, Y., Zhang, X., Zhang, D. *et al.* (2011) High performance supercapacitors based on reduced graphene oxide in aqueous and ionic liquid electrolytes. *Carbon*, **49**, 573–580. doi: 10.1016/j.carbon.2010.09.060

27. Wang, Y., Shi, Z., Huang, Y. *et al.* (2009) Supercapacitor devices based on graphene materials. *J. Phys. Chem. C*, **113**, 13103–13107. doi: 10.1021/jp902214f

28. Hantel, M.M., Kaspar, T., Nesper, R. *et al.* (2011) Partially reduced graphite oxide for supercapacitor electrodes: effect of graphene layer spacing and huge specific capacitance. *Electrochem. Commun.*, **13**, 90–92.

29. Chen, Y., Zhang, X., and Zhang, H. (2012) High-performance supercapacitors based on a graphene–activated carbon composite prepared by chemical activation. *RSC Adv.*, **2012**, 7747–7753.

30. Zhu, Y., Murali, S., and Stoller, M.D. (2011) Carbon-based supercapacitors produced by activation of graphene. *Science*, **332**, 1537–1541.

31. Si, Y. and Samulski, E.T. (2008) Exfoliated graphene separated by platinum nanoparticles. *Chem. Mater.*, **2008** (20), 6792–6797.

32. Zhang, K., Mao, L., Zhang, L.L. *et al.* (2011) Surfactant-intercalated, chemically reduced graphene oxide for high performance supercapacitor electrodes. *J. Mater. Chem.*, **21**, 7302–7307. doi: 10.1039/c1jm00007a

33. Yu, Y., Sun, Y., Cao, C. *et al.* (2014) Graphene-based composite supercapacitor electrodes with diethylene glycol as inter-layer spacer. *J. Mater. Chem. A*, **2014**, 7706–7710. doi: 10.1039/C4TA00905C

34. Wang, J., Gao, Z., Li, Z. *et al.* (2011) Green synthesis of graphene nanosheets/ZnO composites and electrochemical properties. *J. Solid State Chem.*, **184**, 1421–1427. doi: 10.1016/j.jssc.2011.03.006

35. Cheng, Q., Tang, J., and Ma, J. (2011) Graphene and carbon nanotube composite electrodes for supercapacitors with ultra-high energy density. *Phys. Chem. Chem. Phys.*, **2011** (13), 17615–17624. doi: 10.1039/C1CP21910C

36. Jung, N., Kwon, S., and Lee, D. (2013) Synthesis of chemically bonded graphene/carbon nanotube composites and their application in large volumetric capacitance supercapacitors. *Adv. Mater.*, **25**, 6854–6858. doi: 10.1002/adma.201302788

37. Wang, W., Guo, S., Penchev, M. *et al.* (2013) Three dimensional few layer graphene and carbon nanotube foam architectures for high fidelity supercapacitors. *Nano Energy*, **2**, 294–303. doi: 10.1016/j.nanoen.2012.10.001

38. Yu, D. and Dai, L. (2010) Self-assembled graphene/carbon nanotube hybrid films for supercapacitors. *J. Phys. Chem. Lett.*, **1** (2), 467–470. doi: 10.1021/jz9003137

39. Yan, J., Wei, T., Shao, B. *et al.* (2010) Electrochemical properties of graphene nanosheet/carbon black composites as electrodes for supercapacitors. *Carbon*, **48**, 1731–1737. doi: 10.1016/j.carbon.2010.01.014

40. Ma, J., Xue, T., and Qin, X. (2014) Sugar-derived carbon/graphene composite materials as electrodes for supercapacitors. *Electrochim. Acta*, **115**, 566–572. doi: 10.1016/j.electacta.2013.11.028

41. Li, J.J., Ma, Y.W., Jiang, X. *et al.* (2012) Graphene/carbon nanotube films prepared by solution casting for electrochemical energy storage. *IEEE Trans. Nanotechnol.*, **11**, 3–7. doi: 10.1109/TNANO.2011.2158236

42. Qiu, L., Yang, X., Gou, X. *et al.* (2010) Dispersing carbon nanotubes with graphene oxide in water and synergistic effects between graphene derivatives. *Chem. Eur. J.*, **16**, 10653–10658. doi: 10.1002/chem.20100177

43. Lu, X., Dou, H., Gao, B. *et al.* (2011) A flexible graphene/multiwalled carbon nanotube film as a high performance electrode material for supercapacitors.

Electrochim. Acta, **56**, 5115–5121. doi: 10.1016/j.electacta.2011.03.066

44. Nolan, H., Mendoza-Sanchez, B., Kumar, N.A. *et al.* (2014) Nitrogen-doped reduced graphene oxide electrodes for electrochemical supercapacitors. *Phys. Chem. Chem. Phys.*, **16**, 2280–2284. doi: 10.1039/c3cp54877e
45. Jiang, B., Tian, C., and Wang, L. (2012) Highly concentrated, stable nitrogen-doped graphene for supercapacitors: simultaneous doping and reduction. *Appl. Surf. Sci.*, **258**, 3438–3443. doi: 10.1016/j.apsusc.2011.11.091
46. Sun, L., Wang, L., Tian, C. *et al.* (2012) Nitrogen-doped graphene with high nitrogen level via a one-step hydrothermal reaction of graphene oxide with urea for superior capacitive energy storage. *RSC Adv.*, **2012**, 4498–4506. doi: 10.1039/c2ra01367c
47. Du, J.H. and Cheng, H.M. (2012) The fabrication, properties, and uses of graphene/polymer composites. *Macromol. Chem. Phys.*, **213**, 1060–1077. doi: 10.1016/j.electacta.2011.08.054
48. Beidaghi, M. and Wang, C.L. (2011) Micro-supercapacitors based on three dimensional interdigital polypyrrole/C-MEMS electrodes. *Electrochim. Acta*, **56**, 9508–9514. doi: 10.1002/macp.201200029
49. Tong, Z.Q., Yang, Y.N., Wang, J.Y. *et al.* (2014) Layered polyaniline/graphene film from sandwich-structured polyaniline/graphene/polyaniline nanosheets for high-performance pseudosupercapacitors. *J. Mater. Chem. A*, **2**, 4642–4651. doi: 10.1039/c3ta14671e
50. Zhang, K., Zhang, L.L., Zhao, X.S., and Wu, J.S. (2010) Graphene/polyaniline nanofiber composites as supercapacitor electrodes. *Chem. Mater.*, **22**, 1392–1401. doi: 10.1021/cm902876u
51. Mao, L., Zhang, K., Chan, H.S.O., and Wu, J.S. (2012) Surfactant-stabilized graphene/polyaniline nanofiber composites for high performance supercapacitor electrode. *J. Mater. Chem.*, **22**, 80–85. doi: 10.1039/c1jm12869h
52. Wang, H.L., Hao, Q.L., Yang, X.J. *et al.* (2009) Graphene oxide doped polyaniline for supercapacitors. *Electrochem. Commun.*, **11**, 1158–1161. doi: 10.1016/j.elecom.2009.03.036
53. Hao, Q.L., Wang, H.L., Yang, X.J. *et al.* (2011) Morphology-controlled fabrication of sulfonated graphene/polyaniline nanocomposites by liquid/liquid interfacial polymerization and investigation of their electrochemical properties. *Nano Res.*, **4** (4), 323–333. doi: 10.1007/s12274-010-0087-4
54. Hu, L.W., Tu, J.G., Jiao, S.Q. *et al.* (2012) In situ electrochemical polymerization of a nanorod-PANI–Graphenecomposite in a reverse micelle electrolyte and its application in a supercapacitor. *Phys. Chem. Chem. Phys.*, **14**, 15652–15656. doi: 10.1039/c2cp42192e
55. Wang, D.W., Li, F., Zhao, J.P. *et al.* (2009) Fabrication of graphene/polyaniline composite paper via in situ anodic electropolymerization for high-performance flexible electrode. *ACS Nano*, **3**, 1745–1752. doi: 10.1021/nn900297m
56. Feng, X.M., Li, R.M., Ma, Y.W. *et al.* (2011) One-step electrochemical synthesis of graphene/polyaniline composite film and its applications. *Adv. Funct. Mater.*, **21**, 2989–2996. doi: 10.1002/adfm.201100038
57. Sahoo, S., Karthikeyan, G., Nayak, G.C., and Das, C.K. (2011) Electrochemical characterization of in situ polypyrrole coated graphene nanocomposites. *Synth. Met.*, **161**, 1713–1719. doi: 10.1016/j.synthmet.2011.06.011
58. Oliveira, H.P.D., Sydlik, S.A., and Swager, T.M. (2013) Supercapacitors from free-standing polypyrrole/graphene nanocomposites. *J. Phys. Chem. C*, **117**, 10270–10276. doi: 10.1021/jp400344u
59. Li, L.Y., Xia, K.Q., Li, L. *et al.* (2012) Fabrication and characterization of free-standing polypyrrole/graphene oxide nanocomposite paper. *J. Nanopart. Res.*, **14**, 908. doi: 10.1007/s11051-012-0908-3
60. Liu, Y., Zhang, Y., Ma, G.H. *et al.* (2013) Ethylene glycol reduced

graphene oxide/polypyrrole composite for supercapacitor. *Electrochim. Acta*, **88**, 519–525. doi: 10.1016/j.electacta.2012.10.082

61. Davies, A., Audette, P., Farrow, B. *et al.* (2011) Graphene-based flexible supercapacitors: pulse-electropolymerization of polypyrrole on free-standing graphene films. *J. Phys. Chem. C*, **115**, 17612–17620. doi: 10.1021/jp205568v

62. Si, P., Ding, S.J., Lou, X.W. *et al.* (2011) A electrochemically formed three-dimensional structure of polypyrrole/graphene nanoplatelets for high performance supercapacitors. *RSC Adv.*, **1**, 1271–1278. doi: 10.1039/C1RA00519G

63. Carlberg, J.C. and Inganäs, O. (1997) Poly(3,4-ethylenedioxythiophene) as electrode material in electrochemical capacitors. *J. Electrochem. Soc.*, **144** (4), L61–L64.

64. Ryu, K.S., Lee, Y.G., Hong, Y.S. *et al.* (2004) Poly(ethylenedioxythiophene) (PEDOT) as polymer electrode in redox supercapacitor. *Electrochim. Acta*, **50**, 843–847. doi: 10.1016/j.electacta.2004.02.055

65. Patra, S. and Munichandraiah, N. (2007) Supercapacitor studies of electrochemically deposited PEDOT on stainless steel substrate. *J. Appl. Polym. Sci.*, **106**, 1160–1171. doi: 10.1002/app.26675

66. Alvia, F., Ramc, M.K., Basnayakab, P.A. *et al.* (2011) Graphene–polyethylenedioxythiophene conducting polymer nanocomposite based supercapacitor. *Electrochim. Acta*, **56**, 9406–9412. doi: 10.1016/j.electacta.2011.08.024

67. Zhang, J.T. and Zhao, X.S. (2012) Conducting polymers directly coated on reduced graphene oxide sheets as high-performance supercapacitor electrodes. *J. Phys. Chem. C*, **116**, 5420–5426. doi: 10.1021/jp211474e

68. Devaraj, S. and Munichandraiah, N. (2008) Effect of crystallographic structure of MnO_2 on its electrochemical capacitance properties. *J. Phys. Chem. C*, **112**, 4406–4417.

69. Zhao, Y.Q., Zhao, D.D., Tang, P.Y. *et al.* (2012) MnO_2/graphene/nickel foam composite as high performance supercapacitor electrode via a facile electrochemical deposition strategy. *Mater. Lett.*, **76**, 127–130.

70. Wang, W., Guo, S., Bozhilov, K.N. *et al.* (2013) Intertwined nanocarbon and manganese oxide hybrid foam for high-energy supercapacitors. *Small*, **9**, 3714–3721. doi: 10.1002/smll.201300326

71. Ge, J., Yao, H.B., Hu, W. *et al.* (2013) Facile dip coating processed graphene/MnO_2 nanostructured sponges as high performance supercapacitor electrodes. *Nano Energy*, **2**, 505–513.

72. Yang, S., Song, X., Zhang, P. *et al.* (2013) Facile synthesis of nitrogen-doped graphene–ultrathin MnO_2 sheet composites and their electrochemical performances. *ACS Appl. Mater. Interfaces*, **5**, 3317–3322.

73. Wang, B., Park, J., Wang, C. *et al.* (2010) Mn_3O_4 nanoparticles embedded into graphene nanosheets: preparation, characterization, and electrochemical properties for supercapacitors. *Electrochim. Acta*, **55**, 6812–6817.

74. Wu, Z.S., Wang, D.W., Ren, W. *et al.* (2010) Anchoring hydrous RuO_2 on graphene sheets for high-performance electrochemical capacitors. *Adv. Funct. Mater.*, **20**, 3595–3602. doi: 10.1002/adfm.201001054

75. Li, J., Xie, H.Q., Li, Y. *et al.* (2011) Electrochemical properties of graphene nanosheets/polyaniline nanofibers composites as electrode for supercapacitors. *J. Power Sources*, **196**, 10775–10781. doi: 10.1016/j.jpowsour.2011.08.105

76. Xu, J.J., Wang, K., Zu, S.Z. *et al.* (2010) Hierarchical nanocomposites of polyaniline nanowire arrays on graphene oxide sheets with synergistic effect for energy storage. *ACS Nano*, **4** (9), 5019–5026. doi: 10.1021/nn1006539

77. Xu, G.H., Wang, N., Wei, J.Y. *et al.* (2012) Preparation of graphene oxide/polyaniline nanocomposite with assistance of supercritical carbon dioxide for supercapacitor electrodes. *Ind. Eng. Chem. Res.*, **51**, 14390–14398. doi: 10.1021/ie301734f

78. Kumar, N.A., Choi, H.J., Shin, Y.R. *et al.* (2012) Polyaniline-grafted reduced graphene oxide for efficient electrochemical supercapacitors. *ACS Nano*, **6** (2), 1715–1723. doi: 10.1021/nn204688c
79. Zhang, D.C., Zhang, X., Chen, Y. *et al.* (2011) Enhanced capacitance and rate capability of graphene/polypyrrole composite as electrode material for supercapacitors. *J. Power Sources*, **196**, 5990–5996. doi: 10.1016/j.jpowsour.2011.02.090
80. Biswas, S. and Drzal, L.T. (2010) Multilayered nanoarchitecture of graphene nanosheets and polypyrrole nanowires for high performance supercapacitor electrodes. *Chem. Mater.*, **22**, 5667–5671. doi: 10.1021/cm101132g
81. Li, J. and Xie, H.Q. (2012) Synthesis of graphene oxide/polypyrrole nanowire composites for supercapacitors. *Mater. Lett.*, **78**, 106–109. doi: 10.1016/j.matlet.2012.03.013
82. Pham, H.D., Pham, V.H., Oh, E.S. *et al.* (2012) Synthesis of polypyrrole-reduced graphene oxide composites by in-situ photopolymerization and its application as a supercapacitor electrode. *Korean J. Chem. Eng.*, **29** (1), 125–129. doi: 10.1007/s11814-011-0145-y
83. Chang, H.H., Chang, C.K., Tsai, Y.C., and Liao, C.S. (2012) Electrochemically synthesized graphene/polypyrrole composites and their use in supercapacitor. *Carbon*, **50**, 2331–2336. doi: 10.1016/j.carbon.2012.01.056
84. Wang, J.P., Xua, Y.L., Zhu, J.B., and Ren, P.G. (2012) Electrochemical in situ polymerization of reduced graphene oxide/polypyrrole composite with high power density. *J. Power Sources*, **208**, 138–143. doi: 10.1016/j.jpowsour.2012.02.018
85. Wang, Q., Jiao, L., Du Hongmei, D. *et al.* (2014) Fe3O4 nanoparticles grown on graphene as advanced electrode materials for supercapacitors. *J. Power Sources*, **245**, 101–106. doi: 10.1016/j.jpowsour.2013.06.035
86. Li, Z., Wang, J., Niu, L. *et al.* (2014) Rapid synthesis of graphene/cobalt hydroxide composite with enhanced electrochemical performance for supercapacitors. *J. Power Sources*, **245**, 224–231. doi: 10.1016/j.jpowsour.2013.06.121
87. Li, Q., Hu, X., Yang, Q. *et al.* (2014) Electrocapacitive performance of graphene/Co3O4 hybrid material prepared by a nanosheet assembly route. *Electrochim. Acta*, **119**, 184–191. doi: 10.1016/j.electacta.2013.12.066
88. Naoi, K., Naoi, W., Aoyagi, S. *et al.* (2012) New generation "nanohybrid supercapacitor". *Acc. Chem. Res.*, **46** (5), 1075–1083. doi: 10.1021/ar200308h
89. Chae, J.H., Ng, K.C., and Chen, G.Z. (2010) Nanostructured materials for the construction of asymmetrical supercapacitors. *Proc. IMechE' Part A: J. Power Energy*, **224**, 479. doi: 10.1243/09576509JPE861
90. Yu, G., Xie, X., and Pan, L. (2013) Hybrid nanostructured materials for high-performance electrochemical capacitors. *Nano Energy*, **2**, 213–234. doi: 10.1016/j.nanoen.2012.10.006
91. Naoi, K. (2010) "Nanohybrid capacitor": the next generation electrochemical capacitors. *Fuel Cells*, **10** (5), 825–833. doi: 10.1002/fuce.201000041
92. Wu, Z.S., Ren, W., Wang, D.W. *et al.* (2010) High-energy MnO_2 nanowire/graphene and graphene asymmetric electrochemical capacitors. *ACS Nano*, **4** (10), 5835–5842. doi: 10.1021/nn101754k
93. Cheng, Q., Tang, J., Ma, J. *et al.* (2011) Graphene and nanostructured MnO_2 composite electrodes for supercapacitors. *Carbon*, **49**, 2917–2925. doi: 10.1016/j.carbon.2011.02.068
94. Huang, M., Zhang, Y., Li, F. *et al.* (2014) Self-assembly of mesoporous nanotubes assembled from interwoven ultrathin birnessite-type MnO_2 nanosheets for asymmetric supercapacitors. *Sci. Rep.*, **4**, 3878. doi: 10.1038/srep03878
95. Sumboja, A., Foo, C.Y., Wang, X. *et al.* (2013) Large areal mass, flexible and free-standing reduced graphene oxide/manganese dioxide paper for asymmetric supercapacitor device. *Adv. Mater.*, **25**, 2809–2815. doi: 10.1002/adma.201205064

96. Hung, P.J., Chang, K.H., Lee, Y.F. *et al.* (2010) Ideal asymmetric supercapacitors consisting of polyaniline nanofibers and graphene nanosheets with proper complementary potential windows. *Electrochim. Acta*, **55**, 6015–6021. doi: 10.1016/j.electacta.2010.05.058
97. Yu, G., Hu, L., Vosgueritchian, M. *et al.* (2011) Solution-processed graphene/MnO_2 nanostructured textiles for high-performance electrochemical capacitors. *Nano Lett.*, **11**, 2905–2911. doi: 10.1021/nl2013828
98. Fan, Z., Yan, J., Wei, T. *et al.* (2011) Asymmetric supercapacitors based on graphene/MnO_2 and activated carbon nanofiber electrodes with high power and energy density. *Adv. Funct. Mater.*, **21**, 2366–2375. doi: 10.1002/adfm.201100058
99. Wang, H., Liang, Y., Mirfakhrai, T. *et al.* (2011) Advanced asymmetrical supercapacitors based on graphene hybrid materials. *Nano Res.*, **4** (8), 729–736. doi: 10.1007/s12274-011-0129-6
100. Chang, J., Jin, M., Yao, F. *et al.* (2013) Asymmetric supercapacitors based on graphene/MnO_2 nanospheres and graphene/MoO3 nanosheets with high energy density. *Adv. Funct. Mater.*, **23**, 5074–5083. doi: 10.1002/adfm201301851
101. Gao, H., Xiao, F., Ching, C.B. *et al.* (2012) High-performance asymmetric supercapacitor based on graphene hydrogel and nanostructured MnO_2. *ACS Appl. Mater. Interfaces*, **4**, 2801–2810. doi: 10.1021/am300455d
102. Long, C., Wei, T., Yan, J. *et al.* (2013) Supercapacitors based on graphene-supported iron nanosheets as negative electrode materials. *ACS Nano*, **7** (12), 11325–11332. doi: 10.1021/nn405192s
103. Chen, H., Hu, L., Yan, Y. *et al.* (2013) One-step fabrication of ultrathin porous nickel hydroxide-manganese dioxide hybrid nanosheets for supercapacitor electrodes with excellent capacitive performance. *Adv. Energy Mater.*, **3**, 1636–1646. doi: 10.1002/aenm.201300580
104. Jafta, C.J., Nkosi, F., Roux, L.L. *et al.* (2013) Manganese oxide/graphene oxide composites for high-energy aqueous asymmetric electrochemical capacitors. *Electrochim. Acta*, **110**, 228–233. doi: 10.1016/j.electacta.2013.06.096
105. Shi, S., Xu, C., Yang, C. *et al.* (2013) Flexible asymmetric supercapacitors based on ultrathin two-dimensional nanosheets with outstanding electrochemical performance and aesthetic property. *Sci. Rep.*, **3**, 2598. doi: 10.1038/srep02598
106. Amatucci, G.G., Badway, F. *et al.* (2001) An asymmetric hybrid nonaqueous energy storage cell. *J. Electrochem. Soc.*, **148** (8), A930–A939. doi: 10.1149/1.1383553
107. Stoller, M.D., Murali, S., Quarles, N. *et al.* (2012) Activated graphene as a cathode material for Li-ion hybrid supercapacitors. *Phys. Chem. Chem. Phys.*, **14**, 3388–3391. doi: 10.1039/c2cp00017b
108. Aravindan, V., Mhamane, D., Ling, W.C. *et al.* (2013) Nonaqueous lithium-ion capacitors with high energy densities using trigol-reduced graphene oxide nanosheets as cathode-active material. *ChemSusChem*, **6**, 2240–2244. doi: 10.1002/cssc.201300465
109. Kim, H., Cho, M.Y., Kim, M.H. *et al.* (2013) A novel high-energy hybrid supercapacitor with an anatase TiO_2 –reduced graphene oxide anode and an activated carbon cathode. *Adv. Energy Mater.*, **3**, 1500–1506. doi: 10.1002/aenm.201300467
110. Perera, S.D., Rudolph, M., Mariano, R.G. *et al.* (2013) Manganese oxide nanorod–graphene/vanadium oxide nanowire–graphene binder-freepaper electrodes for metaloxide hybrid supercapacitors. *Nano Energy*, **2**, 966–975. doi: 10.1016/j.nanoen.2013.03.018
111. Perera, S.D., Liyanage, A.D., Nijem, N. *et al.* (2013) Vanadium oxide nanowire e graphene binder free nanocomposites paper electrodes for supercapacitors: a facile green approach. *J. Power Sources*, **230**, 130–137. doi: 10.1016/j.jpowsour.2012.11.118
112. Wang, Z.L. and Wu, W. (2012) Nanotechnology-enabled energy

harvesting for self-powered micro-/nanosystems. *Angew. Chem. Int. Ed.*, **51**, 11700–11721. doi: 10.1002/anie.201201656

113. Lee, J.H., Shin, W.H., Lim, S.Y. *et al.* (2013) Modified graphite and graphene electrodes for high-performance lithium ion hybrid capacitors. *Mater. Renewable Sustainable*, **2**, 22. doi: 10.1007/s40243-014-0022-9
114. Gogotsi, Y. and Simon, P. (2011) True performance metrics in electrochemical energy storage. *Science*, **334**, 917–918. doi: 10.1126/science.1213003
115. Arthur, T.S., Bates, D.J., and Dunn, B. (2011) Three-dimensional electrodes and battery architectures. *MRS Bull.*, **36**, 523–531. doi: 10.1557/mrs.2011.156
116. Sun, W. and Chen, X.Y. (2009) Fabrication and tests of a novel three dimensional microsupercapacitor. *Microelectron. Eng.*, **86**, 1307–1310. doi: 10.1016/j.mee.2008.12.010
117. Sun, W., Zheng, R.L., and Chen, X.Y. (2010) Symmetric redox supercapacitor based on micro-fabrication with three-dimensional polypyrrole electrodes. *J. Power Sources*, **195**, 7120–7125. doi: 10.1016/j.jpowsour.2010.05.012
118. Sung, J.H., Kim, S., and Lee, K.H. (2004) Fabrication of all-solid-state electrochemical microcapacitors. *J. Power Sources*, **133**, 312–319. doi: 10.1016/j.jpowsour.2004.02.003
119. Chmiola, J., Largeot, C., Taberna, P.L. *et al.* (2010) Monolithic carbide-derived carbon films for micro-supercapacitors. *Science*, **328**, 480–483. doi: 10.1126/science.1184126
120. Pandolfo, A.G. and Hollenkamp, A.F. (2006) Carbon properties and their role in supercapacitors. *J. Power Sources*, **157**, 11–27. doi: 10.1016/j.jpowsour.2006.02.065
121. Zhang, L.L., Zhou, R., and Zhao, X.S. (2010) Graphene-based materials as supercapacitor electrodes. *J. Mater. Chem.*, **20**, 5983–5992. doi: 10.1039/C000417K
122. Huang, X., Qi, Y., Boey, F. *et al.* (2012) Graphene-based composites. *Chem. Soc. Rev.*, **41**, 666–686. doi: 10.1039/C1CS15078B
123. Byon, H.R., Lee, S.W., Chen, S. *et al.* (2011) Thin films of carbon nanotubes and chemically reduced graphenes for electrochemical micro-capacitors. *Carbon*, **49**, 457–467. doi: 10.1016/j.carbon.2010.09.042
124. Yan, J., Fan, Z.J., Wei, T. *et al.* (2010) Fast and reversible surface redox reaction of graphene-MnO_2 composites as supercapacitor electrodes. *Carbon*, **48**, 3825–3833. doi: 10.1016/j.carbon.2010.06.047
125. Liu, C.G., Yu, Z.N., Neff, D. *et al.* (2010) Graphene-based supercapacitor with an ultrahigh energy density. *Nano Lett.*, **10**, 4863–4868. doi: 10.1021/nl102661q
126. Yoo, J.J., Balakrishnan, K., Huang, J.S. *et al.* (2011) Ultrathin planar graphene supercapacitors. *Nano Lett.*, **11**, 1423–1427. doi: 10.1021/nl200225j
127. Beidaghi, M. and Wang, C.L. (2012) Micro-supercapacitors based on interdigital electrodes of reduced graphene oxide and carbon nanotube composites with ultrahigh power handling performance. *Adv. Funct. Mater.*, **22**, 4501–4510. doi: 10.1002/adfm.201201292
128. Lin, J., Zhang, C., Yan, Z. *et al.* (2013) 3-dimensional graphene carbon nanotube carpet-based microsupercapacitors with high electrochemical performance. *Nano Lett.*, **13**, 72–78. doi: 10.1021/nl3034976
129. Liu, W.W., Feng, Y.Q., Yan, X.B. *et al.* (2013) Superior micro-supercapacitors based on graphene quantum dots. *Adv. Funct. Mater.*, **23**, 4111–4122. doi: 10.1002/adfm.201203771
130. Gao, W., Singh, N., Song, L. *et al.* (2011) Direct laser writing of micro-supercapacitors on hydrated graphite oxide films. *Nat. Nanotechnol.*, **6**, 496–500. doi: 10.1038/nnano.2011.110
131. El-Kady, M.F., Strong, V., Dubin, S. *et al.* (2012) Laser scribing of high-performance and flexible graphene-based electrochemical capacitors.

Science, **1326**, 1326–1330. doi: 10.1126/science.1216744

132. El-Kady, M.F. and Kaner, R.B. (2013) Scalable fabrication of high-power graphene micro-supercapacitors for flexible and on-chip energy storage. *Nat. Commun.*, **4**, 1475–1483. doi: 10.1038/ncomms2446

133. Xue, M.Q., Li, F.W., Zhu, J. *et al.* (2012) Structure-based enhanced capacitance: in situ growth of highly ordered polyaniline nanorods on reduced graphene oxide patterns. *Adv. Funct. Mater.*, **22**, 1284–1290. doi: 10.1002/adfm.201101989

7
Graphene-Based Solar-Driven Water-Splitting Devices

Jian Ru Gong

7.1
Introduction

Human beings are now experiencing the culmination of a fast growth period in economics and technology. But the huge consumption of fossil fuels and the severe deterioration of the environment have restricted the sustainable development of human society. Sufficiently utilizing clean and renewable energy resources is considered as the ultimate solution to the above issues, and has attracted worldwide interest in recent decades [1].

Actually, energy from sunlight that arrives on the earth in 1 h is more than all of the energy consumed by humans in an entire year; thus an affordable future can be certainly achieved if solar energy, the most abundant renewable energy in the earth, is efficiently exploited [2]. However, because of the daily and seasonal variability of sunlight, a cost-effective way in which solar energy can be captured, converted, and stored is highly desired. The most widely recognized method for cost-effective massive energy storage is in the form of chemical bonds. Thus, great attention has been given to the development of highly effective technologies for conversion of solar energy to chemical fuels [3, 4].

Splitting water into hydrogen and oxygen by using sunlight is a promising approach to solar energy storage [1, 4]. Among various technologies, direct photolysis of water upon semiconductors, which was first demonstrated by Fujishima and Honda [5] in 1972, is seen as the best path toward this objective, because it is convenient and cost effective, and has huge potential for further development. Therefore, tremendous efforts have been made during the past 40 years to approach this Holy Grail, that is, solar-driven water splitting [6–10].

For realizing solar-driven water splitting, one requires, at the minimum, a light absorber, fuel-forming catalysts, and an electrolyte [11, 12]. Among them, the light absorber and the catalysts are the two key components that directly determine the final solar conversion efficiency. Hence, most of the research activities in the field of solar-driven water splitting are centralized on the development of light absorbers and catalysts with high efficiency, long durability, and excellent scalability. Several reviews have comprehensively summarized the current achievements

Graphene-based Energy Devices, First Edition. Edited by A. Rashid bin Mohd Yusoff.
© 2015 Wiley-VCH Verlag GmbH & Co. KGaA. Published 2015 by Wiley-VCH Verlag GmbH & Co. KGaA.

in this emerging area and described the common strategies to promote the performance of catalysts [6–10]. However, we are still confronted with many issues, such as the low absorption of incident light, the rapid recombination of the photogenerated charge carriers, the sluggish kinetics of hydrogen or oxygen evolution reactions, the severe back reactions between hydrogen and oxygen, the poor stability of light absorbers and catalysts, and the over-abuse of noble metals [11, 12].

Recently, graphene has stimulated the interests of global researchers because of its unique properties, such as the extremely large surface area, the amazingly high electron mobility and conductivity, and the high optical transparency [13]. Great achievements have been made in revealing the impressive application prospects of graphene in various fields such as biomedicine, electronics, energy storage, and sensors [14–18]. In view of these encouraging achievements, researchers also pay a lot of attention to investigate the potential applications of graphene in the area of solar-driven water splitting, and considerable progress has been made in this emerging field recently [16, 19–22]. In this chapter, we will comprehensively review the recent progress in this area, in order to promote further development of graphene-based solar-driven water-splitting devices.

7.2 Basic Architectures of Solar-Driven Water-Splitting Devices

A large number of solar-driven water-splitting devices have been reported to date [23]. The majority of these proposed device designs can be classified into three general types with respect to their technological maturity and projected manufacturing cost, namely photoelectrochemical (PEC) cells, mixed-colloid photocatalysis systems, and photovoltaic (PV)/electrolyzer tandem devices (Scheme 7.1) [11].

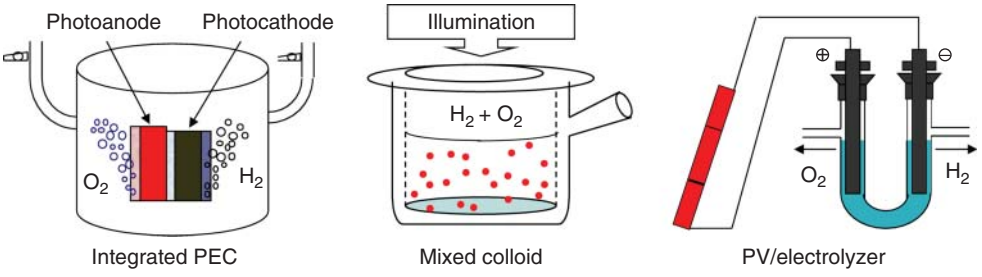

Scheme 7.1 Schematic of three device architectures available for solar-driven water splitting.

PEC devices always exhibit excellent hydrogen production property; especially, those composed of III–V group semiconductors have demonstrated solar-to-hydrogen (STH) efficiencies as high as 12.4% and 18.3% [24–29]. But the poor durability and high manufacturing costs severely restrict their scale-up. Mixed-colloid photocatalysis systems can be considered as a limiting case in

PEC devices, where a colloid particle can be thought of as a short-circuited PEC cell [30]. These colloid systems are much simpler and less expensive to construct and use than PEC cells, but the solar conversion efficiencies reported to date are still far from satisfactory. Also, one needs to expend additional energy to separate the explosive mixtures of hydrogen and oxygen immediately when formed, thereby further reducing the overall efficiency [6, 8]. Meanwhile, current technology can mate solar cells with conventional water electrolysis units to produce hydrogen, which has been proposed as a mature technique to realize solar-driven water splitting by using PV/electrolyzer tandem devices [31, 32]. However, the large potential required for water electrolysis (~1.9 eV) can be achieved only by using tandem solar cells, and an electrolyzer operating at high faradic efficiency always uses noble metal electrocatalysts. To operate such kind of devices at very high efficiencies would be extremely expensive. That is, the key requirements for practical applications, namely efficiency, stability, and scalability, still cannot be simultaneously attained by these reported solar-driven water-splitting devices.

7.3
Promising Prospects of Graphene in Solar-Driven Water-Splitting Devices

Graphene, a two-dimensional (2D) network of hexagonal-structured, sp^2-hybridized carbon atoms, is a rapidly rising star in the horizon of materials science [33, 34]. Its band structure is symmetric about the Dirac point, and its π^*-state conduction band (CB) and the π-state valence band (VB) touch each other at the Dirac point, making graphene to display an amazingly high conductivity and electron transport property [35, 36]. Meanwhile, graphene possess a high work function (4.42 eV), and can accept photogenerated electrons from the CB of most semiconductors [37]. Therefore, similar to the contact between a metal and a semiconductor, a space charge region will certainly form near the surface of a semiconductor when it is contacted with graphene (Scheme 7.2). Moreover, graphene possesses an extremely high specific surface area and is unusually flexible, so it can well spread over the surface of a semiconductor. Thus the graphene/semiconductor interface is nearly infinite, making the space charge region to homogeneously distribute on the surface of semiconductor, thereby significantly promoting the separation of the photogenerated charge carriers; in contrast, the metal particle is always embedded in semiconductor, resulting in the limited distribution of space charge region [38–40]. In addition, the reduction potential of graphene/graphene$^{\cdot-}$ (−0.08 eV vs NHE, pH = 0) is more negative than the reduction potential of H^+/H_2, which means that graphene is also a potential catalyst for hydrogen evolution reaction (HER) [41]. Therefore, we can conclude that graphene can not only act as an electron sink and transporter but also promote the charge separation and catalyze the HER.

More importantly, the band structure of graphene can be tailored by physical methods, such as heteroatom doping, which usually makes graphene an n-type

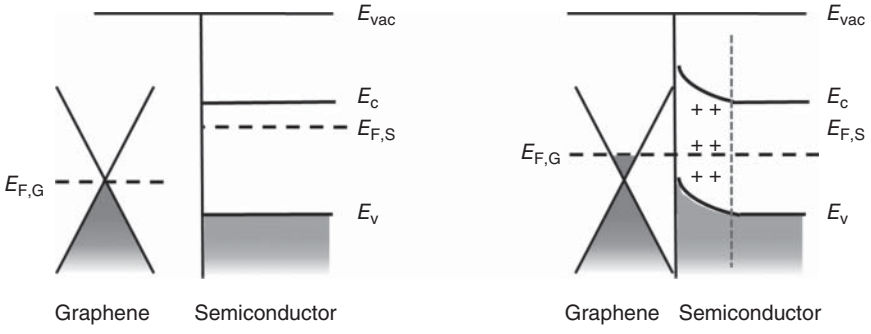

Scheme 7.2 Energy band diagrams of graphene and an n-type semiconductor before and after contact. E_{vac}, vacuum energy; E_c, energy of conduction band minimum; E_v, energy of valence band maximum; $E_{F,G}$, femi level of graphene; and $E_{F,S}$, femi level of the semiconductor.

or p-type semiconductor with a small bandgap by detuning away the Fermi level from the Dirac point [42, 43]. And, a tunable bandgap from insulating to conducting can also be achieved by controlling the reduction degree of graphene oxide (GO). For instance, a bandgap ranging from a few tenths to 4 eV has been obtained by changing the reduction level and the location of the oxidized region of GO (Scheme 7.3) [44, 45]. Thus, functionalized graphene and graphene derivatives are also potential candidate materials that can drive the water-splitting reaction under sunlight irradiation. In summary, the unique properties of graphene make it extremely attractive for its application in solar-driven water-splitting devices.

We will review the great efforts that have been made in the design of graphene-based solar-driven water-splitting devices recently in the subsequent sections. The

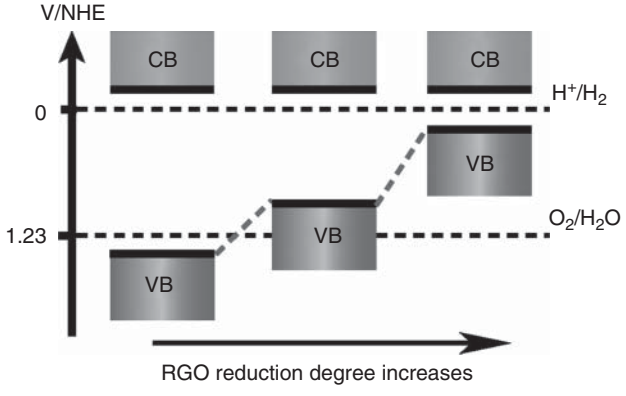

Scheme 7.3 Energy level diagrams of RGO with different reduction degrees in comparison with the potentials for water reduction and oxidation. (Reprinted with permission from Ref. [19]. Copyright (2013), John Wiley & Sons.)

achievements in different types of graphene-based solar-driven water-splitting devices will be summarized, including integrated PEC cells, mixed-colloid systems, and PV/eletrolyzer devices. Finally, we will end this chapter with some perspectives in this emerging area.

7.4 Graphene-Based Integrated Photoelectrochemical Cells

Graphene has been combined with a variety of semiconductors for its application in integrated PEC cells, and many encouraging findings have already been obtained till now, indicating the promising future of graphene in PEC devices. Especially, it has been found that graphene can play different roles during the water-splitting process, such as a conductive scaffold, an electron collection layer, an interfacial charge transporter, an electrocatalyst, or even a photosensitizer.

In earlier works, much attention has been focused on the direct combination of graphene with semiconductors to promote their PEC performance. Ng *et al.* [46] first reported that graphene could improve the hydrogen production rate of a PEC device (Figure 7.1). They fabricated a $BiVO_4$/reduced graphene oxide (RGO) composite photoanode by spin coating, and found that the obtained photoelectrode exhibited a steady evolution of H_2 under visible light irradiation, and a much higher incident photon-to-current conversion efficiency (IPCE) at 400 nm (4.2%) compared to $BiVO_4$ (0.3%) alone. This excellent performance of the $BiVO_4$/RGO

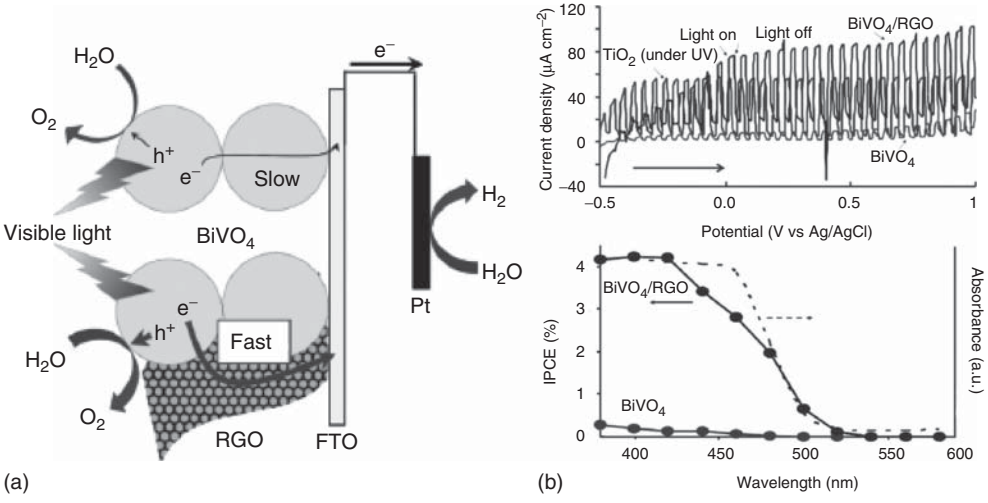

Figure 7.1 (a) Schematic illustration of reduced graphene oxide (RGO) promoting electron migration from $BiVO_4$ to fluorine-doped tin oxide (FTO) glass. (b) Visible light voltage–photocurrent functions of $BiVO_4$, $BiVO_4$/RGO, and TiO_2 (under UV irradiation), and IPCE and diffuse reflectance spectra of $BiVO_4$ and $BiVO_4$/RGO. (Reprinted with permission from Ref. [46]. Copyright (2010), American Chemical Society.)

photoanode was attributed to the presence of RGO, as it acts as an excellent conductive scaffold by efficiently accepting the photogenerated electrons from $BiVO_4$ and rapidly shuttling them to the collecting electrode. Similarly, a WO_3/RGO photoanode was reported to exhibit a significant enhancement in photoresponse compared to pristine WO_3 [47]. But the authors proposed that RGO could not only play a favorable role in enhancing the electron–hole separation but also provide active sites for the electron–hole recombination, and a more positive applied bias is in favor of effective electron–hole separation by means of quick collection and transport of electrons by RGO. Besides, graphene can also promote the photoelectrochemcial activity of sulfide semiconductors. Zhang *et al.* prepared a $Zn_{0.5}Cd_{0.5}S$/reduced graphene oxide ($Zn_{0.5}Cd_{0.5}S$/RGO) photoelectrode by a facile *in situ* photoreduction of GO in the presence of nanoporous $Zn_{0.5}Cd_{0.5}S$ single-crystal-like nanosheets [48]. The $Zn_{0.5}Cd_{0.5}S$/RGO photoelectrode exhibited a higher anodic photocurrent density, a lower zero-current potential, and a higher PEC response than pure $Zn_{0.5}Cd_{0.5}S$ photoelectrodes. This high photochemical activity is ascribed to the presence of RGO, which serves as a conductive scaffold to collect electrons, thus efficiently prolonging the lifetime of photoinduced electrons from the excited $Zn_{0.5}Cd_{0.5}S$ nanosheets. Furthermore, the electrons stored in RGO are readily discharged or scavenged on demand by the applied positive bias to the counterelectrode, making the $Zn_{0.5}Cd_{0.5}S$/RGO photoelectrode highly stable for HER.

Recently, Liu *et al.* fabricated well-defined hybrid films of graphene nanosheet (GN)/CdS quantum dots (QDs) by sequential layer-by-layer (LbL) self-assembly of positively charged, poly(allylamine hydrochloride) (PAH)-modified GNs and negatively charged CdS QDs (Figure 7.2) [49]. It was found that the alternating GN/CdS QD multilayered film showed significantly enhanced PEC activity under visible light irradiation as compared to pure CdS QD and GN films. The enhancement is attributed to the judicious integration of CdS QDs with GNs in an alternating manner, which maximizes the 2D structural advantage of GNs in GN/CdS QD composite films. In this way, photoexcited electrons in CdS QDs are readily and efficiently transferred from the CB of CdS to the neighboring GN scaffold upon visible light irradiation, where the GNs serve serve as an efficient electron collector and transporter, thus suppressing the recombination of photogenerated electron–hole pairs.

However, the contact area between graphene and the semiconductor nanoparticles is always confined, as this planar scaffold can only contact with the bottom part of the nanoparticles. Accordingly, Kim *et al.* [50] modified an iron oxide photoanode by using a graphene/carbon nanotube (CNT) composite conducting scaffold. This composite photoanode showed a much more improved photocurrent compared to the bare Fe_2O_3, which was also higher than those of Fe_2O_3/CNT and Fe_2O_3/graphene photoanodes. This is due to the formation of a more open and highly exposed 3D-like architecture, where CNTs and graphene become the spacer for each other, not only enlarging the contact area between the conducting scaffold and Fe_2O_3 particles but also facilitating partial recovery of the intrinsic conducting ability of graphene and the CNTs.

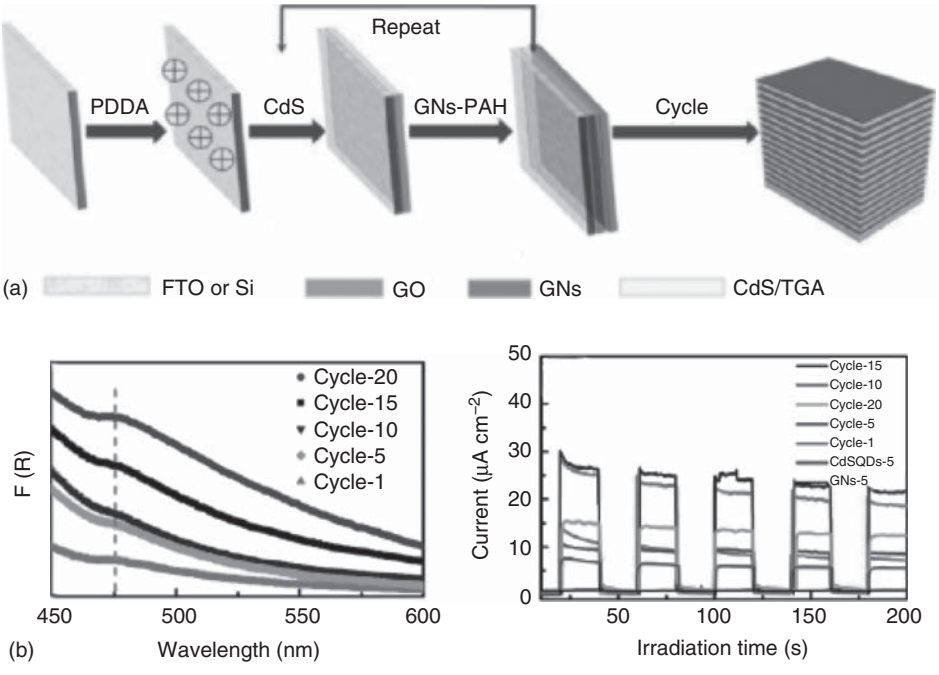

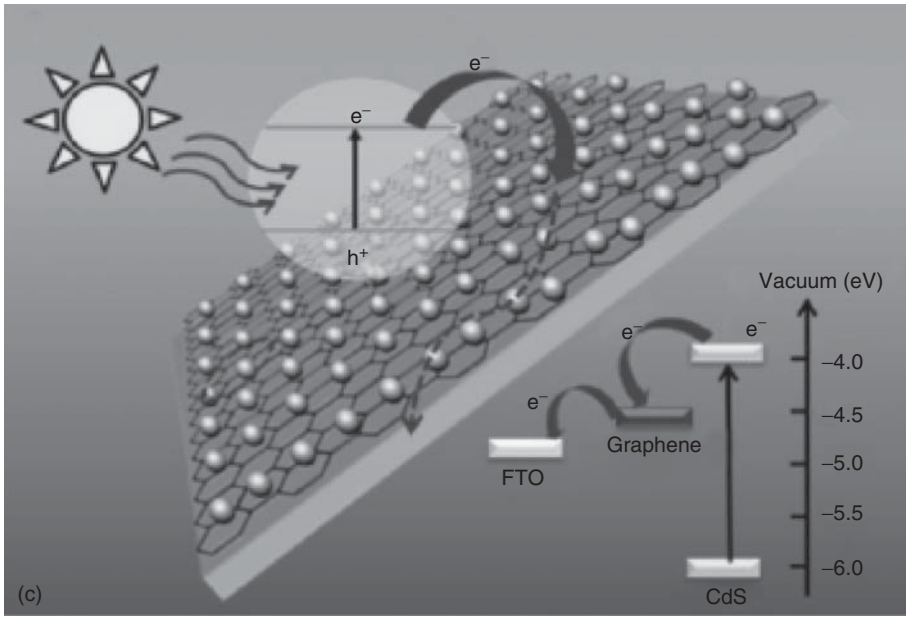

Figure 7.2 (a) Schematic illustration of LbL self-assembly of GN/CdS QD multilayered films. (b) UV–vis absorption spectra and transient photocurrent responses of $(GN/CdS\ QD)_n$ multilayered films with variable deposition cycles ($n = 1, 5, 10, 15, 20$). (c) Schematic illustration of the PEC mechanism over the GN/CdS QD multilayer films. (Reprinted with permission from Ref. [49]. Copyright (2014), American Chemical Society.)

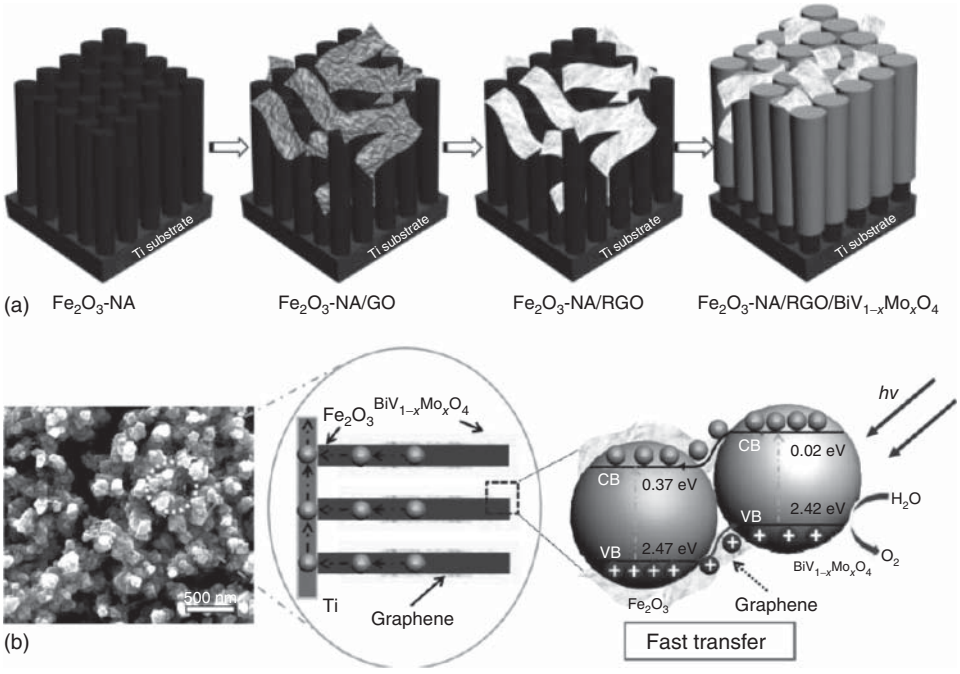

Figure 7.3 (a) Synthetic route to the Fe_2O_3-NA/RGO/$BiV_{1-x}Mo_xO_4$ heterojunction. (b) Schematic for the energy band structure of the Fe_2O_3-NA/RGO/$BiV_{1-x}Mo_xO_4$ heterojunction and the proposed mechanism of PEC water splitting. (Reprinted with permission from Ref. [51]. Copyright (2012), American Chemical Society.)

Graphene as an interfacial charge transporter between two semiconductors has been reported in PEC devices by Hou *et al.* They synthesized a novel heterojunction array of α-Fe_2O_3/RGO/$BiV_{1-x}Mo_xO_4$ core–shell nanorod with RGO as the interlayer (Figure 7.3) [51]. Thanks to the band alignment and potential difference, RGO sheets, as an excellent electron conductor, provide a direct pathway for electrons to transfer from the CB of the $BiV_{1-x}Mo_xO_4$ shell to the CB of the Fe_2O_3 core. Simultaneously, the holes migrate from the VB of Fe_2O_3 via the RGO interlayer to the VB of $BiV_{1-x}Mo_xO_4$, and then are consumed by oxidizing water to form O_2. Thus, the photoinduced charges are efficiently separated, resulting in the enhancement of PEC activity. Lately, a composite photoelectrode consisting of a CdS sensitizer, an RGO charge transporter, and a TiO_2 acceptor was reported [52]. The RGO is demonstrated to play vital roles in alleviating trapped electrons at the heterojunction and serves as a platform for shuttling electrons between CdS and TiO_2. These works open a promising avenue for the design and fabrication of novel graphene-based core–shell heterojunctions for PEC water splitting.

Moreover, Chen *et al.* [53] proposed a novel 2D ternary nanojunction composed of porous graphitic C_3N_4 nanosheets, nitrogen-doped graphene, and layered MoS_2 (Figure 7.4). The constructed 2D/2D layered junction significantly

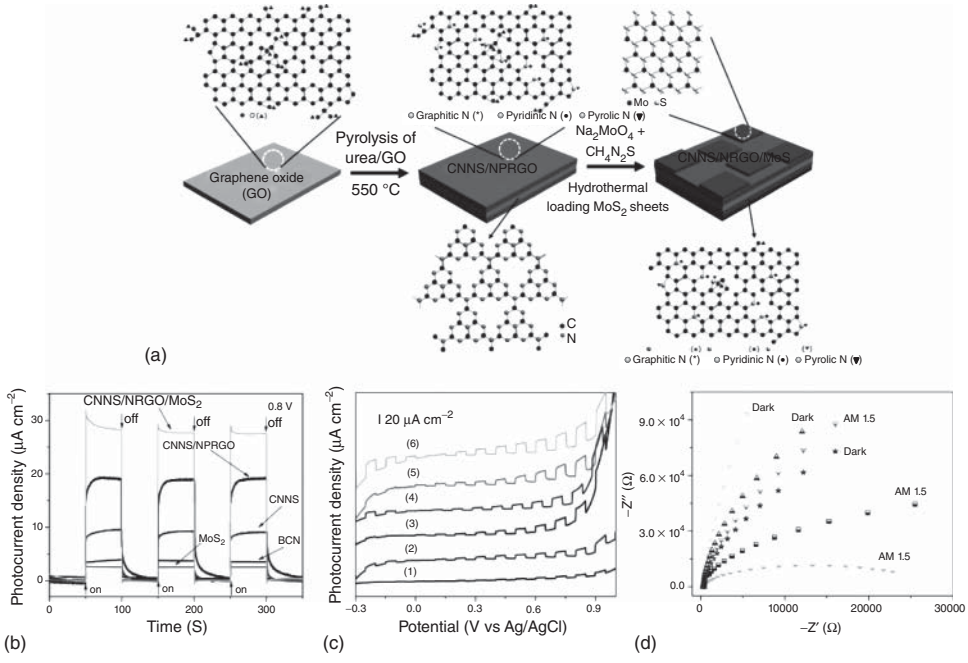

Figure 7.4 (a) Schematic illustration for the synthesis process of the CNNS/NRGO/MoS_2 nanojunction. (b) Transient photocurrent density versus time plotted for different samples in 0.01 M Na_2SO_4 electrolyte under simulated sunlight irradiation. (c) Current–potential plots for BCN (1), CNNS (2), CNNS/NPRGO (3), physical mixture of CNNS/NRGO and MoS_2 (4), CNNS/MoS_2 (5), and CNNS/NRGO/MoS_2 nanojunction (6) irradiated with chopped simulated sunlight. (d) EIS Nyquist plots of the CNNS (△,▽), CNNS/NPRGO (□,□), and CNNS/NRGO/MoS_2 nanojunction (★,○) at a bias of 0.3 V under dark and simulated sunlight irradiation. (Reprinted with permission from Ref. [53]. Copyright (2013), John Wiley & Sons.)

increased the contact area for efficient charge transfer across the interface compared to 0D nanoparticles that were only in point contact, thus exhibiting significantly enhanced PEC activity. Coupling grapheme with layered semiconductors to form a 2D heterojunction provides an effective strategy for improving the photoconversion efficiency.

Wang *et al.* coated the surface of silicon nanowire (SiNW) arrays with RGO by a facile spin-coating method [54]. The resulting SiNW/RGO composite exhibited enhanced PEC properties, with short-circuit photocurrent density more than 4 times higher than that of the pristine SiNWs and more than 600 times higher than that of planar Si/RGO composites. The results of electrochemical impedance spectroscopy measurements suggest that the reduction of trapping and recombination of photogenerated carriers, as well as the remarkable enhancement of PEC properties, can be attributed to the low charge transfer resistance at the SiNW/RGO interface and RGO/electrolyte interface. The above achievements

prove that graphene can also promote the charge transfer at a semiconductor/liquid interface, and the method can provide a convenient and applicable approach to further development of highly active photoelectrodes.

Interestingly, Kim *et al.* [55] introduced a graphene interlayer onto the transparent conductive electrode before the construction of an inverse opaline hematite (a-Fe_2O_3) thin film (Figure 7.5). The graphene interlayer can act a good electron collection layer by efficiently gathering the electrons in a-Fe_2O_3 and rapidly delivering them to the transparent conductive electrode, similar to the electron collection layer in a solar cell. Besides, the graphene layer acts also an excellent electrolyte blocking barrier, by which the charge recombination at the substrate/electrolyte interface is dramatically reduced. Therefore, both the photocurrent density and IPCE of the electrode remarkably improved, which were several times higher than those of the pure inverse opaline hematite photoanode.

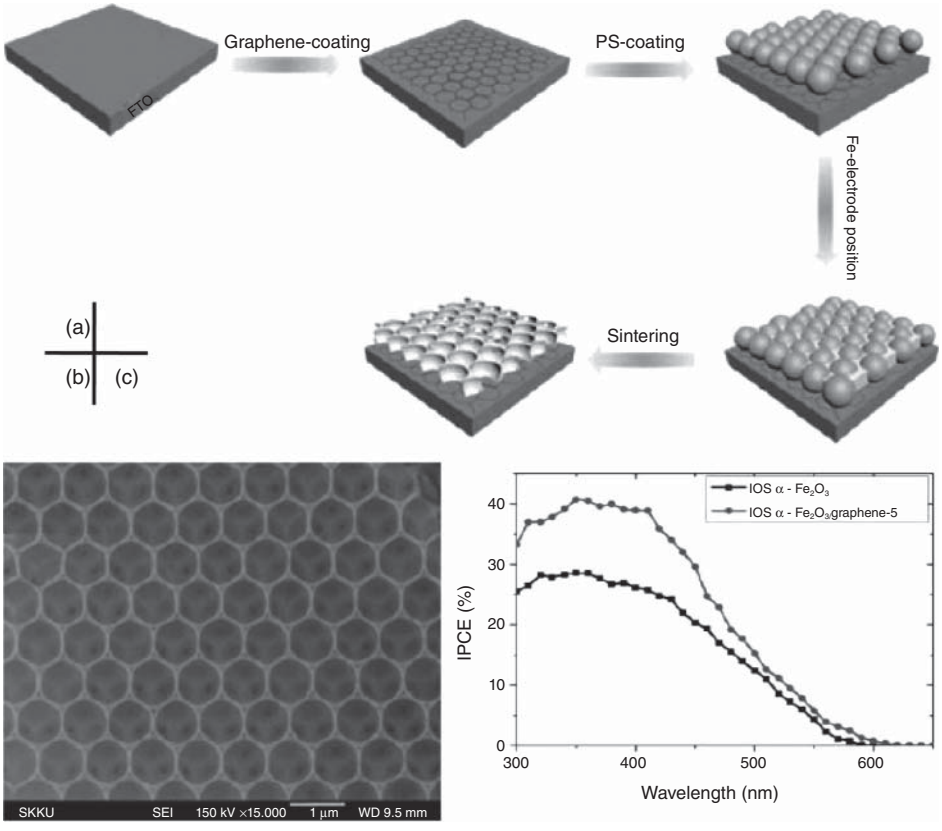

Figure 7.5 (a) Schematic illustration of the fabrication process of the photoanode composed of inverse opal structured α-Fe_2O_3 grown on graphene/FTO substrates. (b) FE-SEM image of the top view of the α-Fe_2O_3 film on graphene. (c) IPCE of α-Fe_2O_3 and α-Fe_2O_3/graphene photoanodes at 0.5 V in 1 M aqueous NaOH electrolyte. (Reprinted with permission from Ref. [55]. Copyright (2013), Royal Society of Chemistry.)

Sim *et al.* [56] transferred a monolayer graphene prepared by chemical vapor deposition (CVD) to a p-type Si wafer, and investigated the role of graphene as a catalyst for solar-driven HER on this Si photocathode (Figure 7.6). They boosted the catalytic activity of graphene by plasma treatment in a nitrogen ambient, as this treatment can induce abundant defects and incorporate nitrogen atoms into the graphene structure, acting as catalytic sites on graphene. This monolayer graphene containing nitrogen impurities exhibited a remarkable increase in the exchange current density and led to a significant anodic shift of the onset of photocurrent from the Si photocathode. Additionally, monolayer graphene shows the passivation effect that suppresses the surface oxidation of Si, thus enabling the operation of the Si photocathode in neutral water. This study shows that graphene itself can be applied to a PEC system as a catalyst with high activity and chemical stability. Meanwhile, the role of graphene as a surface passivation layer is also proved by comparing the behavior of graphene-coated n-type Si(111) photoanodes with that of H-terminated n-type Si(111) photoanodes [57]. It was found that the n-Si/graphene electrodes exhibited stable short-circuit photocurrent densities of over 10 mA cm^{-2} for >1000 s of continuous operation

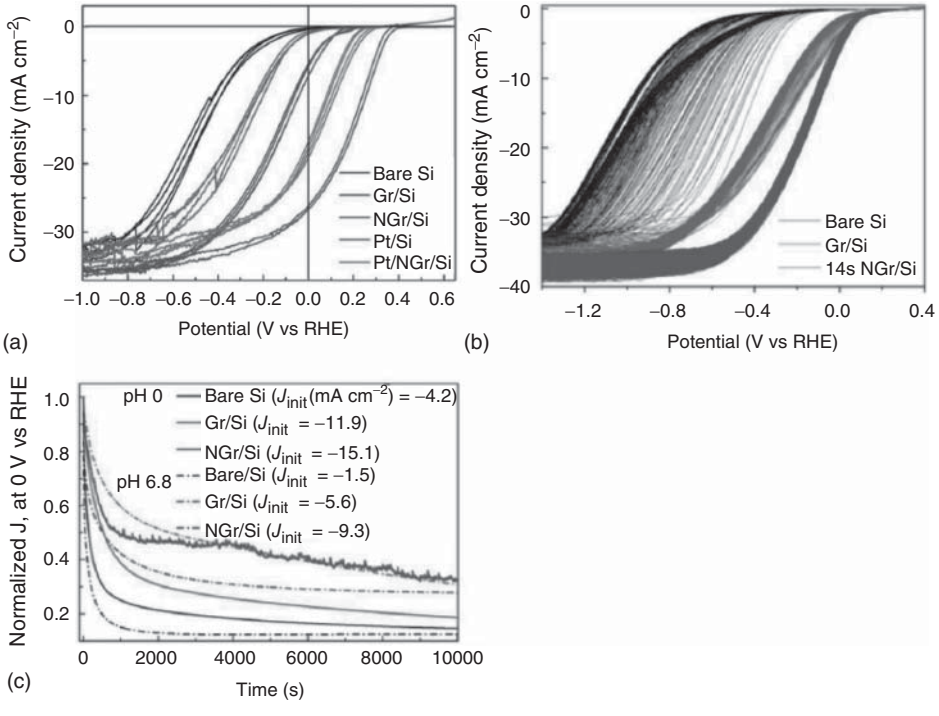

Figure 7.6 (a) Photocurrent density–potential (*J*–*E*) curves for lightly boron doped p-Si electrode deposited with Gr and NGr. (b) The stability test of bare Si, Gr/Si, and NGr/Si photocathodes. (c) Chronoamperometry operation of photocathodes. (Reprinted with permission from Ref. [56]. Copyright (2013), Royal Society of Chemistry.)

in aqueous electrolytes, whereas n-Si-H electrodes yielded a nearly complete decay of the current density within ~100 s.

In addition, graphene can absorb light uniformly over a wide range of wavelengths from the infrared through visible to the ultraviolet region, since it is basically a large aromatic macromolecule without a bandgap. Lin *et al.* [58] constructed an RGO/ZnO heterojunction and investigated its PEC properties (Figure 7.7). They found that the highly photoactive RGO as a photosensitizer

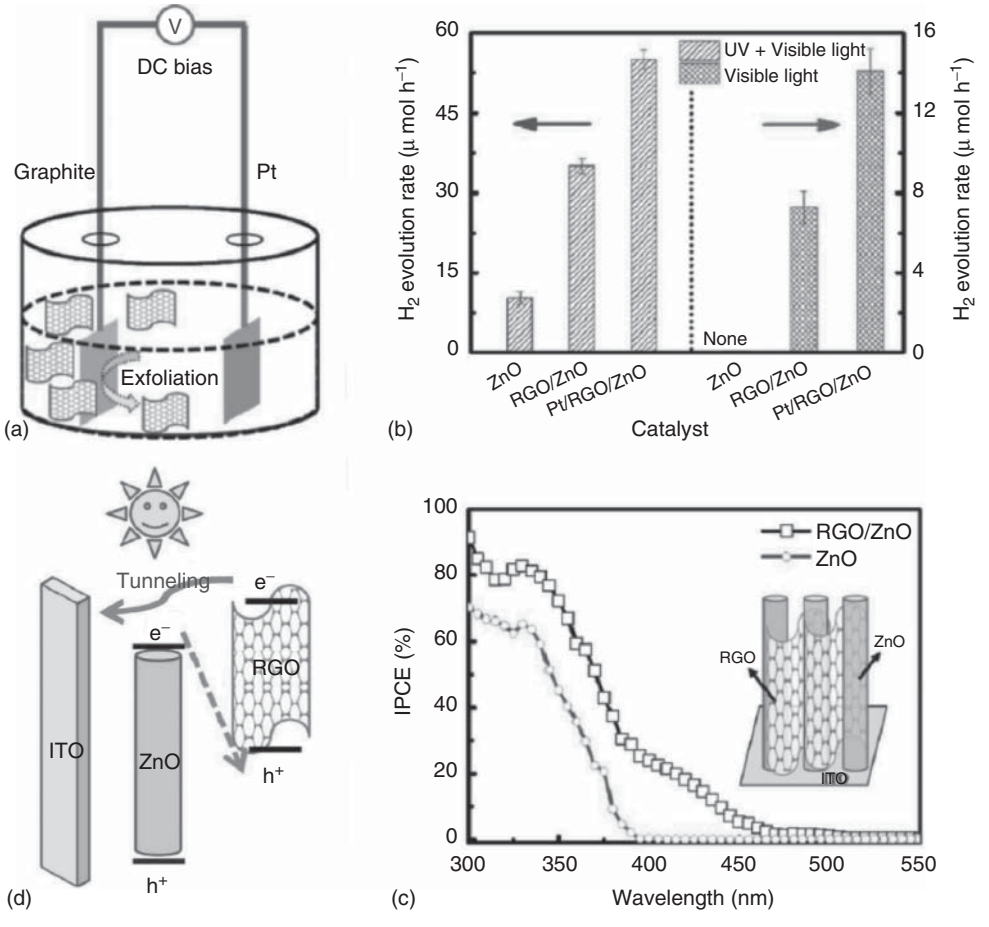

Figure 7.7 (a) Schematic illustration for the EC exfoliation of graphite. (b) Comparison of the photocatalytic performance over bare ZnO, RGO/ZnO, and Pt/RGO/ZnO photoelectrodes under UV–visible light ($\lambda > 300$ nm) and visible light ($\lambda > 400$ nm) irradiation. (c) The measured IPCE spectra of pristine ZnO nanorods and RGO/ZnO nanohybrids in the region 300–550 nm at a potential of 0.4 V (vs Pt) in the two-electrode system (inset: schematic illustration for the 1D ZnO nanorod/2D RGO nanosheet hybrid). (d) The possible schematic process of photoexcited electron–hole transport in the RGO photosensitized ZnO nanoelectrode. (Reprinted with permission from Ref. [58]. Copyright (2012), Royal Society of Chemistry.)

could make H_2 evolution easier and improve the photoconversion ability of ZnO under visible light irradiation. The IPCE of the RGO/ZnO photoanodes at the monochromatic wavelength of 400 nm can go up to 24%.

7.5 Graphene-Based Mixed-Colloid Photocatalytic Systems

The availability of solution-based synthetic strategies for graphene, that is, RGO, which proceeds proceeds through reduction of GO (a highly oxidized and exfoliated product of pristine graphite), provides a great convenience for development of graphene-based mixed-colloid photocatalytic systems, as the residual functional groups on RGO can not only serve as the nucleation sites to anchor nanoparticles but also help in coupling of graphene with other molecules [59, 60]. Thus, graphene-based mixed-colloid photocatalytic systems have been under fast-paced development in the past several years, and it has been found that graphene can play various roles during the photocatalytic hydrogen production process, including an electron acceptor and transporter, a cocatalyst, a photocatalyst, and a photosensitizer [19]. These important scientific achievements have been systemically reviewed recently [19, 61]. Here we will selectively summarize the milestones in this area.

TiO_2/graphene is one of the most investigated graphene-based mixed-colloid systems. Many researchers have proved that graphene can accept the photoinduced electrons from TiO_2 and transport them to reactive sites efficiently, thus promoting separation of the photogenerated electron–hole pairs and finally improving the photocatalytic H_2 production efficiency [37, 62–64]. Meanwhile, the performance of TiO_2/graphene composite is affected by several factors, including the graphene content in the composite [65, 66], interfacial interaction, and the contact area between graphene and TiO_2 [67]. Among various attempts, works on the configuration of TiO_2/graphene composite carried out by Choi group are very impressive (Figure 7.8). Usually, the 2D graphene sheets can only contact the bottom part of the TiO_2 nanoparticles, which limits the electron transport from TiO_2 nanoparticles to graphene. However, Choi group designed a TiO_2/RGO core–shell photocatalyst in which the TiO_2 nanoparticle was fully contacted by the RGO shell, resulting in the easier transfer of the photogenerated electrons from TiO_2 to RGO [68]. Thus, the H_2 production rate was higher than that over RGO sheets loaded with TiO_2. Recently, another efficient way to improve the interfacial interaction by embedding graphene in the matrix of TiO_2 was also proposed by the same group [69]. It was found that the electronic coupling between graphene sheets and TiO_2 matrix was stronger than that in the situation where graphene sheets coupled with the external surface of TiO_2. Accordingly, Zhang *et al.* [70] developed a titania/graphene nanosheet composite through a 2D interface engineering strategy. The special 2D/2D TiO_2 nanosheet/graphene photocatalyst configuration also effectively enhanced charge separation, thus promoting the photodegradation reactions.

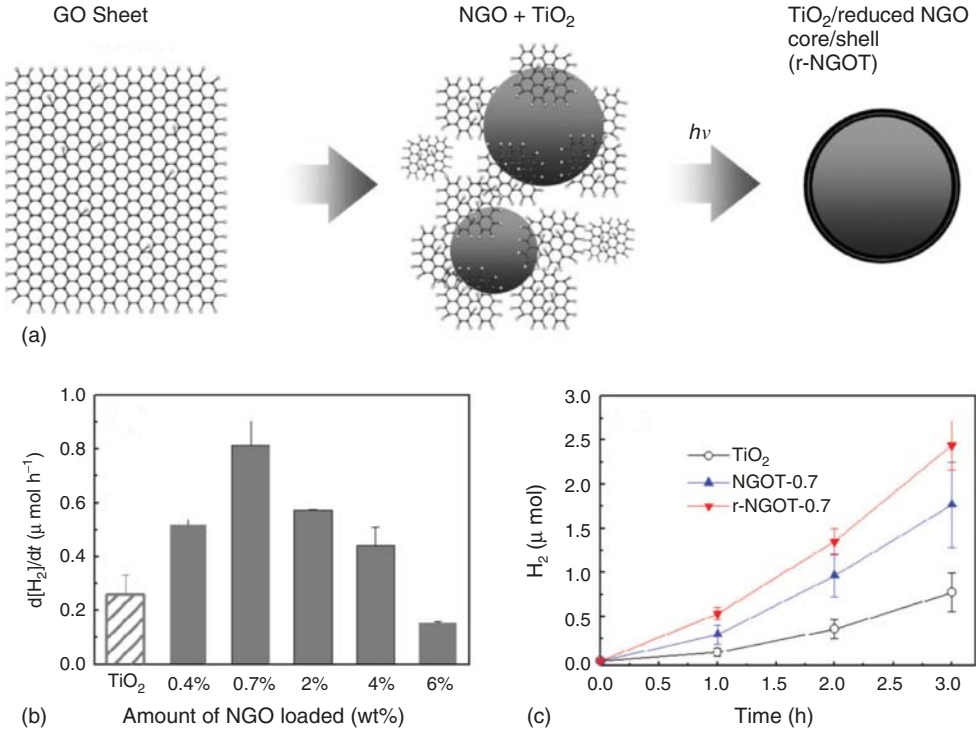

Figure 7.8 (a) Illustration of the preparation procedure of r-NGOT. (b) Hydrogen production rate as a function of the content of NGO in r-NGOT. (c) Time profiles of H_2 production with various photocatalysts. (Reprinted with permission from Ref. [68]. Copyright (2012), American Chemical Society.)

CdS is considered as a promising photocatalyst under visible light because of its narrower bandgap (2.4 eV) and relatively high conduction band position compared to that of TiO_2 [71]. Thus much attention has been paid on combining graphene and CdS. Li *et al.* [72] synthesized a series of RGO/CdS nanocomposites using dimethylsulfoxide (DMSO) as a solvent and investigated the photocatalytic H_2 generation property (Figure 7.9a,b). They found that the nanocomposites with 1.0 wt% RGO and 0.5 wt% Pt exhibited the highest H_2 production under visible light irradiation in a lactic acid solution, and reached an apparent quantum efficiency (AQE) of 22.5% at 420 nm, which was much higher than that of the pure CdS/Pt. The excellent performance is attributed to the role of RGO as an electron acceptor and transporter to separate photogenerated electron–hole pairs in the CdS semiconductor. This interfacial electron–hole separation mechanism of the graphene-supported CdS nanomaterials was further studied by Dong *et al.* [73] through first-principles calculations. It was consistent with Li's assumption that the excited electron in CdS QDs would be injected into graphene and transported along the graphene layer through π^* orbitals, thus achieving efficient interfacial electron–hole separation. Moreover, Kamat *et al.* applied

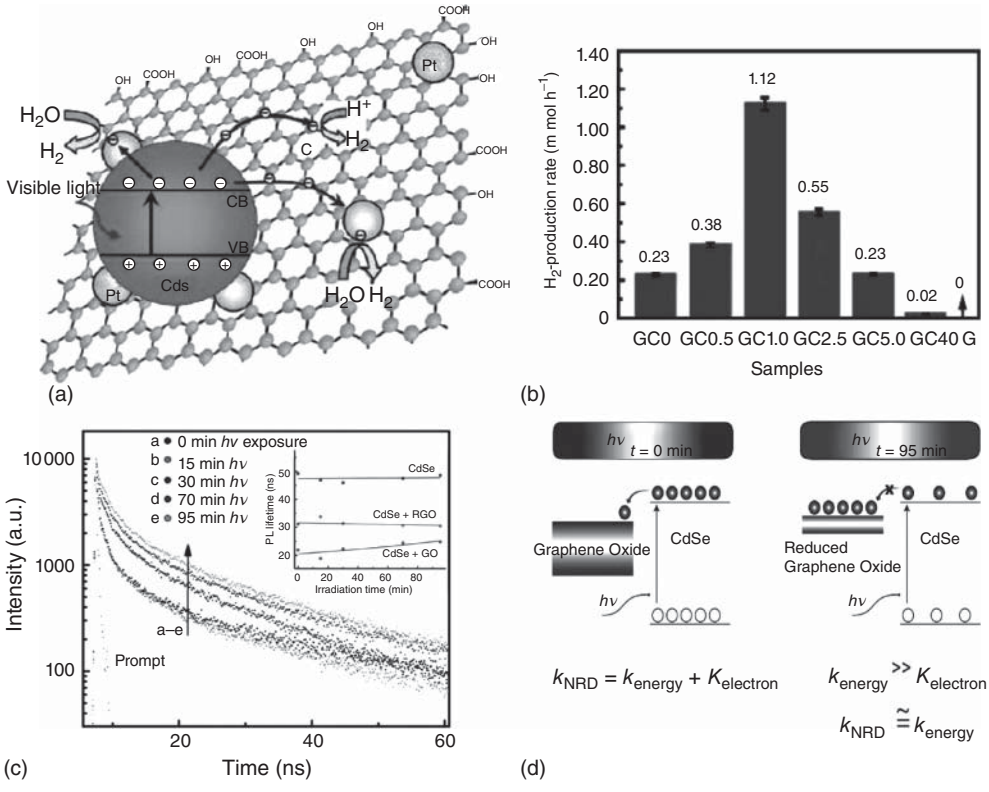

Figure 7.9 (a) Schematic illustration of the charge separation and transfer in the RGO/CdS system under visible light. (b) Comparison of the visible light photocatalytic activity of samples GC0, GC0.5, GC1.0, GC2.5, GC5.0, GC40, and RGO for H_2 production using 10 vol% lactic acid aqueous solution as a sacrificial reagent and 0.5 wt% Pt as a cocatalyst. (Reprinted with permission from Ref. [72]. Copyright (2011), American Chemical Society.) (c) CdSe/GO composites showing increased photoluminescence lifetimes upon visible light light irradiation (>420 nm). (d) Mechanism of energy and electron transfer from photoexcited CdSe colloidal quantum dots to GO and RGO. (Reprinted with permission from Ref. [74]. Copyright (2012), American Chemical Society.)

transient techniques to investigate the kinetics of electron and energy transfer experimentally in a system similar to CdS/graphene, that is, CdSe colloidal QDs/GO composite (Figure 7.9c,d) [74]. They found that the increase in photoluminescence lifetime with prolonged illumination on CdSe/GO composites was related to the different charging in GO. The reason is that the initial illumination on the CdSe/GO composite results in electron transfer from the CdSe CB to GO, while continued illumination results in a decrease in electron transfer rate because of the reduction of GO and eventual storage of electrons in GO. That is, the reduction degree of GO will affect the charge transfer process. Thus, Fu group continuously tuned the reduction degree of RGO in the RGO/$ZnIn_2S_4$ nanocomposite by photoreduction or hydrazine reduction, and systemically

investigated its influence on the photocatalytic performance of the RGO/$ZnIn_2S_4$ nanocomposite [75, 76]. It was found that the highly reductive RGO/$ZnIn_2S_4$ nanocomposite showed significantly enhanced photocatalytic activity for H_2 production under visible light irradiation, as the highly reduced RGO served as a good electron acceptor/mediator to promote photocatalytic water splitting over $ZnIn_2S_4$.

Likewise, several groups found a good application prospect of graphene in dye-sensitized system, where graphene as an electron acceptor and transporter can efficiently promote the electron transfer between the photosensitizer and the catalysts, because of the well-aligned energy levels between the different components [77–79]. Especially, Lu group has carried out much impressive work in this area. In their earlier works, they reported eosin-Y (EY)-sensitized RGO with Pt nanoparticle as a cocatalyst for photocatalytic H_2 evolution under visible light, and obtained an AQE of 9.3% at 520 nm in a triethanolamine (TEOA) solution (Figure 7.10) [80]. RGO was demonstrated to transfer electrons efficiently from

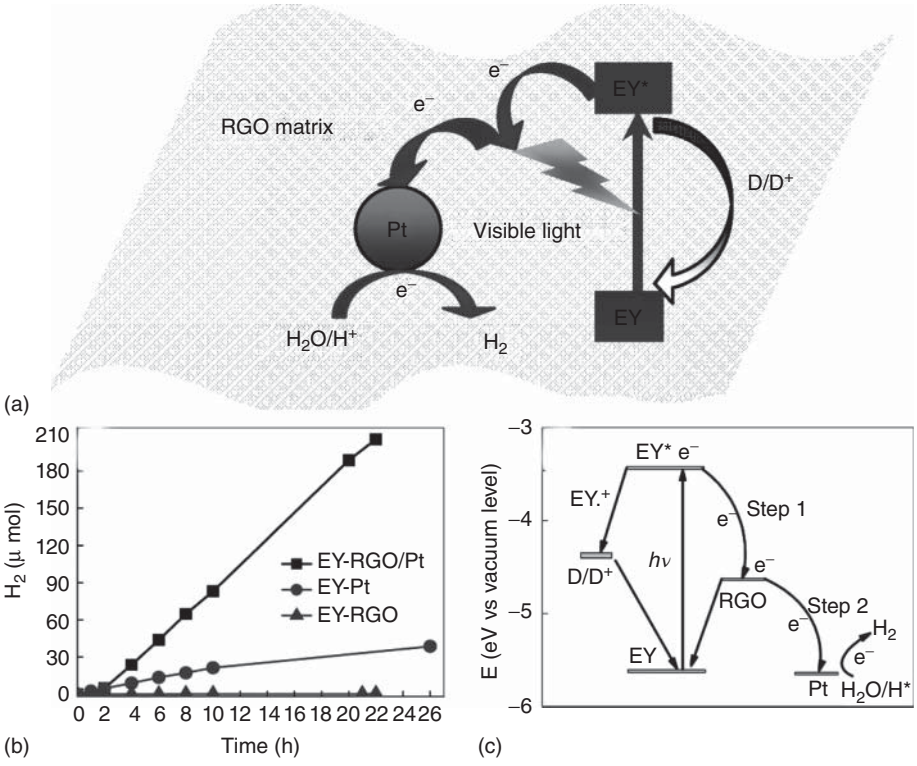

Figure 7.10 (a) Proposed photocatalytic mechanism for hydrogen evolution over EY-RGO/Pt photocatalyst under visible light irradiation. (b) The time courses of hydrogen evolution over EY-Pt, EY-RGO, and EY-RGO/Pt photocatalysts. (c) Energy level diagram for hydrogen evolution over EY-RGO/Pt photocatalyst. (Reprinted with permission from Ref. [80]. Copyright (2011), American Chemical Society.)

the EY photosensitizer to the Pt catalyst, thus enhancing the photocatalytic H_2 evolution. Unfortunately, the photocatalytic activity declined rapidly in the 24-h test. Accordingly, they proposed EY and Rose Bengal (RB) cosensitized RGO/Pt photocatalyst, and found a slight decrease in the photocatalytic activity after 40 h of irradiation [81]. Lately, effects of xanthenes dyes, H_2-evolution catalysts, and sacrificial donors on the H_2 production rate of the dye-sensitized RGO systems were systemically investigated by them. RB-sensitized RGO decorated with Pt cocatalyst using TEOA as the electron donor exhibited the highest activity for H_2 evolution [82]. Considering the high cost and scarcity of Pt, they also developed EY-sensitized cobalt/graphene and $CoSn_xO_y$/graphene hybrids for efficient photocatalytic hydrogen production under visible light irradiation [83, 84].

In addition, researchers have also tried to apply graphene to heterojunction photocatalysts as a conductive mediator so as to improve the electron transfer efficiency. Hou *et al.* [85] synthesized a CdS/TaON core–shell heterojunction coupled with RGO nanosheets (Figure 7.11a,b). This photocatalyst showed a

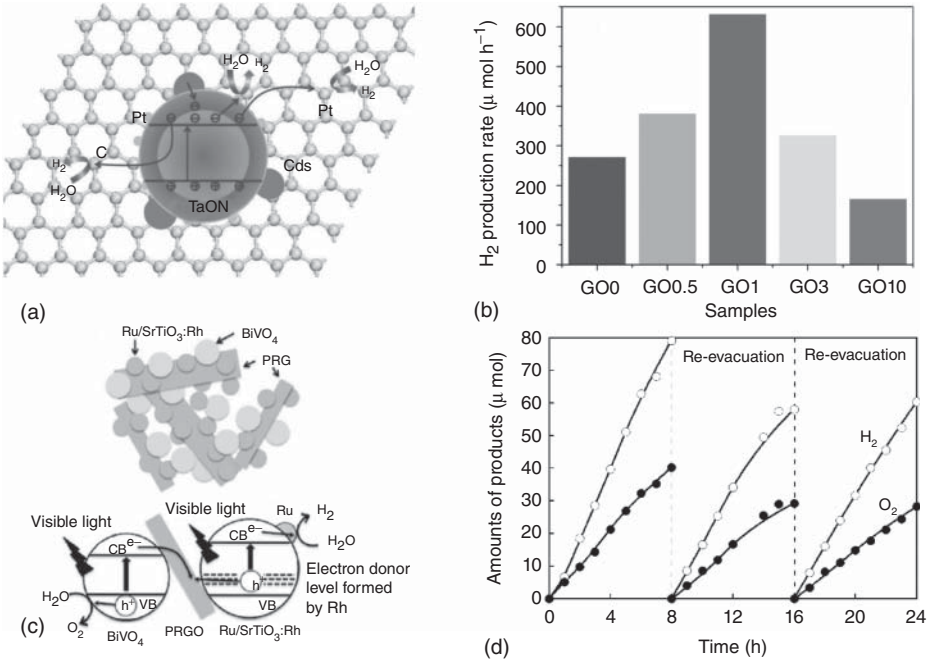

Figure 7.11 (a) Schematic illustration of the charge separation and transfer in the graphene/CdS/TaON system under visible light. (b) Comparison of the visible light photocatalytic activity of samples of CdS/TaON composites using various amounts of GO: 0, 0.5%, 1%, 3%, and 5%. (Reprinted with permission from Ref. [85]. Copyright (2012), Royal Society of Chemistry.) (c) Mechanism of water splitting in a Z-scheme photocatalysis system consisting of Ru/$SrTiO_3$:Rh and RGO/$BiVO_4$ under visible light irradiation. (d) Overall water splitting under visible light irradiation by the (Ru/$SrTiO_3$:Rh)/(RGO/$BiVO_4$) system. (Reprinted with permission from Ref. [89]. Copyright (2011), American Chemical Society.)

stable and high H_2 production rate of 633 μmol h^{-1} under visible light irradiation, which was about 141 times higher than that of the pristine TaON. They ascribed this high photocatalytic activity, first, to the presence of CdS/TaON heterojunction which reduced the photogenerated electron–hole recombination and, second, to involvement of RGO which served as an electron acceptor and transporter to efficiently lengthen the lifetime of the photogenerated charge carriers from the CdS/TaON heterojunction to RGO. Likewise, similar phenomena were demonstrated in other systems such as CdS/RGO/$ZnIn_2S_4$ heterojunction [86], Ru(dcbpy)$_3$/TiO_2/RGO composites [87], and CdS/RGO/MoS_2 composites [88]. These findings have also encouraged scientists to investigate the potential application of graphene as a solid electron mediator to substitute the common redox couples in Z-scheme systems. Amal group constructed a Z-scheme system consisting of RGO/$BiVO_4$ and Ru/$SrTiO_3$:Rh, and proved that RGO could act as an electron mediator to transfer the electrons from the CB of $BiVO_4$ to the impurity levels of Ru/$SrTiO_3$:Rh (Figure 7.11c,d) [89]. Then the electrons in Ru/$SrTiO_3$:Rh reduced water to H_2 on the Ru cocatalyst, while the holes in $BiVO_4$ simultaneously oxidized water to O_2, accomplishing a complete water-splitting cycle. Furthermore, the RGO was stable as an electron mediator over a period of 24 h. This work provides a novel strategy to develop highly efficient Z-scheme systems for overall water splitting.

Graphene is also a promising candidate for a cost-effective cocatalyst to replace noble metals. Zhang *et al.* [41] synthesized a series of RGO/$Zn_xCd_{1-x}S$ photocatalysts using hydrothermal strategy, and found that the RGO/$Zn_{0.8}Cd_{0.2}S$ photocatalyst exhibited a H_2 production rate of 1824 μmol h^{-1} g^{-1} in Na_2S/Na_2SO_3 solution with an AQE of 23.4% at 420 nm, which was even higher than that of the Pt/$Zn_{0.8}Cd_{0.2}S$ (Figure 7.12). It suggests that, besides working as an electron acceptor and transporter, RGO is also an excellent cocatalyst to reduce H^+ to H_2 molecule in this system. This role of graphene was also reported in many other systems such as RGO/TiO_2 [90], RGO/$ZnIn_2S_4$ [91], CdS/RGO [92], and CdS/ZnO/RGO [93]. Moreover, graphene-based composites proved to be good cocatalysts for photocatalytic H_2 generation. Xiang *et al.* [94] prepared a TiO_2/MoS_2/RGO photocatalyst by a two-step hydrothermal process. This composite photocatalyst exhibited a high H_2 production rate of 165.3 μmol h^{-1} under UV light irradiation. They proposed that the positive synergetic effect between MoS_2 and RGO sheets could suppress the charge recombination, improve the interfacial charge transfer, and provide a great number of active adsorption sites and photocatalytic reaction centers. Likewise, the graphene/MoS_2 hybrid was also applied as a cocatalyst for the ZnS photocatalyst, resulting in significantly enhanced photocatalytic activity and good recurrence stability in H_2 evolution from water splitting [95]. Min and Lu [96] further demonstrated the feasibility of the MoS_2/RGO hybrid as a highly active cocatalyst in a dye-sensitized photocatalytic system, where a high AQE of 24.0% was obtained at 460 nm over the EY-sensitized MoS_2/RGO photocatalyst, proving the applicability of the MoS_2/RGO hybrid as a cocatalyst for various photocatalytic systems. Besides, RGO combined with Cu is also a good cocatalyst, as reported by Lu *et al.* [97]

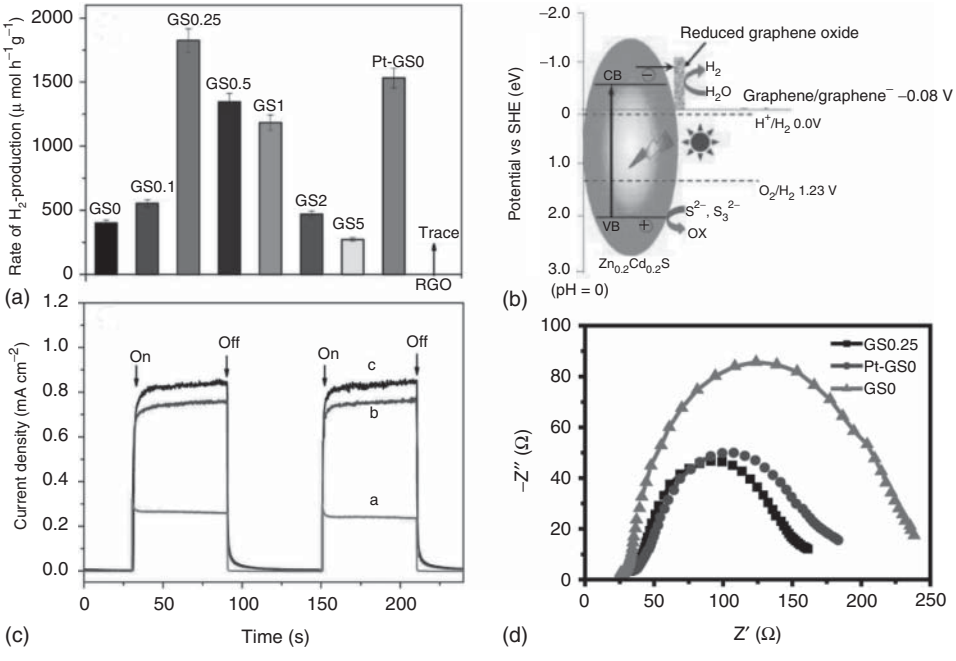

Figure 7.12 (a) Comparison of the photocatalytic H_2 production activity under simulated solar irradiation over different samples. (b) Proposed mechanism for photocatalytic H_2 production under simulated solar irradiation. (c) Transient photocurrent responses and (d) Nyquist plots of $Zn_{0.8}Cd_{0.2}S$, 1 wt% Pt-$Zn_{0.8}Cd_{0.2}S$, and RGO/$Zn_{0.8}Cd_{0.2}S$ samples. (Reprinted with permission from Ref. [41]. Copyright (2012), American Chemical Society.)

The H_2 generation efficiency of Cu/RGO-P25 photocatalyst was about five times higher than that of the RGO-P25 photocatalyst.

As an organic-dye-like macromolecule, graphene functionalized as a "photosensitizer" in photocatalytic systems was reported recently [98–100]. Amal *et al.* [101] simulated the interfacial charge transfer in the graphene/TiO_2 composite by *ab initio* calculations, and found an interesting phenomenon in which electrons could be excited from the upper VB of graphene to the CB of TiO_2 under visible light irradiation, predicting the potential sensitizing effect of graphene in the photocatalytic process (Figure 7.13). Lately, this finding was proved experimentally by Zeng *et al.* [102], as they found that the RGO/TiO_2 composite prepared by the hydrothermal method exhibited a photocatalytic H_2 production rate of 380 μmol h^{-1} under visible light irradiation, with an AQE of about 8.2% at 420 nm. Similarly, Xu *et al.* [103] proved that RGO in the ZnS/RGO nanocomposites acted as a "photosensitizer" instead of an electron reservoir for ZnS.

Furthermore, the potential application of graphene with an open bandgap for water splitting has attracted much attention recently. Teng group [104] first proved that RGO with the bandgap of 2.4–4.3 eV exhibited stable H_2 evolution from an aqueous methanol solution or pure water, even without Pt cocatalyst under

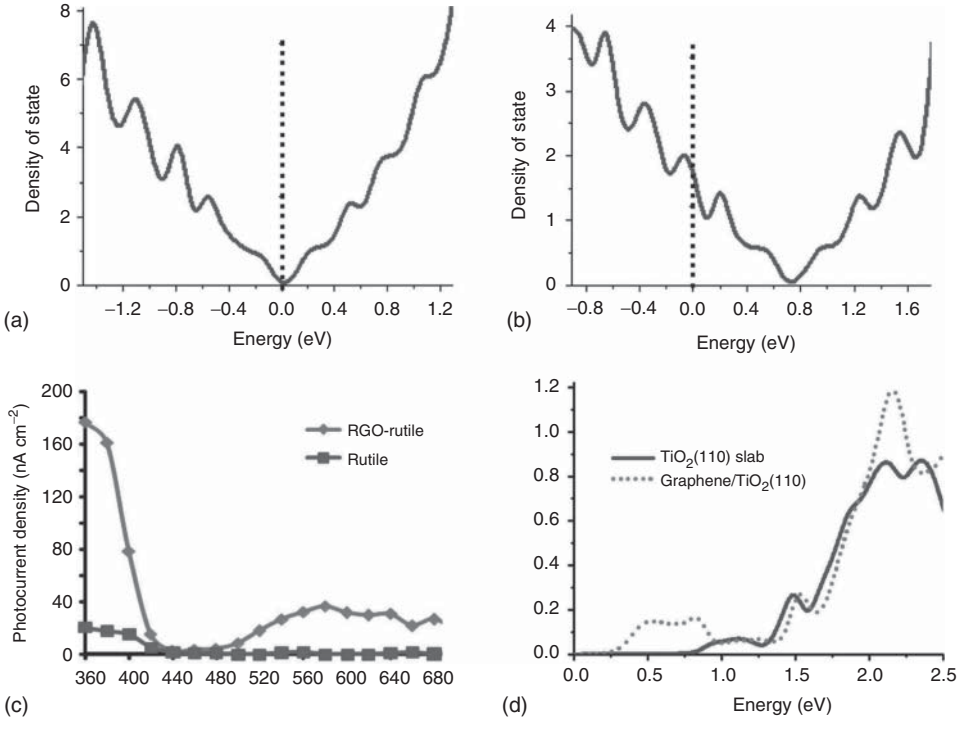

Figure 7.13 DOS plots for (a) free-standing and (b) TiO_2(110) surface-supported graphene. The short dotted lines indicate the Fermi level. (c) Photocurrent action spectra of the TiO_2-only (rutile) film compared with those of RGO/rutile nanocomposite films prepared by the photocatalytic reduction method at a 0 V bias condition. (d) The calculated imaginary part of the dielectric function of the rutile TiO_2(110) surface (red solid line) and the hybrid graphene/TiO_2(110) nanocompoiste (green dot line) for the polarization vector perpendicular to the surface. (Reprinted with permission from Ref. [101]. Copyright (2011), American Chemical Society.)

irradiation with light from a mercury light lamp. They also investigated the photocatalytic activity of RGO at various oxidation levels, and found that there was an inverse relationship between the photocatalytic activity and the amount of the oxygen-containing groups on the RGO sheets [105]. However, an unexpected phenomenon was that the O_2 evolution exhibited a decreasing trend, although the H_2-evolution rate of RGO was stable over time. The reason is that the electronic structure of the RGO with a sufficient oxidation degree is suitable for both the reduction and oxidation of water, but the mutual reduction between the RGO sheets during the photocatalytic reaction narrowed their bandgaps, thus leading to the upward shift of the VB edge and causing the decrease of the O_2 evolution rate. Very recently, nitrogen-doped graphene oxide-quantum dots (NGO-QDs) were demonstrated to be capable of splitting pure water into H_2 and O_2 (Figure 7.14) [106]. The authors found that the prepared NGO-QDs exhibited both p- and n-type conductivity, and formed a novel diode configuration, which was

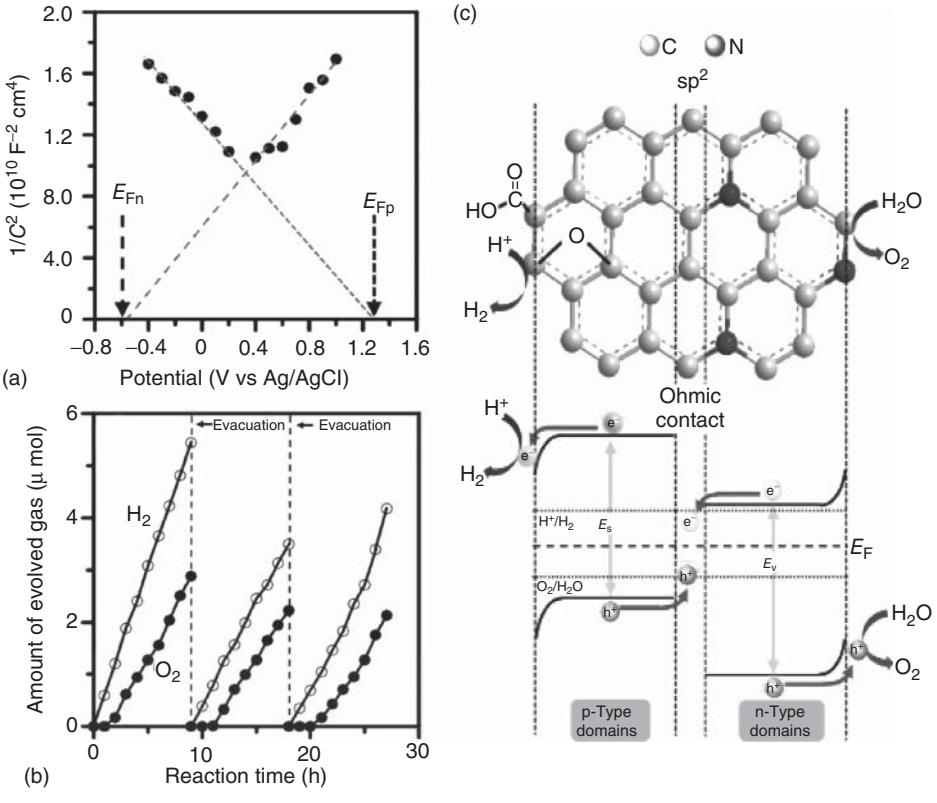

Figure 7.14 (a) Variation of capacitance with the applied potential in 2 M H_2SO_4 presented in the Mott–Schottky relationship for the NGO-QD electrode. (b) Time courses of gas production over photocatalysts suspended in 200 ml of pure water under visible light (420 nm < λ < 800 nm) irradiation. (c) The configuration and energy diagram for the NGO-QD photochemical diode. (Reprinted with permission from Ref. [106]. Copyright (2014), John Wiley & Sons.)

supposed to cause an internal Z-scheme charge transfer mechanism at the QD interface, finally achieving successful overall water splitting under visible light. The work demonstrates that graphene species are promising materials for synthesizing metal-free, cost-effective, and environmentally friendly catalysts for overall water splitting under solar illumination.

7.6 Graphene-Based Photovoltaic/Electrolyzer Devices

The solar cell in a PV/electrolyzer device converts the sunlight into electricity and provides the essential voltage for the electrolysis of water. That is, it determines the upper limit of STH efficiency of a PV/electrolyzer device. Seeking for

effective strategies to improve the efficiency of solar cells is of great importance for a higher STH efficiency in a PV/electrolyzer device. With their unique properties, that is, high optical transparency, high electrical conduction, and mechanical flexibility, graphene and its derivatives have been investigated extensively in the field of solar cells since its first discovery. To day, graphene can not only be used as the electrodes (i.e., transparent anodes, nontransparent anodes, transparent cathodes, and catalytic counterelectrodes) but also be applied as the active layer (i.e., light harvesting material, electron transport layer, hole transport layer, and interfacial layer) in the tandem configuration. These impressive results have been well reviewed by Zhang *et al.*, [107] so we will not elaborate them in detail here.

An electrolyzer is the medium where water is electrolyzed into hydrogen and oxygen. The electrolytic efficiency determines to what extent the electricity produced by a solar cell can be effectively utilized. Actually, it is always restricted by the high overpotential or low faradic efficiency during the electrochemical processes. Modifying the electrodes in an electrolyzer by electrocatalysts is the most efficient strategy to conquer the above problems [108]. However, precious metal-based materials are still a dominant class of electrocatalyst for important energy-related electrochemical conversions, but their inherent corrosion and oxidation problems largely limit their application in sustainable water electrolysis [109].

Carbon materials have been considered as promising alternatives to the state-of-the-art precious metal catalysts in water electrolysis reaction because of their tunable molecular structures, abundance, and strong tolerance to acidic/alkaline environments. Especially, graphene is of paramount interest in electrochemistry, and considerable effort has been made to synthesize graphene-based nanomaterials with enhanced performance toward HER and OER (oxygen evolution reaction).

Chemical modification of graphene by doping with heteroatoms provides an effective way to overcome its low catalytic activity and tailor the electronic structure and electrochemical properties. Particularly, N-doped graphene has been demonstrated as an excellent catalyst for electrochemical reactions because of its unique electronic properties derived from the conjugation between the nitrogen lone-pair electrons and the graphene π system [110, 111]. Xia *et al.* [112] explored the OER mechanism of N-doped armchair and zigzag graphene nanoribbons by using density functional theory (DFT) calculations. They found that the substitution of carbon at the graphene edge by nitrogen resulted in the best performance in terms of overpotentials, and estimated the lowest OER overpotential for armchair nanoribbons to be 0.405 V, which is comparable to those for Pt-containing catalysts. This work suggests that engineering the edge structures of graphene is an effective strategy to increase the efficiency of the N-doped graphene for OER. Zhang group [113] prepared an N-doped graphene/single-walled carbon nanotube (SWCNT) hybrid electrocatalyst (NGSH) by *in situ* doping during CVD growth (Figure 7.15). The one-step approach not only led to the formation of a 3D interconnected network but also brought the intrinsic dispersion of graphene and carbon nanotubes and the dispersion of N-containing functional groups within a highly conductive

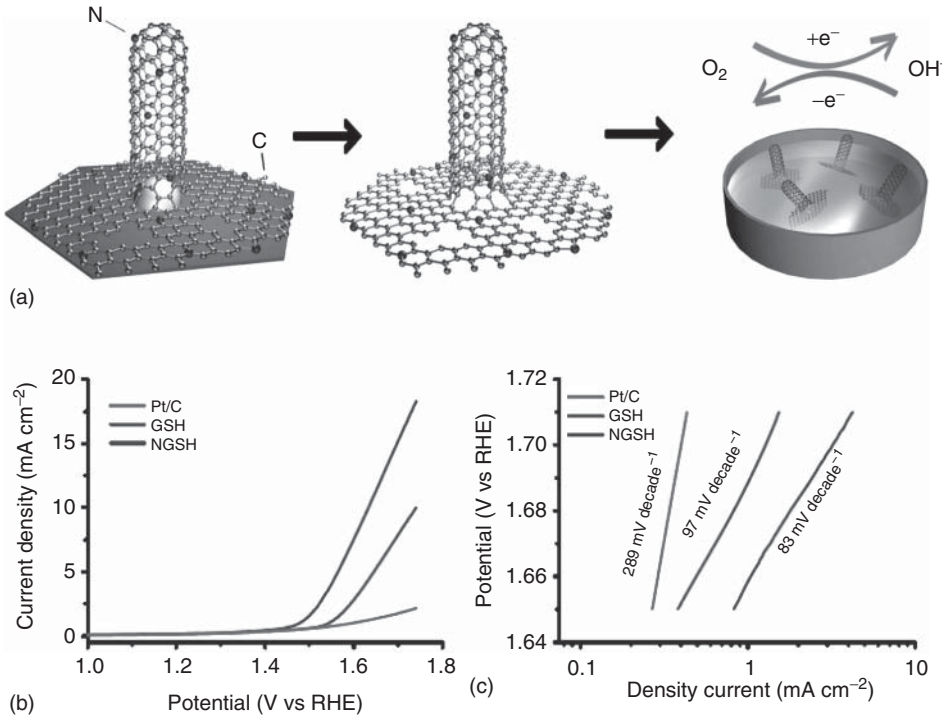

Figure 7.15 (a) One-step growth of nitrogen-doped graphene–carbon nanotube hybrids for oxygen reduction and oxygen evolution reaction. (b) OER currents of Pt/C, GSH, and NGSH electrodes in 0.1 mol l^{-1} KOH solution at a scan rate of 5 mV s^{-1}. (c) Tafel plots of commercial Pt/C, GSH, and NGSH catalysts recorded at 1 mV s^{-1} in 0.1 mol l^{-1} KOH. (Reprinted with permission from Ref. [113]. Copyright (2014), John Wiley & Sons.)

scaffold, thus rendering the hybrid material high-performance electrocatalysts for OER. Qiao *et al.* [114] further proposed a N,O dual-doped graphene–carbon nanotube (denoted as NG-CNT) hydrogel film electrocatalyst via LbL self-assembly strategy. This self-supported material exhibited a surprisingly high OER activity, outperforming even noble (IrO_2) and some transition-metal catalysts. Moreover, the NG-CNT catalyst featured a robust stability in both alkaline and strong acidic solutions. The authors attributed this high OER activity to the dual active sites mechanism originating from the synergy of chemically converted graphene and CNTs. More recently, they designed and synthesized another N,P dual-doped graphene as an electrocatalyst for sustainable and efficient HER [115]. It was demonstrated that the N and P heteroatoms could coactivate the adjacent C atom in the graphene matrix by affecting its valence orbital energy levels to induce a synergistically enhanced reactivity toward HER. The dual-doped graphene showed higher electrocatalytic HER activity than single-doped ones and comparable performance to some of the traditional metallic catalysts.

Moreover, graphene itself can not only be applied as a high-performance metal-free electrocatalyst but also be adopted as a novel catalyst support for HER and OER, as the large specific surface area can facilitate the dispersion of catalyst nanoparticles and suppress their agglomeration while the excellent electrical conductivity can promote the electron transport in the electrode.

MoS_2/graphene hybrid material is the most popular electrocatalyst for HER investigated up to now. Dai *et al.* [116] developed a MoS_2/RGO hybrid material that possessed nanoscopic few-layer MoS_2 structures with an abundance of exposed edges stacked onto graphene. It exhibited superior electrocatalytic activity in the HER relative to other MoS_2 catalysts, with a Tafel slope of ~41 mV/decade. They attributed this excellent activity to the abundance of catalytic edge sites on the MoS_2 nanoparticles and the excellent electrical coupling to the underlying graphene network. Liu *et al.* [117] further proposed a MoS_2/mesoporous graphene foam (MGF) electrocatalyst by *in situ* formation of MoS_2 nanoparticles on 3D MGF. The MoS_2/MGF hybrid showed better catalytic activity than MoS_2/graphene, because of the abundant catalytic sites, the accessible surface area, and unique synergic effect between the MGF support and the active catalyst, as well as the multiple pathways provided by MGF for the efficient diffusion of ions and electrons. More interestingly, Yang *et al.* [118] fabricated a hybrid of alternating MoS_2 sheets and RGO layers via a solvent-evaporation-assisted intercalation method, by which the nanosize of the MoS_2 nanosheets was effectively controlled by leveraging the confinement effect within the 2D graphene layers (Figure 7.16). The resulting MoS_2/RGO composite showed higher current densities and lower onset potentials for HER than the conventional RGO supported MoS_2. Recently, Wang group [119] further introduced a nano-tungsten carbide (WC) dispersant into the classic MoS_2/graphene system, achieving a higher current density for HER. The excellent performance was attributed to the presence of the conductive and electrocatalytically active nano-WC dispersant and the positive synergistic effect between nano-WC/RGO and layered MoS_2.

Meanwhile, various efficient electrocatalysts for OER have been obtained by combining graphene with many transition-metal compounds, especially cobalt compounds. Qiao group [120] reported a 3D OER catalyst composed of N-doped graphene and $NiCo_2O_4$ for water splitting, which exhibited a remarkable OER catalytic activity comparable to that of IrO_2. The well-developed in-plane and out-of-plane pores, 3D conductive networks, and N-doping were proposed to be responsible for the excellent performance. Likewise, a 3D architectured hydrated catalyst fabricated by forming NiCo double hydroxides on N-doped graphene

Figure 7.16 (A) Schematic illustration for the synthesis of various MoS_2/RGO composites based on graphite oxidation, oxidation-induced interlayer expansion/exfoliation, evaporation-assisted intercalation, and space-confined growth. (B) Polarization curves and (C) Tafel plots of (a) MoS_2, (b) MoS_2/RGO_2, (c) MoS_2/e-RGO_2, (d) MoS_2/RGO_1, and (e) MoS_2/RGO_3 composites modified electrodes. (D) Stability for the MoS_2/RGO_2 composite modified electrode with initial polarization curve (black curve) and after 500 cycles (red curve) in 0.5 M H_2SO_4 solution. (Reprinted with permission from Ref. [118]. Copyright (2014), American Chemical Society.)

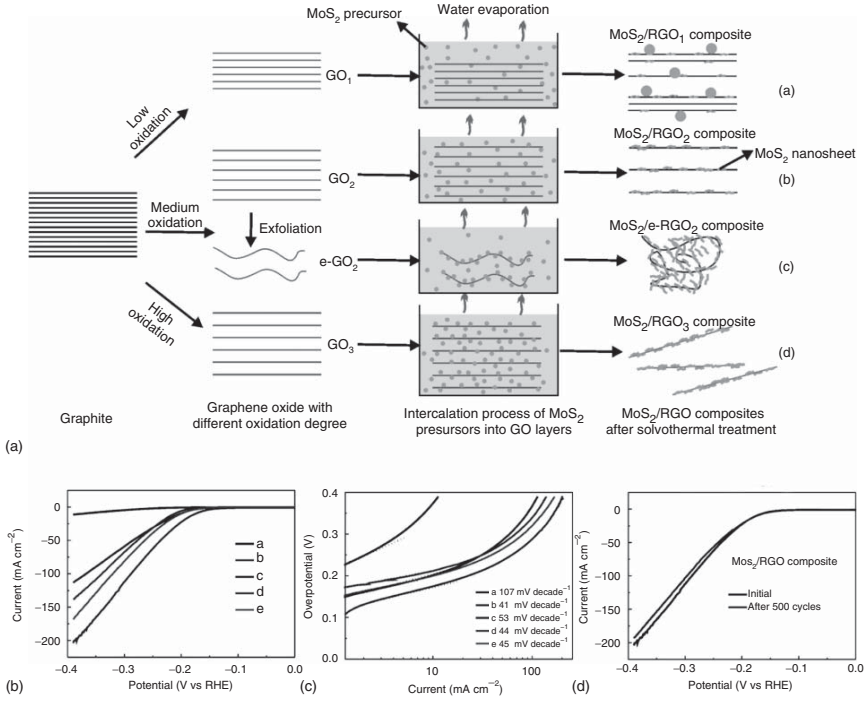
MoS2 precursor
Water evaporation
MoS2/RGO1 composite
GO1
(a)
Low oxidation
MoS2/RGO2 composite
MoS2 nanosheet
GO2
(b)
Medium oxidation
Exfoliation
MoS2/e-RGO2 composite
e-GO2
(c)
High oxidation
MoS2/RGO3 composite
GO3
(d)
Graphite
Graphene oxide with different oxidation degree
Intercalation process of MoS2 presursors into GO layers
MoS2/RGO composites after solvothermal treatment
(a)
Current (mA cm−2)
Potential (V vs RHE)
a
b
c
d
e
(b)
Overpotential (V)
a 107 mV decade−1
b 41 mV decade−1
c 53 mV decade−1
d 44 mV decade−1
e 45 mV decade−1
Current (mA cm−2)
(c)
Mos2/RGO composite
Initial
After 500 cycles
Current (mA cm−2)
Potential (V vs RHE)
(d)

hydrogels was proposed by them [121]. This highly hydrophilic hybrid catalyst (denoted as NG-NiCo) featured favorable electrode kinetics, great durability, and superior activity. Also, the catalytic current of NG-NiCo was even higher than that of IrO_2. Chen *et al.* also obtained a high-performance electrocatalyst by combining 3D crumpled graphene (CG) with cobalt oxide [122]. They concluded that the unique 3D and hollow graphene structure offers a large surface area and stable anchoring sites for CoO nanocrystals, which enables the full use of the catalyst surface area by minimizing agglomeration/restacking of graphene sheets. As a result, the nitrogen-doped CG/CoO hybrid exhibits excellent catalytic activity and durability, making it a high-performance non-precious-metal-based electrocatalyst for OER. More recently, amorphous Co_3O_4/graphene composites (Co_3O_4/GR) were fabricated via LbL assembly onto Indium-Tin-Oxide (ITO) glass and applied as an electrocatalyst for efficient OER in electrolytic water splitting by Zhao *et al.* [123] (Figure 7.17). By adjusting the number of bilayers, the catalytic activity of Co_3O_4/GR composite could be successfully tuned. The

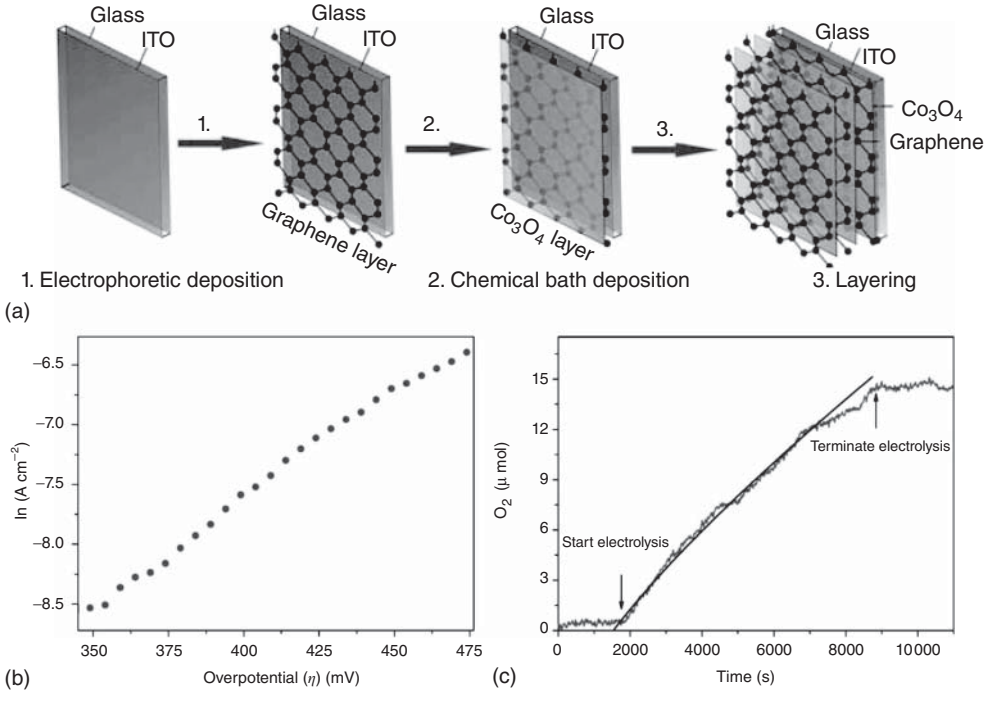

Figure 7.17 (a) Fabrication scheme of a bilayer of the [Co_3O_4/GR] composite. (b) Tafel plot generated from water oxidation using $[Co_3O_4/GR]_{9L}$ in 0.1 M KOH, pH 13.0. (c) The amount of O_2 gas generated with $[Co_3O_4/GR]_{9L}$ (red line), during 2 h electrolysis. The solid line represents the theoretical amount of O_2 calculated from the total charge consumed in electrolysis at a Faradaic efficiency of 100%. (Reprinted with permission from Ref. [123]. Copyright (2013), Royal Society of Chemistry.)

composite exhibits a remarkable catalytic activity for OER in 0.1 M KOH, with a high Faradaic efficiency (95%) and excellent long-term stability.

7.7 Conclusion and Perspective

Graphene has been intensively investigated for the applications in solar-driven water-splitting devices. Considerable progress has already been achieved in recent years, indicating the promising application prospects of graphene in the solar-driven water-splitting area. These impressive achievements further inspire and strengthen the will of researchers to continue their works in this field. Nevertheless, many scientific questions and technological bottlenecks remain unsolved, and the efficiency of graphene-based solar-driven water-splitting devices is still far from satisfactory, which makes it a very challenging research avenue. Achieving the ultimate goal needs close cooperation of researchers in different fields, including chemists, physicists, materials scientists, and engineers. We believe that through the unremitting efforts of all researchers in the related fields, a great breakthrough for hydrogen production by utilizing graphene-based solar-driven water-splitting devices would definitely be realized, providing us with a promising future.

References

1. Turner, J.A. (1999) A realizable renewable energy future. *Science*, **285** (5428), 687–689.
2. Lewis, N.S. (2007) Toward cost-effective solar energy use. *Science*, **315** (5813), 798–801.
3. Walter, M.G., Warren, E.L., McKone, J.R., Boettcher, S.W., Mi, Q.X., Santori, E.A., and Lewis, N.S. (2010) Solar water splitting cells. *Chem. Rev.*, **110** (11), 6446–6473.
4. Newman, J., Hoertz, P.G., Bonino, C.A., and Trainham, J.A. (2012) Review: an economic perspective on liquid solar fuels. *J. Electrochem. Soc.*, **159** (10), A1722–A1729.
5. Fujishima, A. and Honda, K. (1972) Electrochemical photolysis of water at a semiconductor electrode. *Nature*, **238** (5358), 37–38.
6. Kudo, A. and Miseki, Y. (2009) Heterogeneous photocatalyst materials for water splitting. *Chem. Soc. Rev.*, **38** (1), 253–278.
7. Joya, K.S., Joya, Y.F., Ocakoglu, K., and van de Krol, R. (2013) Water-splitting catalysis and solar fuel devices: artificial leaves on the move. *Angew. Chem. Int. Ed.*, **52** (40), 10426–10437.
8. Chen, X., Shen, S., Guo, L., and Mao, S.S. (2010) Semiconductor-based photocatalytic hydrogen generation. *Chem. Rev.*, **110** (11), 6503–6570.
9. Prévot, M.S. and Sivula, K. (2013) Photoelectrochemical tandem cells for solar water splitting. *J. Phys. Chem. C*, **117** (35), 17879–17893.
10. Sivula, K. (2013) Metal oxide photoelectrodes for solar fuel production, surface traps, and catalysis. *J. Phys. Chem. Lett.*, **4** (10), 1624–1633.
11. McKone, J.R., Lewis, N.S., and Gray, H.B. (2014) Will solar-driven water-splitting devices see the light of day? *Chem. Mater.*, **26** (1), 407–414.
12. Osterloh, F.E. (2013) Inorganic nanostructures for photoelectrochemical and photocatalytic water splitting. *Chem. Soc. Rev.*, **42** (6), 2294–2320.

13. Novoselov, K. (2007) Mind the gap. *Nat. Mater.*, **6** (10), 720–721.
14. Guo, S. and Dong, S. (2011) Graphene nanosheet: synthesis, molecular engineering, thin film, hybrids, and energy and analytical applications. *Chem. Soc. Rev.*, **40** (5), 2644–2672.
15. Bonaccorso, F., Sun, Z., Hasan, T., and Ferrari, A.C. (2010) Graphene photonics and optoelectronics. *Nat. Photonics*, **4** (9), 611–622.
16. Chen, D., Zhang, H., Liu, Y., and Li, J. (2013) Graphene and its derivatives for the development of solar cells, photoelectrochemical, and photocatalytic applications. *Energy Environ. Sci.*, **6** (5), 1362–1387.
17. Feng, L. and Liu, Z. (2011) Graphene in biomedicine: opportunities and challenges. *Nanomedicine*, **6** (2), 317–324.
18. Kamat, P.V. (2011) Graphene-based nanoassemblies for energy conversion. *J. Phys. Chem. Lett.*, **2** (3), 242–251.
19. Xie, G., Zhang, K., Guo, B., Liu, Q., Fang, L., and Gong, J.R. (2013) Graphene-based materials for hydrogen generation from light-driven water splitting. *Adv. Mater.*, **25** (28), 3820–3839.
20. Han, L., Wang, P., and Dong, S. (2012) Progress in graphene-based photoactive nanocomposites as a promising class of photocatalyst. *Nanoscale*, **4** (19), 5814–5825.
21. Zhang, N., Zhang, Y., and Xu, Y.-J. (2012) Recent progress on graphene-based photocatalysts: current status and future perspectives. *Nanoscale*, **4** (19), 5792–5813.
22. Xiang, Q.J. and Yu, J.G. (2013) Graphene-based photocatalysts for hydrogen generation. *J. Phys. Chem. Lett.*, **4** (5), 753–759.
23. Grimes, C., Varghese, O., and Ranjan, S. (2008) in *Light, Water, Hydrogen* (eds C. Grimes, O. Varghese, and S. Ranjan), Springer, pp. 115–190.
24. Licht, S. (2001) Multiple band gap semiconductor/electrolyte solar energy conversion. *J. Phys. Chem. B*, **105** (27), 6281–6294.
25. Licht, S., Wang, B., Mukerji, S., Soga, T., Umeno, M., and Tributsch, H. (2000) Efficient solar water splitting, exemplified by RuO_2-catalyzed AlGaAs/Si photoelectrolysis. *J. Phys. Chem. B*, **104** (38), 8920–8924.
26. Licht, S., Wang, B., Mukerji, S., Soga, T., Umeno, M., and Tributsch, H. (2001) Over 18% solar energy conversion to generation of hydrogen fuel; theory and experiment for efficient solar water splitting. *Int. J. Hydrogen Energy*, **26** (7), 653–659.
27. Licht, S., Ghosh, S., Tributsch, H., and Fiechter, S. (2002) High efficiency solar energy water splitting to generate hydrogen fuel: probing RuS_2 enhancement of multiple band electrolysis. *Sol. Energy Mater. Sol. Cells*, **70** (4), 471–480.
28. Licht, S. (2003) Solar water splitting to generate hydrogen fuel: photothermal electrochemical analysis. *J. Phys. Chem. B*, **107** (18), 4253–4260.
29. Licht, S. (2005) Solar water splitting to generate hydrogen fuel - a photothermal electrochemical analysis. *Int. J. Hydrogen Energy*, **30** (5), 459–470.
30. Bard, A.J. (1979) Photoelectrochemistry and heterogeneous photocatalysis at semiconductors. *J. Photochem.*, **10** (1), 59–75.
31. Ganguly, A., Misra, D., and Ghosh, S. (2010) Modeling and analysis of solar photovoltaic-electrolyzer-fuel cell hybrid power system integrated with a floriculture greenhouse. *Energy Buildings*, **42** (11), 2036–2043.
32. Bilgen, E. (2001) Solar hydrogen from photovoltaic-electrolyzer systems. *Energy Convers. Manage.*, **42** (9), 1047–1057.
33. Novoselov, K.S., Geim, aK., Morozov, S.V., Jiang, D., Zhang, Y., Dubonos, S.V., Grigorieva, I.V., and Firsov, A.A. (2004) Electric field effect in atomically thin carbon films. *Science*, **306**, 666–669.
34. Geim, A.K. and Novoselov, K.S. (2007) The rise of graphene. *Nat. Mater.*, **6** (3), 183–191.
35. Avouris, P. (2010) Graphene: electronic and photonic properties and devices. *Nano Lett.*, **10** (11), 4285–4294.
36. Castro Neto, A.H., Guinea, F., Peres, N.M.R., Novoselov, K.S., and Geim, A.K. (2009) The electronic properties

of graphene. *Rev. Mod. Phys.*, **81** (1), 109–162.

37. Wang, X., Zhi, L., and Müllen, K. (2007) Transparent, conductive graphene electrodes for dye-sensitized solar cells. *Nano Lett.*, **8** (1), 323–327.
38. Ioannides, T. and Verykios, X.E. (1996) Charge transfer in metal catalysts supported on doped TiO_2: a theoretical approach based on metal–semiconductor contact theory. *J. Catal.*, **161** (2), 560–569.
39. Donolato, C. (2004) Approximate analytical solution to the space charge problem in nanosized Schottky diodes. *J. Appl. Phys.*, **95** (4), 2184–2186.
40. Zhang, Z. and Yates, J.T. (2012) Band bending in semiconductors: chemical and physical consequences at surfaces and interfaces. *Chem. Rev.*, **112** (10), 5520–5551.
41. Zhang, J., Yu, J.G., Jaroniec, M., and Gong, J.R. (2012) Noble metal-free reduced graphene Oxide-$Zn_xCd_{1-x}S$ nanocomposite with enhanced solar photocatalytic H_2 production performance. *Nano Lett.*, **12**, 4584–4589.
42. Guo, B., Liu, Q., Chen, E., Zhu, H., Fang, L., and Gong, J.R. (2010) Controllable N-doping of graphene. *Nano Lett.*, **10** (12), 4975–4980.
43. Guo, B., Fang, L., Zhang, B., and Gong, J.R. (2011) Doping effect on shift of threshold voltage of graphene-based field-effect transistors. *Electron Lett.*, **47** (11), 663–664.
44. Yan, J.-A., Xian, L., and Chou, M.Y. (2009) Structural and electronic properties of oxidized graphene. *Phys. Rev. Lett.*, **103** (8), 086802.
45. Mathkar, A., Tozier, D., Cox, P., Ong, P., Galande, C., Balakrishnan, K., Leela Mohana Reddy, A., and Ajayan, P.M. (2012) Controlled, stepwise reduction and band gap manipulation of graphene oxide. *J. Phys. Chem. Lett.*, **3** (8), 986–991.
46. Ng, Y.H., Iwase, A., Kudo, A., and Amal, R. (2010) Reducing graphene oxide on a visible-light $BiVO_4$ photocatalyst for an enhanced photoelectrochemical water splitting. *J. Phys. Chem. Lett.*, **1** (17), 2607–2612.
47. Lin, J.D., Hu, P., Zhang, Y., Fan, M.T., He, Z.M., Ngaw, C.K., Loo, J.S.C., Liao, D.W., and Tan, T.T.Y. (2013) Understanding the photoelectrochemical properties of a reduced graphene oxide-WO_3 heterojunction photoanode for efficient solar-light-driven overall water splitting. *RSC Adv.*, **3** (24), 9330–9336.
48. Zhang, J., Zhao, W.T., Xu, Y., Xu, H.L., and Zhang, B. (2014) In-situ photoreducing graphene oxide to create $Zn_{0.5}Cd_{0.5}S$ porous nanosheets/RGO composites as highly stable and efficient photoelectrocatalysts for visible-light-driven water splitting. *Int. J. Hydrogen Energy*, **39** (2), 702–710.
49. Xiao, F.-X., Miao, J., and Liu, B. (2014) Layer-by-layer self-assembly of CdS quantum dots/graphene nanosheets hybrid films for photoelectrochemical and photocatalytic applications. *J. Am. Chem. Soc.*, **136** (4), 1559–1569.
50. Young Kim, J., Jang, J.-W., Hyun Youn, D., Yul Kim, J., Sun Kim, E., and Sung Lee, J. (2012) Graphene-carbon nanotube composite as an effective conducting scaffold to enhance the photoelectrochemical water oxidation activity of a hematite film. *RSC Adv.*, **2** (25), 9415–9422.
51. Hou, Y., Zuo, F., Dagg, A., and Feng, P. (2012) Visible light-driven α-Fe_2O_3 nanorod/graphene/$BiV_{1-x}Mo_xO_4$ core/shell heterojunction array for efficient photoelectrochemical water splitting. *Nano Lett.*, **12** (12), 6464–6473.
52. Yang, H., Kershaw, S.V., Wang, Y., Gong, X., Kalytchuk, S., Rogach, A.L., and Teoh, W.Y. (2013) Shuttling photoelectrochemical electron transport in tricomponent CdS/rGO/TiO_2 nanocomposites. *J. Phys. Chem. C*, **117** (40), 20406–20414.
53. Hou, Y., Wen, Z.H., Cui, S.M., Guo, X.R., and Chen, J.H. (2013) Constructing 2D porous graphitic C_3N_4 nanosheets/nitrogen-doped graphene/layered MoS_2 ternary nanojunction with enhanced photoelectrochemical activity. *Adv. Mater.*, **25** (43), 6291–6297.
54. Huang, Z., Zhong, P., Wang, C., Zhang, X., and Zhang, C. (2013) Silicon

nanowires/reduced graphene oxide composites for enhanced photoelectrochemical properties. *ACS Appl. Mater. Interfaces*, **5** (6), 1961–1966.

55. Zhang, K., Shi, X., Kim, J.K., Lee, J.S., and Park, J.H. (2013) Inverse opal structured α-Fe_2O_3 on graphene thin films: enhanced photo-assisted water splitting. *Nanoscale*, **5** (5), 1939–1944.
56. Sim, U., Yang, T.Y., Moon, J., An, J., Hwang, J., Seo, J.H., Lee, J., Kim, K.Y., Lee, J., Han, S., Hong, B.H., and Nam, K.T. (2013) N-doped monolayer graphene catalyst on silicon photocathode for hydrogen production. *Energy Environ. Sci.*, **6** (12), 3658–3664.
57. Nielander, A.C., Bierman, M.J., Petrone, N., Strandwitz, N.C., Ardo, S., Yang, F., Hone, J., and Lewis, N.S. (2013) Photoelectrochemical behavior of n-type Si(111) electrodes coated with a single layer of graphene. *J. Am. Chem. Soc.*, **135** (46), 17246–17249.
58. Lin, Y.-G., Lin, C.-K., Miller, J.T., Hsu, Y.-K., Chen, Y.-C., Chen, L.-C., and Chen, K.-H. (2012) Photochemically active reduced graphene oxide with controllable oxidation level. *RSC Adv.*, **2** (30), 11258–11262.
59. Singh, V., Joung, D., Zhai, L., Das, S., Khondaker, S.I., and Seal, S. (2011) Graphene based materials: past, present and future. *Prog. Mater. Sci.*, **56** (8), 1178–1271.
60. Huang, X., Yin, Z., Wu, S., Qi, X., He, Q., Zhang, Q., Yan, Q., Boey, F., and Zhang, H. (2011) Graphene-based materials: synthesis, characterization, properties, and applications. *Small*, **7** (14), 1876–1902.
61. Yeh, T.-F., Cihlář, J., Chang, C.-Y., Cheng, C., and Teng, H. (2013) Roles of graphene oxide in photocatalytic water splitting. *Mater. Today*, **16** (3), 78–84. doi: 10.1016/j.mattod.2013.03.006
62. Williams, G., Seger, B., and Kamat, P.V. (2008) TiO_2-graphene nanocomposites. UV-assisted photocatalytic reduction of graphene oxide. *ACS Nano*, **2** (7), 1487–1491.
63. Lightcap, I.V., Kosel, T.H., and Kamat, P.V. (2010) Anchoring semiconductor and metal nanoparticles on a two-dimensional catalyst mat. Storing and shuttling electrons with reduced graphene oxide. *Nano Lett.*, **10** (2), 577–583.
64. Li, N., Liu, G., Zhen, C., Li, F., Zhang, L., and Cheng, H.-M. (2011) Battery performance and photocatalytic activity of mesoporous anatase TiO_2 nanospheres/graphene composites by template-free self-assembly. *Adv. Funct. Mater.*, **21** (9), 1717–1722.
65. Zhang, X.-Y., Li, H.-P., Cui, X.-L., and Lin, Y. (2010) Graphene/TiO_2 nanocomposites: synthesis, characterization and application in hydrogen evolution from water photocatalytic splitting. *J. Mater. Chem.*, **20** (14), 2801–2806.
66. Zhang, X., Sun, Y., Cui, X., and Jiang, Z. (2012) A green and facile synthesis of TiO_2/graphene nanocomposites and their photocatalytic activity for hydrogen evolution. *Int. J. Hydrogen Energy*, **37** (1), 811–815.
67. Fan, W., Lai, Q., Zhang, Q., and Wang, Y. (2011) Nanocomposites of TiO_2 and reduced graphene oxide as efficient photocatalysts for hydrogen evolution. *J. Phys. Chem. C*, **115** (21), 10694–10701.
68. H-i, K., G-h, M., Monllor-Satoca, D., Park, Y., and Choi, W. (2011) Solar photoconversion using graphene/TiO_2 composites: nanographene shell on TiO_2 Core versus TiO_2 nanoparticles on graphene sheet. *J. Phys. Chem. C*, **116** (1), 1535–1543.
69. H-i, K., Kim, S., Kang, J.-K., and Choi, W. (2014) Graphene oxide embedded into TiO_2 nanofiber: effective hybrid photocatalyst for solar conversion. *J. Catal.*, **309**, 49–57.
70. Sun, J., Zhang, H., Guo, L.-H., and Zhao, L. (2013) Two-dimensional interface engineering of a titania–graphene nanosheet composite for improved photocatalytic activity. *ACS Appl. Mater. Interfaces*, **5** (24), 13035–13041.
71. Zhang, K. and Guo, L.J. (2013) Metal sulphide semiconductors for photocatalytic hydrogen production. *Catal. Sci. Technol.*, **3** (7), 1672–1690.
72. Li, Q., Guo, B., Yu, J., Ran, J., Zhang, B., Yan, H., and Gong, J.R. (2011) Highly efficient visible-light-driven

photocatalytic hydrogen production of CdS-cluster-decorated graphene nanosheets. *J. Am. Chem. Soc.*, **133** (28), 10878–10884.

73. Dong, C., Li, X., Jin, P., Zhao, W., Chu, J., and Qi, J. (2012) Intersubunit Electron Transfer (IET) in quantum dots/graphene complex: what features does IET endow the complex with? *J. Phys. Chem. C*, **116** (29), 15833–15838.

74. Lightcap, I.V. and Kamat, P.V. (2012) Fortification of CdSe quantum dots with graphene oxide excited state interactions and light energy conversion. *J. Am. Chem. Soc.*, **134** (16), 7109–7116.

75. Chen, Y., Ge, H., Wei, L., Li, Z., Yuan, R., Liu, P., and Fu, X. (2013) Reduction degree of reduced graphene oxide (RGO) dependence of photocatalytic hydrogen evolution performance over RGO/$ZnIn_2S_4$ nanocomposites. *Catal. Sci. Technol.*, **3** (7), 1712–1717.

76. Ye, L., Fu, J., Xu, Z., Yuan, R., and Li, Z. (2014) Facile one-pot solvothermal method to synthesize sheet-on-sheet reduced graphene oxide (RGO)/$ZnIn_2S_4$ nanocomposites with superior photocatalytic performance. *ACS Appl. Mater. Interfaces*, **6** (5), 3483–3490.

77. Zhu, M., Dong, Y., Xiao, B., Du, Y., Yang, P., and Wang, X. (2012) Enhanced photocatalytic hydrogen evolution performance based on Ru-trisdicarboxybipyridine-reduced graphene oxide hybrid. *J. Mater. Chem.*, **22** (45), 23773–23779.

78. Zhu, M., Li, Z., Xiao, B., Lu, Y., Du, Y., Yang, P., and Wang, X. (2013) Surfactant assistance in improvement of photocatalytic hydrogen production with the porphyrin noncovalently functionalized graphene nanocomposite. *ACS Appl. Mater. Interfaces*, **5** (5), 1732–1740.

79. Xiao, B., Wang, X., Huang, H., Zhu, M., Yang, P., Wang, Y., and Du, Y. (2013) Improved superiority by covalently binding dye to graphene for hydrogen evolution from water under visible-light irradiation. *J. Phys. Chem. C*, **117** (41), 21303–21311.

80. Min, S. and Lu, G. (2011) Dye-sensitized reduced graphene oxide photocatalysts for highly efficient visible-light-driven water reduction. *J. Phys. Chem. C*, **115** (28), 13938–13945.

81. Min, S. and Lu, G. (2012) Dye-cosensitized graphene/Pt photocatalyst for high efficient visible light hydrogen evolution. *Int. J. Hydrogen Energy*, **37** (14), 10564–10574.

82. Min, S. and Lu, G. (2013) Promoted photoinduced charge separation and directional electron transfer over dispersible xanthene dyes sensitized graphene sheets for efficient solar H_2 evolution. *Int. J. Hydrogen Energy*, **38** (5), 2106–2116.

83. Kong, C., Min, S., and Lu, G. (2014) A novel amorphous $CoSn_xO_y$ decorated graphene nanohybrid photocatalyst for highly efficient photocatalytic hydrogen evolution. *Chem. Commun.*, **50** (39), 5037–5039.

84. Kong, C., Min, S., and Lu, G. (2014) Dye-sensitized cobalt catalysts for high efficient visible light hydrogen evolution. *Int. J. Hydrogen Energy*, **39** (10), 4836–4844.

85. Hou, J., Wang, Z., Kan, W., Jiao, S., Zhu, H., and Kumar, R.V. (2012) Efficient visible-light-driven photocatalytic hydrogen production using CdS@TaON core-shell composites coupled with graphene oxide nanosheets. *J. Mater. Chem.*, **22** (15), 7291–7299.

86. Hou, J., Yang, C., Cheng, H., Wang, Z., Jiao, S., and Zhu, H. (2013) Ternary 3D architectures of CdS QDs/graphene/$ZnIn_2S_4$ heterostructures for efficient photocatalytic H_2 production. *Phys. Chem. Chem. Phys.*, **15** (37), 15660–15668.

87. Chen, Y., Mou, Z., Yin, S., Huang, H., Yang, P., Wang, X., and Du, Y. (2013) Graphene enhanced photocatalytic hydrogen evolution performance of dye-sensitized TiO_2 under visible light irradiation. *Mater. Lett.*, **107**, 31–34.

88. Jia, T., Kolpin, A., Ma, C., Chan, R.C.-T., Kwok, W.-M., and Tsang, S.C.E. (2014) A graphene dispersed CdS-MoS_2 nanocrystal ensemble for cooperative photocatalytic hydrogen production

from water. *Chem. Commun.*, **50** (10), 1185–1188.

89. Iwase, A., Ng, Y.H., Ishiguro, Y., Kudo, A., and Amal, R. (2011) Reduced graphene oxide as a solid-state electron mediator in Z-scheme photocatalytic water splitting under visible light. *J. Am. Chem. Soc.*, **133** (29), 11054–11057.
90. Xiang, Q., Yu, J., and Jaroniec, M. (2011) Enhanced photocatalytic H_2-production activity of graphene-modified titania nanosheets. *Nanoscale*, **3** (9), 3670–3678.
91. Zhou, J., Tian, G., Chen, Y., Meng, X., Shi, Y., Cao, X., Pan, K., and Fu, H. (2013) In situ controlled growth of $ZnIn_2S_4$ nanosheets on reduced graphene oxide for enhanced photocatalytic hydrogen production performance. *Chem. Commun.*, **49** (22), 2237–2239.
92. Lv, X.-J., Fu, W.-F., Chang, H.-X., Zhang, H., Cheng, J.-S., Zhang, G.-J., Song, Y., Hu, C.-Y., and Li, J.-H. (2012) Hydrogen evolution from water using semiconductor nanoparticle/graphene composite photocatalysts without noble metals. *J. Mater. Chem.*, **22** (4), 1539–1546.
93. Khan, Z., Chetia, T.R., Vardhaman, A.K., Barpuzary, D., Sastri, C.V., and Qureshi, M. (2012) Visible light assisted photocatalytic hydrogen generation and organic dye degradation by CdS-metal oxide hybrids in presence of graphene oxide. *RSC Adv.*, **2** (32), 12122–12128.
94. Xiang, Q., Yu, J., and Jaroniec, M. (2012) Synergetic effect of MoS_2 and graphene as cocatalysts for enhanced photocatalytic H_2 production activity of TiO_2 nanoparticles. *J. Am. Chem. Soc.*, **134** (15), 6575–6578.
95. Zhu, B., Lin, B., Zhou, Y., Sun, P., Yao, Q., Chen, Y., and Gao, B. (2014) Enhanced photocatalytic H_2 evolution on ZnS loaded with graphene and MoS_2 nanosheets as cocatalysts. *J. Mater. Chem. A*, **2** (11), 3819–3827.
96. Min, S. and Lu, G. (2012) Sites for high efficient photocatalytic hydrogen evolution on a limited-layered MoS_2 cocatalyst confined on graphene sheets–the role of graphene. *J. Phys. Chem. C*, **116** (48), 25415–25424.
97. Lv, X.-J., Zhou, S.-X., Zhang, C., Chang, H.-X., Chen, Y., and Fu, W.-F. (2012) Synergetic effect of Cu and graphene as cocatalyst on TiO_2 for enhanced photocatalytic hydrogen evolution from solar water splitting. *J. Mater. Chem.*, **22** (35), 18542–18549.
98. Kim, C.H., Kim, B.-H., and Yang, K.S. (2012) TiO_2 nanoparticles loaded on graphene/carbon composite nanofibers by electrospinning for increased photocatalysis. *Carbon*, **50** (7), 2472–2481.
99. Bai, X., Wang, L., and Zhu, Y. (2012) Visible photocatalytic activity enhancement of $ZnWO_4$ by graphene hybridization. *ACS Catal.*, **2** (12), 2769–2778.
100. Du, A., Sanvito, S., Li, Z., Wang, D., Jiao, Y., Liao, T., Sun, Q., Ng, Y.H., Zhu, Z., Amal, R., and Smith, S.C. (2012) Hybrid graphene and graphitic carbon nitride nanocomposite: gap opening, electron–hole puddle, interfacial charge transfer, and enhanced visible light response. *J. Am. Chem. Soc.*, **134** (9), 4393–4397.
101. Du, A., Ng, Y.H., Bell, N.J., Zhu, Z., Amal, R., and Smith, S.C. (2011) Hybrid graphene/titania nanocomposite: interface charge transfer, hole doping, and sensitization for visible light response. *J. Phys. Chem. Lett.*, **2** (8), 894–899.
102. Zeng, P., Zhang, Q., Zhang, X., and Peng, T. (2012) Graphite oxide–TiO_2 nanocomposite and its efficient visible-light-driven photocatalytic hydrogen production. *J. Alloys Compd.*, **516**, 85–90.
103. Zhang, Y., Zhang, N., Tang, Z.-R., and Xu, Y.-J. (2012) Graphene transforms wide band gap ZnS to a visible light photocatalyst. The new role of graphene as a macromolecular photosensitizer. *ACS Nano*, **6** (11), 9777–9789.
104. Yeh, T.-F., Syu, J.-M., Cheng, C., Chang, T.-H., and Teng, H. (2010) Graphite oxide as a photocatalyst for hydrogen production from water. *Adv. Funct. Mater.*, **20** (14), 2255–2262.

105. Yeh, T.F., Chan, F.F., Hsieh, C.T., and Teng, H. (2011) Graphite oxide with different oxygenated levels for hydrogen and oxygen production from water under illumination: the band positions of graphite oxide. *J. Phys. Chem. C*, **115** (45), 22587–22597.
106. Yeh, T.-F., Teng, C.-Y., Chen, S.-J., and Teng, H. (2014) Nitrogen-doped graphene oxide quantum dots as photocatalysts for overall water-splitting under visible light illumination. *Adv. Mater.*, **26** (20), 3297–3303.
107. Yin, Z., Zhu, J., He, Q., Cao, X., Tan, C., Chen, H., Yan, Q., and Zhang, H. (2014) Graphene-based materials for solar cell applications. *Adv. Energy Mater.*, **4** (1). doi: 10.1002/aenm.201300574
108. Liang, Y., Li, Y., Wang, H., and Dai, H. (2013) Strongly coupled inorganic/nanocarbon hybrid materials for advanced electrocatalysis. *J. Am. Chem. Soc.*, **135** (6), 2013–2036.
109. Chen, J., Lim, B., Lee, E.P., and Xia, Y. (2009) Shape-controlled synthesis of platinum nanocrystals for catalytic and electrocatalytic applications. *Nano Today*, **4** (1), 81–95.
110. Lin, Z., Waller, G.H., Liu, Y., Liu, M., and Wong, C.-P. (2013) Simple preparation of nanoporous few-layer nitrogen-doped graphene for use as an efficient electrocatalyst for oxygen reduction and oxygen evolution reactions. *Carbon*, **53**, 130–136.
111. Wang, Y., Shao, Y., Matson, D.W., Li, J., and Lin, Y. (2010) Nitrogen-doped graphene and its application in electrochemical biosensing. *ACS Nano*, **4** (4), 1790–1798.
112. Li, M., Zhang, L., Xu, Q., Niu, J., and Xia, Z. (2014) N-doped graphene as catalysts for oxygen reduction and oxygen evolution reactions: theoretical considerations. *J. Catal.*, **314**, 66–72.
113. Tian, G.L., Zhao, M.Q., Yu, D., Kong, X.Y., Huang, J.Q., Zhang, Q., and Wei, F. (2014) Nitrogen-doped graphene/carbon nanotube hybrids: in situ formation on bifunctional catalysts and their superior electrocatalytic activity for oxygen evolution/reduction reaction. *Small*, **10** (11), 2251–2259.
114. Chen, S., Duan, J., Jaroniec, M., and Qiao, S.Z. (2014) Nitrogen and oxygen dual-doped carbon hydrogel film as a substrate-free electrode for highly efficient oxygen evolution reaction. *Adv. Mater.*, **26** (18), 2925–2930.
115. Zheng, Y., Jiao, Y., Li, L.H., Xing, T., Chen, Y., Jaroniec, M., and Qiao, S.Z. (2014) Toward design of synergistically active carbon-based catalysts for electrocatalytic hydrogen evolution. *ACS Nano*, **8** (5), 5290–5296.
116. Li, Y., Wang, H., Xie, L., Liang, Y., Hong, G., and Dai, H. (2011) MoS_2 nanoparticles grown on graphene: an advanced catalyst for the hydrogen evolution reaction. *J. Am. Chem. Soc.*, **133** (19), 7296–7299.
117. Liao, L., Zhu, J., Bian, X., Zhu, L., Scanlon, M.D., Girault, H.H., and Liu, B. (2013) MoS_2 formed on mesoporous graphene as a highly active catalyst for hydrogen evolution. *Adv. Funct. Mater.*, **23** (42), 5326–5333.
118. Zheng, X., Xu, J., Yan, K., Wang, H., Wang, Z., and Yang, S. (2014) Space-confined growth of MoS_2 nanosheets within graphite: the layered hybrid of mos_2 and graphene as an active catalyst for hydrogen evolution reaction. *Chem. Mater.*, **26** (7), 2344–2353.
119. Yan, Y., Xia, B., Qi, X., Wang, H., Xu, R., Wang, J.Y., Zhang, H., and Wang, X. (2013) Nano-tungsten carbide decorated graphene as co-catalysts for enhanced hydrogen evolution on molybdenum disulfide. *Chem. Commun.*, **49** (43), 4884–4886.
120. Chen, S. and Qiao, S.Z. (2013) Hierarchically porous nitrogen-doped graphene-$NiCo_2O_4$ hybrid paper as an advanced electrocatalytic water-splitting material. *ACS Nano*, **7** (11), 10190–10196.
121. Chen, S., Duan, J., Jaroniec, M., and Qiao, S.Z. (2013) Three-dimensional N-doped graphene hydrogel/NiCo double hydroxide electrocatalysts for highly efficient oxygen evolution. *Angew. Chem.*, **52** (51), 13567–13570.
122. Mao, S., Wen, Z., Huang, T., Hou, Y., and Chen, J. (2014) High-performance bi-functional electrocatalysts of 3D crumpled graphene–cobalt oxide

nanohybrids for oxygen reduction and evolution reactions. *Energy Environ. Sci.*, **7** (2), 609.

123. Suryanto, B.H.R., Lu, X., and Zhao, C. (2013) Layer-by-layer assembly of transparent amorphous Co_3O_4 nanoparticles/graphene composite electrodes for sustained oxygen evolution reaction. *J. Mater. Chem. A*, **1** (41), 12726.

8
Graphene Derivatives in Photocatalysis

Luisa M. Pastrana-Martínez, Sergio Morales-Torres, José L. Figueiredo, Joaquim L. Faria, and Adrián M.T. Silva

8.1
Introduction

Nowadays, environmental deterioration in the context of energy production and sustainability is probably one of the most significant concerns of our society. Because of their wide applications in solar energy conversion and environmental remediation, effective semiconductor photocatalyst development has emerged as one of the most important goals in materials science. Some of the most adequately and traditionally studied semiconductors are TiO_2, ZnO, CdS, ZnS, Fe_2O_3, WO_3, and Bi_2WO_4 [1, 2]. When a semiconductor is illuminated with photons of energy $h\nu$ that is equal to or higher than the semiconductor bandgap E_G ($h\nu \geq E_G$), these photons are absorbed and create high energy electron–hole pairs, which dissociate into free photoelectrons in the conduction band and photoholes in the valence band [3]. The photogenerated electrons and holes that migrate to the surface of the semiconductor without recombination can, respectively, reduce and oxidize the reactants adsorbed on the semiconductor surface. Therefore, suppressing the recombination of photogenerated charge carriers and the efficient utilization of visible light are some of the main challenges before making these processes economically feasible [4, 5]. In order to overcome these drawbacks, various strategies have been developed to improve the photocatalytic performance of semiconductor materials, such as the addition of electron donors [6, 7], noble metal loading [8, 9], metal ion or anion doping [10, 11], dye sensitization [12], and fabrication of composite semiconductors [13, 14].

A highly appealing approach toward the development of nanocomposite photocatalysts relies on the combination of semiconductors with carbonaceous materials, including mesoporous carbon and carbon nanotubes [15–17], and more recently, graphene and its derivatives [2, 18].

Graphene is a two-dimensional monolayer of sp^2 carbon atoms bonded in a dense honeycomb crystal structure, which behaves electronically as a zero-gap semiconductor. Since its isolation in 2004 [19], graphene has sparked considerable scientific activity and has now established a broad worldwide community

Graphene-based Energy Devices, First Edition. Edited by A. Rashid bin Mohd Yusoff.
© 2015 Wiley-VCH Verlag GmbH & Co. KGaA. Published 2015 by Wiley-VCH Verlag GmbH & Co. KGaA.

because of its outstanding properties. In particular, this material offers high thermal conductivity (~5000 $W\,m^{-1}\,K^{-1}$), excellent mobility of charge carriers (200 000 $cm^2\,V^{-1}\,s^{-1}$), a large theoretical specific surface area (~2630 $m^2\,g^{-1}$), and good mechanical stability [20, 21]. Graphene oxide (GO) has attracted huge interest as a valuable precursor of graphene because the oxygen functional groups attached on a graphene surface can be partly removed, resulting in the partial restoration of the sp^2 hybridization of carbon [22]. The exfoliation of graphite oxide followed by a reduction process to yield reduced graphene oxide (rGO) offers important advantages, namely the possibility to obtain a tailored hydrophilic surface of graphene, decorated with oxygenated functionalities, by a cost-effective approach. These surface groups can be used to facilitate the anchoring of semiconductor and metal nanoparticles, or even the assembly of macroscopic structures that are relevant to the development of photocatalysts [23–25] and other functionalized materials for many different applications, such as sensors [26], supercapacitors [27], batteries [28], and solar cells [29, 30].

Besides its surface chemistry, GO exhibits a highly heterogeneous electronic structure determined by the interplay of conducting π-states from sp^2 carbon atoms within the large energy gap (σ-states) of the sp^3 matrix [31]. More importantly, significant enhancement of the photocatalytic activity has been frequently observed when graphene derivatives are combined with a semiconductor because of their synergetic interaction encompassing both interfacial electron transfer between the two constituent phases and the enhanced adsorption capacity [2].

This chapter is focused on the synthesis and properties of GO and rGO, as well as on the preparation processes currently used to produce GO/TiO_2 and rGO/TiO_2 photocatalytic composites. The exciting recent progress on the use of graphene-based materials for different applications, including photodegradation of organic pollutants, photocatalytic splitting of H_2O, photocatalytic reduction of CO_2, as well as dye-sensitized solar cells (DSSCs), will be also discussed and summarized. In addition, the prospects and further expected developments of graphene-based materials in these fields will be reviewed.

8.2 Graphene Oxide and Reduced Graphene Oxide

8.2.1 Synthesis

Graphite oxide consists of a bulk solid obtained by strong oxidation of graphite through processes that functionalize the basal planes and increase the interlayer spacing (Figure 8.1).

Graphite oxide can be exfoliated in water or other suitable organic solvents to form GO [33–35]. The synthesis methods of graphite oxide have been recently reviewed [32, 36, 37]. There are three main methods of preparation of graphite oxide, which are the Brodie [38] method, the Staudenmaier [39] method, and the

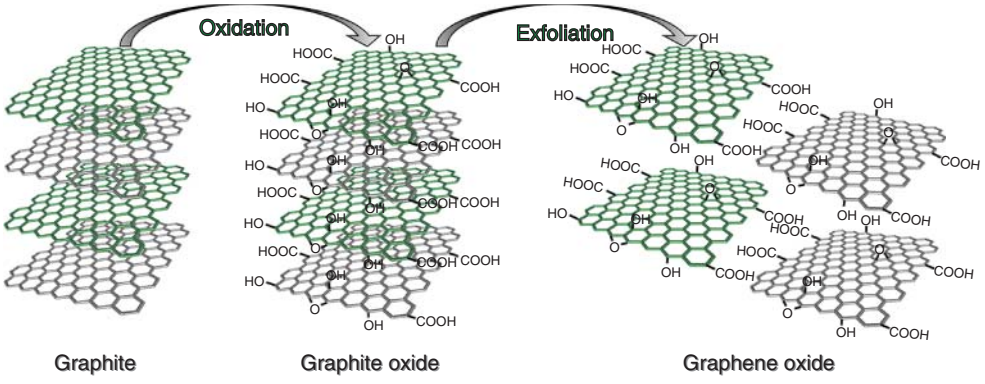

Figure 8.1 Synthesis of graphene oxide. (Adapted from Ref. [32]. Copyright (2012), Royal Society of Chemistry.)

Hummers [40] method. In brief, these methods differ in both the acid medium and the type of oxidizing agent used. The degree of graphite oxidation is dependent upon the synthetic technique and the extent of reaction. The Staudenmaier method typically produces the most oxidized graphite oxide, although the entire synthesis may take several days. However, both this and the Brodie method generate ClO_2 gas, which must be handled with caution because of its high toxicity and tendency to decompose in air violently.

Nowadays, the method most widely used to prepare graphite oxide is the Hummers method, where the oxidation of graphite to graphite oxide is accomplished by treatment with a water mixture of concentrated sulfuric acid, sodium nitrate, and potassium permanganate. Although some modifications have been proposed [41, 42], the main strategy is similar in these methods. The resulting graphite oxide product is usually purified by centrifugation and washed to remove some remaining aggregates and inorganic impurities.

Several structural models for the chemistry of GO have been proposed over the years [37, 43], with that suggested by Lerf and Klinowski (Figure 8.2) being the most accepted. Although the chemistry of GO is still a matter of debate, the latest studies seem to confirm that it exhibits epoxy and hydroxyl groups, mostly at the basal planes of the sheets, and carboxyl groups at the edges. Several methods have been proposed to reduce GO (yielding rGO and partially restoring the sp^2-hybridized network), including chemical [44], thermal [42], electrochemical [45], photocatalytic [46], photothermal [47], sonochemical, and microwave reduction methods.

The amount, type, and location of the oxygen functional groups can be varied by modifying the synthesis conditions, which can have a strong influence on the reactivity of these materials. The rGO obtained differs markedly from pristine graphene without defects, because includes both structural disorder and defects inherited from GO, together with a non-negligible amount of residual oxygen functionalities [22, 44, 48–52] (Figure 8.3). However, the presence of both defects and functional groups also provides potential advantages for the efficient

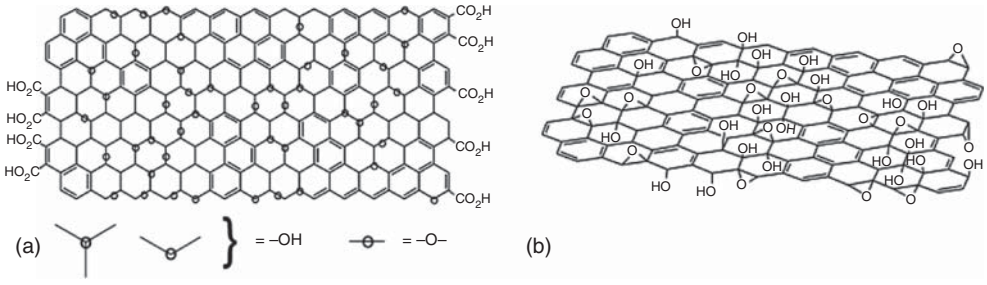

Figure 8.2 Variations of the Lerf–Klinowski model indicating ambiguity regarding the (a) presence or (b) absence of carboxylic acids on the periphery of the basal plane of the graphitic platelets of GO. (Reprinted with permission from Ref. [37]. Copyright (2009), Royal Society of Chemistry.)

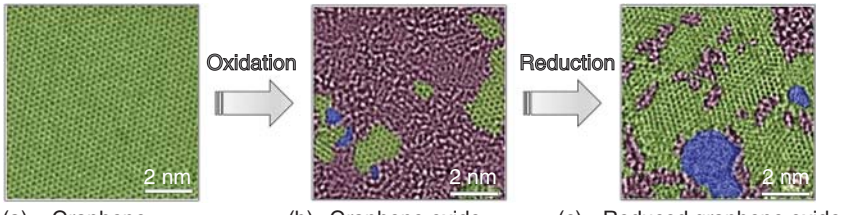

Figure 8.3 Color-coded high-resolution TEM images showing the atomic structures of graphene (a), GO (b), and rGO (c). The green, purple, and blue areas depict ordered graphitic sp^2 domains, disordered and highly oxidized sp^3 domains, and holes on the sheet, respectively. (Adapted from Ref. [52]. Copyright (2010), Wiley-VCH.)

utilization of GO and rGO in the preparation of graphene-based semiconductor composites.

8.2.2 Properties

Because of its specific 2D structure and the presence of various oxygen functional groups, GO exhibits some excellent properties, as previously mentioned. These include electronic, optical, thermal, mechanical, and electrochemical properties, as well as chemical reactivity [53].

Electronic properties, such as the conductivity of GO sheets, depend strongly on their chemical and atomic structures. In fact, they depend upon the degree of structural disorder arising from the presence of a substantial sp^3 carbon fraction [54]. In general, GO films are typically insulating, with an energy gap in the electron density of states [54, 55], and they exhibit sheet resistance (R_s) values of about $1012\,\Omega\,sq^{-1}$ or higher [56]. The intrinsic insulating nature of GO is strongly correlated to the amount of sp^3 C–O bonding [53]. However, the reduction of

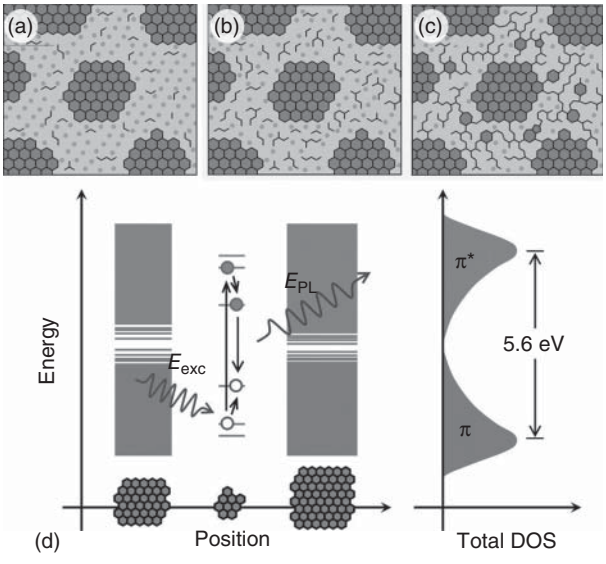

Figure 8.4 Structural models of GO at different stages of reduction. The PL intensity is relatively weak for (a) the as-synthesized GO but increases with reduction as a result of (b) the formation of additional small sp^2 domains between the larger clusters due to evolution of oxygen with reduction. After extensive reduction, the smaller sp^2 domains create (c) percolating pathways among the larger clusters. (d) Representative band structure of GO. The energy levels are quantized with large energy gaps for small fragments due to confinement. A photogenerated e–h pair recombining radiatively is depicted. (Reprinted with permission from Ref. [66]. Copyright (2010), Wiley Online Library.)

GO facilitates the transport of carriers [57, 58] and results in a decrease in R_s by several orders of magnitude, and hence transforms the material into a semiconductor and/or into a graphene-like semimetal [54, 59–63] reaching in some cases the rGO conductivity of about $\sim 1000\,S\,m^{-1}$ [60, 64]. Moreover, the local-density approximation bandgap of GO was found to vary over a range of a few electronvolts, depending on the oxidation level [65]. This result suggests a large potential for tuning the energy gap in GO through the use of controlled reduction processes [53].

GO is also expected to exhibit unique optical properties, as evidenced by its photoluminescence (PL) characteristics [31]. This effect was found to occur from the near-UV to blue to visible to near-infrared (NIR) wavelength range, and it is originated from the recombination of electron–hole (e–h) pairs localized within small sp^2 carbon clusters embedded within a sp^3 matrix. The PL intensity varies with the nature of the reduction treatment, and can be correlated to the evolution of very small sp^2 clusters (Figure 8.4) [66].

The presence of oxygen surface groups can modify the properties of pristine graphene, affecting the adsorption and desorption of molecules and chemical reactions [37]. On the other hand, the solubility of graphene can be tuned to suit different solvents needed for the processing of the composite [34] by

derivatizing graphene with different organic moieties. Functional groups can extend the properties of graphene derivatives, which afford tunability in electrical conductivity as well as optical and photovoltaic properties [67].

To summarize, graphene has an extensive surface area as well as excellent mechanical and optical properties. The optoelectronic and chemical properties are the main differences between graphene and GO. Graphene has excellent conductivity and transparency, while GO is a more opaque insulator. However, GO can be either chemically functionalized or reduced to produce rGO. With these materials, a tunable bandgap can be achieved with a low recombination rate and a high photocurrent response, providing excellent substrates for semiconductor particles.

8.3 Synthesis of Graphene-Based Semiconductor Photocatalysts

TiO_2 has been widely studied and proven as one of the most interesting photocatalysts since the first consolidated contribution focused on a clear understanding of the heterogeneous photocatalytic process in 1972, with the pioneering work of Fujishima and Honda [68]. These authors investigated the electrochemical photolysis of water using a single TiO_2 (rutile) crystal (n-type) as photoanode and a Pt counterelectrode (CE). The interest in photocatalytic processes for environmental applications started to grow in 1977 after Frank and Bard [69] examined the possibilities of using TiO_2 to decompose cyanide in water. Since then, photocatalytic reactions have attracted increased attention. Ample verification of the effectiveness of TiO_2 to generate highly reactive chemical species such as hydroxyl radicals upon UV light illumination, along with its environmentally benign properties (i.e., relatively low toxicity, photostability) and relative inexpensiveness, rendered this semiconductor a key material for the complete destruction of hazardous organic pollutants for many different water/wastewater treatment applications, and also in the fields of energy conversion and air purification [4, 18, 70]. However, the practical application of TiO_2 is severely compromised by two inherent limitations, namely the low quantum yield, which is primarily impaired by the recombination of photogenerated charge carriers, and the poor light-harvesting ability, which is restricted by the wide bandgap of TiO_2 to the Ultraviolet A (UVA) spectral range.

According to the literature, TiO_2 or other inorganic oxides in combination with graphene-based nanosheets can be prepared by different methods. For instance, graphene derivatives have been investigated as substrates for photocatalytic materials including ZnO [71–74], Cu_2O [75, 76], Ag_3PO_4 [77], $BiVO_4$ [78], CdS [79, 80], Fe_2O_3 [81], C_3N_4 [82, 83], Ag/AgX (X = Br, Cl) [84], and TiO_2 [18, 24, 85–93]. The widely used preparation methods are simple mixing and/or sonication, the sol–gel process, as well as hydrothermal and solvothermal methods.

8.3.1
Mixing Method

The simplest route for the preparation of graphene derivative/TiO_2 composites involves mixing and sonication steps, because GO has to be exfoliated when added to an aqueous or organic solution. For example, Bell *et al.* [94] reported the synthesis of rGO/TiO_2 composites where the TiO_2 particles and the GO colloids were mixed ultrasonically, followed by UV-assisted photocatalytic reduction of GO. In another work, Zhang and Pan [95], after mixing and sonication, used a heat treatment under inert atmosphere, which doped carbon atoms into the TiO_2 structure, improving the visible light photocatalytic activity. Morales-Torres *et al.* [93] used GO and the benchmark TiO_2 photocatalyst (P25) to prepare different composites, by a simple method of mixing and sonication, and varying the GO content and the heat-treatment temperature under nitrogen. The best performing photocatalyst was that containing 1.4 wt% GO and treated at 200–300 °C. The improved performance was attributed to the reduction of GO during the thermal treatment and to the good contact between TiO_2 and the carbon phases. Sun *et al.* [83] synthesized a composite polymeric photocatalyst rGO/C_3N_4 by a combined mixing method with a chemical reduction process. C_3N_4 was deposited on the surface of rGO sheets to form a layered composite by polymerizing melamine molecules adsorbed on rGO. Other composite photocatalysts were prepared by mixing ZnO [96] or SnO_2 nanoparticles [97], Ag/AgX (X = Br, Cl) [84] or WO_3 and $BiVO_4$ [98], among others.

8.3.2
Sol–Gel Process

The sol–gel technique is one of the most widely applied methods to obtain an intimate mixing and chemical interaction between GO and TiO_2. The surface of GO sheets is generally available to be combined with titanium alkoxide precursors because of the water solubility and hydrogen bonding ability of GO and because the hydroxyl surface groups of GO can establish oxo or hydroxo bridges with metal centers. Lambert *et al.* [99] reported the synthesis of TiO_2/GO and TiO_2/rGO composites prepared via the hydrolysis of TiF_4 at 60 °C for 24 h in the presence of an aqueous dispersion of GO. The results showed that at higher GO loadings, and without stirring of the reaction medium, a long-range-ordered assembly of TiO_2/GO sheets occurred as a result of self-assembly.

Zhu *et al.* [100] reported a novel and facile process for water-phase synthesis of high-quality graphene/TiO_2 composite nanosheets using $TiCl_3$ both as a reducing agent and a precursor. Chen *et al.* [101] demonstrated the fabrication of graphene sheets wrapped around anatase TiO_2 hollow particles (GS/TiO_2), shown in Figure 8.5, synthesized using a modified method [102]. These TiO_2 hollow particles were then functionalized with aminopropyltriethoxysilane to have a positively charged surface. Negatively charged GO sheets were linked to these functionalized TiO_2 hollow particles via simple electrostatic interaction. The GO was finally

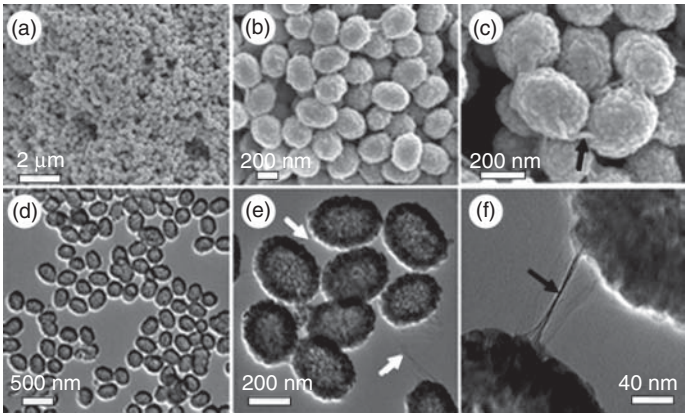

Figure 8.5 (a–c) Field-emission scanning electron microscopy (FESEM) images and (d–f) transmission electron microscopy (TEM) images of the as-prepared GS/TiO_2 composite. The white arrows in (e) indicate the edges of GS, while the black arrow in (c,f) show the folding of GS between connected TiO_2 hollow particles. (Reprinted with permission from Ref. [101]. Copyright (2011), Royal Society of Chemistry.)

reduced to GSs (graphene sheets) by a thermal treatment under an inert atmosphere.

Very recently, a TiO_2/GO composite was successfully prepared by a two-step approach including the in situ growth of a uniform TiC layer on GO sheets and subsequent oxidation of TiC to anatase TiO_2 [103]. The results suggest that TiO_2/GO keeps a morphology similar to that of the pristine GO sheets and that the nanosized anatase TiO_2 particles distribute uniformly and densely on the surface of the GO sheets. TiO_2 particles contact closely with GO via Ti–O–C bonds.

8.3.3
Hydrothermal and Solvothermal Methods

The hydrothermal/solvothermal methods are also effective for the preparation of semiconductor composites and involve reactions under controlled temperature and/or pressure. In these processes, semiconductor nanoparticles or their precursors are loaded on the GO sheets, which are reduced to rGO. In addition, changes in the crystalline phase of TiO_2 are generally observed.

Zhang *et al.* [86] prepared a GO/P25 composite by hydrothermal treatment of GO and Degussa P25 in an ethanol–water solvent. The composite maintained the crystalline structure and surface area identical to those of P25, and GO was reduced by the effect of the hydrothermal treatment. On the other hand, Ding *et al.* [104] synthesized graphene-supported ultrathin anatase TiO_2 nanosheets with exposed (001) high-energy facets by a simple solvothermal method (G/TiO_2 NSs). In this process, anatase TiO_2 nanosheets directly grew on the GO support during the solvothermal method, and then GO was reduced to rGO via a thermal

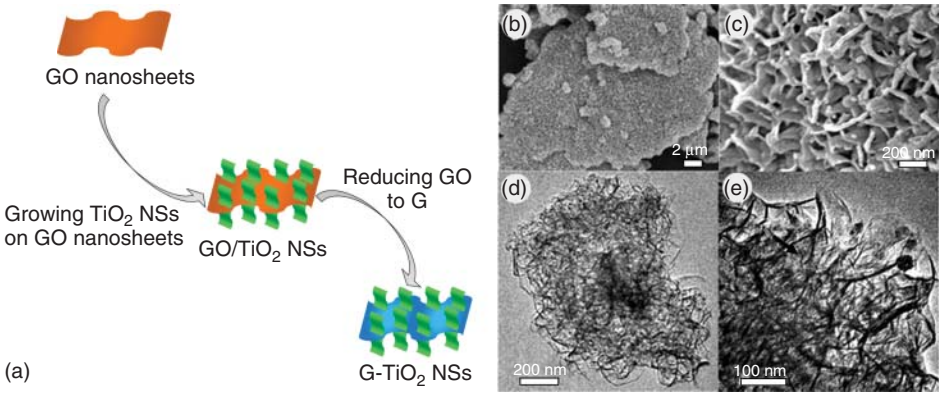

Figure 8.6 (a) Schematic illustration of the formation of graphene-supported TiO_2 nanosheets (G/TiO_2 NSs). (b,c) Scanning electron microscope (SEM) images and (d,e) TEM images of the as-prepared G/TiO_2 NSs. (Adapted with permission from Ref. [104]. Copyright (2011), Royal Society of Chemistry.)

treatment under N_2/H_2, resulting in a unique hybrid structure of graphene/TiO_2 composites (Figure 8.6).

Shen *et al.* [105] found an environmently friendly route for the preparation of graphene/TiO_2 nanocomposites with a one-step hydrothermal method using glucose as the reducing agent. They claim that this process is simple, scalable, and feasible because it utilizes only water and glucose, although the treatment with glucose does not lead to complete reduction under hydrothermal conditions.

Fan *et al.* [85] demonstrated that the hydrothermal method is more appropriate than the UV-assisted photocatalytic approach or even the method implementing hydrazine for GO reduction because of the strongest interaction between both GO and TiO_2 materials obtained using the hydrothermal method. Very recently, Liang *et al.* [106] developed a facile and efficient one-step hydrothermal approach to synthesize chemically bonded TiO_2/rGO nanocomposites with $Ti(SO_4)_2$ and GO as precursors and ethanol–water mixture as the reducing agent. The morphology of TiO_2/rGO nanocomposites revealed that this method leads to efficient dispersion of TiO_2 nanocrystals on the surface of rGO sheets and to close interfacial contact between TiO_2 and rGO.

8.4 Photocatalytic Applications

Significant enhancement of the photocatalytic activity has been frequently observed when GO is combined with TiO_2 as a result of their synergetic interaction encompassing interfacial electron transfer between the two constituent phases. Graphene-based semiconductor photocatalysts have been widely used for the degradation of pollutants, photocatalytic hydrogen generation, and

photocatalytic reduction of CO_2. In this section, the main applications of GO/TiO_2 and rGO/TiO_2 semiconductor photocatalysts are briefly overviewed.

8.4.1 Photodegradation of Organic Pollutants

Some of the most significant applications of rGO/TiO_2 and GO/TiO_2 composites are the detoxification and disinfection of water and wastewater. These composites exhibit high adsorption capacity, extended light absorption range, and enhanced charge separation and transportation properties. In the literature, most of the target pollutants are dyes [86, 88, 107] (such as methylene blue, MB, methyl orange, MO, acid orange 7, AO7, and rhodamine B, RB), although some recent exceptions include a few pharmaceuticals (diphenhydramine, DP and carbamazepine, CBZ) [24, 108], pesticides/herbicides (2,4-dichlorophenoxyacetic acid 2,4-D [109] and polybrominated diphenyl ethers PBDEs) [92], endocrine disruptors (bisphenol A, BPA) [110], cyanobacteria (microcystin-LR, MC-LR), and other compounds (2-methylisoborneol, MIB) [111].

Zhang *et al.* [86] reported the GO/P25 composite as a high-performance photocatalyst. This composite showed a significant enhancement of photocatalytic degradation of MB in water under both UV and visible light irradiation compared to bare P25. The higher performance is due to the $\pi-\pi$ stacking between MB and the aromatic regions of graphene, enhancing the adsorption of the dyes on the surface of the catalyst (Figure 8.7). Moreover, the introduction of graphene extended the light responding range of P25, facilitating a more efficient visible-light-driven photocatalysis.

On the other hand, GO/TiO_2 nanorod composites presented a large enhancement of both MB [88] and AO7 photocatalytic degradation under UV light irradiation and also for *Escherichia coli* bacteria under simulated solar light [112]. Once again, this was mainly justified by the better contact between GO and TiO_2 nanorods and the more effective charge transfer between TiO_2 nanorods and GO sheets. The mechanism of anticharge recombination of the GO/TiO_2 nanorod composite for the photocatalytic degradation of MB under UV light irradiation has also been reported (Figure 8.8) [88]. The authors found that the electrons in the GO sheets could react with adsorbed O_2 to form hydroxyl ($HO^{\bullet}$) radicals. Thus, the effective charge transfer can reduce the charge recombination and increase the photocatalytic activity of TiO_2 nanorods.

Moreover, Ng *et al.* [109] reported the photodegradation of 2,4-D by rGO/TiO_2 thin films, exhibiting a fourfold increase in the rate of degradation compared to the bare TiO_2 films. The enhancement was attributed to the incorporation of graphene into TiO_2, which could ensure the rapid transport of the carriers and suppress recombination, and to the interaction between graphene and the pollutants, which could concentrate the organics near the surface of the catalysts and accelerate the photodegradation process.

Regarding the role of both GO and rGO in extending the photocatalytic activity of TiO_2 under visible light illumination, important advances have been made

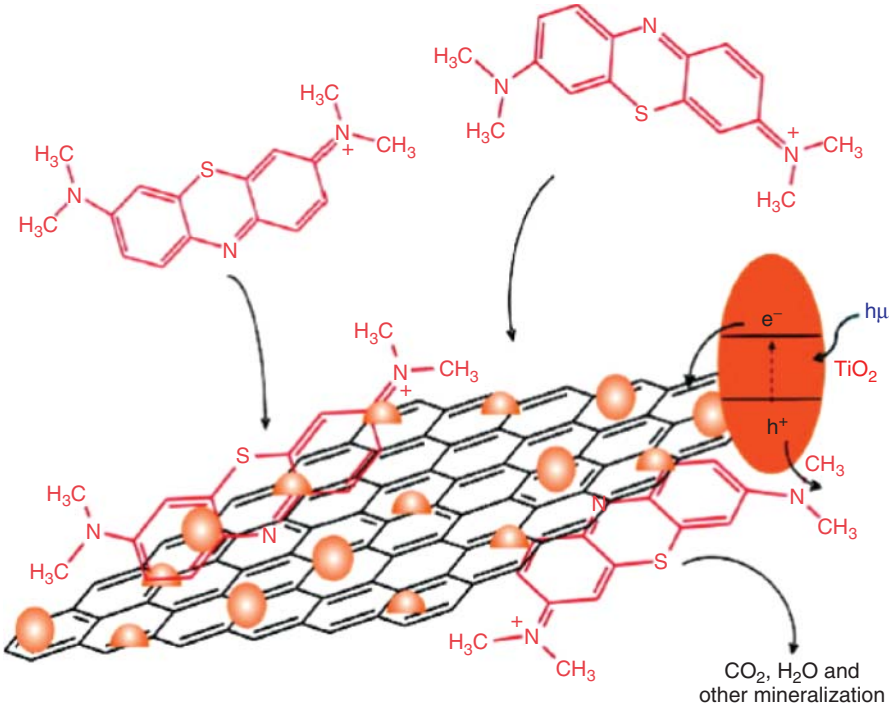

Figure 8.7 Schematic illustration of the P25/graphene composite exemplifying adsorption of methylene blue on graphene sheets and the role of graphene during the photocatalytic degradation of methylene blue. (Reprinted with permission from Ref. [86]. Copyright (2010), American Chemical Society.)

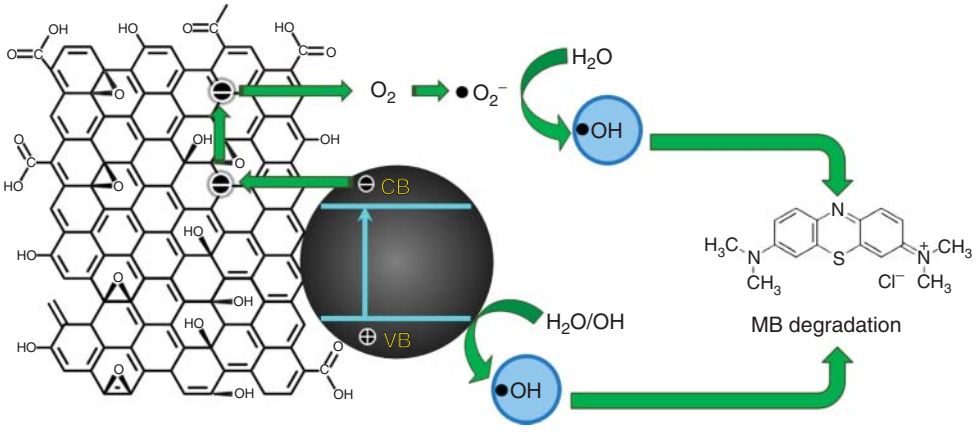

Figure 8.8 Schematic illustration of high photocatalytic activity of TiO_2 nanorods/GO composite for the degradation of MB under UV light irradiation. (Adapted with permission from Ref. [88]. Copyright (2010), Wiley-VCH.)

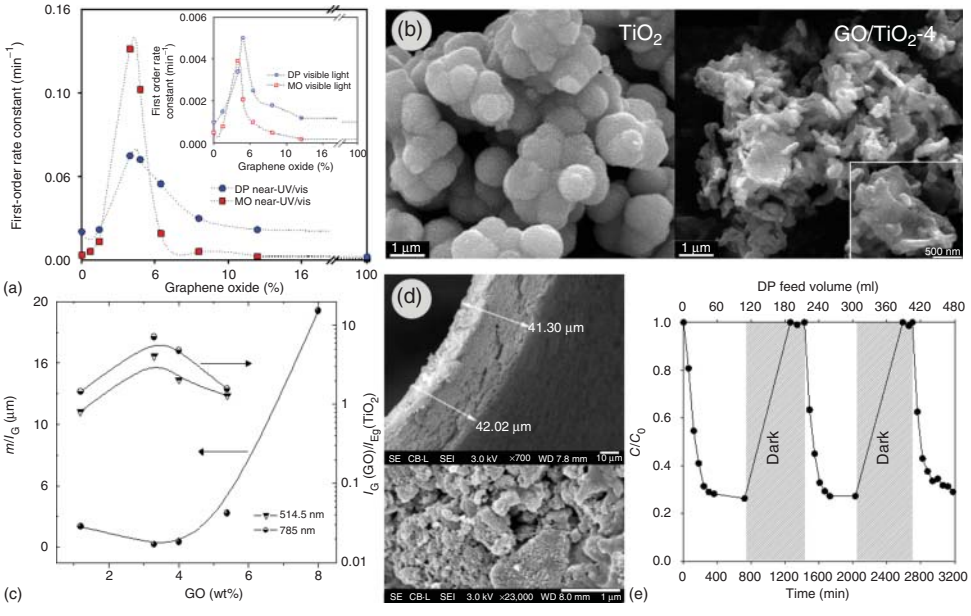

Figure 8.9 (a) Pseudo-first-order reaction rate constant (k) under near-UV/vis and visible light irradiation for DP and MO degradation. (b) SEM micrographs of bare TiO_2 and GO/TiO_2-4. (c) The corresponding GO dependence of the PL background slope (m) to the G peak intensity I_G (left axis) and of the intensity area ratio of the G band to the low-frequency E_g anatase mode $I_G(GO)/I_{Eg}(TiO_2)$ (right axis). (d) SEM micrographs of both wall thickness and external surface of the GO/TiO_2-4 composite immobilized into alginate porous hollow fibers. (e) Photocatalytic degradation of DP over GO/TiO_2-4/APHF in continuous mode under near-UV/vis irradiation. ((a–c) Reprinted with permission from Ref. [24]. Copyright (2012), Elsevier. (d,e) Reprinted with permission from Ref. [91]. Copyright (2013), Elsevier.)

in recent years. Our group [24, 91, 113] reported the photocatalytic activity of GO/TiO_2 composites for the degradation of the pharmaceutical DP and the dye MO under both near-UV/vis and visible light irradiation. The photocatalytic activity of the most active composite GO/TiO_2-4 (composite treated at 200 °C with 4.0 wt% GO, shown in Figure 8.9b) exceeded that of the benchmark P25 photocatalyst for both DP and MO pollutants, especially under visible light (Figure 8.9a). This indicates that GO may effectively enhance the photocatalytic activity of TiO_2 in the visible range without compromising the performance under UV irradiation. The efficiency of the composite was attributed to the optimal assembly and interfacial coupling between the GO sheets and TiO_2 nanoparticles. These results, combined with the distinct quenching of the GO PL under visible and NIR laser excitation (Figure 8.9c), indicate that GO acts either as electron acceptor or electron donor (*sensitizer*) of TiO_2 under UV and visible light, respectively [114].

This active photocatalyst was also immobilized into the matrix of alginate porous hollow fibres (APHF), the resulting material hereafter labelled as GO-TiO_2-4/APHF (Figure 8.9d), as reported elsewhere [91, 115], presenting

considerably high activity and stability in consecutive light–dark cycles of continuous reaction operation for the degradation of DP under near-UV/vis irradiation (Figure 8.9e), which is relevant for future technological applications. The same composite was also stabilized into the pores of ultrafiltration monochannel monoliths, which were tested in a hybrid photocatalytic/ultrafiltration process [116]. The synergetic effects of GO on pollutant adsorption and the photocatalytic degradation capacity of TiO_2 were thoroughly studied, and the influence of the pore size of the monolithic substrate on the deposition morphologies was also elucidated. Moreover, the performance of the novel hybrid process was compared with that of standard nanofiltration with respect to pollutant removal efficiency and energy consumption, providing firm evidence for the former's economic feasibility and efficiency.

In another work, Chen *et al.* [117] reported the visible-light-driven photocatalytic performance of the GO/TiO_2 composites with p/n heterojunction in the degradation of MO. In the aforementioned study, the p-type semiconductor was formed by GO in the GO/TiO_2 composite. Thus, a p/n heterojunction was observed in this composite. Interestingly, this p-type semiconductor could be excited by visible light with wavelengths longer than 510 nm, and acted as a sensitizer and as an electron carrier in the composite, leading to the visible-light-responsive photocatalytic activity.

Another alternative to design high-performance photocatalysts under visible light illumination is the attachment of a visible-light-reactive species. For instance, Wen *et al.* [118] reported the incorporation of Ag into the TiO_2/graphene composite. The increased absorption in the visible light region was originated from the strong interaction between TiO_2 nanoparticles and graphene, as well as the surface plasmon resonance effect of Ag nanoparticles (Figure 8.10). The highly efficient photocatalytic activity is associated with the strong adsorption ability of graphene for aromatic dye molecules, fast photogenerated charge separation due to the formation of Schottky junction between TiO_2 and Ag nanoparticles and the high electron mobility of graphene sheets, as well as the broad absorption in the visible light region. Thus, the photodegradation of MB in the presence of Ag/TiO_2/graphene catalyst under visible light was superior to that with bare P25, graphene, or TiO_2/graphene.

On the other hand, a new nanocomposite consisting of the upconversion (UC) material (YF_3:Yb^{3+}, Tm^{3+}), TiO_2 (P25), and graphene (GR) has been prepared and shown to be an advanced sunlight-activated photocatalyst [119]. During the facile hydrothermal method, the reduction of GO and loading of YF_3:Yb^{3+}, Tm^{3+}, and P25 were achieved simultaneously, and the functionalities of each part were integrated together. The as-prepared ternary UC/P25/GR nanocomposite photocatalyst exhibited large adsorption of dyes, a significantly extended light absorption range, efficient charge separation properties, and superior durability. Indeed, the photocatalytic activity of this novel ternary nanocomposite under sunlight was improved compared with those of P25/GR nanocomposites and bare P25. Overall, this work could provide new insights into the fabrication of ternary composites as

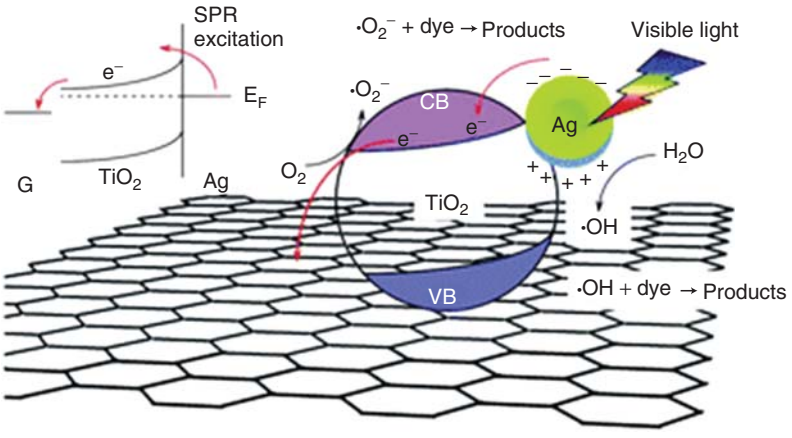

Figure 8.10 Proposed mechanism for the photocatalytic degradation of organic dyes over a $Ag/TiO_2/G$ nanocomposite under visible light irradiation. (Reprinted with permission from Ref. [118]. Copyright (2011), Royal Society of Chemistry.)

high-performance photocatalysts and facilitate their application in environmental protection issues.

Many other photocatalysts have also been incorporated with GO or rGO, including ZnO [120], Fe_3O_4, [121], ZnSe [122], Bi_2WO_6 [123], plasmonic materials (such as Ag/AgBr [124]), and carbon nitride (g-C_3N_4) [125], among others, and they have been reported as efficient photocatalysts for the decomposition of pollutants in water. As already described for TiO_2, the combination of graphene with these other materials can also enhance the adsorption of organic pollutants, extend the photoresponding range, and facilitate the effective charge separation, thereby leading to improved photocatalytic activities.

8.4.2
Photocatalytic Splitting of H_2O

Production of clean hydrogen fuel has been considered as one of the most promising solutions to address the increasing demand for energy and associated environmental concerns [126]. Photocatalytic water splitting into hydrogen and oxygen using semiconductor photocatalysts has been considered as another application of interest for GO semiconductors, because the extension of light absorption to the visible light region for development of solar-driven technologies and the suppression of electron–holes recombination are also key factors in this process.

Zhang *et al.* [127, 128] studied the water-splitting performance using graphene/TiO_2 composites with different loading contents of graphene and both Na_2S and Na_2SO_3 as sacrificial agents under Xe lamp irradiation. The optimal graphene content was found to be 5.0 wt%, with its hydrogen production exceeding more than twice that observed for P25. The enhanced photocatalytic H_2 production activity was due to the deposition of TiO_2 nanoparticles on

graphene sheets, which acted as electron acceptors to efficiently separate the photogenerated charge carriers.

Fan *et al.* [85] studied the efficiency of H_2 evolution for the P25/graphene composite prepared by UV-assisted photocatalytic reduction, hydrazine reduction, and a hydrothermal method. All the composites exhibited better photocatalytic performance for H_2 evolution from methanol aqueous solution than P25 alone, and the P25/graphene composite prepared by the hydrothermal method showed the best performance. The ratio of P25 to graphene in the composite also significantly influenced the photocatalytic performance, and the optimum mass ratio was found to be 5.0 wt%, with the photocatalytic activity of the composite exceeding more than 10 times that of pure P25.

Recently, Lv *et al.* [129] reported the use of graphene sheets in the light-driven water splitting with TiO_2 or CdS. The photocatalytic hydrogen-generating capability of the photocatalysts was investigated in the presence of sacrificial a reagent (Na_2S or Na_2SO_3). The results obtained by the measurements of time-resolved emission spectra, photocurrent generated response, and electrochemical impedance spectra revealed that graphene attached to semiconductor surfaces can efficiently accept and transport electrons from the excited semiconductor, suppressing charge recombination and improving interfacial charge transfer processes. The semiconductor nanoparticle/graphene photocatalysts displayed higher activity for photocatalytic hydrogen evolution, which can be compared with the hydrogen-generating efficiency of systems containing the well-known Pt cocatalyst. Accordingly, the inexpensive and environmentally benign graphene can serve as an alternative cocatalyst for highly efficient hydrogen evolution from the photocatalytic splitting of H_2O.

In addition to TiO_2/graphene and CdS/graphene photocatalysts, a metal-free polymeric photocatalyst, namely graphitic carbon nitride (g-C_3N_4) or $BiVO_4$, combined with graphene has also been reported for efficient H_2 evolution from water splitting. Xiang *et al.* [82] prepared graphene/g-C_3N_4 composite photocatalysts by a combined impregnation–chemical reduction strategy. The resulting composites showed a H_2 evolution rate three times higher than from pure g-C_3N_4 under visible light irradiation, which is due to the efficient charge carrier separation on the photocatalyst (Figure 8.11).

Similarly, Ng *et al.* [130] reported the incorporation of $BiVO_4$ with rGO to improve the photoresponse in visible light. A remarkable 10-fold enhancement in photoelectrochemical water-splitting reaction was observed for the $BiVO_4$/rGO composite compared with pure $BiVO_4$ under visible illumination. This improvement could be attributed to the longer electron lifetime of excited $BiVO_4$ because the electrons were injected to rGO instantly at the site of generation, minimizing charge recombination. It was also observed that GO itself with an appropriate oxygen level and band structure can play the role of photocatalyst in the evolution of both H_2 and O_2. Yeh *et al.* [131] reported that a GO semiconductor photocatalyst with an apparent band gap of 2.4–4.3 eV can steadily produce H_2 from an aqueous methanol solution or pure water even in the absence of Pt as the cocatalyst under visible light irradiation. Usually, the bandgap energy

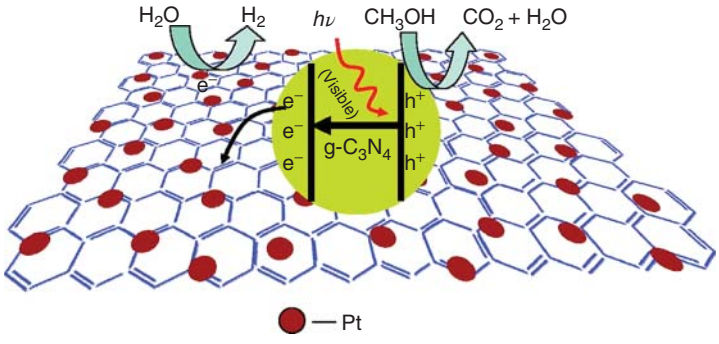

Figure 8.11 Proposed mechanism for the enhanced electron transfer in the graphene/g-C_3N_4 composites. (Reprinted with permission from Ref. [82]. Copyright (2011), American Chemical Society.)

of GO depends on the number of oxygenated sites, and can be modulated by functionalization or cutting them into nanoribbons. When the conduction band edge of GO, which is mainly formed by the anti-bonding π^* orbital, has a higher energy level than that needed for H_2 generation, it can lead to electron injection into the solution phase for H_2 generation.

In another work, Yeh *et al.* [132] investigated the photocatalytic activity of GO, with different amounts of surface oxygen groups, in methanol and $AgNO_3$ solutions for the evolution of H_2 and O_2, respectively. The H_2 evolution was strong and stable over time, whereas the O_2 evolution was negligibly small because of the mutual photocatalytic reduction of the GO with upward shift of the valence band edge under illumination. The conduction band edge of GO showed only negligible change with illumination. When $NaIO_3$ was used as a sacrificial reagent to suppress the mutual reduction mechanism under illumination, strong O_2 evolution was observed over the GO specimens, demonstrating that chemical modification can easily modify the electronic properties of GO for specific photosynthetic applications.

8.4.3
Photocatalytic Reduction of CO_2

The past decades have seen a significant rise in atmospheric carbon dioxide (CO_2) levels resulting from the combustion of hydrocarbon fuels. A solar energy-based technology to recycle CO_2 into a readily transportable hydrocarbon fuel (i.e., a solar fuel) would help reduce atmospheric CO_2 levels and partially fulfill the energy demands within the present hydrocarbon-based fuel infrastructure [133, 134]. Graphene-based materials have also been employed as catalysts for photocatalytic CO_2 conversion. Liang *et al.* [30] investigated the influence of structural defects of graphene on the photocatalytic reduction of CO_2. The two major solution-based pathways for producing graphene, namely oxidation–reduction and solvent exfoliation, resulted in nanoplatelets with

different defect densities. It was demonstrated that the TiO_2/graphene catalysts based on the solvent-exfoliated graphene (SEG) exhibited higher activity than that obtained by the oxidation–reduction method, as a result of fewer defects and enhanced carrier mobility. In comparison with bare TiO_2, the optimized TiO_2/graphene nanocomposites yielded nearly sevenfold improvement in the photoreduction of CO_2.

Tu *et al.* [135] reported the synthesis of robust hollow spheres, consisting of alternating TiO_2 nanosheets and graphene nanosheets (G-$Ti_{0.91}O_2$), by a layer-by-layer deposition method for efficient photocatalytic CO_2 conversion. Compared to the TiO_2/graphene nanocomposites prepared by dispersing TiO_2 nanoparticles on the surface of graphene sheets, G-$Ti_{0.91}O_2$-based hollow spheres exhibited a ninefold enhancement in the photoreduction of CO_2. The enhancement could be attributed to three factors: (i) the ultrathin nature of $Ti_{0.91}O_2$ nanosheets, allowing charge carriers to move rapidly onto the surface; (ii) the sufficiently compact stacking of ultrathin $Ti_{0.91}O_2$ nanosheets with graphene nanosheets, enabling the fast transfer of photogenerated electrons from $Ti_{0.91}O_2$ nanosheets to graphene and thereby enhancing the lifetime of the charge carriers; and (iii) the hollow structure potentially acting as a good photon trap to allow multiple scattering of the incidence light for the enhancement of light absorption.

TiO_2/graphene 2D sandwich-like hybrid nanosheets were prepared in a binary ethylenediamine (En)/H_2O solvent [136]. Abundant Ti^{3+} ions were detected on the surface of TiO_2 of the hybrid, and both methane and ethane were produced by the photoreduction of CO_2 over the prepared hybrid. The total production rate increased with increasing graphene content. The photoinduced electrons from TiO_2 canbe transferred freely along the graphene network for CO_2 reduction, increasing the photocatalytic CO_2 conversion rate. Very recently, Tan *et al.* [137] fabricated rGO/TiO_2 hybrid nanocrystals by a novel and simple solvothermal synthetic route. Anatase TiO_2 particles with an average diameter of 12 nm were uniformly dispersed on the rGO sheet. The prepared rGO/TiO_2 nanocomposites exhibited superior photocatalytic activity in the reduction of CO_2 compared to pristine graphite oxide and pure anatase. The intimate contact between TiO_2 and rGO was proposed to accelerate the transfer of photogenerated electrons from TiO_2 to rGO, leading to effective charge antirecombination and thus enhancing the photocatalytic activity. Furthermore, the photocatalysts were found to be active even under the irradiation of low-power, energy-saving light bulbs, which renders the entire process economically and practically feasible.

Photocatalytic CO_2 conversion to methanol was also investigated over GO as a metal-free photocatalyst [138]. Figure 8.12a shows the photocatalytic methanol formation over GO-1 (Hummers method), GO-2 (modified with 5 ml of H_3PO_4), GO-3 (modified with 10 ml of H_3PO_4), and TiO_2. The activity of methanol formation from photocatalytic CO_2 conversion followed the order: GO-3 > GO-1 > GO-2 > TiO_2 (P-25). The photocatalytic CO_2-to-methanol conversion rate of the modified GO-3 was six times higher than that of P25. The authors propose that, in the photocatalytic reduction, the photogenerated electrons (e^-) and holes (h^+) would migrate to the GO surface and serve as the

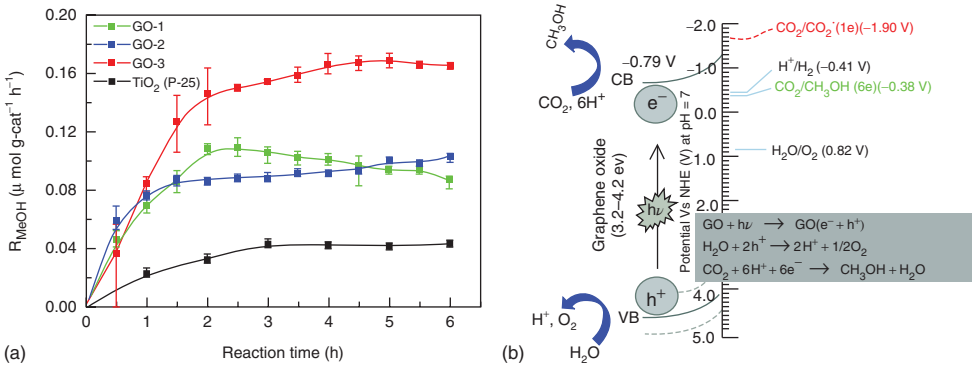

Figure 8.12 (a) Photocatalytic methanol formation (R_{MeOH}) on different GO samples (GO-1, GO-2, GO-3) and TiO_2, using a simulated solar-light source. (b) Schematic illustration of the photocatalytic CO_2 reduction mechanism on GO. (Reprinted with permission from Ref. [138].)

oxidizing and reducing sites, respectively, to react with adsorbed reactants. This indicates that the photogenerated electrons and holes in the irradiated GO can react with the adsorbed CO_2 and H_2O to produce CH_3OH via a six-electron reaction (Figure 8.12b).

8.4.4 Other Applications: Dye-Sensitized Solar Cells

DSSCs, also known as *Grätzel cells*, have been considered as a next-generation renewable power source owing to their relatively high conversion of sunlight into electrical energy, simple fabrication process, and affordable costs, all of which make them competitive with conventional silicon solar cells [139, 140]. Generally, a DSSC is composed of a dye-sensitized nanocrystalline TiO_2 film on a transparent conducting electrode (indium tin oxide, ITO, or fluorine-doped tin oxide, FTO), a CE, and an electrolyte usually containing the I^-/I_3^- redox couple. Upon irradiation, the dyes (also known as the *sensitizers*) are excited, followed by ultrafast electron injection into the conduction band of the semiconductor film. The dye molecule is then regenerated by I^-, which is oxidized to I_3^- and then restored at the CE/electrolyte interface. Despite the high power conversion efficiencies achieved, there still remain several challenging issues for developing DSSCs, including the suppression of charge recombination and the high cost of the Pt-based CE [141].

Graphene-based materials have been explored to act as different components in DSSCs including transparent electrodes, CE materials, and electron transporter/acceptor, showing a great potential in the fabrication of cost-effective DSSCs with promising performances. For example, Wang *et al.* [142] revealed the possibility of using graphene as the transparent electrode in DSSCs. In their work, the obtained graphene thin film showed a high conductivity of 550 S cm^{-1} and a transparency of more than 70% over the 1000–3000 nm range.

Recently, Yeh *et al.* [143] reported the synthesis of rGO prepared by a green photothermal reduction process (P-rGO) and used as the CE on DSSCs. The cell with a P-rGO-based CE showed higher cell efficiency ($\eta = 7.62\%$) when compared with that of the cell having a GO-based CE ($\eta = 0.03\%$). The photoanodes of DSSCs are typically constructed using thick films of TiO_2 nanoparticles, providing anchoring sites for the dye molecules. However, electron transport across disordered TiO_2 nanoparticles is not yet effective enough, and recombination of the photogenerated electrons can take place, decreasing the efficiency of DSSCs. Tang *et al.* [144] reported the G/TiO_2 composite as the photoanode in the fabrication of DSSC. The incorporation of graphene improves the conductivity by a factor of more than 2, and increases the power conversion by a factor of more than 5, in comparison with TiO_2 alone. The better performance of the G/TiO_2 composite was also attributed to the better dye loading on the G/TiO_2 film than on the TiO_2 film.

8.5 Conclusions and Outlook

Because of the unique structure and excellent properties of graphene derivatives, the coupling of both GO and rGO with semiconductor materials presents the possibility to design and fabricate novel graphene-based materials. These photocatalyst composites have attracted extensive attention for their potential in environmental and energy applications because of (i) the interfacial electron transfer between the two constituent phases, (ii) the extended light absorption range, and (iii) the markedly enhanced adsorption capacity for pollutant molecules.

Different methods of synthesis have been developed for fabricating graphene-based semiconductor photocatalysts, such as simple mixing and/or sonication, the sol–gel process, and hydrothermal and solvothermal methods. These composites have been used for a wide variety of photocatalytic applications, ranging from photocatalytic decomposition of organic pollutants, photocatalytic splitting of H_2O, and photocatalytic conversion of CO_2 to the production of fuels and DSSCs.

Despite the demonstrated advances, the studies in this field are still at an early stage of development and further advancements are necessary. For instance, more controlled strategies have to be developed for preparing graphene and its derivatives with high purity, well-defined structure, and lower defects. Special attention should also be paid to the mechanism of photocatalytic enhancement by the graphene-based materials. For this purpose, all aspects in the processing, structure, and properties will need to be better understood and controlled.

Nevertheless, because of the ongoing intensive research on graphene-based materials, these photocatalyst composites are expected to be developed as competitive materials for environmental and energy applications.

Acknowledgments

Financial support for this work was provided by projects PTDC/AAC-AMB/122312/2010 cofinanced by FCT (Fundação para a Ciência e a Tecnologia) and FEDER (ERDF – European Regional Development Fund) through Programme COMPETE (FCOMP-01-0124-FEDER-019503). This work was also partially cofinanced by FCT and FEDER through project PEst-C/EQB/LA0020/2013 (COMPETE), and by QREN, ON2 (North Portugal Regional Operational Programme) and FEDER through projects NORTE-07-0162-FEDER-000050, NORTE-07-0162-FEDER-000015, and NORTE-07-0202-FEDER-038900 in the National Strategic Reference Framework (NSRF). LMPM and SMT acknowledge financial support from FCT grants SFRH/BPD/88964/2012 and SFRH/BPD/74239/2010, respectively. AMTS acknowledges the FCT Investigator 2013 Programme (IF/01501/2013), with financing from the European Social Fund and the Human Potential Operational Programme.

References

1. Gupta, S. and Tripathi, M. (2012) An overview of commonly used semiconductor nanoparticles in photocatalysis. *High Energy Chem.*, **46** (1), 1–9.
2. Xiang, Q., Yu, J., and Jaroniec, M. (2012) Graphene-based semiconductor photocatalysts. *Chem. Soc. Rev.*, **41** (2), 782–796.
3. Herrmann, J.M. (2005) Heterogeneous photocatalysis: state of the art and present applications. *Top. Catal.*, **34** (1-4), 49–65.
4. Fujishima, A., Zhang, X., and Tryk, D.A. (2008) TiO_2 photocatalysis and related surface phenomena. *Surf. Sci. Rep.*, **63** (12), 515–582.
5. Kubacka, A., Fernández-García, M., and Colón, G. (2011) Advanced nanoarchitectures for solar photocatalytic applications. *Chem. Rev.*, **112** (3), 1555–1614.
6. Li, Y., Lu, G., and Li, S. (2003) Photocatalytic production of hydrogen in single component and mixture systems of electron donors and monitoring adsorption of donors by in situ infrared spectroscopy. *Chemosphere*, **52** (5), 843–850.
7. Maeda, K., Higashi, M., Lu, D., Abe, R., and Domen, K. (2010) Efficient nonsacrificial water splitting through two-step photoexcitation by visible light using a modified oxynitride as a hydrogen evolution photocatalyst. *J. Am. Chem. Soc.*, **132** (16), 5858–5868.
8. Murdoch, M., Waterhouse, G.I.N., Nadeem, M.A., Metson, J.B., Keane, M.A., Howe, R.F., Llorca, J., and Idriss, H. (2011) The effect of gold loading and particle size on photocatalytic hydrogen production from ethanol over Au/TiO_2 nanoparticles. *Nat. Chem.*, **3** (6), 489–492.
9. Yu, J., Qi, L., and Jaroniec, M. (2010) Hydrogen production by photocatalytic water splitting over Pt/TiO_2 nanosheets with exposed (001) facets. *J. Phys. Chem. C*, **114** (30), 13118–13125.
10. Weber, A.S., Grady, A.M., and Koodali, R.T. (2012) Lanthanide modified semiconductor photocatalysts. *Catal. Sci. Technol.*, **2** (4), 683–693.
11. Liu, G., Niu, P., Sun, C., Smith, S.C., Chen, Z., Lu, G.Q., and Cheng, H.-M. (2010) Unique electronic structure induced high photoreactivity of sulfur-doped graphitic C_3N_4. *J. Am. Chem. Soc.*, **132** (33), 11642–11648.
12. Kim, W., Tachikawa, T., Majima, T., and Choi, W. (2009) Photocatalysis of dye-sensitized TiO_2 nanoparticles with thin overcoat of Al_2O_3: enhanced activity

for H_2 production and dechlorination of CCl_4. *J. Phys. Chem. C*, **113** (24), 10603–10609.
13. Yin, Z., Wang, Z., Du, Y., Qi, X., Huang, Y., Xue, C., and Zhang, H. (2012) Full solution-processed synthesis of all metal oxide-based tree-like heterostructures on fluorine-doped tin oxide for water splitting. *Adv. Mater.*, **24** (39), 5374–5378.
14. Zhou, W., Yin, Z., Du, Y., Huang, X., Zeng, Z., Fan, Z., Liu, H., Wang, J., and Zhang, H. (2013) Synthesis of few-layer MoS_2 nanosheet-coated TiO_2 nanobelt heterostructures for enhanced photocatalytic activities. *Small*, **9** (1), 140–147.
15. Zhang, L.-W., Fu, H.-B., and Zhu, Y.-F. (2008) Efficient TiO_2 photocatalysts from surface hybridization of TiO_2 particles with graphite-like carbon. *Adv. Funct. Mater.*, **18** (15), 2180–2189.
16. Chen, C., Long, M., Zeng, H., Cai, W., Zhou, B., Zhang, J., Wu, Y., Ding, D., and Wu, D. (2009) Preparation, characterization and visible-light activity of carbon modified TiO_2 with two kinds of carbonaceous species. *J. Mol. Catal. A: Chem.*, **314** (1-2), 35–41.
17. Silva, C.G. and Faria, J.L. (2010) Photocatalytic oxidation of benzene derivatives in aqueous suspensions: synergic effect induced by the introduction of carbon nanotubes in a TiO_2 matrix. *Appl. Catal. Environ.*, **101** (1-2), 81–89.
18. Morales-Torres, S., Pastrana-Martínez, L.M., Figueiredo, J.L., Faria, J.L., and Silva, A.M.T. (2012) Design of graphene-based TiO_2 photocatalysts – a review. *Environ. Sci. Pollut. Res.*, **19**, 3676–3687.
19. Novoselov, K.S., Geim, A.K., Morozov, S.V., Jiang, D., Zhang, Y., Dubonos, S.V., Grigorieva, I.V., and Firsov, A.A. (2004) Electric field effect in atomically thin carbon films. *Science*, **306** (5696), 666–669.
20. Geim, A.K. and Novoselov, K.S. (2007) The rise of graphene. *Nat. Mater.*, **6** (3), 183–191.
21. Geim, A.K. (2009) Graphene: status and prospects. *Science*, **324** (5934), 1530–1534.
22. Pei, S. and Cheng, H.-M. (2012) The reduction of graphene oxide. *Carbon*, **50** (9), 3210–3228.
23. Du, J., Lai, X., Yang, N., Zhai, J., Kisailus, D., Su, F., Wang, D., and Jiang, L. (2010) Hierarchically ordered macro–mesoporous TiO_2–graphene composite films: improved mass transfer, reduced charge recombination, and their enhanced photocatalytic activities. *ACS Nano*, **5** (1), 590–596.
24. Pastrana-Martínez, L.M., Morales-Torres, S., Likodimos, V., Figueiredo, J.L., Faria, J.L., Falaras, P., and Silva, A.M.T. (2012) Advanced nanostructured photocatalysts based on reduced graphene oxide–TiO_2 composites for degradation of diphenhydramine pharmaceutical and methyl orange dye. *Appl. Catal. Environ.*, **123–124**, 241–256.
25. Kamat, P.V. (2009) Graphene-based nanoarchitectures. Anchoring semiconductor and metal nanoparticles on a two-dimensional carbon support. *J. Phys. Chem. Lett.*, **1** (2), 520–527.
26. Yavari, F. and Koratkar, N. (2012) Graphene-based chemical sensors. *J. Phys. Chem. Lett.*, **3** (13), 1746–1753.
27. Jiang, G., Lin, Z., Chen, C., Zhu, L., Chang, Q., Wang, N., Wei, W., and Tang, H. (2011) TiO_2 nanoparticles assembled on graphene oxide nanosheets with high photocatalytic activity for removal of pollutants. *Carbon*, **49** (8), 2693–2701.
28. Kim, I.T., Magasinski, A., Jacob, K., Yushin, G., and Tannenbaum, R. (2013) Synthesis and electrochemical performance of reduced graphene oxide/maghemite composite anode for lithium ion batteries. *Carbon*, **52**, 56–64.
29. Song, J., Yin, Z., Yang, Z., Amaladass, P., Wu, S., Ye, J., Zhao, Y., Deng, W.-Q., Zhang, H., and Liu, X.-W. (2011) Enhancement of photogenerated electron transport in dye-sensitized solar cells with introduction of a reduced graphene oxide–TiO_2 junction. *Chem. Eur. J.*, **17** (39), 10832–10837.
30. Liang, Y.T., Vijayan, B.K., Gray, K.A., and Hersam, M.C. (2011) Minimizing graphene defects enhances titania

nanocomposite-based photocatalytic reduction of CO_2 for improved solar fuel production. *Nano Lett.*, **11** (7), 2865–2870.

31. Loh, K.P., Bao, Q., Eda, G., and Chhowalla, M. (2010) Graphene oxide as a chemically tunable platform for optical applications. *Nat. Chem.*, **2** (12), 1015–1024.
32. Poh, H.L., Sanek, F., Ambrosi, A., Zhao, G., Sofer, Z., and Pumera, M. (2012) Graphenes prepared by Staudenmaier, Hofmann and Hummers methods with consequent thermal exfoliation exhibit very different electrochemical properties. *Nanoscale*, **4** (11), 3515–3522.
33. Ruoff, R. (2008) Graphene: calling all chemists. *Nat. Nano*, **3** (1), 10–11.
34. Paredes, J.I., Villar-Rodil, S., Martínez-Alonso, A., and Tascón, J.M.D. (2008) Graphene oxide dispersions in organic solvents. *Langmuir*, **24** (19), 10560–10564.
35. Bianco, A., Cheng, H.-M., Enoki, T., Gogotsi, Y., Hurt, R.H., Koratkar, N., Kyotani, T., Monthioux, M., Park, C.R., Tascon, J.M.D., and Zhang, J. (2013) All in the graphene family – a recommended nomenclature for two-dimensional carbon materials. *Carbon*, **65**, 1–6.
36. Compton, O.C. and Nguyen, S.T. (2010) Graphene oxide, highly reduced graphene oxide, and graphene: versatile building blocks for carbon-based materials. *Small*, **6** (6), 711–723.
37. Dreyer, D.R., Park, S., Bielawski, C.W., and Ruoff, R.S. (2010) The chemistry of graphene oxide. *Chem. Soc. Rev.*, **39** (1), 228–240.
38. Brodie, B.C. (1859) On the atomic weight of graphite. *Philos. Trans. R. Soc. London*, **149**, 249–259.
39. Staudenmaier, L. (1898) Verfahren zur Darstellung der Graphitsäure. *Ber. Dtsch. Chem. Ges.*, **31** (2), 1481–1487.
40. Hummers, W.S. and Offeman, R.E. (1958) Preparation of graphitic oxide. *J. Am. Chem. Soc.*, **80** (6), 1339–1339.
41. Marcano, D.C., Kosynkin, D.V., Berlin, J.M., Sinitskii, A., Sun, Z., Slesarev, A., Alemany, L.B., Lu, W., and Tour, J.M. (2010) Improved synthesis of graphene oxide. *ACS Nano*, **4** (8), 4806–4814.
42. Botas, C., Álvarez, P., Blanco, C., Santamaría, R., Granda, M., Gutiérrez, M.D., Rodríguez-Reinoso, F., and Menéndez, R. (2013) Critical temperatures in the synthesis of graphene-like materials by thermal exfoliation–reduction of graphite oxide. *Carbon*, **52**, 476–485.
43. Lerf, A., He, H., Forster, M., and Klinowski, J. (1998) Structure of graphite oxide revisited. *J. Phys. Chem. B*, **102** (23), 4477–4482.
44. Stankovich, S., Dikin, D.A., Piner, R.D., Kohlhaas, K.A., Kleinhammes, A., Jia, Y., Wu, Y., Nguyen, S.T., and Ruoff, R.S. (2007) Synthesis of graphene-based nanosheets via chemical reduction of exfoliated graphite oxide. *Carbon*, **45** (7), 1558–1565.
45. Shao, Y., Wang, J., Engelhard, M., Wang, C., and Lin, Y. (2010) Facile and controllable electrochemical reduction of graphene oxide and its applications. *J. Mater. Chem.*, **20** (4), 743–748.
46. Williams, G., Seger, B., and Kamat, P.V. (2008) TiO_2-graphene nanocomposites. UV-assisted photocatalytic reduction of graphene oxide. *ACS Nano*, **2** (7), 1487–1491.
47. Huang, L., Liu, Y., Ji, L.-C., Xie, Y.-Q., Wang, T., and Shi, W.-Z. (2011) Pulsed laser assisted reduction of graphene oxide. *Carbon*, **49** (7), 2431–2436.
48. Gao, X., Jang, J., and Nagase, S. (2009) Hydrazine and thermal reduction of graphene oxide: reaction mechanisms, product structures, and reaction design. *J. Phys. Chem. C*, **114** (2), 832–842.
49. Bagri, A., Mattevi, C., Acik, M., Chabal, Y.J., Chhowalla, M., and Shenoy, V.B. (2010) Structural evolution during the reduction of chemically derived graphene oxide. *Nat. Chem.*, **2** (7), 581–587.
50. Gómez-Navarro, C., Meyer, J.C., Sundaram, R.S., Chuvilin, A., Kurasch, S., Burghard, M., Kern, K., and Kaiser, U. (2010) Atomic structure of reduced graphene oxide. *Nano Lett.*, **10** (4), 1144–1148.
51. Krishnan, D., Kim, F., Luo, J., Cruz-Silva, R., Cote, L.J., Jang, H.D., and Huang, J. (2012) Energetic

graphene oxide: challenges and opportunities. *Nano Today*, **7** (2), 137–152.
52. Erickson, K., Erni, R., Lee, Z., Alem, N., Gannett, W., and Zettl, A. (2010) Determination of the local chemical structure of graphene oxide and reduced graphene oxide. *Adv. Mater.*, **22** (40), 4467–4472.
53. Chen, D., Feng, H., and Li, J. (2012) Graphene oxide: preparation, functionalization, and electrochemical applications. *Chem. Rev.*, **112** (11), 6027–6053.
54. Mattevi, C., Eda, G., Agnoli, S., Miller, S., Mkhoyan, K.A., Celik, O., Mastrogiovanni, D., Granozzi, G., Garfunkel, E., and Chhowalla, M. (2009) Evolution of electrical, chemical, and structural properties of transparent and conducting chemically derived graphene thin films. *Adv. Funct. Mater.*, **19** (16), 2577–2583.
55. Boukhvalov, D.W. and Katsnelson, M.I. (2008) Modeling of graphite oxide. *J. Am. Chem. Soc.*, **130** (32), 10697–10701.
56. Becerril, H.A., Mao, J., Liu, Z., Stoltenberg, R.M., Bao, Z., and Chen, Y. (2008) Evaluation of solution-processed reduced graphene oxide films as transparent conductors. *ACS Nano*, **2** (3), 463–470.
57. Eda, G., Fanchini, G., and Chhowalla, M. (2008) Large-area ultrathin films of reduced graphene oxide as a transparent and flexible electronic material. *Nat. Nano*, **3** (5), 270–274.
58. Wang, S., Chia, P.-J., Chua, L.-L., Zhao, L.-H., Png, R.-Q., Sivaramakrishnan, S., Zhou, M., Goh, R.G.S., Friend, R.H., Wee, A.T.S., and Ho, P.K.H. (2008) Band-like transport in surface-functionalized highly solution-processable graphene nanosheets. *Adv. Mater.*, **20** (18), 3440–3446.
59. Eda, G., Mattevi, C., Yamaguchi, H., Kim, H., and Chhowalla, M. (2009) Insulator to semimetal transition in graphene oxide. *J. Phys. Chem. C*, **113** (35), 15768–15771.
60. Si, Y. and Samulski, E.T. (2008) Synthesis of water soluble graphene. *Nano Lett.*, **8** (6), 1679–1682.
61. Luo, D., Zhang, G., Liu, J., and Sun, X. (2011) Evaluation criteria for reduced graphene oxide. *J. Phys. Chem. C*, **115** (23), 11327–11335.
62. Lee, G., Kim, K.S., and Cho, K. (2011) Theoretical study of the electron transport in graphene with vacancy and residual oxygen defects after high-temperature reduction. *J. Phys. Chem. C*, **115** (19), 9719–9725.
63. Wei, Z., Wang, D., Kim, S., Kim, S.-Y., Hu, Y., Yakes, M.K., Laracuente, A.R., Dai, Z., Marder, S.R., Berger, C., King, W.P., de Heer, W.A., Sheehan, P.E., and Riedo, E. (2010) Nanoscale tunable reduction of graphene oxide for graphene electronics. *Science*, **328** (5984), 1373–1376.
64. Li, D., Muller, M.B., Gilje, S., Kaner, R.B., and Wallace, G.G. (2008) Processable aqueous dispersions of graphene nanosheets. *Nat. Nano*, **3** (2), 101–105.
65. Yan, J.-A., Xian, L., and Chou, M.Y. (2009) Structural and electronic properties of oxidized graphene. *Phys. Rev. Lett.*, **103** (8), 086802.
66. Eda, G., Lin, Y.-Y., Mattevi, C., Yamaguchi, H., Chen, H.-A., Chen, I.S., Chen, C.-W., and Chhowalla, M. (2010) Blue photoluminescence from chemically derived graphene oxide. *Adv. Mater.*, **22** (4), 505–509.
67. Loh, K.P., Bao, Q., Ang, P.K., and Yang, J. (2010) The chemistry of graphene. *J. Mater. Chem.*, **20** (12), 2277–2289.
68. Fujishima, A. and Honda, K., (1972) Electrochemical Photolysis of Water at a Semiconductor Electrode. *Nature*, **238** (5358), 37–38.
69. Frank, S.N. and Bard, A.J. (1977) Heterogeneous photocatalytic oxidation of cyanide ion in aqueous solutions at titanium dioxide powder. *J. Am. Chem. Soc.*, **99** (1), 303–304.
70. Likodimos, V., Dionysiou, D., and Falaras, P. (2010) CLEAN WATER: water detoxification using innovative photocatalysts. *Rev. Environ. Sci. Biotechnol.*, **9** (2), 87–94.
71. Liu, X., Pan, L., Zhao, Q., Lv, T., Zhu, G., Chen, T., Lu, T., Sun, Z., and Sun, C. (2012) UV-assisted photocatalytic synthesis of ZnO–reduced graphene

oxide composites with enhanced photocatalytic activity in reduction of Cr(VI). *Chem. Eng. J.*, **183**, 238–243.

72. Xu, T., Zhang, L., Cheng, H., and Zhu, Y. (2011) Significantly enhanced photocatalytic performance of ZnO via graphene hybridization and the mechanism study. *Appl. Catal. Environ.*, **101** (3-4), 382–387.
73. Akhavan, O. (2011) Photocatalytic reduction of graphene oxides hybridized by ZnO nanoparticles in ethanol. *Carbon*, **49** (1), 11–18.
74. Zhang, C., Zhang, J., Su, Y., Xu, M., Yang, Z., and Zhang, Y. (2014) ZnO nanowire/reduced graphene oxide nanocomposites for significantly enhanced photocatalytic degradation of Rhodamine 6G. *Physica E*, **56**, 251–255.
75. Abulizi, A., Yang, G.-H., and Zhu, J.-J. (2014) One-step simple sonochemical fabrication and photocatalytic properties of Cu_2O–rGO composites. *Ultrason. Sonochem.*, **21** (1), 129–135.
76. Zeng, B., Chen, X., Ning, X., Chen, C., Deng, W., Huang, Q., and Zhong, W. (2013) Electrostatic-assembly three-dimensional CNTs/rGO implanted Cu_2O composite spheres and its photocatalytic properties. *Appl. Surf. Sci.*, **276**, 482–486.
77. Chen, G., Sun, M., Wei, Q., Zhang, Y., and Du, B. (2013) Ag_3PO_4/graphene-oxide composite with remarkably enhanced visible-light-driven photocatalytic activity toward dyes in water. *Journal of Hazardous Material*, **244-245** (0), 86–93.
78. Fu, Y., Sun, X., and Wang, X. (2011) $BiVO_4$–graphene catalyst and its high photocatalytic performance under visible light irradiation. *Mater. Chem. Phys.*, **131** (1-2), 325–330.
79. Pawar, R.C. and Lee, C.S. (2013) Sensitization of CdS nanoparticles onto reduced graphene oxide (RGO) fabricated by chemical bath deposition method for effective removal of Cr(VI). *Mater. Chem. Phys.*, **141** (2-3), 686–693.
80. Weng, B., Liu, S., Zhang, N., Tang, Z.-R., and Xu, Y.-J. (2014) A simple yet efficient visible-light-driven CdS nanowires-carbon nanotube 1D–1D nanocomposite photocatalyst. *J. Catal.*, **309**, 146–155.
81. Guo, S., Zhang, G., Guo, Y., and Yu, J.C. (2013) Graphene oxide–Fe_2O_3 hybrid material as highly efficient heterogeneous catalyst for degradation of organic contaminants. *Carbon*, **60**, 437–444.
82. Xiang, Q., Yu, J., and Jaroniec, M. (2011) Preparation and enhanced visible-light photocatalytic H_2-production activity of graphene/C_3N_4 composites. *J. Phys. Chem. C*, **115** (15), 7355–7363.
83. Sun, Y., Li, C., Xu, Y., Bai, H., Yao, Z., and Shi, G. (2010) Chemically converted graphene as substrate for immobilizing and enhancing the activity of a polymeric catalyst. *Chem. Commun.*, **46** (26), 4740–4742.
84. Zhu, M., Chen, P., and Liu, M. (2011) Graphene oxide enwrapped Ag/AgX (X = Br, Cl) nanocomposite as a highly efficient visible-light plasmonic photocatalyst. *ACS Nano*, **5** (6), 4529–4536.
85. Fan, W., Lai, Q., Zhang, Q., and Wang, Y. (2011) Nanocomposites of TiO_2 and reduced graphene oxide as efficient photocatalysts for hydrogen evolution. *J. Phys. Chem. C*, **115** (21), 10694–10701.
86. Zhang, H., Lv, X., Li, Y., Wang, Y., and Li, J. (2010) P25-graphene composite as a high performance photocatalyst. *ACS Nano*, **4** (1), 380–386.
87. Wang, F. and Zhang, K. (2011) Reduced graphene oxide–TiO_2 nanocomposite with high photocatalystic activity for the degradation of rhodamine B. *J. Mol. Catal. A: Chem.*, **345** (1-2), 101–107.
88. Liu, J., Bai, H., Wang, Y., Liu, Z., Zhang, X., and Sun, D.D. (2010) Self-assembling TiO_2 nanorods on large graphene oxide sheets at a two-phase interface and their anti-recombination in photocatalytic applications. *Adv. Funct. Mater.*, **20** (23), 4175–4181.
89. Akhavan, O., Abdolahad, M., Esfandiar, A., and Mohatashamifar, M. (2010) Photodegradation of graphene oxide sheets by TiO_2 nanoparticles after a photocatalytic reduction. *J. Phys. Chem. C*, **114** (30), 12955–12959.

90. Akhavan, O. and Ghaderi, E. (2009) Photocatalytic reduction of graphene oxide nanosheets on TiO_2 thin film for photoinactivation of bacteria in solar light irradiation. *J. Phys. Chem. C*, **113** (47), 20214–20220.
91. Pastrana-Martínez, L.M., Morales-Torres, S., Papageorgiou, S.K., Katsaros, F.K., Romanos, G.E., Figueiredo, J.L., Faria, J.L., Falaras, P., and Silva, A.M.T. (2013) Photocatalytic behaviour of nanocarbon–TiO_2 composites and immobilization into hollow fibres. *Appl. Catal. Environ.*, **142–143**, 101–111.
92. Lei, M., Wang, N., Zhu, L., Xie, C., and Tang, H. (2014) A peculiar mechanism for the photocatalytic reduction of decabromodiphenyl ether over reduced graphene oxide–TiO_2 photocatalyst. *Chem. Eng. J.*, **241**, 207–215.
93. Morales-Torres, S., Pastrana-Martínez, L.M., Figueiredo, J.L., Faria, J.L., and Silva, A.M.T. (2013) Graphene oxide-P25 photocatalysts for degradation of diphenhydramine pharmaceutical and methyl orange dye. *Appl. Surf. Sci.*, **275**, 361–368.
94. Bell, N.J., Ng, Y.H., Du, A., Coster, H., Smith, S.C., and Amal, R. (2011) Understanding the enhancement in photoelectrochemical properties of photocatalytically prepared TiO_2-reduced graphene oxide composite. *J. Phys. Chem. C*, **115** (13), 6004–6009.
95. Zhang, Y. and Pan, C. (2011) TiO_2/graphene composite from thermal reaction of graphene oxide and its photocatalytic activity in visible light. *J. Mater. Sci.*, **46** (8), 2622–2626.
96. Williams, G. and Kamat, P.V. (2009) Graphene–semiconductor nanocomposites: excited-state interactions between ZnO nanoparticles and graphene oxide†. *Langmuir*, **25** (24), 13869–13873.
97. Paek, S.-M., Yoo, E., and Honma, I. (2008) Enhanced cyclic performance and lithium storage capacity of SnO_2/graphene nanoporous electrodes with three-dimensionally delaminated flexible structure. *Nano Lett.*, **9** (1), 72–75.
98. Ng, Y.H., Iwase, A., Bell, N.J., Kudo, A., and Amal, R. (2011) Semiconductor/reduced graphene oxide nanocomposites derived from photocatalytic reactions. *Catal. Today*, **164** (1), 353–357.
99. Lambert, T.N., Chavez, C.A., Hernandez-Sanchez, B., Lu, P., Bell, N.S., Ambrosini, A., Friedman, T., Boyle, T.J., Wheeler, D.R., and Huber, D.L. (2009) Synthesis and characterization of titania–graphene nanocomposites. *J. Phys. Chem. C*, **113** (46), 19812–19823.
100. Zhu, C., Guo, S., Wang, P., Xing, L., Fang, Y., Zhai, Y., and Dong, S. (2010) One-pot, water-phase approach to high-quality graphene/TiO_2 composite nanosheets. *Chem. Commun.*, **46** (38), 7148–7150.
101. Chen, J.S., Wang, Z., Dong, X.C., Chen, P., and Lou, X.W. (2011) Graphene-wrapped TiO_2 hollow structures with enhanced lithium storage capabilities. *Nanoscale*, **3** (5), 2158–2161.
102. Lou, X.W. and Archer, L.A. (2008) A general route to nonspherical anatase TiO_2 hollow colloids and magnetic multifunctional particles. *Adv. Mater.*, **20** (10), 1853–1858.
103. Cong, Y., Long, M., Cui, Z., Li, X., Dong, Z., Yuan, G., and Zhang, J. (2013) Anchoring a uniform TiO_2 layer on graphene oxide sheets as an efficient visible light photocatalyst. *Appl. Surf. Sci.*, **282**, 400–407.
104. Ding, S., Chen, J.S., Luan, D., Boey, F.Y.C., Madhavi, S., and Lou, X.W. (2011) Graphene-supported anatase TiO_2 nanosheets for fast lithium storage. *Chem. Commun.*, **47** (20), 5780–5782.
105. Shen, J., Yan, B., Shi, M., Ma, H., Li, N., and Ye, M. (2011) One step hydrothermal synthesis of TiO_2-reduced graphene oxide sheets. *J. Mater. Chem.*, **21** (10), 3415–3421.
106. Liang, D., Cui, C., Hu, H., Wang, Y., Xu, S., Ying, B., Li, P., Lu, B., and Shen, H. (2014) One-step hydrothermal synthesis of anatase TiO_2/reduced graphene oxide nanocomposites with enhanced photocatalytic activity. *J. Alloys Compd.*, **582**, 236–240.

107. Nguyen-Phan, T.D., Pham, V.H., Shin, E.W., Pham, H.D., Kim, S., Chung, J.S., Kim, E.J., and Hur, S.H. (2011) The role of graphene oxide content on the adsorption-enhanced photocatalysis of titanium dioxide/graphene oxide composites. *Chem. Eng. J.*, **170** (1), 226–232.

108. Amalraj Appavoo, I., Hu, J., Huang, Y., Li, S.F.Y., and Ong, S.L. (2014) Response surface modeling of Carbamazepine (CBZ) removal by Graphene-P25 nanocomposites/UVA process using central composite design. *Water Res.*, **57**, 270–279.

109. Ng, Y.H., Lightcap, I.V., Goodwin, K., Matsumura, M., and Kamat, P.V. (2010) To what extent do graphene scaffolds improve the photovoltaic and photocatalytic response of TiO_2 nanostructured films? *J. Phys. Chem. Lett.*, **1** (15), 2222–2227.

110. Maroga Mboula, V., Héquet, V., Andrès, Y., Pastrana-Martínez, L.M., Doña-Rodríguez, J.M., Silva, A.M.T., and Falaras, P. (2013) Photocatalytic degradation of endocrine disruptor compounds under simulated solar light. *Water Res.*, **47** (12), 3997–4005.

111. Fotiou, T., Triantis, T.M., Kaloudis, T., Pastrana-Martínez, L.M., Likodimos, V., Falaras, P., Silva, A.M.T., and Hiskia, A. (2013) Photocatalytic degradation of microcystin-LR and Off-odor compounds in water under UV-A and solar light with a nanostructured photocatalyst based on reduced graphene oxide–TiO_2 composite. Identification of intermediate products. *Ind. Eng. Chem. Res.*, **52** (39), 13991–14000.

112. Liu, J., Liu, L., Bai, H., Wang, Y., and Sun, D.D. (2011) Gram-scale production of graphene oxide-TiO_2 nanorod composites: towards high-activity photocatalytic materials. *Appl. Catal. Environ.*, **106** (1–2), 76–82.

113. Pastrana-Martínez, L.M., Morales-Torres, S., Kontos, A.G., Moustakas, N.G., Faria, J.L., Doña-Rodríguez, J.M., Falaras, P., and Silva, A.M.T. (2013) TiO_2, surface modified TiO_2 and graphene oxide-TiO_2 photocatalysts for degradation of water pollutants under near-UV/Vis and visible light. *Chem. Eng. J.*, **224**, 17–23.

114. Chatterjee, D. and Dasgupta, S. (2005) Visible light induced photocatalytic degradation of organic pollutants. *J. Photochem. Photobiol., C*, **6** (2-3), 186–205.

115. Papageorgiou, S.K., Katsaros, F.K., Favvas, E.P., Romanos, G.E., Athanasekou, C.P., Beltsios, K.G., Tzialla, O.I., and Falaras, P. (2012) Alginate fibers as photocatalyst immobilizing agents applied in hybrid photocatalytic/ultrafiltration water treatment processes. *Water Res.*, **46** (6), 1858–1872.

116. Athanasekou, C.P., Morales-Torres, S., Likodimos, V., Romanos, G.E., Pastrana-Martinez, L.M., Falaras, P., Dionysiou, D.D., Faria, J.L., Figueiredo, J.L., and Silva, A.M.T. (2014) Prototype composite membranes of partially reduced graphene oxide/TiO_2 for photocatalytic ultrafiltration water treatment under visible light. *Appl. Catal. Environ.*, **158–159**, 361–372.

117. Chen, C., Cai, W., Long, M., Zhou, B., Wu, Y., Wu, D., and Feng, Y. (2010) Synthesis of visible-light responsive graphene oxide/TiO_2 composites with p/n heterojunction. *ACS Nano*, **4** (11), 6425–6432.

118. Wen, Y., Ding, H., and Shan, Y. (2011) Preparation and visible light photocatalytic activity of Ag/TiO_2/graphene nanocomposite. *Nanoscale*, **3** (10), 4411–4417.

119. Ren, L., Qi, X., Liu, Y., Huang, Z., Wei, X., Li, J., Yang, L., and Zhong, J. (2012) Upconversion-P25-graphene composite as an advanced sunlight driven photocatalytic hybrid material. *J. Mater. Chem.*, **22** (23), 11765–11771.

120. Yoo, D.-H., Cuong, T.V., Luan, V.H., Khoa, N.T., Kim, E.J., Hur, S.H., and Hahn, S.H. (2012) Photocatalytic performance of a Ag/ZnO/CCG multidimensional heterostructure prepared by a solution-based method. *J. Phys. Chem. C*, **116** (12), 7180–7184.

121. Sun, H., Cao, L., and Lu, L. (2011) Magnetite/reduced graphene oxide nanocomposites: one step solvothermal synthesis and use as a novel platform

for removal of dye pollutants. *Nano Res.*, **4** (6), 550–562.

122. Chen, P., Xiao, T.-Y., Li, H.-H., Yang, J.-J., Wang, Z., Yao, H.-B., and Yu, S.-H. (2011) Nitrogen-doped graphene/ZnSe nanocomposites: hydrothermal synthesis and their enhanced electrochemical and photocatalytic activities. *ACS Nano*, **6** (1), 712–719.

123. Gao, E., Wang, W., Shang, M., and Xu, J. (2011) Synthesis and enhanced photocatalytic performance of graphene-Bi_2WO_6 composite. *Phys. Chem. Chem. Phys.*, **13** (7), 2887–2893.

124. Zhu, M., Chen, P., and Liu, M. (2012) Ag/AgBr/graphene oxide nanocomposite synthesized via oil/water and water/oil microemulsions: a comparison of sunlight energized plasmonic photocatalytic activity. *Langmuir*, **28** (7), 3385–3390.

125. Liao, G., Chen, S., Quan, X., Yu, H., and Zhao, H. (2012) Graphene oxide modified g-C_3N_4 hybrid with enhanced photocatalytic capability under visible light irradiation. *J. Mater. Chem.*, **22** (6), 2721–2726.

126. Maeda, K. and Domen, K. (2010) Photocatalytic water splitting: recent progress and future challenges. *J. Phys. Chem. Lett.*, **1** (18), 2655–2661.

127. Zhang, X.-Y., Li, H.-P., Cui, X.-L., and Lin, Y. (2010) Graphene/TiO_2 nanocomposites: synthesis, characterization and application in hydrogen evolution from water photocatalytic splitting. *J. Mater. Chem.*, **20** (14), 2801–2806.

128. Zhang, X., Sun, Y., Cui, X., and Jiang, Z. (2012) A green and facile synthesis of TiO_2/graphene nanocomposites and their photocatalytic activity for hydrogen evolution. *Int. J. Hydrogen Energy*, **37** (1), 811–815.

129. Lv, X.J., Fu, W.F., Chang, H.X., Zhang, H., Cheng, J.S., Zhang, G.J., Song, Y., Hu, C.Y., and Li, J.H. (2012) Hydrogen evolution from water using semiconductor nanoparticle/graphene composite photocatalysts without noble metals. *J. Mater. Chem.*, **22** (4), 1539–1546.

130. Ng, Y.H., Iwase, A., Kudo, A., and Amal, R. (2010) Reducing graphene oxide on a visible-light $BiVO_4$ photocatalyst for an enhanced photoelectrochemical water splitting. *J. Phys. Chem. Lett.*, **1** (17), 2607–2612.

131. Yeh, T.-F., Syu, J.-M., Cheng, C., Chang, T.-H., and Teng, H. (2010) Graphite oxide as a photocatalyst for hydrogen production from water. *Adv. Funct. Mater.*, **20** (14), 2255–2262.

132. Yeh, T.-F., Chan, F.-F., Hsieh, C.-T., and Teng, H. (2011) Graphite oxide with different oxygenated levels for hydrogen and oxygen production from water under illumination: the band positions of graphite oxide. *J. Phys. Chem. C*, **115** (45), 22587–22597.

133. Dhakshinamoorthy, A., Navalon, S., Corma, A., and Garcia, H. (2012) Photocatalytic CO_2 reduction by TiO_2 and related titanium containing solids. *Energy Environ. Sci.*, **5** (11), 9217–9233.

134. Izumi, Y. (2013) Recent advances in the photocatalytic conversion of carbon dioxide to fuels with water and/or hydrogen using solar energy and beyond. *Coord. Chem. Rev.*, **257** (1), 171–186.

135. Tu, W., Zhou, Y., Liu, Q., Tian, Z., Gao, J., Chen, X., Zhang, H., Liu, J., and Zou, Z. (2012) Robust hollow spheres consisting of alternating titania nanosheets and graphene nanosheets with high photocatalytic activity for CO_2 conversion into renewable fuels. *Adv. Funct. Mater.*, **22** (6), 1215–1221.

136. Tu, W., Zhou, Y., Liu, Q., Yan, S., Bao, S., Wang, X., Xiao, M., and Zou, Z. (2013) An in situ simultaneous reduction-hydrolysis technique for fabrication of TiO2-graphene 2D sandwich-like hybrid nanosheets: graphene-promoted selectivity of photocatalytic-driven hydrogenation and coupling of CO_2 into methane and ethane. *Adv. Funct. Mater.*, **23** (14), 1743–1749.

137. Tan, L.-L., Ong, W.-J., Chai, S.-P., and Mohamed, A. (2013) Reduced graphene oxide-TiO_2 nanocomposite as a promising visible-light-active photocatalyst for the conversion of carbon dioxide. *Nanoscale Res. Lett.*, **8** (1), 465.

138. Hsu, H.-C., Shown, I., Wei, H.-Y., Chang, Y.-C., Du, H.-Y., Lin, Y.-G.,

Tseng, C.-A., Wang, C.-H., Chen, L.-C., Lin, Y.-C., and Chen, K.-H. (2013) Graphene oxide as a promising photocatalyst for CO_2 to methanol conversion. *Nanoscale*, **5** (1), 262–268.

139. O'Regan, B. and Gratzel, M. (1991) A low-cost, high-efficiency solar cell based on dye-sensitized colloidal TiO_2 films. *Nature*, **353** (6346), 737–740.

140. Chen, D., Zhang, H., Liu, Y., and Li, J. (2013) Graphene and its derivatives for the development of solar cells, photoelectrochemical, and photocatalytic applications. *Energy Environ. Sci.*, **6** (5), 1362–1387.

141. Yella, A., Lee, H.-W., Tsao, H.N., Yi, C., Chandiran, A.K., Nazeeruddin, M.K., Diau, E.W.-G., Yeh, C.-Y., Zakeeruddin, S.M., and Grätzel, M. (2011) Porphyrin-sensitized solar cells with cobalt (II/III)–based redox electrolyte exceed 12 percent efficiency. *Science*, **334** (6056), 629–634.

142. Wang, X., Zhi, L., and Müllen, K. (2007) Transparent, conductive graphene electrodes for dye-sensitized solar cells. *Nano Lett.*, **8** (1), 323–327.

143. Yeh, M.-H., Lin, L.-Y., Chang, L.-Y., Leu, Y.-A., Cheng, W.-Y., Lin, J.-J., and Ho, K.-C. (2014) Dye-sensitized solar cells with reduced graphene oxide as the counter electrode prepared by a green photothermal reduction process. *ChemPhysChem*, **15** (6), 1175–1181.

144. Tang, Y.B., Lee, C.S., Xu, J., Liu, Z.T., Chen, Z.H., He, Z., Cao, Y.L., Yuan, G., Song, H., Chen, L., Luo, L., Cheng, H.M., Zhang, W.J., Bello, I., and Lee, S.T. (2010) Incorporation of graphenes in nanostructured TiO_2 films via molecular grafting for dye-sensitized solar cell application. *ACS Nano*, **4** (6), 3482–3488.

9
Graphene-Based Photocatalysts for Energy Applications: Progress and Future Prospects

Wanjun Wang, Donald K.L. Chan, and Jimmy C. Yu

9.1
Introduction

Graphene, a two-dimensional sheet of sp^2-hybridized carbon with one atom thickness, has become a rapidly rising star on the horizon of materials science [1–5]. Because of its planar structure, graphene can be wrapped up into zero-dimensional spherical fullerenes with the introduction of pentagons, rolled along a given direction into one-dimensional carbon nanotubes (CNTs), or staked into three-dimensional graphite [6]. Therefore, graphene is recognized as the basic building block of all-dimensional carbon materials. It has an ultrahigh theoretical surface area of 2630 $m^2\ g^{-1}$, a mobility of 200 000 $cm^2\ V^{-1}\ s^{-1}$ at a carrier density of ~1012 cm^{-2}, and the highest electrical conductivity at room temperature (106 S cm^{-1}) [7–9]. The strong mechanical properties of graphene with Young's modulus of ~1 TPa, breaking strength of 42 N m^{-1}, and excellent thermal conductivity (3000–5000 W $m^{-1}\ K^{-1}$) are also favorable for various applications [10, 11]. The measured white-light absorbance of suspended single-layer graphene is 2.3% with a negligible reflectance (<0.1%), indicating excellent optical transparency [12]. On account of these unique properties, graphene has been utilized in diverse areas such as nanoelectronics and optoelectronics [13–17], energy storage [18, 19], supercapacitors [20–22], biosensors [23–28], catalysis [29–32], and drug delivery [33].

Since the discovery of the photocatalytic splitting of water on TiO_2 electrodes by Fujishima and Honda [34] in 1972, photocatalysis has attracted intense attention during the past decades because of its potential for environmental purification and energy applications. This green technology is based on the unique electronic structure of semiconductors, which consist of a filled valence band (VB) and an empty conduction band (CB). When the semiconductor absorbs a photon with energy equal to or higher than the band gap energy (E_g), electrons will be excited from the VB to the CB, leaving positive holes in the VB. The photogenerated holes and electrons after separation will move to the photocatalysts surface, triggering the chemical oxidation or reduction process by separated holes or electrons, respectively [35–38]. The whole process is regarded as an energy conversion process of solar

Graphene-based Energy Devices, First Edition. Edited by A. Rashid bin Mohd Yusoff.
© 2015 Wiley-VCH Verlag GmbH & Co. KGaA. Published 2015 by Wiley-VCH Verlag GmbH & Co. KGaA.

energy to chemical energy, which can be used to drive various chemical reactions to achieve diverse applications, including photocatalytic hydrogen (H_2) evolution, CO_2 reduction, and pollutant degradation. Therefore, the search for various semiconductors as photocatalysts has been an intensively pursued topic in the past decades. To date, hundreds of photocatalysts have been developed, typically TiO_2, ZnO, CdS, Bi_2WO_4 $Pb_2Sn_2O_6$, and $NaTaO_3$ [39–46]. However, the practical applications of this technique are still limited by the ineffective utilization of the whole solar spectrum, insufficient quantum efficiency, or the possible photocorrosion of the photocatalysts [47]. A variety of strategies have been developed to improve the semiconductor photocatalytic performances, such as adding electron–hole donors [48–50], noble metal loading [51], metal/nonmetal ion doping [52–55], dye sensitization [56, 57], and composite photocatalysts [58–62].

The discovery of graphene has provided an alternative strategy to modify semiconductor photocatalysts. Because of its unique atom-thick 2D structure, excellent transparency, high specific surface area, locally conjugated aromatic system, superior electron mobility, and high chemical and electrochemical stability, graphene is an ideal candidate for photocatalyst carriers or promoters. For example, Kamat and coworkers [63, 64] synthesized graphene oxide (GO)/TiO_2 nanocrystalline composites by sonicating TiO_2 nanoparticles and GO in ethanol and demonstrated the feasibility of using graphene as an electron-transfer medium in the graphene/TiO_2 composite photocatalysts. This pioneering work has stimulated extensive research on the preparation, modification, and application of graphene-based semiconductor photocatalysts. There are a number of excellent reviews written on the design and preparation of graphene-based photocatalysts from the chemist's point of view [65–67]. There is no doubt that the discovery of graphene will bring about enormous opportunities in solar energy conversion by photocatalysis.

This chapter is intended to give a systematic, updated summary of the current status of graphene-based nanocomposites applied in photocatalysis for energy applications, including photocatalytic H_2 evolution, CO_2 reduction, and photocatalytic pollutant degradation. The contents are organized into two major sections. The first is a brief review on several important preparation strategies for graphene-based photocatalysts, to benefit synthetic chemists who are interested in this emerging field of novel functional materials. The second section is about the energy applications of graphene-based photocatalysts, which are divided into the above-mentioned three parts. Finally, we conclude with some critical issues in this emerging field awaiting further explorations. We also hope that this chapter can serve as a tutorial review to benefit materials scientists exploring applications of graphene-based photocatalysts.

9.1.1 Synthesis of Graphene-Based Photocatalysts

Graphene has been introduced into a variety of semiconductors to construct graphene-based photocatalysts. These photocatalysts mainly include metal

oxides (TiO_2, ZnO, WO_3, SnO_2, Cu_2O, Fe_2O_3, NiO, MnO_2, ZrO_2, etc.), sulfides (ZnS, CuS, SnS_2, CdS, etc.), oxy-acid salts (Bi_2WO_6, $BiVO_4$, $Sr_2Ta_2O_7$, $ZnFe_2O_4$, $LaMnO_3$, $InNbO_4$, and Bi_2MoO_6, etc.), silver/silver halides (Ag/AgCl and Ag/AgBr), and metal-free photocatalysts (g-C_3N_4 and α-S_8). The synthetic methods can be classified into two major categories: the *ex situ* hybridization strategy and the *in situ* growth strategy.

9.1.2 *Ex Situ* Hybridization Strategy

This strategy refers to the physical mixing of graphene nanosheets and presynthesized or commercially available nanocrystals in solutions. To achieve an intimate interaction between graphene and nanocrystals, the nanocarystals or the graphene nanosheets are often premodified to be enriched with functional groups. For example, benzyl mercaptan (BM)-capped CdS quantum dots of 3 nm size were presynthesized and then attached effectively on reduced graphene oxide (RGO) [68]. In this process, the benzene rings not only anchored to CdS but also interacted with RGO via π−π stacking, acting as interlinkers between RGO and the CdS dots. Similarly, GO/RGO sheets can also be premodified with adhesive polymers for anchoring the nanoparticles. Liu *et al.* [69] has employed amphiphilic biopolymers, such as bovine serum albumin (BSA) protein, to modify the RGO surface via the π−π interaction. This functionalized RGO can be used as a universal adhesive layer to absorb various kinds of metal nanoparticles including Au, Ag, Pt, and Pd.

9.1.3 *In Situ* Growth Strategy

The *ex situ* hybridization strategy often results in nonuniformity, particle aggregation, and weak interaction between GO/RGO and photocatalysts. This will significantly limit the charge transportation between graphene and photocatalysts, resulting in poor activity. Therefore, *in situ* growth is the most popular synthetic strategy to fabricate graphene-based photocatalysts. It can not only produce uniform surface coverage of nanocrystals by controlling the nucleation sites on GO/RGO but also facilitate the anchoring of nanocrystals on graphene, thus achieving intimate interaction between photocatalysts and graphene.

9.1.3.1 Hydrothermal Method

Hydrothermal synthesis is a powerful and versatile tool for the synthesis of inorganic nanocrystals. It is particularly important for the synthesis of graphene/photocatalyst composites, because GO can be *in situ* reduced to RGO under hydrothermal conditions. Combining with the precursors of photocatalysts, one-pot reaction for the fabrication of graphene/photocatalysts composite could be achieved simply by using GO as the graphene source. The photocatalyst nanocrystals are *in situ* grown on RGO that is produced as a result of GO deoxygenation simultaneously during the hydrothermal synthesis.

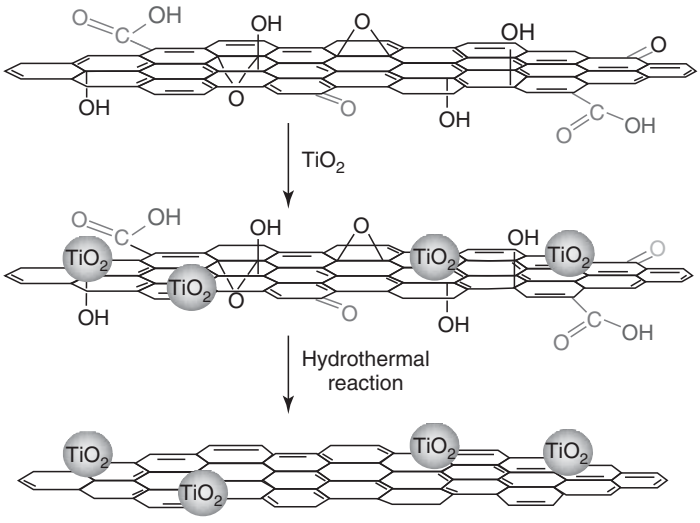

Figure 9.1 Graphical illustration for the synthesis of TiO_2/RGO nanocomposite by a hydrothermal method. (Reprinted with permission from Ref. [70]. Copyright (2013), Elsevier Ltd.)

Typically, the RGO/TiO_2 (P25) composite has been synthesized in one step simply by using GO and TiO_2 as the stating materials [70]. GO was obtained from natural graphite powder by using the modified Hummers method [71]. RGO/TiO_2 can be synthesized under hydrothermal condition at 150 °C for 5 h, without adding any surfactants or templates. As shown in Figure 9.1, the one-step formation process of the suspendable TiO_2/RGO nanocomposites is based on the initial formation of the strongly coupled TiO_2/GO nanocomposite and the subsequent *in situ* reduction of GO to RGO during the hydrothermal treatment. The hydrothermally formed supercritical water with unique properties, such as strong electrolytic solvent power, high diffusion coefficient, and ion molecules, can exhibit strong reducing power during the hydrothermal reaction, resulting in the cleavage reactions of various heterolytic bonds [72] and finally leading to the deoxygenation of GO and *in situ* anchoring of TiO_2 particles on RGO.

Single-layer RGO/CdS quantum dot nanocomposites were synthesized by this one-step method from GO and $Cd(CH_3COO)_2$ in dimethylsulfoxide (DMSO), thus avoiding the low-yield production and the aggregation of single-layer graphene sheets [73]. DMSO acted as both the solvent and the sulfur source. Our group has also synthesized WO_3 nanorods/graphene composites by using GO and Na_2WO_4 as the starting materials [74]. Uniform WO_3 nanorods/grapheme composites were thus prepared. The existence of graphene in the composites facilitated the electron transfer, light absorption, and electrical conductivity. As a result, the visible-light photocatalytic performance and the gas sensing property of WO_3 nanorods were improved by up to 2.2 and 25 times, respectively.

Besides using pure water as the solvent, we also developed a cysteine-assisted hydrothermal method to fabricate In_2S_3 nanosheets/graphene composites [75].

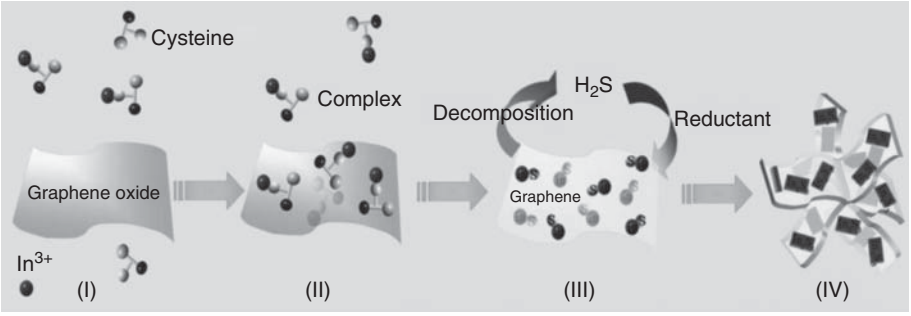

Figure 9.2 Schematic diagram of the synthetic route for In_2S_3 nanosheets/grapheme composites. (Reprinted with permission from Ref. [75]. Copyright (2013), Elsevier Ltd.)

As shown in Figure 9.2, cysteine acts as a sulfide source and a grafting molecule, facilitating the *in situ* incorporation of In_2S_3 nanosheets with GO supports. During the hydrothermal process, the breaking of S–C bonds results in the formation of In_2S_3 nuclei and the release of H_2S [76]. The reduction of GO to RGO is therefore accelerated because of the additional reducing ability of H_2S. This leads to the intimate connection between RGO and In_2S_3 nanosheets [77]. The partial overlap or coalescence of RGO sheets would also result in the formation of a 3D cross-linked architecture. These studies indicate that the *in situ* hydrothermal method is effective in synthesizing photocatalyst/graphene composites in a simple way that may be amenable for commercial production.

9.1.3.2 Electrochemical and Electrophoretic Deposition

Electrochemical and electrophoretic deposition are other popular ways to prepare graphene nanocomposites. They are particularly attractive approaches for thin-film-based materials synthesis without the requirement for postsynthetic transfer of the composite materials. For example, nanostructures of ZnO [78], Cu_2O [79], MnO_2 [80], and ZrO_2 [81] have been successfully deposited on RGO films. Generally, a constant current is first applied to seed nanoparticles (such as ZnO) on RGO, followed by the growth of nanoparticles under the constant potential mode. During this synthetic process, the conductivity of RGO plays an important role in determining the sample morphology. High-quality hexagonal ZnO nanorods can grow only when the RGO has a high conductivity [78]. Moreover, ordered nanostructures can also be prepared by using a porous, hard template such as a mesoporous silica film [82]. The CdSe nanocrystals were electrochemically deposited on the graphene surface through the pores of the precoated silica film. Consequently, an ordered CdSe/graphene film was produced after removing the silica templates by HF etching.

9.1.3.3 Chemical Vapor Deposition

Chemical vapor deposition (CVD) is another useful method to uniformly grow semiconductor metal oxides on graphene substrates. Kim *et al.* [83] has grown ZnO nanoneedles on graphene using vapor-phase epitaxy. They found that the

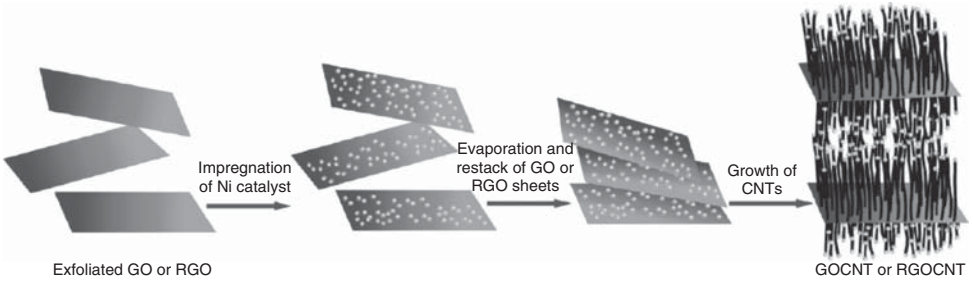

Figure 9.3 Experimental steps of pillaring GO and RGO platelets with CNTs. (Reprinted with permission from Ref. [85]. Copyright (2010), American Chemical Society.)

enhanced ZnO nanoneedle nucleation at step edges and kinks on graphene surfaces could result in higher vertical alignments than those grown on SiO_2/Si. In another study, ZnO nanorod/graphene heterogeneous nanostructures were fabricated by tuning the CVD growth temperature, with denser nanorod arrays at the ripple boundary of graphene [84].

Besides metal oxide, also chemically exfoliated RGO was pillared with CNTs by *Zhang et al.* [85] by utilizing the CVD method. As shown in Figure 9.3, a nickel nitrate solution was added to chemically exfoliated GO or RGO platelets in water. Upon drying at 60 °C, Ni-containing GO or RGO platelets were obtained, which were subsequently used as the catalyst to grow CNTs using the CVD method with acetonitrile as the carbon source. This composite material with RGO layers pillared by CNTs formed a robust three-dimensional (3D) porous structure of specific surface area as high as 352 $m^2\ g^{-1}$. The growth of one-dimensional (1D) CNTs can be controlled by varying the catalyst loading and the CVD time. The CNT-pillared RGO composite materials exhibited an excellent visible-light-driven photocatalytic performance in the degradation of rhodamine B. The high adsorption ability, efficient photosensitized electron injection, and retarded electron–radical recombination make the composite material an excellent photocatalyst. This work also shows the possibility of CNT/RGO composites as a new family of metal-free photocatalysts.

9.1.3.4 **Photochemical Reaction**

The photochemical reaction is another important method to synthesize photocatalyst/graphene composites. It has been reported that GO could be reduced to RGO simply by light irradiation of a GO solution. The complete reduction of GO to RGO can be achieved within 80 min in a sealed reactor when irradiated with a Xe lamp [86, 87]. Therefore, when combined with photocatalysts, the GO can be *in situ* reduced and coated on photocatalysts, as the photogenerated electrons can even accelerate this reduction process. For example, TiO_2/graphene nanocomposites were prepared by mixing GO and TiO_2 nanoparticles in ethanol by UV-induced photochemical reactions [64]. In addition, WO_3/RGO and $BiVO_4$/RGO were also prepared by the same methods under visible light irradiation [88].

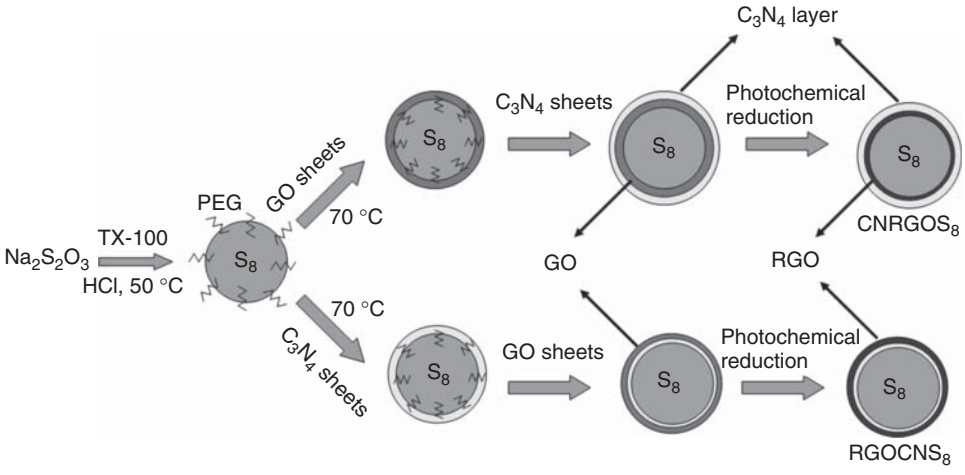

Figure 9.4 Schematic illustration of the two different synthetic pathways for the preparation of α-sulfur co-wrapped with graphene and C_3N_4 sheets by photochemical reaction. (Reprinted with permission from Ref. [89]. Copyright (2013), American Chemical Society.)

The photochemical reduction is also applicable to construct graphene-wrapped core–shell structures. Our group has prepared RGO and g-C_3N_4 (CN) nanosheets co-wrapped α-S_8 as a new family of metal-free photocatalysts [89]. Two distinctive structures were fabricated by wrapping RGO and CN sheets in different orders. As shown in Figure 9.4, sulfur particles were first wrapped by a layer of GO sheets and then wrapped by CN sheets, while, the other way, sulfur particles were first wrapped by CN sheets followed by GO sheets. In this process, Triton X-100 (a surfactant with a poly(ethylene glycol) (PEG) chain) was used as a capping agent for sulfur particles to introduce hydrophilic groups onto the surface and to limit the size of sulfur particles to the submicrometer region. The GO sheets were finally reduced to RGO sheets by the photochemical technique. It is known that it is difficult to wrap RGO directly on semiconductors because of the lack of functional groups. Therefore, this method is of particular importance to fabricate hierarchical RGO-wrapped structures, as GO can be readily *in situ* reduced to RGO at the final step of synthesis simply by light irradiation.

9.2 Energy Applications

9.2.1 Photocatalytic Hydrogen Evolution

Hydrogen (H_2) is regarded as an excellent source of clean energy. Among various processes, H_2 evolution from photocatalytic water splitting is promising because it utilizes solar energy, while traditional methods such as electrolysis and steam

reforming rely heavily on fossil fuels. In the water-splitting process, electrons in the CB reduce water molecules to form H_2 while holes in the VB reduce water molecules to form O_2. In the past decades, researches have been focused on the fabrication of advanced materials to deal with the limitations of typical photocatalysts such as TiO_2, which are mainly electron–hole recombination and light absorption limited to the UV region [90–93].

Because of its excellent electrical properties, graphene has been combined with photocatalysts to improve their conductivity and hence activity in H_2 evolution. For example, a composite photocatalyst of TiO_2 and graphene sheets (GSs) was prepared by the calcination of precursors at 450 °C [94]. The study found that the TiO_2/GS composite showed a highest rate of H_2 production at 5 wt% C/Ti ratio. To further improve the photocatalytic activity, GSs were premodified before combining with the TiO_2. Gao and Sun [95] have synthesized a sulfonated grapheme oxide (SG)/TiO_2 composite by ultrasonic mixing of SG sheets and TiO_2 spheres. Under neutral pH (pH 7), the SG/TiO_2-2 composite with the optimal amount of 2% SG achieved the highest hydrogen evolution rate (~260 μmol h^{-1}), which is more than 11 times higher than that of pure TiO_2 and P25. They also found that SG/TiO_2 composites exhibited high hydrogen production efficiency over a wide pH range (from pH 3 to 11), as shown in Figure 9.5. In contrast, the activity of GO/TiO_2 decreased rapidly under alkaline conditions. The tight coordination between the SG sheets and TiO_2 spheres could prevent the damage of SG/TiO_2 composites in alkaline solutions. This feature of SG/TiO_2 is important for practical application, because photocatalysts are required to be active under different pH conditions.

Besides TiO_2-based photocatalysts, graphene has also been used to improve the activity of metal sulfide. CdS is a widely studied semiconductor photocatalyst because of its narrow bandgap (2.4 eV). However, the use of CdS has been limited by its poor photostability [97]. Upon irradiation of light, CdS will be oxidized by

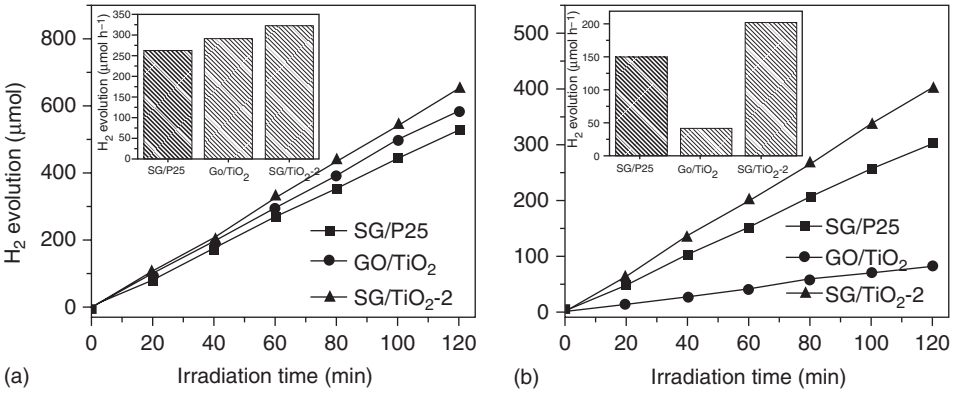

Figure 9.5 Hydrogen production activity of SG/TiO_2-2, GO/TiO_2 (2 wt% of GO), and SG/P25 (2 wt% of SG) under pH 3 (a) and pH 11 (b) (inset: average hydrogen evolution rate). (Reprinted with permission from Ref. [95]. Copyright (2014), Elsevier Ltd.)

photogenerated holes to release the toxic Cd^{2+}. Jia *et al.* [98] fabricated a series of N-doped graphene/CdS nanocomposites for water splitting. N-doped graphene acted as a charge collector to promote the separation and transfer of the photogenerated charge carriers. Comparative studies showed that the order of activity is N-doped graphene/CdS > graphene/CdS > GO/CdS > CdS. The photostability of N-doped graphene/CdS was also found to be better than that of the traditional Pt/CdS systems.

In another study, Tang *et al.* synthesized a composite of CuInZnS and graphene using a hydrothermal method [99]. With an optimal graphene content of 2%, the rate of H_2 production reached 3.8 mmol $h^{-1}g^{-1}$ under visible light, which was higher than that of pure CuInZnS by 1.84 times. The enhancement was attributed to the suppression of charge recombination and improved interfacial charge transfer.

GO alone was reported as an environmentally friendly photocatalyst for H_2 evolution [100]. Because of the highly hydrophilic nature of GO, a cocatalyst is not required. The study also showed that the activity of GO was related to its oxidation level.

9.2.2
Photocatalytic Reduction of Carbon dioxide

Semiconductor-mediated photocatalytic reduction of carbon dioxide (CO_2) to fuels is promising because it can be a solution to both global warming and energy shortage problems. However, this process has been limited by low conversion rates, making it far from ideal for practical applications. As a promising material in different aspects of photocatalysis, graphene has also been studied for its application in the conversion of CO_2 [101, 102].

Liang *et al.* [103] prepared graphene nanoplatelets with different defect densities by two major solution-based pathways, namely oxidation–reduction and solvent exfoliation. The as-prepared graphene nanoplatelets were combined with P25 (TiO_2) to form nanocomposites for the photoreduction of CO_2. The study revealed that less defective graphene exhibited a significantly larger enhancement in photocatalytic activity of P25, especially under visible light. A later study by Tan *et al.* [104] also showed that RGO-modified anatase TiO_2 has a higher activity then pure anatase, producing methane with a rate of 0.135 μmol g^{-1} h^{-1} under visible light.

Robust hollow spheres consisting of molecular-scale alternating $Ti_{0.91}O_2$ nanosheets and graphene nanosheets were fabricated by a layer-by-layer assembly technique [96]. The 2D $Ti_{0.91}O_2$ nanosheets and graphene nanosheets were contacted in molecular scale to assemble hollow sphere morphology. The photocatalytic CO_2 conversion in the presence of water vapor was investigated. It was found that CO was the major product and a relatively small amount of CH_4 was obtained on the graphene/$Ti_{0.91}O_2$ hollow spheres with rates of 8.91 and 1.14 μmol g^{-1} h^{-1}, respectively (Figure 9.6). The total conversion yield of CO_2 by graphene/$Ti_{0.91}O_2$ hollow spheres was five times higher than by $Ti_{0.91}O_2$ hollow

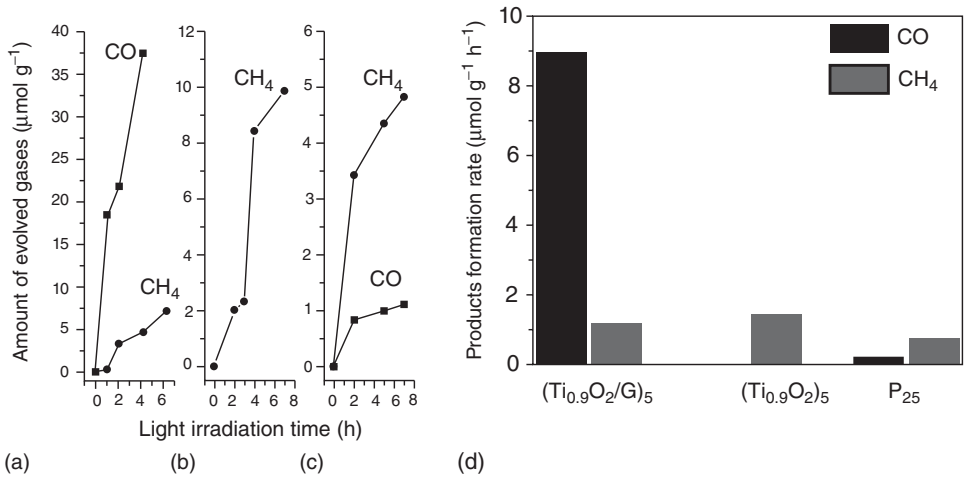

Figure 9.6 Photocatalytic CH_4 and CO evolution amounts for (a) G/$(Ti_{0.91}O_2)_5$ spheres, (b) $(Ti_{0.91}O_2)_5$ spheres, and (c) P25. (d) Comparison of the average product formation rates. (Reprinted with permission from Ref. [96]. Copyright (2012), Wiley-VCH.)

spheres, indicating that graphene was effective in improving the photocatalytic activity of $Ti_{0.91}O_2$. The enhancement was mainly attributed to the compact stacking of ultrathin $Ti_{0.91}O_2$ nanosheets with graphene nanosheets, allowing the fast transfer of electrons from $Ti_{0.91}O_2$ to graphene, thus enhancing the lifetime of the charge carriers.

The photocatalytic conversion of CO_2 to methanol simply by GO has also been reported [105]. GO samples were prepared using a modified Hummer's method. The conversion rate was 0.172 μmol g^{-1} h^{-1} under visible light, which is sixfold higher than that of the pure TiO_2. Isotope tracer analyses with $^{13}CO_2$ was performed to confirm that methanol originated from CO_2 and not from the photodecomposition of GO. X-ray photoelectron spectroscopy (XPS) studies also showed that the majority of the oxygenated functional groups remained chemically stable after the photocatalytic reaction.

9.2.3
Environmental Remediation

Nanostructured photocatalysts for the degradation of various water contaminants have been extensively studied. Photoexcited electrons and holes at the surface of a photocatalyst are able to react with other species adsorbed on the surface. For example, electrons can react with O_2 and H_2O to give $\bullet O_2^-$ and $\bullet HO_2$, while the holes can react with H_2O or OH^- to give •OH [106]. These highly reactive species are able to attack molecules around the surface of the photocatalyst, resulting in the degradation of the molecules. Here, we give some examples of highly efficient graphene-based composite photocatalysts for the degradation of water contaminants.

9.2.3.1 Photodegradation of Organic Dyes

Graphene was combined with P25 to give a high-performance photocatalyst under both UV and visible light [107]. The composite showed higher activity in the photodegradation of methylene blue than both pure P25 and a P25/carbon nanotube composite. Addition of graphene resulted in enhanced adsorption, extended light absorption range, and efficient charge separation.

Our group has reported a hydrothermal approach to synthesize visible-light-driven In_2S_3 nanosheets/graphene composites [75]. In the degradation of methyl orange, a highly stable azo dye, the composite with 1% graphene had an apparent rate more than five times higher than that of pure In_2S_3. The enhanced photocatalytic activity can be attributed to the perfect interfacial contact between the two components and the efficient charge separation. In another study, we synthesized WO_3 nanorods/graphene for high-efficiency visible-light-driven photocatalysis [74]. It was found that the existence of graphene in the composites facilitated electron transfer, light absorption, and electrical conductivity. As a result, the visible light photocatalytic degradation of rhodamine B 6G and the gas sensing property of WO_3 nanorods were improved by up to 2.2 and 25 times, respectively.

9.2.3.2 Water Disinfection

Traditional water disinfection photocatalysts are mainly Ag-based materials, which inevitably causes potential Ag^+ contamination. In this context, graphene wrapping was particularly important to protect the photocatalysts from photocorrosion. Sun's group has demonstrated the preparation of various composite photocatalysts, including GO/CdS [108], GO/TiO_2/Ag [109], and sulfonated GO/ZnO/Ag [110]. Under visible light, both composites showed enhanced efficiency and photostability in the inactivation of *Escherichia coli* when compared to their counterparts without adding GO. Metal-free photocatalyst is another solution to avoid metallic secondary contamination, as no metal ions exist in the photocatalyst. For example, our group has constructed a graphene and g-C_3N_4 co-wrapped sulfur particle as a metal-free photocatalysts for water disinfection under visible light [90].

Bi-based photocatalysts are also widely used to combine with graphene for water disinfection. It was shown that the Bi_2MoO_6/RGO nanocomposite had a significantly higher efficiency in the inactivation of *E. coli* K-12 than pure Bi_2MoO_6 [111]. The study also suggested that RGO exhibited certain toxic effects on *E. coli* K-12, but not as strong as the photocatalytic antibacterial effect. The improvement was attributed to the growth of highly ordered Bi_2MoO_6 on graphene and the electron accepting ability of graphene.

9.3 Conclusions and Outlook

Graphene-based photocatalysts hold great potential for being used as robust materials to address energy issues. In this chapter, the current status of the

synthesis and energy applications of graphene-based photocatalysts was summarized. The introduction of graphene into various semiconductor photocatalysts can effectively improve the photocatalytic performance, owing to the extended light absorption range, high adsorption capacity, specific surface area, and superior electron conductivity of graphene. In spite of the remarkably rapid progress, some challenges still exist. For example, the interfacial contact between the semiconductor and graphene needs to be strengthened to fully exploit the special properties of graphene. Most of the synthetic routes for graphene-based photocatalysts are still through "hard" integration on the surface of graphene nanosheets, which is unfavorable to utilize the advantage of the 2D structure of graphene [112]. Therefore, the development of more efficient synthesis methods for integrating graphene and photocatalysts at the molecular or even atomic level are highly anticipated. To increase the interfacial connection, some interfacial mediators, possibly transition-metal ions or metal nanoparticles, may be developed to optimize the charge transfer at the interface of graphene-based photocatalysts.

Most of the reported graphene-based photocatalysts are focused on binary components, in which graphene is only coupled with one single photocatalyst. The development of ternary or multicomponent graphene-based hybrid nanostructures may provide new insight into constructing novel 3D nanoarchitectures with enhanced photocatalytic activities. This area is pioneered by Hayashi and coworkers, who have observed a remarkably high photocurrent generation in a ternary composite of porphyrin, ZnO nanoparticles, and RGO as a hierarchical electron transfer cascade system [113]. In this regard, more efforts should be devoted to constructing multicomponent graphene-based photocatalysts. Finally, the energy applications of graphene-based photocatalysts are still at infancy. Further development in this field would require multidisciplinary efforts from chemistry, physics, and materials science.

References

1. Geim, A.K. (2009) Graphene: status and prospects. *Science*, **324**, 530–1534.
2. Allen, M.J., Tung, V.C., and Kaner, R.B. (2009) Honeycomb carbon: a review of graphene. *Chem. Rev.*, **110**, 132–145.
3. Rao, C.N.R., Sood, A.K., Subrahmanyam, K.S. *et al.* (2009) Graphene: the new two-dimensional nanomaterial. *Angew. Chem. Int. Ed.*, **48**, 7752–7777.
4. Chang, H.X. and Wu, H.K. (2013) Graphene-based nanomaterials: synthesis, properties, and optical and optoelectronic applications. *Adv. Funct. Mater.*, **23**, 1984–1997.
5. Yang, K., Feng, L., Shi, X. *et al.* (2013) Nano-graphene in biomedicine: theranostic applications. *Chem. Soc. Rev.*, **42**, 530–547.
6. Geim, A.K. and Novoselov, K.S. (2007) The rise of graphene. *Nat. Mater.*, **6**, 183–191.
7. Zhu, Y., Murali, S., Cai, W. *et al.* (2010) Graphene and graphene oxide: synthesis, properties, and applications. *Adv. Mater.*, **22**, 3906–3924.
8. Du, X., Skachko, I., Barker, A. *et al.* (2008) Approaching ballistic transport in suspended graphene. *Nat. Nanotechnol.*, **3**, 491–495.
9. Huang, X., Yin, Z.Y., Wu, S.X. *et al.* (2011) Graphene-based materials: synthesis, characterization, properties, and applications. *Small*, **7**, 1876–1902.

10. Lee, C., Wei, X.D., Kysar, J.W. *et al.* (2008) Measurement of the elastic properties and intrinsic strength of monolayer graphene. *Science*, **321**, 385–388.
11. Balandin, A.A., Ghosh, S., Bao, W. *et al.* (2008) Superior thermal conductivity of single-layer graphene. *Nano Lett.*, **8**, 902–907.
12. Nair, R.R., Blake, P., Grigorenko, A.N. *et al.* (2008) Fine structure constant defines visual transparency of graphene. *Science*, **320**, 1308–1308.
13. Wang, Q.H., Kalantar-Zadeh, K., Kis, A. *et al.* (2012) Electronics and optoelectronics of two-dimensional transition metal dichalcogenides. *Nat. Nanotechnol.*, **7**, 699–712.
14. Osada, M. and Sasaki, T. (2012) Two-dimensional dielectric nanosheets: novel nanoelectronics from nanocrystal building blocks. *Adv. Mater.*, **24**, 210–228.
15. Hirsch, A., Englert, J.M., and Hauke, F. (2013) Wet chemical functionalization of graphene. *Acc. Chem. Res.*, **46**, 87–96.
16. Dubois, S.M.M., Zanolli, Z., Declerck, X. *et al.* (2009) Electronic properties and quantum transport in graphene-based nanostructures. *Eur. Phys. J. B*, **72**, 1–24.
17. Dragoman, M. and Dragoman, D. (2009) Graphene-based quantum electronics. *Prog. Quantum Electron.*, **33**, 165–214.
18. Sun, Y.Q., Wu, Q., and Shi, G.Q. (2011) Graphene based new energy materials. *Energy Environ. Sci.*, **4**, 1113–1132.
19. Cao, X.H., Shi, Y.M., Shi, W.H. *et al.* (2011) Preparation of novel 3D graphene networks for supercapacitor applications. *Small*, **7**, 3163–3168.
20. Huang, Y., Liang, J.J., and Chen, Y.S. (2012) An overview of the applications of graphene-based materials in supercapacitors. *Small*, **8**, 1805–1834.
21. Jiang, H., Lee, P.S., and Li, C.Z. (2013) 3D carbon based nanostructures for advanced supercapacitors. *Energy Environ. Sci.*, **6**, 41–53.
22. Dong, L., Chen, Z.X., Yang, D. *et al.* (2013) Hierarchically structured graphene-based supercapacitor electrodes. *RSC Adv.*, **3**, 21183–21191.
23. Wang, Z.J., Zhou, X.Z., Zhang, J. *et al.* (2009) Direct electrochemical reduction of single-Layer graphene oxide and subsequent functionalization with glucose oxidase. *J. Phys. Chem. C*, **113**, 14071–14075.
24. He, Q.Y., Sudibya, H.G., Yin, Z.Y. *et al.* (2010) Centimeter-long and large-scale micropatterns of reduced graphene oxide films: fabrication and sensing applications. *ACS Nano*, **4**, 3201–3208.
25. Pumera, M. (2011) Graphene in biosensing. *Mater. Today*, **14**, 308–315.
26. He, Q.Y., Wu, S.X., Gao, S. *et al.* (2011) Transparent, flexible, all-reduced graphene oxide thin film transistors. *ACS Nano*, **5**, 5038–5044.
27. Wang, Z.J., Zhang, J., Chen, P. *et al.* (2011) Staphylococcus aureus DNA with reduced graphene oxide-modified electrodes. *Biosens. Bioelectron.*, **26**, 3881–3886.
28. Cao, X.H., He, Q.Y., Shi, W.H. *et al.* (2011) Graphene oxide as a carbon source for controlled growth of carbon nanowires. *Small*, **7**, 1199–1202.
29. Lightcap, I.V. and Kamat, P.V. (2013) Graphitic design: prospects of graphene-based nanocomposites for solar energy conversion, storage, and sensing. *Acc. Chem. Res.*, **46**, 2235–2243.
30. Zhu, J., Holmen, A., and Chen, D. (2013) Carbon nanomaterials in catalysis: proton affinity, chemical and electronic properties, and their catalytic consequences. *ChemCatChem*, **5**, 378–401.
31. Machado, B.F. and Serp, P. (2012) Graphene-based materials for catalysis. *Catal. Sci. Technol.*, **2**, 54–75.
32. Wu, S.X., He, Q.Y., Zhou, C.M. *et al.* (2012) Synthesis of Fe_3O_4 and Pt nanoparticles on reduced graphene oxide and their use as a recyclable catalyst. *Nanoscale*, **4**, 2478–2483.
33. Zhang, Y., Nayak, T.R., Hong, H. *et al.* (2012) Graphene: a versatile nanoplatform for biomedical applications. *Nanoscale*, **4**, 3833–3842.
34. Fujishima, A. and Honda, K. (1972) Electrochemical photolysis of water at a

semiconductor electrode. *Nature*, **238**, 37–38.

35. Kudo, A. and Miseki, Y. (2009) Heterogeneous photocatalyst materials for water splitting. *Chem. Soc. Rev.*, **38**, 253–278.
36. Chen, X.B., Shen, S.H., Guo, L.J. *et al.* (2010) Semiconductor-based photocatalytic hydrogen generation. *Chem. Rev.*, **110**, 6503–6570.
37. Wheeler, D.A., Wang, G.M., Ling, Y.C. *et al.* (2012) Nanostructured hematite: synthesis, characterization, charge carrier dynamics, and photoelectrochemical properties. *Energy Environ. Sci.*, **5**, 6682–6702.
38. Hoffmann, M.R., Martin, S.T., Choi, W. *et al.* (1995) Environmental applications of semiconductor photocatalysis. *Chem. Rev.*, **95**, 69–96.
39. Asahi, R., Morikawa, T., Ohwaki, T. *et al.* (2001) Visible-light photocatalysis in nitrogen-doped titanium oxides. *Science*, **293**, 269–271.
40. Yu, S., Yun, H.J., Kim, Y.H. *et al.* (2014) Carbon-doped TiO_2 nanoparticles wrapped with nanographene as a high performance photocatalyst for phenol degradation under visible light irradiation. *Appl. Catal., B*, **144**, 893–899.
41. Wang, W.J., Zhang, L.S., An, T.C. *et al.* (2011) Comparative study of visible-light-driven photocatalytic mechanisms of dye decolorization and bacterial disinfection by B–Ni-codoped TiO_2 microspheres: the role of different reactive species. *Appl. Catal., B*, **108-109**, 108–116.
42. Chen, D.M., Wang, K.W., Xiang, D.G. *et al.* (2014) Significantly enhancement of photocatalytic performances via core–shell structure of ZnO@mpg-C_3N_4. *Appl. Catal., B*, **147**, 554–561.
43. Long, L.Z., Yu, X., Wu, L.P. *et al.* (2014) Nano-CdS confined within titanate nanotubes for efficient photocatalytic hydrogen production under visible light illumination. *Nanotechnology*, **25**, 035603.
44. Zhang, Y.H. and Xu, Y.J. (2014) Bi_2WO_6: a highly chemoselective visible light photocatalyst toward aerobic oxidation of benzylic alcohols in water. *RSC Adv.*, **4**, 2904–2910.
45. Wang, W.J., Bi, J.H., Wu, L. *et al.* (2008) Hydrothermal synthesis and performance of a novel nanocrystalline $Pb_2Sn_2O_6$ photocatalyst. *Nanotechnology*, **19**, 505705.
46. Liu, D.R., Wei, C.D., Xue, B. *et al.* (2010) Synthesis and photocatalytic activity of N-doped $NaTaO_3$ compounds calcined at low temperature. *J. Hazard. Mater.*, **182**, 50–54.
47. Zhang, N., Zhang, Y.H., and Xu, Y.J. (2012) Recent progress on graphene-based photocatalysts: current status and future perspectives. *Nanoscale*, **4**, 5792–5813.
48. Park, H. and Choi, W. (2003) Photoelectrochemical investigation on electron transfer mediating behaviors of polyoxometalate in UV-illuminated suspensions of TiO_2 and Pt/TiO_2. *J. Phys. Chem. B*, **107**, 3885–3890.
49. Li, Y.X., Lu, G.X., and Li, S.B. (2003) Photocatalytic production of hydrogen in single component and mixture systems of electron donors and monitoring adsorption of donors by in situ infrared spectroscopy. *Chemosphere*, **52**, 843–850.
50. Maeda, K., Higashi, M., Lu, D.L. *et al.* (2010) Efficient nonsacrificial water splitting through two-step photoexcitation by visible light using a modified oxynitride as a hydrogen evolution photocatalyst. *J. Am. Chem. Soc.*, **132**, 5858–5868.
51. Murdoch, M., Waterhouse, G.I.N., Nadeem, M.A. *et al.* (2011) The effect of gold loading and particle size on photocatalytic hydrogen production from ethanol over Au/TiO_2 nanoparticles. *Nat. Chem.*, **3**, 489–492.
52. Weber, A.S., Grady, A.M., and Koodali, R.T. (2012) Lanthanide modified semiconductor photocatalysts. *Catal. Sci. Technol.*, **2**, 683–693.
53. Gurunathan, K. (2004) Photocatalytic hydrogen production using transition metal ions-doped γ-Bi_2O_3 semiconductor particles. *Int. J. Hydrogen Energy*, **29**, 933–940.
54. Hou, Y.D., Wang, X.C., Wu, L. *et al.* (2008) N-Doped SiO_2/TiO_2 mesoporous nanoparticles with enhanced

photocatalytic activity under visible-light irradiation. *Chemosphere*, **72**, 414–421.

55. Liu, G., Niu, P., Sun, C.H. *et al.* (2010) Unique electronic structure induced high photoreactivity of sulfur-doped graphitic C_3N_4. *J. Am. Chem. Soc.*, **132**, 11642–11648.
56. Youngblood, W.J., Lee, S.H.A., Maeda, K. *et al.* (2009) Visible light water splitting using dye-sensitized oxide semiconductors. *Acc. Chem. Res.*, **42**, 1966–1973.
57. Kim, W., Tachikawa, T., Majima, T. *et al.* (2009) Photocatalysis of dye-sensitized TiO_2 nanoparticles with thin overcoat of Al_2O_3: enhanced activity for H_2 production and dechlorination of CCl_4. *J. Phys. Chem. C*, **113**, 10603–10609.
58. Chen, D., Zhang, H., Hu, S. *et al.* (2008) Preparation and enhanced photoelectrochemical performance of coupled bicomponent $ZnO-TiO_2$ nanocomposites. *J. Phys. Chem. C*, **112**, 117–122.
59. Chen, X.F., Wang, X.C., and Fu, X.Z. (2009) Hierarchical macro/mesoporous TiO_2/SiO_2 and TiO_2/ZrO_2 nanocomposites for environmental photocatalysis. *Energy Environ. Sci.*, **2**, 872–877.
60. Zhang, L.L., Zhang, H.C., Huang, H. *et al.* (2012) Ag_3PO_4/SnO_2 semiconductor nanocomposites with enhanced photocatalytic activity and stability. *New J. Chem.*, **36**, 1541–1544.
61. Yin, Z.Y., Wang, Z., Du, Y.P. *et al.* (2012) Full solution-processed synthesis of all metal oxide-based tree-like heterostructures on fluorine-doped tin oxide for water splitting. *Adv. Mater.*, **24**, 5374–5378.
62. Zhou, W.J., Yin, Z.Y., Du, Y.P. *et al.* (2013) Synthesis of few-layer MoS_2 nanosheet-coated TiO_2 nanobelt heterostructures for enhanced photocatalytic activities. *Small*, **9**, 140–147.
63. Lightcap, I.V., Kosel, T.H., and Kamat, P.V. (2010) Anchoring semiconductor and metal nanoparticles on a two-dimensional catalyst mat. storing and shuttling electrons with reduced graphene oxide. *Nano Lett.*, **10**, 577–583.
64. Williams, G., Seger, B., and Kamat, P.V. (2008) TiO_2-graphene nanocomposites. UV-assisted photocatalytic reduction of graphene oxide. *ACS Nano*, **2**, 1487–1491.
65. An, X.Q. and Yu, J.C. (2011) Graphene-based photocatalytic composites. *RSC Adv.*, **1**, 1426–1434.
66. Xiang, Q.J., Yu, J.G., and Jaroniec, M. (2012) Graphene-based semiconductor photocatalysts. *Chem. Soc. Rev.*, **41**, 782–796.
67. Huang, X., Qi, X.Y., Boey, F. *et al.* (2012) Graphene-based composites. *Chem. Soc. Rev.*, **41**, 666–686.
68. Feng, M., Sun, R.Q., Zhan, H.B. *et al.* (2010) Lossless synthesis of graphene nanosheets decorated with tiny cadmium sulfide quantum dots with excellent nonlinear optical properties. *Nanotechnology*, **21**, 075601.
69. Liu, J., Fu, S., Yuan, B. *et al.* (2010) Toward a universal "adhesive nanosheet" for the assembly of multiple nanoparticles based on a protein-induced reduction/decoration of graphene oxide. *J. Am. Chem. Soc.*, **132**, 7279–7281.
70. Wang, P., Wang, J., Wang, X.F. *et al.* (2013) One-step synthesis of easy-recycling TiO_2-rGO nanocomposite photocatalysts with enhanced photocatalytic activity. *Appl. Catal., B*, **132–133**, 452–459.
71. Xu, Y., Bai, H., Lu, G. *et al.* (2008) Flexible graphene films via the filtration of water-soluble noncovalent functionalized graphene sheets. *J. Am. Chem. Soc.*, **130**, 5856–5857.
72. Zhou, Y., Bao, Q., Tang, L.A.L. *et al.* (2009) Hydrothermal dehydration for the "green" reduction of exfoliated graphene oxide to graphene and demonstration of tunable optical limiting properties. *Chem. Mater.*, **21**, 2950–2956.
73. Cao, A., Liu, Z., Chu, S. *et al.* (2010) A facile one-step method to produce graphene–CdS quantum dot nanocomposites as promising optoelectronic materials. *Adv. Mater.*, **22**, 103–106.
74. An, X.Q., Yu, J.C., Wang, Y. *et al.* (2012) WO_3 nanorods/graphene nanocomposites for high-efficiency

visible-light-driven photocatalysis and NO_2 gas sensing. *J. Mater. Chem.*, **22**, 8525–8531.

75. An, X.Q., Yu, J.C., Wang, F. *et al.* (2013) One-pot synthesis of In_2S_3 nanosheets/graphene composites with enhanced visible-light photocatalytic activity. *Appl. Catal., B*, **129**, 80–88.

76. Zhao, P., Huang, T., and Huang, K. (2007) Fabrication of indium sulfide hollow spheres and their conversion to indium oxide hollow spheres consisting of multipore nanoflakes. *J. Phys. Chem. C*, **111**, 12890–12897.

77. Chang, K. and Chen, W. (2011) l-Cysteine-assisted synthesis of layered MoS_2/Graphene composites with excellent electrochemical performances for lithium ion batteries. *ACS Nano*, **5**, 4720–4728.

78. Yin, Z., Wu, S., Zhou, X. *et al.* (2010) Electrochemical deposition of ZnO nanorods on transparent reduced graphene oxide electrodes for hybrid solar cells. *Small*, **6**, 307–312.

79. Wu, S., Yin, Z., He, Q. *et al.* (2010) Electrochemical deposition of semiconductor oxides on reduced graphene oxide-based flexible, transparent, and conductive electrodes. *J. Phys. Chem. C*, **114**, 11816–11821.

80. Yu, G.H., Hu, L.B., Vosgueritchian, M. *et al.* (2011) Solution-processed graphene/MnO_2 nanostructured textiles for high-performance electrochemical capacitors. *Nano Lett.*, **11**, 2905–2911.

81. Du, D., Liu, J., Zhang, X.Y. *et al.* (2011) One-step electrochemical deposition of a graphene-ZrO_2 nanocomposite: preparation, characterization and application for detection of organophosphorus agents. *J. Mater. Chem.*, **21**, 8032–8037.

82. Kim, Y.T., Han, J.H., Hong, B.H. *et al.* (2010) Electrochemical synthesis of CdSe quantum dot array on graphene basal plane using mesoporous silica thin film templates. *Adv. Mater.*, **22**, 515–518.

83. Kim, Y.J., Lee, J.H., and Yi, G.C. (2009) Vertically aligned ZnO nanostructures grown on graphene layers. *Appl. Phys. Lett.*, **95**, 213101.

84. Lin, J., Penchev, M., Wang, G. *et al.* (2010) Heterogeneous graphene nanostructures: ZnO nanostructures grown on large-area graphene layers. *Small*, **6**, 2448–2452.

85. Zhang, L.L., Xiong, Z.G., and Zhao, X.S. (2010) Pillaring chemically exfoliated graphene oxide with carbon nanotubes for photocatalytic degradation of dyes under visible light irradiation. *ACS Nano*, **4**, 7030–7036.

86. Li, X.H., Chen, J.S., Wang, X.C. *et al.* (2012) A green chemistry of graphene: photochemical reduction towards monolayer graphene sheets and the role of water adlayers. *ChemSusChem*, **5**, 642–646.

87. Li, X.H., Chen, J.S., Wang, X.C. *et al.* (2011) Metal-free activation of dioxygen by graphene/g-C_3N_4 nanocomposites: functional dyads for selective oxidation of saturated hydrocarbons. *J. Am. Chem. Soc.*, **133**, 8074–8077.

88. Ng, Y.H., Iwase, A., Bell, N.J. *et al.* (2011) Semiconductor/reduced graphene oxide nanocomposites derived from photocatalytic reactions. *Catal. Today*, **164**, 353–357.

89. Wang, W.J., Yu, J.C., Xia, D.H. *et al.* (2013) Graphene and g-C_3N_4 nanosheets cowrapped elemental α-Sulfur as a novel metal-free heterojunction photocatalyst for bacterial inactivation under visible-light. *Environ. Sci. Technol.*, **47**, 8724–8732.

90. Chen, X. and Mao, S.S. (2007) Titanium dioxide nanomaterials: synthesis, properties, modifications, and applications. *Chem. Rev.*, **107**, 2891–2959.

91. Xie, G.C., Zhang, K., Guo, B.D. *et al.* (2013) Graphene-based materials for hydrogen generation from light-driven water splitting. *Adv. Mater.*, **25**, 3820–3839.

92. Chang, H.X. and Wu, H.K. (2013) Graphene-based nanocomposites: preparation, functionalization, and energy and environmental applications. *Energy Environ. Sci.*, **6**, 3483–3507.

93. Chen, D., Zhang, H., Liu, Y. *et al.* (2013) Graphene and its derivatives for the development of solar cells, photoelectrochemical, and photocatalytic

applications. *Energy Environ. Sci.*, **6**, 1362–1387.

94. Zhang, X.Y., Li, H.P., Cui, X.L. *et al.* (2010) Graphene/TiO_2 nanocomposites: synthesis, characterization and application in hydrogen evolution from water photocatalytic splitting. *J. Mater. Chem.*, **20**, 2801–2806.

95. Gao, P. and Sun, D.D. (2014) Hierarchical sulfonated graphene oxide–TiO_2 composites for highly efficient hydrogen production with a wide pH range. *Appl. Catal., B*, **147**, 888–896.

96. Tu, W.G., Zhou, Y., Liu, Q. *et al.* (2012) Robust hollow spheres consisting of alternating titania nanosheets and graphene nanosheets with high photocatalytic activity for CO_2 conversion into renewable fuels. *Adv. Funct. Mater.*, **22**, 1215–1221.

97. Yu, J.C., Wu, L., Lin, J. *et al.* (2003) Microemulsion-mediated solvothermal synthesis of nanosized CdS-sensitized TiO_2 crystalline photocatalyst. *Chem. Commun.*, 1552–1553.

98. Jia, L., Wang, D., Huang, Y. *et al.* (2011) Highly durable N-doped graphene/CdS nanocomposites with enhanced photocatalytic hydrogen evolution from water under visible light irradiation. *J. Phys. Chem. C*, **115**, 11466–11473.

99. Tang, X., Tay, Q., Chen, Z. *et al.* (2013) CuInZnS-decorated graphene nanosheets for highly efficient visible-light-driven photocatalytic hydrogen production. *J. Mater. Chem. A*, **1**, 6359–6365.

100. Yeh, T., Syu, J., Cheng, C. *et al.* (2010) Graphite oxide as a photocatalyst for hydrogen production from water. *Adv. Funct. Mater.*, **20**, 2255–2262.

101. Tran, P.D., Wong, L.H., Barber, J. *et al.* (2012) Recent advances in hybrid photocatalysts for solar fuel production. *Energy Environ. Sci.*, **5**, 5902–5918.

102. Roy, S.C., Varghese, O.K., Paulose, M. *et al.* (2010) Toward solar fuels: photocatalytic conversion of carbon dioxide to hydrocarbons. *ACS Nano*, **4**, 1259–1278.

103. Liang, Y., Vijayan, B.K., Gray, K.A. *et al.* (2011) Minimizing graphene defects enhances titania nanocomposite-based photocatalytic reduction of CO_2 for improved solar fuel production. *Nano Lett.*, **11**, 2865–2870.

104. Tan, L., Ong, W., Chai, S. *et al.* (2013) Reduced graphene oxide-TiO_2 nanocomposite as a promising visible-light-active photocatalyst for the conversion of carbon dioxide. *Nanoscale Res. Lett.*, **8**, 465.

105. Hsu, H., Shown, I., Wei, H. *et al.* (2013) Graphene oxide as a promising photocatalyst for CO_2 to methanol conversion. *Nanoscale*, **5**, 262–268.

106. Hu, X., Li, G., and Yu, J.C. (2010) Design, fabrication, and modification of nanostructured semiconductor materials for environmental and energy applications. *Langmuir*, **26**, 3031–3039.

107. Zhang, H., Lv, X., Li, Y. *et al.* (2010) P25-graphene composite as a high performance photocatalyst. *ACS Nano*, **4**, 380–386.

108. Gao, P., Liu, J., Sun, D.D. *et al.* (2013) Graphene oxide–CdS composite with high photocatalytic degradation and disinfection activities under visible light irradiation. *J. Hazard. Mater.*, **250–251**, 412–420.

109. Liu, L., Bai, H., Liu, J. *et al.* (2013) Multifunctional graphene oxide-TiO_2-Ag nanocomposites for high performance water disinfection and decontamination. *J. Hazard. Mater.*, **261**, 214–223.

110. Gao, P., Ng, K., and Sun, D.D. (2013) Sulfonated graphene oxide–ZnO–Ag photocatalyst for fast photodegradation and disinfection under visible light. *J. Hazard. Mater.*, **262**, 826–835.

111. Zhang, Y., Zhu, Y., Yu, J. *et al.* (2013) Enhanced photocatalytic water disinfection properties of Bi_2MoO_6–RGO nanocomposites under visible light irradiation. *Nanoscale*, **5**, 6307–6310.

112. Zhang, Y., Tang, Z.R., Fu, X. *et al.* (2011) Engineering the unique 2D mat of graphene to achieve graphene-TiO_2 nanocomposite for photocatalytic selective transformation: what advantage

does graphene have over its forebear carbon nanotube? *ACS Nano*, **5**, 7426–7435.

113. Hayashi, H., Lightcap, I.V., Tsujimoto, M. *et al.* (2011) Electron transfer cascade by organic/inorganic ternary composites of porphyrin, zinc oxide nanoparticles, and reduced graphene oxide on a tin oxide electrode that exhibits efficient photocurrent generation. *J. Am. Chem. Soc.*, **133**, 7684–7687.

10
Graphene-Based Devices for Hydrogen Storage

Hou Wang and Xingzhong Yuan

10.1
Introduction

In the twenty-first century, renewable, environment-friendly, and sustainable alternative energy sources are urgently demanded because of the aggravating energy problems related to fossil fuel consumption and global warming [1, 2]. Among these candidate energy sources, hydrogen has been considered as one of the ultimate clean fuels because of its environmental compatibility, easy production, and nonpolluting properties [3]. However, the storage of hydrogen has been identified as the most difficult challenge. For practical applications, hydrogen storage demands high gravimetric and volumetric densities, fast reaction kinetics, a low H_2 absorption temperature, good reversibility, and low cost. Therefore, much research effort has been focused on how to develop hydrogen storage systems that can satisfy the conditions mentioned above. Current hydrogen storage technologies, such as cryogenic liquid storage, high-pressure gas cells, low-temperature adsorbates, metal hydrides, and chemical storage, have not been able to meet all the industry requirements [4]. To achieve economic feasibility, hydrogen storage materials with high gravimetric and volumetric densities – specified by the Department of Energy targets of 6.0 wt% mass ratio and 45 kg m^{-3} volumetric capacity by 2010 – need to be developed urgently [5].

Undoubtedly, the developments of hydrogen storage techniques strongly depend on achievements of materials science [2]. In order to accomplish such a target, the key aspects are designing novel materials and developing synthesis processes that allow precise control over the structural and chemical characteristics of the material, as well as seeking greener and cost effective material synthesis processes for the widespread utilization of such devices [6, 7]. In the past decade, there has been a strong focus on the use of carbon nanotubes (CNTs) for the fabrication of hydrogen energy storage devices. Besides being lightweight, CNTs present many advantages, including a large surface area (up to 1315 m^2 g^{-1}) and mass producability. However, many disadvantages have limited its widespread applications, such as the presence of toxic residual metallic impurities that are very difficult to remove and the high manufacturing cost [8].

Graphene-based Energy Devices, First Edition. Edited by A. Rashid bin Mohd Yusoff.
© 2015 Wiley-VCH Verlag GmbH & Co. KGaA. Published 2015 by Wiley-VCH Verlag GmbH & Co. KGaA.

Recent studies indicate that graphene-based materials may become the most promising candidates because of their low weight, chemical inertness, low price, and safety for everyday use in mobile applications [9].

Graphene is the basic building block of graphitic materials of all other dimensionalities; it can be wrapped up into 0D fullerene, rolled into 1D nanotube, or stacked into 3D graphite (Figure 10.1) [10]. It is a planar monolayer of carbon atoms arranged in a two-dimensional honeycomb lattice with sp^2 hybridization and has a carbon–carbon bond length of 0.142 nm [11]. This unique structure endows graphene with various superior properties, including excellent thermal conductivity (5300 $W\,mK^{-1}$) and mobility of charge carriers, electrical ($\sim$2000 $S\,cm^{-1}$) and mechanical (Young's modulus, $\sim$1100 GPa) properties, specific magnetism, and a large surface area ($\sim$2630 $m^2\,g^{-1}$) [1]. These properties attract enormous scientific attention during recent years in various fields, such as field-effect transistors, solar cells, sensors, supercapacitors, and transparent electrodes. Because of its excellent chemical properties, large surface area, and geometry, graphene has great potential for applications in hydrogen storage devices. Up to now, two main methods, namely storage of molecular hydrogen or storage of atomic hydrogen based on hydrogen spillover, have been adopted for hydrogen storage in graphene-based materials.

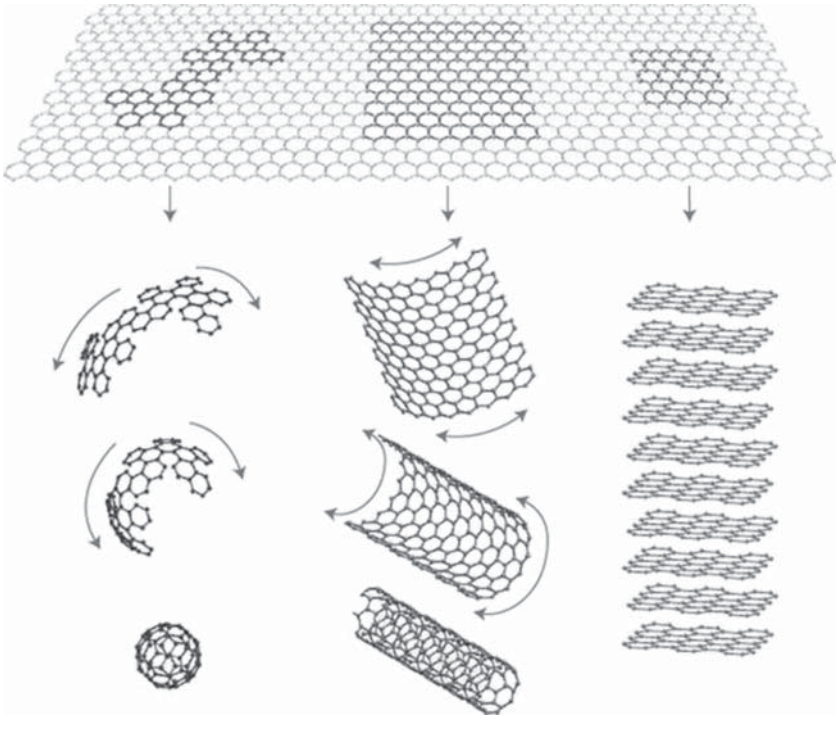

Figure 10.1 Graphene, the parent of all graphitic forms. The lattice and reciprocal lattice of graphene. (Adapted from Ref. [10].)

10.2
Storage of Molecular Hydrogen

In the process of storage, the most stable configuration is that in which H_2 is physisorbed above the center of a hexagon of graphene [12]. The interaction of nonpolar H_2 molecules with the physisorption substrates in graphene-based system is mainly London dispersion (instantaneous dipole–dipole-induced forces) [13]. The spatial distribution of molecular hydrogen adsorbed on graphene is delocalized and involves an essentially free lateral motion of H_2 (Figure 10.2). Few-layer graphene could achieve chemical storage of ~5 wt% of hydrogen by Birch reduction [14]. Hydrogenated samples containing sp^3 C–H bonds are stable at room temperature, and hydrogen can be progressively removed by heating or irradiation with light. This interesting phenomenon can be explained in terms of the competition between the gain in energy due to the formation of C–H bonds and the energy cost associated with the in-plane expansion of the C–C lattice. Besides, the corrugation of the layered graphene sheet and the controlled inversion of its curvature result in fast storage with gravimetric capacities of 8 wt% and release of hydrogen by external control of the local curvature at room conditions [15]. The large variation of H binding energy makes chemisorption a favorable process on convex sites and hydrogen release a favorable process on graphene concave sites. Graphene can also be defect-engineered to develop effective hydrogen storage media [16]. Although none of the defects was found to be detrimental to hydrogen anchoring, only the single vacancy showed promising hydrogen binding in the ideal range. Two high-defect-density structures constructed using vacancies and combined Stone–Wales defects and vacancies yielded gravimetric densities of 5.81% and 7.02%, respectively, with the van der Waals functional.

Moreover, graphene frameworks with the three-dimensional (3D) network nanostructure were confirmed to possess high hydrogen storage capacity based on theoretical predictions and experimental results [17]. Three-dimensional

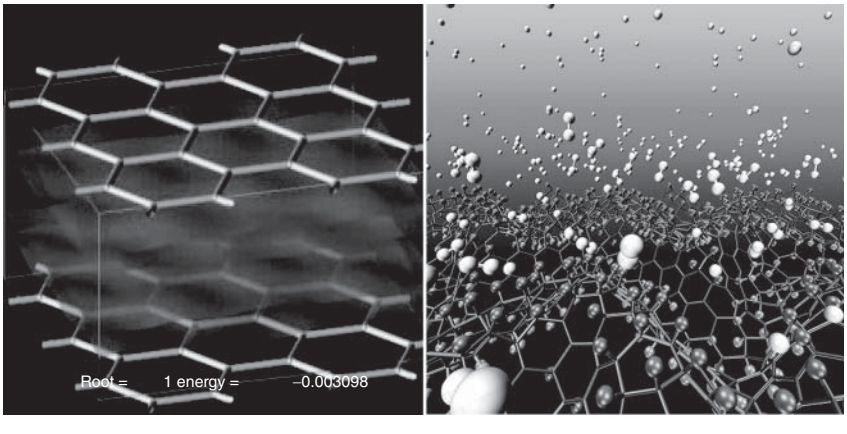

Figure 10.2 Graphene for hydrogen storage. (Adapted from Refs [13, 15].)

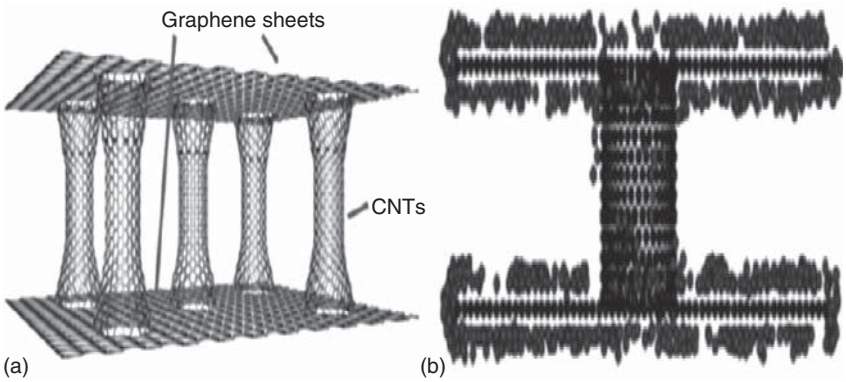

Figure 10.3 (a) Schematic of three-dimensional pillared graphene array. (b) Snapshots of hydrogen adsorption on pillared graphene. (Adapted from Ref. [20].)

graphene has a relatively large specific surface area and high aspect ratio, which, together with the multiple-lattice layered graphitic structure, are very helpful for hydrogen storage [18]. For example, Kim *et al.* constructed hierarchical micro and mesoporous metallomacrocycle-graphene frameworks (MGFs) using two distinct building blocks (graphene oxide (GO) and metallomacrocycles) [19]. The resulting materials exhibited H_2 adsorption capacity of 1.54 wt% at 77 K and 1 bar with a large hysteresis resulting from the flexible, pillared structure of the MGF. Three factors synergistically acted to improve the H_2 storage capacity of MGFs: (i) more sp^2 C species which serve as the H_2 uptake site are exposed since the GO layers are significantly reduced; (ii) high-valent Ni(III) open metal centers as strong Lewis acidic sites appeared at the pores; and (iii) the microporous nature of MGFs might be especially suited for H_2 uptake. Wu and his group [20] investigated the adsorption of molecular hydrogen on 3D pillared graphene structure (the combination of CNTs and graphene sheets) under various environments using molecular dynamics simulations (Figure 10.3). The efficiency of hydrogen storage in this structure is determined by (i) both binding energy and binding force from the pillared graphene interacting with hydrogen, and (ii) hydrogen flow from the edges of graphene sheets to enter the internal structure (empty space). The authors claimed that low temperature, high pressure, and a large gap between graphene sheets maximized the hydrogen storage capacity. The key to obtaining higher hydrogen capacity would be utilizing 1D spacers for enhancing the synergistic effect between the spacers and graphene sheets. Aboutalebi *et al.* [21] acquired high hydrogen capacity (up to 2.6 wt%) at room temperature by using unique 3D platforms of GO layers with 1D CNTs as building blocks. Compared to GO, multiwalled carbon nanotubes (MWCNTs), and rGO/MWCNT, GO/MWCNT composites have the highest hydrogen adsorption value at different hydrogen pressures (Figure 10.4a). The much higher hydrogen uptake in this hybrid is due to an increase in accessible and effective open surface. Individual and fully separated CNTs that entangled between separated GO sheets lead to no bundling of MWCNTs (Figure 10.4b).

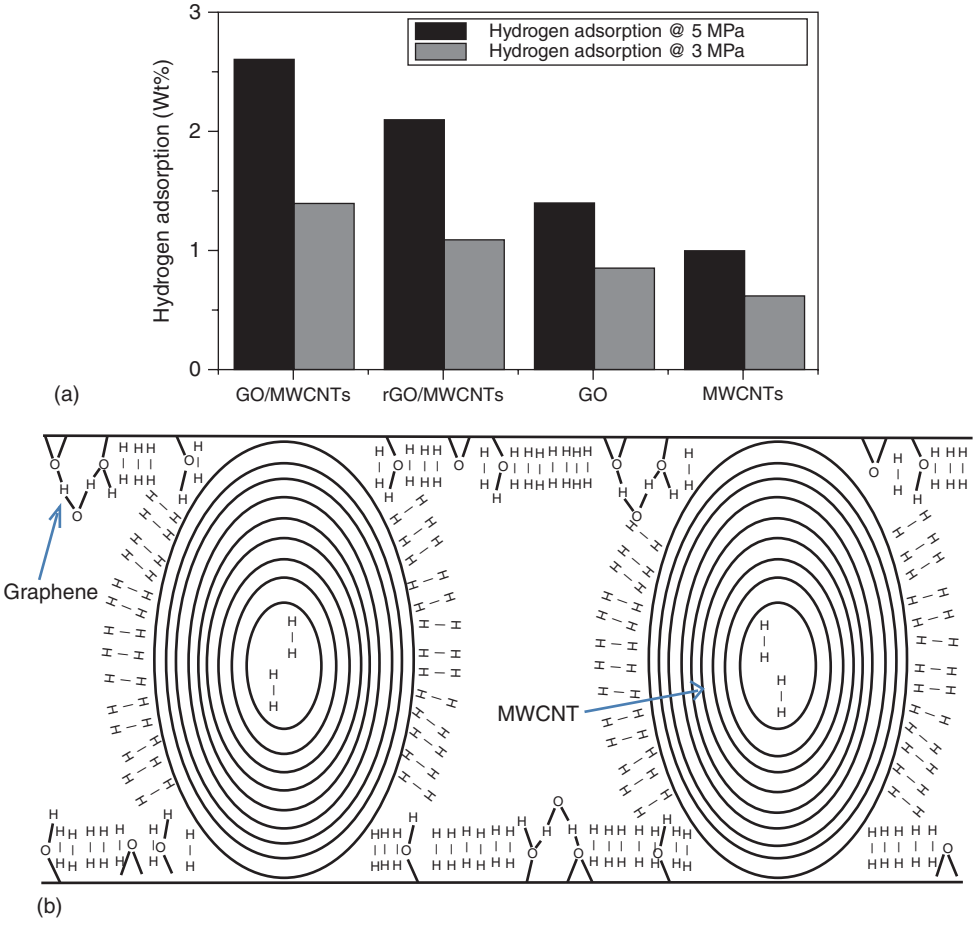

Figure 10.4 (a) Comparative hydrogen adsorption of GO, MWCNTs, and GO/MWCNT and rGO/MWCNT composites at different hydrogen pressures. (b) Schematic representing of hydrogen storage on GO/MWCNTs. (Reproduced with permission from Ref. [21].)

10.2.1 Graphene-Based Metal/Metal Oxide

GO or graphene-based metal/metal oxide nanoparticles can also be used for hydrogen storage [22]. With the interlayer distance of 6.5 Å, multilayered GO modulated by thermal annealing could achieve the maximum storage capacity of 4.8 wt% at 77 K and 9.0 MPa pressure [23]. H_2 molecules were stored via graphitic sp^2 carbon parts and mainly physisorbed in the entire region, especially on the edge of GO. The presence of O and OH functional groups on GO sheets plays a role of a spacer to separate the carbon layers. In addition, GO with different functional groups may serve as buildings block to fabricate various graphene-based metal/metal oxide nanoparticles for hydrogen storage. In

general, the anchoring/decorating nanoparticles are alkali metal (Li, Na, K, Ca) and transition-metal atoms/metal oxide (Ti, Pt, Sc, Pd, TiO_2, V_2O_5) [22, 24–34].

Coulomb and Kubas interactions between the transition metal or alkaline metal and hydrogen molecules are strong enough to provide significant capacity for the binding of H_2 [24]. For instance, graphene decorated with Ca atoms with a Ca–Ca distance of 10 Å without clustering of the Ca atoms could reach the gravimetric capacity of ~5 wt% hydrogen because up to six H_2 molecules were bond to a Ca atom with a binding energy of ~0.2 eV/H_2 [28]. The van der Waals interaction plays an important role on the binding of H_2 molecules with Ca-decorated graphene [29]. Graphene can be metallized by accepting charge from adsorbed Li atoms to its π^* bands so that each positively charged Li atom can absorb up to four H_2 molecules by polarizing them [31]. By adjusting the coverage of Li atoms on both sides, the hydrogen storage capacity can be increased to 16 wt%. It was found that the clustering of Ti adatoms is hindered by the repulsive Coulomb interactions between metal adatoms due to the strong bonding between metal adatom and graphene. Because Ti can bind up to eight H_2 molecules on two sides of the boron-substituted graphene, the theoretical hydrogen storage capacity of such metal/graphene hybrid with boron substitution can reach 7.9 wt% [26]. Similarly, yttrium decorated graphene may also be acted as a potential carrier for high density hydrogen storage [35]. Because each yttrium could attach six hydrogen molecules with average adsorption energy of −0.568 eV per hydrogen molecule, the hydrogen storage capacity of this material was 5.78 wt%. Moreover, Hong *et al.* [34] prepared graphene oxide-wrapped transition-metal oxide composite materials by the dehydration reaction and hydrogen bonding (Figure 10.5a). These materials showed an enhancement of hydrogen storage capacity compared to those of the pristine transition-metal oxides, from 0.16 wt% for V_2O_5 (0.58 wt% for TiO_2) to 1.36 wt% for GO/V_2O_5 (1.26 wt% for GO/TiO_2) (Figure 10.5b).

10.2.2
Doped Graphene

Another possibility is to use doped graphene, especially with boron [36–38], aluminum [39], silicon [40], or nitrogen [41], for significant enhancement of H_2 binding capacity. The presence of boron modifies the symmetry of the energy landscape because of both the larger boron size (with respect to carbon) and its stronger interaction with hydrogen molecules [36]. For instance, Li *et al.* [37] showed that the hydrogen storage capacity might reach up to 15.1 wt% on Be/B-doped graphene for double-sided adsorption. Strong electron interaction occurred between H_2 molecules and graphene system decorated with B and Be atoms. Ao *et al.* [39] found that the hydrogen uptake process in N-doped graphene layer can easily occur under an electric field applied perpendicularly. N-doped graphene is a promising hydrogen storage material with a storage capacity of up to 6.73 wt%, which is attributed to hydrogen dissociative adsorption and diffusion on N-doped graphene with low energy barriers. The dopant atoms (Ti, Zn, Zr, Al, and N) have a great effect on the interactions between graphene sheets and

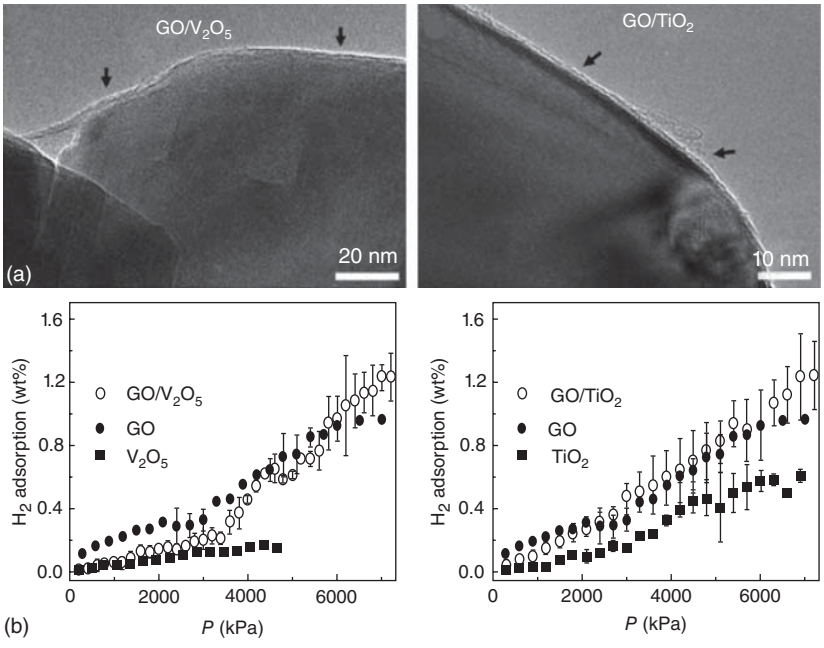

Figure 10.5 (a) Transmission electron microscopy (TEM) images of GO/V_2O_5 and GO/TiO_2. (b) High-pressure H_2 adsorption of V_2O_5, GO, GO/V_2O_5, TiO_2, GO, and GO/TiO_2. (Adapted from Ref. [34].)

hydrogen molecules [42]. The doped metallic atoms could greatly change the local electron structures of the graphene sheet, whereas the doped N atom could not. Thus, the doped Al, Zn, Zr, and Ti atoms increased the H_2 storage ability of the graphene sheet, whereas the doped N atom did not affect the H_2 storage ability of the graphene sheet.

10.3 Storage of Atomic Hydrogen Based on Hydrogen Spillover

Hydrogen spillover is anticipated to be a promising phenomenon to increase the capacity of graphene-based hydrogen storage materials with the help of the "bridges" between the catalysts and graphene surface [43, 44]. Graphene-based materials are doped with metal catalysts, which dissociate the H_2 molecules into H atoms, and then the H atoms migrate from metal to graphene and further diffuse on the supporting sheet [45] (Figure 10.6). The common catalyst particles in graphene-based materials are typically Pt, Pd, or Ni (or other transition metals) [45–49]. Compared to undoped graphene, it was experimentally observed that the hydrogen storage capacities of graphene/Pt and graphene/Pd samples were enhanced by factors of 2.23 and 2.32 as a result of the spillover effect [50]. Moreover, the amount of metal particles and the metal particle size decorating

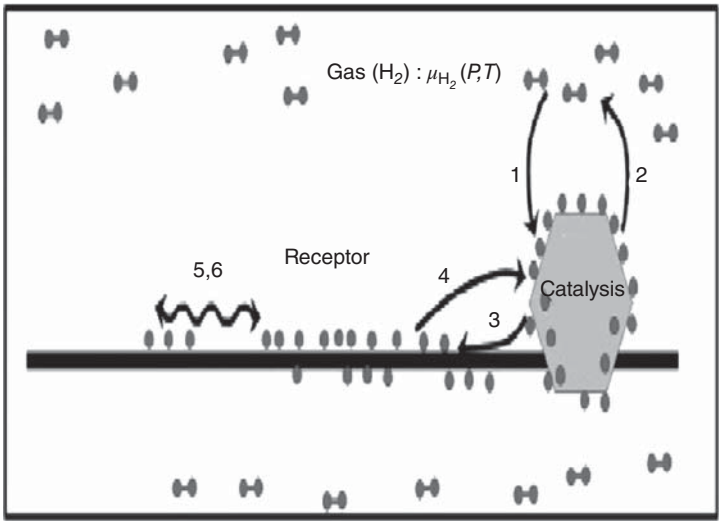

Figure 10.6 Schematic description of the hydrogen spillover process. (Adapted from Ref. [45].)

the graphene have great effects on the hydrogen spillover. Although the spillover effect has been experimentally observed, it has never been clear why it is favorable for molecular hydrogen to dissociate on a catalyst into its atomic form and further to spill over graphene sheets.

Chen *et al.* [44] illustrated facile pathways for hydrogen spillover from a Pt particle onto a graphitic basal plane using density functional theory. Their result indicated that H atom diffusion with chemisorbed state in graphitic materials is energetically difficult because it requires C–H bond breaking, and hydrogen spillover would occur probably via physisorption of H atoms (Figure 10.7). But their work has not directly addressed the role of support and bridge materials. Hydrogen storage by spillover on graphene also acts as a phase nucleation process [47]. Possible nucleation centers can be the metal particles, which lower the reaction (H_2 dissociation) transition state as a catalyst and reduce the nucleation barrier. Nano-thermodynamics of hydrogen spillover has indicated that it is possible for spillover of H to occur from a metal cluster to the hydrogenated graphene and that H uptake via the spillover can increase with the temperature and reduction of the substrate [48]. Meanwhile, this process does not require full saturation of the metal clusters before the spillover. Recently, Han *et al.* [49] found that the particular geometry of the chair-like all-paired configuration of hydrogen adatoms had a large barrier against hydrogen migration along the graphene-like carbon surface. However, hydrogen spillover could occur with the graphene surface if some moving catalyst is introduced. Hydrogen storage in Ni–B nanoalloy-doped 3D graphene material was reported by Wang and coworkers [51]. The graphene doped with Ni (0.83 wt%) and B (1.09 wt%) showed the best hydrogen storage capacity of

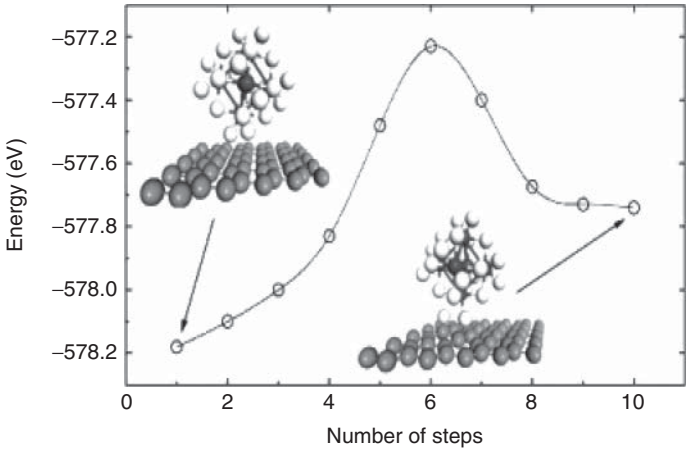

Figure 10.7 Spillover of hydrogen from Pt_6 (upper inset) to the graphene sheet (lower inset). The line is drawn as a guide to the eye. (Adapted from Ref. [44].)

4.4 wt% at 77 K and 106 kPa, which was better than that of pristine graphene and all carbon-based materials (Figure 10.8). Different from the predominantly physical adsorption on graphene, doping with appropriate content of Ni–B alloys can lead to the dissociative chemisorption of hydrogen molecules by spillover. The hydrogen molecules first attach themselves to the Ni–B nanoalloys, become dissociated

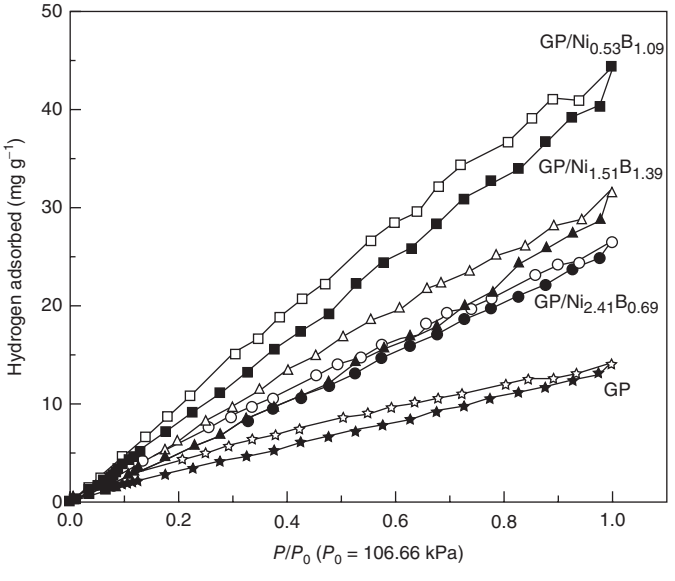

Figure 10.8 Hydrogen adsorption and desorption isotherms of graphene (GP), GP/$Ni_{2.41}B_{0.69}$, GP/$Ni_{1.51}B_{1.39}$, and GP/$Ni_{0.83}B_{1.09}$ at 77 K (adsorption data are shown as closed shapes, desorption data as open shapes). (Adapted from Ref. [51].)

to hydrogen atoms, and diffuse to the sites of the graphene to form the C–H bond. However, the mechanisms of hydrogen storage based on hydrogen spillover in 3D graphene-based materials are partly unclear and need to be further explored.

In summary, as new and unique 2D carbon nanomaterials, graphene-based materials have been applied to construct different and promising hydrogen storage devices. As high-performance energy storage materials, it is extremely crucial for individual graphene layers to obtain careful, rational nanoarchitectonic design and proper spacing. Moreover, in order to enhance the storage performance, one has to see how to combine graphene with these functional materials including metal or metal oxides, polymers, metal organic framework, and others to utilize their synergistic effect. Among the numerous potential dopants, the most suitable and efficient dopants have to be selected, and methods for the improved storage behavior of graphene materials have to be researched. Thus, the study of graphene-based hydrogen storage devices can be a challenging and highly promising research topic.

References

1. Yan, L., Zheng, Y.B., Zhao, F. *et al.* (2012) Chemistry and physics of a single atomic layer: strategies and challenges for functionalization of graphene and graphene-based materials. *Chem. Soc. Rev.*, **41**, 97–114.
2. Sun, Y.Q., Wu, Q., and Shi, G.Q. (2011) Graphene based new energy materials. *Energy Environ. Sci.*, **4**, 1113–1132.
3. Lian, G., Zhang, X., Zhang, S. *et al.* (2012) Controlled fabrication of ultrathin-shell BN hollow spheres with excellent performance in hydrogen storage and wastewater treatment. *Energy Environ. Sci.*, **5**, 7072–7080.
4. Wang, Y.S., Yuan, P.F., Li, M. *et al.* (2012) Metal decorated monolayer BC_2N for hydrogen storage. *Comput. Mater. Sci.*, **60**, 181–185.
5. Department of Energy (1999) A Multiyear Plan for the Hydrogen R&D Program.
6. Wang, H., Yuan, X., Wu, Y. *et al.* (2013) Graphene-based materials: fabrication, characterization and application for the decontamination of wastewater and wastegas and hydrogen storage/generation. *Adv. Colloid Interface Sci.*, **195–196**, 19–40.
7. Sevilla, M. and Mokaya, R. (2014) Energy storage applications of activated carbons: supercapacitors and hydrogen storage. *Energy Environ. Sci.*, **7**, 1250–1280.
8. Singh, V., Joung, D., Zhai, L. *et al.* (2011) Graphene based materials: past, present and future. *Prog. Mater. Sci.*, **56**, 1178–1271.
9. Pumera, M. (2011) Graphene-based nanomaterials for energy storage. *Energy Environ. Sci.*, **4**, 668–674.
10. Geim, A.K. and Novoselov, K.S. (2007) The rise of graphene. *Nat. Mater.*, **6**, 183.
11. Slonczewski, J.C. and Weiss, P.R. (1958) Band structure of graphite. *Phys. Rev.*, **109**, 272.
12. Arellano, J.S., Molina, L.M., Rubio, A. *et al.* (2000) Density functional study of adsorption of molecular hydrogen on graphene layers. *J. Chem. Phys.*, **112**, 8114.
13. Patchkovskii, S., Tse, J.S., Yurchenko, S.N. *et al.* (2005) Graphene nanostructures as tunable storage media for molecular hydrogen. *Proc. Natl. Acad. Sci. U.S.A.*, **102**, 10439–10444.
14. Subrahmanyam, K.S., Kumar, P., Maitra, U. *et al.* (2011) Chemical storage of hydrogen in few-layer graphene. *Proc. Natl. Acad. Sci. U.S.A.*, **108**, 2674–2677.
15. Tozzini, V. and Pellegrini, V. (2011) Reversible hydrogen storage by

controlled buckling of graphene layers. *J. Phys. Chem. C*, **115**, 25523–25528.
16. Yadav, S., Zhu, Z., and Singh, C.V. (2014) Defect engineering of graphene for effective hydrogen storage. *Int. J. Hydrogen Energy*, **39**, 4981–4995.
17. Burress, J.W., Gadipelli, S., Ford, J. *et al.* (2010) Graphene oxide framework materials: theoretical predictions and experimental results. *Angew. Chem. Int. Ed.*, **49**, 8902–8904.
18. Wang, Y., Wang, K., Guan, C. *et al.* (2011) Surface functionalization-enhanced spillover effect on hydrogen storage of Ni–B nanoalloy-doped activated carbon. *Int. J. Hydrogen Energy*, **36**, 13663–13668.
19. Kim, T.K., Cheon, J.Y., Yoo, K. *et al.* (2013) Three-dimensional pillared metallomacrocycle–graphene frameworks with tunable micro- and mesoporosity. *J. Mater. Chem. A*, **1**, 8432–8437.
20. Wu, C.D., Fang, T.H., and Lo, J.Y. (2012) Effects of pressure, temperature, and geometric structure of pillared graphene on hydrogen storage capacity. *Int. J. Hydrogen Energy*, **37**, 14211–14216.
21. Aboutalebi, S.H., Aminorroaya-Yamini, S., Nevirkovets, I. *et al.* (2012) Enhanced hydrogen storage in graphene oxide-MWCNTs composite at room temperature. *Adv. Energy Mater.*, **2**, 1439–1446.
22. Parambhath, V.B., Nagar, R., and Ramaprabhu, S. (2012) Effect of nitrogen doping on hydrogen storage capacity of palladium decorated graphene. *Langmuir*, **28**, 7826–7833.
23. Kim, B.H., Hong, W.G., Yu, H.Y. *et al.* (2012) Thermally modulated multilayered graphene oxide for hydrogen storage. *Phys. Chem. Chem. Phys.*, **14**, 1480–1484.
24. Kim, G., Jhi, S., Lim, S. *et al.* (2009) Crossover between multipole Coulomb and Kubas interactions in hydrogen adsorption on metal-graphene complexes. *Phys. Rev. B*, **79**, 155437.
25. Chu, S., Hu, L., Hu, X. *et al.* (2011) Titanium-embedded graphene as high-capacity hydrogen-storage media. *Int. J. Hydrogen Energy*, **36**, 12324–12328.
26. Park, H. and Chung, Y. (2010) Hydrogen storage in Al and Ti dispersed on graphene with boron substitution: first-principles calculations. *Comput. Mater. Sci.*, **49**, S297–S301.
27. Wang, L., Lee, K., Sun, Y. *et al.* (2009) Graphene oxide as an ideal substrate for hydrogen storage. *ACS Nano*, **3**, 2995–3000.
28. Lee, H., Ihm, J., Cohen, M.L. *et al.* (2010) Calcium-decorated graphene-based nanostructures for hydrogen storage. *Nano Lett.*, **10**, 793–798.
29. Wang, V., Mizuseki, H., He, H.P. *et al.* (2012) Calcium-decorated graphene for hydrogen storage: a van der Waals density functional study. *Comput. Mater. Sci*, **55**, 180–185.
30. Wu, M., Gao, Y., Zhang, Z. *et al.* (2012) Edge-decorated graphene nanoribbons by scandium as hydrogen storage media. *Nanoscale*, **4**, 915–920.
31. Zhou, W., Zhou, J., Shen, J. *et al.* (2012) First-principles study of high-capacity hydrogen storage on graphene with Li atoms. *J. Phys. Chem. Solids*, **73**, 245–251.
32. Zhou, M., Lu, Y., Zhang, C. *et al.* (2010) Strain effects on hydrogen storage capability of metal-decorated graphene: a first-principles study. *Appl. Phys. Lett.*, **97**, 103109.
33. Reunchanl, P. and Jhi, S. (2011) Metal-dispersed porous graphene for hydrogen storage. *Appl. Phys. Lett.*, **98**, 093103.
34. Hong, W.G., Kim, B.H., Lee, S.M. *et al.* (2012) Agent-free synthesis of graphene oxide/transition metal oxide composites and its application for hydrogen storage. *Int. J. Hydrogen Energy*, **37**, 7594–7599.
35. Liu, W., Liu, Y., and Wang, R. (2014) Prediction of hydrogen storage on Y-decorated graphene: a density functional theory study. *Appl. Surf. Sci.*, **296**, 204–208.
36. Firlej, L., Kuchta, B., Wexler, C. *et al.* (2009) Boron substituted graphene: energy landscape for hydrogen adsorption. *Adsorption*, **15**, 312–317.
37. Li, D., Ouyang, Y., Li, J. *et al.* (2012) Hydrogen storage of beryllium adsorbed on graphene doping with boron: first-principles calculations. *Solid State Commun.*, **152**, 422–425.
38. Beheshti, E., Nojeh, A., and Servati, P. (2011) A first-principles study of

calcium-decorated, boron-doped graphene for high capacity hydrogen storage. *Carbon*, **49**, 1561–1567.

39. Ao, Z.M., Jiang, Q., Zhang, R.Q. *et al.* (2009) Al doped graphene: a promising material for hydrogen storage at room temperature. *J. Appl. Phys.*, **105**, 074307.

40. Cho, J.H., Yang, S.J., Lee, K. *et al.* (2011) Si-doping effect on the enhanced hydrogen storage of single walled carbon nanotubes and graphene. *Int. J. Hydrogen Energy*, **36**, 12286–12295.

41. Ao, Z.M., Hernández-Nieves, A.D., Peeters, F.M. *et al.* (2012) The electric field as a novel switch for uptake/release of hydrogen for storage in nitrogen doped graphene. *Phys. Chem. Chem. Phys.*, **14**, 1463–1467.

42. Zhang, H., Luo, X., Lin, X. *et al.* (2013) Density functional theory calculations of hydrogen adsorption on Ti-, Zn-, Zr-, Al-, and N-doped and intrinsic graphene sheets. *Int. J. Hydrogen Energy*, **38**, 14269–14275.

43. Psofogiannakis, G.M., Steriotis, T.A., Bourlinos, A.B. *et al.* (2011) Enhanced hydrogen storage by spillover on metal-doped carbon foam: an experimental and computational study. *Nanoscale*, **3**, 933–936.

44. Chen, L., Cooper, A.C., Pez, G.P. *et al.* (2007) Mechanistic study on hydrogen spillover onto graphitic carbon materials. *J. Phys. Chem. C*, **111**, 18995–19000.

45. Wu, H., Fan, X., Kuo, J. *et al.* (2011) DFT Study of hydrogen storage by spillover on graphene with boron substitution. *J. Phys. Chem. C*, **115**, 9241–9249.

46. Wang, L. and Yang, R.T. (2008) New sorbents for hydrogen storage by hydrogen spillover–a review. *Energy Environ. Sci.*, **1**, 268–279.

47. Lin, Y., Ding, F., and Yakobson, B.I. (2008) Hydrogen storage by spillover on graphene as a phase nucleation process. *Phys. Rev. B*, **78**, 041402.

48. Singh, A.K., Ribas, M.A., and Yakobson, B.I. (2009) H-spillover through the catalyst saturation: an ab Initio thermodynamics study. *ACS Nano*, **3**, 1657–1662.

49. Han, S.S., Jung, H., Jung, D.H. *et al.* (2012) Stability of hydrogenation states of graphene and conditions for hydrogen spillover. *Phys. Rev. B*, **85**, 155408.

50. Huang, C.C., Pu, N.W., Wang, C.A. *et al.* (2011) Hydrogen storage in graphene decorated with Pd and Pt nano-particles using an electroless deposition technique. *Sep. Purif. Technol.*, **82**, 210–215.

51. Wang, Y., Guo, C.X., Wang, X. *et al.* (2011) Hydrogen storage in a Ni–B nanoalloy-doped three-dimensional graphene material. *Energy Environ. Sci.*, **4**, 195–200.

11
Graphene-Supported Metal Nanostructures with Controllable Size and Shape as Advanced Electrocatalysts for Fuel Cells

Minmin Liu and Wei Chen

11.1
Introduction

Because of the dramatically increasing energy consumption, fossil fuel depletions, limited supply of these natural resources, and environmental pollution all over the world [1, 2], intense efforts are being made by many researchers to find clean, environmentally friendly, renewable, and sustainable energy storage systems, including batteries, diesel/generator units, supercapacitors, and fuel cells, among others [3, 4]. Of these energy devices, fuel cells (FCs) are expected to become a potential energy source with the advantages of abundance and nontoxicity of the small organic molecular fuels, high energy density and conversion efficiency, and clean and environmentally friendly products. FCs are a type of electrical energy converting devices that generate electrical energy from chemical energy via the reactions between the oxidation of chemical fuels (hydrogen, methanol, formic acid, or ethanol) at the anode and the reduction of oxygen at the cathode at the interface of the electrocatalyst and electrolyte [5]. Electrocatalysts play crucial roles in determining the performance of a fuel cell. Meanwhile, the performance of an electrocatalyst is strongly dependent on its size, shape, and composition. Therefore, the design and fabrication of electrocatalysts are of top priority among the components in a fuel cell. Structure-controlled synthesis and surface functionalization of inorganic metals or metal oxides are effective routes in improving the stability and performance of electrocatalysts.

Graphene is an atomically thin two-dimensional (2D) carbon sheet with a hexagonal-packed lattice structure and has attracted increasing research interests in both scientific studies and technological development since it was discovered by Geim *et al.* [6] in 2004. In recent years, graphene materials with different forms have been synthesized, such as 2D graphene nanosheets (GNSs), 1D graphene nanoribbons (GNRs), and 0D graphene quantum dots (GQDs) [7]. Graphene possesses the chemical and physical advantages of high surface area ($\sim 2600\ m^2\ g^{-1}$), chemical and thermal stability, distinct long-range π conjugation and graphitized basal plane structure, and a broad potential window, as well as excellent electrical conductivity ($10^5 - 10^6\ S\ m^{-1}$) and mechanical properties [8–11]. With these

Graphene-based Energy Devices, First Edition. Edited by A. Rashid bin Mohd Yusoff.
© 2015 Wiley-VCH Verlag GmbH & Co. KGaA. Published 2015 by Wiley-VCH Verlag GmbH & Co. KGaA.

amazing properties, graphene and graphene-based nanomaterials have been accepted as promising candidates as new 2D supporting materials in many application fields such as batteries, biosensors, FCs, photovoltaic devices, and supercapacitors [5, 12]. Researches on the interactions between metal nanomaterials and graphene have disclosed that a charge transfer across the interface of graphene and metals occurs according to the graphene–metal spacing and the Fermi level difference between the metal and graphene [13]. As an excellent support material, GNSs not only provide large surface area for loading nanoparticles but also enhance the stability of the supported nanomaterials by preventing the decorated nanoparticles (NPs) from aggregating. Because of the high electronic conductivity, through hybridization with graphene, the electronic conductivity of the electrocatalysts based on metal or metal oxide NPs could also be improved effectively [14]. On the basis of the above discussion, graphene-supported nanostructures with optimized morphologies could be a class of promising electrocatalysts for FCs. In recent years, various graphene-based nanocatalysts, including precious and nonprecious metals, nonmetals and metal oxides, and so on, have been studied extensively. In this chapter, we highlight the recent progress of graphene-supported metal and metal oxide nanocatalysts with controllable size and shape for FC applications.

11.2 Fuel Cells

As a kind of promising clean energy source, FC has attracted much attention in last decades. The theoretical cell voltage of a hydrogen-powered FC is 1.23 V, based on the low calorific value of hydrogen [15]. FCs can be classified into five categories according to the electrolyte used: alkaline fuel cells (AFCs), phosphoric acid fuel cells (PAFCs), proton exchange membrane fuel cells (PEMFCs), molten carbonate fuel cells (MCFCs), and solid oxide fuel cells (SOFCs). In detail, PEMFCs include direct methanol fuel cells (DMFCs), direct formic acid fuel cells (DFAFCs), and direct ethanol fuel cells (DEFCs) [15]. The various types of FCs could be divided into high-temperature and low-temperature cells according to their operate temperature. High-temperature FCs include MCFCs and SOFCs, while low-temperature FCs comprise AFCs, PEMFCs, and PAFCs. On the other hand, on the basis of the treatment modes, FCs could also be classified as direct, indirect, or regenerative. Moreover, according to the chronological order of their development, FCs can be sorted as first generation (PAFCs), second generation (MCFCs), and third generation (SOFCs, PEMFCs). Besides, biofuel cells, for example, microbial fuel cells (MFCs) [16] and enzymatic biofuel cells (EBFCs) [17], have also seen great development in recent years.

Among all these types of FCs, PEMFC is a prospective technology to power portable electronic devices, transportation vehicles, and stationary grids because of its higher energy density, lower operation temperature, and lower environmental impact compared to high-temperature fuel cells (MCFCs, SOFCs) [3].

Besides, PEMFC shows superior start-up/shut-down characteristics and superior load-following, although it has the drawbacks of lower electrical efficiency and complicated gas treatment processes [15].

Presently, the next generation of PEMFCs operating at higher temperatures (<90 °C) are being developed with enhanced fuel cell reaction kinetics, especially for the oxygen reduction reaction (ORR) on cathode, enhanced contamination tolerance, improved heat rejection capability, and water management [18]. Here, PEMFCs are mainly introduced.

11.2.1 Configuration and Design of PEMFCs

Figure 11.1 demonstrates a typical structure of a PEMFC, showing the conversion of the chemical energy stored in H_2 into electrical energy. In a hydrogen-powered fuel cell, H_2 is oxidized at the anode while O_2 is reduced at the cathode. At the anode, H_2 gas fuel can be substituted by small organic molecular fuels, such as formic acid, methanol, ethanol, and so on. At the cathode, O_2 is generally selected to collect the electrons released from fuel because of its high electronegativity. On one hand, protons flow from the anode to the cathode, crossing the proton exchange membrane inside of the FC. On the other hand, electrons flow from the fuel oxidation reaction (at anode) to the ORR (at cathode) outside the FC. The proton migration into the fuel cell and the electron flow out of the cell form a complete current circuit [3]. The electrodes are the energy conversion reaction sites for anodic and cathodic reactions. The products of the oxidation of the fuel at the anode and oxygen reduction at the cathode are CO_2 and H_2O, which are clean and environmentally friendly gases. Therefore, ultralow or zero emission of environmental pollutants is one of the greatest advantages of PEMFCs over thermal engines. Nevertheless, electrocatalysts on both the anode and the cathode play an

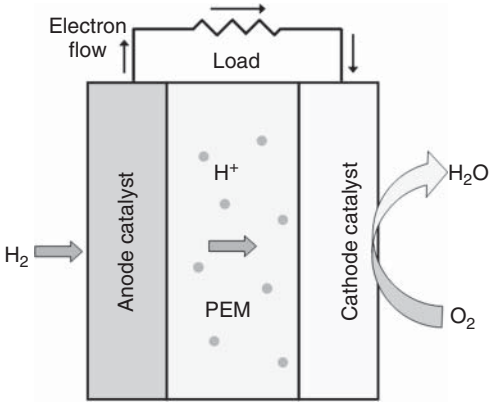

Figure 11.1 Schematic diagram of a hydrogen-powered proton exchange membrane fuel cell (PEMFC).

important role for reducing the electrochemical overpotentials and achieving a high voltage output [3].

Despite considerable recent advances, existing FC technology suffers from drawbacks. Platinum (Pt)-based materials have been accepted to be the highest active electrocatalysts for both fuel oxidation and ORR. However, in addition to the high cost and scarcity of Pt, the other major disadvantage of Pt-based electrocatalysts is that they tend to get inactivated by agglomeration or CO (carbon monoxide) poisoning. The instability and poor durability of the Pt electrocatalysts could seriously impact the whole performance of an FC. Up to now, to resolve these problems, carbon materials such as active carbon, carbon nanotubes (CNTs), graphene, carbon dots (CDs), and GQDs have been widely studied as electrocatalyst supporting materials [15]. The role of nanocarbons is to support metal catalysts and facilitate the anodic or cathodic reaction, which is possible because of their light weight and large surface area. A recent work showed a substantial loss of the Pt surface area over time in PEMFCs during the stop-and-go driving of an electric car; this depletion exceeded the Pt dissolution rates observed upon holding it at a constant potential for extended time spans [19]. Therefore, how to improve the durability and reliability of electrocatalysts is still a major challenge for FCs in practical operating environments [18]. Several typical PEMFCs are introduced below.

11.2.2 Direct Methanol Fuel Cells (DMFCs)

As a subcategory of PEMFC, DMFCs take the advantages of low operating temperature, high energy efficiency, low exhaustion, and the fast start-up of the fuel and show potential for various applications, such as vehicle propulsion, stationary low power generation, and as replacement for the battery in electronic equipment such as cameras and notebooks [15].

The theoretical open-circuit voltage (OCV) of a methanol–oxygen fuel cell is 1.18 V [20]. The methanol oxidation reaction (MOR) procedure involves methanol adsorption, the subsequent dissociation into adsorbed intermediates, and their oxidation. There are several important parameters to evaluate the catalytic performance of a catalyst for MOR, such as the electrochemical surface area (ECSA), oxidation current density, and the onset potential of MOR. ECSA determines the available catalytically active site numbers for an electrochemical reaction and accounts for the available conductive paths to transfer electrons to and from the electrode surface. Meanwhile, another parameter, the ratio I_f/I_b, is an essential key to qualitatively describe the catalyst's tolerance to poisoning intermediates. Here, I_f represents the forward oxidation peak current which is associated with the oxidation of freshly chemisorbed species, and I_b is the reverse oxidation peak current which primarily originates from the removal of carbonaceous species incompletely oxidized in the forward scan. A larger I_f/I_b ratio usually indicates the higher tolerance of a catalyst to the poisoning species on the catalyst surface [21]. A higher I_f/I_b ratio with large I_f and more negative

onset potential in the forward scan reflects a much higher catalytic efficiency for MOR and the highly efficient removal of the excessive incompletely oxidized species on the catalyst surface, such as CO and other carbonaceous residues. CO is widely accepted as a kind of main poisoning intermediate species absorbed on the surface of catalysts, especially Pt-based catalysts, which could largely reduce the performance of catalysts and the overall fuel cell. Depending on the oxidation of methanol with CO generation or not, a dual-pathway mechanism has been proposed to explain the MOR process, which can be simply represented as in Equation 11.1:

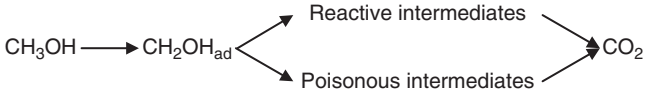

(11.1)

The total reaction can be expressed as

$$CH_3OH + H_2O \rightarrow CO_2 + 6H^+ + 6e^- \tag{11.2}$$

It has been proposed that chemically synthesized graphene can improve the tolerance toward CO poisoning for MOR, because the residual oxygenated functional groups on the graphene surface can react and remove the carbonaceous species produced during the electrode reactions [22, 23]. For instance, for Pt NPs supported on reduced graphene oxide (rGO), the oxygen-containing surface species (e.g., OH) on the rGO surface can remove the adsorbed CO (CO_{ad}) on catalyst surface during MOR:

$$rGO + H_2O \rightarrow rGO\text{-}(OH)_{ads} + H^+ + e^- \tag{11.3}$$

$$Pt\text{-}CO_{ads} + rGO(OH)_{ads} \rightarrow CO_2 + H^+ + Pt + rGO + e^- \tag{11.4}$$

Therefore, with graphene as support, the electrocatalytic performance of catalysts can be enhanced. On the other hand, electrochemical reactions involve the electric charge transfer through the electrode/electrolyte interface. The driving force of an electrode reaction is controlled not only by parameters such as the concentration, pressure, and temperature but also by the electrical force, that is, the electrode potential. The electric force can affect the charge transfer through the electrode/electrolyte interface and can be altered by an applied external voltage in an electrochemical cell. The high electron mobility of graphene can enhance the electron transfer process during the MOR, especially for low-conductive catalyst materials.

The cathode reaction generally refers to the ORR, which plays an essential role in determining the performance of an FC. However, the electron-transfer kinetics of ORR is sluggish, which greatly limits the application of FCs. The ORR process is complicated and usually considered to proceed through an efficient $4e^-$ reduction of O_2 to H_2O (in acid) or OH^- (in alkaline) (Equation 11.5), or a less efficient two-step $2e^-$ reduction pathway, forming H_2O_2 (in acid) or HO_2^- (in

alkaline) as intermediates and further being oxidized to H_2O and OH^-, respectively (Equation 11.6) [3].

$$O_2 + 4H^+ + 4e^- \rightarrow 2H_2O \text{ or } O_2 + 2H_2O + 4e^- \rightarrow 4OH^- \tag{11.5}$$

$$\begin{aligned} &O_2 + 4H^+ + 2e^- \rightarrow H_2O_2 + 2H^+ + 2e^- \rightarrow 2H_2O \quad \text{or} \\ &O_2 + H_2O + 2e^- \rightarrow HO_2^- + OH^-; \quad HO_2^- + H_2O + 2e^- \rightarrow 3OH^- \end{aligned} \tag{11.6}$$

The rotating disk electrode (RDE) technique is widely utilized to investigate ORR kinetic information. The kinetic current density can be derived from the following equations:

$$\frac{1}{J} = \frac{1}{J_K} + \frac{1}{J_L} = \frac{1}{J_K} + \frac{1}{B\omega^{\frac{1}{2}}} \tag{11.7}$$

$$B = 0.62nFAD_O^{\frac{2}{3}}\omega^{\frac{1}{2}}\nu^{-\frac{1}{6}}C_{O_2} \tag{11.8}$$

$$i_k = nFAkC_{O_2} \tag{11.9}$$

where J represents the measured current density, J_K and J_L are the kinetic and diffusion limiting current density, respectively, ω is the rotation rate of the electrode, n is the electron transfer number, F is the Faraday constant, C_O is the bulk concentration of O_2 dissolved in the electrolyte, D_O is the O_2 diffusion coefficient, ν is the electrolyte kinematic viscosity, and k is the electron transfer rate constant. Besides, the rotation ring-disk electrode (RRDE) can be used to estimate the ORR performance of a catalyst with an auxiliary ring electrode. The electron transfer numbers (n) can be obtained from the ring and disk current information, as given by the following equation:

$$n = \frac{4I_D}{I_D + I_R/N} \tag{11.10}$$

I_D and I_R stand for the disk current and ring current, respectively, and N represents the RRDE collection efficiency. The percentage of H_2O_2 collected on the ring electrode which generated at the disk electrode could be calculated according to the following equation:

$$\%H_2O_2 = \frac{2I_R/N}{I_D + I_R/N} \times 100\% \tag{11.11}$$

According to the theory, a linear sweep voltammetry (LSV) curve with a more positive half-wave potential, a steeper polarization curve, and a higher current density suggest better catalytic efficiency.

The main advantages of DMFCs include the low cost and abundance of methanol in nature, the easy storage and transport of methanol in the liquid stste, and the clean products CO_2 and H_2O. Meanwhile, DMFCs also possess the superiority of high energy density as well as low operating pressure and temperature [15]. However, an obvious disadvantage of DMFCs is that methanol

can easily cross over from the anode to the cathode side through the polymer membranes, which can decrease the cathode potential and reduce fuel efficiency due to the MOR on cathode catalysts [24]. To overcome the methanol crossover, enormous efforts have been made on developing methanol-tolerant Pt-based and Pt-free cathode electrocatalysts [10].

11.2.3 Direct Formic Acid Fuel Cells (DFAFCs)

Fuel cells that use formic acid as fuel at the anode are called *direct formic acid fuel cells*, in which formic acid is oxidized at the anode and oxygen is reduced at the cathode. Dilute aqueous formic acid is considered to be a safe liquid fuel at room temperature and it also has the advantages of ease of handling, transportion, and storage compared to hydrogen gas. Meanwhile, the theoretical OCV of a DFAFC (~1.48 or 1.45 V) is higher than that of methanol–oxygen (1.18 V) and hydrogen–oxygen (1.23 V) fuel cells. More importantly, formic acid shows much lower crossover effect compared to methanol in DMFCs [25], which will reduce the cost by using much thinner membranes and improve the performance of the entire fuel cell by increasing the concentration of formic acid. In addition, the mechanism of formic acid oxidation reaction (FAOR) shows a dual pathway, that is, the direct dehydrogenation route, which removes two H atoms and produces CO_2 directly (Equation 11.12), and the indirect dehydration (Equation 11.13) route, which removes a H_2O molecule and generates the poisonous intermediate CO_{ads} species,further oxidizing it to CO_2 [26]:

$$HCOOH \rightarrow CO_2 + 2H^+ + 2e^- \tag{11.12}$$

$$HCOOH \rightarrow CO_{ads} + H_2O \rightarrow CO_2 + 2H^+ + 2e^- \tag{11.13}$$

In electrochemical studies, the current peaks in the forward scan are usually ascribed to the oxidation of formic acid via the dehydrogenation pathway (Equation 11.12) and oxidation of carbon monoxide formed via the dehydration (Equation 11.13). The current peak in the reverse scan may be attributed to the direct oxidation of formic acid and the removal of the incompletely oxidized carbonaceous species, such as CO, $HCOO^-$, and HCO^-, accumulated on the surface of catalyst during the forward scan. Similar to the MOR, the ratio of the forward and backward peak currents, I_f/I_b, can also be used to qualitatively estimate the CO tolerance of the catalyst. Enhanced electrocatalytic activity of formic acid oxidation has been achieved on graphene-supported catalysts compared to commercial Pd/C, Pt/C, or other carbon-material-supported catalysts by engineering the morphology and composition of the materials [12, 20, 25, 27–31].

11.2.4 Direct Alcohol Fuel Cells (DAFCs) and Biofuel Cells

Direct alcohol fuel cells (DAFCs) have also been attracting increasing interest owing to their higher theoretical energy density combined with the less toxicity of ethanol than methanol. The reaction mechanism of ethanol oxidation on Pt-based electrocatalysts is complex. According to the proposed mechanism, acetaldehyde, acetic acid, or CO_2 can be formed through different reaction pathways. It has been found that the catalytic activities of Pd-based electrocatalysts for the alcohol oxidation reaction (AOR) are prominent only in alkaline media. The reaction mechanism of ethanol oxidation on Pd in alkaline media was proposed as the following [32]:

$$Pd + CH_3CH_2OH + 3OH^- \rightarrow Pd-CH_3CO_{ads} + 3H_2O + 3e^- \quad (11.14)$$

$$Pd + OH^- \leftrightarrow Pd-OH_{ads} + e^- \quad (11.15)$$

$$Pd-CH_3CO_{ads} + Pd-OH_{ads} \rightarrow Pd-CH_3COOH + Pd \quad (11.16)$$

It was suggested that Equation 11.16 is the rate-determining step. To date, various graphene-supported metal materials have been successfully designed as electrocatalysts for DAFCs [33–36].

In recent years, biochemical fuel cells have attracted much attention as a novel type of clean energy source. In biochemical fuel cells, biocatalysts are used for conversing chemical energy to electrical energy to meet the energy needs. The chemical energy can come from Nature's solutions, even a living organism (e.g., glucose from the blood stream). Abundant organic raw materials such as methanol, organic acids, or glucose can be used as fuels for the oxidation process, and molecular oxygen or H_2O_2 can act as the oxidants to be reduced [15].

At present, PEMFC systems with lower output power (<10 kW) are primarily used in residential buildings for power, heating, and warm water as portable households applications. PEMFCs with larger output power levels (50–250 kW) are used as back-up power (secure energy supply) and low-temperature heating and premium power supply [15]. However, although substantial progress has been achieved in fuel cells, the wide commercialization and performance these cells are still limited by the high cost of and the low catalytic activities of the Pt-based catalysts, especially the sluggish electron-transfer kinetics of ORR. It should be noted that carbon supports are usually used in the state-of-the-art commercial catalysts. However, the degradation of nanocatalysts and the severe corrosion of carbon supports in a real fuel cells can lead to rapid performance loss of the catalysts. As a new member of carbon materials, graphene exhibits unique physical and chemical properties, such as large specific surface area, ultrahigh electrical conductivity, excellent mechanical properties, and high stability [37]. These extraordinary properties make graphene a type of promising catalyst support. In the last decade, various graphene-based materials have been designed and studied as electrocatalysts for fuel cells. Here, we summarize the fuel cell catalysts based on graphene-supported metal nanostructures with controllable size and shape.

11.3
Graphene-Based Metal Nanostructures as Electrocatalysts for Fuel Cells

The electrocatalysts in fuel cells are generally considered to determine the cost and the overall performance of the cells [38]. As described above, although Pt-based nanomaterials are the most active electrocatalysts for both anode and cathode reaction processes in fuel cells, the application of pure Pt catalysts are limited by its high cost, limited occurrence in nature, poor durability, and the easy self-poisoning by the carbon monoxide intermediate produced in electrode reactions. To solve these problems, one effective approach is alloying noble metals with nonprecious metals to decrease the cost and improve the tolerance toward CO species. Previous studies have revealed that alloyed metal nanocomposites show much higher electrocatalytic activities than single-metal nanomaterials. Another method is to prepare the catalysts with controlled size and shape to lower the cost and optimize the catalytic activity [39]. On the other hand, it is also accepted that the electrocatalytic performances of catalysts are strongly dependent on the surface morphology and chemical composition as well as the shape and size of the nanomaterials [38, 40]. The combination of metal nanocrystals with graphene can produce hybrid nanocatalysts with different morphologies, resulting in improved electronic conductivity and stability [14, 41].

Compared to the CNT-based supports, graphene shows the following advantages. First, the 2D structure of graphene sheets with both sides exposed to the solution leads to a larger active surface area than the 1D tube structure [42]. Second, metal NPs can be uniformly distributed on graphene-based supports, while NPs on CNTs sometimes tend to aggregate as a result of the large curvature of the CNTs wall. Moreover, compared to CNTs, the chemically converted graphene or rGO exhibits better tolerance toward CO poisoning in MOR because the remaining oxygen-containing groups on graphene surface can react and remove the carbonaceous species [22].

To date, graphene-based nanostructures with different morphologies, such as metal nanoclusters, metal NPs, core–shell, hollow, flower-like, and nanodendritic nanostructures, have been successfully prepared and investigated as fuel cell electrocatalysts. The preparation methods mainly include chemical reduction, *in situ* growth, self-assembly, electrodeposition, microwave-assisted processing, and impregnation/thermal processing, among others.

11.3.1
Graphene-Supported Metal Nanoclusters

Bulk coinage metals, such as Au, Ag, Cu, are chemically inert, which is due to their filled d bands. Their inertness leads to higher activation barriers compared to other transition metals with partially filled d bands. However, when the size of the materials is reduced to the scale of nanoclusters (NCs, <2 nm), the Au catalysts with their d band shifted closer to the Fermi level show strikingly different properties from those of bulk Au and Au NPs (2 nm < NPs < 100 nm). Moreover,

the Au nanoclusters with small size as well as a narrow d band and size distribution are favorable for O_2 adsorption, which is advantageous for the ORR in fuel cells [43, 44].

Generally, to decrease the core size and improve the stability, tiny nanoclusters have to be capped by protecting ligands, which might block the surface active sites as well as the mass and electron transfer, resulting in low electrocatalytic activities. At the same time, because of the extremely high surface energy or Gibbs free energy of small-sized particles, the surfactant-free metal nanoclusters are easy to dissolve, aggregate, and sinter during electrocatalysis. Introducing metal nanoclusters and NPs onto the surface of GNSs and other carbon supports is an effective approach to overcome these drawbacks and improve the electrochemical stability [45–48]. The hybridization between metal clusters and the sp^2 dangling bonds at the defect sites of graphene could obviously improve the stability of the composites [49]. Actually, the simplest single-carbon-vacancy defect on graphene was found to play an important role in catalyzing CO oxidation and increasing the interaction between metal clusters and graphene sheets [50]. The results from density functional theory (DFT) calculations show that metal nanoclusters supported on graphene with carbon vacancies are more stable than those on defect-free graphene [51]. Moreover, theoretical calculations predict that the hybrid nanostructures of metal nanoclusters decorated on graphene have improved catalytic activity through the enhanced charge transfer between the clusters and graphene. In fact, numerous experimental studies have shown that rGO/metal nanocluster composites display outstanding electrocatalytic performance.

A typical procedure to prepare graphene-supported metal clusters is simultaneously reducing the mixture of metal precursors and GO (graphene oxide) in a single step. Through this method, Tang and coworkers [44] successfully synthesized Au NCs/rGO hybrids with clean surfaces without using any protecting or reducing agents. In the synthesis, by ultrasonic treatment of a mixture of $HAuCl_4$ and rGO solution for 10 min, Au NCs/rGO hybrids with 1.8 nm Au nanoclusters were obtained. As shown by the scanning electron microscopy (SEM) and transmission electron microscopy (TEM) images (Figure 11.2), the monodisperse Au nanoclusters are evenly dispersed on the surface of rGO sheets. In the proposed synthetic mechanism, rGO with electron-donor property (electron donor) can strongly anchor the positive Au (III) ions (electron acceptor) and thus the gold ions can be *in situ* reduced to clusters on the surface of rGO nanosheets. In the following electrochemical studies, the obtained Au NCs/rGO composite showed excellent electrocatalytic performance toward ORR with an onset potential comparable to that of commercial Pt/C catalyst [44].

With GNSs as supports, surfactant-free Ir_xV binary alloy nanoclusters have also been successfully prepared in the presence of ethylene glycol (EG) at 120 °C for 3 h [52]. The average core diameter of the Ir_xV clusters is ~2 nm. The Ir_xV/rGO nanostructures displayed composition-dependent catalytic activities toward ORR, and the Ir_2V/rGO hybrid demonstrated the best catalytic performance in alkaline electrolyte among the studied Ir_xV/rGO hybrids with different ratios of Ir to V.

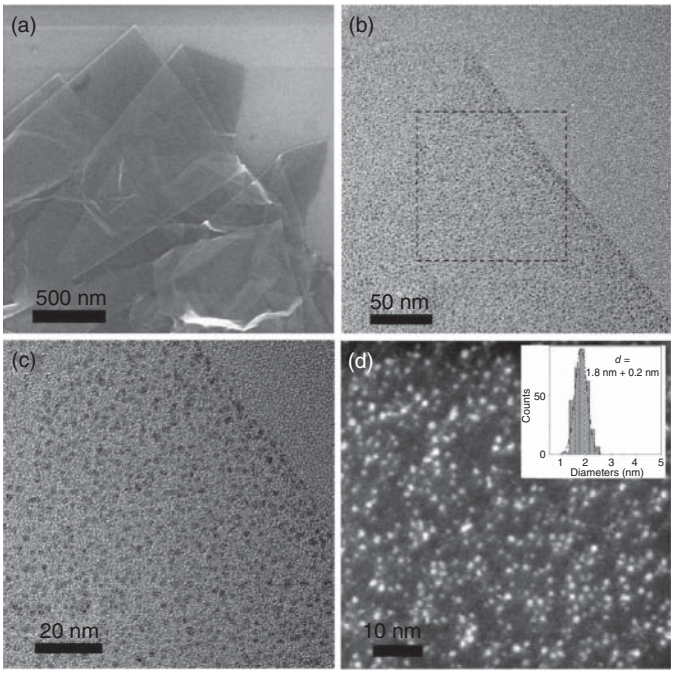

Figure 11.2 SEM (a), TEM (b,c), and HAADF (d) images of the as-synthesized Au nanoclusters decorated on reduced GO. Inset in (d) shows the size histogram of the Au nanoclusters with an average size of 1.8 ± 0.2 nm. (Reprinted with permission from Ref. [44]. Copyright (2012), American Chemical Society.)

From these studies, it can be seen that introducing metal nanoclusters onto graphene sheets could remarkably enhance their stability and electrocatalytic activity. The defect sites and oxygen functionalities on the graphene surface can provide reactive sites for the nucleation and growth of metal cluster catalysts and facilitate the *in situ* growth of graphene-supported nanocrystals.

11.3.2
Graphene-Supported Monometallic and Alloy Metal Nanoparticles (NPs)

In addition to metal nanoclusters, much work has been done on the synthesis of graphene-supported monometallic (Au [53], Pt [54–58], and Pd [27, 59]) or metal alloy (PtPd [33, 36, 60, 61], PtRu [62–64], PtAu [12, 28, 35, 65], PdAg [66, 67], PtFe [68, 69], PtCo [14, 70, 71], PtNi [72–75], PtPdAu [76, 77]) NPs and their electrocatalytic activities for fuel cells [42]. Among the alloy nanostructures, PtRu NPs have received special attention because of their high catalytic performance as both anodic and cathodic catalysts. For example, PtRu NPs decorated on graphenes (PtRu/GNs, <10 nm) were successfully prepared by Dong *et al.* [62], using the EG reduction method. Figure 11.3A,B shows the catalytic activities of the PtRu NPs supported on different carbon supports for methanol and ethanol

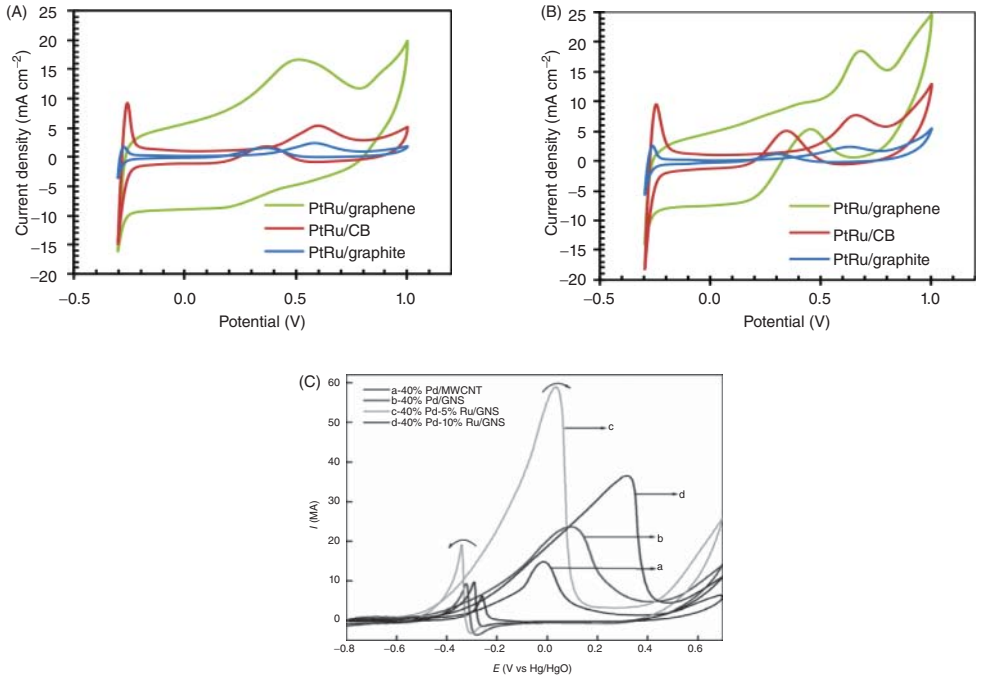

Figure 11.3 Electrocatalytic activities of PtRu NPs supported on graphene, graphite, and Vulcan XC-72R carbon black for methanol (A) and ethanol (B) oxidation in 0.5 M H_2SO_4 + 1 M CH_3OH solution (A) and 0.5 M H_2SO_4 + 1 M CH_3CH_2OH solution (B), potential scan rate 50 mV s^{-1}. (Reprinted with permission from Ref. [62]. Copyright (2010), Elsevier.) (C) CV curves of 40%Pd/MWCNT, 40%Pd/GNs, 40%Pd-5%Ru/GNs, and 40%Pd-10%Ru/GNs catalysts in 1 M KOH + 1 M CH_3OH; potential scan rate 50 mV s^{-1}. (Reprinted with permission from Ref. [64]. Copyright (2013), Elsevier.)

oxidation. Obviously, PtRu/GNs exhibit improved electrocatalytic performance compared to the PtRu catalysts supported on graphite and Vulcan XC-72R carbon black (CB). In another work, Singh and Awasthi [64] prepared PtRu/GNs composites by a microwave-assisted polyol reduction method and studied their catalytic activity for methanol electroxidation. As can be seen in Figure 11.3C, Pd supported on graphene shows more negative onset potential and higher current density for methanol oxidation in comparison with Pd supported on multiwalled carbon nanotubes (MWCNTs). And, PdRu/GNs exhibit much higher poisoning tolerance than Pd//GNs and Pd/MWCNTs.

Graphene-supported Pd and Pd-based alloy NPs have been found to have excellent catalytic activity and tolerance, especially toward CO and methanol, during the cathodic ORR process in fuel cells [78]. For example, graphene-supported monodisperse Pd NPs (4.5 nm) were synthesized by solution-phase reduction of $Pd(acac)_2$ aceylacetonate (acac) with morpholine borane in a solution mixture of oleylamine and 1-octadecene (Figure 11.4a) [27]. The Pd NPs were assembled on graphene sheets uniformly, and the Pd/GNs showed enhanced catalytic activity

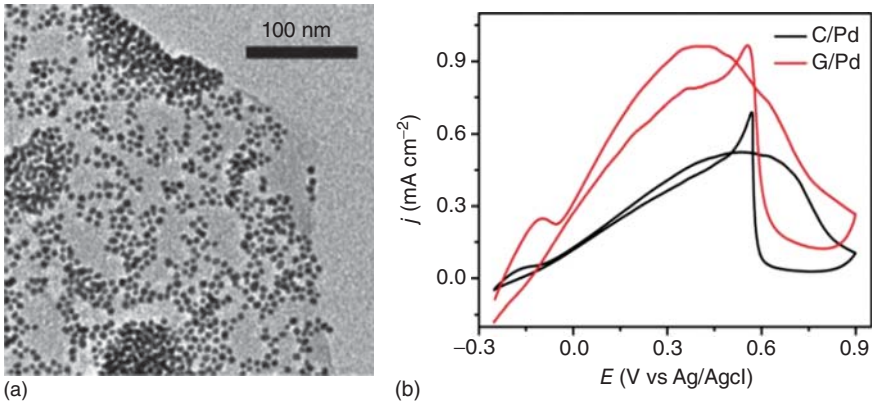

Figure 11.4 (a) TEM image of G/Pd NPs and (b) cyclic voltammograms (CVs) of FAOR catalyzed on G/Pd NP modified electrode in N_2-saturated 0.1 M $HClO_4$ + 0.1 M HCOOH solution at a scan rate of 50 mV s^{-1}. (Reprinted with permission from Ref. [27]. Copyright (2013), Royal Society of Chemistry.)

for formic acid electroxidation, as shown in Figure 11.4b. These studies demonstrate that graphene has great application potential as a support to enhance the stability and catalytic activities of metal NPs.

Zhang *et al.* [12] prepared PtAu alloy NPs decorated on GNSs (PtAu/GNs, 3.2 nm) via a facile synthesis method, using the cationic polyelectrolyte poly (diallyldimethylammonium chloride) (PDDA) as a stabilizing agent (Figure 11.5a–d). PtAu/GNs exhibited improved catalytic efficiency for formic acid oxidation compared to PtAu alloy NPs supported on CB and the commercial Etek-Pt/C catalyst. From the cyclic voltammograms (CVs) shown in Figure 11.5e, formic acid oxidation has much lower onset potentials on the PtAu/GNs and PtAu/CB than that on Etek-Pt/C. Moreover, the peak current densities obtained on PtAu/GNs (2.310 A mg_{Pt}^{-1}) and PtAu/CB (1.682 A mg_{Pt}^{-1}) are much larger than that from Etek-Pt/C (0.182 A mg_{Pt}^{-1}). The X-ray diffraction (XRD) patterns of PtAu/GN and PtAu/CB (Figure 11.5f) indicate the formation of alloy PdAu nanocrystals on GNs and CB.

Metal NPs deposited on GNSs via *in situ* growth method usually lack the desired size and morphology control, which will hamper their potential application in catalysis. The self-assembly process can provide a method to assemble uniform NPs on GNSs. For instance, in a recent work [68], FePt alloy NPs (~7 nm) were first synthesized and then assembled onto the surface of graphene (FePt/GNs) by a self-assembly method. The ORR activity of the FePt/GNs showed almost no change after 10 000 potential scans, suggesting that graphene can greatly enhance the stability and durability of metal NPs supported on it.

In addition to noble metals, metal oxide NPs supported on graphene have also been successfully fabricated and studied as ORR electrocatalysts. For example, Guo *et al.* [13] reported the assembly of Co/CoO NPs on GNs and their application as ORR catalyst for fuel cells. In another report, Cu_2O NPs

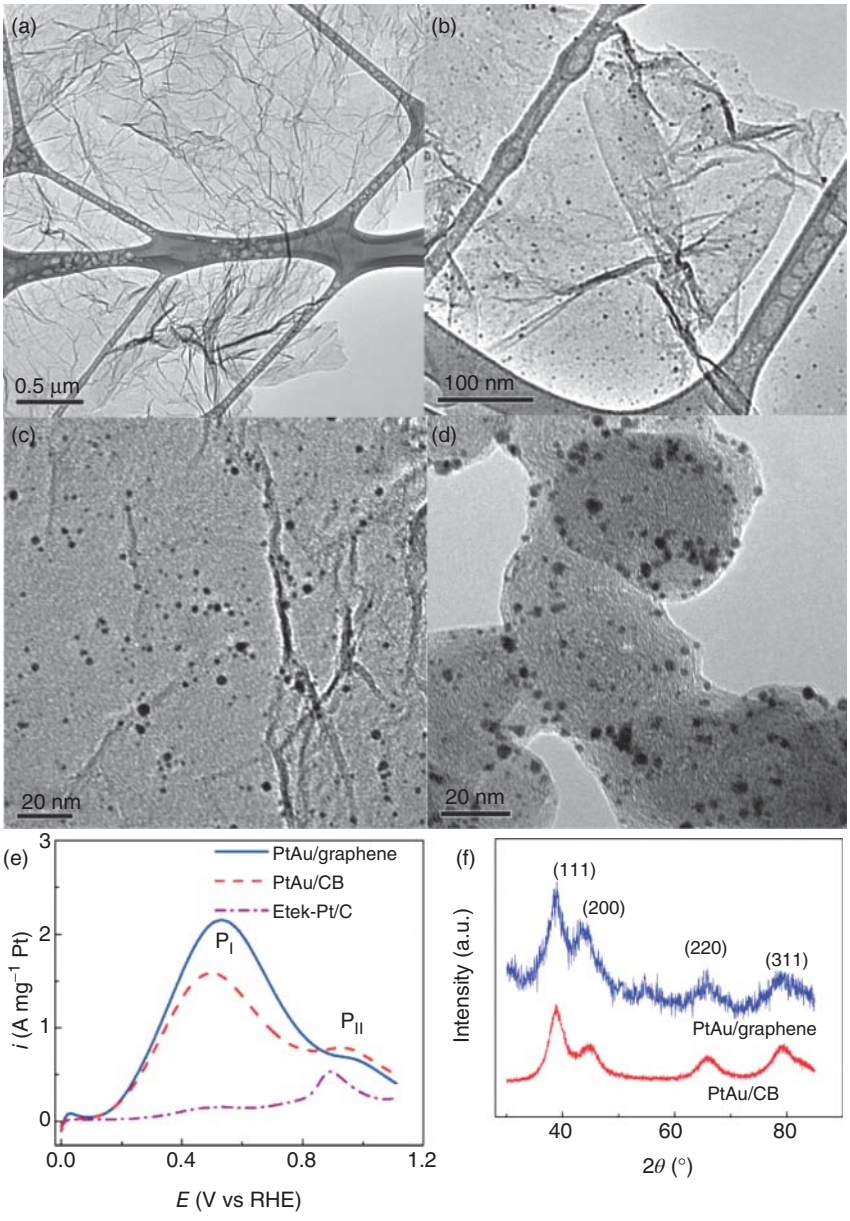

Figure 11.5 TEM images of (a) graphene nanosheets, (b,c) PtAu/GNs, and (d) PtAu/CB. (e) CV curves of formic acid oxidation on PtAu/GN, PtAu/CB, and commercial Etek-Pt/C in N_2-saturated 0.5 M H_2SO_4 + 0.5 M HCOOH solution. (f) XRD patterns of PtAu/GN and PtAu/CB. (Reprinted with permission from Ref. [12]. Copyright (2011), American Chemical Society.)

(~4 nm in diameter) dispersed on rGO (Cu_2O/rGO) were prepared with a facile method by reducing copper acetate in the presence of diethylene glycol [79]. The Cu_2O/rGO hybrid showed high catalytic activity for ORR and outstanding tolerance to methanol and CO in an alkaline medium. Other graphene-supported nanocomposites with novel structures have also been synthesized. For instance, graphene-supported noble metal and transition-metal oxide hybrids, such as Pd NPs/MnO_2 nanolamella (Pd/MNL/GNs) MnO_2 nanolamella (MNL), have been successfully synthesized by a typical EG synthetic route [29]. The obtained Pd/MNL/GNs were found to be efficient catalysts for both MOR and FAOR in fuel cells, which opens a new design opportunity for the fabrication of electrocatalysts with high catalytic performance. It should be pointed out that, at present, NP is the most common morphology that can be easily obtained and utilized. The *in situ* growth of NPs on graphene surface could maximize the contact between them and thus enhance their interaction and electrocatalytic performance for both anode and cathode reactions in fuel cells.

11.3.3
Graphene-Supported Core–shell Nanostructures

Graphene-based bimetallic core–shell nanocrystals are important candidates for future heterogeneous catalysts. Unlike doped or alloyed nanostructures, all the surface atoms of core–shell composites can be regulated and controlled to the desired active components [80]. In the core–shell heterostructures, core NPs are encapsulated and sheltered by an outside shell which prevents them from being removed and aggregating during the electrocatalytic processes. The outer metal shell is usually strained and thus can present prominent catalytic properties [81]. When applied in fuel cells, the strong electronic and ligand interactions between the core and the shell are more favorable for the electrocatalytic performance than when using monometallic materials [82]. Meanwhile, studies have also revealed that not only the core–shell/GN interactions but also the dimensions (thickness) of the core and shell play an important role in affecting the catalytic activities.

One kind of core–shell structure contains metal NPs as core and metal oxide NPs as shell. A series of Co/CoO/GN nanostructures with tunable Co size and CoO thickness were formed by exposing self-assembled Co/GNs hybrids in air for oxidation [13]. The as-synthesized Co/CoO/GNs composites exhibited comparable activity to and much better stability than the commercial Pt/C catalyst, suggesting their potential application for the ORR. Generally, core–shell nanostructures can be obtained by growing crystalline overlayers outside the core nanocrystals [83]. Besides, the core–shell structures can also be achieved by chemical leaching or electrochemical dealloying of the base metal in the catalysts [84] as well as through the impulsive galvanic replacement method [85] proposed by Adzic and Kokkinidis.

Previous studies have shown that core–shell nanomaterials with a transition metal as core and a base noble metal as shell offer many advantages. The electronic properties of the outer noble metal can be adjusted by regulating the

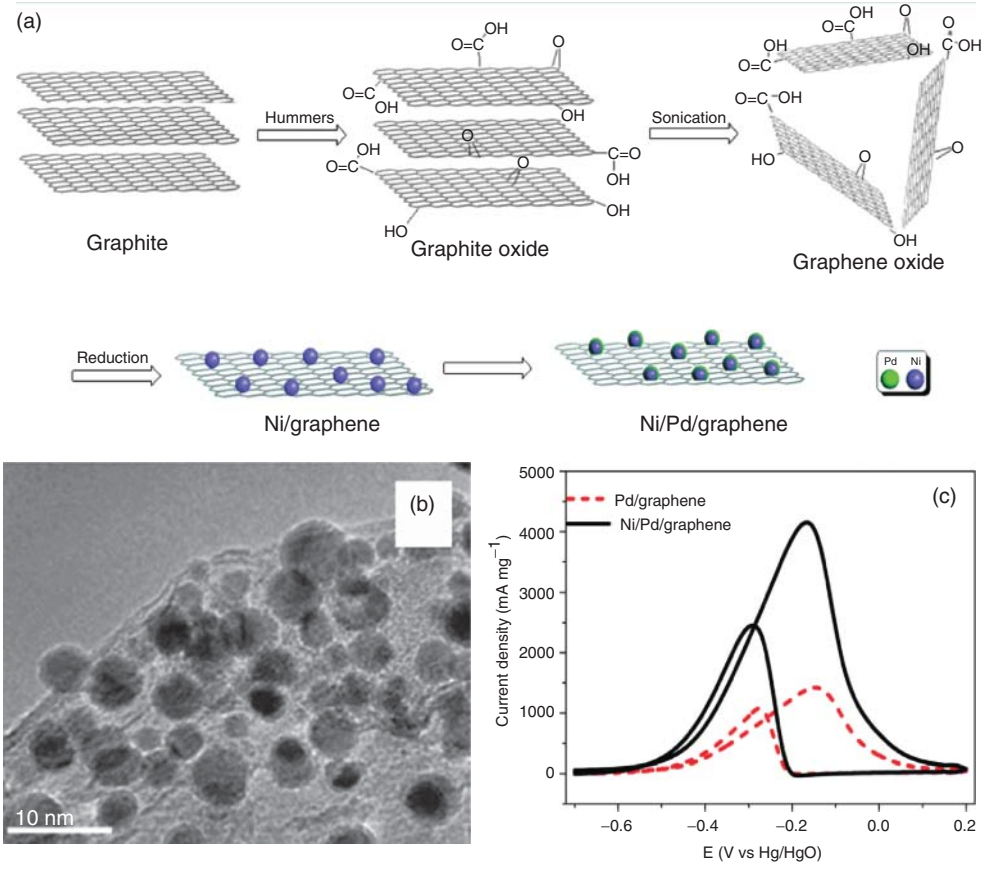

Figure 11.6 (a) Schematic illustration of the preparation process of graphene-supported Ni/Pd core–shell structures (Ni/Pd/GNs). (b) TEM image of Ni/Pd/GNs. (c) CV curves of ethanol oxidation on the Ni/Pd/GNs and Pd/GNs in 1.0 M KOH + 1.0 M ethanol solution, scanning rate: 50 mV s^{-1}. (Reprinted with permission from Ref. [85]. Copyright (2012), Royal Society of Chemistry.)

base metal content of the core. Zhang *et al.* [85] prepared graphene-supported Ni/Pd core–shell structures (Ni/Pd/GN, 4 nm) via a two-step process combining the microwave synthesis and a galvanic replacement procedure, as shown in Figure 11.6a. In the synthesis, the mixture of graphite oxide in EG solution and nickel nitrate was subjected to microwave (MW) heating in a microwave oven. The obtained Ni/graphene compound was then isolated and added to the H_2PdCl_4 solution under stirring for 14 h, resulting in well-dispersed Ni/Pd core–shell NPs on graphene. From the TEM characterization (Figure 11.6b), the formed core–shell structures were found to be uniformly dispersed on GNSs. The electrochemical measurements (Figure 11.6c) showed that the peak current density of ethanol oxidation on the obtained Ni/Pd/GNs was three times higher than that of the Pd/GN electrocatalyst with the same Pd loading.

Core–shell nanocrystals with thin or porous shells are desired for application in catalysis. The porous shell facilitates the elecrocatalysis process and provides free access of chemical species and electrolyte from the outside to the core surface inside [86]. Therefore, the electrocatalytic activity of graphene-supported core–shell nanostructures can be improved by optimizing the shell structure.

11.3.4 Graphene-Supported Hollow Nanostructures

Since the electrocatalysis processes occur on the surface atoms of catalysts, the large quantities of bulk atoms inside materials are actually not involved in the catalysis reactions. Therefore, noble metal materials with a hollow structure attract great interest as electrocatalysts for fuel cells, which will largely reduce the loading of precious metals and at the same time bring about enhanced catalytic activity compared to bulk catalysts [38]. The hollow nanostructures have the advantages of enhanced surface area, low density, and efficient utilization of noble metals. Similar to the hollow structure, the ring-like structure can greatly increase the active surface area because both exterior and interior surfaces can be utilized for catalytic reactions [38, 87]. Another kind of hollow nanostructures with a porous shell could also greatly increase the active surface area for catalytic process and decrease the cost of the noble metals. Generally, hollow nanostructures could be prepared by hard-template and soft-template methods. The hard-template method involves the tedious and complicated preparation and removal of the template before and after the synthesis, which may destroy the as-prepared hollow nanostructures. The soft-template method involves the addition of some specific surfactants, which might cause the formation of byproducts. The introduction of impurities further makes the products unsuitable for applications [88].

Recently, the galvanic replacement reaction was reported as an efficient route to prepare hollow nanostructures by using base metals such as, Fe, Co, or Ag as sacrificial templates. For instance, the standard reduction potentials of Ag^{+}/Ag and Pd^{2+}/Pd are +0.7991 and +0.915 V (vs normal hydrogen electrode (NHE)), respectively. Based on the different reduction potentials, PdAg hollow nanorings have been prepared via a galvanic replacement reaction between Pd^{2+} and the Ag NPs on GNs [38]. In the preparation, graphene-supported Ag NPs (Ag/GNs) were first synthesized by refluxing the mixture of $AgNO_3$ and GO solution in the presence of sodium citrate (reducing agent). The oxygen functional groups on the GO surface work as nucleation sites and facilitate the seeding and *in situ* growth of Ag NPs. The highly crystalline ring-shaped nanocrystals can be observed clearly in the high-resolution TEM (HRTEM) images (Figure 11.7a,b). Figure 11.7c–e shows the elemental mapping images, indicating that Ag and Pd are evenly distributed in the shell of the nanorings. The as-synthesized PdAg nanorings supported on graphene exhibited excellent methanol tolerance in ORR process, which provides a promising way for the preparation of methanol-tolerant cathode catalysts for fuel cells.

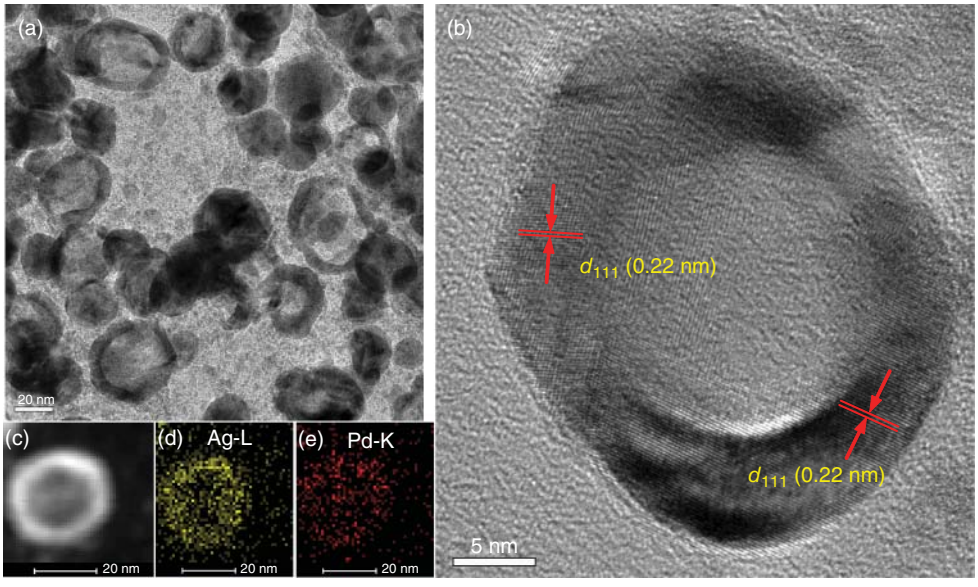

Figure 11.7 High-resolution TEM micrographs (a,b) of the as-prepared PdAg nanorings supported on GNs at different magnifications. (c) High-angle annular dark field (HAADF) micrograph of single PdAg nanoring and (d,e) the corresponding elemental mapping for Ag and Pd. (Reprinted with permission from Ref. [38]. Copyright (2013), Wiley-VCH.)

In another study, Pt hollow nanostructures were *in situ* grown on GNSs (Pt–H–GNs), by using the galvanic replacement reaction between $PtCl_6^{2-}$ and Co/GNs hybrids. Because the standard reduction potential of $PtCl_6^{2-}$/Pt (0.735 V vs standard hydrogen electrode (SHE)) is much higher than that of the Co^{2+}/Co (0.277 V vs SHE), Co NPs predeposited on GNSs can be easily depleted and replaced by assembled Pt NPs with hollow morphology. The synergetic effect between Pt hollow structures and the graphene support could enhance the electrocatalytic activities for the anodic methanol oxidation [89]. Hollow ternary Pt/Pd/Cu nanoboxes supported on a porous 3D GN framework (PtPdCu/3DGF) have been developed via a novel dual solvothermal route by Hu *et al.* [34]. Similarly, 3DGF-supported PdCu nanocubes (PdCu/3DGF) were first prepared as core via a solvothermal treatment in EG at 160 °C. And the ternary Pt/PdCu/3DGF structure was then obtained by heating the mixture of PdCu/3DGF and H_2PtCl_6 solution in EG at 160 °C for another 3 h. The as-prepared 3D porous hybrid materials were found to be efficient ethanol oxidation electrocatalysts [34].

The galvanic replacement method provides a rapid, simple, effective, high-quality, and reproducible process for synthesizing hollow structures without posttreatment [65, 88]. Graphene-supported hollow-like metal electrocatalysts obtained through this way can efficiently utilize the surface of the materials and thus largely decrease the use of noble metals, which are beneficial for their application in fuel cell catalysts.

11.3.5
Graphene-Supported Cubic Nanostructures

Since the electrocatalytic activity, selectivity, and stability of metal materials are strongly dependent on their morphologies (size, shape, composition, etc.), it is important to synthesize graphene-supported metal nanocatalysts with controlled morphology. Recently, Lu *et al.* [90] synthesized PtPd alloy nanocubes supported on reduced graphene oxide (PtPd/rGO) by a one-pot synthesis with polyvinylpyrrolidone (PVP) as the protecting agent. In the synthesis, *N*,*N*-dimethylformamide (DMF) was used as a bifunctional solvent to dissolve and reduce the metal precursors. Figure 11.8a shows the schematic diagram of the synthesis, including two steps: (i) In the first step, GO was reduced and acted as nucleation sites to anchor metal nanocrystals through the strong contact between them, and (ii) in the second,

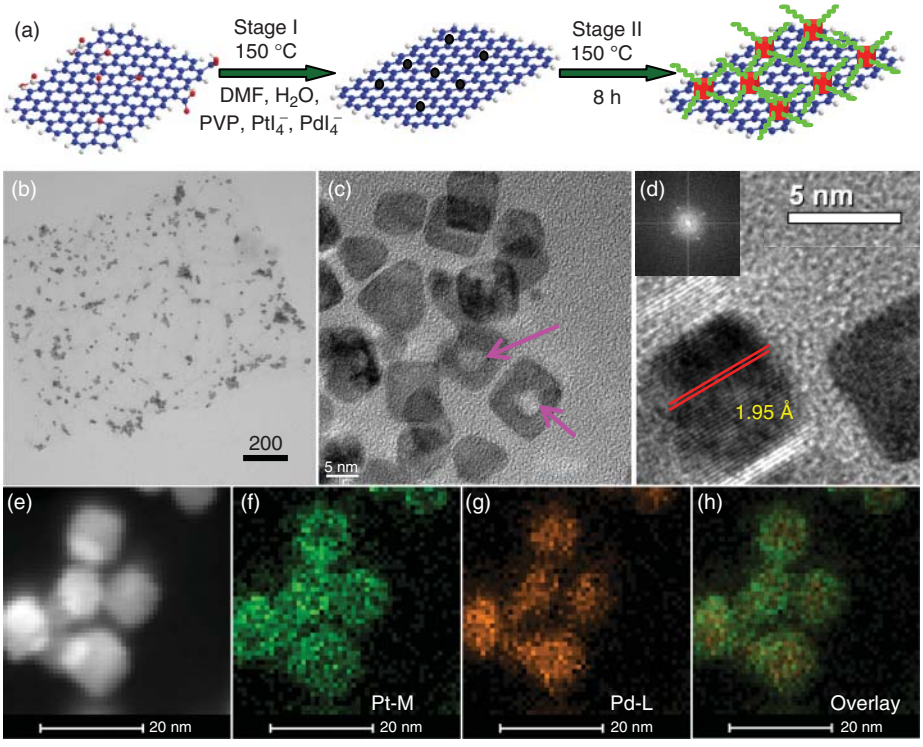

Figure 11.8 (a) Schematic diagram of the one-pot hydrothermal synthesis of rGO-supported PtPd alloy nanocubes (PtPd/rGO). (b) TEM and (c,d) HRTEM images of the PtPd/rGO at different magnifications. The inset in (d) shows the fast fourier transform (FFT) pattern of an individual PtPd nanocrystal. (e) The high-angle annular dark field scanning transmission electron microscope (HAADF-STEM) image of PtPd/rGO and the corresponding elemental mapping of (f) Pt, (g) Pd, and (h) the overlay. (Reprinted with permission from Ref. [90]. Copyright (2013), American Chemical Society.)

the formation and growth of nuclei into a cubic shape took place in the presence of PVP. Figure 11.8b–h shows the TEM and element mapping images, revealing that 82% of PtPd nanocubes with the average size of 8.5 nm are uniformly dispersed on the rGO surface. The obtained PtPd/rGO composite displayed enhanced electrocatalytic performance for MOR compared to the unsupported PtPd alloy nanocubes and commercial Pt/C, including improved ECSA, larger current density, and more negative onset potential. Moreover, the PtPd/rGO showed much enhanced stability and durability during the methanol oxidation process, indicating that graphene sheets can act as excellent catalyst supports for enhancing the electrocatalytic performance and durability of electrocatalysts.

Besides, the cube-like nanomaterials can also be prepared by other methods. For instance, the cubic PtPd/rGO nanostructures were synthesized via another one-pot but surfactant-free method by using DMF as the solvent and reducing agent to reduce GO and the metal precursors [61]. Well-dispersed Cu nanocubes on graphene paper (Cu-GP) have been prepared by electrodeposition, in which $CuCl_2$ was deposited on GNSs at −0.4 V (vs saturated calomel electrode (SCE)) [91].

It is well documented that metal nanomaterials with exposed high-index facets have enhanced catalytic performance [92]. Therefore, by coupling metal nanocrystals with high-index facets to GNSs, their electrocatalytic performance may be enhanced. Lu *et al.* [93] demonstrated the formation of graphene-supported PtPd alloy concave nanocubes (C-PtPd/rGO) via a facile one-pot hydrothermal synthetic strategy. To prepare C-PtPd/rGO, a mixture of K_2PtCl_4 and Na_2PdCl_4 in the molar ratio of 1 : 1, PVP, NaI, and GO in DMF solution was placed in a Teflon-lined stainless steel autoclave and reacted at 130 °C for 5 h. As shown in Figure 11.9, PtPd alloy concave nanocubes with an average size of 13.8 nm could be easily tailored via the hydrothermal process in the presence of GO. Here, GO plays an important role in the formation of C-PtPd/rGO not only as a support but also as a morphology-directing agent because of the various functional groups on its surface. In sharp contrast, only PtPd alloy nanocubes were obtained in the absence of GO. The HRTEM image (Figure 11.9d) clearly indicates the presence of the {730} high-index facet. The obtained C-PtPd/rGO material exhibited enhanced electrocatalytic activity and high durability toward MOR. For instance, the peak current density from MOR was up to 381 mA mg^{-1}, which is nearly four times higher than that of the commercial Pt/C catalyst. Besides, after 1000 voltammetric cycles, the ECSA of the C-PtPd/rGO displayed only 9.96% loss, and there was no loss in the peak current density for MOR. The improved electrocatalytic performance could be due to the high-index facets exposed on the surface and the strong interaction between the graphene support and catalysts [93].

11.3.6
Graphene-Supported Nanowires and Nanorods

Two-dimensional (2D) nanowire (NW) and nanorod materials have received increasing attention as electrocatalysts in fuel cells, such as PtPd [94], FePt [95], FePtPd [96], Pd/FePt [97], CoPt [95], AuPtPd [77], and PdAg [98], for ORR [95],

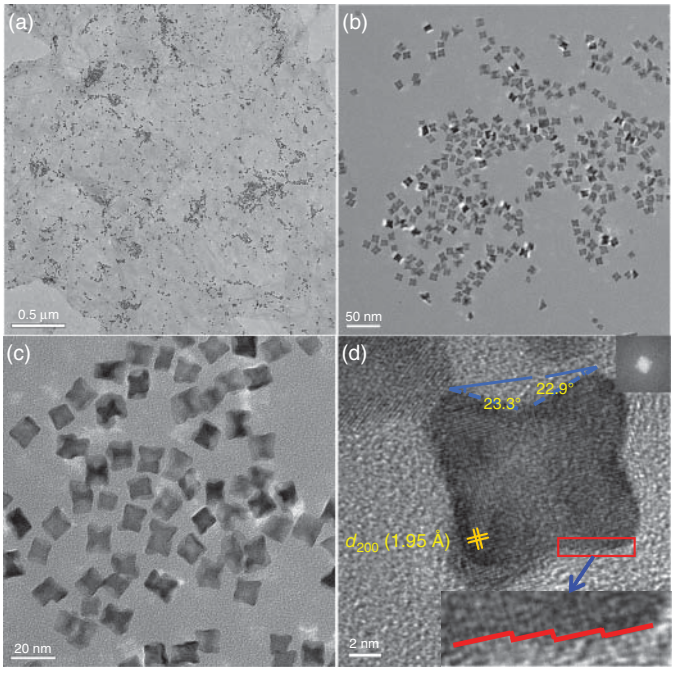

Figure 11.9 (a,b) TEM images of the as-synthesized C-PtPd/rGO at different magnifications. (c,d) HRTEM images of the C-PtPd/rGO at different magnifications. The inset in the top right of (d) is the FFT pattern of the concave nanocube, and the inset at the bottom shows a zoomed-in image of the selected area marked by the red rectangle in (d). (Reprinted with permission from Ref. [93]. Copyright (2014), Royal Society of Chemistry.)

ethanol oxidation reaction (EOR) [77], and FAOR [98] processes. The successful synthesis of branched platinum nanowires supported on rGO (BPtNW/rGO) was demonstrated through a facile one-step wet chemical reduction approach by using HCOOH as reducing agent without adding any surfactant [30]. As shown in Figure 11.10, the formed Pt nanowires have a diameter of 3–4 nm and a length about 5–20 nm, which can be affected by the addition of different Pt precursors. The BPtNW/rGO composite exhibited much higher mass and specific activities than commercial Pt/C for methanol oxidation. Hu *et al.* [99] also prepared ternary Pd_2/PtFe NWs supported on 3D graphene (Pd_2/PtFe/3DGF) for FAOR in an acid electrolyte. The Pd_2/PtFe/3DGF was prepared via a dual solvothermal method, which included two steps. First, PtFe NWs with tens of nanometers in length and 2–5 nm in diameter were fabricated on graphene sheets. Pd was then deposited onto the PtFe/3DGF composites. In the electrocatalytic measurements of formic acid oxidation on the Pd_2/PtFe/3DGF catalyst, two current peaks were observed in both the forward and backward directions, which can be attributed to the FAOR characteristics of both PtFe and Pd. Such results indicate the favorably synergetic effect between PtFe and Pd. Moreover, Pd_2/PtFe/3DGF exhibited the

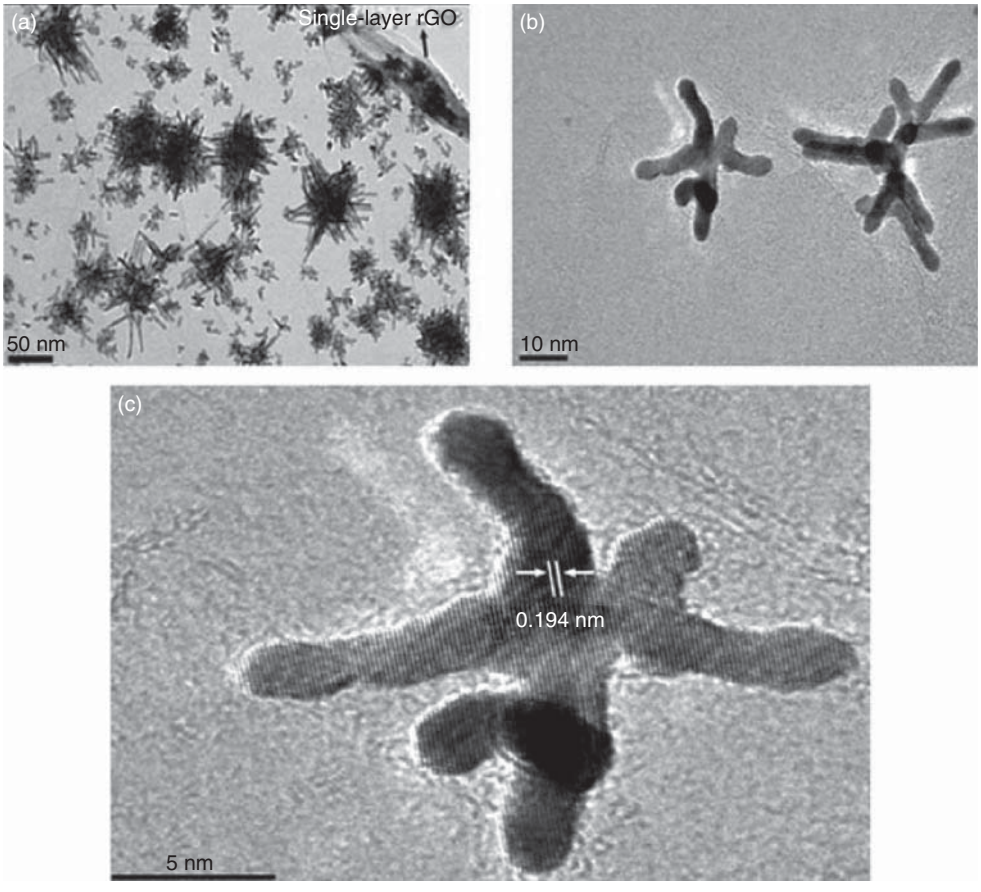

Figure 11.10 TEM (a,b) and HRTEM (c) images of the BPtNW/rGO hybrids at different magnifications. (Reprinted with permission from Ref. [30]. Copyright (2012), Royal Society of Chemistry.)

lowest onset potential, the largest oxidation current, and the highest stability for formic acid oxidation among all the catalysts studied.

Graphene-supported metal oxide nanostructures have also been fabricated and investigated as catalysts for ORR [100]. Wu *et al.* [101] prepared graphene-supported manganese oxides (MnO_2/G) with different crystalline structures and morphologies. The effects of the MnO_2 structures on the ORR catalytic activities were also studied. It was found that the electrocatalytic performances of the MnO_2/G hybrids for ORR decreased in the sequence α-MnO_2 nanowires > amorphous MnO_x NPs > β-MnO_2 microprisms. Among these materials, α-MnO_2 nanowires have the highest catalytic property for O_2 reduction reaction via a four-electron pathway and the highest durability in alkaline solutions.

Furthermore, it was found that the doping of Cu or Ni in MnO_2 catalysts can lower the activation energy and improve their ORR performance [102]. The RRDE results revealed that the electron transfer numbers are 3.5, 3.4, and 3.1, respectively, for ORR on Ni/α-MnO_2, Cu/α-MnO_2, and α-MnO_2 nanowires. All the electrochemical results indicate that the electrocatalytic activities for ORR decrease in the order Ni/α-MnO_2 > Cu/α-MnO_2 > α-MnO_2. The Ni-doped α-MnO_2 hybrid materials exhibited the highest catalytic activity for ORR with a half-wave potential comparable to that of commercial 20% Pt/C catalyst but with a much higher stability than Pt/C.

In addition to graphene-supported nanowire structures, metal nanorods supported on graphene have also been fabricated and their catalytic activities for both anode and cathode reactions have been studied. For instance, by taking advantage of the positively charged gold and Au/PtAg nanorods, the metal nanorods can be self-assembled on the negatively charged graphene sheets to form Au/PtAg nanorod/graphene hybrids [103]. As a kind of anode catalyst, the Au/PtAg/GN hybrids showed higher catalytic activity and electrochemical stability toward MOR than pure Au/Pt and Au/AgPt alloy nanorods. In another work, highly uniform Co_3O_4 nanorods supported on reduced graphene oxide (Co_3O_4/rGO) were prepared through a simple hydrothermal process. As a class of cathode electrocatalyst, the Co_3O_4/rGO hybrids showed outstanding catalytic performance toward ORR [104].

Graphene-based 2D nanowires and nanorods, especially with the compositions of binary or ternary alloys, could decrease the use of noble metals and enhance the stability of eletrocatalysts. Notably, transition-metal oxide nanowires or nanorods supported on graphene with excellent electrocatalytic activities hold a promising application as fuel cell catalysts because of their low cost and high durability.

11.3.7
Graphene-Supported Flower-Like Nanostructures

The highly rough external surface of flower-like and nanodendrite structures can provide high surface area and may significantly increase their electrocatalytic performance as fuel cell catalysts [31, 105]. Hoefelmeyer *et al.* [106] proposed a "seeded growth" mechanism for the formation of flower-like Rh NPs. By using a one-pot chemical reduction method, Chen and coworkers [107] synthesized a Pt nanoflower nanostructure supported on 3D graphene oxide (PtNF/GO) with high yield and good size monodispersity. The formation process and mechanism of the flower-like PtNF/GO nanostructures were proposed by the authors. In the synthesis, GO acted as a stabilizer to avoid the aggregation of PtNFs, and ethanol was used as both the reducing agent and dispersant. It was suggested that the reduction of $PtCl_4^{2-}$ on the Pt nanocrystals formed in the early stage leads to the formation of Pt nanoflowers. The as-prepared PtNF/GO hybrids exhibited improved electrocatalytic activities for MOR with larger ECSA, lower onset potential, higher I_f/I_b ratio, and larger methanol oxidation current in comparison with the Pt black catalyst. Recently, Wang *et al.* [108] reported

a simple and efficient method to fabricate flower-shaped Pd NPs supported on graphene (FSPd/GN, 20–30 nm) via a mild stirring process in an ice bath without adding any reducing agent. Under gentle stirring, FSPd NPs were formed at the nucleation sites instead of single particles. The role graphene played in the FSPd/GN synthesis process was also investigated. It was found that, with decreasing GO concentration, the size of Pt NPs increases, even resulting in aggregates. Moreover, without the presence of GO, no Pd NP or nanoflower could be formed in the synthesis. The FSPd/GN composite showed remarkable electrocatalytic performance for ORR and the glucose oxidation reaction.

Flower-like Au NPs supported on reduced graphene oxide (Au NP/rGO) were also prepared by a facile, one-pot, green approach using regenerated silk fibroin (RSF) as both a reducing agent for GO and $AuCl_4^-$ and a bonding agent for anchoring Au NPs onto the surface of rGO sheets [109]. Figure 11.11 shows SEM (a,b), TEM (c,d), and HRTEM (e) images of the Au NP/rGO hybrids at a reaction time of 5 min. It can be seen that the rGO-supported flower-like Au NPs have

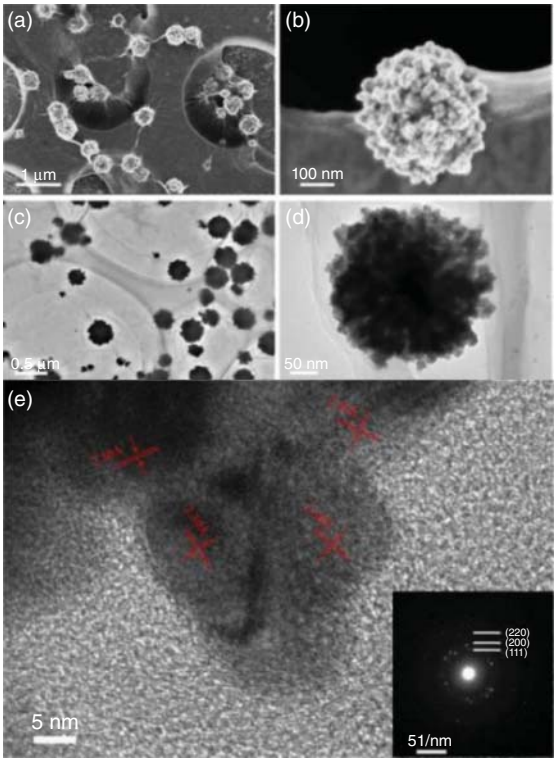

Figure 11.11 SEM (a,b), TEM (c,d), and HRTEM (e) images of flower-like Au NPs supported on rGO sheets at a reaction time of 5 min. The lattice spacing of 2.30 Å can be indexed to the (111) facet of Au. The inset of (e) is the select area electron diffraction (SAED) pattern of flower-like Au NPs. (Reprinted with permission from Ref. [109]. Copyright (2013), American Chemical Society.)

a size of 200–300 nm with rough surfaces, which is composed of 10-nm NPs (Figure 11.11e). The size of the Au nanoflowers is dependent on the reaction time and temperature. The electrochemical experiments indicated that the Au NP/rGO hybrids have excellent catalytic performance toward ORR.

Bimetallic flower-like PtAu NPs supported on graphene (PtAu/GN) nanostructures were successfully prepared by the simultaneous electrodeposition of Pt and Au precursors onto a graphene-decorated glass carbon electrode (GCE) [110]. The morphology, composition, and electrocatalytic activity of the PtAu/GN nanostructures could be easily tailored by varying the molar ratio between the Pt and Au precursors. The PtAu/GN hybrid with the Pt/Au ratio of 2 : 1 showed the highest catalytic activity toward ORR and MOR because of the synergistic role of the Au and Pt. Meanwhile, graphene played a significant role in enhancing the electrocatalytic performance and the long-term durability of the catalyst.

A low-cost bimetallic FePt flower-like nanocluster uniformly dispersed on rGO (FePt/rGO) with the average size of 4 nm was synthesized by solvothermal technique using EG/water as both the reducing agent and solvent without any surfactant [111]. The morphology of the FePt/rGO nanostructures could be adjusted by simply controlling the GO concentration. At a lower GO concentration, FePt/rGO hybrids with a flower-like shape could be formed. However, only NPs were obtained at a higher GO concentration. Markedly, FePt NPs or nanoclusters were homogeneously dispersed on rGO sheets, and no aggregation was observed. These results reveal the important role of graphene in the synthesis. The as-synthesized flower-like FePt/rGO hybrids showed remarkably higher electrocatalytic performance and enhanced durability for ORR compared to the FePt NPs supported on rGO and 60% commercial Pt/C catalyst.

From the above, it can be seen that flower-like nanostructures supported on graphene with the advantage of 3D nanostructures show substantial promise as electrocatalysts with lower cost, increased surface area, and higher electrocatalytic activity compared to commercial Pt/C catalysts.

11.3.8
Graphene-Supported Nanodendrites

Some dendrite-like nanostructures and their properties have been reported, such as Au/GNs with Raman enhancement effect and PtAu bimetallic dendritic NPs with high catalytic properties [112, 113]. Three-dimensional Pt-on-Pd bimetallic nanodendrites supported on PVP-functionalized GNSs (TP-BNGN) with the average size of 15 nm have been successfully fabricated via a wet-chemical procedure [21]. As shown in Figure 11.12, in this study, small single-crystal Pt nanobranches supported on porous Pd nanocrystals were directly grown onto the surface of GNSs. By simply tuning the synthesis parameters, such as the concentrations of graphene and the Pt precursor, the number of nanobranches of TP-BNGN and thus the electrocatalytic properties could be easily controlled. It was found that the Pd seeds play an important role in forming the dendritic nanostructure. The growth of Pt branches can probably be attributed to the

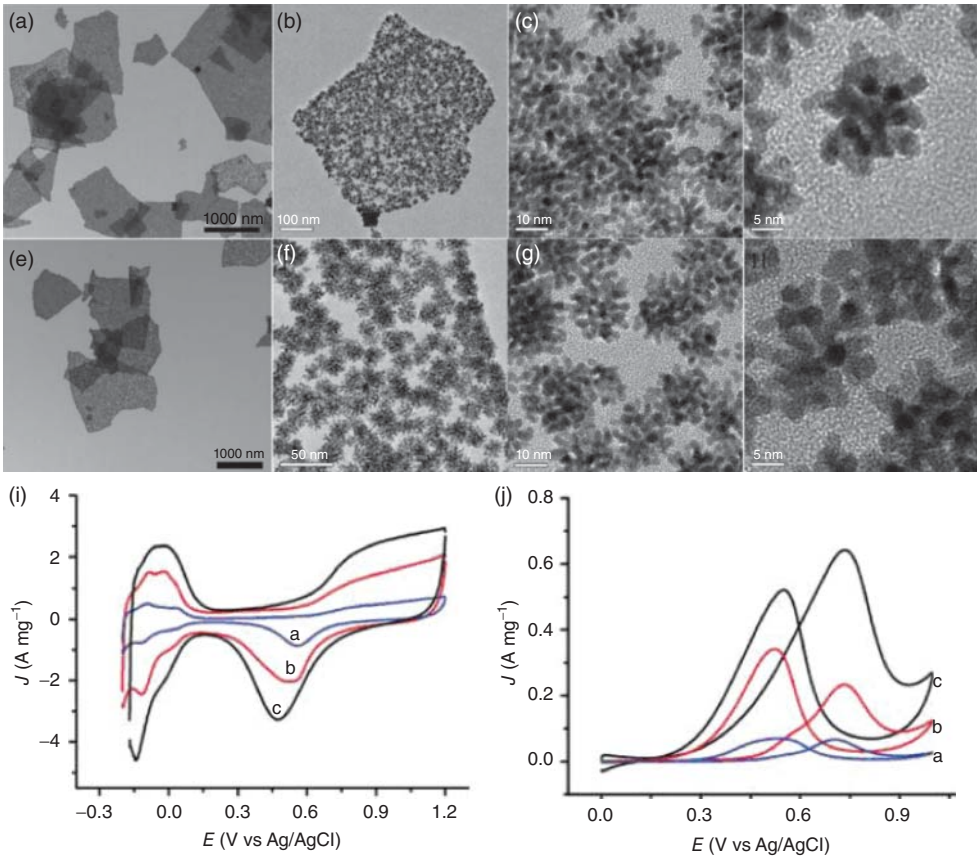

Figure 11.12 TEM images of the TP-BNGN with lower (A–D) and higher (E–H) concentration of K_2PtCl_4 at different magnifications. (I) CVs of platinum black (PB) (blue), E-TEK catalyst (red), and TP-BNGN (black) modified GC electrodes (GCEs) in a N_2-naturated 0.5 M H_2SO_4 solution at the scan rate of 20 mV s^{-1}. (J) CVs of PB (blue), E-TEK catalyst (red), and TP-BNGN (black) modified GCEs in a 0.5 M H_2SO_4 + 1 M CH_3OH at the scan rate of 50 mV s^{-1}. (Reprinted with permission from Ref. [21]. Copyright (2010), American Chemical Society.)

high reduction rate and (111) facet epitaxial growth of Pt mediated by Pd seeds with (111) facets. Most importantly, the electrochemical results (Figure 11.12I,J) demonstrate that the as-prepared TP-BNGN hybrids have superior electrocatalytic activity for MOR compared to the commercial E-TEK Pt/C and Pt black catalysts. The high-index facets of the nanodendrite catalyst may also contribute to its high electrocatalytic activity.

Graphene-based nanodendrites with well-defined morphology of metal nanobranches can be formed as a result of the different growth rates of two different metals along a specific crystal face. The design of the dendritic morphology could efficiently increase the electrocatalytic activity of graphene-based catalysts.

11.3.9
Other Graphene-Supported 2D or 3D Nanostructures

In recent years, 2D and 3D nanostructured materials have been used in many fields, such as energy storage and conversion and chemical sensors. Recently, a novel, bendable N-doped graphene/CNT/Co_3O_4 paper was prepared on a large scale through a self-assembly method and a hydrothermal treatment process [114]. The N-doped graphene/CNT/Co_3O_4 paper acted as a promising electrocatalyst toward oxygen reduction with long-term durability and excellent tolerance to methanol poisoning. The excellent electrocatalytic activities might be due to the synergistic effects of three components. In the hybrid, CNTs existing between GNSs can efficiently prevent graphene from restacking and increase the basal spacing as well as the electrical conductivity.

Currently, the three-dimensional porous graphene framework (3DGF) with abundant macropores has been attracting huge interest because of its unique structure and properties [34, 115–117]. The efficient dispersion of catalysts on porous 3DGF and the multidimensional electron/mass transport pathways due to the rich macroporosity of 3DGF network could enhance the catalytic activity for both anode and cathode reactions [59, 115]. Wang *et al.* [59] studied the catalytic activity of Pd NPs supported on three-dimensional reduced graphene oxide (Pd/TRGO) for formic acid electroxidation. Compared to Pd NPs supported on CB, the Pd/TRGO composite exhibited enhanced catalytic activity with much higher current density of FAOR.

In another work, Wu and coworkers [115] successfully synthesized Fe_3O_4 NPs supported on 3D graphene aerogel hybrids (Fe_3O_4/N-GAs) through hydrothermal assembly and thermal treatment, as shown in Figure 11.13A. Compared to Fe_3O_4 NPs supported on N-doped CB and N-doped graphene sheets, Fe_3O_4/N-GAs showed a more positive onset potential as well as higher cathodic current density and electron transfer number for the ORR in alkaline medium (Figure 11.13B,C).

11.4
Conclusions

In this chapter, we summarized graphene-supported nanostructures as electrocatalysts for fuel cells. The properties of these hybrid electrocatalysts can be tailored by controlling the size, shape, and composition of the nanomaterials. The graphene-supported metal materials exhibit outstanding electrocatalytic performance for either anodic oxidation or cathodic reduction reactions in fuel cells. The excellent catalytic performance is generally attributed to the strong interaction and synergy effects between graphene and the electrocatalysts. The introduction of nanomaterials to the surface of GNSs can lower the overpotentials of many electrochemical redox reactions. Besides, as an ideal support material, graphene can not only improve the electrocatalytic performance but also greatly enhance the stability and durability of the electrocatalysts. To realize the practical application

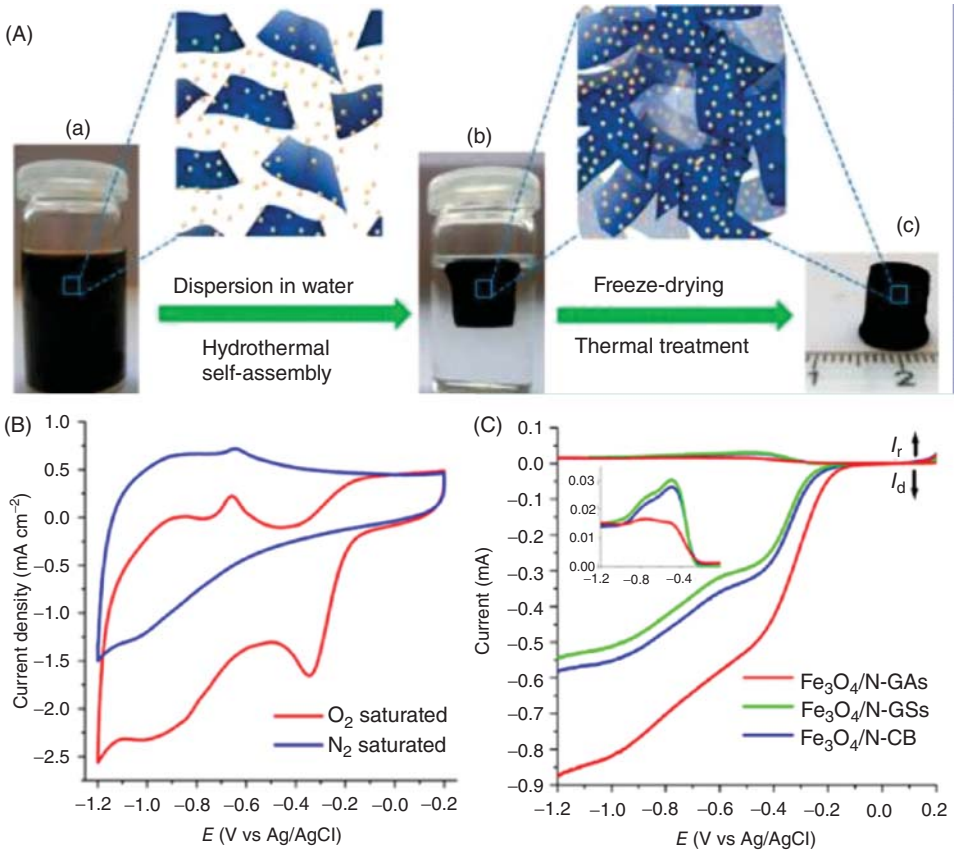

Figure 11.13 (A) Schematic diagram of the fabrication process of the 3D Fe_3O_4/N-GAs catalyst. (B) CVs of Fe_3O_4/N-GAs in N_2- and O_2-staturated 0.1 M KOH solution at a scan rate of 100 mV s^{-1}. (C) RRDE tests of the ORR on Fe_3O_4/N-GAs, Fe_3O_4/N-GSs, and Fe_3O_4/N-CB in an O_2-saturated 0.1 M KOH electrolyte at a rotation rate of 1600 rpm. The inset shows the ring current as a function of the electrode potential. (Reprinted with permission from Ref. [115]. Copyright (2012), American Chemical Society.)

of graphene-based nanostructures in fuel cells, the size and morphology of electrocatalysts on graphene need to be further investigated and optimized.

Acknowledgments

This work was supported by the National Natural Science Foundation of China (Grant Nos 21275136, 21043013) and the Natural Science Foundation of Jilin province, China (No. 201215090).

References

1. Liu, M., Zhang, R., and Chen, W. (2014) *Chem. Rev.*, **114**, 5117.
2. Liu, H., Song, C., Zhang, L., Zhang, J., Wang, H., and Wilkinson, D.P. (2006) *J. Power Sources*, **155**, 95.
3. Guo, S., Zhang, S., and Sun, S. (2013) *Angew. Chem. Int. Ed.*, **52**, 8526.
4. Huang, X., Qi, X., Boey, F., and Zhang, H. (2012) *Chem. Soc. Rev.*, **41**, 666.
5. Tan, C., Huang, X., and Zhang, H. (2013) *Mater. Today*, **16**, 29.
6. Novoselov, K.S., Geim, A.K., Morozov, S.V., Jiang, D., Zhang, Y., Dubonos, S.V., Grigorieva, I.V., and Firsov, A.A. (2004) *Science*, **306**, 666.
7. Wang, H., Maiyalagan, T., and Wang, X. (2012) *ACS Catal.*, **2**, 781.
8. Wang, D.-W. and Su, D. (2014) *Energy Environ. Sci.*, **7**, 576.
9. Chen, D., Tang, L., and Li, J. (2010) *Chem. Soc. Rev.*, **39**, 3157.
10. Tan, Y., Xu, C., Chen, G., Zheng, N., and Xie, Q. (2012) *Energy Environ. Sci.*, **5**, 6923.
11. Tang, Q., Zhou, Z., and Chen, Z.F. (2013) *Nanoscale*, **5**, 4541.
12. Zhang, S., Shao, Y., Liao, H.-G., Liu, J., Aksay, I.A., Yin, G., and Lin, Y. (2011) *Chem. Mater.*, **23**, 1079.
13. Guo, S.J., Zhang, S., Wu, L.H., and Sun, S.H. (2012) *Angew. Chem. Int. Ed.*, **51**, 11770.
14. Wang, Y., Yuan, R., Chai, Y., Yuan, Y., Bai, L., and Liao, Y. (2011) *Biosens. Bioelectron.*, **30**, 61.
15. Vielstich, W., Lamm, A., and Gasteiger, H.A. (2003) *Handbook of Fuel Cells: Fundamentals, Technology, and Applications*, John Wiley & Sons, Ltd, Chichester, Hoboken, NJ, p. 4v.
16. Logan, B.E., Hamelers, B., Rozendal, R., Schröder, U., Keller, J., Freguia, S., Aelterman, P., Verstraete, W., and Rabaey, K. (2006) *Environ. Sci. Technol.*, **40**, 5181.
17. Liu, C., Alwarappan, S., Chen, Z., Kong, X., and Li, C.-Z. (2010) *Biosens. Bioelectron.*, **25**, 1829.
18. Wang, Y.-J., Wilkinson, D.P., and Zhang, J. (2011) *Chem. Rev.*, **111**, 7625.
19. Zhang, J., Sasaki, K., Sutter, E., and Adzic, R.R. (2007) *Science*, **315**, 220.
20. Venkateswara Rao, C., Cabrera, C.R., and Ishikawa, Y. (2011) *J. Phys. Chem. C*, **115**, 21963.
21. Guo, S., Dong, S., and Wang, E. (2010) *ACS Nano*, **4**, 547.
22. Li, Y., Gao, W., Ci, L., Wang, C., and Ajayan, P.M. (2010) *Carbon*, **48**, 1124.
23. Sharma, S., Ganguly, A., Papakonstantinou, P., Miao, X., Li, M., Hutchison, J.L., Delichatsios, M., and Ukleja, S. (2010) *J. Phys. Chem. C*, **114**, 19459.
24. Jeon, I.-Y., Yu, D., Bae, S.-Y., Choi, H.-J., Chang, D.W., Dai, L., and Baek, J.-B. (2011) *Chem. Mater.*, **23**, 3987.
25. Bong, S., Uhm, S., Kim, Y.-R., Lee, J., and Kim, H. (2010) *Electrocatalysis*, **1**, 139.
26. Yu, X. and Pickup, P.G. (2008) *J. Power Sources*, **182**, 124.
27. Jin, T., Guo, S.J., Zuo, J.L., and Sun, S.H. (2013) *Nanoscale*, **5**, 160.
28. Wang, S., Wang, X., and Jiang, S.P. (2011) *Phys. Chem. Chem. Phys.*, **13**, 6883.
29. Huang, H. and Wang, X. (2013) *Phys. Chem. Chem. Phys.*, **15**, 10367.
30. Luo, Z., Yuwen, L., Bao, B., Tian, J., Zhu, X., Weng, L., and Wang, L. (2012) *J. Mater. Chem.*, **22**, 7791.
31. Chai, J., Li, F., Hu, Y., Zhang, Q., Han, D., and Niu, L. (2011) *J. Mater. Chem.*, **21**, 17922.
32. Fang, X., Wang, L., Shen, P.K., Cui, G., and Bianchini, C. (2010) *J. Power Sources*, **195**, 1375.
33. Yang, X., Yang, Q., Xu, J., and Lee, C.-S. (2012) *J. Mater. Chem.*, **22**, 8057.
34. Hu, C., Cheng, H., Zhao, Y., Hu, Y., Liu, Y., Dai, L., and Qu, L. (2012) *Adv. Mater.*, **24**, 5493.
35. Huang, Z., Zhou, H., Li, C., Zeng, F., Fu, C., and Kuang, Y. (2012) *J. Mater. Chem.*, **22**, 1781.
36. Chen, X., Cai, Z., Chen, X., and Oyama, M. (2014) *J. Mater. Chem. A*, **2**, 315.
37. Pumera, M. and Wong, C.H.A. (2013) *Chem. Soc. Rev.*, **42**, 5987.
38. Liu, M., Lu, Y., and Chen, W. (2013) *Adv. Funct. Mater.*, **23**, 1289.
39. Liang, Y., Li, Y., Wang, H., and Dai, H. (2013) *J. Am. Chem. Soc.*, **135**, 2013.

40. Varghese, B., Teo, C.H., Zhu, Y., Reddy, M.V., Chowdari, B.V.R., Wee, A.T.S., Tan, V.B.C., Lim, C.T., and Sow, C.H. (2007) *Adv. Funct. Mater.*, **17**, 1932.
41. Vasquez, Y., Sra, A.K., and Schaak, R.E. (2005) *J. Am. Chem. Soc.*, **127**, 12504.
42. Xu, C., Wang, X., and Zhu, J. (2008) *J. Phys. Chem. C*, **112**, 19841.
43. Lu, Y. and Chen, W. (2012) *Chem. Soc. Rev.*, **41**, 3594.
44. Yin, H., Tang, H., Wang, D., Gao, Y., and Tang, Z. (2012) *ACS Nano*, **6**, 8288.
45. Liu, M.M. and Chen, W. (2013) *Nanoscale*, **5**, 12558.
46. Liu, M.M., Liu, R., and Chen, W. (2013) *Biosens. Bioelectron.*, **45**, 206.
47. Wei, W.T. and Chen, W. (2012) *J. Power Sources*, **204**, 85.
48. Liu, M.M., Wei, W.T., Lu, Y.Z., Wu, H.B., and Chen, W. (2012) *Chin. J. Anal. Chem.*, **40**, 1477.
49. Yoo, E., Okada, T., Akita, T., Kohyama, M., Honma, I., and Nakamura, J. (2011) *J. Power Sources*, **196**, 110.
50. Zhou, M., Zhang, A., Dai, Z., Zhang, C., and Feng, Y.P. (2010) *J. Chem. Phys.*, **132**, 194704.
51. Yoo, E., Okata, T., Akita, T., Kohyama, M., Nakamura, J., and Honma, I. (2009) *Nano Lett.*, **9**, 2255.
52. Zhang, R.Z. and Chen, W. (2013) *J. Mater. Chem. A*, **1**, 11457.
53. Wang, F.-B., Wang, J., Shao, L., Zhao, Y., and Xia, X.-H. (2014) *Electrochem. Commun.*, **38**, 82.
54. Xu, X., Zhou, Y., Yuan, T., and Li, Y. (2013) *Electrochim. Acta*, **112**, 587.
55. Qian, Y., Wang, C., and Le, Z.-G. (2011) *Appl. Surf. Sci.*, **257**, 10758.
56. Zhou, Y.-G., Chen, J.-J., Wang, F.-B., Sheng, Z.-H., and Xia, X.-H. (2010) *Chem. Commun.*, **46**, 5951.
57. Zhu, C., Guo, S., Zhai, Y., and Dong, S. (2010) *Langmuir*, **26**, 7614.
58. Huang, H., Chen, H., Sun, D., and Wang, X. (2012) *J. Power Sources*, **204**, 46.
59. Wang, Y., Liu, H., Wang, L., Wang, H., Du, X., Wang, F., Qi, T., Lee, J.-M., and Wang, X. (2013) *J. Mater. Chem. A*, **1**, 6839.
60. Li, S.-S., Lv, J.-J., Hu, Y.-Y., Zheng, J.-N., Chen, J.-R., Wang, A.-J., and Feng, J.-J. (2014) *J. Power Sources*, **247**, 213.
61. Chen, X., Cai, Z., Chen, X., and Oyama, M. (2014) *Carbon*, **66**, 387.
62. Dong, L., Gari, R.R.S., Li, Z., Craig, M.M., and Hou, S. (2010) *Carbon*, **48**, 781.
63. Xu, X., Zhou, Y., Lu, J., Tian, X., Zhu, H., and Liu, J. (2014) *Electrochim. Acta*, **120**, 439.
64. Awasthi, R. and Singh, R.N. (2013) *Carbon*, **51**, 282.
65. Guo, S., Dong, S., and Wang, E. (2009) *J. Phys. Chem. C*, **113**, 5485.
66. Liu, J., Zhou, H., Wang, Q., Zeng, F., and Kuang, Y. (2012) *J. Mater. Sci.*, **47**, 2188.
67. Feng, L., Gao, G., Huang, P., Wang, X., Zhang, C., Zhang, J., Guo, S., and Cui, D. (2011) *Nanoscale Res. Lett.*, **6**, 1.
68. Guo, S. and Sun, S. (2012) *J. Am. Chem. Soc.*, **134**, 2492.
69. Ji, Z., Zhu, G., Shen, X., Zhou, H., Wu, C., and Wang, M. (2012) *New J. Chem.*, **36**, 1774.
70. Yan, Z., Wang, M., Huang, B., Liu, R., and Zhao, J. (2013) *Int. J. Electrochem. Sci.*, **8**, 149.
71. Yue, Q., Zhang, K., Chen, X., Wang, L., Zhao, J., Liu, J., and Jia, J. (2010) *Chem. Commun.*, **46**, 3369.
72. Wang, C., Chi, M., Wang, G., van der Vliet, D., Li, D., More, K., Wang, H.-H., Schlueter, J.A., Markovic, N.M., and Stamenkovic, V.R. (2011) *Adv. Funct. Mater.*, **21**, 147.
73. Cui, C., Gan, L., Li, H.-H., Yu, S.-H., Heggen, M., and Strasser, P. (2012) *Nano Lett.*, **12**, 5885.
74. Luo, B., Xu, S., Yan, X., and Xue, Q. (2013) *J. Electrochem. Soc.*, **160**, F262.
75. Zhang, K., Yue, Q., Chen, G., Zhai, Y., Wang, L., Wang, H., Zhao, J., Liu, J., Jia, J., and Li, H. (2011) *J. Phys. Chem. C*, **115**, 379.
76. Zhang, Y., Gu, Y.-E., Lin, S., Wei, J., Wang, Z., Wang, C., Du, Y., and Ye, W. (2011) *Electrochim. Acta*, **56**, 8746.
77. Zhu, C., Guo, S., and Dong, S. (2012) *J. Mater. Chem.*, **22**, 14851.
78. Yin, H., Liu, S., Zhang, C., Bao, J., Zheng, Y., Han, M., and Dai, Z. (2014) *ACS Appl. Mater. Interfaces*, **6**, 2086.
79. Yan, X.-Y., Tong, X.-L., Zhang, Y.-F., Han, X.-D., Wang, Y.-Y., Jin, G.-Q.,

Qin, Y., and Guo, X.-Y. (2012) *Chem. Commun.*, **48**, 1892.
80. Henning, A.M., Watt, J., Miedziak, P.J., Cheong, S., Santonastaso, M., Song, M., Takeda, Y., Kirkland, A.I., Taylor, S.H., and Tilley, R.D. (2013) *Angew. Chem. Int. Ed.*, **52**, 1477.
81. Ferrer, D., Torres-Castro, A., Gao, X., Sepúlveda-Guzmán, S., Ortiz-Méndez, U., and José-Yacamán, M. (2007) *Nano Lett.*, **7**, 1701.
82. Chen, H., Li, Y., Zhang, F., Zhang, G., and Fan, X. (2011) *J. Mater. Chem.*, **21**, 17658.
83. Lauhon, L.J., Gudiksen, M.S., Wang, D., and Lieber, C.M. (2002) *Nature*, **420**, 57.
84. Mani, P., Srivastava, R., and Strasser, P. (2008) *J. Phys. Chem. C*, **112**, 2770.
85. Zhang, M., Yan, Z., Sun, Q., Xie, J., and Jing, J. (2012) *New J. Chem.*, **36**, 2533.
86. Zhang, Q., Lee, I., Joo, J.B., Zaera, F., and Yin, Y. (2012) *Acc. Chem. Res.*, **46**, 1816.
87. Luo, B., Xu, S., Yan, X., and Xue, Q. (2012) *J. Power Sources*, **205**, 239.
88. Guo, S., Dong, S., and Wang, E. (2008) *Chem. Eur. J.*, **14**, 4689.
89. Xiao, Y.-P., Wan, S., Zhang, X., Hu, J.-S., Wei, Z.-D., and Wan, L.-J. (2012) *Chem. Commun.*, **48**, 10331.
90. Lu, Y., Jiang, Y., Wu, H., and Chen, W. (2013) *J. Phys. Chem. C*, **117**, 2926.
91. Gao, H., Wang, Y., Xiao, F., Ching, C.B., and Duan, H. (2012) *J. Phys. Chem. C*, **116**, 7719.
92. Tian, N., Zhou, Z.Y., Sun, S.G., Ding, Y., and Wang, Z.L. (2007) *Science*, **316**, 732.
93. Lu, Y., Jiang, Y., and Chen, W. (2014) *Nanoscale*, **6**, 3309.
94. Guo, S., Dong, S., and Wang, E. (2010) *Chem. Commun.*, **46**, 1869.
95. Guo, S., Li, D., Zhu, H., Zhang, S., Markovic, N.M., Stamenkovic, V.R., and Sun, S. (2013) *Angew. Chem. Int. Ed.*, **125**, 3549.
96. Guo, S., Zhang, S., Sun, X., and Sun, S. (2011) *J. Am. Chem. Soc.*, **133**, 15354.
97. Mazumder, V., Chi, M., More, K.L., and Sun, S. (2010) *J. Am. Chem. Soc.*, **132**, 7848.
98. Lu, Y. and Chen, W. (2011) *ACS Catal.*, **2**, 84.
99. Hu, C., Zhao, Y., Cheng, H., Hu, Y., Shi, G., Dai, L., and Qu, L. (2012) *Chem. Commun.*, **48**, 11865.
100. Zhang, J., Guo, C., Zhang, L., and Li, C.M. (2013) *Chem. Commun.*, **49**, 6334.
101. Wu, J., Zhang, D., Wang, Y., and Wan, Y. (2012) *Electrochim. Acta*, **75**, 305.
102. Lambert, T.N., Davis, D.J., Lu, W., Limmer, S.J., Kotula, P.G., Thuli, A., Hungate, M., Ruan, G., Jin, Z., and Tour, J.M. (2012) *Chem. Commun.*, **48**, 7931.
103. Feng, L.L., Gao, G., Huang, P., Wang, X.S., Zhang, C.L., Zhang, J.L., Guo, S.W., and Cui, D.X. (2011) *Nanoscale Res. Lett.*, **6**, 551.
104. Wang, M., Huang, J., Wang, M., Zhang, D., Zhang, W., Li, W., and Chen, J. (2013) *Electrochem. Commun.*, **34**, 299.
105. Liang, H., Li, Z., Wang, W., Wu, Y., and Xu, H. (2009) *Adv. Mater.*, **21**, 4614.
106. Hoefelmeyer, J.D., Niesz, K., Somorjai, G.A., and Tilley, T.D. (2005) *Nano Lett.*, **5**, 435.
107. Chen, X., Su, B., Wu, G., Yang, C.J., Zhuang, Z., Wang, X., and Chen, X. (2012) *J. Mater. Chem.*, **22**, 11284.
108. Wang, Q., Cui, X., Guan, W., Zheng, W., Chen, J., Zheng, X., Zhang, X., Liu, C., Xue, T., Wang, H., Jin, Z., and Teng, H. (2013) *J. Phys. Chem. Solids*, **74**, 1470.
109. Xu, S.J., Yong, L., and Wu, P.Y. (2013) *ACS Appl. Mater. Interfaces*, **5**, 654.
110. Hu, Y., Zhang, H., Wu, P., Zhang, H., Zhou, B., and Cai, C. (2011) *Phys. Chem. Chem. Phys.*, **13**, 4083.
111. Chen, D., Zhao, X., Chen, S., Li, H., Fu, X., Wu, Q., Li, S., Li, Y., Su, B.-L., and Ruoff, R.S. (2014) *Carbon*, **68**, 755.
112. Jasuja, K. and Berry, V. (2009) *ACS Nano*, **3**, 2358.
113. Guo, S., Li, J., Dong, S., and Wang, E. (2010) *J. Phys. Chem. C*, **114**, 15337.
114. Li, S.-S., Cong, H.-P., Wang, P., and Yu, S.-H. (2014) *Nanoscale*, **6**, 7534.
115. Wu, Z.-S., Yang, S., Sun, Y., Parvez, K., Feng, X., and Müllen, K. (2012) *J. Am. Chem. Soc.*, **134**, 9082.

116. Dong, X., Wang, X., Wang, L., Song, H., Zhang, H., Huang, W., and Chen, P. (2012) *ACS Appl. Mater. Interfaces*, **4**, 3129.

117. Qiu, H.J., Dong, X.C., Sana, B., Peng, T., Paramelle, D., Chen, P., and Lim, S. (2013) *ACS Appl. Mater. Interfaces*, **5**, 782.

12
Graphene-Based Microbial Fuel Cells

Yezhen Zhang and Jian Shan Ye

12.1
Introduction

Energy (also known as *energy resources*, including coal, oil, natural gas, water, wind, sunlight, etc.) is the basic ingredient for human survival and as the driving force of social development plays a very important role in human society. The great development in the energy utilization pattern has made huge changes in human society. The use of fire was the first step to civilization, which enhanced the ability of humans to conquer nature. With the invention of the steam engine, the new era of steam power came into being which was not available for ancient humans. Industrialization and economic growth were supported by fossil fuels during the past century. Nowadays, fastest developments in the history of humans are taking place in industry, agriculture, high-tech industry, and so on. Development of the economy and the increasing population make the demand for energy increase rapidly. But the nonrenewable fossil energy reserves are becoming more and more scarce. Obviously, they may run out very soon. The energy crisis has been deepening because of the critical shortage of resources and low efficiency in their exploitation and utilization, as well as severe pollution that has brought about serious environmental problem such as the greenhouse effect, ozone depletion, acid rain, water pollution, and so on. The increasing energy depletion and environmental pollution problems constitute one of the biggest challenges of this century.

At present, most of the energy in biomass is wasted directly. In the United States, it takes 15 GW of electricity to deal with the organic wastewater, which accounts for 3% of the total output power [1]. But there is about 1.5×10^3 GW of potential energy contained in wastewater [2]. As the world's largest developing country, China accounts for a large proportion of energy production and consumption. Along with the accelerating process of industrialization, wastewater discharges have also increased dramatically in China. Rivers, lakes, and groundwater are seriously polluted, which greatly affect people's health. The exploitation of clean and green renewable energy is urgently required.

At present, the main countries in the world are actively developing various kinds of new energy sources, such as solar energy, hydropower, wind energy, biomass

Graphene-based Energy Devices, First Edition. Edited by A. Rashid bin Mohd Yusoff.
© 2015 Wiley-VCH Verlag GmbH & Co. KGaA. Published 2015 by Wiley-VCH Verlag GmbH & Co. KGaA.

energy, nuclear energy, geothermal energy, and so on. Of these, biomass energy has attracted strong scientific interest because of its abundance. It can be derived from plants and animals, including crop waste, wood, aquatic plants, and so on, in addition to urban sewage, industrial wastewater, and animal dung. Biomass energy is the world's fourth largest resource, next only to coal, oil, and natural gas. Its total quantity is extremely high, it can be recycled, and it is considered as a pollution-free energy source. So the effective utilization of biomass energy is of great significance to solve the problem of environment pollution and energy shortage.

At present, biomass energy is derived mainly through three ways, namely direct combustion, biological chemical conversion, and thermal chemical conversion. Direct combustion is the burning of the biomass directly. Its efficiency is low and it produces a large amount of dust and particulate matter, which seriously pollutes the environment; at the same time, there is the potential risk of fire. Biological chemical conversion uses biomass to generate methane gas through fermentation by microorganisms under an anaerobic environment. Thermal chemical conversion is a technology that changes biomass into gaseous or liquid fuel under certain conditions through gasification, carbonization, pyrolysis, or liquefaction. However, at present, electricity is the most convenient way of energy utilization. Can we convert biomass directly into electricity? The microbial fuel cell (MFC) may make it possible.

12.2 MFC

12.2.1 The Working Principle of MFC

MFC is a novel electrochemical device that directly converts chemical energy into electricity using electrochemical technology [3]. The most common type is the dual-chamber MFC. Its working principle is as follows: Under an anaerobic environment, the microorganisms in the anode chamber used as a biological catalyst can decompose organics of the substrate and release metabolites containing electrons, protons, and so on. The electrons can be passed to the anode by appropriate electronic intermediaries and then passed to the cathode through an external circuit. The protons reach the cathode through an exchange membrane. In the cathode chamber, electrons, protons, and electron receptors (commonly used oxygen) are combined, so the whole electron transfer process of MFC is completed. Figure 12.1 shows the working principle of an MFC. For example, with glucose as the anode fuel and oxygen as the cathode electron acceptor, the equation is as follows:

The anode reaction:

$$C_6H_{12}O_6 + 6H_2O \rightarrow 6CO_2 + 24H^+ + 24e^- \tag{12.1}$$

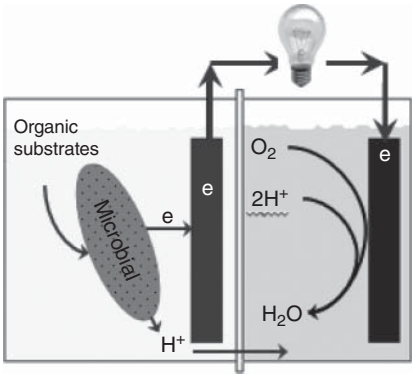

Figure 12.1 Schematic of the working principle of MFC.

The cathode reaction:

$$6O_2 + 24H^+ + 24e^- \rightarrow 12H_2O \tag{12.2}$$

The whole reaction:

$$C_6H_{12}O_6 + 6O_2 \rightarrow 6CO_2 + 12H_2O$$

12.2.2 The Advantages of MFCs

MFC, as a new energy technology, can make use of industrial wastewater and domestic sewage as fuel to produce electricity directly [4–13]. Compared to other energy sources, it has the following advantages: (i) It offers high energy conversion efficiency. It can directly change the chemical energy that is stored in the substrate into electrical energy. So it has high energy conversion efficiency in theory. (ii) It is of low cost. There are a variety of organic and inorganic substances, such as crop stalks, wood, leaves, sewage, industrial wastewater, and even animal waste, that can be used as the anode fuel, which is free usually. If we use oxygen as the electron acceptor in the cathode, it can also significantly reduce the cost because of its ready availability in the atmosphere and not requiring any energy input [14]. (iii) It requires only mild operating conditions. It works under atmospheric pressure, which is different from the existing thermal conversion process, thus making the battery maintenance cheap and secure. (iv) It is environmentally friendly. The main gas released by MFC is carbon dioxide, which can be absorbed by plants. (v) It offers a long run time. In theory, if the environment is suitable for bacteria, it can realize self-renewal and repeated use, without worrying about energy depletion. As a new green energy technology, MFC can greatly reduce the sewage treatment cost and solve the energy crisis.

12.2.3 The Classification of MFCs

So far, though many scientific workers are in engaged in MFC research, no international classification method of MFCs has been set up. MFCs can be divided into different types based on different classifications.

12.2.3.1 Dual-Chamber and Single-Chamber MFCs

Dual-chamber MFC is mainly composed of the anode chamber and the cathode chamber, which are separated by a proton exchange membrane [15, 16]. The proton exchange membrane can realize oxygen and bacteria isolation and prevent oxygen seeping into the anode chamber and affecting the bacteria. Meanwhile,

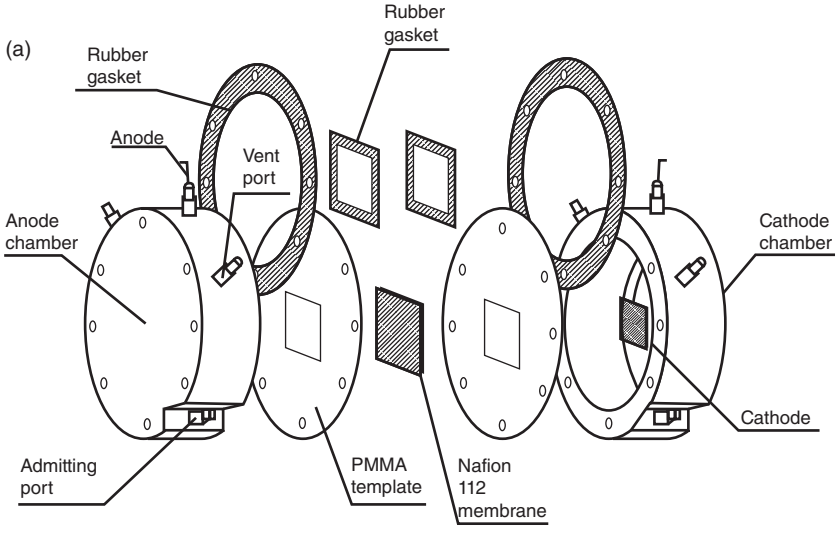

Figure 12.2 Schematic (a) and photograph (b) of the dual-chamber MFC.

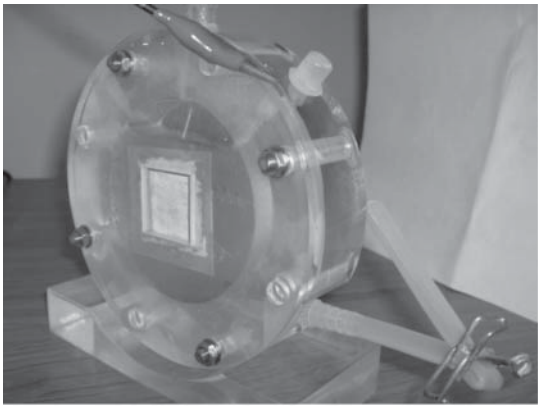

Figure 12.3 Configuration of the single-chamber MFC.

protons can cross the proton membrane to the cathode chamber, keeping the charge and acidity balance. Bacteria, the culture medium, and the electrode materials have a great influence on efficiency of electricity production. The MFC shown in Figure 12.2 has been designed by our group [17] and is constructed by using two round poly(methyl methacrylate) templates. The anodic or cathodic compartment is an inner cylinder in each template. The two compartments are screwed together and separated by two poly(methyl methacrylate) disk gaskets with a Nafion 112 membrane.

Because of the convenient construction and simple operation, dual-chamber MFC is one of the most common configurations under current laboratory level, but the presence of the proton exchange membrane causes high internal resistance, so the power output density is low, thereby reducing its potential application.

The single-chamber MFC is shown in Figure 12.3. The cathode chamber is omitted. The cathode and proton membrane are pressed together, so the distance between the anode and the cathode is reduced and the transfer resistance is much less than that of a dual-chamber MFC. This type of MFC uses oxygen as the electron acceptor directly, without aeration, which can reduce the operation cost. But it still has the following disadvantages. (i) Because of the short distance between the anode and the cathode, it is easy for oxygen to pass through the cathode, which will increase the level of dissolved oxygen in the anode chamber and affect the activity of the anode anaerobic microorganisms. At the same time, the oxygen can be used as the electron acceptor for electrogenesis of the microorganism, which will reduce the electron and energy recovery, thus affecting the coulomb efficiency and power output of the MFC [18–20]. (ii) Presently, platinum is widely used as the efficient cathode catalyst for the oxygen reduction reaction in MFCs. Platinum is very expensive, which therefore increases the cost of MFCs. (iii) The proton exchange membrane is omitted, so the catalyst contacts with the electrolyte directly, and it is easy to cause catalyst poisoning by the components of the substrate existing in wastewater, resulting in a decrease in

the power output and even causing system paralysis. (iv) So far, the preparation process of the cathode remains complex, so it is difficult to realize scaling up of the whole system.

In short, as a member of emerging MFC types and because of its unique configuration design, single-chamber MFCs are being focused on by more and more researchers toward improving their adaptability and performance.

12.2.3.2 Direct and Indirect MFCs

Depending on the type of electron transfer, MFCs can be divided into direct MFCs [21–24] and indirect MFCs [25]. Direct MFCs can transfer electrons to the electrode directly without a mediator. These bacteria mainly include *Geobacteraceae, Clostridium butyricum, Alcaligenes faecalis, Rhodoferax ferrireducens, Pseudomonas aeruginosa,* and *Shewanella putrefaciens* [26–28]. In an indirect MFC, it is difficult to realize the electron transfer directly. It needs the addition of a mediator to the anode chamber to achieve electron transfer. Direct MFC is the subject of most research because of its practicality. By combining with genetic engineering, it would be possible to design efficient microorganisms to increase the power output greatly.

12.2.3.3 Heterotrophic, Photosynthetic Autotroph, and Sediment MFCs

On the basis of the nutrition type, MFCs can be divided into heterotrophic, photosynthetic autotroph, and sediment MFCs [29–32]. A heterotrophic MFC usually uses anaerobic bacteria as the biological catalyst and is one of the most common types of MFCs. Photosynthetic autotroph MFC refers to a cyanobacterium or light-sensitive microbial and converts light into electricity. Sediment MFC uses the potential difference between the sediments and liquid phase to produce electricity. Compounds contained in the sediments, such as sugars and organic acids, can be decomposed by the microbes in the sediments. The sea surface has a lot of dissolved oxygen. One can place the anode in the marine sediments and cathode in the surface waters. The two parts are then connected by a wire. The organics in sediment are decomposed by the bacteria, releasing electrons, which can be passed to the cathode by the wire. Protons and electrons in the cathode zone are combined into water (Figure 12.4). So, the sediment MFC can achieve electricity by using seawater. Because of the rich substrates, freedom from maintenance, and continuous power generation, sediment MFCs are promising candidates to be used as energy devices in remote waters.

12.2.3.4 Intermittent and Continuous MFCs

Depending on their operation, MFCs can be divided into intermittent and continuous MFCs. An intermittent MFC needs to change the culture regularly. This type of MFC can improve the flexibility of experiments, which has several advantages in the testing of the performance of the anode material, proton exchange membrane, catalyst, and so on. But it is difficult to employ it for industrial use because it is time consuming.

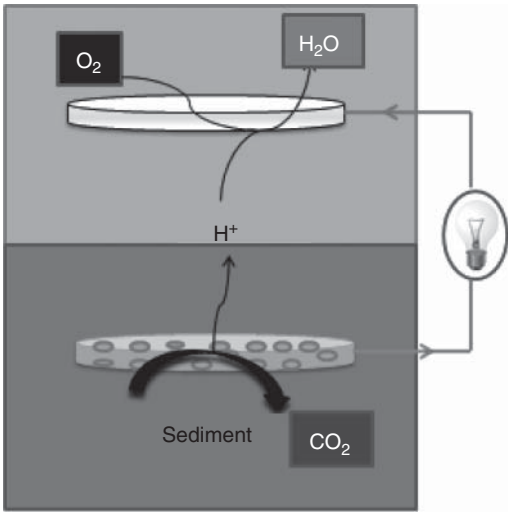

Figure 12.4 Schematic of the sediment MFC.

Continuous MFC uses a peristaltic pump to realize the circulation, so it is suitable for large-scale wastewater treatment.

12.2.3.5 Pure Bacteria and Mixed Bacteria MFCs

Depending on the microbial species, MFCs can be divided into pure bacteria MFCs and mixed bacteria MFCs. Pure bacteria have the advantages of high electron transfer efficiency and faster growth rate, and can realize quick start, but they are vulnerable to pollution even during the purification operation because it is hard to completely isolate the bacteria from the rest of the world. Therefore, they are usually used in laboratory research. Mixed bacteria generally are obtained from the bottom of the sea sediment or activated sludge of a sewage plant. Compared to pure bacteria, mixed bacteria do not require a strictly sterile environment and the operation condition is simple, so most research is focused in this direction.

12.3 The Development History of MFCs

In the eighteenth century, the Italian biologist Galvani found that frog's leg responded to current stimulation, which led to the realization that there is a certain relationship between biology and electricity. The first observation of an electrical current generated by bacteria is generally credited to Potter [33] in 1911. He successfully created the world's first MFC, but very few practical advances were made in this field in the subsequent decades. In 1931, Cohen found that the power density increased after adding potassium ferricyanide [34], but it was still too low. Until the middle of the twentieth century, the United

States wanted to develop a bio-fuel cell to make use of astronauts' waste, which brought MFCs to a certain degree of development. After the 1980s, with the wide application of electron mediators, research on MFCs increased sharply. Major breakthroughs appeared in the 1990s. Using mixed bacteria as the biological catalyst, and with domestic sewage and industrial wastewater as the substrate, it increased the likelihood of actual operation in sewage treatment. MFCs have seen great progress in the field of environment and chemistry.

12.4 The Application Prospect of MFC

Because of the shortage of resources and environmental pollution, research on the utilization of biomass energy is becoming more and more important. MFC, with its unique way of producing electricity, has become the focus in the green energy field and has broad application prospects.

12.4.1 Micro Batteries Embedded in the Body

With increasing use of artificial organ devices that require low energy consumption, such as cardiac pacemakers, it is necessary to find a stable, reliable, and long-lasting power supply for these electronic components. If glucose and dissolved oxygen, which exist in the human blood, can be used as fuel, one can build an MFC to supply the power for artificial organ devices. In theory, glucose will be completely oxidized into carbon dioxide and water, with no poisoning to human body, and can be used for life.

12.4.2 Mobile Power Supply

Oxygen and organics widely exist in nature. MFC can be used for supplying power to robots to make them self-supporting. When the power is low, the intelligent robot can obtain raw materials from Nature at any time, so it will have the ability to survive independently.

12.4.3 Photosynthesis to Produce Electricity

Plants can produce sugar through photosynthesis, and the stem can transport sugar to all parts of the plant. If sugar can be transported to the fixed MFC directly, to be used as bacterial nutrients, then one can achieve the goal of photosynthesis to produce electricity. If this method can be realized, forests would become a sustainable green energy resource, converting light into electricity continuously.

12.4.4 Biosensor

If the bacterium is affected by harmful substances, its activity will fall and the number of electrons passing to the electrode will decrease, finally causing a voltage change. This is the working principle of biosensors. A biosensor can be used for online monitoring of lakes or rivers, installed at the entrance of a sewage treatment plant to detect pollutant emissions, or used to determine the location where the pollution occurred [35, 36]. If the relation between the electrical signals generated in MFC and the biochemical oxygen demand (BOD) is linear over a certain range, then online monitoring of BOD of wastewater can be realized. Kim [37] has reported a BOD sensor that has been in operation for over 5 years in a stable manner without any servicing, which is longer than any previously reported.

12.4.5 Power Supply in Remote Areas or Open Sea

Some of the remote areas may be away from the power grid, so it is difficult to set up high-voltage transmission lines, with the resulting inconvenience to users in such areas. Meanwhile, there is a large amount of organic matter in crop straw, and burning of crop straw is widespread in China, causing serious air pollution. If straw or other agriculture refuse can be used by the MFC, environmental pollution can be reduced and the demand for electricity in remote rural areas can be met. Similarly, the sediment MFCs can be used for supplying power in the open sea.

12.4.6 Treatment of Organic Wastewater

Sewage treatment has significant social and environmental benefits, but its large energy consumption and high operation cost make poor economic benefit. MFCs can use the organics in the wastewater as fuel and generate electricity at the same time. Compared to traditional wastewater treatment processes, it has several obvious advantages. (i) It has high energy utilization. The conventional anaerobic treatment process converts the organics in wastewater into methane or hydrogen, which are then used as fuels to generate power. This indirect way greatly reduces the efficiency of power generation. (ii) Sludge discharge is reduced. Traditional wastewater treatments produce a large amount of sludge and need a lot of money to be spent in dealing with it. However, MFC has the advantage of less sludge discharge. (iii) MFCs are environment friendly. Usually, hydrogen sulfide gas is generated in a conventional anaerobic treatment process, which will pollute the environment if not treated. In MFC, it is difficult to generate the harmful gas because electrons are transformed into current directly.

12.5 Problems Existing in the MFCs

MFCs are involved in many fields such as biology, chemistry, and materials science. So far, researchers have done a lot of meaningful research on them, but they are still in the laboratory stage and have not realized industrialization. At the current level, there are some reasons for this. (i) First is the low output power density. It is several orders of magnitude lower than in conventional batteries. This puts far from being used in industrial applications. (ii) The cost of MFCs is high. In order to improve the efficiency of electron transfer, it is often necessary to add a mediator to improve the output, which makes the operation cost to increase and brings in pollution problems at the same time. Platinum or other precious metals are commonly used as catalysts, which increases the battery running cost. (iii) The model is difficult to be scaled up. Because of the structure and operation characteristics, the MFCs reported are not suitable for large-scale wastewater treatment processes. Therefore, we need to develop new reactors for practical applications.

In short, MFC, as an emerging technology, has shown incomparable superiority. Once industrialized, it will produce immeasurable social benefits and environmental benefits.

12.6 Graphene-Based MFC

12.6.1 Anode

The low power density of MFCs is one of the main obstacles for their practical applications [38, 39]. There are many factors affecting the performance of MFCs, which include the cell design, inoculum, proton exchange material, and so on [24, 40–45] materials play a profound role in influencing the power output by determining the actual surface area for bacteria to anchor and affecting the electrode resistance. Therefore, a high-performance anode material is most essential to improve the power output of MFCs.

Traditionally, carbon materials, such as carbon cloth and carbon paper, are commonly used as anode material in MFCs because of their high conductivity, good stability, and biocompatibility. However, the pores of such materials can be clogged by the bacteria, resulting in cell death and significant reduction of the power output [46]. Carbon nanotubes have also been explored to improve the performance of MFCs [47]. But carbon nanotubes are toxic to bacteria because of the heavy metal catalyst residue, which could lead to proliferation inhibition and cell death [48, 49].

Recently, graphene, as an intriguing material, has been attracting scientific interest because of its great application potentials in various fields such as

batteries and supercapacitors [50–52]. It has a unique nanostructure and extraordinary properties, such as high surface area, excellent conductivity, outstanding mechanical strength, and extraordinary electrocatalytic activity, among others [53–55]. Graphene can be synthesized by the chemical oxidation–reduction treatment of graphite [56, 57], in which heavy metal catalysts are not used, which makes for its good biological compatibility. It is a desired property for application in MFCs.

Much research has been done on graphene anodes. He *et al.* [58] used the biocompatible chitosan and vacuum-stripped graphene as an efficient bioanode and delivered a remarkable maximum power density of 1530 mW m^{-2} in a mediatorless MFC, which is much higher than that obtained from a carbon cloth anode. Hou *et al*. [59] has fabricated a novel anode by electrochemically reducing graphene oxide and coating polyaniline nanofibers afterward on the surface of a carbon cloth. When used as anode, it gave a maximum power density of 1390 mW m^{-2}. The great improvement is attributed to the high conductivity and large specific surface area of graphene. Xiao *et al.* [60] used crumpled graphene to modify both the anode and cathode in an MFC. Higher electricity generation was achieved because of the higher electrical conductivity, larger surface area, and catalytic activity of the crumpled graphene. It produced the highest maximum power density of 3.6 W m^{-3}, which is twice that when using activated carbon. Liu *et al.* [61] used an electrochemical method to deposit graphene on a carbon cloth to fabricate the MFC anode. It improved the power density and energy conversion efficiency by 2.7 and 3 times, respectively. This was attributed to the high biocompatibility of graphene, which can promote bacterial growth on the electrode surface and accelerate the electron transfer. Wang *et al.* [62] developed a three-dimensional reduced graphene oxide/nickel foam as anode for MFC. It provides a large accessible surface area for microbial colonization and a uniform macroporous scaffold for effective mass diffusion of the culture medium. The MFC produced a volumetric power density of 661 W m^{-3} and could be operated effectively in a batch mode for at least a week. Xie *et al*. [63] used a graphene/sponge composite and a stainless steel current collector as anode. It appeared to be promising for large-scale applications. Yuan *et al*. [64] used a one-pot method to prepare a microbially reduced graphene, which exhibited comparable conductivity and physical characteristics. The maximum power density of the MFC was 1905 mW m^{-2} and the coulombic efficiency was 54%. Their work demonstrates that the construction of the bacteria/graphene network is an effective alternative to improve the MFC's performance. Zhao *et al.* [65] synthesized positively charged ionic liquid-functionalized graphene nanosheets that were used as the anode in an MFC, which proved effective for high biocurrent generation and power output.

In brief, the power output can be greatly improved by using graphene or its compounds as anodes, through improving the surface area of electrode, adhesion of bacteria, and efficiency of electron transfer. It provides significant prospects for developing large-scale MFCs.

12.6.2 Membrane

For the dual-chamber MFC, protons need to be passed to the cathode chamber with sufficient speed, because a large number of protons accumulating in the anode chamber will reduce the PH value and harm the microorganisms on the anode. By far, the most commonly used proton membrane is the Nafion membrane produced by DuPont. The Nafion membrane has good selectivity and offers small resistance. But it is expensive, so much research is devoted to the study of the proton exchange membrane.

Khilari *et al.* [66] developed a proton exchange polymer membrane consisting of graphene oxide, poly(vinyl alcohol), and silicotungstic acid. The power achieved was higher than that while using a Nafion 117 membrane. A maximum power density of 1.9 $W\,m^{-3}$ was obtained when acetate wastewater was treated in the MFC equipped with the membrane. Therefore, it can be used as an efficient and inexpensive separator for MFCs.

Although the study on proton membrane preparation is not pursued intensively at present, we believe that low-priced and good-quality proton membranes can be prepared with the development of science.

12.6.3 Cathode

Because of the high oxidation potential, availability in the environment, low cost (it is free), and clean nature, oxygen is an ideal electron acceptor in the cathode of MFCs. However, because of the poor kinetics of the oxygen reduction reaction, most of the cathode materials cannot efficiently employ oxygen as the final electron acceptor directly. So it requires an efficient catalyst to accelerate the reaction. Presently, platinum is widely used as an efficient catalyst because of its excellent catalytic activity. But because of its high cost and limited supply, alternative catalysts with high catalytic activity and low cost should be developed on high priority.

Recently, graphene, as an intriguing family member of carbon allotropes, has been widely used as catalyst for oxygen reduction. Qin *et al*. [67] used nitrogen-doped graphene nanosheets to catalyze oxygen reduction. Graphene shows the high activity, improved kinetics, and excellent long-term stability for the oxygen reduction reaction. The MFC with the nitrogen-doped graphene nanosheets as cathode catalyst performs even better than when using the commercial Pt/C (Pt 10%) catalysts. Feng *et al*. [68] uses an easy-to-operate and low-temperature method to synthesize nitrogen-doped graphene in gram-scale quantities. They used nitrogen-doped graphene as the cathode catalyst, and obtained a maximum power density comparable to that from a conventional platinum catalyst. Later, they [69] enhanced the catalytic activity by the implantation of nitrogen active sites with mesoporous graphitic carbon nitride. It exhibited super electrocatalytic activity and durability. When used as cathode catalyst in MFCs, the power density increased greatly, thereby offering a new, high-performance, and less expensive

cathode material. Gnana Kumar *et al.* [70] used a MnO_2 nanotube/graphene oxide nanocomposite to modify the electrode, which exhibited a maximum power density of 3359 mW m^{-2}, which is 7.8-fold higher than that with the unmodified electrode and comparable with that with the Pt/C modified electrode. Li *et al*. [71] synthesized iron- and nitrogen-functionalized graphene as a non-precious-metal catalyst. It showed high electrocatalytic activity toward the oxygen reduction reaction and achieved the highest power density of 1149.8 mW m^{-2}.

In short, with the progress of the research, graphene will be more and more widely used in MFCs.

References

1. McCarty, P.L., Bae, J., and Kim, J. (2011) Domestic wastewater treatment as a net energy producer-can this be achieved? *Environ. Sci. Technol.*, **45** (17), 7100–7106.
2. Logan, B.E. (2004) Extracting hydrogen electricity from renewable resources. *Environ. Sci. Technol.*, **38** (9), 160a–167a.
3. Logan, B.E., Hamelers, B., Rozendal, R.A. *et al.* (2006) Microbial fuel cells: methodology and technology. *Environ. Sci. Technol.*, **40** (17), 5181–5192.
4. Logan, B.E. (2005) Simultaneous wastewater treatment and biological electricity generation. *Water Sci. Technol.*, **52** (1-2), 31–37.
5. Rozendal, R.A., Hamelers, H.V.M., Rabaey, K. *et al.* (2008) Towards practical implementation of bioelectrochemical wastewater treatment. *Trends Biotechnol.*, **26** (8), 450–459.
6. Song, Y.C., Yoo, K.S., and Lee, S.K. (2010) Surface floating, air cathode, microbial fuel cell with horizontal flow for continuous power production from wastewater. *J. Power Sources*, **195** (19), 6478–6482.
7. Sun, J., Hu, Y.Y., Bi, Z. *et al.* (2009) Improved performance of air-cathode single-chamber microbial fuel cell for wastewater treatment using microfiltration membranes and multiple sludge inoculation. *J. Power Sources*, **187** (2), 471–479.
8. Lefebvre, O., Tan, Z., Shen, Y.J. *et al.* (2013) Optimization of a microbial fuel cell for wastewater treatment using recycled scrap metals as a cost-effective cathode material. *Bioresour. Technol.*, **127**, 158–164.
9. Gong, D. and Qin, G. (2012) Treatment of oilfield wastewater using a microbial fuel cell integrated with an up-flow anaerobic sludge blanket reactor. *Desalin. Water Treat.*, **49** (1-3), 272–280.
10. Zhang, L.J., Tao, H.C., Wei, X.Y. *et al.* (2012) Bioelectrochemical recovery of ammonia-copper(II) complexes from wastewater using a dual chamber microbial fuel cell. *Chemosphere*, **89** (10), 1177–1182.
11. Zhuang, L., Yuan, Y., Wang, Y.Q. *et al.* (2012) Long-term evaluation of a 10-liter serpentine-type microbial fuel cell stack treating brewery wastewater. *Bioresour. Technol.*, **123**, 406–412.
12. Wang, Y.P., Liu, X.W., Li, W.W. *et al.* (2012) A microbial fuel cell-membrane bioreactor integrated system for cost-effective wastewater treatment. *Appl. Energy*, **98**, 230–235.
13. Mardanpour, M.M., Esfahany, M.N., Behzad, T. *et al.* (2012) Single chamber microbial fuel cell with spiral anode for dairy wastewater treatment. *Biosens. Bioelectron.*, **38** (1), 264–269.
14. Liu, H., Ramnarayanan, R., and Logan, B.E. (2004) Production of electricity during wastewater treatment using a single chamber microbial fuel cell. *Environ. Sci. Technol.*, **38** (7), 2281–2285.
15. Liu, X.Y., Du, X.Y., Wang, X. *et al.* (2013) Improved microbial fuel cell performance by encapsulating microbial cells with a nickel-coated sponge. *Biosens. Bioelectron.*, **41**, 848–851.
16. Wang, Y.Q., Li, B., Zeng, L.Z. *et al.* (2013) Polyaniline/mesoporous tungsten

trioxide composite as anode electrocatalyst for high-performance microbial fuel cells. *Biosens. Bioelectron.*, **41**, 582–588.
17. Zhang, Y., Mo, G., Li, X., *et al*. (2011) A graphene modified anode to improve the performance of microbial fuel cells. *J. Power Sources*, **196**, 5402–5407.
18. Liu, H. and Logan, B.E. (2004) Electricity generation using an air-cathode single chamber microbial fuel cell in the presence and absence of a proton exchange membrane. *Environ. Sci. Technol.*, **38** (14), 4040–4046.
19. Liu, H., Cheng, S.A., and Logan, B.E. (2005) Power generation in fed-batch microbial fuel cells as a function of ionic strength, temperature, and reactor configuration. *Environ. Sci. Technol.*, **39** (14), 5488–5493.
20. Cheng, S., Liu, H., and Logan, B.E. (2006) Increased power generation in a continuous flow MFC with advective flow through the porous anode and reduced electrode spacing. *Environ. Sci. Technol.*, **40** (7), 2426–2432.
21. Bond, D.R., Holmes, D.E., Tender, L.M. *et al.* (2002) Electrode-reducing microorganisms that harvest energy from marine sediments. *Science*, **295** (5554), 483–485.
22. Kim, B.H., Ikeda, T., Park, H.S. *et al.* (1999) Electrochemical activity of an Fe(III)-reducing bacterium, Shewanella putrefaciens IR-1, in the presence of alternative electron acceptors. *Biotechnol. Tech.*, **13** (7), 475–478.
23. Kim, H.J., Park, H.S., Hyun, M.S. *et al.* (2002) A mediator-less microbial fuel cell using a metal reducing bacterium, Shewanella putrefaciense. *Enzyme Microb. Technol.*, **30** (2), 145–152.
24. Park, H.S., Kim, B.H., Kim, H.S. *et al.* (2001) A novel electrochemically active and Fe(III)-reducing bacterium phylogenetically related to Clostridium butyricum isolated from a microbial fuel cell. *Anaerobe*, **7** (6), 297–306.
25. Park, D.H., Laivenieks, M., Guettler, M.V. *et al.* (1999) Microbial utilization of electrically reduced neutral red as the sole electron donor for growth and metabolite production. *Appl. Environ. Microbiol.*, **65** (7), 2912–2917.
26. Rabaey, K., Boon, N., Siciliano, S.D. *et al.* (2004) Biofuel cells select for microbial consortia that self-mediate electron transfer. *Appl. Environ. Microbiol.*, **70** (9), 5373–5382.
27. Reimers, C.E., Tender, L.M., Fertig, S. *et al.* (2001) Harvesting energy from the marine sediment-water interface. *Environ. Sci. Technol.*, **35** (1), 192–195.
28. Bond, D.R. and Lovley, D.R. (2003) Electricity production by Geobacter sulfurreducens attached to electrodes. *Appl. Environ. Microbiol.*, **69** (3), 1548–1555.
29. Lowy, D.A. and Tender, L.M. (2008) Harvesting energy from the marine sediment-water interface III. Kinetic activity of quinone- and antimony-based anode materials. *J. Power Sources*, **185** (1), 70–75.
30. Lowy, D.A., Tender, L.M., Zeikus, J.G. *et al.* (2006) Harvesting energy from the marine sediment-water interface II – Kinetic activity of anode materials. *Biosens. Bioelectron.*, **21** (11), 2058–2063.
31. Wilcock, W.S.D. and Kauffman, P.C. (1997) Development of a seawater battery for deep-water applications. *J. Power Sources*, **66** (1-2), 71–75.
32. Tender, L.M., Reimers, C.E., Stecher, H.A. *et al.* (2002) Harnessing microbially generated power on the seafloor. *Nat. Biotechnol.*, **20** (8), 821–825.
33. Potter, M.C. (1911) Electrical effects accompanying the decomposition of organic compounds. *Proc. R. Soc. London, Ser. B*, **84** (571), 260–276.
34. Cohen, B. (1931) The bacterial culture as an electrical half-cell. *J. Bacteriol.*, **21**, 18–19.
35. Chang, I.S., Jang, J.K., Gil, G.C. *et al.* (2004) Continuous determination of biochemical oxygen demand using microbial fuel cell type biosensor. *Biosens. Bioelectron.*, **19** (6), 607–613.
36. Chang, I.S., Moon, H., Jang, J.K. *et al.* (2005) Improvement of a microbial fuel cell performance as a BOD sensor using respiratory inhibitors. *Biosens. Bioelectron.*, **20** (9), 1856–1859.
37. Kim, B.H., Chang, I.S., Gil, G.C. *et al.* (2003) Novel BOD (biological oxygen demand) sensor using mediator-less microbial fuel cell. *Biotechnol. Lett.*, **25** (7), 541–545.

38. Holzman, D.C. (2005) Microbe Power!. *Environ. Health Perspect.*, **113**, A754–A757.
39. Bullen, R.A., Arnot, T.C., Lakeman, J.B., *et al*. (2006) Biofuel cells and their development. *Biosens. Bioelectron.*, **21**, 2015–2045.
40. Gil, G.C., Chang, I.S., Kim, B.H. *et al.* (2003) Operational parameters affecting the performance of a mediator-less microbial fuel cell. *Biosens. Bioelectron.*, **18**, 327–334.
41. Oh, S.E. and Logan, B.E. (2006) Proton exchange membrane and electrode surface areas as factors that affect power generation in microbial fuel cells. *Appl. Microbiol. Biotechnol.*, **70**, 162–169.
42. Thygesen, A., Poulsen, F.W., Min, B. *et al.* (2009) The effect of different substrates and humic acid on power generation in microbial fuel cell operation. *Bioresour. Technol.*, **100**, 1186–1191.
43. Mohan, Y. and Das, D. (2009) Effect of ionic strength, cation exchanger and inoculum age on the performance of microbial fuel cells. *Int. J. Hydrogen Energy*, **34**, 7542–7546.
44. Butler, C.S. and Nerenberg, R. (2010) Performance and microbial ecology of air-cathode microbial fuel cells with layered electrode assemblies. *Appl. Microbiol. Biotechnol.*, **86**, 1399–1408.
45. Joo-Youn, N., Hyun-Woo, K., and Hang-Sik, S. (2010) Ammonia inhibition of electricity generation in single-chambered microbial fuel cells. *J. Power Sources*, **195**, 6428–6433.
46. Rabaey, K. and Verstraete, W. (2005) Microbial fuel cells: novel biotechnology for energy generation. *Trends Biotechnol.*, **23**, 291–298.
47. Tsai, H.Y., Wu, C.C., Lee, C.Y. *et al.* (2009) Microbial fuel cell performance of multiwall carbon nanotubes on carbon cloth as electrodes. *J. Power Sources*, **194**, 199–205.
48. Flahaut, E., Durrieu, M.C., Remy-Zolghadri, M. *et al.* (2006) Study of the cytotoxicity of CCVD carbon nanotubes. *J. Mater. Sci.*, **41**, 2411–2416.
49. Magrez, A., Kasas, S., Salicio, V. *et al.* (2006) Cellular toxicity of carbon-based nanomaterials. *Nano Lett.*, **6**, 1121–1125.
50. Yoo, E., Kim, J., Hosono, E. *et al.* (2008) Large reversible Li storage of graphene nanosheet families for use in rechargeable lithium ion batteries. *Nano Lett.*, **8**, 2277–2282.
51. Wang, X., Zhi, L., and Mullen, K. (2007) Transparent, conductive graphene electrodes for dye-sensitized solar cells. *Nano Lett.*, **8**, 323–327.
52. Vivekchand, S.R.C., Rout, C.S., Subrahmanyam, K.S. *et al.* (2008) Graphene-based electrochemical supercapacitors. *J. Chem. Sci.*, **120**, 9–13.
53. McAllister, M.J., Li, J.L., Adamson, D.H. *et al.* (2007) Single sheet functionalized graphene by oxidation and thermal expansion of graphite. *Chem. Mater.*, **19**, 4396–4404.
54. Geim, A.K., Novoselov, K.S. *et al.* (2007) Detection of individual gas molecules adsorbed on grapheme. *Nat. Mater.*, **6**, 183–191.
55. Lee, C., Wei, X.D., and Kysar, J.W. (2008) Intrinsic response of graphene vapor sensors. *Science*, **321**, 385–388.
56. Stankovich, S., Dikin, D.A., Piner, R.D. *et al.* (2007) Synthesis of graphene-based nanosheets via chemical reduction of exfoliated graphite oxide. *Carbon*, **45**, 1558–1565.
57. Stankovich, S., Piner, R.D., Chen, X.Q. *et al.* (2006) Stable aqueous dispersions of graphitic nanoplatelets via the reduction of exfoliated graphite oxide in the presence of poly(sodium 4-styrenesulfonate). *J. Mater. Chem.*, **16**, 155–158.
58. He, Z., Liu, J., Qiao, Y. *et al.* (2012) Architecture engineering of hierarchically porous chitosan/vacuum-stripped graphene scaffold as bioanode for high performance microbial fuel cell. *Nano Lett.*, **12**, 4738–4741.
59. Hou, J., Liu, Z., and Zhang, P. (2013) A new method for fabrication of graphene/polyaniline nanocomplex modified microbial fuel cell anodes. *J. Power Sources*, **224**, 139–144.
60. Xiao, L., Damien, J., Luo, J. *et al.* (2012) Crumpled graphene particles for microbial fuel cell electrodes. *J. Power Sources*, **208**, 187–192.

61. Liu, J., Qiao, Y., Guo, C.X. *et al.* (2012) Graphene/carbon cloth anode for high-performance mediatorless microbial fuel cells. *Bioresour. Technol.*, **114**, 275–280.
62. Wang, H., Wang, G., Ling, Y. *et al.* (2013) High power density microbial fuel cell with flexible 3D graphene-nickel foam as anode. *Nanoscale*, **5**, 10283–10290.
63. Xie, X., Yu, G., Liu, N. *et al.* (2012) Graphene-sponges as high-performance low-cost anodes for microbial fuel cells. *Energy Environ. Sci.*, **5**, 6862–6866.
64. Yuan, Y., Zhou, S., Zhao, B. *et al.* (2012) Microbially-reduced graphene scaffolds to facilitate extracellular electron transfer in microbial fuel cells. *Bioresour. Technol.*, **116**, 453–458.
65. Zhao, C., Wang, Y., Shi, F. *et al.* (2013) High biocurrent generation in Shewanella-inoculated microbial fuel cells using ionic liquid functionalized graphene nanosheets as an anode. *Chem. Commun.*, **49**, 6668–6670.
66. Khilari, S., Pandit, S., Ghangrekar, M.M. *et al.* (2013) Graphene oxide-impregnated PVA-STA composite polymer electrolyte membrane separator for power generation in a single-chambered microbial fuel cell. *Ind. Eng. Chem. Res.*, **52**, 11597–11606.
67. Ci, S., Wu, Y., Zou, J. *et al.* (2012) Nitrogen-doped graphene nanosheets as high efficient catalysts for oxygen reduction reaction. *Chin. Sci. Bull.*, **57**, 3065–3070.
68. Feng, L., Chen, Y., and Chen, L. (2011) Easy-to-operate and low-temperature synthesis of gram-scale nitrogen-doped graphene and its application as cathode catalyst in microbial fuel cells. *ACS Nano*, **5**, 9611–9618.
69. Feng, L., Yang, L., Huang, Z. *et al.* (2013) Enhancing electrocatalytic oxygen reduction on nitrogen-doped graphene by active sites implantation. *Sci. Rep.*, **3**, 3306–3306.
70. Gnana Kumar, G., Awan, Z., Suk Nahm, K. *et al.* (2014) Nanotubular MnO2/graphene oxide composites for the application of open air-breathing cathode microbial fuel cells. *Biosens. Bioelectron.*, **53**, 528–534.
71. Li, S., Hu, Y., Xu, Q. *et al.* (2012) Iron- and nitrogen-functionalized graphene as a non-precious metal catalyst for enhanced oxygen reduction in an air-cathode microbial fuel cell. *J. Power Sources*, **213**, 265–269.

13
Application of Graphene-Based Materials to Improve Electrode Performance in Microbial Fuel Cells

Li Xiao and Zhen He

13.1
Introduction

The microbial fuel cell (MFC) is a bioelectrochemical device that uses microbial metabolism to catalyze the oxidation of organic compounds and to convert the energy stored in the chemical bonds to electrical energy [1]. A typical MFC consists of two compartments separated by an ion exchange membrane (Figure 13.1). In the anode compartment, exoelectrogenic bacteria oxidize organic matter and release electrons to an anode electrode (Reaction 13.1). These electrons travel through an external circuit to a cathode electrode for reducing electron acceptors (e.g., O_2, Reaction 13.2). The electron movement is driven by the difference in redox potentials between the anode and cathode reactions. An important task for MFC development is to improve the power output, which is investigated through optimizing the reactor configuration and operating conditions, understanding microbial activities, and exploring new electrode and membrane materials. In particular, electrode materials and catalysts (including their modifying materials) are of strong interest because of their significant role in determining the internal resistance of an MFC and appearance of new materials due to rapid development in materials science [2, 3].

$$\text{Anode:} \quad \text{Organics} \rightarrow CO_2 + H^+ + e^- \tag{13.1}$$

$$\text{Cathode:} \quad O_2 + H^+ + e^- \rightarrow H_2O \tag{13.2}$$

The features of ideal electrode materials and catalysts for MFCs include high surface area, high electrical conductivity, good stability, good biocompatibility, and low cost [1]. The electrode performance can be improved through appropriate modification with coating additional materials. With the development of nanotechnologies, nanostructured materials have been extensively studied to improve the performance of both anode and cathode electrodes in MFCs. For example, a carbon nanotube (CNT)/polyaniline (PANI) composite and the

Graphene-based Energy Devices, First Edition. Edited by A. Rashid bin Mohd Yusoff.
© 2015 Wiley-VCH Verlag GmbH & Co. KGaA. Published 2015 by Wiley-VCH Verlag GmbH & Co. KGaA.

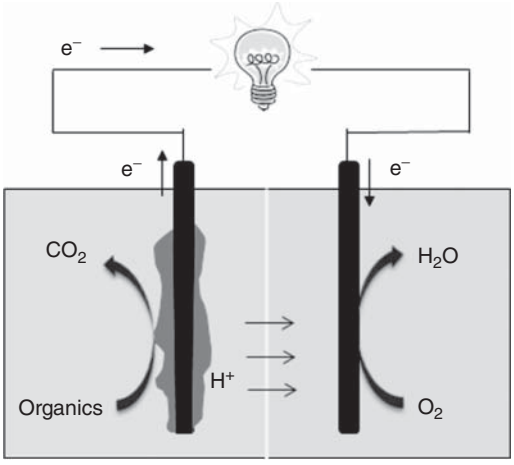

Figure 13.1 Schematic diagram of a microbial fuel cell.

associated nanostructured PANI/mesoporous TiO_2 composite could increase power production through improving the anode electrode [4, 5]. The cathode electrodes need to be coated with appropriate catalysts to reduce terminal electron acceptors and to improve the cathode reaction rate [6, 7]. The most commonly used cathode catalyst is platinum (Pt), which is an expensive precious metal. Several alternative catalysts have been studied, such as manganese oxides, metal tetramethoxy phenylephrine (CoTMPP and FeCoTMPP), and metal phthalocyanine (FePc, CoPc, and FeCuPc) [8]. More information on the MFC electrode materials can be obtained from a recent review [3].

Among the new materials, graphene is an emerging candidate for electrode applications in MFCs [9]. Graphene has some unique and desirable properties as an electrode material: high electrical conductivity, large surface area, appreciable electrocatalytic activity, good chemical and microbial stability, and low production cost [10–12]. Graphene can be processed into different forms (e.g., graphene sheets, graphene particles, and graphene oxide (GO)), and can also be chemically functionalized (e.g., nitrogen-doped graphene (NG), PANI graphene, and some metal-supported graphene). Graphene-based materials have been extensively studied in many electrochemical applications, such as solar cells, ultracapacitors, and lithium-based rechargeable batteries [13–15]. Graphene has also been studied in MFCs, as either anode or cathode material, for improving electricity generation. Both the promises and limitations of graphene-based materials create opportunities and also challenges for MFC applications. The following sections summarize the applications of graphene-based materials in MFCs, present the current status of their development, and discuss the advancement and challenges in using them to improve MFC performance.

13.2 Graphene Materials for Anode Electrodes in MFCs

The features of an ideal material for MFC anode electrodes include high electrical conductivity, strong resistance to corrosion, high specific surface area and high porosity, good biocompatibility, low cost, and convenient manufacturing. Graphene-based materials have some of the above features, such as a higher electrical conductivity than many commonly used carbon materials which allow electrons to move freely across the plane in delocalized orbitals due to their special structure [11], good biocompatibility for bacterial growth, and excellent corrosion resistance in liquid. Table 13.1 summarizes the graphene anode electrodes reported in MFC studies. The following sections introduce several major graphene-based materials that have been studied as anode electrodes in MFCs.

13.2.1 Graphene Nanosheets

Graphene nanosheets (GNSs) are flat monolayers of carbon atoms tightly packed into the two-dimensional (2D) honeycomb lattices, which are the basis of

Table 13.1 Graphene and modified graphene for anode electrode.

Anode material	Anode substrate	Cathode material	Electron acceptor	Reactor configuration	Maximum power density ($W\,m^{-2}$)	References
G/SSM	Glucose	CP	Fe(III)	Dual chamber	2.67	[16]
GONRs/CP	Acetate	CP	Fe(III)	Dual chamber	0.03	[17]
G/CC	Glucose	CC	Fe(III)	Dual chamber	0.05	[18]
CGP/CC	Acetate	CB	Fe(III)	Dual chamber	0.48	[19]
MRG/CC	Acetate	Pt + CC	O_2	Single chamber	1.91	[20]
G-S/SSM	Glucose	Pt + CC		Dual chamber	1.57	[21]
CHI/VSG	Glucose	CC	Fe(III)	Dual chamber	1.53	[22]
PANI-ERGNO/CC	Acetate	CF	Fe(III)	Dual chamber	1.39	[23]
G/PANI foam	Lactate	CC	Fe(III)	Dual chamber	0.77	[24]
G/PEDOT/CP	Glucose	CC	Fe(III)	Dual chamber	0.87	[25]
G/Ni/Ti	Acetate	Pt + CC	O_2	Single chamber	0.001	[26]
IL-GNS/CP	Lactate	CP	Fe(III)	Dual chamber	0.60	[27]
rGO-Ni foam	Lactate	GS	Fe(III)	Dual chamber	27.00 ($W\,m^{-3}$)	[28]
PPy-GO/GF	Lactate	CF	Fe(III)	Dual chamber	1.33	[29]
GNRs/PANI/CP	Lactate	CP	Fe(III)	Dual chamber	0.86	[30]

G, graphene; SSM, stainless steel mesh; GONR, graphene oxide nanoribbon; CP, carbon paper; CC, carbon cloth; CB, carbon brush; CF, carbon felt; CGP, crumpled graphene particle; MRG, microbially reduced graphene; G-S, graphene-sponge; CHI/VSG, chitosan/vacuum-stripped graphene; PANI-ERGNO/CC, polyaniline-electrochemically reducing graphene oxide on the surface of carbon cloth; PEDOT, poly(3,4-ethylenedioxythiophene); IL, ionic liquid (1-(3-aminopropyl)-3-methylimidazolium bromide); PPy, polypyrrole; GNRs: graphene nanoribbons; and GS, graphite stick.

graphene-related materials. There are several different methods to apply GNSs onto anode surfaces in MFCs. The most straightforward way is to physically coat existing anode electrode materials with GNSs using some binding agents. For example, GNSs that were obtained by the chemical oxidation–reduction treatment of graphite were mixed with PTFE (polytetrafluoroethylene), and then the mixture was applied on the surface of SSM (plain stainless steel mesh) as the anode electrode (G/SSM anode) of an MFC [16]. This MFC produced a maximum power density of 2.67 W m^{-2}, which was 18 times larger than that obtained from an MFC with the bare SSM anode, demonstrating that the GNSs could improve electricity generation in MFCs via improving the adhesion of bacteria and the efficiency of electron transfer (Figure 13.2) [16]. Instead of using the physical coating method, Liu and coworkers [18] adopted an electrochemical method, in which GO was electrophoretically transported to the surface of a carbon cloth (CC) electrode in a two-electrode cell under 0.3 mA cm^{-2} anodic current and then reduced to GNSs under 0.6 mA cm^{-2} cathodic current; in that way, they determined the optimal deposition time that gave the best performance of the MFC. In their system, a large number of bacterial cells were observed to adhere to the GNS/CC (G/CC) surface forming a thick biofilm, while only a few cells were attached on the surface of the CC electrode containing no GNSs. These results demonstrated that the GNS modification could improve the biocompatibility of the electrode [18]. Mink *et al.* grew a GNS layer on a thin nickel film by using a chemical vapor deposition method at atmospheric pressure and applied the film as an anode electrode in a micro-MFC, which produced ~1 nW of power from

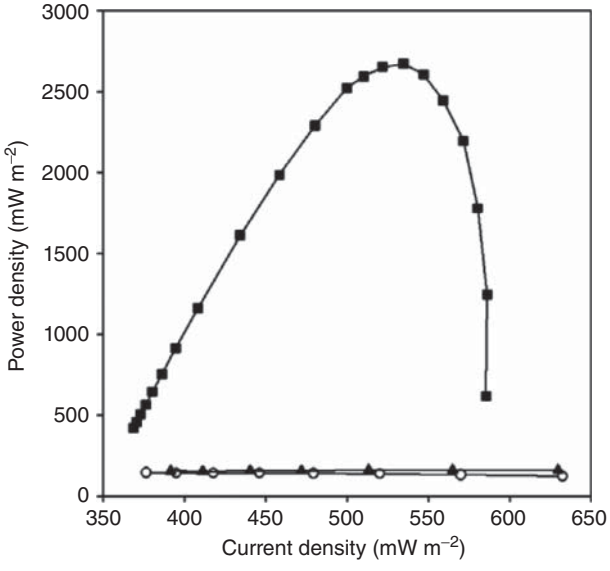

Figure 13.2 Power density curves of MFCs operated with a plain SSM (circle), polytetrafluoroethylene modified SSM (triangle), and graphene modified SSM (square). (Reproduced with permission from Ref. [16].)

wastewater, indicating the potential application of GNSs for lab-on-a-chip MFC devices [26].

As a typical flat-sheet material, GNSs applied to an anode electrode tend to stack as a result of the strong van der Waals attraction between the sheets during the coating process, thereby compromising their high accessible surface area. It was found that GO can be reduced to GNSs by heterotrophic, metal-reducing bacteria [31]. This discovery opens up the possibility of producing GNSs *in situ* in the early stage of the MFC operation, thereby avoiding the additional coating steps and thus alleviating the stacking problem of GNSs [20]. This was demonstrated in an MFC in which GO was microbiologically reduced to GNSs by the anode biofilm, and meanwhile assembling the GNSs automatically on the biofilm to form a bacteria/graphene network [20]. The GNSs reduced by the microbe exhibited conductivity and physical characteristics comparable to those of the chemically reduced products.

In addition to the stacking problem, there is another issue hampering further formation of biofilm on the surface of GNSs. Most electrochemically active bacteria are negatively charged, and, therefore, there are classical electrostatic repulsions between the bacteria and GNSs (negatively charged π-electron cloud), which slow down the bacterial loading and lower the total amount of bacteria on the surface of GNSs. To solve this problem, conductive and positively charged polymers were used to modify graphene anodes, thereby improving the electrostatic attraction between positively charged polymers and negatively charged bacterial cells and resulting in improved performance of the MFCs. For example, the surface of GNSs was decorated with poly(3,4-ethylenedioxythiophene) (PEDOT) by galvanostatic electropolymerization to fabricate a G/PEDOT anode in a H-type MFC, whose maximum power density with the G/PEDOT anode was about 2.5 times that of the one with GNSs without polymer modification [25]. It was also shown that the performance of an MFC could be improved by functionalizing GNSs with positively charged ionic liquids such as (1-(3-aminopropyl)-3-methylimidazolium bromide) [27].

13.2.2
Three-Dimensional Graphene

The transition of graphene from two-dimensional (2D) sheets to 3D particles may also solve the stacking problem of graphene sheets. The 3D crumpled graphene particles are produced by taking advantage of strong π–π stacking at the ridges in an aerosol-assisted capillary compression process [32]. The crumpled graphene particles have much higher surface area than regular graphene sheets because of the former's unique 3D open structure, which could provide more space for biofilm formation on the anode electrode (Figure 13.3) [19, 32]. As a result, a dual-chamber MFC with an anode electrode modified with crumpled graphene particles produced a higher maximum power density ($3.6\,W\,m^{-3}$) than that with an anode electrode modified with flat graphene sheets ($2.7\,W\,m^{-3}$) [19].

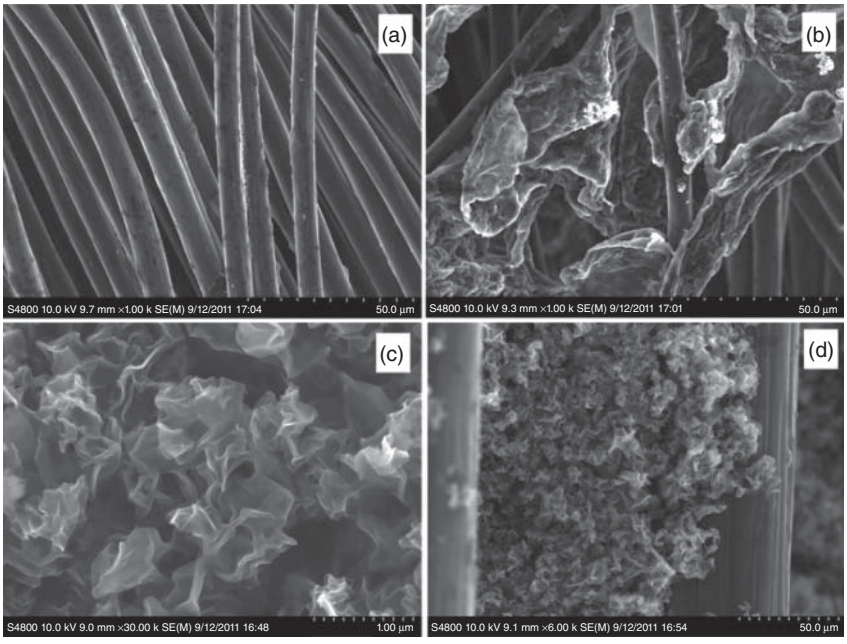

Figure 13.3 Scanning electron microscopy (SEM) images of unmodified carbon cloth electrode (a), graphene-sheet-modified carbon cloth electrode (b), crumpled graphene particles (c), and crumpled-graphene-particle-modified carbon cloth electrode (d). (Reproduced with permission from Ref. [19].)

Ice segregation-induced self-assembly (ISISA) is an effective method to produce macroporous 3D materials [33]. By using this method, a biocompatible chitosan (CHI)/vacuum-stripped graphene (VSG) composite was produced with a hierarchically porous structure composed of macropores formed by the layered-branched architecture and micropores from porous VSG; the maximum power density produced in an MFC using the CHI/VSG anode electrode was 78 times higher than that using a CC anode electrode [22].

Three-dimensional graphene electrodes can also be fabricated by coating some special materials having open porous structures with 2D GNSs. For example, coating sponges with graphene (G-S (graphene-sponge)) by using a simple and scalable dip-and-dry process could give an open porous structure to facilitate electrolyte transport and a high surface area to benefit efficient oxidation of organic matter and transfer of electrons [21]. One problem of the G-S is its low conductivity, which can be addressed by using SSM as current collectors for the G-S electrode (G-S/SSM) [21]. The maximum power density generated by the MFC using the G-S/SSM anode ($1.57\,W\,m^{-2}$) was about 14 times that with the G-S anode ($0.11\,W\,m^{-2}$), demonstrating that the SSM effectively improved the conductivity of the G-S electrode [21]. Other porous materials that have high electrical conductivity, such as nickel foam, have also been studied to create 3D

graphene. It was reported that a high-performance MFC anode was obtained by employing nickel foam as a 3D scaffold and coated with graphene sheets [28]. The nickel foam had similar open porous structure as that of the sponge materials but with much higher conductivity [21, 28].

13.2.3 Graphene Oxide

GO shows similar mechanical properties as graphene but poorer conductivity; therefore, it is not considered as a suitable electrode material. However, appropriate modifications may compensate for the poor conductivity of GO. For example, multiwalled carbon nanotubes (MWCNTs) were used as a precursor to fabricate graphene oxide nanoribbons (GONRs), which had a high length-to-diameter ratio and could act as nanowires; the edge structure of GONR offered plenty of space for chemical modification, which could improve its electrocatalytic capability. The GONR network was coated on carbon paper (CP) by the electrophoretic deposition method, and the GONR/CP anode electrode could successfully improve the electricity generation of an MFC compared to the raw CP anode electrode [17]. It was also reported that the MFC with polypyrrole (PPy)/GO-modified graphite felt showed better performance than graphene-only modified graphite felt, suggesting that some conductive polymers such as PPy can also improve the conductivity of GO [29].

13.3 Graphene Materials for Cathode Electrodes in MFCs

Cathode reaction is a key factor that limits the MFC performance, and oxygen is a commonly used electron acceptor in the cathode because of its large availability and high reducing potential [1]. There are two pathways of ORR (oxygen reduction reaction) occurring in aqueous solution: the four-electron reduction pathway from O_2 directly to H_2O, and the indirect two-electron reduction pathway from O_2 to H_2O_2 and then to H_2O. Basically, ORR proceeds favorably via the four-electron reduction pathway on platinum-group catalysts, while the two-electron ORR pathway occurs on carbon-based materials such as activated carbon and carbon black [34]. However, hydrogen peroxide is undesirable in MFCs because it can damage the membrane or electrode materials. Moreover, the slow kinetics of the two-electron ORR limits the energy performance of MFCs when carbon-based materials are used as cathode electrodes. Because of the high cost of platinum material, it is highly desirable to have an alternative cathode material/catalyst that can also facilitate four-electron ORR but is less expensive. It was found that graphene had excellent catalytic activity for the disproportionation of H_2O_2, which facilitated the four-electron ORR with a low overpotential in neutral media [35]. This finding provides the theoretical basis for the application of graphene as cathode material/catalyst instead of platinum-group materials for

Table 13.2 Graphene and modified graphene for cathode electrodes.

Cathode material	Electron acceptor	Anode material	Anode substrate	Reactor configuration	Maximum power density ($W\,m^{-2}$)	References
CGP/CC	O_2	CC	Acetate	Dual chamber	0.44	[19]
Fe-N-G/CP	O_2	CF	Acetate	Single chamber	1.15	[36]
FeTsPc-G/CP	O_2	CP	Glucose/yeast	Dual chamber	0.82	[37]
MnO2-G/CP	O_2	CF	Acetate	Single chamber	2.08	[38]
G/CC	O_2	CC	Acetate	Dual chamber	0.32	[39]
NG/CC	O_2	CB	Acetate	Single chamber	1.35	[40]
NGNSs/CC	O_2	CC	Acetate	Dual chamber	0.54	[41]
Co_3O_4/NG/GC	O_2	CG	Lactate	Dual chamber	1.34	[42]
PANI-GNS/GF	O_2	GF	Acetate	Single chamber	0.10	[43]
I-NG/CC	O_2	CF	Acetate	Single chamber	1.62	[44]
MnO_2-NTs/G	O_2	CC	Acetate	Single chamber	4.68 ($W\,m^{-3}$)	[45]
Pt-Co/G/CC	O_2	CC	Glucose	Single chamber	1.38	[46]
NG/CP	O_2	CC	Acetate	Dual chamber	0.78	[34]
MnO_2/GO/CC	O_2	CC	Glucose	Single chamber	3.36	[47]
PNCN/G/CP	O_2	CB	Acetate	Single chamber	1.16	[48]

CB, carbon brush; FeTsPc, iron tetrasulfophthalocyanine; NG, nitrogen-doped graphene; NGNSs, nitrogen doped graphene nanosheets; GC, glass carbon; CGs, carbon granules; GF, graphite felt; GNSs, graphene nanosheets; I-NG, implantation of nitrogen active sites to NG sheets; and PNCN, porous nitrogen-doped carbon nanosheet.

MFCs. Table 13.2 summarizes the graphene-based materials used as cathode electrodes in MFCs.

13.3.1 Bare Graphene

When GNSs were directly coated on a CC cathode electrode in a dual-chamber MFC, the resulting maximum power density was more than eight times that with the unmodified CC, demonstrating that graphene could greatly improve the cathode performance and thus electricity generation in MFCs [19]. Similar to the case with anode electrodes, GNSs can be also formed *in situ* on the surface of the cathode electrode by reducing GO. When GO was reduced by bacteria in a biocathode MFC, graphene/biofilm composites were produced on the cathode electrode (Figure 13.4), and this biocathode was shown to be capable of enhancing the ORR [39]. The GNSs used on cathode electrodes also have the stacking problem, which decreases the surface area and conductivity, and this effect can be eliminated by making 3D crumpled graphene particles [32]. It was reported that the cathode electrode with 3D crumpled graphene particles generated higher power density than with flat 2D graphene sheets [19].

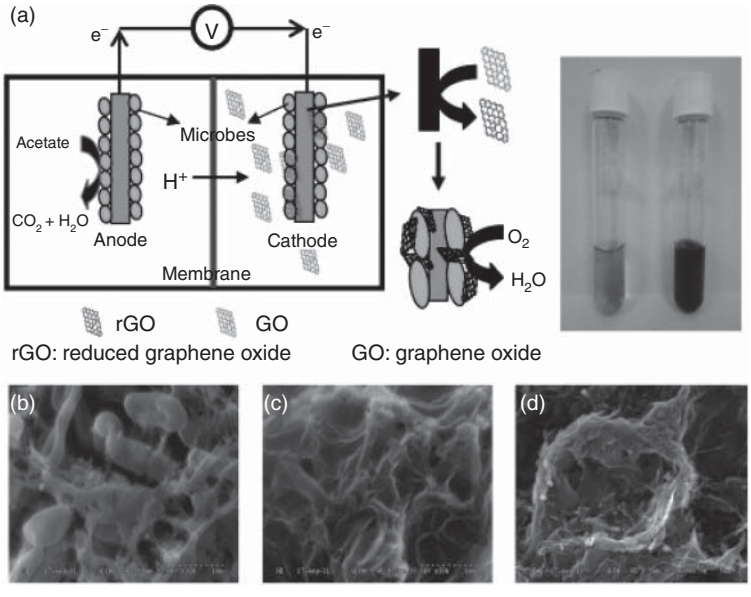

Figure 13.4 (a) Schematic configuration of microbial fuel cell with the microbially reduced graphene as cathode electrode. (b) SEM image of cathode electrode before fabrication with graphene. (c,d) SEM images of graphene with biofilm. (Reproduced with permission from Ref. [39].)

13.3.2
Polymer Coating with Graphene as a Dopant

The electrocatalytic activity of conductive polymers could be improved through doping graphene materials. PANI is one of the most widely used conductive polymers, and exhibits electrocatalytic activity toward the ORR. It has been demonstrated that the MFCs with a PANI-coated cathode generated more electrical energy than those without the PANI coating [43, 49]. When PANI was doped with a certain amount of GNS to form a PANI–GNS cathode, the power density was further improved compared with the non-graphene-doped cathode electrode. The mass ratio between aniline and graphene was optimized to be 9 : 1 in order to achieve the highest maximum power density ($0.10\,W\,m^{-2}$) for this type of cathode electrode [43].

13.3.3
Metal Coating with Graphene as a Supporter

Transition metals are well known for their catalytic activity because of their ability to adopt multiple oxidation states and to form complexes. However, most transition metals have lower catalytic activities for ORR than platinum, and thus their applications are either linked with platinum (via forming alloys) or improved through modification. Graphene was used as a support to prepare a

Pt/cobalt cathode electrode, which exhibited similar performance at a Pt loading rate of 15 wt% as that of a Pt/C-modified cathode electrode with 20 wt% Pt [46]. A composite of MnO_2/GNS was prepared by a direct redox reaction between graphene and potassium permanganate under microwave irradiation, in which graphene acted as both a reducing agent and a highly conductive substrate [38]. Because of the good electrical properties of graphene and the unique structure of the MnO_2/GNS composite, the cathode electrode with MnO_2/GNS as a cathode catalyst resulted in high catalytic activity and generated a maximum power density of 2.08 W m^{-2}, which was much higher than that of the MFC with pure MnO_2 catalyst (1.47 W m^{-2}) (Figure 13.5) [38]. The catalytic activity of MnO_2 can be affected by its structure, particle size, and synthesis methods. For example, among different structures of MnO_2, the catalytic performance follows the sequence β- < λ- < γ- < α-MnO_2 [45]. Tubular shaped MnO_2 exhibits high surface area and could easily accommodate oxygen in its tunnels, thereby favoring the adsorption and cleavage of O–O bonds, which promotes the ORR kinetics. It was reported that α-MnO_2 nanotubes (MnO_2-NTs) supported by graphene or GO used as cathode catalysts could effectively improve the performance of MFCs [45, 47]. Iron is another commonly used transition-metal catalyst. It was found that iron tetrasulfophthalocyanine (FeTsPc)-functionalized graphene could efficiently catalyze ORR in the cathode of a dual-chamber MFC, in which tetrasulfophthalocyanine as a negatively charged and water-soluble aromatic macromolecule prevented the stacking of GNSs [37].

13.3.4 Nitrogen-Doped Graphene

Recently, doping graphene with nitrogen atoms was shown to be an effective method to intrinsically benefit graphene's electronic properties. NG has been found to have a high electrocatalytic activity, improved kinetics, and long-term stability for ORR in MFCs [34, 40, 41]. In NG, there are different types of N species that may play different roles during the ORR process. Graphitic N is capable of reducing O_2 to H_2O_2 via absorbed OHH intermediates through a two-electron ORR pathway, while pyridinic and pyrrolic N might convert the ORR from a two-electron-dominating process to a four-electron-dominating process [50]. Therefore, the high content of pyridinic N and pyrrolic N in NG may facilitate the desired four-electron ORR pathway. A simple way to increase the content of pyridinic N and pyrrolic N is to increase the total number of nitrogen active sites. It was found that the implantation of nitrogen active sites to NG (I-NG) with mesoporous g-C_3N_4 introduced a large number of nitrogen sites on the surface of NG (Figure 13.6) [44]. I-NG with high content nitrogen has the strong ability of weakening the O–O bond via the bonding between oxygen and nitrogen, and the MFC using I-NG as a cathode catalyst produced a much higher power density than the normal NG MFC and even Pt/C MFC [44]. However, how to selectively increase the content of pyridinic N and pyrrolic N in NG for

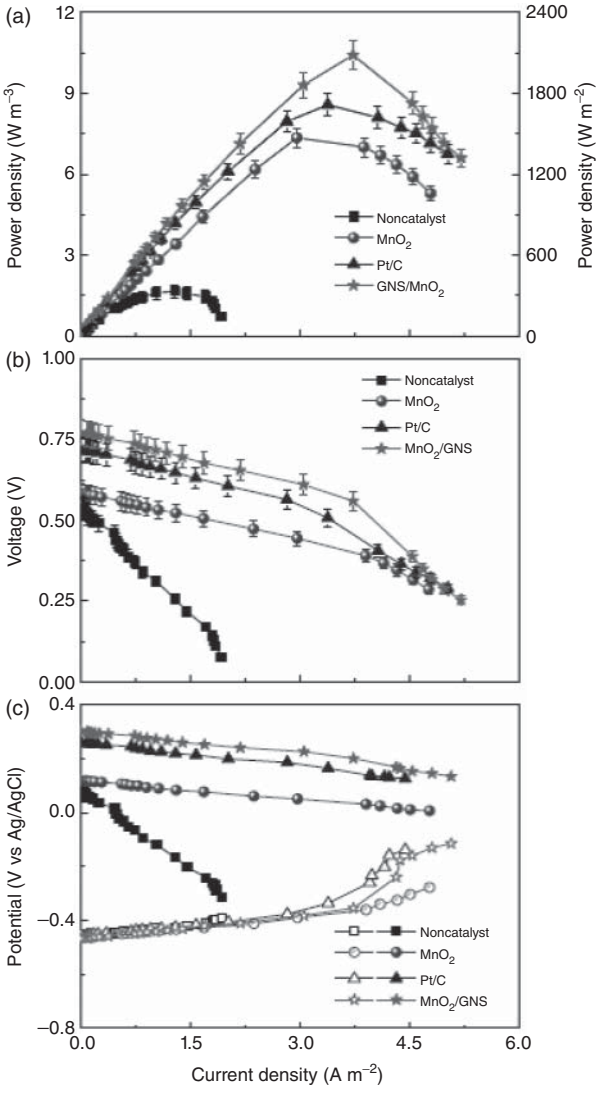

Figure 13.5 Performance of MFC equipped with non-catalyst cathode, MnO_2 cathode, Pt/C cathode, and MnO_2/GNS cathode: (a) power density curves, (b) cell voltage curves, and (c) anode and cathode polarization curves (cathode: filled symbols; anode: open symbols). Reproduced with permission from Ref. [38].

ORR on the cathode electrodes of MFCs remains unclear and warrants further investigation.

Metal elements, such as Fe and Co, are also used to modify NG electrode [36, 42], and in some cases they can also promote the ORR through the four-electron pathway [51, 52]. It was reported that iron in the graphene-based catalyst

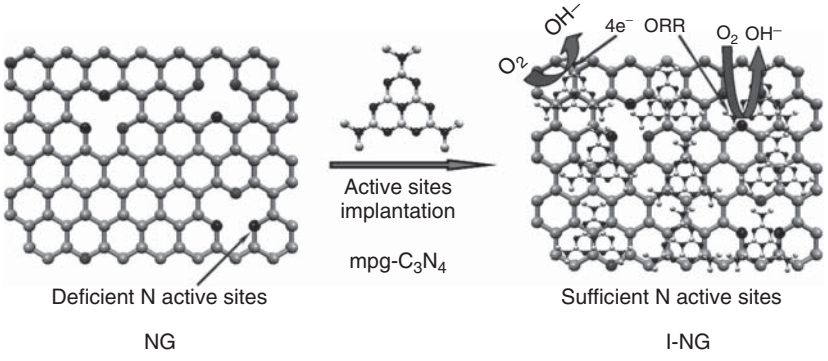

Figure 13.6 Schematic diagrams of synergistic interactions between NG and mesoporous graphene-C_3N_4. (Reproduced with permission from Ref. [44].)

could stabilize the incorporation of nitrogen within the graphene matrix, which promoted electron transfer for oxygen reduction; iron could also facilitate the disproportionation of undesirable H_2O_2, which could enhance the ORR through the desired four-electron pathway [51, 52]. As a result, the MFC with iron- and nitrogen-functionalized graphene (Fe-N-G) as a cathode catalyst achieved higher power density than the one with graphene or Pt/C [36]. A nanocomposite of cobaltosic oxide and nitrogen-doped graphene (Co_3O_4/NG) was prepared by the facile hydrothermal method and used as a cathode catalyst for ORR in a dual-chamber MFC [42]: Co_3O_4/NG highly improved the ORR in the MFC because of the improved catalytic activity due to the synergetic chemical coupling effects between Co_3O_4 and NG [42].

13.4 Outlook

Despite the great promise of graphene-based materials for improving electricity generation in MFCs, there are some challenges that must be addressed toward their future applications.

Firstly, the procedure for preparing graphene-based electrode/catalyst is still complex. A typical approach of preparing graphene electrodes is through three steps: chemical synthesis of GO from graphite according to Hummers' method; reduction of GO to graphene by a chemical reducing agent; and coating the graphene on the surface of a support by a binder such as PTFE or Nafion [29]. Some electrochemical methods can combine the second and third steps through directly reducing GO on the support [29]. Those complex procedures may increase the cost associated with preparation/manufacturing, especially for larger scale MFCs which require a large amount of materials. Moreover, the preparation procedures highly affect graphene's properties (e.g., different surface areas due to different stacking levels of graphene sheets). Therefore, developing

new and simple preparation methods for graphene electrodes is a great challenge. Although NG shows better catalytic activity on ORR in MFCs, it is not well understood how different types of N species contribute to the ORR process. In addition, accurate control of the nitrogen content and doping sites in NG during the preparation process needs to be further investigated.

Secondly, the stability of graphene materials as electrode/catalysts must be examined, especially for metal-coated graphene materials, because the metal could be corroded/oxidized in the aqueous electrolyte. In most published work, the MFCs were operated from several days to a few months. A long-term operation (>1 year) will be desired; in addition, for those MFCs that are designed for wastewater treatment, actual wastewater should be used to investigate the electrode performance during long-term operation.

Thirdly, various graphene-based materials were proposed and studied in MFCs; however, it is not clear which is the optimal form of graphene that can achieve the best performance. Cross-comparison of different studies is not possible because of significant differences in MFC configuration/operation, substrates, and membrane/electrode materials. Thus, a systematic investigation of different graphene-based materials will be needed to identify the optimal material.

Last but not least, scaling up graphene-based electrodes remains challenging. All the studies of graphene-based MFCs were conducted in small-scale reactors (<1000 ml). Systematic scaling up of MFCs is a key to the success of this technology. Although graphene-based materials are demonstrated to be effective in improving MFC's performance in bench-scale systems, they should be manufactured to accommodate large-scale MFCs, for example, 3D electrodes rather than 2D electrodes.

References

1. Logan, B.E., Hamelers, B., Rozendal, R., Schröder, U., Keller, J., Freguia, S. *et al.* (2006) Microbial fuel cells: methodology and technology. *Environ. Sci. Technol.*, **40**, 5181–5192.
2. Fu, L., You, S.-J., Zhang, G.-Q., Yang, F.-L., and Fang, X.-H. (2011) PB/PANI-modified electrode used as a novel oxygen- reduction cathode in microbial fuel cell. *Biosens. Bioelectron.*, **26**, 1975–1979.
3. Zhou, M., Chi, M., Luo, J., He, H., and Jin, T. (2011) An overview of electrode materials in microbial fuel cells. *J. Power Sources*, **196**, 4427–4435.
4. Qiao, Y., Li, C., Bao, S., and Bao, Q. (2007) Carbon nanotube/polyaniline composit as anode material for microbial fuel cells. *J. Power Sources*, **179**, 79–84.
5. Qiao, Y., Bao, S., Li, C., Cui, X., Lu, Z., and Guo, J. (2007) Nanostructured polyaniline/titanium dioxide composite anode for microbial fuel cells. *ACS Nano*, **2**, 113–119.
6. Wang, H., Wu, Z., Plaseied, A., Jenkins, P., Simpson, L., Engtrakul, C. *et al.* (2011) Carbon nanotube modified air-cathodes for electricity production in microbial fuel cells. *J. Power Sources*, **196**, 7465–7469.
7. Feng, L., Yan, Y., Chen, Y., and Wang, L. (2011) Nitrogen-doped carbon nanotubes as efficient and durable metal-free cathodic catalysts for oxygen reduction in microbial fuel cells. *Energy Environ. Sci.*, **4**, 1892–1899.
8. Kim, B.H., Chang, I.S., and Gadd, G.M. (2007) Challenges in microbial fuel

cell development and operation. *Appl. Microbiol. Biotechnol.*, **76**, 485–494.
9. Filip, J. and Tkac, J. (2014) Is graphene worth using in biofuel cells? *Electrochim. Acta*, **136**, 340–354.
10. Geim, A.K. and Novoselov, K.S. (2007) The rise of graphene. *Nat. Mater.*, **6**, 183–191.
11. Novoselov, K.S., Geim, A.K., Morozov, S.V., Jiang, D., Zhang, Y., Dubonos, S.V. *et al.* (2004) Electric field effect in atomically thin carbon films. *Science*, **306**, 666–669.
12. Pumera, M. (2009) Electrochemistry of graphene: new horizons for sensing and energy storage. *Chem. Rec.*, **9**, 211–223.
13. Paek, S.M., Yoo, E., and Honma, I. (2009) Enhanced cyclic performance and lithium storage capacity of SnO_2/graphene nanoporous electrodes with three-dimensionally delaminated flexible structure. *Nano Lett.*, **9**, 72–75.
14. Wang, X., Zhi, L., and Müllen, K. (2008) Transparent, conductive graphene electrodes for dye-sensitized solar cells. *Nano Lett.*, **8**, 323–327.
15. Zhang, L.L., Zhou, R., and Zhao, X.S. (2010) Graphene-based materials as supercapacitor electrodes. *J. Mater. Chem.*, **20**, 5983–5992.
16. Zhang, Y., Mo, G., Li, X., Zhang, W., Zhang, J., Ye, J. *et al.* (2011) A graphene modified anode to improve the performance of microbial fuel cells. *J. Power Sources*, **196**, 5402–5407.
17. Huang, Y.-X., Liu, X.-W., Xie, J.-F., Sheng, G.-P., Wang, G.-Y., Zhang, Y.-Y. *et al.* (2011) Graphene oxide nanoribbons greatly enhance extracellular electron transfer in bio-electrochemical systems. *Chem. Commun. (Camb.)*, **47**, 5795–5797.
18. Liu, J., Qiao, Y., Guo, C.X., Lim, S., Song, H., and Li, C.M. (2012) Graphene/carbon cloth anode for high-performance mediatorless microbial fuel cells. *Bioresour. Technol.*, **114**, 275–280.
19. Xiao, L., Damien, J., Luo, J., Jang, H.D., Huang, J., and He, Z. (2012) Crumpled graphene particles for microbial fuel cell electrodes. *J. Power Sources*, **208**, 187–192.
20. Yuan, Y., Zhou, S., Zhao, B., Zhuang, L., and Wang, Y. (2012) Microbially-reduced graphene scaffolds to facilitate extracellular electron transfer in microbial fuel cells. *Bioresour. Technol.*, **116**, 453–458.
21. Xie, X., Yu, G., Liu, N., Bao, Z., Criddle, C.S., and Cui, Y. (2012) Graphene–sponges as high-performance low-cost anodes for microbial fuel cells. *Energy Environ. Sci.*, **5**, 6862.
22. He, Z., Liu, J., Qiao, Y., Li, C., and Tan, T. (2012) Architecture engineering of hierarchically porous chitosan/vacuum-stripped graphene scaffold as bioanode for high performance microbial fuel cell. *Nano Lett.*, **12**, 4738–4741.
23. Hou, J., Liu, Z., and Zhang, P. (2013) A new method for fabrication of graphene/polyaniline nanocomplex modified microbial fuel cell anodes. *J. Power Sources*, **224**, 139–144.
24. Yong, Y., Dong, X., Chan-Park, M., Song, H., and Chen, P. (2012) Macroporous and monolithic anode based on polyaniline hybridized three-dimensional graphene for high-performance microbial fuel cells. *ACS Nano*, **6**, 2394–2400.
25. Wang, Y., Zhao, C., Sun, D., Zhang, J.-R., and Zhu, J.-J. (2013) A Graphene/Poly (3,4-ethylenedioxythiophene) Hybrid as an anode for high-performance microbial fuel cells. *ChemPlusChem*, **78**, 823–829.
26. Mink, J.E., Qaisi, R.M., and Hussain, M.M. (2013) Graphene-based flexible micrometer-sized microbial fuel cell. *Energy Technol.*, **1**, 648–652.
27. Zhao, C., Wang, Y., Shi, F., Zhang, J., and Zhu, J.-J. (2013) High biocurrent generation in Shewanella-inoculated microbial fuel cells using ionic liquid functionalized graphene nanosheets as an anode. *Chem. Commun. (Camb.)*, **49**, 6668–6670.
28. Wang, H., Wang, G., Ling, Y., Qian, F., Song, Y., Lu, X. *et al.* (2013) High power density microbial fuel cell with flexible 3D graphene-nickel foam as anode. *Nanoscale*, **5**, 10283–10290.
29. Lv, Z., Chen, Y., Wei, H., Li, F., Hu, Y., Wei, C. *et al.* (2013) One-step electrosynthesis of polypyrrole/graphene oxide composites for microbial fuel cell application. *Electrochim. Acta*, **111**, 366–373.
30. Zhao, C., Gai, P., Liu, C., Wang, X., Xu, H., Zhang, J. *et al.* (2013) Polyaniline networks grown on graphene

nanoribbons-coated carbon paper with a synergistic effect for high-performance microbial fuel cells. *J. Mater. Chem. A*, **1**, 12587.

31. Salas, E.C., Sun, Z., Luttge, A., and Tour, J.M. (2010) Reduction of graphene oxide via bacterial respiration. *ACS Nano*, **4**, 4852–4856.
32. Luo, J., Jang, H.D., Sun, T., Xiao, L., He, Z., Katsoulidis, A.P. *et al.* (2011) Compression and aggregation-resistant particles of crumpled soft sheets. *ACS Nano*, **5**, 8943–8949.
33. Gutiérrez, M., Ferrer, M., and del Monte, F. (2008) Ice-templated materials: sophisticated structures exhibiting enhanced functionalities obtained after unidirectional freezing and ice-segregation-induced self-assembly. *Chem. Mater.*, **203**, 634–648.
34. Liu, Y., Liu, H., and Wang, C. (2013) Sustainable energy recovery in wastewater treatment by microbial fuel cells: stable power generation with nitrogen-doped graphene cathode. *Environ. Sci.*, **47**, 13889–13895.
35. Wu, J., Wang, Y., Zhang, D., and Hou, B. (2011) Studies on the electrochemical reduction of oxygen catalyzed by reduced graphene sheets in neutral media. *J. Power Sources*, **196**, 1141–1144.
36. Li, S., Hu, Y., Xu, Q., Sun, J., Hou, B., and Zhang, Y. (2012) Iron- and nitrogen-functionalized graphene as a non-precious metal catalyst for enhanced oxygen reduction in an air-cathode microbial fuel cell. *J. Power Sources*, **213**, 265–269.
37. Zhang, Y., Mo, G., Li, X., and Ye, J. (2012) Iron tetrasulfophthalocyanine functionalized graphene as a platinum-free cathodic catalyst for efficient oxygen reduction in microbial fuel cells. *J. Power Sources*, **197**, 93–96.
38. Wen, Q., Wang, S., Yan, J., Cong, L., Pan, Z., Ren, Y. *et al.* (2012) MnO_2–graphene hybrid as an alternative cathodic catalyst to platinum in microbial fuel cells. *J. Power Sources*, **216**, 187–191.
39. Zhuang, L., Yuan, Y., Yang, G., and Zhou, S. (2012) In situ formation of graphene/biofilm composites for enhanced oxygen reduction in biocathode microbial fuel cells. *Electrochem. Commun.*, **21**, 69–72.
40. Feng, L., Chen, Y., and Chen, L. (2011) Easy-to-operate and low-temperature synthesis of gram-scale nitrogen-doped graphene and its application as cathode catalyst in microbial fuel cells. *ACS Nano*, **5**, 9611–9618.
41. Ci, S., Wu, Y., Zou, J., Tang, L., Luo, S., Li, J. *et al.* (2012) Nitrogen-doped graphene nanosheets as high efficient catalysts for oxygen reduction reaction. *Chin. Sci. Bull.*, **57**, 3065–3070.
42. Su, Y., Zhu, Y., Yang, X., Shen, J., Lu, J., Zhang, X. *et al.* (2013) A highly efficient catalyst toward oxygen reduction reaction in neutral media for microbial fuel cells. *Ind. Eng. Chem. Res.*, **52**, 6076–6082.
43. Ren, Y., Pan, D., Li, X., Fu, F., Zhao, Y., and Wang, X. (2013) Effect of polyaniline-graphene nanosheets modified cathode on the performance of sediment microbial fuel cell. *J. Chem. Technol. Biotechnol.*, **88**, 1946–1950.
44. Feng, L., Yang, L., Huang, Z., Luo, J., Li, M., Wang, D. *et al.* (2013) Enhancing electrocatalytic oxygen reduction on nitrogen-doped graphene by active sites implantation. *Sci. Rep.*, **3**, 3306.
45. Khilari, S., Pandit, S., Ghangrekar, M.M., Das, D., and Pradhan, D. (2013) Graphene supported α-MnO2 nanotubes as a cathode catalyst for improved power generation and wastewater treatment in single-chambered microbial fuel cells. *RSC Adv.*, **3**, 7902.
46. Yan, Z., Wang, M., Huang, B., Liu, R., and Zhao, J. (2013) Graphene supported Pt-Co alloy nanoparticles as cathode catalyst for microbial fuel cells. *Int. J. Electrochem. Sci.*, **8**, 149–158.
47. Gnana Kumar, G., Awan, Z., Suk Nahm, K., and Xavier, J.S. (2014) Nanotubular MnO_2/graphene oxide composites for the application of open air-breathing cathode microbial fuel cells. *Biosens. Bioelectron.*, **53**, 528–534.
48. Wen, Q., Wang, S., Yan, J., Cong, L., Chen, Y., and Xi, H. (2014) Porous nitrogen-doped carbon nanosheet on graphene as metal-free catalyst for oxygen reduction reaction in air-cathode

microbial fuel cells. *Bioelectrochemistry*, **95**, 23–28.

49. Li, C., Ding, L., Cui, H., Zhang, L., Xu, K., and Ren, H. (2012) Application of conductive polymers in biocathode of microbial fuel cells and microbial community. *Bioresour. Technol.*, **116**, 459–465.
50. Lai, L., Potts, J.R., Zhan, D., Wang, L., Poh, C.K., Tang, C. *et al.* (2012) Exploration of the active center structure of nitrogen-doped graphene-based catalysts for oxygen reduction reaction. *Energy Environ. Sci.*, **5**, 7936–7942.
51. Wang, P., Wang, Z., Jia, L., and Xiao, Z. (2009) Origin of the catalytic activity of graphite nitride for the electrochemical reduction of oxygen: geometric factors vs. electronic factors. *Phys. Chem. Chem. Phys.*, **11**, 2730–2740.
52. Chlistunoff, J. (2011) RRDE and voltammetric study of ORR on pyrolyzed Fe/polyaniline catalyst. *J. Phys. Chem. C*, **115**, 6496–6507.

14
Applications of Graphene and Its Derivative in Enzymatic Biofuel Cells

A. Rashid bin Mohd Yusoff

14.1
Introduction

A century ago, Potter [1] was the first to demonstrate the concept of a microbial biofuel cell. Later, in the 1960s, the US National Aeronautics and Space Administration (NASA) demonstrated power generation from human waste on the space shuttles [2]. Since then, the biofuel cell has attracted huge attention because it generates power from many substances such as urea and methane. In 1964, Yahiro *et al.* reported the first enzyme-based biofuel cell, where glucose oxidase (GO_x) was used as the anodic catalyst and glucose as the fuel [3]. Although numerous and interesting advances have been made during the past decades, the performance of biofuel cells in terms of power density, lifetime, and operational stability are still far below those of chemical fuel cells. Even though the enzyme-based biofuel cell basically has orders of magnitude higher power density, owing to the fragile nature of the enzyme [4, 5], however, it has limited lifetime (7–10 days) and only partially oxidizes the fuel. The poor stability and efficiency are due to the mediators in which the electrons are transported between the enzyme's active site and the electrode. Mediators (either in solution or immobilized at the electrode surface) in enzymatic biofuel cells usually consist of organic dyes or organometallic complexes. In general, the enzyme can eliminate the need for a membrane separator (Figure 14.1). In order to overcome this shortcoming, carbon nanotubes (CNTs) have been selected to reduce the electron transfer resistance and increase the electrode surface area [6–9], through the covalent binding between the enzyme and CNTs. Recently, the idea of using redox mediators have been put forward to increase the electron transfer rate, in which the redox potential of the mediator lies between those of the enzyme and the electrode, leading to a gradual shuttle of electrons from the enzyme to the mediator and finally to the electrode [8].

Graphene, a flat and two-dimensional (2D) sheet of CNTs, has recently sparked huge interest as the electrode owing to its excellent conductivity and large surface area ($\sim 2630\ m^2\ g^{-1}$) [11]. Moreover, it has recently been demonstrated that the three-dimensional (3D) architectures of this 2D nanostructure carbon can serve as novel 3D electrochemical electrodes in various applications such as

Graphene-based Energy Devices, First Edition. Edited by A. Rashid bin Mohd Yusoff.
© 2015 Wiley-VCH Verlag GmbH & Co. KGaA. Published 2015 by Wiley-VCH Verlag GmbH & Co. KGaA.

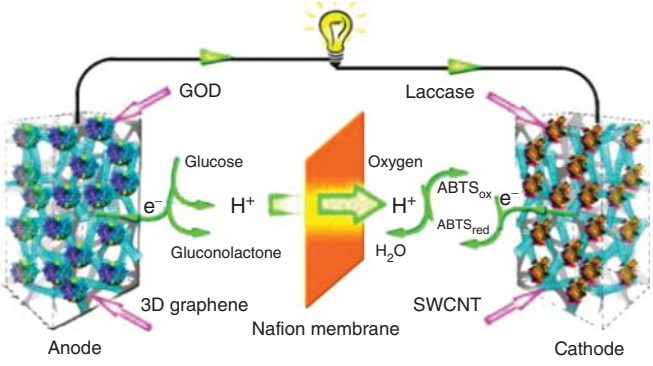

Figure 14.1 Schematic structure of EBFC along with a 3D graphene/SWCNT hybrid electrode. (Reproduced with permission from Ref. [10]. Copyright (2014), American Chemical Society.)

energy storage [12], energy conversion [13], as well as biological and chemical sensing [14]. Efforts have also been made to achieve synergistic integration of 3D graphene and CNTs for applications such as electrochemical biosensors [15], field-emitter devices [16], and double-layer capacitors [17]. In a recent study [10], single-walled carbon nanotube (SWCNT)-decorated 3D graphene was used as both anode and cathode in enzymatic biofuel cells (EBFCs) (Figure 14.1). The authors demonstrated that EBFCs equipped with enzyme-functionalized 3D graphene/SWCNT hybrid electrodes exhibited greatly improved performance compared to previously reported devices, specifically with the open-circuit voltage (E_{cell}^{ocv}) nearly reaching the theoretical limit (~1.2 V), a high power output density (2.27 ± 0.11 or 45.38 ± 2.1 mW cm^{-2}), and good long-term stability (only ~20% drop in E_{cell}^{ocv} after 30 days).

Since graphene is seeing a steady increase in importance in EBFC research, this review will be based on the research activities on membraneless and modified anodic and cathodic EBFCs, although in the realization of graphene or its derivatives in the fabrication of EBFCs in this relatively new area of research there is limited literature available.

14.2 Membraneless Enzymatic Biofuel Cells

In 2009, Liu *et al.* [18] pioneered the work on fabricating membraneless EBFCs employing graphene sheets as anode and cathode. The anode consisted of a gold electrode, where it had been co-immobilized with glucose oxidase using a silica sol–gel matrix. Meanwhile, the cathode was prepared by co-immobilizing with bilirubin oxidase. Figure 14.2 shows the graphene-based membraneless EBFCs along with their test setup and schematic configuration.

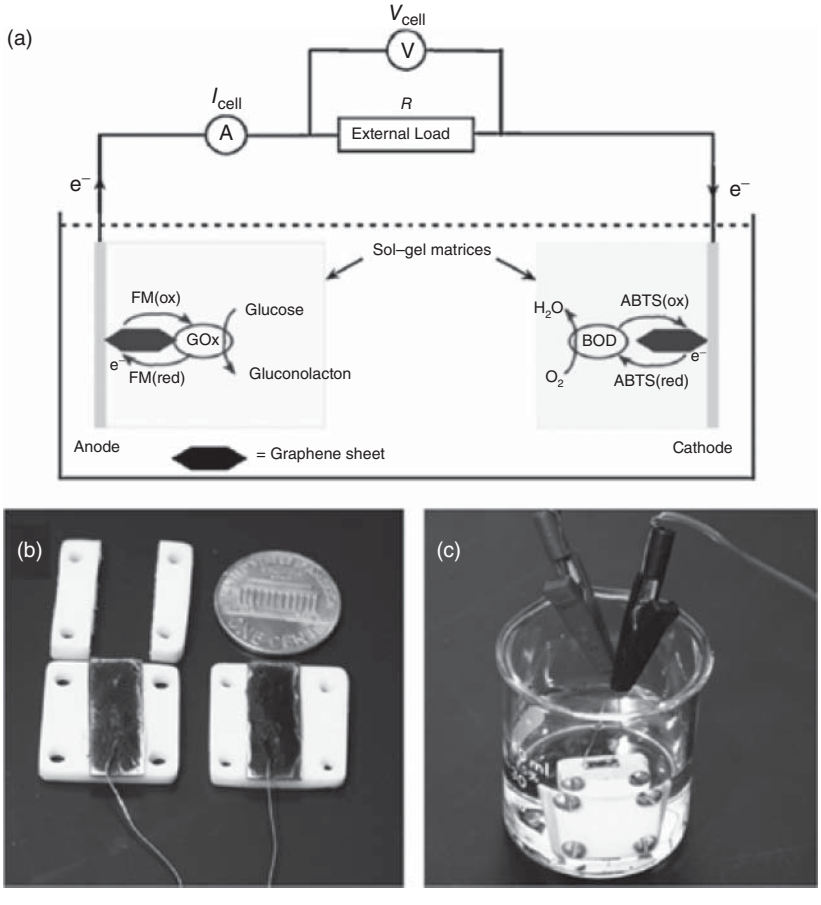

Figure 14.2 (a) Graphene-based membraneless EBFC components. (b) EBFC test setup. (c) Schematic configuration of graphene-based membraneless EBFCs. (Reproduced with permission from Ref. [18]. Copyright (2010), Elsevier.)

To determine the suitability of graphene as the electrode in EBFCs, Liu *et al.* performed a cyclic voltammetric analysis by means of graphene-, SWCNT-, and graphene-based anodes in phosphate-buffered saline (PBS) without glucose. From Figure 14.3A, the catalytic generated current from glucose can be seen, indicating that graphene has retained the bioactivity of the GO_x. Moreover, the graphene-catalyzed current is two times higher than that of the SWCNT, and the bioactivity of the graphene/BOD (bilirubin oxidase) complex was also observed. A similar behavior was also observed by employing a graphene-based cathode, an SWCNT-based cathode in air-saturated PBS solution, and a graphene-based cathode in N_2-saturated PBS solution (Figure 14.3B).

Finally, employing the so-called optimized anode and cathode, the authors fabricated their membraneless EBFCs, where the redox mediators were co-immobilized with graphene and the enzyme onto the anode and cathode,

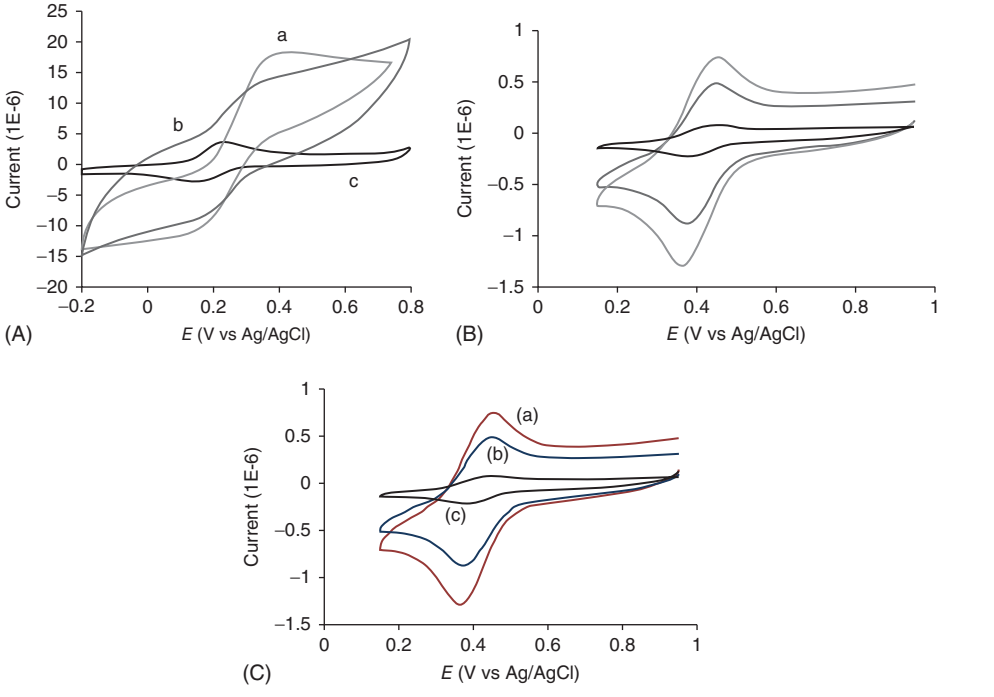

Figure 14.3 (A) Cyclic voltammogram of (a) graphene-based anode, (b) SWCNT-based anode in 100 mM glucose solution, and (c) graphene-based anode in PBS (PH 7.4) without glucose (scan rate: 500 mV s^{-1}). (B) Cyclic voltammogram of (a) graphene-based cathode, (b) SWCNT-based cathode in air-saturated PBS solution (pH 7.4), and (c) graphene-based cathode in N_2-saturated PBS solution (pH 7.4) (scan rate: 1 mV s^{-1}). (Reproduced with permission from Ref. [18]. Copyright (2010), Elsevier.)

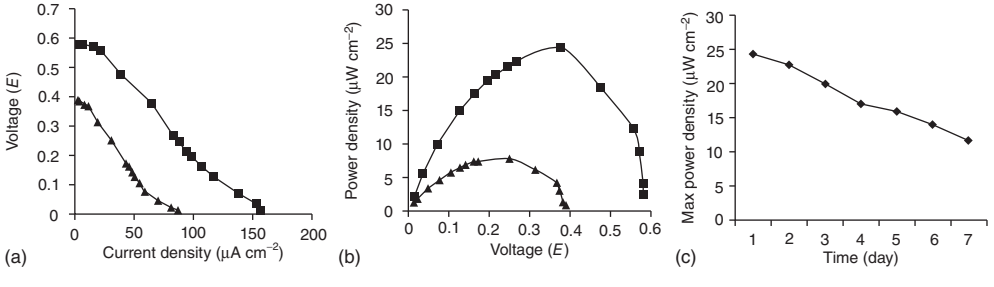

Figure 14.4 (a) Current–voltage behaviors of (■) graphene-based EBFC and (▲) SWCNT-based EBFC with different external loads in 100 mM glucose solution. (b) Power densities at different cell voltage for (■) graphene-based EBFC and (▲) SWCNT-based EBFC in 100 mM glucose solution. (c) Stability of the assembled graphene-based EBFC as a function of time. The external load in the test was 15 kΩ. Other conditions are the same as those in (a,b). (Reproduced with permission from Ref. [18]. Copyright (2010), Elsevier.)

respectively. The performance of the graphene-based membraneless EBFCs was significantly higher than that of SWCNT-based membraneless EBFC in terms of the open-circuit voltage (V_{oc}) and the maximum current density (J_{sc}) (Figure 14.4a). The V_{oc} and J_{sc} for graphene- and SWCNT-based EBFCs were 0.58 ± 0.05 and 0.39 ± 0.04 V, respectively, and 156.6 ± 25 and 86.8 ± 13 μm cm^{-2}, respectively. Furthermore, the maximum power densities of the graphene- and SWCNT-based EBFC were 24.3 ± 4 and 7.8 μW, respectively (Figure 14.4b). The performance of graphene-based EBFC lasted for only 7 days (Figure 14.4c).

The same research group made another attempt based on an electropolymerized pyrrole-immobilized enzyme/graphene sheet composite electrode [19]. Although the performance of this type of EBFCs was slight poor compared to their previous work, this work gives the insight that graphene could successfully be used in EBFCs.

14.3 Modified Bioanode and Biocathode

14.3.1 Electrochemically Reduced Graphene Oxide and Multiwalled Carbon Nanotubes/Zinc Oxide

Another interesting study was reported by Palanisamy *et al*., in which the EBFC was prepared based on simple GO_x-immobilized electrochemically reduced graphene oxide (rGO) as bioanode and laccase-immobilized multiwalled carbon nanotube (MWCNT)/zinc oxide (ZnO) as biocathode [20]. Their proposed rGO/GO_x-modified electrodes showed superior and well-defined redox peaks at −0.458 and −0.413 V compared to other modified electrodes such as graphene oxide (GO)/GO_x and glassy carbon electrode (GCE)/GO_x (Figure 14.5A). This indicates that their proposed rGO/GO_x biocomposite can efficiently transport electrons at the electrode surface. They also demonstrated that the immobilization was stable at the composite biocathode with the presence of well-defined redox peaks for the laccase/MWCNT/ZnO-modified electrode (Figure 14.5B). Their fabricated EBFCs achieved a V_{oc} of 0.055 V and power density up to 54 nW cm^{-2}.

14.3.2 Graphene/Single-Walled Carbon Nanotubes

Recent work (2014) by Prasad *et al.* [10] have demonstrated new EBFCs utilizing enzyme-functionalized 3D graphene/SWCNTs hybrid electrodes. The anodic V_{oc} of the 3D graphene/SWCNT/GO_x hybrid electrode was approximately −0.58 V (Figure 14.6a). On the other hand, GO_x-coated bare 3D graphene exhibited only about −0.12 V, highlighting the critical role of SWCNTs. The cathodic V_{oc} of the laccase-coated 3D graphene electrode was nearly 0 V (Figure 14.6b).

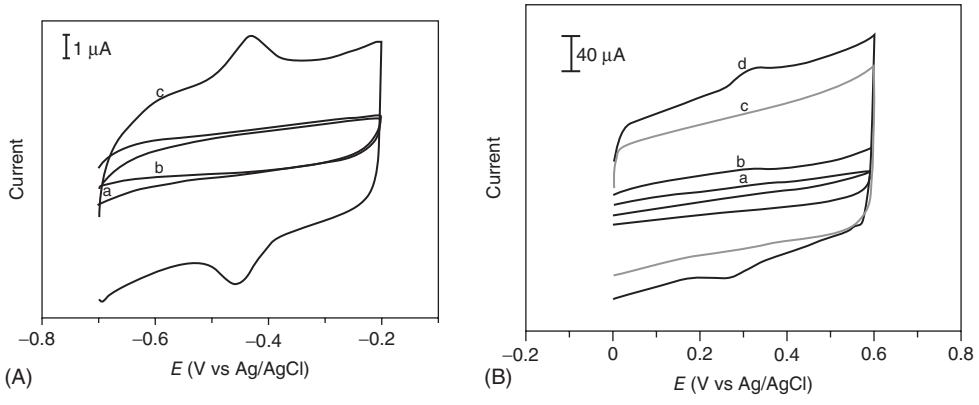

Figure 14.5 (A) Cyclic voltammograms obtained at (a) bare GCE/GO_x–, (b) GO/GO_x–, and (c) ERGO/GO_x-film-modified GCEs in deoxygenated PBS at 50 mV s^{-1} scan rate. (B) Cyclic voltammograms obtained at (a) bare GCE, (b) ZnO, (c) MWCNT, and (d) MWCNT/ZnO/laccase film modified GCEs in deoxygenated PBS at 50 mV s^{-1} scan rate. (Reproduced with permission from Ref. [20]. Copyright (2012), Electrochemical Science Group.)

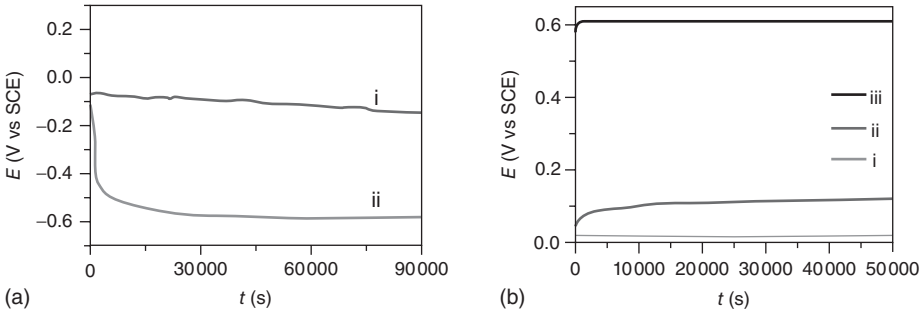

Figure 14.6 (a) Open-circuit potential of (i) the 3D graphene/GOD anode and (ii) 3D graphene/SWCNT/GOD anode in pH 5.0 electrolyte solution containing 30 mM glucose. (b) The open-circuit potential (measured in pH 5.0 electrolyte solution saturated with O_2) of (i) 3D graphene/laccase cathode, (ii) 3D graphene/SWCNT/laccase cathode, and (iii) 3D graphene/SWCNT/laccase cathode (with 0.5 mM ABTS). (Reproduced with permission from Ref. [10]. Copyright (2012), The American Chemical Society.)

The authors attributed this poor performance to the poor adhesion of laccase proteins on the graphene surface. However, significant enhancements have been observed on the 3D graphene/SWCNT/laccase electrode, namely ~0.11 V. Although a distinct improvement has been documented, it is still far from the theoretical value (0.61 V) [21, 22]. Their constructed EBFCs based on 3D graphene/SWCNTs/GO_x (anode) and 3D graphene/SWCNT/laccase (cathode) utilizing ferrocene monocarboxylic acid (FMCA) as mediator demonstrated a remarkably high V_{oc} of about ~1.20 V. They recorded the highest power density of 2.27 ± 0.11 mW cm^{-2} for glucose-based EBFCs. In addition, the lifetime

dropped by 20% after 30 days. Today, the research on graphene-based EBFCs has just begun; however, the reported works highlighted above demonstrate that graphene-based composites are potential candidates for use in the development of efficient EBFCs in the future.

14.4 Conclusion

In summary, we have pointed out some excellent works on biofuel cells based on graphene and its derivatives. As their future prospects, graphene could be used to fabricate high-performance biofuel cells by immobilization of various different enzymes. The development of EBFCs is likely to have a remarkable impact on homeland security as well as the aerospace and healthcare industry due to the fact that they are able to provide high power output. Despite all advances made in the field of high-performance EBFCs, their lifetime should also be prioritized since the best lifetime of EBFCs to date drop by almost 20% from its initial value after only 30 days.

Acknowledgment

This work was supported by the Human Resources Development program (No. 20134010200490) of the Korea Institute of Energy Technology Evaluation and Planning (KETEP) grant funded by the Korea government, Ministry of Trade, Industry and Energy.

References

1. Potter, M.C. (1912) Electrical effects accompanying the decomposition of organic compounds. *Proc. R. Soc. London, Ser. B*, **84** (571), 260–276.
2. FuelCellToday *http://www.fuelcelltoday.com/history* (accessed 3 September 2014).
3. Yahiro, A.T., Lee, S.M., and Kimble, D.O. (1964) Bioelectrochemistry: I. Enzyme utilizing bio-fuel cell studies. *Biochim. Biophys. Acta*, **88** (2), 375–383.
4. Barton, S.C., Gallaway, J., and Atanassov, P. (2004) Enzymatic biofuel cells for implantable and microscale devices. *Chem. Rev.*, **104** (10), 4867–4886.
5. Kim, J., Jia, H., and Wang, P. (2006) Challenges in biocatalysis for enzyme based biofuel cells. *Biotechnol. Adv.*, **24** (3), 296–308.
6. Gao, F., Yan, Y., Su, L., Wang, L., and Mao, L. (2007) An enzymatic glucose/O_2 biofuel cell: preparation, characterization and performance in serum. *Electrochem. Commun.*, **9** (5), 989–996.
7. Li, C.-Z., Choi, W.-B., and Chuang, C.-H. (2008) Size effects on the photoelectrochemical activities of single wall carbon nanotubes. *Electrochim. Acta*, **54** (2), 821–828.
8. Lim, J., Malati, P., Bonet, F., and Dunn, B. (2007) Nanostructured sol–gel electrodes for biofuel cells. *J. Electrochem. Soc.*, **154** (2), A140–A145.
9. Liu, Y. and Dong, S. (2007) A biofuel cell harvesting energy from glucose–air and fruit juice–air. *Biosens. Bioelectron.*, **23** (4), 593–597.
10. Prasad, K.P., Chen, Y., and Chen, P. (2014) Three-dimensional graphene-carbon nanotube hybrid for high

performance enzymatic biofuel cells. *ACS Appl. Mater. Interfaces*, **6** (5), 3387–3393.

11. Stoller, M.D., Park, S., Zhu, Y., An, J., and Ruoff, R.S. (2008) Graphene-based ultracapacitors. *Nano Lett.*, **8** (10), 3498–3502.
12. Pumera, M. (2011) Graphene-based nanomaterials for energy storage. *Energy Environ. Sci.*, **4** (3), 668–674.
13. Kamat, P.V. (2011) Graphene-based nanoassemblies for energy conversion. *J. Phys. Chem. Lett.*, **2** (3), 242–251.
14. Liu, Y., Dong, X., and Chen, P. (2012) Biological and chemical sensors based on graphene materials. *Chem. Soc. Rev.*, **41** (6), 2283–2307.
15. Shao, Y., Wang, J., Wu, H., Liu, J., Aksay, I.A., and Lin, Y. (2010) Graphene based electrochemical sensors and biosensors: a review. *Electroanalysis*, **22** (10), 1027–1036.
16. Verma, V.P., Das, S., Lahiri, I., and Choi, W. (2010) Large-area graphene on polymer film for flexible and transparent anode in field emission device. *Appl. Phys. Lett.*, **96** (20), 203108.
17. Miller, J.R., Outlaw, R.A., and Holloway, B.C. (2010) Graphene double-layer capacitor. *Science*, **329** (5999), 1637–1639.
18. Liu, C., Alwarappan, S., Chen, Z., Kong, X., and Li, C.-Z. (2010) Membraneless enzymatic biofuel cells based on graphene nanosheets. *Biosens. Bioelectron.*, **25** (7), 1829–1833.
19. Liu, C., Chen, Z., and Li, C.-Z. (2011) Surface engineering of graphene-enzyme nanocomposites for miniaturized biofuel cell. *IEEE Trans. Nanotechnol.*, **10** (1), 59–62.
20. Palanisamy, S., Cheemalapati, S., and Chen, S.-M. (2012) An enzymatic biofuel cell based on electrochemically reduced graphene oxide and multiwalled carbon nanotubes/zinc oxide modified electrode. *Int. J. Electrochem. Sci.*, **7** (11), 11477–11487.
21. Harris, D.C. (2010) *Quantitative Chemical Analysis*, 8th edn, W. H. Freeman and Company, New York, p. 298.
22. Chen, Y., Prasad, K.P., Wang, X.W., Pang, H.C., Yan, R.Y., Than, A., Chan-Park, M.B., and Chen, P. (2013) Enzymeless multi-sugar fuel cells with high power output based on 3D graphene–Co_3O_4 hybrid electrodes. *Phys. Chem. Chem. Phys.*, **15** (23), 9170–9176.

15
Graphene and Its Derivatives for Highly Efficient Organic Photovoltaics

Seung J. Lee and A. Rashid bin Mohd Yusoff

15.1
Introduction

In the past few years, graphene has attracted enormous attention because of its interesting properties and great potential for various applications [1–12]. In particular, its applications in economical and efficient energy-based optoelectronic devices, such as photovoltaic systems, lithium-ion secondary batteries, photocatalysts, and supercapacitors, have attracted great attention. Thus, for practical applications, graphene must be available in large quantities, but the availability and processability of graphene have been the rate-limiting steps in its true evaluation [13–15]. One major drawback in synthesizing and applying graphene in optoelectronic devices is overcoming the strong cohesive van der Waals energy of the π-stacked layers in graphite [16]. To date, various physical and chemical methods have been proposed to produce individual single- or few-layer graphene.

There are two chemical approaches to synthesize graphene from different carbon sources: the "top-down" and "bottom-up" approaches. The top-down technique includes the chemical exfoliation of graphite [7, 13] and the longitudinal unzipping of carbon nanotubes (CNTs) [17, 18]. On the other hand, the bottom-up method includes chemical vapor deposition (CVD) [3, 9–21] and organic synthesis [22–25]. The most popular technique used so far is the chemical reduction of graphene oxide, although it suffers from a few drawbacks [26–28]. Moreover, in many optoelectronic devices, graphene has to be mixed with other materials to form nanocomposites, which leads to interesting properties. The main focus of this review is the current research activities on graphene and its derivatives, including conductive electrodes, the active layer, the charge transport layer, and the sensitizer.

Graphene-based Energy Devices, First Edition. Edited by A. Rashid bin Mohd Yusoff.
© 2015 Wiley-VCH Verlag GmbH & Co. KGaA. Published 2015 by Wiley-VCH Verlag GmbH & Co. KGaA.

15.2 Various Applications in Solar Cells

Graphene, the emerging outstanding material that could change the way electronic components are made and help computing performance continue to grow, is everywhere in the research world these days. Numerous interesting and impressive results have been reported, where transparent graphene is employed as anodes [29–38], nontransparent anodes [39, 40], and transparent cathodes [41–44], as well as where graphene is used as the active layer, for example, light harvesting material [45–47], Schottky junction [48–51], electron transport layer (ETL) [52–56], hole transport layer (HTL) [57–61], both HTL and ETL [59], and interfacial layer in the tandem configuration [62–64].

15.2.1 Conductive Electrodes

15.2.1.1 Transparent Conductive Anodes

For many years, carbon nanotubes [65–67] and nanowires [68, 69] have been widely employed as alternative materials for electrodes (anode or cathode) in OSCs (organic solar cells). However, the roughness of these thin films was comparable to or higher than that of the frequently used indium tin oxide (ITO) films, resulting in significant shunt losses. In searching for a suitable replacement, graphene has attracted much attention with its one-atom thick, two-dimensional crystalline arrangement of carbon atoms with a quasi-linear dispersion relation and predicted mobility on the order of $10^6\,cm^2\,V^{-1}{\cdot}s^{-1}$ for a charge carrier concentration $10^{12}\,cm^{-2}$ [1]. The graphene monolayer usually has a transparency of 97–98% [70], and the sheet resistance (R_{sr}) of undoped graphene is on the order of 6 kΩ [71]. Graphene films are suitable for applications as transparent conductive electrodes where low R_{sr} and high optical transparency are essential.

It has been demonstrated that graphene can be used as transparent conductive anodes for the flexible OSCs [32]. A device structure: graphene/PEDOT:Poly Polystyrene sulfonate (PSS)/copper phthalocyanine (CuPc)/C_{60}/bathocuproine (BCP)/Al (Figure 15.1a). Graphene films have been synthesized by CVD on a thermally annealed polycrystalline nickel surface. The grown graphene films were later transferred to a transparent flexible substrate such as poly(ethylene terephthalate) (PET) (Figure 15.1b). The transparency is in the range of 72% at $230\,\Omega\,sq.^{-1}$ and 91% at $8.3\,k\Omega\,sq.^{-1}$ According to this study, the authors obtained a short-circuit current density (J_{sc}) of $4.73\,mA\,cm^{-2}$, an open-circuit voltage (V_{oc}) of 0.48 V, and a fill factor (FF) of 52%, leading to 1.18% power conversion efficiency (PCE). As a comparison, they also fabricated a control device using ITO as the transparent conductive anode on PET, giving J_{sc}, V_{oc}, FF, and PCE of $4.69\,mA\,cm^{-2}$, 0.48 V, 57%, and 1.27%, respectively. Although the CVD-grown graphene demonstrated higher Rsr, the solar cell demonstrates an output power density nearly 93%, and more sensitive to the anode conductivity, and to its

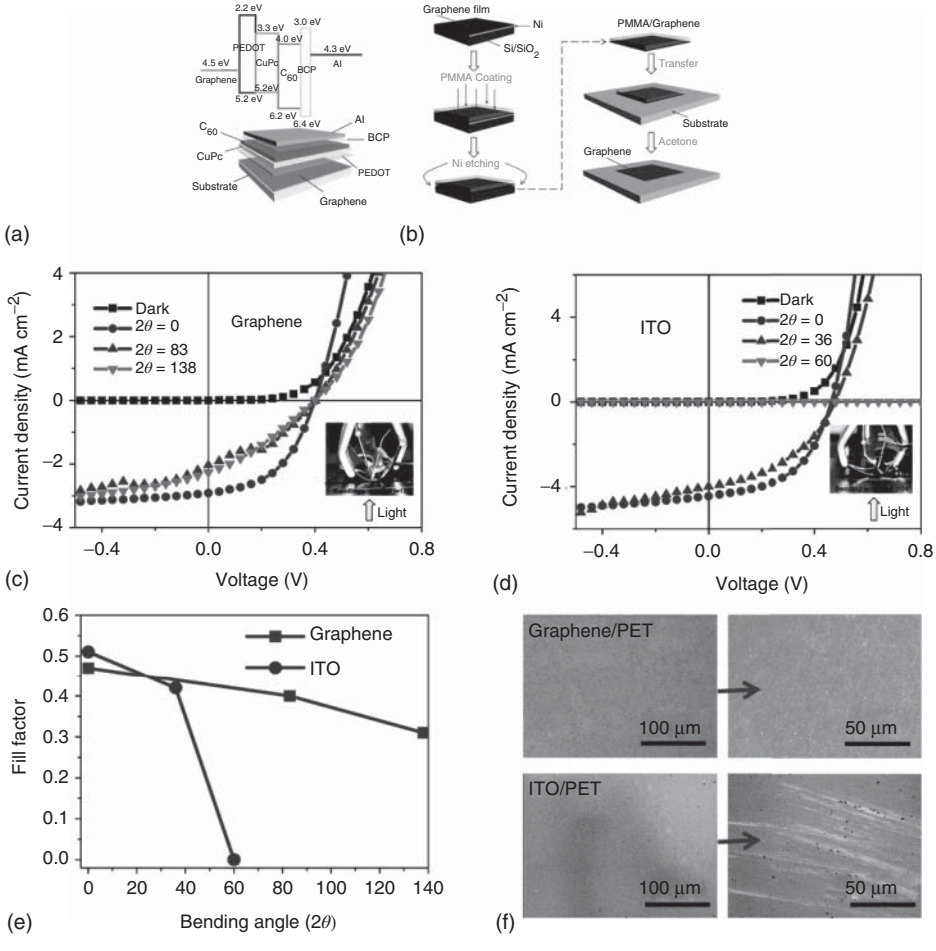

Figure 15.1 (a) Schematic representation of the energy level alignment (top) and construction of the heterojunction organic solar cell fabricated with graphene as anodic electrode: CVD graphene/Poly(3,4-ethylenedioxythiophene)(PEDOT)/CuPc/C_{60}/BCP/Aluminum (Al). (b) Schematic of the CVD graphene transfer process onto transparent substrates. Current density versus voltage characteristics of CVD graphene (c) or ITO (d) photovoltaic cells under 100 mW cm^{-2} AM1.5G spectral illumination for different bending angles. Insets show the setup employed in the experiments. (e) Fill factor dependence of the bending angle for CVD graphene and ITO devices. (f) SEM images showing the surface structure of CVD graphene (top) and ITO (bottom) photovoltaic cells after being subjected to the bending angles described in (a) and (b). (Reproduced with permission from Ref. [32]. Copyright (2010), American Chemical Society.)

capacity to pull holes from the active layers. In addition, the flexibility of CVD-grown graphene solar cell withstood bending angles (curvature radius, surface strain) of up to 138° (4.1 mm, 2.4%) (Figure 15.1c) compared to that fabricated on ITO/PET, where it could only withstand bending up to 36° (15.9 mm, 0.8%) (Figure 15.1d). The authors also noted a gradual deterioration of FF and PCE in the CVD-graphene compared to a rapid decrement of the FF to 0 under a bending of 60° (Figure 15.1e). The bad performance of ITO/PET solar cell is due to the formation of microcracks (Figure 15.1f).

In addition, chemically reduced graphene oxide (rGO) has also been used as the transparent conductive anode in OSCs [31]. The chemically modified rGO was transferred from SiO_2/Si to PET substrates and exhibited R_{sr} of 720 Ω sq.$^{-1}$ along with 40% transparency (Figure 15.2a). They could achieve the highest transmittance of 88% with 4-nm-thick rGO, but R_{sr} significantly increased to 16 kΩ sq.$^{-1}$ A complete structure consists of the construction rGO/PEDOT:PSS/Poly(3-hexylthiophene-2,5-diyl) regioregular (P3HT):PCBM/TiO_2/Al. Their best device provided a J_{sc} of 4.39 mA cm^{-2}, V_{oc} of 0.56 V, FF of 32%, and PCE of 0.78% (Figure 15.2b). The fabricated flexible OSCs demonstrated such an impressive

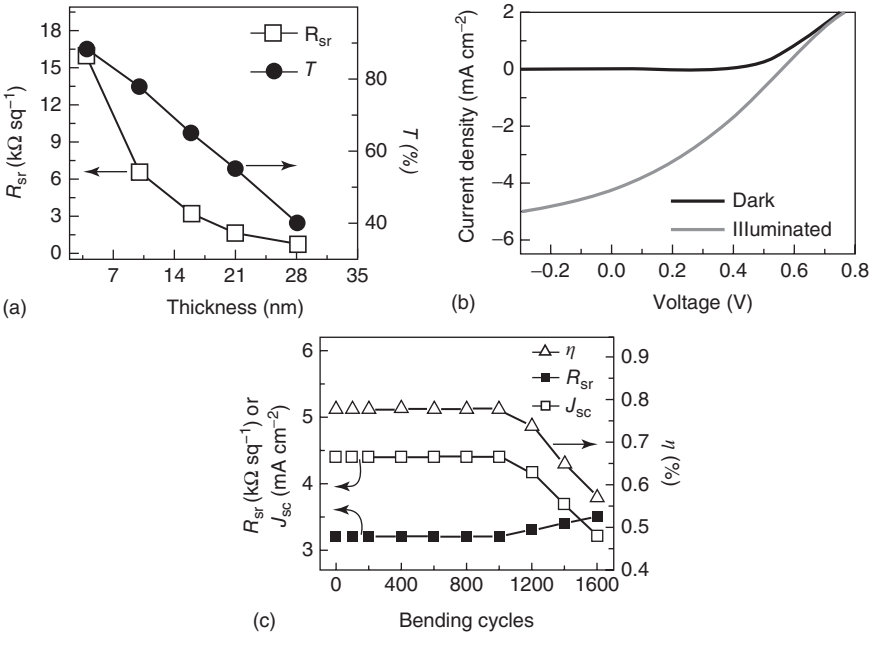

Figure 15.2 (a) Sheet resistance (R_{sr}) and transmittance (T) of an rGO film as a function of its thickness. (b) J–V curves of organic photovoltaic (OPV) devices on rGO/PET under 100 mW cm^{-2} AM1.5G simulated globe sun illumination with rGO film thickness of 21 nm. (c) The short-circuit current density (J_{sc}), overall power conversion efficiency (η), and the sheet resistance (R_{sr}) are plotted as a function of the number of bending cycle. (Reproduced with permission from Ref. [31]. Copyright (2010), American Chemical Society. (c) The short-circuit current density.)

performance that it could sustain 1600 bending cycles (2.9% tensile strain) (Figure 15.2c). This indicates that the CVD-grown rGO is highly mechanically flexible.

Despite the fact that much attention has been given to graphene's application in OSCs, it has also demonstrated its potential as the transparent anode electrode for dye-sensitized solar cells (DSSCs) [30]. The obtained graphene films exhibited a high conductivity of 550 S cm^{-1} and transparency of more than 70% over 1000–3000 nm. These high-conductivity graphene films were prepared by suspending graphite flakes in water, followed by centrifugation at 4000 rpm for 30 min and drying by evaporation under vacuum. In this study, spiro-OMeTAD (hole transport material) and porous TiO_2 (electron transport material) were used along with Au as cathode. A complete device consists of the arrangement graphene/TiO_2/dye.spiro-OMeTAD/Au (Figure 15.3a). Figure 15.3b,c shows the energy diagram along with the $J-V$ characteristics of the device illuminated under AM solar light (1 sun). The obtained graphene DSSCs demonstrated a J_{sc} of 1.01 mA cm^{-2}, V_{oc} of 0.7 V, FF of 36%, and PCE of 0.26%. For comparison, for FTO-based DSSCs the values are J_{sc} of 3.02 mA cm^{-2}, V_{oc} of 0.76 V, FF of 36%, and efficiency of 0.84%. They attributed the lower photovoltaic performance of graphene-based DSSCs to the series resistance (R_s) of the device, the relatively low transmittance of the electrode, and the electronic interfacial change.

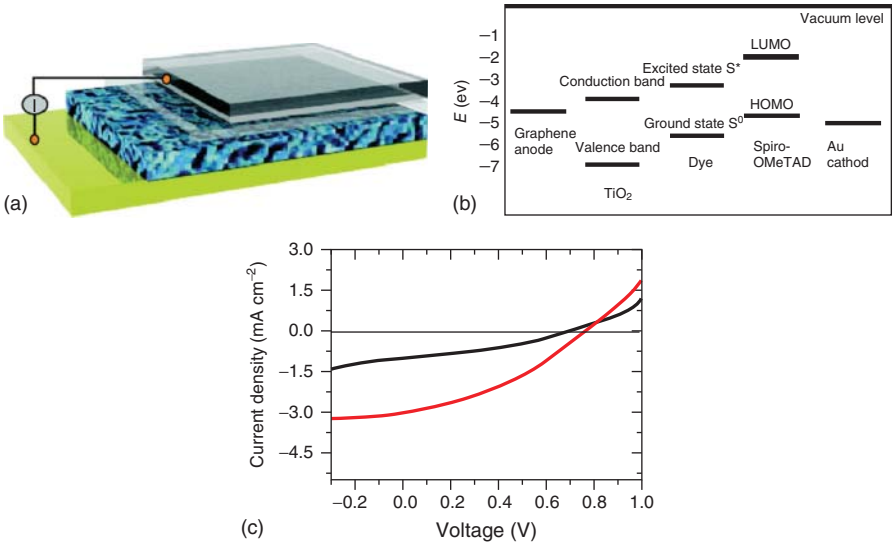

Figure 15.3 Illustration and performance of solar cells based on graphene electrodes. (a) Illustration of dye-sensitized solar cell using graphene film as electrode: the four layers from bottom to top are Au, dye-sensitized heterojunction, compact TiO_2, and graphene film. (b) The energy level diagram of graphene/TiO_2/dye/spiro-OMeTAD/Au device. (c) $I-V$ curve of graphene-based cell (black) and the FTO-based cell (red), illuminated under AM solar light (1 sun). (Reproduced with permission from Ref. [30]. Copyright (2008), American Chemical Society.)

15.2.1.2 Transparent Conductive Cathodes

In addition to the few attempts that made use of graphene as a transparent conductive anode, there have also been simultaneous attempts to utilize graphene as a transparent conductive cathode. Recently, Yin *et al.* [41] have demonstrated the application of highly conducting rGO films on quartz. The transparent rGO was prepared by transferring the hydrazine-vapor-grown rGO film onto a 3-amino-propyl-triethoxysilane (APTES) substrate and then thermally annealing the film. In brief, the rGO exhibited an R_{sr} of 420 Ω sq.$^{-1}$ at 61% transmittance. OSCs with the structure quartz/rGO/ZnO NRs/P3HT/PEDOT:PSS/Au were fabricated. With this structure, a J_{sc} of 1.43 mA cm^{-2}, V_{oc} of 0.66 V, and FF of 33%, leading to 0.31% PCE, have been obtained.

In addition, Bi *et al.* [42] have employed graphene synthesized by ambient pressure-CVD as the front electrode of CdTe solar cells. Their graphene films were synthesized on Cu foils and later transferred to a glass substrate (Figure 15.4a). In this study, the layer of the graphene films could be controlled by controlling the flow rates of H_2, CH_4, and Ar. A low H_2 flow rate promoted self-limited growth but too low a H_2 flow rate could possibly leave carbon islands. The R_{sr} of the graphene film was 220 Ω sq.$^{-1}$ with 84% transparency. The PCE of 4.17% was obtained using the device configuration glass/graphene/ZnO/CdS/CdTe/(graphene paste) (Figure 15.4b). Moreover, graphene has also been used in lead sulfide (PbS) quantum-dot (QD) solar cells (Figure 15.4c) [44]. The obtained PCEs of PbS QD-based devices fabricated on ITO/ZnO, graphene/PEDOT:Polyethylene glycol (PEG)(PC)/ZnO, and graphene/RG-1200/ZnO were 5.1%, 4.2%, and 3.9%, respectively (Figure 15.4d). The obtained PCEs of P3HT-based devices fabricated on ITO/ZnO, graphene/PEDOT:PEG(PC)/ZnO, and graphene/RG-1200/ZnO were 0.4%, 0.3%, and 0.5%, respectively (Figure 15.4e). Along with the development of PbS QD solar cells, the authors investigated the use of graphene as a more effective, less expensive conducting electrode material to replace ITO.

Graphene is normally hydrophobic, which hampers the direct growth of functional semiconductors. Using a composite-modified graphene, Zhang *et al.* [43] were able to improve the wettability of the graphene surface by thermally evaporating very thin Al nanoclusters. Besides providing improved surface wettability, the thin Al nanoclusters on graphene provided a more energetically favorable cathode interface by lowering the work function of graphene for better energy alignment with the organic acceptor (Figure 15.5a). Using an Al-TiO_2/SLG cathode, the optimized inverted OSCs provided an average efficiency of 1.59%. For comparison, inverted OSCs fabricated on Al-TiO_2/ITO demonstrated a J_{sc} of 9.11 mA cm^{-2}, V_{oc} of 0.63 V, FF of 60.1%, and PCE of 3.45% (Figure 15.5b). The low photovoltaic performance of the former was due to the high resistance of the graphene used, although the surface roughness was comparable to that of Al-TiO_2/ITO.

Table 15.1 summarizes the related published works utilizing highly transparent graphene and its derivatives in various photovoltaic devices.

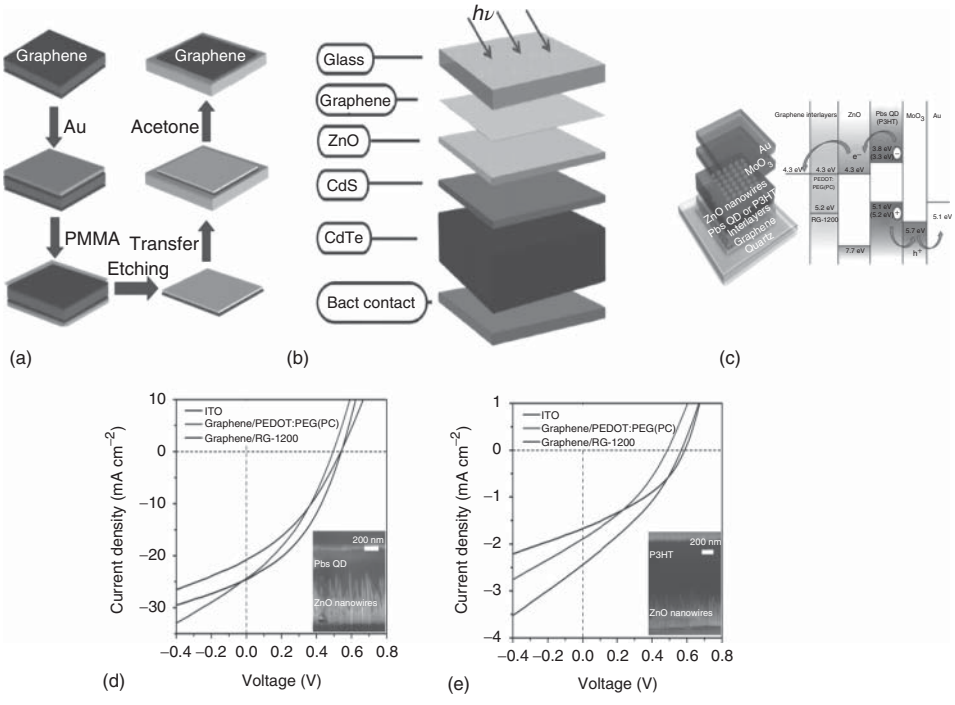

Figure 15.4 (a) Schematic diagram of the transfer process for the APCVD graphene. (b) Schematic diagram the glass/graphene/ZnO/CdS/CdTe/(graphite paste) solar cell and hybrid graphene/ZnO nanowire solar cells. (c) Schematic diagram of the graphene cathode hybrid solar cells: graphene deposited on quartz is covered by a polymer (PEDOT:PEG(PC) or RG-1200), followed by the ZnO seed layer and 400-nm-long ZnO nanowires. The nanowires are then infiltrated and covered with PbS QDs (300 nm) or P3HT (700 nm) and finally with MoO_3 (25 nm)/Au (100 nm) top electrodes. (d) *J*–*V* characteristics under 100 mW cm^{-2} AM1.5G illumination of the champion graphene-based PbS QD device with different polymer interlayers, demonstrating performance comparable to that of an ITO reference cell. (e) *J*–*V* characteristics of representative graphene-based P3HT devices with different polymer interlayers, compared with an ITO reference device. Insets in (c) and (d) show the SEM cross-sectional images of the complete devices, showing substantial infiltration of the photoactive materials (PbS QD or P3HT) into the nanometer-scale gaps between ZnO nanowires. (Reproduced with permission from Refs [42, 44]. Copyright (2011) and (2013), Wiley VCH and American Chemical Society, respectively.)

15.2.2 Active Layer

15.2.2.1 Light-Harvesting Materials

Blending graphene to the P3HT induces a strong quenching of the photoluminescence of the P3HT, corresponding a strong electron/energy transfer from the P3HT to the graphene. For example, Liu *et al.* [45] prepared a solution-processable functionalized graphene via a two-step method, namely an oxidation

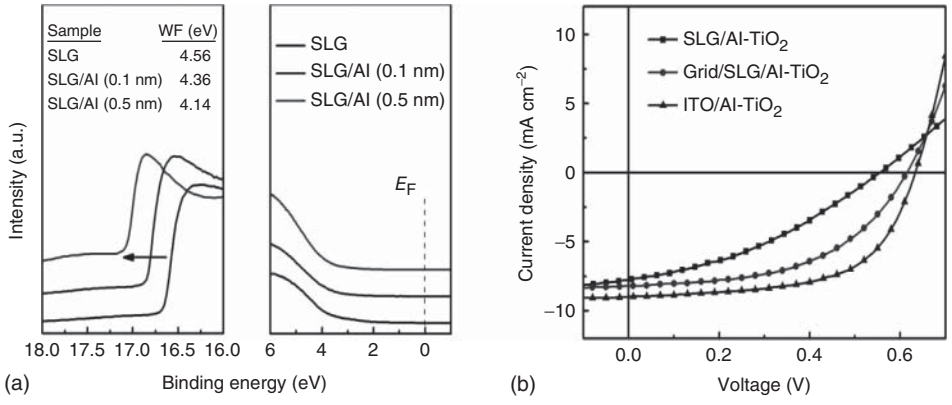

Figure 15.5 (a) UPS spectra and calculated WFs of SLG and SLG/Al (0.1 and 0.5 nm) samples. (b) *J–V* characteristics of a representative set of inverted PSCs with the device structure cathode/P3HT:PC_{61}BM (220 nm)/MoO_3 (14 nm)/Ag (100 nm). (Reproduced with permission from Ref. [43]. Copyright (2013), American Chemical Society.)

Table 15.1 Previously reported works on graphene or rGO as electrodes in various OSCs.

Material	Electrode	Transparency (R_{sr}, T)	Device structure	PCE (%)	References
rGO	Transparent anode	1.8 kΩ sq.$^{-1}$ at $T \sim 70\%$	Glass/rGO/TiO_2/dye/spiro-OMeTAD/Au	0.26	[30]
rGO	Transparent anode	3.2 kΩ sq.$^{-1}$ at $T \sim 65\%$	PET/rGO/PEDOT:PSS/P3HT:PCBM/TiO_2/Al	0.78	[31]
CVD-graphene	Transparent anode	0.25 kΩ sq.$^{-1}$ at $T \sim 92\%$	Quartz/graphene/PEDOT:PSS/CuPc:C_{60}/BCP/Ag	0.85	[36]
rGO-CNT	Transparent anode	0.6 kΩ sq.$^{-1}$ at $T \sim 87\%$	Glass/rGO-CNT/PEDOT:PSS/P3HT:PCBM/Ca:Al	0.85	[33]
CVD-graphene	Transparent anode	3.5 kΩ sq.$^{-1}$ at $T \sim 89\%$	PET/graphene/PEDOT:PSS/CuPc:C_{60}/BCP/Al	1.18	[32]
CVD-graphene	Transparent anode	0.08 kΩ sq.$^{-1}$ at $T \sim 90\%$	Quartz/graphene/MoO_3+PEDOT:PSS/P3HT:PCBM/LiF/Al	2.5	[34]
Tetracyanoquinodimethane (TCNQ)-graphene	Transparent anode	0.278 kΩ sq.$^{-1}$ at $T \sim 92\%$	Glass/TCNQ-graphene/PEDOT:PSS/P3HT:PCBM/Ca/Al	2.58	[37]
Au-doped graphene	Transparent anode	0.293 kΩ sq.$^{-1}$ at $T \sim 90\%$	Au/graphene/PEDOT:PSS/ZnO/ITO	3.04	[38]
rGO	Transparent anode	0.42 kΩ sq.$^{-1}$ at $T \sim 61\%$	Quartz/rGO/ZnO/P3HT/PEDOT:PSS/Au	0.31	[41]
Al-TiO2 modified graphene	Transparent anode	1.2 kΩ sq.$^{-1}$ at $T \sim 96\%$	Au/graphene/Al-TiO_2/P3HT:PCBM/MoO_3/Ag	2.58	[43]
CVD-graphene	Transparent anode	0.3 kΩ sq.$^{-1}$ at $T \sim 92\%$	Glass/graphene/PEDOT:PEG(PC)/ZnO/PbS QD(P3HT)/MoO_3/Au	4.2(0.5)	[44]

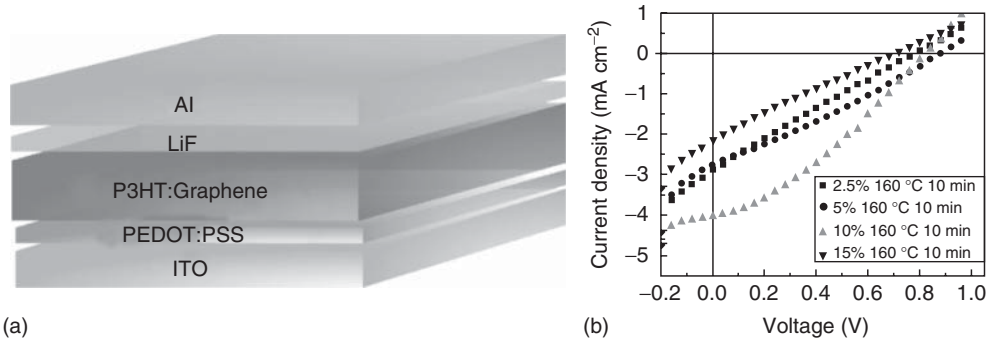

Figure 15.6 (a) Schematic structure of devices with P3HT:graphene thin film as the active layer: ITO (~17 Ω sq.$^{-1}$)/PEDOT:PSS (40 nm)/P3HT:graphene (100 nm)/LiF (1 nm)/Al (70 nm). (b) *J*–*V* characteristics of the P3HT:graphene-based photovoltaic devices with different graphene contents (2.5, 5, 10, and 15 wt%) under simulated AM1.5G 100 mW cm^{-2} illumination without annealing and with annealing at 160 °C for 10 min. (Reproduced with permission from Ref. [45]. Copyright (2009), Wiley VCH.)

and an organic functionalization step, and finally used it as the active layer in the OSCs. The first step was carried out using a modified Hummers method [72] followed by a chemical functionalization process due to the fact that the graphene oxide sheet is hydrophilic in nature. In this study, the conventional structure of ITO/PEDOT:PSS/P3HT:graphene/LiF/Al was used (Figure 15.6a). First, the PCE increased and then decreased with the increase in the graphene content. It was demonstrated that a device consisting of 10 wt% of graphene exhibited superior performance with PCE of 1.1%, V_{oc} of 0.72, J_{sc} of 4.0 mA cm^{-2}, and FF of 38% under simulated AM1.5G conditions at 100 mW cm^{-2} after heat treatment at 160 °C for 10 min. (Figure 15.6b).

Soluble conjugated polymers and fullerene have been frequently used as electron donor (D) and acceptor (A) to improve the charge separation [1–5]. Yu *et al.* [60] demonstrated that the CH_2OH-terminated regioregular P3HT can be grafted into the carboxylic groups of GO via an esterification reaction. The product is soluble in common organic solvents, facilitating structure–property characterization and device fabrication by solution processing. In their study, the authors demonstrated that by using chemically grafted graphene-P3HT as active layer along with thermally evaporated C_{60}, the obtained PCE increased by 200% compared to the device with P3HT/C_{60} active layer under AM1.5 illumination (100 mW cm^{-2}) (Figure 15.7).

One of the most commonly used techniques to solubilize conjugated polymer systems is via lateral attachment of flexible side chains, and it has been very successful in solubilizing small graphene molecules [73]. However, because of the maximum number of the flexible side chains, in the case of graphenes, with increasing size the intergraphene attraction rapidly overtakes the solubilization forces, making it less effective. Thus, in order to reduce the tendency of forming insoluble aggregates by large graphene nanostructures, Yan *et al.* [46] proposed

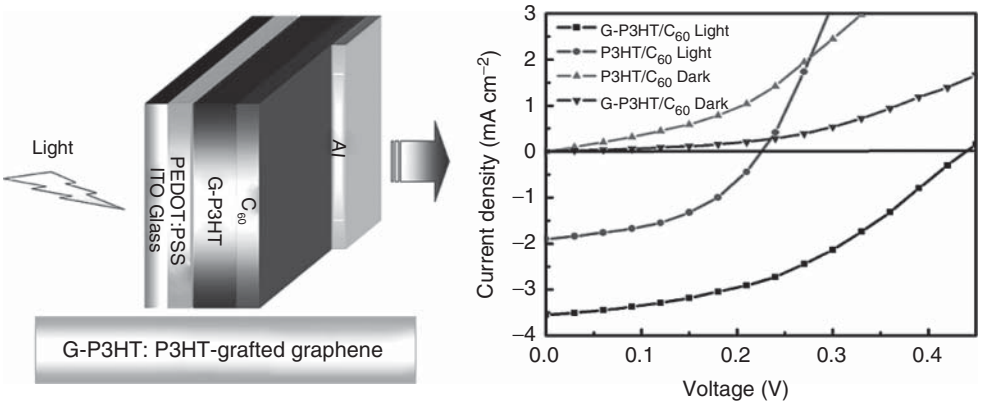

Figure 15.7 (a) Schematic and (b) current–voltage characteristics of the photovoltaic devices using P3HT/C_{60} or G-P3HT/C_{60} as the active layer. (Reproduced with permission from Ref. [60]. Copyright (2010), American Chemical Society.)

a method to shield the graphene layers from each other by enclosing them in all three dimensions (Figure 15.8a). The authors synthesized solution-processable graphene QDs with uniform sizes, which were then used as a sensitizer for solar cells. However, the performance of their device was poor due to a significantly low J_{sc} and V_{oc} (Figure 15.8b). They attributed the low J_{sc} to the low affinity of QDs toward the oxide surfaces.

Graphene quantum dot (GQD) can also be synthesized from graphene sheets (GSs) via a hydrothermal approach [74], where GSs are obtained by thermal oxidation of GO sheets followed by a dialysis process. The sizes of the obtained GQDs were mainly in the range 5–15 nm (Figure 15.9a). Gupta *et al.* [47] used hybrid OSCs with the structure ITO/PEDOT:PSS/P3HT:ANI-GQDs/LiF/Al in their study. For a comparison, the OSCs utilizing P3HT/ANI-GS with ANI-GS contents of 0.5, 1, 3, 5, 10, and 15 wt% (ratio to P3HT) were also measured (Figure 15.9b). As seen from Figure 15.9b, a higher FF for the P3HT/ANI-GQD device was obtained compared to the GS device. Although the obtained PCE showed significant improvement from the previously discussed GQD-based solar cells, the J_{sc} was still significantly low compared to the current state-of-the-art devices. More investigations are needed to understand and improve the performance of GQD-based solar cells.

15.2.2.2 **Schottky Junctions**

The first and successful attempt to replace silicon with carbon-based material in a solar cell was by using diamond-like amorphous film (a-C). Despite the successful formation of p-type a-C/n-type silicon junction, a-C is mainly a unipolar semiconductor, thereby making it difficult to process dopants and eliminating defects. Hence, recently, Li *et al.* [49b] attempted to deposit GS on an n-Si wafer to fabricate solar cells with a PCE of 1.5% (Figure 15.10a). Later, improvements were carried out by Feng *et al.* [75], in which they used a silicon

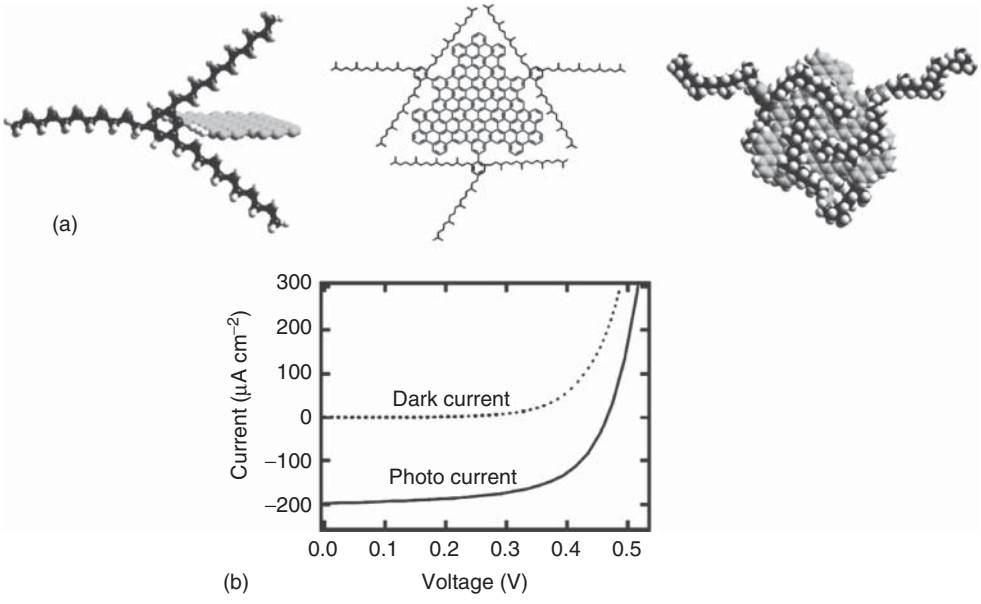

Figure 15.8 (a) Strategy to make large graphene quantum dots soluble. (b) The current–voltage characteristics of a typical nanocrystalline TiO_2 solar cell sensitized by QDs in the dark and under illumination, respectively. (Reproduced with permission from Ref. [46]. Copyright (2009), Wiley VCH.)

pillar array (SPA) to replace the planar Si (Figure 15.10b). The advantage of SPA over planar Si is that the former can improve the harvesting of the incident light. Their proposed graphene/SPA Schottky junction solar cells demonstrated a V_{oc} of 0.47 V, J_{sc} of 15.19 mA cm^{-2}, and PCE of 2.90%. Later, the same group further improved the photovoltaic performance by using chemically doped graphene with HNO_3, where the PCE increased to 4.35% (Figure 15.10c) [76]. This seems intriguing because the PCE of the Schottky junction solar cells again improved to 8.6%, as reported by Miao *et al.* [48]. In their work, they used p-type doped bis(trifluoromethanesulfonyl)amide [$(CF_3SO_2)_2NH$] (TFSA), whereby R_{sr} decreased by 70% (Figure 15.10d). Finally in 2013, Zhang *et al.* [77] reported the highest PCE for graphene/Si Schottky junction solar cells via both surface modification and graphene doping. In their study, P3HT was used as the electron blocking layer, whereby the performance was significantly improved from 7.65% to 10.30% after HNO_3 doping (Figure 15.10e). This is the best reported value for graphene-based Schottky junction solar cells to date. Despite the big improvement in the field of graphene-based Schottky junction solar cells, there is still room for much improvement including the following:

1) The trade-off between conductivity and transparency of the graphene films needs to be fully optimized.
2) The ability to tune the sheet resistance must be seriously taken into consideration, because it leads to a high series resistance.

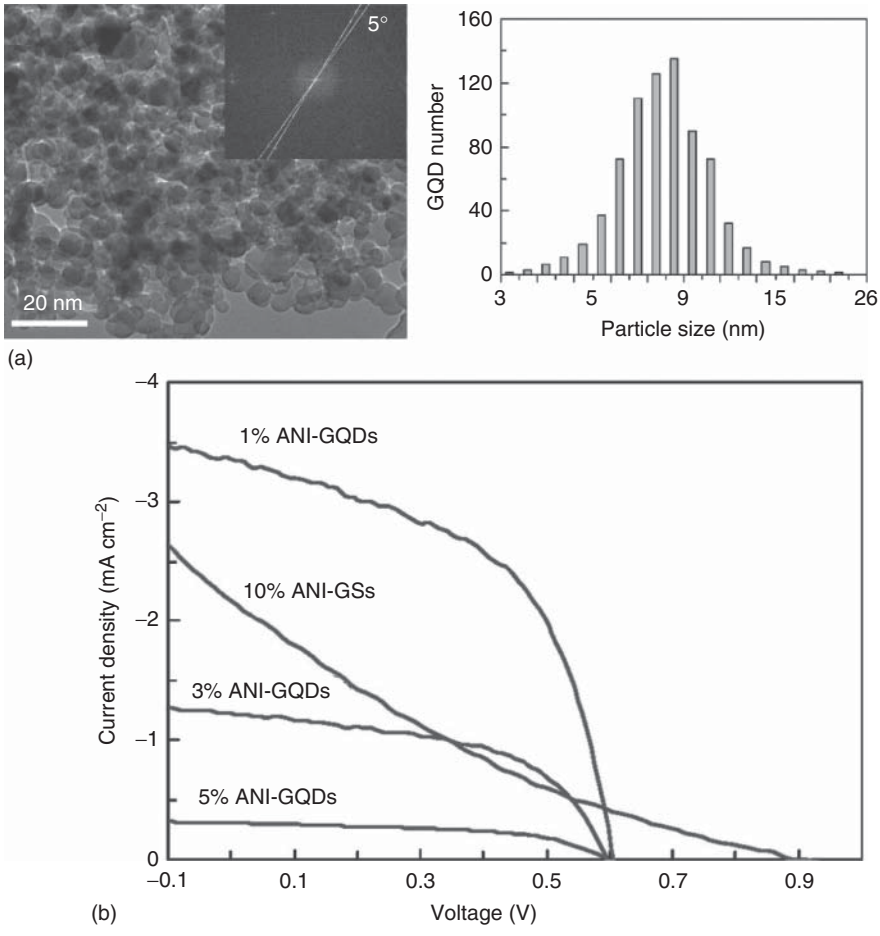

Figure 15.9 (a) TEM image and diameter distribution of the GQDs. (b) *J–V* characteristics of the photovoltaic devices based on ANI-GQDs with different GQD content and ANI-GS (under optimized condition) annealed at 160 °C for 10 min, under AM1.5G 100 mW cm^{-2} illumination. (Reproduced with permission from Ref. [47]. Copyright (2009), Wiley VCH.)

15.2.3 Charge Transport Layer

15.2.3.1 Hole Transport Layer

A few years later, in 2010, Li *et al.* [57] demonstrated for the first time the use of GO as the HTL in a polymer solar cell (PSC). In their work, the structure consisted of ITO/GO/P3HT:PCBM/Al, as shown in Figure 15.11. In addition, two sets of devices were fabricated for comparison: ITO/P3HT:PCBM/Al and ITO/PEDOT:PSS/P3HT:PCBM/Al. The ITO-based device gave a J_{sc} of 9.84 mA cm^{-2}, V_{oc} of 0.45 V, FF of 41.5%, and PCE of 1.8%. On the other hand,

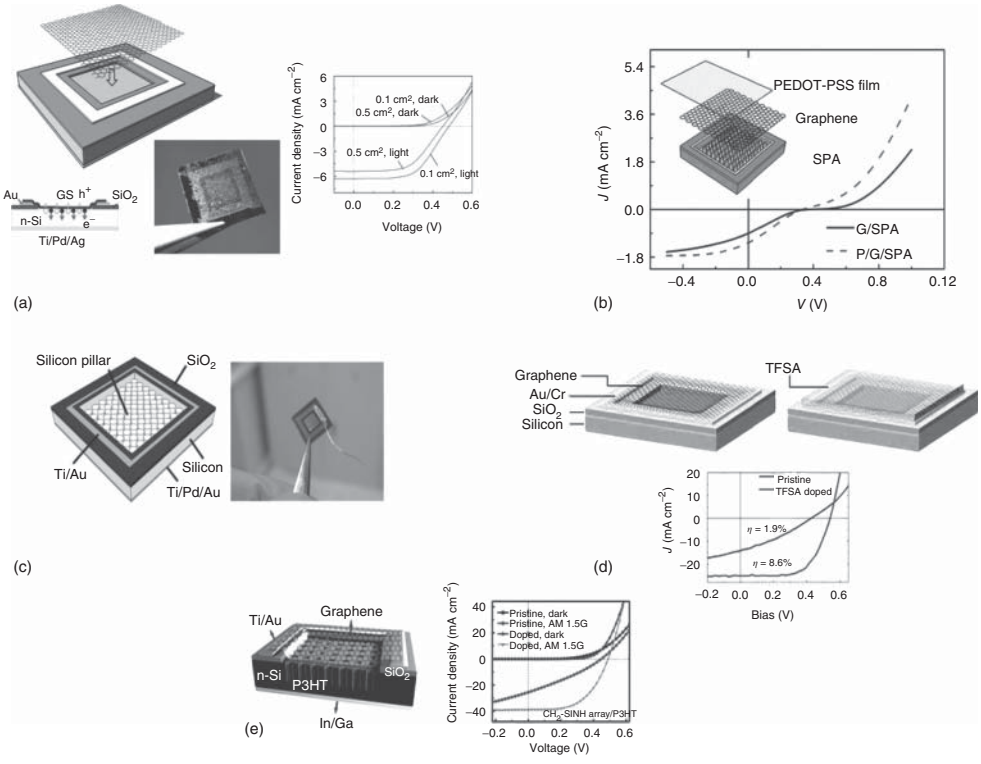

Figure 15.10 (a) Schematic illustration and photograph of the graphene-on-silicon Schottky junction solar cell configuration. (b) The light *J*–*V* curves of G/SPA and P/G/SPA solar cells. (c) Schematic view of a G/SiPA Schottky solar cell and photograph of a G/SiPA solar cell with 0.09 cm^2 junction area. Silver wire was glued to the front electrode for test with silver paste. (d) Configurations of pristine and TFSA-doped graphene-on-silicon Schottky junction solar cell, and their photovoltaic behaviors. (e) Photovoltaic characteristics of the FLG/P3HT/SiNH array before and after HNO_3 doping. (Reproduced with permission from Refs [48, 49b, 76, 77]. Copyrights (2011), (2012), and (2013), Wiley VCH, The American Chemical Society, and The Royal Chemical Society, respectively.)

the PEDOT:PSS-based device showed a significantly higher J_{sc} of 11.15 mA cm^{-2}, V_{oc} of 0.58 V, FF of 56.9%, and PCE of 3.6%. For the GO-based device, the values were J_{sc} of 11.40 mA cm^{-2}, V_{oc} 0.57 V, FF of 54.3%, and PCE 3.5%. The improved performance of the GO-based device was due to the matching of the work function of GO and P3HT, which was found to be 4.9 eV compared to that of pristine GO of 4.6 eV. The higher work function of GO is due to the large electronegativity of oxygen (O) atoms, which produce surface C–C dipoles.

Gao *et al.* [78] developed a simple method to modify the anode interfacial layer of inverted PSCs. The GO layer was spin-coated on top of the active layer P3HT:PCBM at 2000 rpm for 45 s. No heat treatment was carried out after the deposition of the GO layer, and for comparison a control device was fabricated utilizing PEDOT:PSS and without any interfacial layer. The GO, PEDOT:PSS,

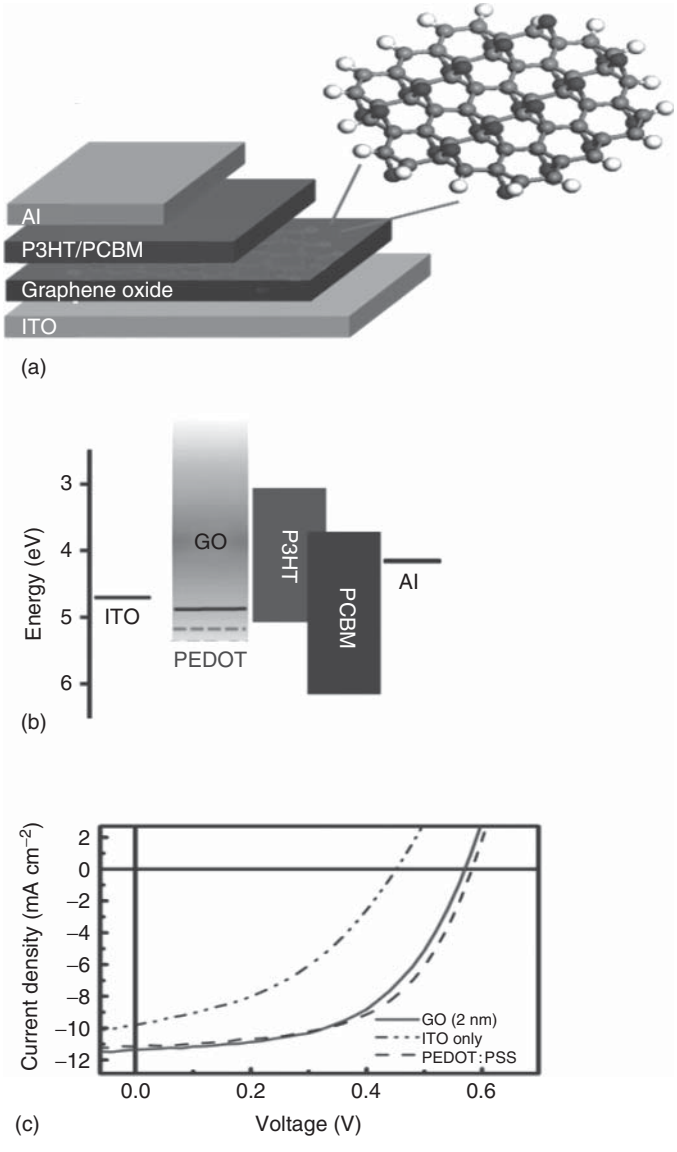

Figure 15.11 (a) Schematic of the photovoltaic device structure consisting of ITO/GO/P3HT:PCBM/Al. (b) Energy level diagrams of the bottom electrode ITO, interlayer materials (PEDOT:PSS, GO), P3HT (donor), and PCBM (acceptor), and the top electrode Al. (c) Current–voltage characteristics of photovoltaic devices with no hole transport layer (curve labeled as ITO), with 30-nm PEDOT:PSS layer, and 2-nm-thick GO film. (Reproduced with permission from Ref. [57]. Copyright (2010), of Wiley VCH.)

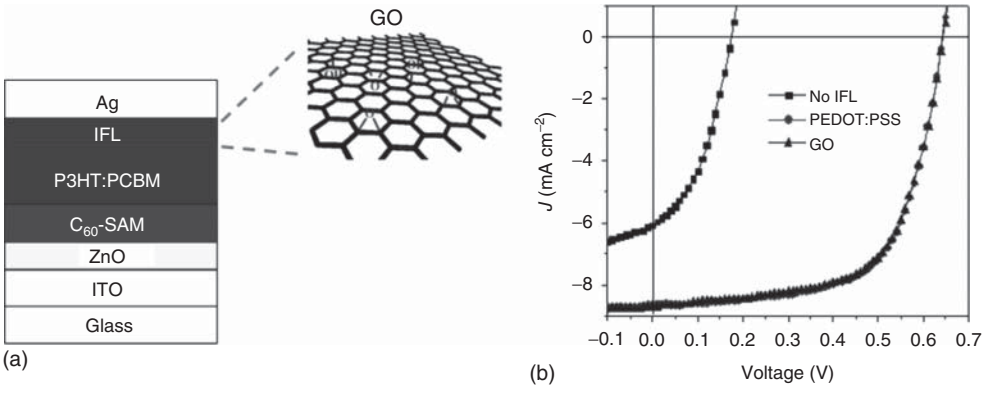

Figure 15.12 (a) Device configuration of the inverted PSCs using GO as hole selective interfacial layer. The right images show the schematic structure of GO. (b) The current density versus voltage (*J*–*V*) characteristics of the inverted PSCs without interface layer, with a 50-nm PEDOT:PSS layer, and with a 2.1-nm GO layer. (Reproduced with permission from Ref. [78]. Copyright (2010), American Physical Society.)

and PSC without the interfacial layer gave PCEs of 3.13%, 3.54%, and 0.43%, respectively (Figure 15.12). A major drawback in the GO-based PSCs is the slightly lower FF of 58.2% compared to that of PEDOT:PSS-based PSC of 63.7%. On the other hand, the poor performance of PSCs without the presence of an anode interfacial layer is attributed to the potential formation of undesirable interfacial dipole through the charge-transfer interactions between PCBM and Ag [79].

In addition, Yun *et al.* [58] carried out a comparative study of solution-processed conventional rGO and *p*-toulenesulfonyl hydrazine (prGO) as HTLs in conventional PSCs. Both prGO and rGO films exhibited 10^5 times higher conductivity than GO films. Unlike GO and rGO, prGO shows a uniform morphology on the ITO surface (Figure 15.13a–c). Thus, prGO provides better PSC performance than GO and rGO (Figure 15.13d). In addition, prGO-based device also demonstrated better lifetime compared with other devices based on GO and rGO (Figure 15.13e).

The hole extraction property of GO arises from two factors: (i) doping of the adjacent donor polymer in active layer by periphery –COOH groups of GO to minimize the contact resistance, and (ii) transporting holes through its basal plane to be collected on the anode [57–59, 78, 80]. Thus, to improve the hole transport capability, Liu *et al.* [81] proposed sulfated GO with $-OSO_3H$ groups (Figure 15.14a). The obtained product GO-OSO_3H showed a superior hole extraction layer as a result of the matching work function for ohmic contact with the active materials. The significantly improved FF from 58% to 71% (Figure 15.14b) was due to the higher conductivity of GO-OSO_3H, being 1.3 S m^{-1} compared to that of GO of 0.004 S m^{-1}. Consequently, the PCE of GO-OSO_3H-based PSCs was 4.37%, where the control device employing GO-based PSCs was 3.34%.

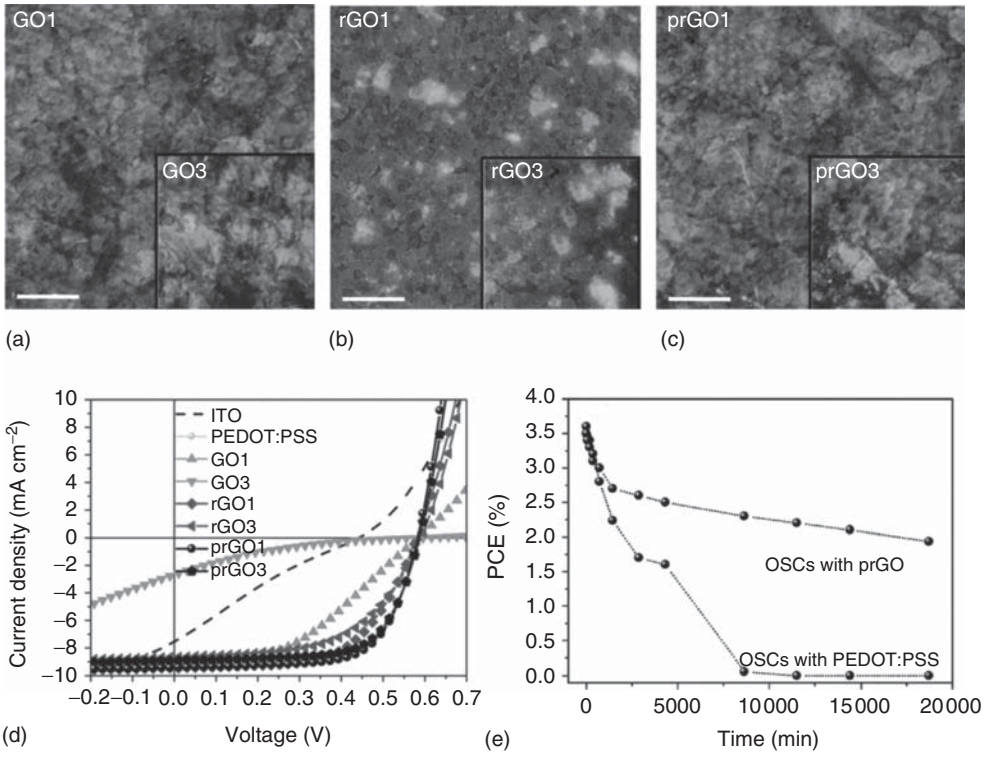

Figure 15.13 AFM height images of (a) GO, (b) rGO, and (c) prGO. The scale bar in the AFM images represents 1 μm. (d) *J–V* curves of PSCs based on different anode interfacial layers. (e) Changes in PCE of a conventional PEDOT:PSS-based OSC and an OSC with the prGO anode interfacial layer during exposure to air. (Reproduced with permission from Ref. [58]. Copyright (2011), Wiley VCH.)

Furthermore, the device performance was nearly independent of the GO-OSO_3H layer thickness (Figure 15.14c).

Jeon *et al.* [82], on the other hand, demonstrated high-performance PSCs by employing moderately reduced GO by a simple and fast thermal annealing. The GO films were annealed at 150, 250, or 350 °C for 10 min in air. The reduction of was confirmed by the uniformity and less aggregation of GO films as shown by atomic force microscopy (AFM) (Figure 15.15a–d). Another evidence for the reduction was the significant decrease of the C–O peak intensity in the X-ray photoelectron (XPS) spectra (Figure 15.15e–f). Further confirmation of the reduction of GO could be observed from the conductivity values of GO films with and without thermal annealing at 250 °C, where the conductivity of the treated GO films increased from 8×10^{-6} to $1.8\,S\,m^{-1}$. Consequently, the ITO/GO/P3HT:PCBM/LiF/Al PSCs exhibited 3.98% PCE compared to ITO/PEDOT:PSS/P3HT:PCBM/LiF/Al PSCs with 3.85% PCE. The

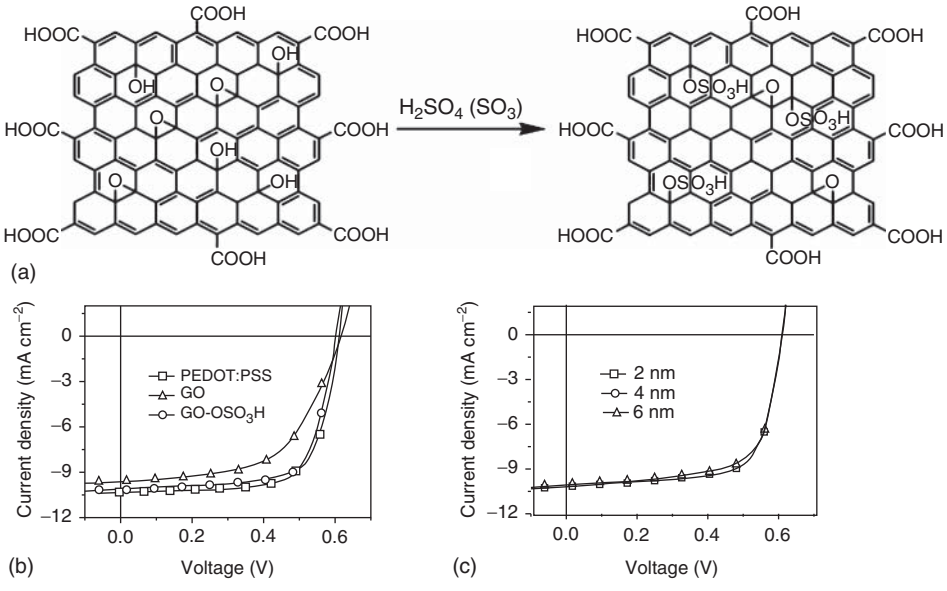

Figure 15.14 (a) Synthetic route to GO-OSO_3H. (b) Current density versus voltage curves of the PSC devices with PEDOT:PSS (25 nm), GO (2 nm), or GO-OSO_3H (2 nm) as the HEL. (c) Current density versus voltage curves of the PSC devices with GO-OSO_3H as HEL with different thicknesses. (Reproduced with permission from Ref. [81]. Copyright (2012), American Chemical Society.)

slight improvement is due to the increase in FF from 63 to 66 in PEDOT:PSS-based PSCs. Furthermore, GO-based PSCs demonstrated better stability than PEDOT:PSS-based PSCs.

A novel treatment of GO was demonstrated by Murray *et al.* [83] through the oxidative chemical exfoliation of graphene powders, which were later deposited via Langmuir–Blodgett (LB) assembly followed by low-level ozone exposure. The resulting GO films exhibited a PCE of 7.39% compared to that of PEDOT:PSS films with a PCE of 7.46% (Figure 15.16a). Moreover, GO-based PSCs showed a 5× improvement in thermal aging lifetime and 20× improvement in humid ambient lifetime compared to PEDOT:PSS-based PSCs (Figure 15.16b,c).

15.2.4
Electron Transport Layer

Taking into account its high electron mobility, graphene and its derivatives have also been used as an ETL. Unlike HTL, ETL should have a low work function in order to match the lowest unoccupied molecular orbital (LUMO) level of the acceptor in the active layer to facilitate electron extraction. Moreover, ETL should efficiently transport electrons to minimize R_s for better photovoltaic performance.

Liu *et al.* [59] published their work on GO-based ETL by using the cesium-neutralized GO for PSCs. By replacing the periphery –COOH groups with

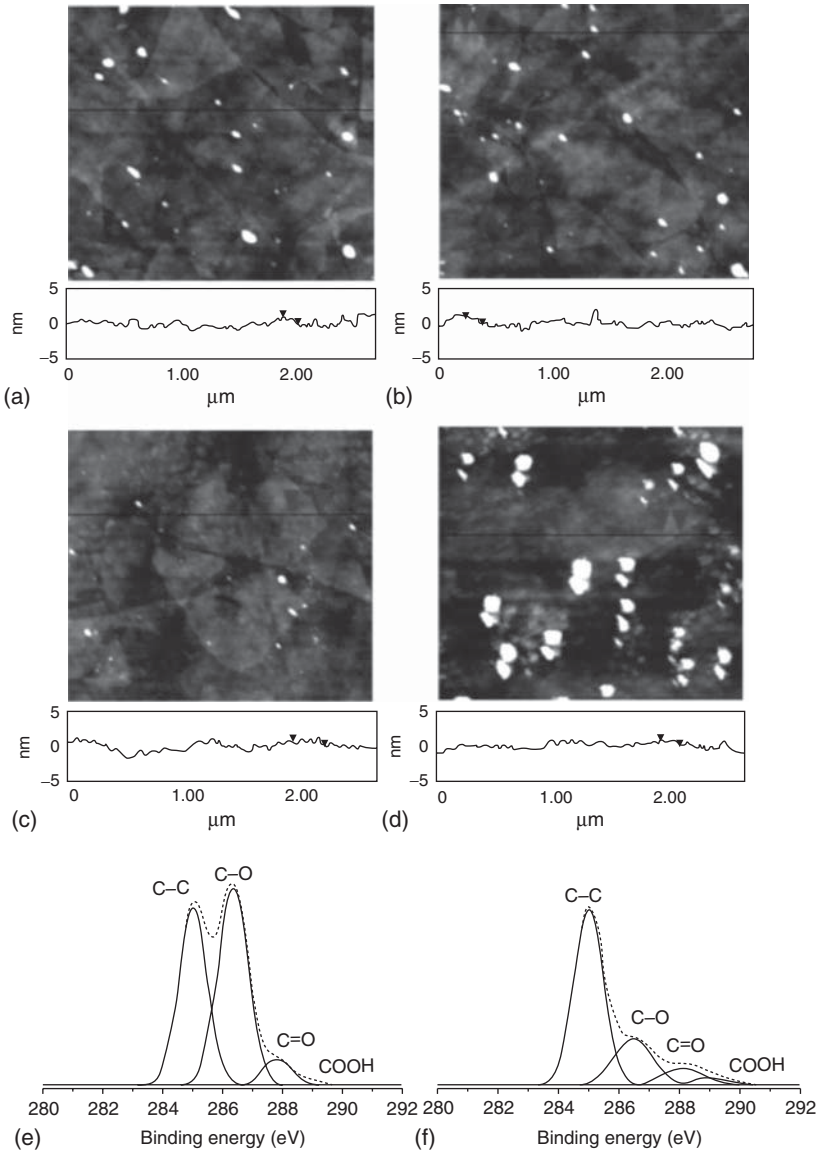

Figure 15.15 AFM topography image of a GO without thermal treatment (a) and thermally treated GO at 150 °C (b), 250 °C (c), and 350 °C (d). XPS spectra of GO without thermal treatment (e) and thermally treated GO at 250 °C (f). (Reproduced with permission from Ref. [82]. Copyright (2012), Elsevier.)

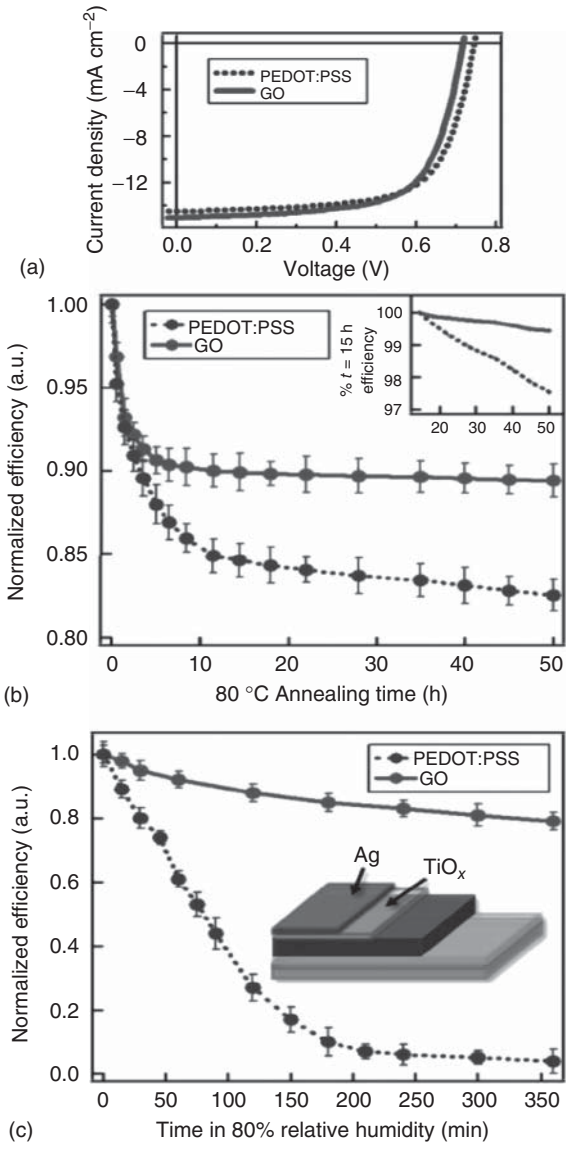

Figure 15.16 (a) Current versus voltage plots under AM1.5G solar simulated light for OPVs fabricated with PEDOT:PSS and GO IFLs. Durability characteristics of PTB7:$PC_{71}BM$ solar cells with PEDOT:PSS and GO IFLs. (b) Thermal degradation of encapsulated devices at 80 °C under N_2 atmosphere. Inset: Plot of the data between 15 and 50 h as a percentage of the efficiency at $t = 15$ h. (c) Environmental degradation of unencapsulated devices fabricated with air-stable electrodes at 80% relative humidity and 25 °C. Inset: Schematic of the device geometry used for humidity degradation testing. (Reproduced with permission from Ref. [83]. Copyright (2011), American Chemical Society.)

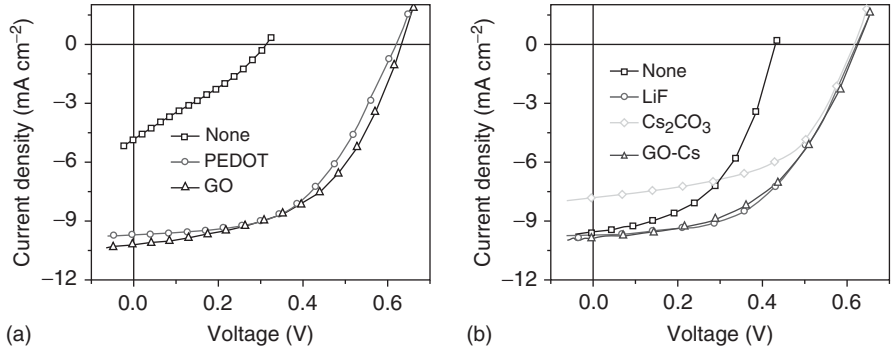

Figure 15.17 (a) *J–V* curves of devices (ITO/interlayer/P3HT:PCBM/LiF/Al) with different hole-extraction interlayers. (b) *J–V* curves of devices (ITO/PEDOT:PSS/P3HT:PCBM/interlayer/Al) with different electron-extraction interlayers. (Reproduced with permission from Ref. [59]. Copyright (2012), Wiley VCH.)

–COOC groups, the work function of GO/Cs-modified AL could be reduced to 4.0 eV. This reduction well matches the LUMO level of PCBM. The modification can be seen from the fabricated conventional and inverted devices. Their conventional device (ITO/GO/P3HT:PCBM/GO-Cs/Al) provided a J_{sc} of 10.30 mA cm^{-2}, V_{oc} of 0.61 V, FF of 59%, and a PCE of 3.67% (Figure 15.17a). On the other hand, the inverted device (ITO/GO-Cs/P3HT:PCBM/GO/Al) provided a J_{sc} of 10.69 mA cm^{-2}, V_{oc} of 0.51 V, FF of 54%, and PCE of 2.97% (Figure 15.17b).

Another example has been reported by Wang *et al.* [84], in which they developed a novel facile stamping process to directly transfer graphene onto the active layer. In this study, they doped the graphene with HNO_3, leading to a graphene oxide film. The transferred GO ETL enhanced the J_{sc} and PCE of the device because of efficient electron charge transport and extraction from the active layer to Al top electrode. Additionally, the PSCs employing a double stack of GO and titanium oxide (TiO_x) interlayer demonstrated the best PCE of 7.5% for poly[N- 9′-heptadecanyl-2,7-carbazole-alt-5,5-(4,7-di-2-thienyl-2′,1′,3′-benzothiadiazole] (PCDTBT):$PC_{71}BM$-based PSCs (Figure 15.18a). They attributed this significant improvement with respect to the control device to the synergistic effect of improved charge transport and enhanced optical field amplitude. In addition to high-performance PSCs, devices with the GO ETL also exhibit a long lifetime of over 30 days' storage in air (Figure 15.18b).

15.2.4.1 Interfacial Layer in Tandem Solar Cells

The first attempt to utilize graphene or its derivatives as the interfacial layer in tandem solar cells was made by Tung *et al.* [64]. These authors obtained a significant increase in the solution viscosity by mixing GO dispersions (0.1–2 wt%) into PEDOT:PSS. Consequently, the PEDOT:PSS/GO mixture provided 2–3 orders of magnitude higher viscosity compared to either pristine GO or PEDOT:PSS. It suggests that gelation favors strong interactions between GO and PEDOT:PSS. In addition, the mixture of GO and PEDOT:PSS also showed increased electrical

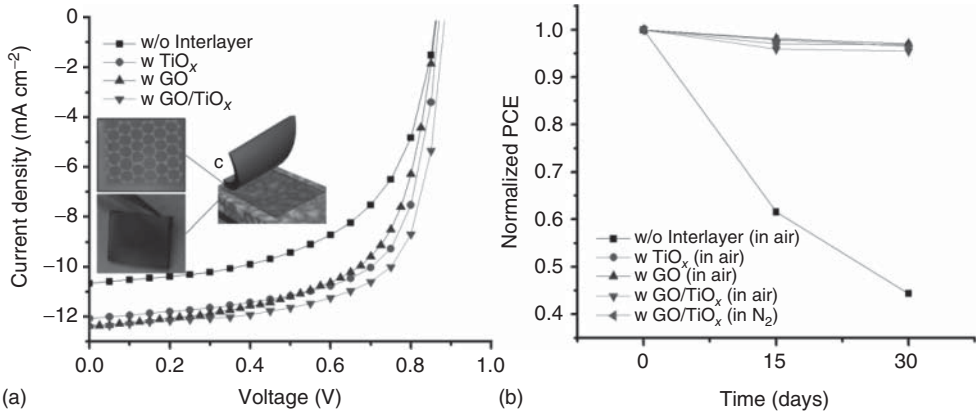

Figure 15.18 (a) *J–V* characteristics of PCDTBT:$PC_{71}BM$ BHJ without an ETL layer and with ETL layers of TiO_x, GO, and GO/TiO_x. (b) Normalized PCE from device-stability test under ambient conditions in air or N_2 atmosphere as a function of time. w/o = without. (Reproduced with permission from Ref. [84]. Copyright (2013), Wiley VCH.)

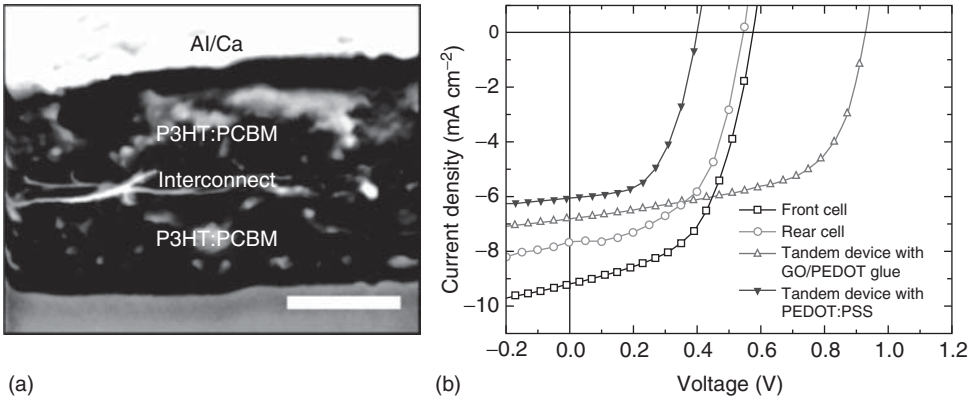

Figure 15.19 (a) Cross-sectional SEM image of an as-fabricated tandem device. The two subcells and the interconnecting layer can be clearly distinguished. Scale bar = 150 nm. (b) *I–V* characteristics of separately prepared front cell and rear cell along with tandem cells laminated with PEDOT:PSS only and GO/PEDOT gel, respectively. (Reproduced with permission from Ref. [64]. Copyright (2011), American Chemical Society.)

conductivity (~0.4 S cm^{-1}) compared to PEDOT:PSS (~0.025 S cm^{-1}). As shown in Figure 15.19, the V_{oc} of the tandem cell is 0.94 V, which is nearly 84% of the sum of the V_{oc}'s of the front and rear subcells, thereby demonstrating that these two subcells are connected in series architecture. In this study, the authors obtained 4.14% PCE, which was higher than that of its front and rear subcells. Their control tandem cell (without GO) provided lower V_{oc} and PCE. These lower V_{oc} and PCE were attributed to the inefficient separation of the front and rear subcells.

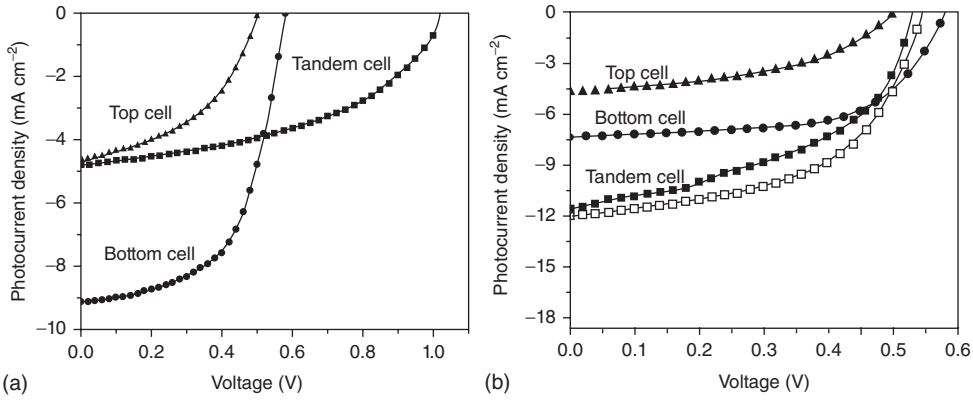

Figure 15.20 (a) *J–V* characteristics of the reference single cell (ITO/PEDOT:PSS/P3HT:PCBM/LiF/Al (bottom cell), ITO/MoO_3/ZnPc:C_{60}/LiF/Al (top cell)), and a series-connected tandem cell under light illumination. (b) *J–V* characteristics of the reference single cells (characterized individually from the parallel-connected tandem cell) and parallel connected tandem cell under light illumination. The theoretical *J–V* curve of the tandem cell is also constructed by summing up the *J–V* curves of the single cells (the line with hollow squares). (Reproduced with permission from Ref. [62]. Copyright (2011), Wiley VCH.)

The same authors also demonstrated the use of GO:single-walled carbon nanotube (SWCNT) as the interconnecting layer in both inverted and conventional tandem solar cells [63]. In this study, the authors employed the same polymer as active layers for the front and rear subcells. The PCEs for conventional and inverted tandem cells were 4.10% and 3.50%, respectively. It is worth noting that the sum of the V_{oc}'s for the conventional and inverted cells is less than the ideal V_{oc}'s for tandem cells.

Moreover, another example of integrating graphene in tandem solar cells can be found in the work of Tong *et al.* [62]. In this study, the work function of graphene could be increased from 4.2 to 5.5 eV by increasing the thickness of the MoO_3 film. By using graphene/MoO_3 as the interconnecting layer in series-connected tandem solar cells, they could achieve a PCE of 2.3% with a V_{oc} of 1.0 V, J_{sc} of 4.8 mA cm^{-2}, and FF of 48% (Figure 15.20a). In the case of parallel-connected tandem solar cells, with MoO_3/graphene/MoO_3 as the interconnecting layer, a PCE of 2.9% was demonstrated (Figure 15.20b). Utilizing this structure, a V_{oc} of 0.52 V, J_{sc} of 11.6 mA cm^{-2}, and FF of 48% were demonstrated. This suggests that graphene can be successfully used to connect the front and rear subcells to multiply the V_{oc} and J_{sc} for achieving high-performance tandem solar cells.

Recently, our groups also demonstrated tandem solar cells utilizing titanium oxide (TiO_x)/GO as the interconnecting layer in a regular architecture [85]. In these tandem cells, we used poly[(4,4′-bis(3-ethylhexyl)dithieno[3,2-*b*:″3′-*d*]silole)-2,6-diyl-alt-(2,5-(3-(2-ethylhexyl)thiophen-2-yl)thiazolo)[5,4-*d*]thiazole]: indene-C_{60} bisadduct (PSEHTT:ICBA) and poly[(4,4′-bis(2-ethylhexyl)dithieno

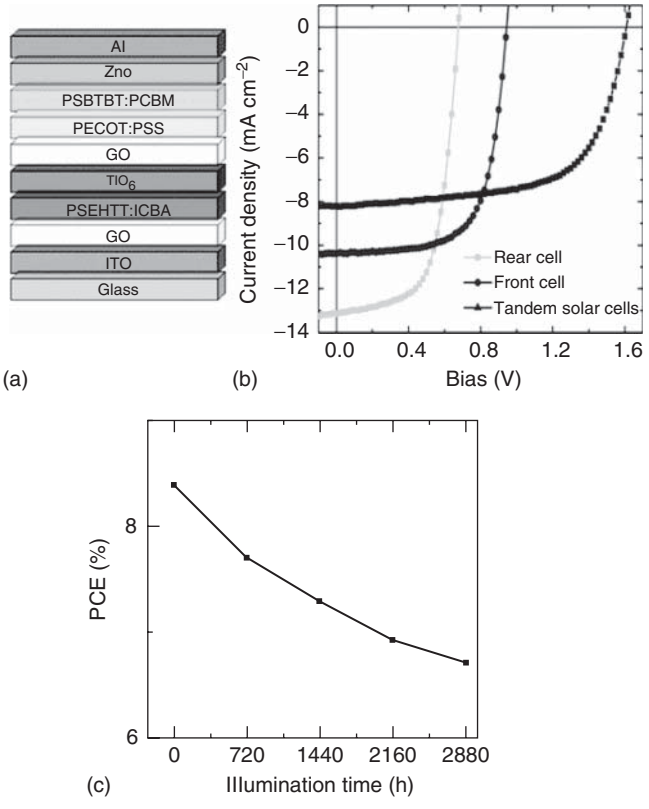

Figure 15.21 (a) Device structure of the polymer tandem solar cells with TiO_2/GO as the recombination layer. (b) Average *J*–*V* characteristics of front, rear (green and red, respectively), and tandem solar cells, under AM1.5 100 mW cm^{-2} illumination. (c) Efficiency decays of organic tandem solar cells. Data is plotted every 720 h and averaged over 117 identical devices. (Reproduced with permission from Ref. [85]. Copyright (2013), Royal Society of Chemistry.)

[3,2-*b*:2′,3′-*d*]silole)-2,6-diyl-alt-(2,1,3-benzothiadiazole)-4,7-diyl]:[6, 6]-phenyl-C_{70} butyric acid methyl ester (PSBTBT:$PC_{70}BM$) as the front and rear subcells' active layers (Figure 15.21a). Our proposed interconnecting layer successfully connected the front and rear subcells, leading to an ideal V_{oc} of 1.62 V (0.94 and 0.68 V, respectively). This ideal sum of the front and rear V_{oc}'s gives a PCE of 8.40% (Figure 15.21b). Moreover, these tandem cells also exhibited excellent lifetime, in which the PCE only degraded 20% from its initial value after 2880 h of continuous illumination (Figure 15.21c). Although our proposed interconnecting layer provided the ideal V_{oc}, the deposition step of TiO_x required special attention, which may lead to other crucial problems.

15.3 Conclusion

In this chapter, we systematically summarized the recent advances of graphene and its derivatives in organic photovoltaics (OPVs). Although huge progress has already been achieved, research in this area can still be considered as in its early stages and a lot of issues remain unsolved: for instance, tackling the lower conductivities of the chemically modified graphene, developing novel approaches to blend single-layer graphene sheets into polymer matrices, and improving the application of graphene-based OPVs in terms of the mechanism used to explain the impact of graphene. This is due to the fact that the current explanation is based on certain assumptions, and the performance of graphene-based OPV devices is still far below their state-of-the-art counterparts.

Acknowledgment

This work was supported by the Human Resources Development program (No. 20134010200490) of the Korea Institute of Energy Technology Evaluation and Planning (KETEP) grant funded by the Korea government Ministry of Trade, Industry and Energy.

References

1. Geim, A.K. and Novoselov, K.S. (2007) The rise of graphene. *Nat. Mater.*, **6** (3), 183–191.
2. Bolotin, K.I., Ghahari, F., Shulman, M.D., Stormer, H.L., and Kim, P. (2009) Observation of the fractional quantum Hall effect in graphene. *Nature*, **462** (7270), 196–199.
3. Kim, K.S., Zhao, Y., Jang, H., Lee, S.Y., Kim, J.M., Kim, K.S., Ahn, J.H., Kim, P., Choi, J.Y., and Hong, B.H. (2009) Large-scale pattern growth of graphene films for stretchable transparent electrodes. *Nature*, **457** (7230), 706–710.
4. Stankovich, S., Dikin, D.A., Dommett, G.H.B., Kohlhaas, K.M., Zimney, E.J., Stach, E.A., Piner, R.D., Nguyen, S.T., and Ruoff, R.S. (2006) Graphene-based composite materials. *Nature*, **442** (7100), 282–286.
5. Eda, G., Fanchini, G., and Chhowalla, M. (2008) Large-area ultrathin films of reduced graphene oxide as a transparent and flexible electronic material. *Nat. Nanotechnol.*, **3** (5), 270–274.
6. Obraztsov, A.N. (2009) Chemical vapour deposition: making graphene on a large scale. *Nat. Nanotechnol.*, **4** (4), 212–213.
7. Park, S. and Ruoff, R.S. (2009) Chemical methods for the production of graphenes. *Nat. Nanotechnol.*, **4** (4), 217–224.
8. Geim, A.K. (2009) Graphene: status and prospects. *Science*, **324** (5934), 1530–1534.
9. Li, D. and Kaner, R.B. (2008) Graphene-based materials. *Science*, **320** (5880), 1170–1171.
10. Li, X.L., Wang, X.R., Zhang, L., Lee, S.W., and Dai, H.J. (2008) Chemically derived, ultrasmooth graphene nanoribbon semiconductors. *Science*, **319** (5867), 1229–1232.
11. Li, X.S., Cai, W.W., An, J.H., Kim, S., Nah, J., Yang, D.X., Piner, R., Velamakanni, A., Jung, I., Tutuc, E., Banerjee, S.K., Colombo, L., and Ruoff, R.S. (2009) Large-area synthesis of high-quality and uniform graphene films on copper foils. *Science*, **324** (5932), 1312–1314.

12. Stoller, M.D., Park, S.J., Zhu, Y.W., An, J.H., and Ruoff, R.S. (2008) Graphene-based ultracapacitors. *Nano Lett.*, **8** (10), 3498–3502.
13. Novoselov, K.S., Geim, A.K., Morozov, S.V., Jiang, D., Zhang, Y., Dubonos, S.V., Grigorieva, I.V., and Firsov, A.A. (2004) Electric field effect in atomically thin carbon films. *Science*, **306** (5696), 666–669.
14. Si, Y. and Samulski, E.T. (2008) Synthesis of water soluble graphene. *Nano Lett.*, **8** (6), 1679–1682.
15. Shen, J.F., Hu, Y.Z., Li, C., Qin, C., Shi, M., and Ye, M.X. (2009) Layer-by-layer self-assembly of graphene nanoplatelets. *Langmuir*, **25** (11), 6122–6128.
16. Schniepp, H.C., Li, J.L., McAllister, M.J., Sai, H., Herrera-Alonso, M., Adamson, D.H., Prud'homme, R.K., Car, R., Saville, D.A., and Aksay, I.A. (2006) Functionalized single graphene sheets derived from splitting graphite oxide. *J. Phys. Chem. B*, **110** (17), 8535–8539.
17. Kosynkin, D.V., Higginbotham, A.L., Sinitskii, A., Lomeda, J.R., Dimiev, A., Price, B.K., and Tour, J.M. (2009) Longitudinal unzipping of carbon nanotubes to form graphene nanoribbons. *Nature*, **458** (7240), 872–876.
18. Jiao, L.Y., Wang, X.R., Diankov, G., Wang, H.L., and Dai, H.J. (2010) Facile synthesis of high-quality graphene nanoribbons. *Nat. Nanotechnol.*, **5** (5), 321–325.
19. Sutter, P.W., Flege, J.I., and Sutter, E.A. (2008) Epitaxial graphene on ruthenium. *Nat. Mater.*, **7** (5), 406–411.
20. Dedkov, Y.S., Fonin, M., Rudiger, U., and Laubschat, C. (2008) Rashba effect in the graphene/ni(111) system. *Phys. Rev. Lett.*, **100** (10), 107602.
21. Reina, A., Jia, X.T., Ho, J., Nezich, D., Son, H.B., Bulovic, V., Dresselhaus, M.S., and Kong, J. (2009) Large area, few-layer graphene films on arbitrary substrates by chemical vapor deposition. *Nano Lett.*, **9** (1), 30–35.
22. Wu, J.S., Pisula, W., and Müllen, K. (2007) Graphenes as potential material for electronics. *Chem. Rev.*, **107** (3), 718–747.
23. Zhi, L.J. and Müllen, K. (2008) A bottom-up approach from molecular nanographenes to unconventional carbon materials. *J. Mater. Chem.*, **18** (13), 1472–1484.
24. Yang, X.Y., Dou, X., Rouhanipour, A., Zhi, L.J., Rader, H.J., and Müllen, K. (2008) Two-dimensional graphene nanoribbons. *J. Am. Chem. Soc.*, **130** (13), 4216–4217.
25. Yan, X., Cui, X., and Li, S.L. (2010) Synthesis of large, stable colloidal graphene quantum dots with tunable size. *J. Am. Chem. Soc.*, **132** (17), 5944–5945.
26. Eda, G. and Chhowalla, M. (2010) Chemically derived graphene oxide: towards large-area thin-film electronics and optoelectronics. *Adv. Mater.*, **22** (22), 2392–2415.
27. Wei, D.C. and Liu, Y.Q. (2010) Controllable synthesis of graphene and its applications. *Adv. Mater.*, **22** (30), 3225–3241.
28. Dreyer, D.R., Park, S., Bielawski, C.W., and Ruoff, R.S. (2010) The chemistry of graphene oxide. *Chem. Soc. Rev.*, **39** (1), 228–240.
29. Bae, S., Kim, H., Lee, Y., Xu, X.F., Park, J.S., Zheng, Y., Balakrishnan, J., Lei, T., Kim, H.R., Song, Y.I., Kim, Y.J., Kim, K.S., Ozyilmaz, B., Ahn, J.H., Hong, B.H., and Iijima, S. (2010) Roll-to-roll production of 30-inch graphene films for transparent electrodes. *Nat. Nanotechnol.*, **5** (8), 574–278.
30. Wang, X., Zhi, L., and Mullen, K. (2007) Transparent, conductive graphene electrodes for dye-sensitized solar cells. *Nano Lett.*, **8** (1), 323–327.
31. Yin, Z.Y., Sun, S.Y., Salim, T., Wu, S.X., Huang, X.A., He, Q.Y., Lam, Y.M., and Zhang, H. (2010) Organic photovoltaic devices using highly flexible reduced graphene oxide films as transparent electrodes. *ACS Nano*, **4** (9), 5263–5268.
32. Gomez De Arco, L., Zhang, Y., Schlenker, C.W., Ryu, K., Thompson, M.E., and Zhou, C. (2010) Continuous, highly flexible, and transparent graphene films by chemical vapor deposition for organic photovoltaics. *ACS Nano*, **4** (5), 2865–2873.
33. Tung, V.C., Chen, L.-M., Allen, M.J., Wassei, J.K., Nelson, K., Kaner, R.B., and Yang, Y. (2009) Low-temperature solution processing of graphene – carbon

nanotube hybrid materials for high-performance transparent conductors. *Nano Lett.*, **9** (5), 1949–1955.

34. Wang, Y., Tong, S.W., Xu, X.F., Özyilmaz, B., and Loh, K.P. (2011) Interface engineering of layer-by-layer stacked graphene anodes for high-performance organic solar cells. *Adv. Mater.*, **23** (13), 1514–1518.
35. Lee, Y.-Y., Tu, K.-H., Yu, C.-C., Li, S.-S., Hwang, J.-Y., Lin, C.-C., Chen, K.-H., Chen, L.-C., Chen, H.-L., and Chen, C.-W. (2011) Top laminated graphene electrode in a semitransparent polymer solar cell by simultaneous thermal annealing/releasing method. *ACS Nano*, **5** (8), 6564–6570.
36. Park, H., Brown, P.R., Bulović, V., and Kong, J. (2011) Graphene as transparent conducting electrodes in organic photovoltaics: studies in graphene morphology, hole transporting layers, and counter electrodes. *Nano Lett.*, **12** (1), 133–140.
37. Hsu, C.-L., Lin, C.-T., Huang, J.-H., Chu, C.-W., Wei, K.-H., and Li, L.-J. (2012) Layer-by-layer Graphene/TCNQ stacked films as conducting anodes for organic solar cells. *ACS Nano*, **6** (6), 5031–5039.
38. Li, S., Luo, Y., Lv, W., Yu, W., Wu, S., Hou, P., Yang, Q., Meng, Q., Liu, C., and Cheng, H.-M. (2011) Vertically aligned carbon nanotubes grown on graphene paper as electrodes in lithium-ion batteries and dye-sensitized solar cells. *Adv. Energy Mater.*, **1** (4), 486–490.
39. Lin, T., Huang, F., Liang, J., and Wang, Y. (2011) A facile preparation route for boron-doped graphene, and its CdTe solar cell application. *Energy Environ. Sci.*, **4** (3), 862–865.
40. Liang, J., Bi, H., Wan, D., and Huang, F. (2012) Novel Cu Nanowires/Graphene as the back contact for CdTe solar cells. *Adv. Funct. Mater.*, **22** (6), 1267–1271.
41. Yin, Z., Wu, S., Zhou, X., Huang, X., Zhang, Q., Boey, F., and Zhang, H. (2010) Electrochemical deposition of ZnO nanorods on transparent reduced graphene oxide electrodes for hybrid solar cells. *Small*, **6** (2), 307–312.
42. Bi, H., Huang, F., Liang, J., Xie, X., and Jiang, M. (2011) Transparent conductive graphene films synthesized by ambient pressure chemical vapor deposition used as the front electrode of CdTe solar cells. *Adv. Mater.*, **23** (38), 3202–3206.
43. Zhang, D., Xie, F.X., Lin, P., and Choy, W.C.H. (2013) Al-TiO_2 composite-modified single-layer graphene as an efficient transparent cathode for organic solar cells. *ACS Nano*, **7** (2), 1740–1747.
44. Park, H., Chang, S., Jean, J., Cheng, J.J., Araujo, P.T., Wang, M.S., Bawendi, M.G., Dresselhaus, M.S., Bulovic, V., Kong, J., and Gradecak, S. (2013) Graphene cathode-based ZnO nanowire hybrid solar cells. *Nano Lett.*, **13** (1), 233–2339.
45. Liu, Z., Liu, Q., Huang, Y., Ma, Y., Yin, S., Zhang, X., Sun, W., and Chen, Y. (2008) Organic photovoltaic devices based on a novel acceptor material:graphene. *Adv. Mater.*, **20** (20), 3924–3930.
46. Yan, X., Cui, X., Li, B., and Li, L.-S. (2010) Large, solution-processable graphene quantum dots as light absorbers for photovoltaics. *Nano Lett.*, **10** (5), 1869–1873.
47. Gupta, V., Chaudhary, N., Srivastava, R., Sharma, G.D., Bhardwaj, R., and Chand, S. (2011) Luminescent graphene quantum dots for organic photovoltaic devices. *J. Am. Chem. Soc.*, **133** (26), 9960–9963.
48. Miao, X., Tongay, S., Petterson, M.K., Berke, K., Rinzler, A.G., Appleton, B.R., and Hebard, A.F. (2012) High efficiency graphene solar cells by chemical doping. *Nano Lett.*, **12** (6), 2745–2750.
49. (a) Song, J., Yin, Z., Yang, Z., Amaladass, P., Wu, S., Ye, J., Zhao, Y., Deng, W.-Q., Zhang, H., and Liu, X.-W. (2011) Enhancement of photogenerated electron transport in dye-sensitized solar cells with introduction of a reduced graphene oxide–TiO_2 junction. *Chem. A Eur. J.*, **17** (39), 10832–10837; (b) Li, X., Zhu, H., Wang, K., Cao, A., Wei, J., Li, C., Jia, Y., Li, Z., Li, X., and Wu, D. (2010) Graphene-on-silicon schottky junction solar cells. *Adv. Mater.*, **22** (25), 2743–2748.
50. Wang, H., Yang, Y., Liang, Y., Cui, L.-F., Sanchez Casalongue, H., Li, Y., Hong, G., Cui, Y., and Dai, H. (2011) $LiMn_{1-x}Fe_xPO_4$ nanorods grown

on graphene sheets for ultrahigh-rate-performance lithium ion batteries. *Angew. Chem. Int. Ed.*, **50** (32), 7364–7368.

51. Lin, Y.X., Li, X.M., Xie, D., Feng, T.T., Chen, Y., Song, R., Tian, H., Ren, T.L., Zhong, M.L., Wang, K.L., and Zhu, H.W. (2013) Graphene/semiconductor heterojunction solar cells with modulated antireflection and graphene work function. *Energy Environ. Sci.*, **6** (1), 108–115.
52. Wang, S., Goh, B.M., Manga, K.K., Bao, Q., Yang, P., and Loh, K.P. (2010) Graphene as atomic template and structural scaffold in the synthesis of graphene-organic hybrid wire with photovoltaic properties. *ACS Nano*, **4** (10), 6180–6186.
53. Guo, C.X., Yang, H.B., Sheng, Z.M., Lu, Z.S., Song, Q.L., and Li, C.M. (2010) Layered graphene/quantum dots for photovoltaic devices. *Angew. Chem. Int. Ed.*, **49** (17), 3014–3017.
54. Zhou, W., Zhu, J., Cheng, C., Liu, J., Yang, H., Cong, C., Guan, C., Jia, X., Fan, H.J., Yan, Q., Li, C.M., and Yu, T. (2011) A general strategy toward graphene/metal oxide core–shell nanostructures for high-performance lithium storage. *Energy Environ. Sci.*, **4** (12), 4954–4961.
55. Yang, N., Zhai, J., Wang, D., Chen, Y., and Jiang, L. (2010) Two-dimensional graphene bridges enhanced photoinduced charge transport in dye-sensitized solar cells. *ACS Nano*, **4** (2), 887–894.
56. Tang, Y.-B., Lee, C.-S., Xu, J., Liu, Z.-T., Chen, Z.-H., He, Z., Cao, Y.-L., Yuan, G., Song, H., Chen, L., Luo, L., Cheng, H.-M., Zhang, W.-J., Bello, I., and Lee, S.-T. (2010) Incorporation of graphenes in nanostructured TiO_2 films via molecular grafting for dye-sensitized solar cell application. *ACS Nano*, **4** (6), 3482–3488.
57. Li, S.-S., Tu, K.-H., Lin, C.-C., Chen, C.-W., and Chhowalla, M. (2010) Solution-processable graphene oxide as an efficient hole transport layer in polymer solar cells. *ACS Nano*, **4** (6), 3169–3174.
58. Yun, J.-M., Yeo, J.-S., Kim, J., Jeong, H.-G., Kim, D.-Y., Noh, Y.-J., Kim, S.-S., Ku, B.-C., and Na, S.-I. (2011) Solution-processable reduced graphene oxide as a novel alternative to PEDOT:PSS hole transport layers for highly efficient and stable polymer solar cells. *Adv. Mater.*, **23** (42), 4923–4928.
59. Liu, J., Xue, Y., Gao, Y., Yu, D., Durstock, M., and Dai, L. (2012) Hole and electron extraction layers based on graphene oxide derivatives for high-performance bulk heterojunction solar cells. *Adv. Mater.*, **24** (17), 2228–2233.
60. Yu, D., Yang, Y., Durstock, M., Baek, J.-B., and Dai, L. (2010) Soluble P3HT-grafted graphene for efficient bilayer-heterojunction photovoltaic devices. *ACS Nano*, **4** (10), 5633–5640.
61. Kim, J., Tung, V.C., and Huang, J. (2011) Water processable graphene oxide:single walled carbon nanotube composite as anode modifier for polymer solar cells. *Adv. Energy Mater.*, **1** (6), 1052–1057.
62. Tong, S.W., Wang, Y., Zheng, Y., Ng, M.-F., and Loh, K.P. (2011) Graphene intermediate layer in tandem organic photovoltaic cells. *Adv. Funct. Mater.*, **21** (23), 4430–4435.
63. Tung, V.C., Kim, J., and Huang, J. (2012) Graphene oxide: single-walled carbon nanotube-based interfacial layer for all-solution-processed multijunction solar cells in both regular and inverted geometries. *Adv. Energy Mater.*, **2** (3), 299–303.
64. Tung, V.C., Kim, J., Cote, L.J., and Huang, J.X. (2011) Sticky interconnect for solution-processed tandem solar cells. *J. Am. Chem. Soc.*, **133** (24), 9262–9265.
65. Rowell, M.W., Topinka, M.A., McGehee, M.D., Prall, H.-J., Dennler, G., Sariciftci, N.S., Hu, L., and Gruner, G. (2006) Organic solar cells with carbon nanotube network electrodes. *Appl. Phys. Lett.*, **88** (3), 233506.
66. Wu, J., Becerril, H.A., Bao, Z., Liu, Z., Chen, Y., and Peumans, P. (2008) Organic solar cells with solution-processed graphene transparent electrodes. *Appl. Phys. Lett.*, **92** (26), 263302.
67. Wang, X., Zhi, L., Tsao, N., Tomović, Ž., Li, J., and Müllen, K. (2008) Transparent carbon films as electrodes in organic solar cells. *Angew. Chem.*, **120** (16), 3032–3034.

68. Kang, M.-G., Xu, T., Park, H.J., Luo, X., and Guo, L.J. (2010) Efficiency enhancement of organic solar cells using transparent plasmonic Ag nanowire electrodes. *Adv. Mater.*, **22** (39), 4378–4383.
69. Lee, J.-Y., Connor, S.T., Cui, Y., and Peumans, P. (2008) Solution-processed metal nanowire mesh transparent electrodes. *Nano Lett.*, **8** (2), 689–692.
70. Nair, R., Blake, P., Grigorenko, A.N., Novoselov, K.S., Booth, T.J., Stauber, T., Peres, N.M.R., and Geim, A.K. (2008) Fine structure constant defines visual transparency of graphene. *Science*, **320** (5881), 1308.
71. Blake, P., Brimicombe, P.D., Nair, R.R., Booth, T.J., Jiang, D., Schedin, F., Ponomarenko, L.A., Morozov, S.V., Gleeson, H.F., Hill, E.W., Geim, A.K., and Novoselov, K.S. (2008) Graphene-based liquid crystal device. *Nano Lett.*, **8** (6), 1704–1708.
72. Hummers, W.S. and Offeman, R.E. (1958) Preparation of graphitic oxide. *J. Am. Chem. Soc.*, **80** (6), 1339–1339.
73. Li, L.S. and Yan, X. (2010) Colloidal graphene quantum dots. *J. Phys. Chem. Lett.*, **1** (17), 2572–2576.
74. Liua, J. and Li, X. (2014) Hydrothermal synthesis of CdTe quantum dots–TiO_2–graphene hybrid. *Phys. Lett. A*, **378** (4), 405–407.
75. Feng, T., Xie, D., Lin, Y., Zhao, H., Chen, Y., Tian, H., Ren, T., Li, X., Li, Z., Wang, K., Wu, D., and Zhu, H. (2012) Efficiency enhancement of graphene/silicon-pillar-array solar cells by HNO3 and PEDOT-PSS. *Nanoscale*, **4** (6), 2130–2133.
76. Feng, F.T., Xie, D., Lin, Y., Zang, Y., Ren, T., Song, R., Zhao, H., Tian, H., Li, X., Zhu, H., and Liu, L. (2011) Graphene based Schottky junction solar cells on patterned silicon-pillar-array substrate. *Appl. Phys. Lett.*, **99** (23), 233505.
77. Zhang, X., Xie, C., Jie, J., Zhang, X., Wu, Y., and Zhang, W. (2013) High-efficiency graphene/Si nanoarray Schottky junction solar cells via surface modification and graphene doping. *J. Mater. Chem. A*, **1** (22), 6593–6601.
78. Gao, Y., Yip, H.P., Hau, S.K., O'Malley, K.M., Cho, M.C., Chen, H., and Jen, A.K.-Y. (2010) Anode modification of inverted polymer solar cells using graphene oxide. *Appl. Phys. Lett.*, **97** (20), 203306.
79. Akaike, K., Kanai, K., Ouchi, Y., and Seki, K. (2009) Influence of side chain of [6,6]-phenyl-C_{61}-butyric acid methyl ester on interfacial electronic structure of [6,6]-phenyl-C_{61}-butyric acid methyl ester/Ag substrate. *Appl. Phys. Lett.*, **94** (4), 043309.
80. Gao, Y., Yip, H.L., Chen, K.-S., O'Malle, K., Acton, M.O., Sun, Y., Ting, G., Chen, H.Z., and Jen, A.K.-Y. (2011) Surface doping of conjugated polymers by graphene oxide and its application for organic electronic devices. *Adv. Mater.*, **23** (16), 1903–1908.
81. Liu, J., Xue, Y., and Dai, L. (2012) Sulfated graphene oxide as a hole-extraction layer in high-performance polymer solar cells. *J. Phys. Chem. Lett.*, **3** (14), 1928–1933.
82. Jeon, Y.-J., Yun, J.-M., Kim, D.-Y., Na, S.-I., and Kim, S.-S. (2012) High-performance polymer solar cells with moderately reduced graphene oxide as an efficient hole transporting layer. *Sol. Energy Mater. Sol. Cells*, **105** (2-3), 96–102.
83. Murray, I.P., Lou, S.J., Cote, L.J., Loser, S., Kadleck, C.J., Xu, T., Szarko, J.M., Rolczynski, B.S., Johns, J.E., Huang, J.X., Yu, L.P., Chen, L.X., Marks, T.J., and Hersam, M.C. (2011) Graphene oxide interlayers for robust, high-efficiency organic photovoltaics. *J. Phys. Chem. Lett.*, **2** (24), 3006–3012.
84. Wang, D.H., Kim, J.K., Seo, J.H., Park, I., Hong, B.H., Park, J.H., and Heeger, A.J. (2013) Transferable graphene oxide by stamping nanotechnology: electron-transport layer for efficient bulk-heterojunction solar cells. *Angew. Chem. Int. Ed.*, **52** (10), 2874–2880.
85. Yusoff, A.R.B.M., da Silva, W.J., Kim, H.P., and Jang, J. (2013) Extremely stable all solution processed organic tandem solar cells with TiO_2/GO recombination layer under continuous light illumination. *Nanoscale*, **5** (22), 11051–11057.

16
Graphene as Sensitizer

Mohd A. Mat-Teridi, Mohd A. Ibrahim, Norasikin Ahmad-Ludin, Siti Nur Farhana Mohd Nasir, Mohamad Yusof Sulaiman, and Kamaruzzaman Sopian

16.1
Graphene as Sensitizer

Recently, graphene has received great attention as a sensitizer because of its advantageous physical properties that are suitable for use in many electronic devices. At present, most effort is concentrated on solar cells, which could be divided into those in which graphene acts as the active medium and those that use graphene as a transparent or distributed electrode material. The former use the same principle of operation as already discussed for photodetectors, and, in principle, would benefit from their uniform absorption over a broad spectral range [1]. However, owing to the low intrinsic optical absorption of graphene, such devices would require complex interferometric or plasmonic enhancement structures [2] to achieve the desired responsivity, and thus are unlikely to be widely used in the near future. Instead, the use of graphene as a transparent electrode in either quantum dot or dye-sensitized solar cells (DSSCs) has proved highly beneficial. Doping can vary the position of the Fermi level in graphene significantly, so such electrodes have been used as conducting media for both electrons [3] and holes [4]. With the cost of grapheme produced by liquid-phase or thermal exfoliation coming down [5], we can expect wide use of graphene in DSSCs, especially in applications where mechanical flexibility is of paramount importance.

The use of graphene in next-generation lithium-ion batteries (LIBs) is currently being widely studied. Cathodes traditionally used in commercial LIBs frequently suffer from poor electrical conductivity, which can be overcome by the addition of graphite and carbon black to the electrode formulation. Graphene, with its sheet-like morphology, can not only act as an advanced conductive filler but may also give rise to novel core–shell or sandwich-type nanocomposite structures [6]. The resulting increase in electrical conductivity of these new morphologies would help in overcoming one of the key limitations of LIBs – their low specific power density. Lastly, the high thermal conductivity of graphene may be advantageous when it comes to high current loads that generate significant amounts of heat within the battery system. As anodes, graphene nanosheets can be used to

Graphene-based Energy Devices, First Edition. Edited by A. Rashid bin Mohd Yusoff.
© 2015 Wiley-VCH Verlag GmbH & Co. KGaA. Published 2015 by Wiley-VCH Verlag GmbH & Co. KGaA.

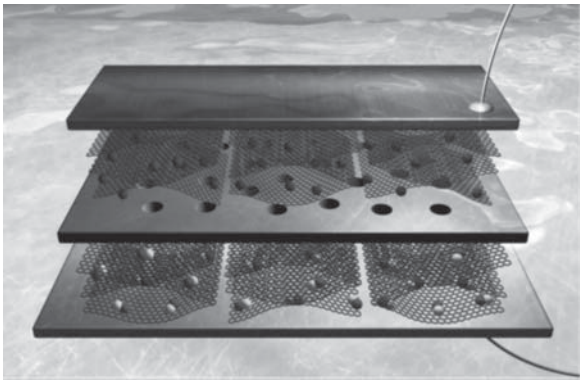

Figure 16.1 In a supercapacitor device, two high-surface-area graphene-based electrodes (net hexagonal planes up and bottom) are separated by a membrane (hole mambrane in the middle). Upon charging, the anions (white and grey merged small spheres) and cations (single grey spheres on the top) of the electrolyte accumulate in the vicinity of the graphene surface. The ions are electrically isolated from the carbon material by the electrochemical double layer, which serves as a molecular dielectric [8].

intercalate lithium reversibly into the layered crystals. Graphene nanosheets used in conjunction with carbon nanotubes (CNTs) and fullerenes (C_{60}) can increase the battery charge capacity [7].

Supercapacitors (Figure 16.1) are based on the storage of energy in electrochemical double-layer capacitors [8]. The superior rate performance of these state-of-the-art devices (compared to LIBs) is based on the predominantly electrostatic storage of electrical energy which is determined by the combination of a high-surface-area activated carbon material and the nanoscopic charge separation at the electrode/electrolyte interface. Graphene is an obvious choice for this application, offering high intrinsic electrical conductivity, an accessible and defined pore structure, good resistance to oxidative processes, and high temperature stability. Currently, the prototype grapheme-based electrochemical double-layer capacitors lead the field in capacitance as well as energy and power densities [9]. Although the characteristics of graphene supercapacitors are very encouraging, there are still issues that must be addressed before the commercial use of such systems. In particular, the irreversible capacitance of graphene-based supercapacitors is still too high, which could probably be improved by reducing the number of defects or choosing a better electrolyte.

There are also reports on the use of graphene nanosheets as a support material for platinum catalysts for fuel cells [10]. Unlike carbon black, which is the baseline support material for platinum catalysts, graphene decreases the platinum particle size to below 1 nm because of the strong interaction between the platinum atoms and graphene [11]. The strong interaction between platinum and graphene and the small particle size lead to increased catalytic activity in direct methanol fuel cells. Common benchmark materials in energy-related applications (graphite, carbon black, and activated carbon) will only be replaced if graphene is proved to be

superior in terms of both performance and cost. The fact that graphene of suitable grades for such applications is already available in scalable amounts might speed its progression into real devices.

The use of graphene in the dye sensitized solar cells (DSSCs) and organic photovoltaics (OPVs) has increased the overall conversion efficiency of such devices, but its function in solar cells is still under investigation because there are many functional factors that are still unclear. It was suggested that graphene can absorb molecules (hydrocarbon) or atoms (hydrogen) and the defects act as a conducting channel [12]. In general, an increase in photocurrent has been observed when using graphene in a DSSC or an OPV due to the better light harvesting and higher scatter effect of naked graphene photoanode paste. A graphene photoanode can generate extra photocurrent without any energetic or structural changes in the semiconductor [13]. The performance of the natural dye anthocyanin greatly improves with the addition of graphene (up to 2.4 times) [14]. Irrespective of whether graphene is added to TiO_2 by forming a film composite or by coadsorption with the dye onto the TiO_2 photoanode as a constituent of the dye mixture, an increase in efficiency has been obtained. Graphene provides better conducting pathways for the photogenerated electrons, thus increasing the current and decreasing the resistance. It was also observed that a longer electron lifetime could be achieved in the presence of graphene, suppressing unwanted electron recombination [14].

Graphene is also used as a counterelectrode in DSSCs and OPVs due to its high electrical conductivity with large specific surface area (theoretically 2630 $m^2\ g^{-1}$). It is a flat carbon nanosheet of sp^2-bonded carbon atoms and possesses very high mobility of charge carriers (200 000 $cm^2\ V^{-1}\ s^{-1}$) which arises from its unique two-dimensional carbon structure [15]. Various studies have been made to optimize the use of graphene as counterelectrode in DSSCs and OPVs so as to replace the Pt counterelectrode which is obtained from expensive Pt precursors. Recently, a graphene thin film was grown using hot filament chemical vapor deposition (HFCVD), and an electrical conversion efficiency of 4.3% was achieved, showing considerably high electrocatalytic activity toward the reduction of I^{-3} ions in the redox electrolyte [16]. It was also revealed that the content of graphene and carbon black in composite counterelectrodes is very important for fabricating DSSCs and OPVs with high catalytic performance and fast interfacial electron transfer [17]. Employment of thermally reduced graphene oxide (RGO) as electrocatalyst on the counterelectrodes gave satisfactory current and voltage but very poor fill factor [18]. The graphene-based multiwalled carbon nanotube (GMWNT) structure was one of the candidates for the counterelectrode for DSSCs and OPVs [19].

The combination of graphene/titania photoanode improved the photovoltaic performance of cadmium sulfide quantum dot-sensitized solar cells because of the smaller electron transfer resistance and lower frequency peak than in pristine titania electrode, which indicates that the electron transport rate is increased by incorporating graphene into the titania electrode [20]. Graphene quantum dots (GQDs) are considered an emerging class of nanomaterials with unique photonic and electric properties [21]. GQDs can be used as a cathode buffer additive for

inverted polymer solar cells, as they exhibit excellent hole-blocking and electron-transfer capability. They can also reduce the charge recombination and improve the charge transfer at the cathode/polymer active layer interface [21].

16.2 Graphene as Storage Current Collector

Nowadays, increasing demand for graphene in many energy device applications has shown that graphene has high potential and is valuable. In energy devices such as solar cells, batteries, and supercapacitors, the current collector plays important roles and functions as an effective collector or transports charge carriers (e.g., electrons and holes). The charge carriers are transported from or to the active materials/electrolyte interface during the charge separation process including the excitation and charge and discharge processes. Therefore, suitable materials such as graphene are required to be used as a desired current collector. The advantages of graphene in terms of the nature of the material (excellent electrons transport, thermodynamic stability, surface wettability, and high electrical conductivity) and better surface contact (including graphene/electrolyte and graphene/active material) make it suitable to be used as the current collector [22, 23]. However, the main factor that influences many energy devices is the excellent electron transport along the atomically thin layer. The mobility of electrons in graphene can reach 15 000 $cm^2\ V^{-1}\ s^{-1}$ [24], which means that graphene can transport electrons very fast and makes it very desirable to be applied in energy devices. Furthermore, the high electrical conductivity can make the device operate at maximum power by influencing the electron transport. This is due to the high electrical conductivity of the material, and the high electron transport will provide a high conductive pathway within the material. These phenomena will improve the performance of the devices. Next, the high surface area also can affect the performance of the devices. Maximizing the surface area provides a large number of active sites in the material. It would seem that better contact between the material and the active layer/electrolyte will increase the number of traveling electrons. This happens through the modification of the size of the particles. In other words, better contact with the active layer/electrolyte and graphene is highly desirable to reduce the contact resistance and lead to high transfer of electrons as well as high power and rate capabilities [25–30]. As reported by Li and Morris [22] and Holm [31], considering classical contact theory, a diffusion resistance will be inevitably formed at two surfaces meeting at a limited number of contact spots for charge transport. Therefore, it will lead to a considerable contact resistance at the asperity interface of the current collector and the active materials or electrolyte.

In addition, as explained in detail by Holm's theory, the electrical resistivity of the contact spots will affect the diffusion resistance in the functioning of the current collector [31–33]. This will affect the interface links between the current collector and the active material/electrolyte. In other words, the material to be used as current collectors should have superior electrical conductivity, which makes

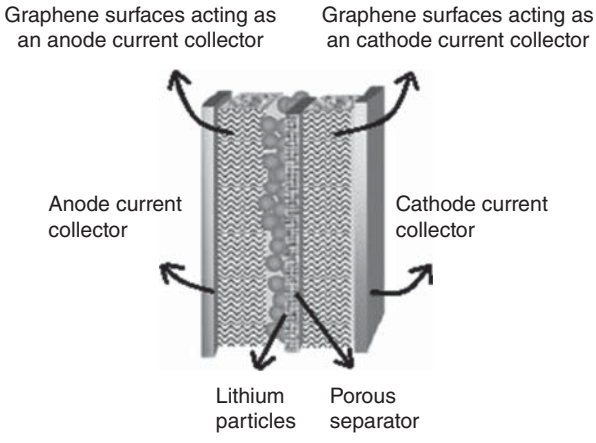
Graphene surfaces acting as an anode current collector
Graphene surfaces acting as an cathode current collector
Anode current collector
Cathode current collector
Lithium particles
Porous separator

Figure 16.2 Structure of a fully surface-enabled lithium ion-exchange cell. It contains an anode current collector and nanostructured graphene at the anode, a Li-ion source (e.g., pieces of Li foil or surface-stabilized Li powder), a porous separator, and a nanostructured functional graphene at the cathode [35].

graphene very attractive to be used as an ideal bridge to obtain better adsorption between the interfaces. Better adsorption means better contact in term of a wide surface area attached between the materials, and thus it will reduce the diffusion resistance. Therefore, high adsorption will improve the electron transfer along the material and enhance the mobility of the electrons.

In term of absorption, graphene absorbs only 2% of the light spectrum [34], which makes graphene very useful as a current collector in energy devices. Other factors such as thermodynamic stability and surface wettability also can effect the performance of the devices. Both these factors can be avoided by minimizing the irreversible redox process and reducing corrosion. This factor will reduce the lifetime and performance of the devices. Graphene has been proved to be a superior and most desirable material to be applied for high performance in many energy devices. As will be discussed later, graphene in energy devices has been used in different parts and for different functions due to their advantages when used as anode and cathode, as shown in Figure 16.2.

16.2.1 Anode Current Collector

Normally in these devices, two components play important roles in the performance, namely the anode and the cathode. Each of these components is responsible for enhancing the performance related to electronic conductivity and ionic diffusivity [36]. However, anode as a negative material has been the subject of many studies because of its easy fabrication, high performance, and abundant availability, compared to the cathode material which is rare, expensive to produce, and of low performance. Furthermore, being the main component, the anode

material will have a bigger impact on the performance of the device than the cathode material [37]. Graphene is the best candidate for implementation as the anode material. This is due to the physical properties of graphene, which fulfill the entire requirements as an anode candidate. The advantages of the graphene are its high electrical conductivity, large surface area, unique heterogeneous electron transfer and charge carrier rates, widely applicable electrocatalytic activity, and low production cost [38–42]. Currently, the anode materials have been in focus more in LIBs and fuel cells for energy storage and as photoanode in solar cells.

16.2.1.1 Li-Ion Storage

LIBs are devices that are can store and supply electricity over a certain period, and the device consists of an anode and a cathode. As a most promising material, graphene has been used in LIBs as the anode. The advantage of using graphene in LIBs is that the device gives higher energy capacities and longer cycle lifetimes. This battery is suitable to be used in electric vehicles [43, 44]. Commercially, graphite has been employed as an anode material for LIBs because of its high coulombic efficiency [42], which means that the reversible charging and discharging under intercalation potentials with a reasonable specific capacity is higher. Nevertheless, since the introduction of graphene in this field, significant improvements have been realized with enormous increase in power output of the device and also reduced charging time [45–47]. The specific capacitance has increased from 372 $mAh\,g^{-1}$ (commercial) to 1264 $mAh\,g^{-1}$ and the durability also has increased up to 848 compared to commercial devices of only 240. The results suggest that the physical properties of the graphene have helped in the improvement of LIBs through its high electrical conductivity, vast surface area, and unique heterogeneous electron transfer and charge carrier rates.

In order to improve the performance of the devices incorporated with graphene, the focus of the studies has been on composite materials with graphene. Graphene has been doped with Fe_2O_3, SnO_2, C_{60}, CNTs, and Mn_3O_4 [7, 48–50]. However, the performance has been poorer than that with only graphene nanosheets. This may be due to the material composite itself, which has low electrical conductivity and gives effect to the composite. The results may suggest that the electron transfer also may be affected by the presence of other materials. However, one can conclude that graphene is a superior anode electrode material in LIB applications.

16.2.1.2 Fuel Cells

In commercial applications of fuel cells, only carbonaceous materials have been used as anode [51]. Such materials are graphite, modified graphite, non-graphitic carbon, and graphene. Among the carbonaceous materials, graphene shows excellent improvement due to its advantageous physical properties. Theoretically, graphene is a unique material which has zero-bandgap semimetal properties and exhibits a large conductive behavior under the influence of an electrical field [52, 53]. The interlayer forces in graphene are also small (van der Waals force)

and the distance between the layers is large (3.35 Å) [54], which allow Li ions to diffuse easily between the graphene sheets. The easy transport and diffusion of electrons in graphene result in excellent performance.

In biofuel cells, graphene has been used without any membrane in enzymatic biofuel cells as reported by Liu *et al.* [55]. In their study, they employed graphene to fabricate the anode and cathode. The study compared the anode made by gold and graphene nanosheets as electrode dopants. The results showed a large improvement with a maximum power density of $24.3 \pm 4\,\mu W$ at 0.38 V (load 15 kΩ), which was nearly two times greater than when using gold ($7.8 \pm 1.1\,\mu W$ at 0.25 V (load 15 kΩ)). The improvement is related to the large surface area of the graphene, high electron transfer, and high electrical conductivity. The stability and durability of the material also improved, as shown by storage in pH 7.4 phosphate buffer solutions at 4 °C and testing every day with a 15-kΩ external load. After a week, the power output was found to decay slowly and eventually reach 50%. However, the result is still amazing when compared to those achieved with the gold, where the power output decayed by more than 50% after a week. From this result, one can conclude that graphene is an ideal material to be applied as anode material in fuel cells application.

16.2.2
Cathode Current Collector

Generally, the cathode current collector has been the monopoly of precious metals, such as platinum and gold, and aluminum. As is well known, all these materials are superior materials and fulfill all the requirements. In order to obtain better quality cathodes as current collectors, the candidates should have suitable materials without change in their structure. The only problem with all these materials is their cost, which keeps increasing every year, making the fabrication of energy devices a high-cost process [56]. Because of this, other suitable materials have been studied and investigated. The main candidates for replacing precious metals are transition metals such as Ni, Mn, Co, V, Fe, and C [57]. Among these materials, V has shown much promise because it can reversibly intercalate with lithium, as shown by Shembel *et al.* [58]. Also, V has a range of oxidation states from +2 to +5. Other materials only accommodate one-electron transfer processes. Apart from that, V is also known to possess high energy density and excellent cyclability, as shown by Ding *et al.* [59]. However, there are some issues that make V a low-performing cathode current collector, such as the low electric conductivity and slow diffusion of electrons or ions in V [56].

Recently, graphene synthesized from graphite has been shown to be the most desired and suitable candidate, mainly because of the nature of the material, high stability, and durability, and low cost in processing [60]. Compared to the other materials, graphene can be produced at low cost and it is abundantly available. Because of working in a very thin layer, graphene can reduce the resistance and increase the conductivity.

16.2.2.1 Li-Ion Storage

Graphene has been employed in lithium-based rechargeable batteries because of its superior characteristics. In the LIBs, the cathode plays a very important role in terms of the performance of the devices. However, many of the studies have been focused on graphene as an anode current collector. In the early study of Liu *et al.* [61], they reported the nanocomposite $Li_3V_2(PO_4)_3$ (LVP)/graphene as a cathode in LIBs. In the presence of graphene, the devices showed very high rate performance and cyclability for LIBs. This is due to the large surface area of graphene, which gets adsorbed and attached tightly to LVP. Consequently, Li^+ ions can easily intercalate and exfoliate, resulting in high electron conductivity and electrochemical performance. A similar situation also happens with other composite such as $LiFePO_4$/graphene [62, 63], $LiMn_2O_4$/graphene [64, 65], and $LiMn_{1-x}FexPO_4$/graphene [38]. Thus it can be concluded that electron-conducting graphene networks are formed, resulting in huge improvements in the electronic conductivity and electrochemical properties of the materials.

16.2.2.2 Fuel Cells

Graphene also has made a big impact on the fabrication of fuel cells. Much interest has been shown in graphene in fuel cell application as the anode and cathode current collectors because of its advantages such as the large surface area, excellent electrical conductivity, improved electrocatalytic activity, better enzymatic binding ability, and low production cost [39, 66]. Qu *et al.* [66] and Brownson and Banks [67] reported that the graphene doped with nitrogen acted as a metal-free electrode and exhibited improved electrocatalytic activity, long-term operation stability, and tolerance to crossover effect compared to Pt for oxygen reduction via a four-electron pathway in alkaline solutions producing water as a by-product. In proton exchange membrane fuel cells (PEMFCs), as successfully reported by Jafri *et al.* [68], replacing commercial Pt catalysts by Pt-loaded graphene nanosheets and nitrogen-doped graphene nanosheets resulted in improved performance of the cell in terms of electrical conductivity and adsorption. This is because the presence of nitrogen in graphene creates defects or increases the surface area for the platinum nanoparticles (NPs) to attach to. Therefore, the adsorption and electron transport are improved, leading to improvement in the electrical conductivity of the fuel cell. Similar results were also reported by Zhang *et al.* [69]. They demonstrated that Pt NPs could be deposited on graphite submicrometer particles using an ethylene glycol reduction method to be used for polymer electrolyte membrane fuel cells. The results have been compared with those of CNT and carbon black doped with Pt, and showed massive improvement in the electrocatalytic activity and enhanced durability. Further studies have been done using graphene as a catalyst in fuel cell technology, which showed many improvements in terms of the performance and life cycle of the cells. Overall, it can be concluded that involving graphene in fuel cells can lead to enhanced electrocatalytic activity and durability and improved adsorption of the surface, as reported by Xin *et al.* [70], showing that graphene in the form of oxide or with nitrogen doping will result in superior characteristics which will help improve fuel cell devices.

16.3
Graphene as Photoanode Additive

Graphene-based composites can improve the strength of composite materials through the advantages of graphene in terms of its mechanical, chemical, and electronic properties. The addition of graphene to the composite can increase the level of the operational temperature, decrease in the moisture level, provide good insulation against lightning strikes, and improve the compressive strength [11]. However, there is also a disadvantage of additives with fluid-based nanomaterials. Mixing of additives could change surface properties of the particles, which may result in an unacceptable level of impurities. The sample may contain agglomerates of larger particles and may require a specific test to determine the exact properties. It is a major challenge to nanoparticles, which is related to their high surface area [71].

16.3.1
DSSC Application

Currently, the efficiency of low-cost, dye-sensitized solar cells (DSSCs) has reached 12.3% under air mass 1.5 global (AM 1.5G) [72]. The performance of these devices mainly depends on how efficient the charge transport is in the TiO_2 film. Extensive research on TiO_2 films has been carried out, especially on the electron mobility improvement and hybrid material development. In the case of electron transport enhancement, the incorporation of graphene into the TiO_2 matrix evidently improves it, minimizes charge recombination, and enhances the cell performance [73]. To understand the mechanism of electron transport in graphene/TiO_2 composites, the particle size dependence of TiO_2 was studied using conducting atomic force microscopy (c-AFM) [74]. The photoanode composites were prepared using a doctor-blade method through a modified one-step solvothermal reaction. Significantly, this study identified that the electron transport is more active when the particle size of TiO_2 is smaller, which improves the charge mobility as well. The graphene composite in a DSSC device led to a power conversion efficiency of about 7.26% with a short-circuit current density $J_{sc} = 13.1\,mA\,cm^{-2}$ and an open-circuit voltage $V_{oc} = 0.771\,V$. It was seen that smaller TiO_2 particles provide larger surface area of the composite electrodes and continuously enhance the electron mobility network of the device.

The use of graphene as a composite porous film during the synthesis of integrated graphene sheets and anatase TiO_2 NPs was investigated in detail by Kusumawati *et al.* [75]. Two types of solution were prepared with a modified Hummer's method by adding anatase TiO_2 particles, terpineol, ethanol, and single-layer graphene oxide (SGO) sheets to form a sticky paste. Then, ethyl cellulose powder was dissolved in ethanol before both solutions were sonicated using an ultrasonic horn. The layers of TiO_2/SGO paste were deposited on fluorine doped tin oxides (FTO) glass by doctor-blading. The multistep process was performed to obtain the exact thickness of the films before annealing them

at 500 °C for 15 min. The final step required immersing the TiO_2 films in a $TiCl_4$ solution and heating once more at 500 °C. RGO increases the performance of the photoelectrode by enhancing the charge transport by 60% in the layer conductivity with the presence of 1.2 wt% RGO. The RGO improved the specific surface area of the films, resulting in higher loading of dye to absorb more solar irradiance spectrum. The conversion efficiency of the solar cell with integration of the graphene content increased up to 12% because of the increase in the short-circuit current density J_{sc}. This result is almost similar to that from DSSC-based redox electrolyte with zinc porphyrin dye, which gave the highest cell efficiency without the graphene content. Furthermore, the enhancement in charge transfer from graphene to titania can be understood through the calculation method of the interface, as reported by Du *et al.* [76]. The three-dimensional (3D) model plotted the large density of interface graphene and TiO_2(110) surface with the equilibrium distance of 0.275 nm. The model stimulated the accumulation of holes in titania-supported graphene where the charge transfer occurred from the graphene layer to the TiO_2(110) in the ground electronic state. It means that the electron in the upper valence band can be directly excited from graphene to the conduction band under visible light irradiation.

Study on the combination of graphene and a dye as photosensitizer for DSSC was carried out by Esteban and Enriquez [14]. DSSCs with TiO_2 and an anthocyanin/graphene volume ratio of 1 : 2 achieved an efficiency of ~0.436% and a short-circuit current J_{sc} of 1.47 mA cm^{-2}. The natural dye anthocyanin in the presence of graphene performed 2.4 times more efficiently than with the anthocyanin dye alone. The existence of graphene in the photoanode composite improved the charge carrier mobility and increased the surface area, which made the electron transport more efficient, as suggested by Yang *et al.* [73]. However, this does not improve the overall efficiency of the cell because of the use of natural dyes. According to our understanding, a natural dye generally produces low efficiency of the cell because of low generation of electronic charge and poor connectivity between the TiO_2 photoanode and sensitizer materials [77]. Moreover, the efficiency of a cell using betanin-based natural dye is still around 2% only [78]. With the advantageous properties of graphene, a graphene-based composite is more appropriate, which will enhance the charge mobility and cell efficiency rather than applied to sensitizer materials.

16.3.2 OPV Application

A lot of work has been carried out to develop high-performance, functionalized, graphene-based anode electrodes and additives for organic solar cell applications. Graphene-based materials are used as additives for donor or donor–acceptor material in the bulk heterojunction (BHJ) OPVs [79].

Liu *et al.* [80] investigated soluble, functionalized graphene used as an acceptor for an OPV device. The graphene was prepared using a two-step method, an oxidation treatment followed by an organic functionalization step, in order to

form solution-processable, functionalized graphene (SPF-graphene). The active layer of the OPV was deposited using a spin-coating method with mixed solutions of poly(3-hexylthiophene-1,3-diyl) (P3HT) and SPF-graphene in the organic solvent 1,2-dichlorobenzene onto a precoated conducting polymer layer of indium tin oxide (ITO) glass substrate. The layer with 10 wt% SPF-graphene content and 100 nm thickness of the active layer resulted in a power conversion efficiency of about 1.1% with a short circuit-current J_{sc} of 4.0 mA cm^{-2} and open-circuit voltage V_{oc} of 0.72 V. The findings of this study suggested that the graphene can be used as acceptor material because of its low cost, simple preparation, and inertness under ambient conditions.

Most recent study, Yong and Tour [81] speculated that the efficiency of a nanostructured graphene-based OPV can reach up to 12% (single-cell junction) and 24% (tandem cell junction). However, further investigation of the actual cells is needed. At present, the actual experimental results show that the integration of graphene into single cell and tandem cell in the OPV devices has the potential to enhance the molecular interaction and improve the cell's efficiency. Kim and coworkers [82] demonstrated a functionalized reduced graphene oxide (FrGO) as a hole-transporting layer using a one-step reduction of novel phenylhydrazine in OPVs. The performance of FrGO with fluorine atoms increased the OPV efficiencies by removing the oxygen functional group attached to graphene oxide (GO). Moreover, the FrGO-based OPV produced via one-step reduction is a suitable interface material and stable to poly(3,4-ethylenedioxythiophene) :poly(styrenesulfonate) (PEDOT:PSS). They extended their experiments using FrGO by fabricating various OPV systems, including thieno[3,4-*b*]thiophene/benzodithiophene:[6,6]-phenyl C71-butyric acid methylester (PTB7:$PC_{71}BM$) and P3HT:indene-C60 bisadduct (ICBA). The FrGO OPV based on PTB7:$PC_{71}BM$ afforded a power conversion efficiency of 6.71%, V_{oc} of 0.70 V, J_{sc} of 14.84 mA cm^{-2}, and fill factor (FF) of 65.1%. This cell efficiency is almost similar to that of the PEDOT:PSS OPVs (6.85%) based on PTB7:PC71BM. Although the cell efficiency of PEDOT:PSS is higher, it gave poor cell stability, high acidity, low hygroscopic stability, and instability of electrical properties [83].

16.3.3 Lithium-Ion Battery

Many researchers have demonstrated the potential of LIBs for favorable energy storage due to their light weight, high energy density, and suitability for portable energy devices and vehicles. Recently, many studies have investigated new electrode materials based on metal oxide/graphene composites as the anode material, which have better specific capacities for higher energy density. The composite tin oxide (SnO_2)/graphene as anode material for LIBs application was investigated by Guo and coworkers [84]. This composite was prepared through a simple wet chemical method using GO and tin(II) chloride dehydrates. The SnO_2/graphene composite performed excellently for lithium intercalation/deintercalation with an initial discharge of 1995.8 mAh g^{-1} and charge capacity of 1923.5 mAh g^{-1}.

The anode composite also maintained high performance after 40 cycles, with a reversible discharge capacity of about 1545.7 mAh g^{-1} at a current density of 1 A g^{-1}.

Tang *et al.* [85] investigated CuInZnS (CIZS)-coated graphene as anode material for rechargeable LIB application. The CIZS/graphene composites were prepared using a hydrothermal process where the precursors of RGO, zinc acetate dehydrate, indium(III) chloride tetrahydrate, copper chloride, and thioacetamide, were added together in distilled water. The mixture was sonicated for half an hour before heating in an autoclave at 180 °C for 18 h. The prepared sample was centrifuged, cleaned with ethanol, and desiccated in air. Combination of CIZS with highly conductive graphene showed a great performance in initial discharge capacity and high current density over 480 cycles. This device demonstrated enhanced initial discharge capacity (1623 mAh g^{-1} at 100 mA g^{-1}), good repeatability/rate capability (2000 mA g^{-1}), and stable cycling life. It performed with better quality, high rate capacity, and cycling stability with the presence of graphene as anode material for lithium battery applications.

16.3.4 Sensor Application

Research on the hybrid nanostructure of graphene coupled with nanocrystals (NCs) has received much attention in energy devices and sensing applications, which offers wide opportunities for variation of new material structure and properties. Characteristics of catalysts based on noble metal (Au [86, 87], Ag [88, 89], Pt [90], and Pd [91]) and metal oxide (SnO_2 [92]) NCs decorated with graphene should include sensitivity, selectivity, and dynamic response for biosensor, optical sensor, and gas sensor application.

Huang *et al.* [89] investigated AgNP/polydopamine (Pdop)-coated graphene. Graphene was prepared with Pdop using a modest method by oxidation of dopamine at room temperature before being mixed together with AgNPs. The nanocomposite was later used as a modified electrode to test electrochemical sensing with the model of guanine and adenine. Promising results of the AgNP/graphene nanocomposite electrode were obtained by detecting at the trace level adenine and guanine in fish sperm. In a similar study with a different metal, Zhang *et al.* [90] investigated a facile method on PtNP/Pdop with RGO nanosheets for electrochemical sensing. The Pt/Pdop/RGO-modified electrode demonstrated the minimum detection level and high sensitivity to detect of H_2O_2 as a model molecule. Good dispersion of PtNPs on the Pdop-RGO surface indicated an effective method of synthesis and showed large electrocatalytic activity for the reduction of H_2O_2 and O_2. The performance of these nanocomposites is more favorable and better than that of a glassy carbon electrode in the progress toward electrocatalysts for biosensing application.

For a semiconductor substrate, flexible layers based on graphene nanoplatelets (GNPs) which were used as measuring layer in force sensors was carried out by Janczak and Wroblewski [93]. The composite material consisted of GNP as the

nano-carbon filler in toluene solution and CNTs with polymethylmethacrylate (PMMA) matrix as comparison sample, where both samples were prepared using screen printing method. After sonicating for 1 h, the solutions were evaporated, leaving behind a paste. Later, the paste was printed twice on a roll mill with a silicon carbide (SiC) roller. Sensor structures were fabricated by printing polymer nanoplatelet or polymer nanotube areas with polymer-silver contact as electrodes. The performance of the sensor based on GNP, with the GNP content between 1.5 and 2 wt%, showed relatively high changes in tensile force from about 10 N to 20 kN compared to CNT- based sensors.

16.3.5
Transparent Conductive Films

Commonly, ITO and FTO are the most popular transparent conducting films as front electrode in thin-film solar cells. Because of the high demand for these conducting films and their high cost, there is a necessity to find alternative materials. Graphene has similar characteristics as ITO and FTO with high electrical mobility, high flexibility [94], and good optical transparency, but at a low cost. Furthermore, interface modifications studies between graphene and organic layers has shown similar yield as an ITO substrate in an OPV cell [95]. The modification of the interface was done by introducing a thin double-hole injection layer (D-HIL) between PEDOT:PSS and the graphene surface. This study demonstrated the potential of graphene as transparent conductor for both anode and cathode applications.

Furthermore, graphene films were grown on Cu foils using ambient-pressure chemical vapor deposition (APCVD) and annealed at 1000 °C for 30 min in a CVD chamber. The transparent conducting films (TCFs) based on graphene were considered as favorable materials, which maintained a high optical transparency between 97% (single layer film) and 84% (seven graphene layers) [96] within the wavelength range of 350–2200 nm. The structure of device consisted of glass/graphene/ZnO/CdS/CdTe/(graphite paste), which gave a photovoltaic efficiency of 4.17%. The efficiency of the cell is quite low, and requires further improvement possibly based on the TCF preparation method and stacking of the interface materials layer by layer. The formation of new TCF-based graphene has the potential to be a low-cost, transparent conducting electrode, providing large optical transparency and good electrical sheet resistance.

Multicomponent hybrid of TCF as an alternative to ITO was introduced by Kholmanov *et al.* [97]. The hybrid TCFs, composed of AuNPs, Ag nanowires (NWs), and RGO platelets, were prepared on glass slides using a spin-coating method. The RGO nanoplatelets work as an insulation layer for covering AgNWs, which show better performance with a low sheet resistance R_s and maintain good optical transmittance compared to Ag TCFs. The findings from this study are consistent with those of Zhu *et al.* [98] on graphene/metal grid hybrid components with $R_s = 20\,\Omega\,\text{sq.}^{-1}$ at $T_{550} = 90\%$.

16.3.6
Photocatalytic Application

A highly efficient and stable photocatalytic activity on hydrogen evolution was established by Min and Lu [99]. The H_2 production was demonstrated using a Pt catalyst-deposited graphene sheet and co-sensitized with Eosin Y (EY) and Rose Bengal (RB). Upon illumination with visible light irradiation (520 and 550 nm), the quantum yield of the photocatalysis was up to 37.3%, which enhanced the forward electron transfer from the photoexcited dye molecules to the Pt catalyst. Simultaneously, the combination of two dyes (EY and RB) as co-sensitizers enhanced the absorption in the visible region, which ensured more efficient utilization of the incident light energy.

In a recent study by Min and Lu [100], the photocatalyst of RB-sensitized graphene sheets decorated with Pt demonstrated the maximum apparent quantum efficiency of ~18.5% at the wavelength of 550 nm. The photocatalytic activity of dispersible graphene sheets showed more operational efficiency by enhancing the electron transport and minimizing the recombination of the charge in the H_2 evolution. The energy conversion occurred in the bulky interface with more active sites of dispersed graphene NPs compared to GO and multiwalled carbon nanotubes (MWCNTs). This work showed the great potential of using conductive and dispersible graphene sheet in solar energy conversion and photocatalysis.

GO incorporation in the compound catalytic process has been recognized as an alternative to photocatalysis in the photodegradation of pollutants. Zhu *et al.* [101] investigated a photocatalyst on silver/silver halide (Ag/AgBr and Ag/AgCl) with GO nanosheets, demonstrating excellent performance as a stable plasmonic photocatalyst for the photodegradation of methyl orange (MO) pollutant under visible-light irradiation. The preparation of hybrid nanocomposites of Ag/AgX (X = Br, Cl)/GO was carried out by mixing a GO aqueous solution and silver nitrate with cetyltrimethylammonium bromide (CTAB) or cetyltrimethylammonium chloride (CTAC) surfactants in a chloroform solution. The photocatalytic performance showed that the Ag/AgX/GO exhibited a higher adsorptive capacity (71–85%) for MO molecules compared to the bare Ag/AgX (25%).

16.4
Graphene as Cathode Electrocatalyst

Fuel cell technology is very desirable because it is a clean technology with high efficiency. However, the requirements for cathode materials such as platinum and the slow oxygen reduction reaction in the cathode are major issues that have to be tackled before large-scale industrial production of fuel cells can begin. Others factors that limit large-scale production include the cost of production, poor durability, fuel crossover effect, and CO poisoning [102–107]. To counter these problems, the improvement or replacement of commercial cathode electrocatalysts is a major strategy to improve the technology. Much work has been done using other

cheap and nonpoisoning materials such as Fe, Co, Mo, and W [102–107]. These issues are serious and challenging the field of fuel cell technology. Furthermore, researchers have discovered that non-precious-metal catalysts were able to catalyze the oxygen reduction reaction, such as cobalt phthalocyanine [108] including N-coordinated transition-metal macromolecules, chalcogenides, oxynitrides, carbonitrides, and also transition metal-doped conductive polymers [109–112]. Among the materials mentioned above, nitrogen-doped carbon material (carbonitrides) such as CNTs, nanotube cups, ordered mesoporous graphitic arrays, and graphene [66, 113–117, 118, 119], are the most promising materials because of their advantages such as low cost of production and good durability, which means more cycles and nontoxic material. Among the carbon materials, graphene or N-doped graphene has shown amazing results where the electrocatalytic activity in an alkaline electrolyte for the oxygen reduction reaction gave more improvement compared to the others [120]. This is due to the characteristics of graphene which are better than those of the others. Based on our knowledge, the electrocatalytic activity of graphene in presence of nitrogen is expected to be one of the major factors in the development of fuel cells in order to achieve high oxygen reduction reaction.

16.4.1 N-Doped Graphene

As reported by Liu *et al.* and Yang *et al.* [121, 122], nitrogen can be doped into graphene in the pyridinic, pyrolic, and graphitic forms. The pyridinic form is obtained by the attachment of N atoms to the edges of the graphene plane. Then the N atom is attached to two carbon atom and releases one p-electron to the p system. In the pyrolic system, the N atom is attached to the heterocyclic rings where it is bonded to two carbon atoms and donates two p-electrons to the p system. Furthermore, the graphitic N atom is associated with the graphene layer and replaces the carbon atom within the graphene plane. As a result, nitrogen can have a large impact on the electronic structure and the mechanism of activity improvement. It can be concluded that there is a relationship between nitrogen and the oxygen reduction reaction.

Based on the study of nitrogen-doped graphene, nitrogen can affect the oxygen reduction reaction activity. Improving the oxygen reduction reaction activity will improve the electrocatalytic activity because the former depends on the nitrogen content. Maximizing the nitrogen doping will improve the oxygen reduction reaction activity, originally a $2e^-$ to $4e^-$ dominated process, as reported by Lai *et al.* [123]. As a conclusion of the doping studies, increasing the nitrogen doping leads to an increase in the number of active sites and thus improve the oxygen reduction reaction as well as the electrocatalytic activity. In addition, the current density can increase by about three times (60%) compared to the original value with 20 wt% Pt/C [66].

The development of nitrogen-doped graphene does not only depend on the nitrogen content but also on the structural and morphological properties

[124]. Thus, introducing the N-doped graphene with high surface areas of up to 1500 $m^2 g^{-1}$ resulted in very high electrocatalytic activity for the oxygen reduction reaction, leading to improved fuel cell performance [118]. In addition, the results revealed the low onset voltage for the oxygen reduction reaction in an alkaline medium and high methanol tolerance compared to the commercial 20 wt% Pt/C. The work was done by preparing mesoporous nitrogen-doped graphene, where the carbonization of nucleobases dissolved in an all-organic ionic liquid took place via hard templating with silica NPs. Then, the nanopores of modified graphene took the lead. The presence of Pluronic F127 resulted in a composite of graphene with excellent electrocatalytic activity and durability [125]. Overall, the development of new structures and morphologies of graphene composites for the cathode electrocatalytic activity can give fresh hope to fabricate the ideal fuel cell with excellent electrocatalytic activity and durability.

16.4.2 B-, P-, S-, and Se-Doped Graphene

In order to improve the electrocatalytic activity, elements other than N have also been tried and doped, such as boron, phosphorous, sulfur, and selenium. The first successful trial was by Sheng *et al.* [126], who doped graphene with boron. They found that the doping resulted in improvement in the electrocatalytic activity and durability. Their results showed improvement by increasing the boron content, which also shifted the onset and peak potential. These results also suggest that the doping element can play a major role in improving the electrocatalytic performance.

Furthermore, phosphorous also was chosen to dope with graphene. As a result, and as reported by Peng *et al.* [127], the content of the dopant affected the performance in terms of improved electrocatalytic activity and stability. The result is very similar to that obtained when doping with nitrogen. This may be due to the fact that phosphorous is in the same group as nitrogen, which has same number of valence electrons and, most importantly, exhibits similar chemical properties. Overall, the result is better than with commercial Pt/C.

Moreover, one of the similarities between boron and phosphorus is that they are more electronegative than carbon. These gave the idea to Yang *et al.* and Jin *et al.* [128, 129] to start working with sulfur, which has 0.03 electronegativity, and selenium, with similar electronegativity as carbon. The results showed improvement in the electrocatalytic activity and long-term stability. In general, a dopant that is similar to nitrogen can, when doped with graphene, enhance the electrocatalytic activity and long-term stability compared to commercial Pt/C.

The development of low-cost and high-performance graphene as electrocatalysts for fuel cells is quite promising and a lot of work has been done toward this. The idea is to replace commercial Pt, which is expensive and gives only limited performance. The results reported by researchers give new hope for the future. We

are studying different materials such as nitrogen-, boron-, phosphorous-, sulfur-, and selenium-doped graphene, which have shown high performance. Based on this review, a few suggestions can be made:

- Doping graphene with suitable materials give excellent improvement in the electrocatalytic activity and can be the most promising method. However, many factors need to be considered, such as the dopant materials, the technique of deposition, the dopant content, and, most important, the defect of the materials.
- Improvements must be made not only of the dopant of the cathode electrocatalysts but also to the surface active sites of electrocatalysts. Such improvement can be done by modifying the surface morphology in terms of increased reduction current density which affects the electrocatalytic activity by providing excellent onset potential. This also may enhance the electron conductivity.
- To date, the better performance of cathode electrocatalysts is achieved in alkaline media. However, we also need to consider acidic media. This is because acidic media are used in the commercial proton exchange membrane fuel cells. In addition, the mechanism in acidic media also needs to be explored.

16.5 Conclusions

As the most promising material for energy production and storage devices, graphene has shown great potential in all applications toward green technology devices. The development of graphene consists of its preparation, deposition, fabrication, and testing. The most important aspects of graphene that lead to improved performance of devices are its advantageous characteristics. In addition, the material is abundantly available, cheap to manufacture, and easy to fabricate. Having discussed and summarized energy production and storage devices such as solar cells, supercapacitors, LIBs, fuel cells, sensors, and transparent conducting films in the presence of graphene, it can be concluded that the graphene has a wide and diverse impact, which is leading to high performance of the devices. However, it can be said that the exploration of graphene is just in the early stage and still a lot needs to be investigated and improved. In the future, in order to make graphene as an ideal candidate, modifications of the material need to be done. We have to start with improving all its characteristics such as conductivity, surface area, electron transfer rate, and charge carrier rate. The stability and adsorption of the material also need to be improved. Regarding deposition and fabrication, the current techniques need to be improved, for which greener and more energy efficient alternatives need to be considered to avoid carbon pollution. Finally, for commercialization, a few things need to be tackled, such as scalability, reproducibility, continuity of energy output, storage capability, characterization of graphene, cost, and environmental issues.

Acknowledgment

This work was supported by the Government of Malaysia through the National University of Malaysia Grant ICONIC-2013-005.

References

1. Nair, R.R., Blake, P.A., Grigorenko, N., Novoselov, K.S., Booth, T.J., Stauber, T., Peres, N.M.R., and Geim, A.K. (2008) Fine structure constant defines visual transparency of graphene. *Science*, **320**, 1308.
2. Echtermeyer, T.J., Britnell, L., Jasnos, P.K., Lombardo, A., Gorbachev, R.V., Grigorenko, A.N., Geim, A.K., Ferrari, A.C., and Novoselov, K.S. (2011) Strong plasmonic enhancement of photovoltage in graphene. *Nat. Commun.*, **2**, 458–462.
3. Wang, X., Zhi, L.J., and Mullen, K. (2008) Transparent, conductive graphene electrodes for dye-sensitized solar cells. *Nano Lett.*, **8** (1), 323–327.
4. Li, S.S., Tu, K.H., Lin, C.C., Chen, C.W., and Chhowalla, M. (2010) Solution-processable graphene oxide as an efficient hole transport layer in polymer solar cells. *ACS Nano*, **4** (6), 3169–3174.
5. Segal, M. (2009) Selling graphene by the ton. *Nat. Nanotechnol.*, **4**, 612–614.
6. Yang, S.B., Feng, X.L., Ivanovici, S., and Mullen, K. (2010) Fabrication of graphene encapsulated oxide nanoparticles: towards high-performance anode materials for lithium storage. *Angew. Chem. Int. Ed.*, **49** (45), 8408–8411.
7. Yoo, E.J., Kim, J., Hosono, E., Zhou, H.-S., Kudo, T., and Honma, I. (2008) Large reversible Li storage of graphene nanosheet families for use in rechargeable lithium ion batteries. *Nano Lett.*, **8** (8), 2277–2282.
8. Simon, P. and Gogotsi, Y. (2008) Materials for electrochemical capacitors. *Nat. Mater.*, **7**, 845–854.
9. Stoller, M.D., Park, S.J., Zhu, Y.W., An, J.H., and Ruoff, R.S. (2008) Graphene-based ultracapacitors. *Nano Lett.*, **8** (10), 3498–3502.
10. Yoo, E.J., Okata, T., Akita, T., Kohyama, M., Nakamura, J., and Honma, I. (2009) Enhanced electrocatalytic activity of Pt subnanoclusters on graphene nanosheet surface. *Nano Lett.*, **9** (6), 2255–2259.
11. Novoselov, K.S., Fal'ko, V.I., Colombo, L., Gellert, P.R., Schwab, M.G., and Kim, K. (2012) A roadmap for graphene. *Nature*, **490**, 192–200.
12. Peres, N.M.R. (2010) The transport properties of graphene: an introduction. *Rev. Mod. Phys.*, **82**, 2673–2700.
13. Javier, D., Pablo, P.B., Miguel, G., Gustavo, M.M., Luis, O., Juan, B., and Eva, M.B. (2012) Photocurrent enhancement in dye-sensitized photovoltaic devices with titania-graphene composite electrode. *Electroanal. Chem.*, **683**, 43–46.
14. Esteban, A.C.M.S. and Enriquez, E.P. (2013) Graphene-anthocyanin mixture as photosensitizer for dye-sensitized solar cell. *Sol. Energy*, **98**, 392–399.
15. Park, S. and Ruoff, R.S. (2009) Chemical methods for production of graphenes. *Nat. Nanotechnol.*, **4**, 217–224.
16. Hyung-Kee, S., Minwu, S., Sadia, A., Shaheer, A., and Hyung, S.S. (2013) New counter electrode of hot filament chemical vapour deposited graphene thin film for dye sensitized solar cell. *Chem. Eng. J.*, **222**, 464–471.
17. Xiaohuan, M., Kai, P., Qingjiang, P., Wei, Z., Lei, W., Yongping, L., Guohui, T., and Guofeng, W. (2013) Highly crystalline graphene/carbon black composite counter electrodes with controllable content: synthesis, characterization and application in dye-sensitized solar cell. *Electrochem. Acta*, **96**, 155–163.
18. Archontoula, N., Dimitrios, T., Lambrini, S., Vassilios, D., Costas, G., and Panagiotis, L. (2013) Study of the thermal reduction of graphene oxide and of its application as electrocatalyst in quasi-solid state dye-sensitized solar cells in combination with PEDOT. *Electrochem. Acta*, **111**, 698–706.

19. Hyonkwang, C., Hyunkook, K., Sookhyun, H., Wonbong, C., and Minhyon, J. (2011) Dye-sensitized solar cells using graphene-based carbon nano composite as counter electrode. *Sol. Energy Mater. Sol. Cells*, **95** (1), 323–325.
20. Junchang, Z., Jihuai, W., Fuda, Y., Zhang, L., and Jianwang, L. (2013) Improving the photovoltaic performance of cadmium sulfide quantum dots-sensitized solar cell by graphene/titania photoanode. *Electrochem. Acta*, **96**, 110–116.
21. Hong, B.Y., Yong, Q.D., Xizu, W., Si, Y.K., Bin, L., and Chang, M.L. (2013) Graphene quantum dots-incorporated cathode buffer for improvement of inverted polymer solar cells. *Sol. Energy Mater. Sol. Cells*, **117**, 214–218.
22. Li, L. and Morris, J.E. (1997) Electrical conduction models for isotropically conductive adhesive joints. *IEEE Trans. Compon. Packag. Manuf. Technol. Part A*, **20**, 3–5.
23. Bo, Z., Zhu, W., Ma, W., Wen, Z., Shuai, X., Chen, J., Yan, J., Wang, Z., Cen, K., and Feng, X. (2013) Vertically oriented graphene bridging active-layer/current-collector interface for ultrahigh rate supercapacitors. *Adv. Mater.*, **25** (40), 5799–5806.
24. Wang, Y., Chen, X.H., Zhong, Y.L., Zhu, F.R., and Loh, K.P. (2009) Large area, continuous, few-layered graphene as anodes in organic photovoltaic devices. *Appl. Phys. Lett.*, **95**, 063302–063304.
25. Biswas, S. and Drzal, L.T. (2010) Multilayered nano architecture of graphene nanosheets and polypyrrole nanowires for high performance supercapacitor electrodes. *Chem. Mater.*, **22** (20), 5667–5670.
26. Shaijumon, M.M., Ou, F.S., Ci, L., and Ajayan, P.M. (2008) Synthesis of hybrid nanowire arrays and their application as high power supercapacitor electrodes. *Chem. Commun.*, **20**, 2373–2275.
27. An, K.H., Kim, W.S., Park, Y.S., Moon, J.M., Bae, D.J., Lim, S.C., Lee, Y.S., and Lee, Y.H. (2001) Electrochemical properties of high-power supercapacitors using single-walled carbon nanotube electrodes. *Adv. Funct. Mater.*, **11** (5), 387–392.
28. Huang, C.-W., Teng, H., Kuo, P.-L., and Teng, H. (2012) Electric double layer capacitors based on a composite electrode of activated mesophase pitch and carbon nanotubes. *J. Mater. Chem.*, **22** (15), 7314–7322.
29. Du, C.S., Yeh, J., and Pan, N. (2005) High power density supercapacitors using locally aligned carbon nanotube electrodes. *Nanotechnology*, **16** (4), 350–353.
30. An, K.H., Kim, W.S., Park, Y.S., Choi, Y.C., Lee, S.M., Chung, D.C., Bae, D.J., Lim, S.C., and Lee, Y.H. (2001) Supercapacitors using single-walled carbon nanotube electrode. *Adv. Mater.*, **13** (7), 497–500.
31. Holm, R. (2000) *Electric Contacts: Theory and Application*, Springer, Berlin.
32. Morozov, S.V., Novoselov, K.S., Katsnelson, M.I., Schedin, F., Elias, D.C., Jaszczak, J.A., and Geim, A.K. (2008) Giant intrinsic carrier mobilities in graphene and its bilayer. *Phys. Rev. Lett.*, **100**, 016602–016607.
33. Du, X., Skachko, I., Barker, A., and Andrei, E.Y. (2008) Approaching ballistic transport in suspended graphene. *Nat. Nanotechnol.*, **3**, 491–495.
34. Alivisatos, A.P., Gur, I., Fromer, N.A., Chen, C.P., and Kanaras, A.G. (2007) Hybrid solar cells with prescribed nanoscale morphologies based on hyperbranched semiconductor nanocrystals. *Nano Lett.*, **7** (2), 409–413.
35. Zhu, Y.W., Murali, S., Stoller, M.D., Ganesh, K.J., Cai, W.W., Ferreira, P.J., Pirkle, A., Wallace, R.M., Cychosz, K.A., Thommes, M., Su, D., Stach, E.A., and Ruoff, R.S. (2011) Carbon-based supercapacitors produced by activation of graphene. *Science*, **332**, 1537–1540.
36. Park, M., Zhang, X., Chung, M., Less, G.B., and Sastry, A.M. (2010) A review of conduction phenomena in Li-ion batteries. *J. Power. Sources*, **195** (24), 7904–7929.
37. Takahashi, M., Ohtsuka, H., Akuto, K., and Sakurai, Y. (2005) Confirmation of long-term cyclability and high thermal stability of LiFePO4 in prismatic

lithium-ion cells. *J. Electrochem. Soc.*, **152** (5), A899–A904.
38. Geim, A.K. and Novoselov, K.S. (2007) The rise of graphene. *Nat. Mater.*, **6**, 183–191.
39. Chen, D., Tang, L., and Li, J. (2010) Graphene-based materials in electrochemistry. *Chem. Soc. Rev.*, **39** (8), 3157–3180.
40. Pumera, M. (2009) Electrochemistry of graphene: new horizons for sensing and energy storage. *Chem. Rec.*, **9** (4), 211–223.
41. Brownson, D.A.C. and Banks, C.E. (2011) Graphene electrochemistry: fabricating amperometric biosensors. *Analyst*, **136** (10), 2084–2089.
42. Liang, M. and Zhi, L. (2009) Graphene-based electrode materials for rechargeable lithium batteries. *J. Mater. Chem.*, **19** (33), 5871–5878.
43. Lian, P., Zhu, X., Liang, S., Li, Z., Yang, W., and Wang, H. (2010) Large reversible capacity of high quality graphene sheets as an anode material for lithium-ion batteries. *Electrochim. Acta*, **55**, 3909–3914.
44. Guo, P., Song, H., and Chen, X. (2009) Electrochemical performance of graphene nanosheets as anode material for lithium-ion batteries. *Electrochem. Commun.*, **11** (6), 1320–1324.
45. Paek, S.-M., Yoo, E., and Honma, I. (2009) Enhanced cyclic performance and lithium storage capacity of SnO2/graphene nanoporous electrodes with three-dimensionally delaminated flexible structure. *Nano Lett.*, **9** (1), 72–75.
46. Pan, D., Wang, S., Zhao, B., Wu, M., Zhang, H., Wang, Y., and Jiao, Z. (2009) Li storage properties of disordered graphene nanosheets. *Chem. Mater.*, **21** (14), 3136–3142.
47. Uthaisar, C. and Barone, V. (2010) Edge effects on the characteristics of Li diffusion in graphene. *Nano Lett.*, **10** (8), 2838–2842.
48. Zhou, G., Wang, D.-W., Li, F., Zhang, L., Li, N., Wu, Z.-S., Wen, L., Lu, G.Q., and Cheng, H.-M. (2010) Graphene-wrapped Fe3O4 anode material with improved reversible capacity and cyclic stability for lithium ion batteries. *Chem. Mater.*, **22** (18), 5306–5313.
49. Wang, H., Cui, L.-F., Yang, Y., Casalongue, H.S., Robinson, J.T., Liang, Y., Cui, Y., and Dai, H. (2010) Mn3O4 – graphene hybrid as a high-capacity anode material for lithium ion batteries. *J. Am. Chem. Soc.*, **132** (40), 13978–13980.
50. Wang, X., Zhou, X., Yao, K., Zhang, J., and Liu, Z. (2010) A SnO2/graphene composite as a high stability electrode for lithium ion batteries. *Carbon*, **49** (1), 133–139.
51. Wu, Y.P., Rahm, E., and Holze, R. (2003) Carbon anode materials for lithium ion batteries. *J. Power. Sources*, **114** (2), 228–236.
52. Novoselov, K.S., Geim, A.K., Morozov, S.V., Jiang, D., Zhang, Y., Dubonos, S.V., Grigorieva, I.V., and Firsov, A.A. (2004) Electric field effect in atomically thin carbon films. *Science*, **306**, 666–669.
53. Partoens, B. and Peeters, F.M. (2006) From graphene to graphite: electronic structure around the K point. *Phys. Rev. B*, **74**, 075404-1–075404-11.
54. Zabel, H. and Solin, S.A. (eds) (1992) *Graphite Intercalation Compound II*, Springer-Verlag.
55. Liu, C., Alwarappan, S., Chen, Z., Kong, X., and Li, C.-Z. (2010) Membraneless enzymatic biofuel cells based on graphene nanosheets. *Biosens. Bioelectron.*, **25** (7), 1829–1833.
56. Bazito, F.F.C. and Torresi, R.M. (2006) Cathodes for lithium ion batteries: the benefits of using nanostructured materials. *J. Braz. Chem. Soc.*, **17** (4), 627–642.
57. Fergus, J.W. (2010) Recent developments in cathode materials for lithium ion batteries. *J. Power Sources*, **195** (4), 939–954.
58. Shembel, E., Apostolova, R., Nagirny, V., Aurbach, D., and Markovsky, B. (1999) Synthesis, investigation and practical application in lithium batteries of some compounds based on vanadium oxides. *J. Power Sources*, **80** (1-2), 90–97.
59. Ding, N., Feng, X., Liu, S., Xiu, J., Fang, X., Lieberwirth, I., and Chen, C. (2009) High capacity and excellent cyclability of vanadium (IV) oxide in lithium

battery applications. *Electrochem. Commun.*, **11** (3), 538–541.

60. Huang, Y.-H., Park, K.-S., and Goodenough, J.B. (2006) Improving lithium batteries by tethering carbon-coated LiFePO4 to polypyrrole. *J. Electrochem. Soc.*, **153** (12), A2282–A2286.
61. Liu, H., Gao, P., Fang, J., and Yang, G. (2011) Li3V2(PO4)3/graphene nanocomposites as cathode material for lithium ion batteries. *Chem. Commun. (Camb.)*, **47** (32), 9110–9112.
62. Su, C., Bu, X., Xu, L., Liu, J., and Zhang, C. (2012) A novel LiFePO4/graphene/carbon composite as a performance-improved cathode material for lithium-ion batteries. *Electrochim. Acta*, **64**, 190–195.
63. Yang, J., Wang, J., Wang, D., Li, X., Geng, D., Liang, G., Gauthier, M., Li, R., and Sun, X. (2012) 3D porous LiFePO4/graphene hybrid cathodes with enhanced performance for Li-ion batteries. *J. Power Sources*, **208** (15), 340–344.
64. Kim, J.-G., Kim, H.-K., Jegal, J.-P., Kim, K.-H., Kim, J.-Y., Park, S.-H., and Kim, K.-B. (2012) Nanocomposites of reduced graphene oxide for energy storage applications. *Proc. Int. Conf. Nanomaterials: Appl. Prop.*, **1** (4), 04NEA07-1–04NEA07-3.
65. Bak, S.-M., Nam, K.-W., Lee, C.-W., Kim, K.-H., Jung, H.-C., Yang, X.-Q., and Kim, K.-B. (2011) Spinel LiMn2O4/reduced graphene oxide hybrid for high rate lithium ion batteries. *J. Mater. Chem.*, **21** (43), 17309–17315.
66. Qu, L., Baek, Y.J.-B., and Dai, L. (2010) Nitrogen-doped graphene as efficient metal-free electrocatalyst for oxygen reduction in fuel cells. *ACS Nano*, **4** (3), 1321–1326.
67. Brownson, D.A.C. and Banks, C.E. (2010) Graphene electrochemistry: an overview of potential applications. *Analyst*, **135**, 2768–2778.
68. Jafri, R.I., Rajalakshmi, N., and Ramaprabhu, S. (2010) Nitrogen doped graphene nanoplatelets as catalyst support for oxygen reduction reaction in proton exchange membrane fuel cell. *J. Mater. Chem.*, **20** (34), 7114–7117.
69. Zhang, S., Shao, Y., Li, X., Nie, Z., Wang, Y., Liu, J., Yin, G., and Lin, Y. (2010) Low-cost and durable catalyst support for fuel cells: graphite submicronparticles. *J. Power Sources*, **195** (2), 457–460.
70. Xin, Y., Liu, J.-G., Zhou, Y., Liu, W., Gao, J., Xie, Y., Yin, Y., and Zou, Z. (2010) Preparation and characterization of Pt supported on graphene with enhanced electrocatalytic activity in fuel cell. *J Power Sources*, **196** (3), 1012–1018.
71. Abdin, Z., Alim, M.A., Saidur, R., Islam, M.R., Rashmi, W., and Mekhilef, S. (2013) Solar energy harvesting with the application of nanotechnology. *Renew. Sustain. Energy Rev.*, **26**, 837–852.
72. Yella, A., Lee, H.-W., Tsao, H.N., Yi, C., Chandiran, A.K., Nazeeruddin, M.K., Diau, E.W.G., Yeh, C.Y., Zakeeruddin, S.M., and Grätzel, M. (2011) Porphyrin-sensitized solar cells with cobalt (II/III)–based redox electrolyte exceed 12 percent efficiency. *Science*, **334**, 629–634.
73. Yang, N., Zhai, J., Wang, D., Chen, Y., and Jiang, L. (2010) Two-dimensional graphene bridges enhanced photoinduced charge transport in dye-sensitized solar cells. *ACS Nano*, **4**, 887–894.
74. He, Z., Phan, H., Liu, J., Nguyen, T.-Q., and Tan, T.T.Y. (2013) Understanding TiO2 size-dependent electron transport properties of a graphene-TiO2 photoanode in dye-sensitized solar cells using conducting atomic force microscopy. *Adv. Mater.*, **25**, 6900–6904.
75. Kusumawati, Y., Martoprawiro, M.A., and Pauporté, T. (2014) Effects of graphene in graphene/TiO2 composite films applied to solar cell photoelectrode. *J. Phys. Chem. C*, **118** (19), 9974–9981.
76. Du, A., Ng, Y.H., Bell, N.J., Zhu, Z., Amal, R., and Smith, S.C. (2011) Hybrid graphene/titania nanocomposite: interface charge transfer, hole doping, and sensitization for visible light response. *J. Phys. Chem. Lett.*, **2**, 894–899.
77. Narayan, M.R. (2012) Review: dye sensitized solar cells based on natural

photosensitizers. *Renew. Sustain. Energy Rev.*, **16**, 208–215.
78. Sandquist, C. and McHale, J.L. (2011) Improved efficiency of betanin-based dye-sensitized solar cells. *J. Photochem. Photobiol., A*, **221**, 90–97.
79. Iwan, A. and Chuchmal, A. (2012) Perspectives of applied graphene: polymer solar cells. *Prog. Polym. Sci.*, **37** (12), 1805–1828.
80. Liu, Q., Liu, Z., Zhang, X., Zhang, N., Yang, L., and Yin, S. (2008) Organic photovoltaic cells based on an acceptor of soluble graphene. *Appl. Phys. Lett.*, **92**, 223303–223306.
81. Yong, V. and Tour, J.M. (2010) Theoretical efficiency of nanostructured graphene-based photovoltaics. *Small*, **6** (2), 313–318.
82. Kim, S.-H., Lee, C.-H., Yun, J.-M., Noh, Y.-J., Kim, S.-S., Lee, S., Jo, S.M., Joh, H.-I., and Na, S.-I. (2014) Fluorine-functionalized and simultaneously reduced graphene oxide as a novel hole transporting layer for highly efficient and stable organic photovoltaic cells. *Nanoscale*, **6**, 7183–7187.
83. Boopathi, K.M., Raman, S., Mohanraman, R., Chou, F.-C., Chen, Y.-Y., Lee, C.-H., Chang, F.-C., and Chu, C.-W. (2014) Solution-processable bismuth iodide nanosheets as hole transport layers for organic solar cells. *Sol. Energy Mater. Sol. Cells*, **121**, 35–41.
84. Guo, Q., Zheng, Z., Gao, H., Ma, J., and Qin, X. (2013) SnO2/graphene composite as highly reversible anode materials for lithium ion batteries. *J. Power Sources*, **240**, 149–154.
85. Tang, X., Yao, X., Chen, Y., Song, B., Zhou, D., and Kong, J. (2014) CuInZnS-decorated graphene as a high-rate durable anode for lithium-ion batteries. *J. Power Sources*, **257**, 90–95.
86. Gong, J., Zhou, T., Song, D., and Zhang, L. (2010) Monodispersed Au nanoparticles decorated graphene as an enhanced sensing platform for ultrasensitive stripping voltammetric detection of mercury (II). *Sens. Actuators B*, **150** (2), 491–497.
87. Ge, S., Yan, M., Lu, J., Zhang, M., Yu, F., and Yu, J. (2012) Electrochemical biosensor based on graphene oxide–Au nanoclusters composites for l-cysteine analysis. *Biosens. Bioelectron.*, **31** (1), 49–54.
88. Cui, S., Pu, H., Lu, G., Wen, Z., Mattson, E.C., and Hirschmugl, C. (2012) Fast and selective room-temperature ammonia sensors using silver nanocrystal-functionalized carbon nanotubes. *ACS Appl. Mater. Interfaces*, **4** (9), 4898–4904.
89. Huang, K.-J., Wang, L., Wang, H.-B., Gan, T., Wu, Y.-Y., and Li, J. (2013) Electrochemical biosensor based on silver nanoparticles–polydopamine–graphene nanocomposite for sensitive determination of adenine and guanine. *Talanta*, **114**, 43–48.
90. Zhang, Q.-L., Xu, T.-Q., Wei, J., Chen, J.-R., Wang, A.-J., and Feng, J.-J. (2013) Facile synthesis of uniform Pt nanoparticles on polydopamine-reduced graphene oxide and their electrochemical sensing. *Electrochim. Acta*, **112**, 127–132.
91. Kong, L., Lu, X., Bian, X., Zhang, W., and Wang, C. (2010) Accurately tuning the dispersity and size of palladium particles on carbon spheres and using carbon spheres/palladium composite as support for polyaniline in H2O2 electrochemical sensing. *Langmuir*, **26** (8), 5985–5990.
92. Lin, Q., Li, Y., and Yang, M. (2012) Tin oxide/graphene composite fabricated via a hydrothermal method for gas sensors working at room temperature. *Sens. Actuators B*, **173**, 139–147.
93. Janczak, D. and Wróblewski, G. (2012) Screen printed resistive pressure sensors fabricated from polymer composites with graphene nanoplatelets. XIV International PhD Workshop OWD2012, pp. 171–175.
94. Yin, Z., Sun, S., Salim, T., Wu, S., Huang, X., and He, Q. (2010) Organic photovoltaic devices using highly flexible reduced graphene oxide films as transparent electrodes. *ACS Nano*, **4** (9), 5263–5268.
95. Park, H., Chang, S., Smith, M., Gradecak, S., and Kong, J. (2013) Interface engineering of graphene

for universal applications as both anode and cathode in organic photovoltaics. *Sci. Rep.*, **3**, 1–8.

96. Bi, H., Huang, F., Liang, J., Xie, X., and Jiang, M. (2011) Transparent conductive graphene films synthesized by ambient pressure chemical vapor deposition used as the front electrode of CdTe solar cells. *Adv. Mater.*, **23**, 3202–3206.

97. Kholmanov, I.N., Stoller, M.D., Edgeworth, J., Lee, W.H., Li, H., and Lee, J. (2012) Nanostructured hybrid transparent conductive films with antibacterial properties. *ACS Nano*, **6** (6), 5157–5163.

98. Zhu, Y., Sun, Z., Yan, Z., Jin, Z., and Tour, J.M. (2011) Rational design of hybrid graphene films for high-performance transparent electrodes. *ACS Nano*, **5** (8), 6472–6479.

99. Min, S. and Lu, G. (2012) Dye-cosensitized graphene/Pt photocatalyst for high efficient visible light hydrogen evolution. *Int. J. Hydrogen Energy*, **37** (14), 10564–10574.

100. Min, S. and Lu, G. (2013) Promoted photoinduced charge separation and directional electron transfer over dispersible xanthene dyes sensitized graphene sheets for efficient solar H2 evolution. *Int. J. Hydrogen Energy*, **38** (5), 2106–2116.

101. Zhu, M., Chen, P., and Liu, M. (2011) Graphene oxide enwrapped Ag/AgX (X = Br, Cl) nanocomposite as a highly efficient visible-light plasmonic photocatalyst. *ACS Nano*, **5** (6), 4529–4536.

102. Gasteiger, H.A. and Markovic, N.M. (2009) Just a dream or future reality? *Science*, **324**, 48–49.

103. Lefevre, M., Proietti, E., Jaouen, F., and Dodelet, J.P. (2009) Iron-based catalysts with improved oxygen reduction activity in polymer electrolyte fuel cells. *Science*, **324**, 71–74.

104. Wu, G., More, K.L., Johnston, C.M., and Zelenay, P. (2011) High-performance electrocatalysts for oxygen reduction derived from polyaniline, iron, and cobalt. *Science*, **332**, 443–447.

105. Levy, R.B. and Boudart, M. (1973) Platinum-like behavior of tungsten carbide in surface catalysis. *Science*, **181**, 547–5479.

106. Jaouen, F., Proietti, E., Lefèvre, M., Chenitz, R., Dodelet, J.-.P., Wu, G., Chung, H.T., Johnston, C.M., and Zelenay, P. (2011) Recent advances in non-precious metal catalysis for oxygen-reduction reaction in polymer electrolyte fuel cells. *Energy Environ. Sci.*, **4** (1), 114–130.

107. Chen, Z.W., Higgins, D., Yu, A.P., Zhang, L., and Zhang, J.J. (2011) A review on non-precious metal electrocatalysts for PEM fuel cells. *Energy Environ. Sci.*, **4** (9), 3167–3192.

108. Jasinski, R. (1964) A new fuel cell cathode catalyst. *Nature*, **201**, 1212–1213.

109. Bashyam, R. and Zelenay, P. (2006) A class of non-precious metal composite catalysts for fuel cells. *Nature*, **443**, 63–66.

110. Gong, K., Yu, P., Su, L., Xiong, S., and Mao, L. (2007) Polymer-assisted synthesis of manganese dioxide/carbon nanotube nanocomposite with excellent electrocatalytic activity toward reduction of oxygen. *J. Phys. Chem. C*, **111** (5), 1882–1887.

111. Collman, J.P., Devaj, N.K., Decreau, R.A., Yang, Y., Yan, Y.L., Ebina, W., Eberspacher, T.A., and Chidsey, C.E.D. (2007) A cytochrome c oxidase model catalyzes oxygen to water reduction under rate-limiting electron flux. *Science*, **315**, 1565–1568.

112. Jensen, B.W., Jensen, O.W., Forsyth, M., and MacFarlane, D.R. (2008) High rates of oxygen reduction over a vapor phase-polymerized PEDOT electrode. *Science*, **321**, 671–674.

113. Gong, K.P., Du, F., Xia, Z.H., Durstock, M., and Dai, L.M. (2009) Nitrogen-doped carbon nanotube arrays with high electrocatalytic activity for oxygen reduction. *Science*, **323**, 760–764.

114. Xiong, W., Du, F., Liu, Y., Perez, A., Supp, M., Ramakrishnan, T.S., Dai, L.M., and Jiang, L. (2010) 3-D carbon nanotube structures used as high performance catalyst for oxygen reduction reaction. *J. Am. Chem. Soc.*, **132** (45), 15839–15841.

115. Nagaiah, T.C., Kundu, S., Bron, M., Muhler, M., and Schuhmann, W. (2010) Nitrogen-doped carbon nanotube as a highly efficiency cathode catalyst for the

oxygen reduction reaction in alkaline medium. *Electrochem. Commun.*, **12**, 338–341.

116. Tang, Y.F., Allen, B.L., Kauffman, D.R., and Star, A. (2009) Electrocatalytic activity of nitrogen-doped carbon nanotube cups. *J. Am. Chem. Soc.*, **131** (37), 13200–13201.

117. Liu, R.L., Wu, D.Q., Feng, X.L., and Mullen, K. (2010) Nitrogen-doped ordered mesoporous graphitic arrays with high electrocatalytic activity for oxygen reduction. *Angew. Chem. Int. Ed.*, **49** (14), 2565–2569.

118. Yang, W., Fellinger, T.P., and Antonietti, M.J. (2011) Efficient metal-free oxygen reduction in alkaline medium on high-surface-area mesoporous nitrogen-doped carbons made from ionic liquids and nucleobases. *J. Am. Chem. Soc.*, **133** (2), 206–209.

119. Yu, D.S. and Dai, L.M. (2010) Self-assembled graphene/carbon nano-tube hybrid films for supercapacitors. *J. Phys. Chem. Lett.*, **1** (2), 467–470.

120. Sheng, Z.H., Tao, L., Chen, J.J., Bao, W.J., Wang, F.B., and Xia, X.H. (2011) Catalyst-free synthesis of nitrogen-doped graphene via thermal annealing graphite oxide with melamine and its excellent electrocatalysis. *ACS Nano*, **5** (6), 4350–4358.

121. Liu, H.T., Liu, Y.Q., and Zhu, D.B. (2011) Chemical doping of graphene. *J. Mater. Chem.*, **21** (10), 3335–3345.

122. Yang, Z., Nie, H., Chen, X., Chen, X., and Huang, S. (2013) Recent progress in doped carbon nanomaterials as effective cathode catalysts for fuel cell oxygen reduction reaction. *J. Power Sources*, **236**, 238–249.

123. Lai, L.F., Potts, J.R., Zhan, D., Wang, L., Poh, C.K., Tang, C.H., Gong, H., Shen, Z.X., Lin, J.Y., and Ruoff, R.S. (2012) Exploration of the active center structure of nitrogen-doped graphene-based catalysts for oxygen reduction reaction. *Science*, **5**, 7936–7942.

124. Matter, P.H., Zhang, L., and Ozkan, U.S. (2006) The role of nanostructure in nitrogen-containing carbon catalysts for the oxygen reduction reaction. *J. Catal.*, **239** (1), 83–96.

125. Sun, Y.Q., Li, C., and Shi, G.Q. (2012) Nanoporous nitrogen doped carbon modified graphene as electrocatalyst for oxygen reduction reaction. *J. Mater. Chem.*, **22** (25), 12810–12816.

126. Sheng, Z.H., Gao, H.L., Bao, W.J., Wang, F.B., and Xia, X.H. (2012) Synthesis of boron doped graphene for oxygen reduction reaction in fuel cells. *J. Mater. Chem.*, **22**, 390–395.

127. Liu, Z.W., Peng, F., Wang, H.J., Yu, H., Zheng, W.X., and Yang, J. (2011) Phosphorus-doped graphite layers with high electrocatalytic activity for the O2 reduction in an alkaline medium. *Angew. Chem. Int. Ed.*, **50** (14), 3257–3261.

128. Yang, Z., Yao, Z., Fang, G.Y., Li, G.F., Nie, H.G., Zhou, X.M., Chen, X., and Huang, S.M. (2012) Sulfur-doped graphene as an efficient metal-free cathode catalyst for oxygen reduction. *ACS Nano*, **6** (1), 205–211.

129. Jin, Z.P., Nie, H.G., Yang, Z., Liu, Z., Zhou, X.M., Xu, X.J., and Huang, S.M. (2012) Metal-free selenium doped carbon nanotube/graphene networks as a synergistically improved cathode catalyst for oxygen reduction reaction. *Nanoscale*, **4** (20), 6455–6460.

Index

a

activated carbons (ACs) 174
activated graphene-based electrodes
– EDLC materials 178
– electrochemical activation 177
– graphene with KOH 178
– partially reduced graphite oxide 177
AFM, *see* atomic force microscopy (AFM)
$Ag/TiO_2/G$ nanocomposite 262
aminopropyltriethoxysilane 255
anode current collector
– energy storage devices 412
– fuel cells 412, 413
– Li-ion batteries 412
anode materials, LIBs
– carbon coated graphene synthesis 93
– cathodic exfoliation of graphite 94
– Co_3O_4/GNS nano composite materials 96, 97, 99
– diffusion mechanism 87
– electrochemical exfoliation 93
– GNS/Fe_3O_4 composite materials 96, 97
– graphene nanoribbon 87
– graphene nanosheets 85, 89, 92, 95, 96
– graphene paper 91
– graphite oxides 89
– holey graphene 93, 94
– LiC_2 formation 86
– porous graphene 92
– pure graphene 98
– randomly stacked HGs 93, 94
– reduced graphene oxide 99, 100
– Si/GNS composite 97, 100
– Si/graphene composite 99, 102
– SnO_2/graphene composite 98, 101
apparent quantum efficiency (AQE) 228, 230
asymmetric capacitors 193
– activated graphene 194
– conductive polymers 194
– electron transport 193
– graphene-based electrodes 196
– graphene–MnO_2–textiles 195
– high-voltage asymmetric supercapacitor 193
– hybrid supercapacitors 195
– nanosized or porous materials 193
atomic force microscopy (AFM) 2, 14
atomic layer deposition (ALD) 98, 136
Au NP/RGO hybrids 330

b

biofuel cells 314
biological chemical conversion method 340
biomass energy
– biological chemical conversion method 340
– direct combustion 340
– plants and animals 340
– pollution-free energy source 340
– thermal chemical conversion 340
Bragg's law 22
Brodie method 250

c

carbon aerogels 174
carbon allotropes 350
carbon black (CB) composites 153, 179
carbon coated graphene (GSNC) 92
carbon dioxide, photocatalytic reduction 285
carbon material composites, graphene
– carbon black (CB) 153
– carbon nanotubes (CNT) 153
– mesoporous carbon spheres (MCS) 154
carbon nanotubes (CNTs) 153, 174
– applications 372
– electron transfer resistance 371

Graphene-based Energy Devices, First Edition. Edited by A. Rashid bin Mohd Yusoff.
© 2015 Wiley-VCH Verlag GmbH & Co. KGaA. Published 2015 by Wiley-VCH Verlag GmbH & Co. KGaA.

carbon nanotubes (CNTs) (*contd.*)
– redox mediators 371
– single-walled CNTs (SWCNTs) 372
carbon nanowires (CNWs) 174
carbon/oxygen ratio (C/O ratio) 87
cathode current collector
– fabrication of energy devices 413
– fuel cells 414
– graphene synthesis, graphite 413
– Li-ion battery 414
– low electric conductivity 413
– transition metals 413
cathode electrodes, MFCs
– electricity generation 362
– graphene and modified graphene 362
– microbially-reduced graphene 363
– non-catalyst cathode 365
– ORR 361
– platinum-group materials 361
– polymer coating 363
– synergistic interactions, NG and mpg-C_3N_4 366
– transition metal coating 363, 364
cathode materials, LIBs
– CA-G/LFP, annealing 103, 108
– charge/discharge tests 101, 104
– GO and LFP/C 102, 108
– graphene-coated Li 100, 103
– graphene-sandwiched LNMO structure 102, 107
– $LiFePO_4$, G/LFP and CA-G/LFP, cycling performance 103, 109
– $LiMn_{1/3}Ni_{1/3}Co_{1/3}O_2$ (LMNCO), preparation 101, 105, 106
– lithium ion diffusion pathways 103, 109
– pure GO and porous graphene-coated $LiFePO_4$ 103, 109
– spray drying method 100
– $VO_{2.07}$RGO composite film 101, 104, 405
CdS/TaON core-shell heterojunction 231, 232
characterization of graphene
– AFM 14
– PL measurement 23
– Raman spectroscopy 23
– SEM 16
– TEM/SEAD/EELS 16
– XPS 20
– XRD 21
charge transport layer
– ETL, *see* electron transport layer (ETL)
– HTL, *see* hole transport layer (HTL)
chemical approaches, graphene synthesis 379
chemical vapor deposition (CVD) 1, 3, 4, 148, 175, 281, 358
chemically modified graphene (CMG)
– CV plots 126
– SEM image 126
– TEM image 126
– ultracapacitor test cell assembly 126
composite material, GO
– Ag/graphene 9, 10
– Au samples 9
– Co, Ni and Cu samples 9, 11
– europium in lanthanoids and palladium 12
– graphene–polymer nanocomposites 11–13
– hybrid materials 8
– structural property and chemical bonding 8
conducting polymer composites, graphene
– advantages 158
– aniline polymerization 161
– electrochemical polymerization process 163
– graphene nanocomposites, supercapacitors 159
– *in situ* polymerization 160
– PANI nanowires 162, 163
– PANI-graphene composites 159
– PANI/GO nanocomposites 160
– PANI/rGO nanocomposite 161, 164
conduction band (CB) 277
conductive electrodes
– cathodes, transparent 384
– transparent anodes, *see* transparent conductive anodes
continuous MFC 345
shell nanostructures 322
cubic nanostructures 326
CVD graphene 125
cyclic voltammetric analysis 373

d

2D flexible anode materials
– chemical deposition/hydrothermal reaction 70
– Co_3O_4 nanosheets/GS film 72
– Coulombic efficiency 69
– CVD 69
– Fe_3O_4 nanospindles/GS film 71, 72
– holey graphene paper 67, 68
– Si NWs/GS/RGO electrode 71, 72
– SnO_2 nanoparticles/GS paper 71
2D flexible cathode materials
– graphene paper 73

– $LiFePO_4$/GF cathode and $Li_4Ti_5O_12$/GF anode 73, 74
– V_2O_5/graphene paper 73
3D macroscopic graphene
– α-FeOOH/GS and Fe_3O_4/GS aerogels 75, 76
– aerogel 74
– Fe_3O_4/GS aerogel 75
– GO 75
– hydrothermal treatment 75
– solvothermal treatment 77
direct alcohol fuel cells (DAFCs) 314
direct formic acid fuel cells (DFAFCs)
– CO_2 directl and indirect dehydration route 313
– definition 313
– electrocatalytic activity 313
– electrochemical studies 313
– FAOR 313
– OCV 313
– oxidized carbonaceous species 313
direct methanol fuel cells (DMFCs)
– advantages 310, 312
– electrode/electrolyte interface 311
– electron transfer numbers 312
– graphene surface 311
– I_f/I_b ratio 310
– LSV curve 312
– OCV 310
– ORR process 311
– polymer membranes 313
– Pt-based catalysts 311
– RDE technique 312
double-layer capacitance, graphene
– carbon nanostructures composite electrodes 179
– electrodes 177, 180
– reduction of graphene oxide 176
dual-chamber MFC 342, 343
dye-sensitized solar cells (DSSCs)
– electrical conductivity 409
– electron mobility network 415
– electron transport enhancement 415
– graphene/titania photoanode 409
– hybrid materials development 415
– natural dye anthocyanin 416
– redox electrolyte, zinc porphyrin dye 416
– solvothermal reaction 415
– visible light irradiation 416

e

electrical double layer capacitors (EDLCs) 106, 145, 174, 180
electrochemical capacitors (ECs)
– EDLCs 174
– fundamentals 172
– hybrid ECs 174
– pseudocapacitive materials 174
– pseudocapacitors 174
– Ragone plot 172
electrochemical method 358
electrochemical sensing 418
electrochemically reduced graphene oxide (ERGO)/PANI composite 132, 375
electrode materials, graphene capacitors
– double-layer capacitance 176
– pseudocapacitive composite materials 183
electron transport layer (ETL) 395, 398, 399
energy resources
– biomass 339
– electricity 340
– environmental pollution 339
– fire 339
– human society 339
environmental remediation
– organic dyes, photodegradation 287
– water disinfection 287
epitaxial growth 148
equivalent series resistance (ESR) 174
exfoliation, graphene
– description 1
– mechanical cleavage 3, 4

f

fabrication graphene oxide (GO) 420
Faradaic mechanism 174
FePt/rGO nanostructures 331
field-emission scanning electron microscopy (FESEM) 256
fluorine tin oxide (FTO) electrode 117
fossil fuels, industrialization and economic growth 339
FSPd/GN synthesis 330
fuel cells (FC)
– anodic oxidation/cathodic reduction reactions 333
– carbon-based materials 114
– carbon nanotube-based supports 315
– classification 308
– DAFCs and biofuel cells 314
– DFAFCs 313
– DMFCs 313
– electrocatalysts 315
– electrochemical redox reactions 333
– high-temperature 308
– hydrogen storage materials 115
– metal alloy nano-composites 315

fuel cells (FC) (*contd.*)
– metal nanoparticles 315
– nanoclusters 316, 317
– nitrogen-doped graphene 114, 116
– Pd NPs 318, 319
– PEMFCs 309, 310
– preparation methods 315
– PtRu NPs 317, 318
– treatment modes 308
– types of 308
full width at half maximum (FWHM) 21, 24
fullerenes 174
functionalization of graphene oxide (FrGO) 417

g

G-metal oxide nanocomposites 130
gas-phase synthesis 1
GNR, *see* graphene nanoribbon (GNR)
GNS, *see* graphene nanosheets (GNS)
GO-TiO_2 nanorod composites 258
graphene
– carbon material composites 153
– characterization 2, 12
– CNTs 295
– disadvantages 295
– 2D of sp^2-hybridized carbon atoms 171
– EDLCs devices 123
– efficiency 241
– electroactive species 123
– energy 215
– environmental and energy applications 267
– faradic process 123
– fields 216
– GO and rGO, *see* graphene oxide (GO)
– graphitic carbon forms 171, 172, 296
– heterogeneous electronic structure 250
– high-performance energy 304
– human beings 215
– hydrogen production 241
– hydrogen storage technologies 295
– issues 137
– light absorber and electrocatalyst 215
– mesopore and macropore structures 124
– metal oxides composites 154
– metal oxides-conducting polymer composites 158, 164
– mixed colloid photocatalytic systems, *see* mixed colloid photocatalytic systems
– molecular hydrogen storage, *see* hydrogen storage
– optical property modification 25
– optoelectric application 39
– photocatalysis, *see* photocatalysis
– photocatalytic applications, *see* photocatalytic applications
– photoelectrochemical cells, *see* photoelectrochemical cells
– photoelectrons 249
– photovoltaic/electrolyzer devices, *see* photovoltaic/electrolyzer devices
– polymer composites, *see* polymer composites
– potential dopants 304
– properties 171
– semiconductor photocatalysts, *see* semiconductor photocatalysts
– sluggish kinetics, hydrogen/oxygen 216
– solar-driven water-splitting devices, *see* solar-driven water-splitting devices
– sp^2 carbon atoms 249, 277
– specific power *vs.* energy 124
– specific surface area 123
– supercapacitors, *see* supercapacitors
– superior properties 296
– synthesis 1, 267
– TiO_2 composite photocatalysts 278
– various fields 296
– water upon semiconductors 215
graphene nanoribbon (GNR) 87
graphene nanosheets (GNS) 85, 96
graphene oxide (GO)
– absorption spectra 27
– diffraction rings 17
– EELS spectrum 17, 19
– oxygen plasma treatment 32
– PL spectra 35
– properties 253
– Raman spectra 26
– reduction 1
– SAED pattern 17, 18
– synthesis 252
– TEM measurements 16, 18
– thermal annealing 22, 25
graphene oxide nanoribbons (GONRs) 361
graphene quantum dot (GQD)
– cathode buffer additive 409
– electron transfer capability 410
– hole blocking 410
– photonic and electric properties 409
graphene sheets (GS) 94
graphene synthesis methods
– chemical exfoliation method 149
– chemical vapor deposition (CVD) 150, 151
– electrochemical capacitor performance 147, 148
– graphene oxide (GO) chemical structure, 149

– liquid-phase exfoliation 149
– mechanical exfoliation 148
– reduced graphene oxides (rGO) 149
graphene, sensitizer
– doping 407
– electronic devices 407
– energy devices applications 410
– intrinsic optical absorption 407
– lithium-ion batteries 407
– supercapacitors 408
graphene-activated carbon (GAC) composite. 178
graphene-based anode materials, LIBs
– composites 56
– graphite, 3D network 54
– heteroatomic doping 55
– Irreversible/reversible Li storage 55
– Li_2C_6 intercalation mechanism 55
– lithium adsorption 54
– metal oxides composites 62
– oxygen-containing functional groups or heteroatoms sites 54
– Si/Sn composites 58
– transport mechanism in disordered carbon 54
– van der Waals forces 56
graphene-based cathode materials, LIBs
– $LiFePO_4$ 52
– $LiMn_{0.75}Fe_{0.25}PO_4$ nanorods 52
– $LiMPO_4$ 51
– V_2O_5 52
graphene-based electrodes, supercapacitors
– EDLC materials 151
– electrochemical capacitors 152
– flexible supercapacitors 152
– microwave exfoliated GO (MEGO) 152
– N-doped graphene sheets (NGS) 152
– rGO electrodes 151
graphene-based energy devices
– fuel cells 114
– Li-ion batteries 85
– Li-sulfur batteries 111
– solar cells 116
– supercapacitors 105
graphene-based materials
– anode electrodes, MFCs 357
– electrochemical applications 356
– microbial fuel cell 356
– optimal material 367
– small-scale reactors 367
graphene-based MFC
– carbon nanotubes 348
– cathode 350
– electricity generation 349
– electrode resistance 348
– proton membrane 350
graphene-based supercapacitors
– energy-related applications 408
– platinum catalysts 408
– rGO electrodes 153
– supercapacitor device 408
graphene-single-walled carbon nanotubes 375
graphene-supported metal nanostructures
– alloy metal nanoparticles 321
– application fields 308
– BPtNW/RGO hybrids at magnifications 328
– chemical and physical advantages 307
– shell nanostructures 322, 323
– cubic nanostructures 325–327
– 2D/3D nanostructures 333
– 3D Fe_3O_4/N-GAs catalyst 334
– electrical energy 307
– and FC, *see* fuel cells (FC)
– Fermi level difference 308
– flower-like nanostructures 330, 331
– graphene-based nanocatalysts 308
– high resolution TEM micrographs 323, 324
– hollow nanostructures 324
– inorganic metals/metal oxides 307
– nanoclusters 317
– nanodendrites 332
– nanowires and nanorods 329
– potential energy source 307
– TP-BNGN 332
graphene/g-C_3N_4 composites 264
graphene–CdS/TaON system 231

h

Helmholtz double layer 174
heterotrophic MFC 344
hexagonal boron nitride (h-BN) 3
hexylamine-modified graphene 8
highest occupied molecular orbital (HOMO) 23, 30
highly ordered pyrolytic graphite (HOPG) 3
hole transport layer (HTL)
– AFM topography, GO 396
– anode interfacial layer 393
– charge transfer interactions 393
– device configuration, inverted PSCs 393
– hole extraction property, GO 393
– photovoltaic device structure 392
– polymer solar cells (PSCs) 390
– PSS-based PSCs 395

hole transport layer (HTL) (*contd.*)
– solution-processed conventional rGO 393
– surface C –C dipoles 391
holey graphene (HG) 93, 94
hollow nanostructures 324
Holm's theory 410
hot filament chemical vapor deposition (HFCVD) 409
humidity degradation testing 397
Hummer's method 7, 175, 366, 415
hybrid electrochemical capacitors 174
hydrogen evolution reaction (HER) 236, 238
Hydrogen spillover 303
hydrogen storage
– C–H bonds 297
– doped-graphene 301
– efficiency 298
– graphene-based metal/metal oxide 301
– hydrogen adsorption 299
– lattice-layered graphitic structure 298
– MGFs 298
– physisorption substrates 297
– sp^3 C-H bonds 297
– spillover 301
– Stone–Wales defects 297
– three-dimensional pillared graphene array 298
hydrothermal/solvothermal methods 256, 279

i

In-situ Raman technique 86
incident photon-to-current efficiency (IPCE) 219, 224
indirect MFC 344
interfacial layer, tandem solar cells 398, 400, 401
intermittent MFC 344
irreversible redox process 411

l

Lerf–Klinowski model 252
Li-sulfur batteries
– G-S hybrid, formation 113, 115
– G-S-CNF multilayered coaxial nanocomposites 113, 115
– RGO/CMK-3/S composite 111, 114
light-harvesting materials
– chemically grafted graphene-P3HT 387
– conjugated systems polymers 387
– current-voltage characteristics, photovoltaic devices 388
– GQDs 388, 390
– graphene thin film 387
– oxidation and organic functionalization 387
– soluble conjugated polymers and fullerene 387
lithium ion batteries (LIBs)
– anode materials 54, 85, 418
– application 417
– cathode materials 51, 100
– charging/discharging process 51
– conductive graphene 418
– electrodes 51
– principle 50
– rocking chair battery 51
– schematic representation 50
– theoretical capacity 51
– three-dimensional macroscopy 74
– two-dimensional macroscopy 67
lithium storage mechanisms of anode materials
– alloying-dealloying mechanism 58
– conversion mechanism 57, 58
– intercalation-deintercalation mechanism 57, 58
lithium-ion capacitors (LIC)
– activated microwave expanded graphite oxide (a-MEGO) 198
– asymmetric capacitors 205
– conventional Li-ion based hybrid systems 198
– Faradaic process 195
– LIBs 195
– nanohybrid capacitor (NHC) 198
– V_2O_5 nanowires (VNWs) 199
low energy electron diffraction (LEED) patterns 2, 4
lowest occupied molecular orbital (LUMO) 23, 30

m

membraneless EBFCs
– current–voltage behaviors 374
– graphene based 372, 373
– redox mediators 373
– silica sol–gel matrix 372
mesoporous carbon spheres (MCS) composites 154
mesoporous graphene foams (MGF) 238
metal oxides composites
– cobalt and nickel oxides 157, 158
– conversion mechanism 62
– graphene/NiO composite 64
– GS/Fe_3O_4 composite 63
– hydrothermal method 62
– manganese oxides (MnO_2 and Mn_3O_4) 156

– *in-situ* chemical synthesis 63
– nitrogen-doped graphene 64
– preparation methods 63
– redox reaction 154
– ruthenium oxide (RuO_2) 155
– SnO_2 nanoparticles 62
– sponge/rGO, and sponge/rGO/MnO_2 157
– vanadium oxides nanomaterials 158
metal oxides-conducting polymer composites
– 3D conductive layer wrapping method 164
– graphene/MnO_2 (GM) 164, 165
metallomacrocycle-graphene frameworks (MGFs) 298
MFC anode electrodes
– 3D graphene electrodes 360, 361
– graphene and modified graphene 357
– graphene nanosheets 357
– graphene oxide (GO) 361
micro-supercapacitors
– 2D design 201
– carpet-based microsupercapacitors 202
– fabrication procedures 202
– GO/CNT 201
– graphene quantum dots (GQD) 202
– laser reduction technique 203
– laser scribing method 203
– rGO electrodes 201
microbial fuel cell (MFC)
– advantages 341
– biosensor 347
– classification 342
– development history 345
– dual-chamber 340
– electrochemical device 340
– electrode applications 356
– electron movement 355
– electron transfer process 340
– high cost 348
– internal resistance 355
– ion exchange membrane 355
– low output power density 348, 355
– micro batteries 346
– mobile power supply 346
– nanotechnologies 355
– photosynthesis and stem 346
– power density curves 358
– power supply, remote areas/open sea 347
– sewage treatment 347
– social and environmental benefits 348
– unmodified carbon cloth electrode 360
microelectromechanical systems (MEMS) 199
mixed bacteria MFC 345
mixed colloid photocatalytic systems
– CdS/TaON core-shell heterojunction 231, 232
– CdSe/GO composite 229
– DOS plots 234
– dye-sensitized system 230
– EY-RGO/Pt photocatalyst 230
– graphene–CdS/TaON system 231
– H_2-production rate 227
– 2 M H_2SO_4 235
– NGO-QDs 234
– organic dye-like macromolecular 233
– photocatalytic hydrogen production 227, 233
– r-NGOT 228
– reduced graphene oxide 227
– RGO-ZnxCd1-xS photocatalysts 232
– RGO/CdS nanocomposites 228, 229
– RGO/$ZnIn_2S_4$ nanocomposite 229, 230
– stable H_2 evolution 233
– TEOA 230
– TiO_2/graphene 227
– TiO_2/MoS_2/RGO photocatalyst 232
– titania-graphene nanosheet composite 227
– Z-scheme systems 231, 232
modified graphene 8
molybdenum disulfide (MoS_2) 3
Monte Carlo simulation 2
multiwalled carbon nanotubes (MWCNTs) 361
multiwalled carbon nanotubes/zinc oxide 375

n

nanorods 329
nanowires 329
natural dye anthocyanin 409
nitrogen-doped graphene (NG) 350, 364, 366, 367
nitrogen-doped graphene oxide-quantum dots (NGO-QDs) 234, 235
number of graphene (NGP) layers 21

o

onion like carbons (OLCs) 174
optical microscopy 2
optical property modification, graphene
– absorption 26
– annealed GO 25
– oxygen plasma treatment, PL properties 29
– Pd grafted graphene oxide 35
– substrate effect 30
optical sensor and gas sensor application 418
optoelectric application, graphene
– Dirac equation 39

optoelectric application, graphene (*contd.*)
– dye-sensitized solar cells consist 41
– GTCFs37 42
– indium tin oxide (ITO) 41, 42
– OLED 41
– photodetectors 43
– photoexcited electron kinetics 40
– saturable absorber 43
organic dyes, photodegradation 287
organic light emitting device (OLED) 41, 43
organic photovoltaic cells (OPV)
– bulk heterojunction (BHJ) 416
– nanostructured graphene 417
– oxidation treatment 416
organic solar cell (OSC) 380
oxidized graphene (OG) 26, 28
oxygen evolution reaction (OER)
– dual-doped graphene 237
– N-doped armchair and zigzag graphene nanoribbons 236
oxygen reduction reaction 350

p

P25-graphene composite 259
partially reduced graphite oxide (GOpr) 177
PEDOT-graphene nanocomposite 136
photoanode additive, graphene
– DSSCs, *see* dye-sensitized solar cells (DSSCs)
– additives 415
photocatalysts, graphene synthesis
– electrochemical and electrophoresis deposition 281
– *ex situ* hybridization strategy 279
– *in situ* growth strategy 279
– semiconductors 278
photocatalytic activity, hydrogen evolution 420
photocatalytic applications
– CO_2 266
– DSSCs 266
– H_2O 264
– photodegradation, organic pollutants 262
– TiO_2 257
photocatalytic hydrogen evolution 283
photochemical reaction 282
photoelectrochemical cells (PECs)
– α-Fe_2O_3 andα-Fe_2O_3/graphene photoanodes 224
– α-Fe_2O_3/RGO/$BiV_{1-x}Mo_xO_4$ core-shell nanorod 222
– bare Si, Gr–Si and NGr–Si photocathodes 225
– $BiVO_4$/RGO photoanode 220
– chronoamperometry operation 225
– CNNS/NRGO/MoS_2 nanojunction 223
– CNT and graphene 220
– current–potential plots, BCN 223
– 2D ternary nanojunction 222
– EC exfoliation of graphite 226
– fabrication process, photoanode 224
– FE-SEM image 224
– GNs–CdS QDs 220, 221
– graphene interlayer 224
– graphene with semiconductors 219
– heterojunction array 222
– H_2-production 219
– IPCE 224
– iron oxide photoanode 220
– monolayer graphene 225
– n-Si/graphene electrodes 225
– photocurrent density–potential curves 225
– photoexcited electron–hole transport 226
– planar Si/rGO composite 223
– RGO/ZnO heterojunction 226
– STH efficiencies 216
– transient photocurrent density *vs.* time plotted 223
– water splitting process 219
– WO_3-RGO photoanode 220
– $Zn_{0.5}Cd_{0.5}S$ nanosheets 220
– $Zn_{0.5}Cd_{0.5}S$/reduced grapheme oxide 220
– $Zn_{0.5}Cd_{0.5}S$/RGO photoelectrode 220
photoluminesces (PL) measurement 3, 14, 23
photosynthetic autotrophs MFC 344
photovoltaic/electrolyzer devices
– carbon materials 236
– chemical modification 236
– Co_3O_4/graphene composites 240
– CoO nanocrystals 240
– 3D architectured hydrated catalyst 238
– electrocatalytic HER activity 237
– electrodes 236
– MoS_2/graphene hybrid material 238
– MoS_2/RGO composite 238
– N-doped graphene and $NiCo_2O_4$ 238
– NG-CNT catalyst 237
– OER mechanism, N-doped armchair and zigzag graphene nanoribbons 236
– overpotential/faradic efficiency 236
– solar cell 235
– Tafel plot 240
– unique properties 236
physical coating method 358
Polyaniline (PANI)-graphene nanocomposites 133, 184

polyethylenedioxythiophene (PEDOT) composites 185
polymer composites
– ALD 136
– PANI-graphene nanocomposites 133
– PEDOT-graphene nanocomposite 136
– 2p orbitals, carbon atoms 129
– PPy-graphene nanocomposite 135
– supercapacitors 129
polymer tandem solar cells 401
polymethyl methacrylate (PMMA) spheres 69
polypyrrole (PPy)-graphene nanocomposite 135
polystyrene (PS) colloidal particles 69
polythiophene (PTh) composites 136
polythiophene (PTh)/GO composites 135
porous graphene nanosheets (PGNs) 107
power generation, human wastes 371
PPy composites 184
proton exchange membrane fuel cells (PEMFCs)
– anodic/cathodic reaction 310
– carbon materials 310
– H_2 gas fuel 309
– Pt electrocatalysts 310
– ultralow/zero emissions, environmental pollutants 309
pseudocapacitive materials
– carbon-based materials 175
– conducting polymer, graphene 183
– graphene 175
– graphene/ PANI composites 184
– graphene/ PEDOT composites 185
– graphene/PPy composites 184
– metal oxides 175
– redox reactions 175
pseudocapacitors
– electrode materials 146
– energy storage mechanism 145
– Faradaic manner 174
PtAu/GN nanostructures 331
PtNF/GO nanostructures 329
pure bacteria MFC 345

r

Ragone plots 137, 173
Raman spectroscopy 2
randomly stacked HGs (RSHGs) 93, 94
reduced graphene oxide (RGO), *see also* graphene oxide (GO)
– $BiVO_4$
– concept of spacer 128
– EDLC preparation 177
– electrochemical performance 126
– mechanical and electrical properties 125
– MoS_2 238
– N-doped 125
– PANI nanocomposites 129
– PEDOT composite 134
– synthesization 87

s

scanning electron microscopy (SEM) 2
scanning tunneling microscopy (STM) 2
Schottky junction solar cells
– electron blocking layer 389
– graphene-on-silicon 391
– sheet resistance 389
– surface modification 389
sediment MFC 344
selective area electron diffraction (SAED) pattern 17
semiconductor photocatalysts
– hazardous organic pollutants 254
– hydrothermal and solvothermal methods 257
– mixing method 255
– sol–gel process 256
– TiO_2 254
sensor application 418, 419
Si/Sn composites
– alloying mechanism 58
– CVD technique 62
– morphologies 59
– nanoparticles on graphene sheets 60
– Si nanowire (Si NW)/GS composite 61
– Si/grapnene composites 60, 61
– Sn/graphene composites 61
single wall carbon nanotube (SWCNT) 195, 236
single-chamber MFC 343, 344
solar cells
– active layer 385
– conductive electrodes 380
– dye sensitized applications 117
– graphene/PEDOT-PSS composite electrode 117
– graphene/TiO_2/dye/spiro-OMeTAD/Au device 117
– light harvesting material 380
– near IR range 116
solar-driven water-splitting devices
– bandgap ranging 218
– classification 216
– graphene possesses 217
– H^+/H_2 217
– heteroatom doping 217

solar-driven water-splitting devices (*contd.*)
– hexagonal structured sp^2-hybridized carbon atoms 217
– metal electrocatalysts 217
– mixed colloid photocatalysis systems 216
– n-type semiconductor before and after contacts 218
– PEC devices 216
– PV/electrolyzer tandem devices 217
– RGO with reduction degree 218
solar-to-hydrogen (STH) efficiencies
– PEC devices 216
– PV/electrolyzer device 235
solid electrolyte interphase (SEI) 98
solution based graphene
– chemical exfoliation 7
– intercalation 7
– ultra sonication 6
solution-processable functionalized graphene (SPF-graphene) 417
sp^2 bonding 1
Staudenmeier method 251
storage current collector, graphene
– charge separation process 410
– electrical conductivity 410
– energy devices 410
– lithium ion-exchange cell 411
– surface wettability 411
– thermodynamic stability 411
supercapacitors (SCs)
– carbon electrode materials 110
– CVD graphene 125
– EDLCs 106, 128, 145
– electrochemical tests 107, 112
– electrode materials 180, 181
– energy and power densities 147
– GO samples, tests 107, 113
– graphene-based porous materials 107, 112, 124
– graphene/metal oxide nanocomposites 128
– material 106, 111, 175
– performance metric 146
– PGNs 107
– power density 147
– pseudocapacitor 106, 145
– ultracapacitors 123
SWCNT based anode 374
synthesis, graphene
– composite material, graphene oxide 8
– CVD growth of graphene 4
– epitaxial growth 4
– mechanical cleavage 3
– solution based graphene 5

t

thermal chemical conversion 340
TiO_2/MoS_2 composites
– characterization 66
– graphene/TiO_2 66
– intercalation mechanism 65
– three-dimensional graphene network (MoS_2/3DGN) 65
– TONRAs-GS nanocomposite 66
TiO_2 nanorods-GO composite 259
transition metal oxides
– EDLC 186
– graphene 186
– graphene/manganese oxide composites 186
– pseudocapacitive materials composites 191
– RuO_2 188
– supercapacitors 189, 192
transmission electron microscopy (TEM) 2, 13, 252, 256, 257
transparent conductive anodes
– electronic interfacial change 383
– energy level alignment 381
– indium tin oxide (ITO) 380
– optical transparency 380
– reduced graphene oxide (rGO) 382
– sheet resistance 382
– solar cell, graphene electrodes 383
transparent conductive cathodes
– APCVD graphene 385
– functional semiconductors 384
– glass substrate 384
– photovoltaic devices 384
transparent conductive films (TCFs) 419

v

valence band (VB) 277

w

wastewater treatment process 347
water disinfection 287

x

X-ray diffraction (XRD) 2, 21
X-ray photoelectron (XPS) 20

y

Young's modulus 277

z

$Zn_{0.5}Cd_{0.5}S$ photoelectrodes 220